NUREG/CR--4994

TI89 011629

Core-Concrete Interactions Using Molten Steel with Zirconium on a Basaltic Basemat: The SURC-4 Experiment

Manuscript Completed: March 1989
Date Published: April 1989

Prepared by
F. R. Copus, R. F. Blose*, J. E. Brockmann,
R. D. Gomez, D. A. Lucero

Sandia National Laboratories
Albuquerque, NM 87185

*Ktech Corporation, Albuquerque, NM

Prepared for
Division of Systems Research
Office of Nuclear Regulatory Research
U.S. Nuclear Regulatory Commission
Washington, D.C. 20555
NRC FIN A1218

AVAILABILITY NOTICE

Availability of Reference Materials Cited in NRC Publications

Most documents cited in NRC publications will be available from one of the following sources:

1. The NRC Public Document Room, 2120 L Street, NW, Lower Level, Washington, DC 20555

2. The Superintendent of Documents, U.S. Government Printing Office, P.O. Box 37082, Washington, DC 20013-7082

3. The National Technical Information Service, Springfield, VA 22161

Although the listing that follows represents the majority of documents cited in NRC publications, it is not intended to be exhaustive.

Referenced documents available for inspection and copying for a fee from the NRC Public Document Room include NRC correspondence and internal NRC memoranda; NRC Office of Inspection and Enforcement bulletins, circulars, information notices, inspection and investigation notices; Licensee Event Reports; vendor reports and correspondence; Commission papers; and applicant and licensee documents and correspondence.

The following documents in the NUREG series are available for purchase from the GPO Sales Program: formal NRC staff and contractor reports, NRC-sponsored conference proceedings, and NRC booklets and brochures. Also available are Regulatory Guides, NRC regulations in the *Code of Federal Regulations*, and *Nuclear Regulatory Commission Issuances*.

Documents available from the National Technical Information Service include NUREG series reports and technical reports prepared by other federal agencies and reports prepared by the Atomic Energy Commission, forerunner agency to the Nuclear Regulatory Commission.

Documents available from public and special technical libraries include all open literature items, such as books, journal and periodical articles, and transactions. *Federal Register* notices, federal and state legislation, and congressional reports can usually be obtained from these libraries.

Documents such as theses, dissertations, foreign reports and translations, and non-NRC conference proceedings are available for purchase from the organization sponsoring the publication cited.

Single copies of NRC draft reports are available free, to the extent of supply, upon written request to the Office of Information Resources Management, Distribution Section, U.S. Nuclear Regulatory Commission, Washington, DC 20555.

Copies of industry codes and standards used in a substantive manner in the NRC regulatory process are maintained at the NRC Library, 7920 Norfolk Avenue, Bethesda, Maryland, and are available there for reference use by the public. Codes and standards are usually copyrighted and may be purchased from the originating organization or, if they are American National Standards, from the American National Standards Institute, 1430 Broadway, New York, NY 10018.

DISCLAIMER NOTICE

ABSTRACT

An inductively heated experiment, SURC 4, was executed as part of the ex-vessel core debris interaction program in order to investigate the additional effects of zirconium metal oxidation on core debris/concrete interactions using molten stainless steel as the core debris simulant. The Ex-Vessel Core Debris Interaction Program is designed to measure, model, and assess the variety of source terms produced during core debris/concrete interactions. These source terms include thermal energy released to both the reactor basemat and the containment environment as well as flammable gas, condensible vapor, and toxic or radioactive aerosols produced during the course of a severe reactor accident. These source terms are the governing phenomena in all realistic containment integrity evaluations or risk consequence analyses. The results of the SURC 4 test showed that zirconium reactions have two major impacts on core-concrete interactions. First is a dramatic increase in temperature and gas release. Second is the extensive production of low density oxide foam. Neither of these two phenomena are accounted for using current computer models. The SURC 4 experiment eroded a total of 25 cm of basaltic concrete during 62 minutes of sustained interaction using 200 kg of 304 stainless steel to which 20 kg of zirconium metal was added subsequent to ablating 4-6 cm of concrete. The meltpool temperature during the test ranged from 1500°C before zirconium addition to 1650°C during the zirconium-steel-concrete phase of the test which lasted 42 minutes. Large increases in erosion rate, gas production, and aerosol release were also measured shortly after Zr metal was introduced to the melt. Measured erosion rates increased from 15 cm/hr to 30 cm/hr, gas release increased from 60 slpm to 130 slpm, and aerosol production increased from .5g/sec to 10g/sec. Additional measurements indicated that the effluent gas was composed of 85% H_2, 10% CO, 3% H_2O and 2% CO_2 and that the aerosols released were comprised primarily of tellurium and stainless steel component oxides. In addition, post-test analysis of the SURC 4 crucible revealed that in the process of ablating 25 cm of basaltic concrete, the zirconium-steel attack created large amounts of a foamy black-green by-product that was very porous, had a composition that was 17-18% Zr, and had a density of .7 to 1.2 g/cm^3. The information from SURC 4 was used as input to an OECD code comparison exercise designed to test the applicability of current accident analysis computer models.

CONTENTS

LIST OF FIGURES

LIST OF FIGURES, CONT'D

LIST OF FIGURES, CON'T

LIST OF FIGURES, CON'T

PAGE

LIST OF TABLES

LIST OF TABLES, CON'T

PAGE

1. GENERAL

The Ex-Vessel Core Debris Interactions Program is intended to measure, model, and assess the thermal, gas evolution, and aerosol source terms produced during core debris-concrete interactions that might occur following a severe nuclear reactor accident. These source terms are the governing phenomena in any postaccident containment integrity analysis or risk evaluation. A matrix of eight tests is being conducted as part of the program. This matrix is designated as the SURC (SUSTAINED URANIA-CONCRETE) test series.

In addition to extending the existing data base to include more prototypic core debris-concrete interactions, the SURC experiments are designed to provide information necessary to validate three important aspects of ex-vessel core debris-concrete interactions models. These are (1) heat transfer mechanisms, (2) gas release chemistry, and (3) vaporization release of aerosols. Both integral tests using UO_2-ZrO_2 materials (SURC 1, SURC 2, SURC 5, and SURC 6) as well as separate effects tests using stainless steel (SURC 3, SURC 4, SURC 7, and SURC 8) will be conducted.

The first two tests in the SURC series were designed to be integral tests using a 250 kg mixture of 69^{W}/o UO_2-22^{W}/o ZrO_2-9^{W}/o Zr over a 40 cm diameter concrete basemat formed from either limestone concrete (SURC 1) or basaltic concrete (SURC 2). Tests three and four in the SURC series were designed to be separate effects tests using stainless steel which investigated the additional effects of zirconium metal oxidation on sustained core debris concrete interactions. In tests SURC 3 and SURC 4, Zr metal was added to molten stainless steel to create meltpools with up to 10% Zr interacting with two different concrete basemats. The tests were inductively heated in order to sustain the molten attack and lasted as long as four hours. The molten steel charge ablated either limestone (SURC 3) or basaltic (SURC 4) concrete until steady state erosion and gas release were established. Zirconium metal was then added to the meltpool, and its effects on gas release rates and gas chemistry were observed. Together, SURC 3 and SURC 4 are expected to provide validation data for gas release chemistry models in the CORCON code, particularly with regard to the severity and duration of any coking effects that are predicted to produce extraordinary amounts of carbon monoxide immediately after the zirconium is fully oxidized. At present, the CORCON code calculates that the H_2O and CO_2 released from the concrete will be almost totally reduced by Zr in the melt forming ZrO_2, H_2, and elemental carbon. Virtually no gas other than hydrogen is predicted to be released during this reduction phase. After nearly all of the Zr metal is oxidized, the residual elemental carbon is expected to react with CO_2 or H_2O to form carbon monoxide. When this occurs, the gas release rate is expected to double the steady state value since two moles of gas are produced from each mole of gas evolved from the concrete. SURC 3 and SURC 4 were instrumented to test this predicted behavior.

The SURC 4 experiment used 200 kg of 304 stainless steel and 20 kg of Zr metal as the charge materials. It was designed to be a comprehensive test examining the additional effects of zirconium metal addition to molten steel interacting with basaltic concrete. The goals of the experiment were to measure in detail the gas evolution, aerosol generation, and erosion characteristics associated with steel-zirconium-concrete interactions.

The SURC 4 experiment was conducted in a 60 cm diameter interaction crucible constructed with a 40 cm diameter basaltic concrete cylinder in the base of a magnesium oxide (MgO) annulus. A 10 cm thick, circular cover of MgO was fabricated and placed on top of the crucible. The interaction crucible and induction coil were housed in a sealed, water cooled, aluminum containment vessel. A picture of this vessel and some of the rest of the test apparatus is shown in Figure 1.1. The vessel was 180 cm high, 120 cm in diameter and contained feedthroughs for the induction power leads, instrumentation leads, and an exhaust gas port connected to the flow and aerosol sampling instrumentation. The interaction crucible was instrumented with numerous thermocouple arrays cast into the concrete cylinder, MgO annulus and MgO cover. A 280 kW induction power supply and coil were used to heat and melt the 200 kg stainless charge within the test article and to sustain the interaction for the duration of the experiment. Additionally, 6 kg of fission product simulants were dissolved into the melt to study fission product release. Flowrates of generated gases were measured using a sharp edge concentric orifice, a laminar flow device and two dry gas clocks. Gaseous effluents produced during the experiment were monitored and sampled using an infrared gas analyzer, mass spectrometer, and by an integral grab sample technique. Aerosols were captured on filters, cascade impactors and a cascade cyclone. Erosion characteristics were measured using type K, S, and C thermocouples in order to define the meltpool temperature and overall heat balance as well as the axial erosion rate. The apparatus was sealed and purged with argon gas in order to direct the majority of the reaction gas and aerosol effluents through a 5 cm diameter flow pipe. The SURC 4 test was run at local atmospheric pressure (.83 atm) and at an ambient temperature of 25°C.

The zirconium metal was added to the meltpool after a constant rate of concrete erosion was established via a single tube, manually actuated, delivery system attached vertically to the containment vessel. The tube contained 50 Zr cylinders each with a diameter of 3.3 cm and a length of 7.6 cm. Each cylinder weighed 400 g and the total charge weighed 20 kg. Deposition into the meltpool was accomplished by opening a ball valve to the gas flow line, dropping the Zr metal, and closing the ball valve to reestablish flow through the exit port.

The SURC 4 test was designed to provide comprehensive, redundant, and well-characterized information on the steel-zirconium-concrete interaction which would be suited for code validation

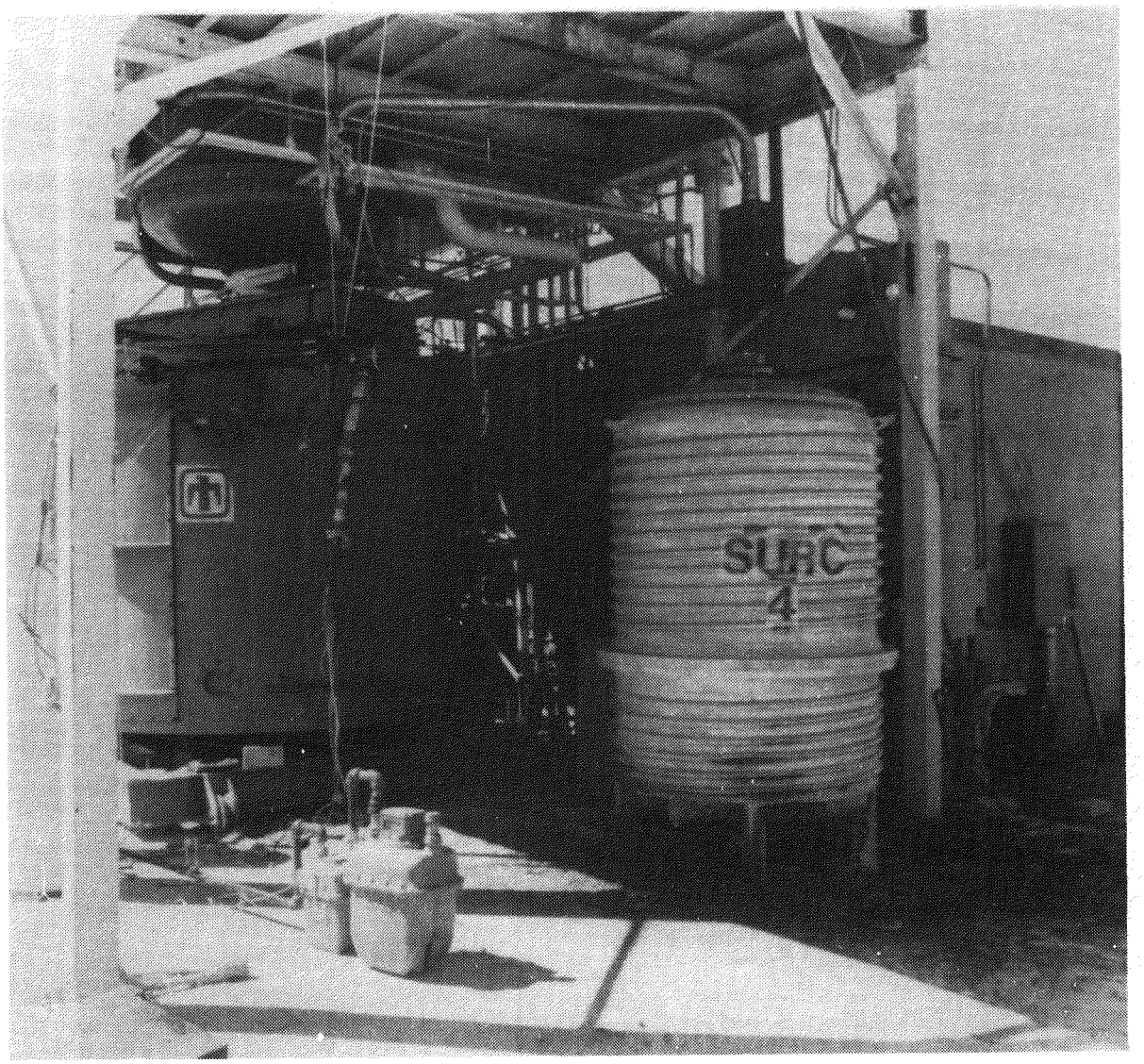

Figure 1.1 - SURC 4 Overview Photograph

efforts. The SURC 4 test ran for a total of 162 minutes. The data return was excellent and all of the test goals were successfully met.

2. MATERIALS

The interaction crucible used in the SURC-4 experiment is of cylindrical geometry and is shown in Figure 2.1. The crucible consists of three major components; the lower crucible, upper crucible and cover. The annulus of the upper and lower crucible and the cover are cast using a MgO castable refractory material. Basaltic concrete is cast into the base of the lower crucible. A detailed description of the interaction crucible including dimensions and thermocouple locations will be discussed later in Section 3.2.

2.1 Magnesium Oxide (MgO)

The annulus of the crucible was cast using an MgO castable material manufactured by Kaiser Refractories called K/R Cast-98. This material is a superior MgO castable produced from critically sized 98+% MgO periclase and bonded with a special chromate composition. K/R Cast-98 can be vibrated to exceptionally high densities. This material resists melt penetration and provides outstanding resistance to highly basic slags. This material also has excellent volume stability and is commonly used for crucibles in the steel industry. The chemical composition of K/R Cast-98 is shown in Table 2.1.

The MgO castable was mixed by placing a known mass of dry material into a clean paddle-type mixer. Clean drinking water was then added 5% by weight to the castable material and mixed for at least two minutes. Once a homogeneous mixture was achieved, the mix was carefully placed into the casting forms with small scoops and shovels. Two types of vibrators, operating at 10,000 to 12,000 vibrations/minute were used to densify the mix and remove entrained air. A pneumatically operated eccentric vibrator was attached to the brackets mounted to the steel casting forms. Another mechanical vibrator called a "stinger" was inserted directly into the mix to enhance densification.

After casting, the mix was cured at ambient temperature (15 to 35 C) for 24 hours. Then the forms were placed into an oven and initially heated at a rate of 40 C/hour to 265 C. The casting was held at temperature for 12 hours. The total curing cycle took 24 hours. During the baking period, two K-type thermocouples were connected to a strip chart recorder to monitor the curing temperature. One thermocouple measured the ambient oven temperature, the other thermocouples was cast into the annulus and measured the actual temperature of the annulus. Figure 2.2 shows a plot of the oven and crucible temperature versus time for the lower crucible annulus.

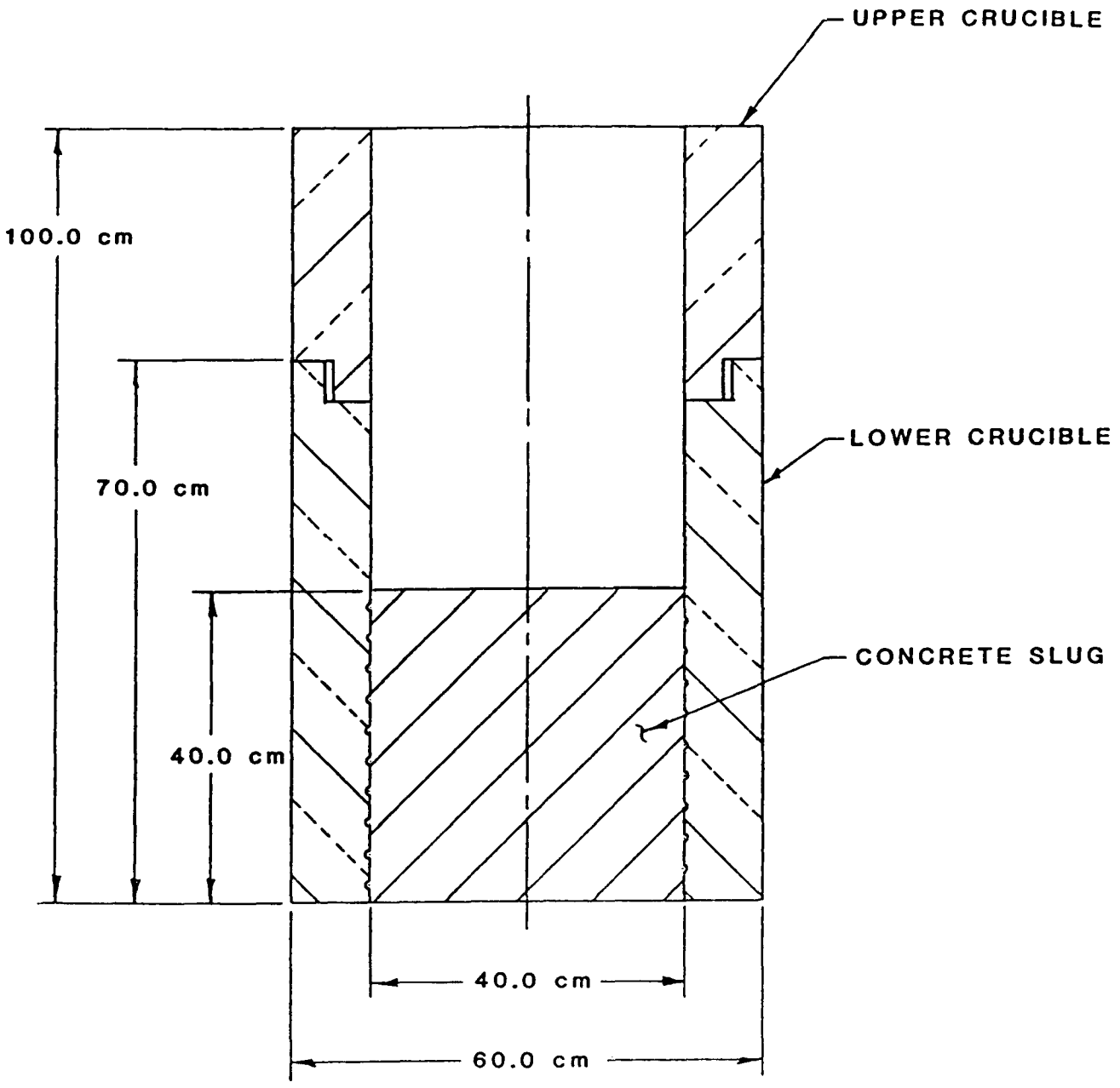

Figure 2.1 - Interaction Crucible, SURC-4 Experiment

Table 2.1

Chemical Composition of K/R Cast-98*
MgO Castable Refractory

Oxide	Weight %
MgO	97.1
SiO_2	0.4
Al_2O_3	0.1
Fe_2O_3	0.3
CaO	1.0
Cr_2O_3	1.1

* K/R Cast-98 is a product of Kaiser Refractories, 300 Lakeside Drive, Oakland, CA 94643.

Data Obtained from Basic Ramming and Casting Mixes Bulletin Published by Kaiser Refractories.

The thermal behavior of the K/R Cast-98 was characterized by thermal gravimetric analysis (TGA), shown in Figure 2.3. This analysis was performed with a Dupont 790 thermal analysis apparatus with a 1870 K DTA cell and Model 950 TGA attachment.

The TGA was performed in dry air with a flowrate of 50 cc/min. The heating rate was 10 K/min from room temperature to 1400 K. The sample had been air cured for 24 hours, baked at 470° K for 24 hours, then allowed to air cool for an additional 24 hours prior to thermal analysis. Weight losses indicated in the thermogram are attributed to the release of free and bound water. This sample shows a 4.0 weight-percent loss due to release of free and bound water between ambient temperature and 700 K. From 700 K to 1000 K, an additional 0.2 percent-weight loss of bound was observed, which is probably due to the decomposition of brucite ($Mg(OH)_2$).

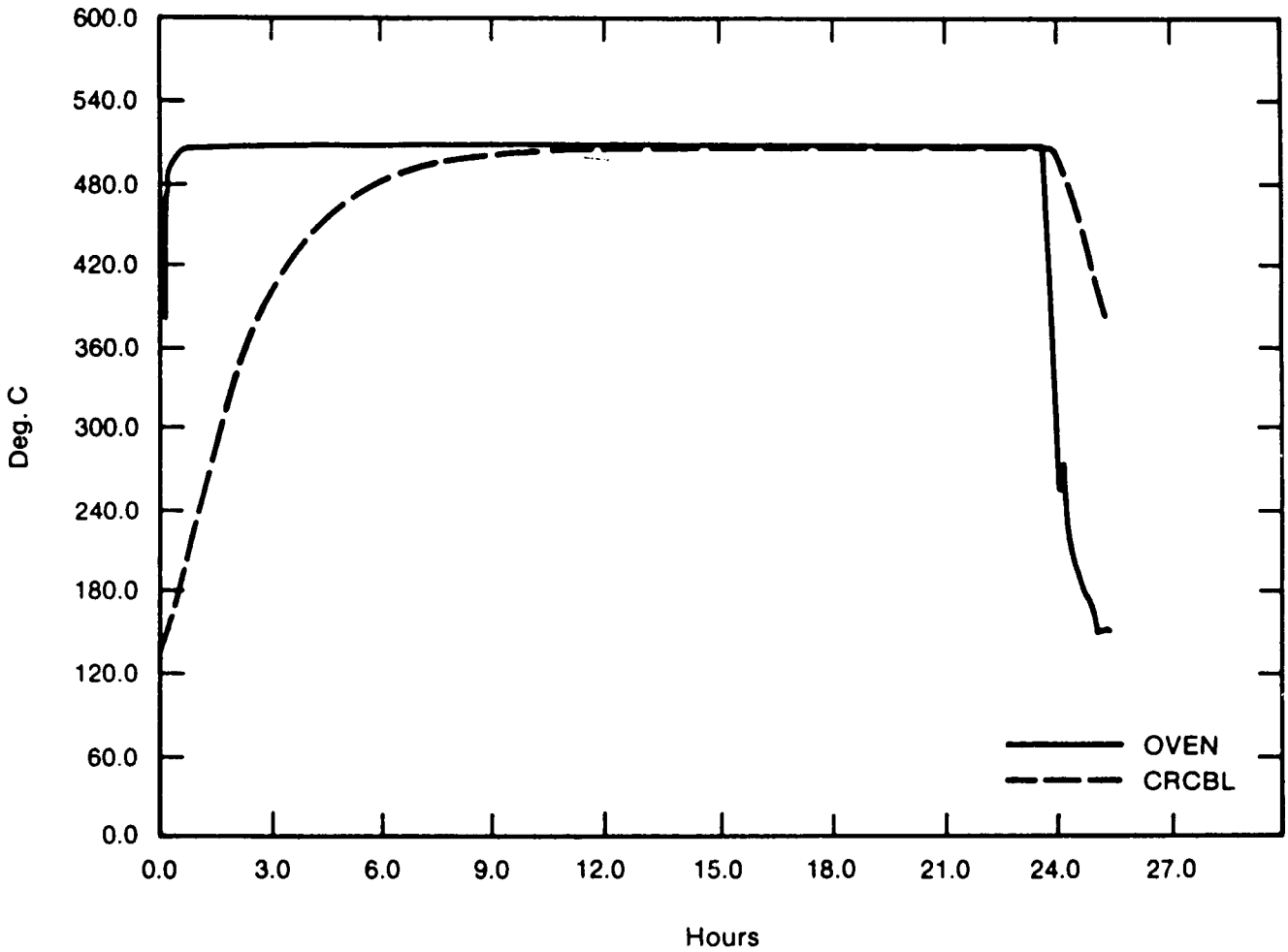

Figure 2.2 - Elevated Temperature Cure for the Annulus of the Lower Crucible.

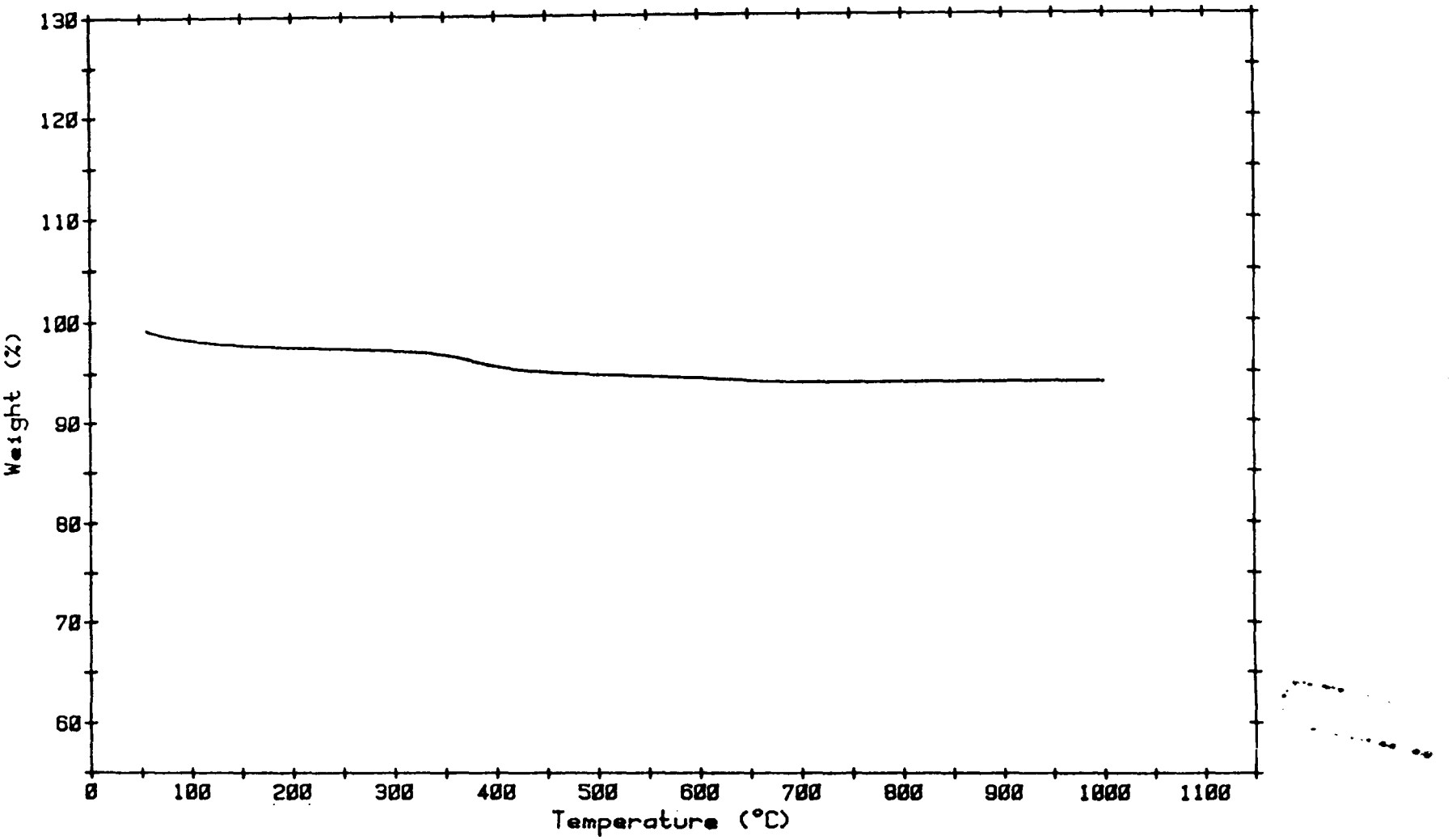

Figure 2.3 - Thermograph of MgO K/R Cast 98: Air-Cure 24 hours, Baked at 470 K for 24 Hours.

The thermal properties of the castable K/R Cast-98 have been extensively investigated. In addition to industry data, experiments were conducted at Sandia to study the thermal response of the MgO to intense heating conditions similar to those expected during an experiment. These experiments were carried out at the Sandia Solar Tower where a MgO specimen was subjected to incident solar fluxes in the range of 6.5×10^5 W/m^2 to 1.4×10^6 W/m^2. The test specimen was 45 cm x 45 cm x 8 cm and was cast of the K/R Cast-98 material. The test specimen was well instrumented with 17, 1.5 mm diameter type K thermocouples, located from 0.3 cm to 6.3 cm below the exposed surface. The test specimen was mounted in a frame compatible with the Solar Tower assemblies. The incident flux was monitored by heat flux gauges deployed along the top and side of the test specimen. The back of the test specimen was well insulated in order to approximate an adiabatic boundary condition.

A typical thermal history of the specimen is shown in Figure 2.4. As one can see, the temperature rise is interrupted at 373 K. This is due to the release of the free water in the castable material. The material continued to be heated until approximately 1673 K, then the solar heat flux was removed and the test specimen was allowed to cool.

The data were analyzed by the "PROPTY" code using methods developed by J. V. Beck (Beck, 1985). The code determines the thermal conductivity of a material that fits a set of temperature response curves for specific interval and boundary conditions.

The PROPTY prediction of the thermal conductivity of the MgO is shown in Figure 2.6. The presence of the free water within the castable material causes minor problems in the analysis of the experimental data. As shown in Figure 2.5, the predicted thermal conductivity is slightly higher for "wet" or uncured material than it is for "dry" or fully dehydrated MgO castable. A check of the relative accuracy of the values of the conductivity is demonstrated by comparing the predicted thermal response with the actual experimental data. As shown in Figure 2.6, excellent agreement is achieved. The absolute values of thermal conductivity (k) are dependent on the initial value set in the PROPTY code. This value is fixed, and the values of k at other temperatures are allowed to vary in order to determine the best value of k.

Thermal conductivity data for 98% dense magnesium oxide are also shown in Figure 2.5. It is readily apparent that the thermal conductivity of the K/R Cast-98 is much less than the highly densified Mgo. The conductivity of the castable material is quite dependent on density and method of preparation. Another determination of the thermophysical properties of K/R Cast-98 was performed by Purdue University and is described in Appendix A. The density of the K/R Cast-98 material was also investigated. The bulk density of the material used in SURC 4 was found to be 2680 kg/m^3 as compared to the theoretical density for MgO of 3590 kg/m^3.

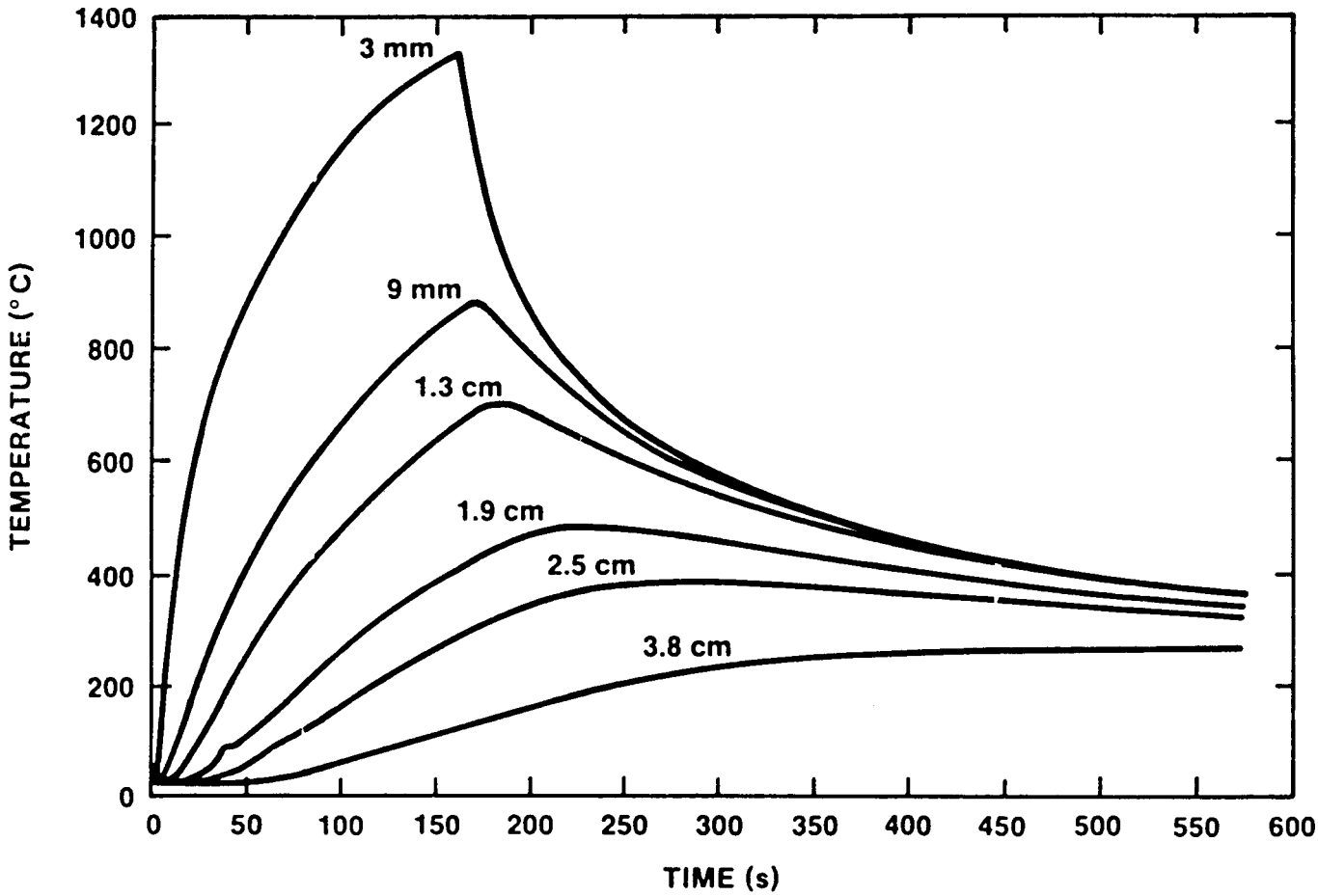

Figure 2.4 - Representative Temperature History of an MgO Sample Exposed to Solar Heat Flux 1.4 x 10^6 W/m^2

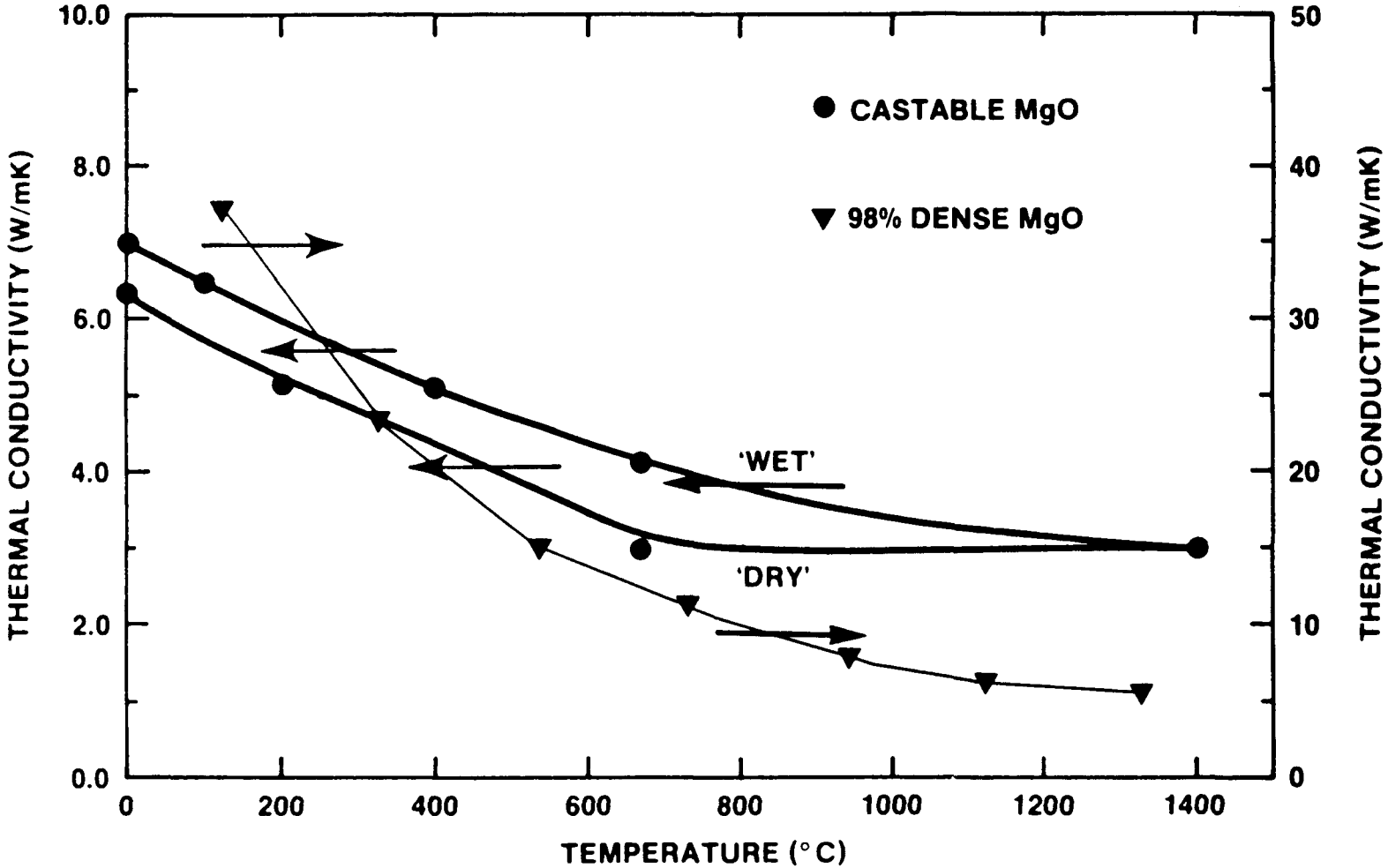

Figure 2.5 - "PROPTY" Thermal Conductivity Prediction for Castable MgO Material. Also shown are data for 98% dense material. Note the significantly different scale used for the thermal conductivity of the highly dense material.

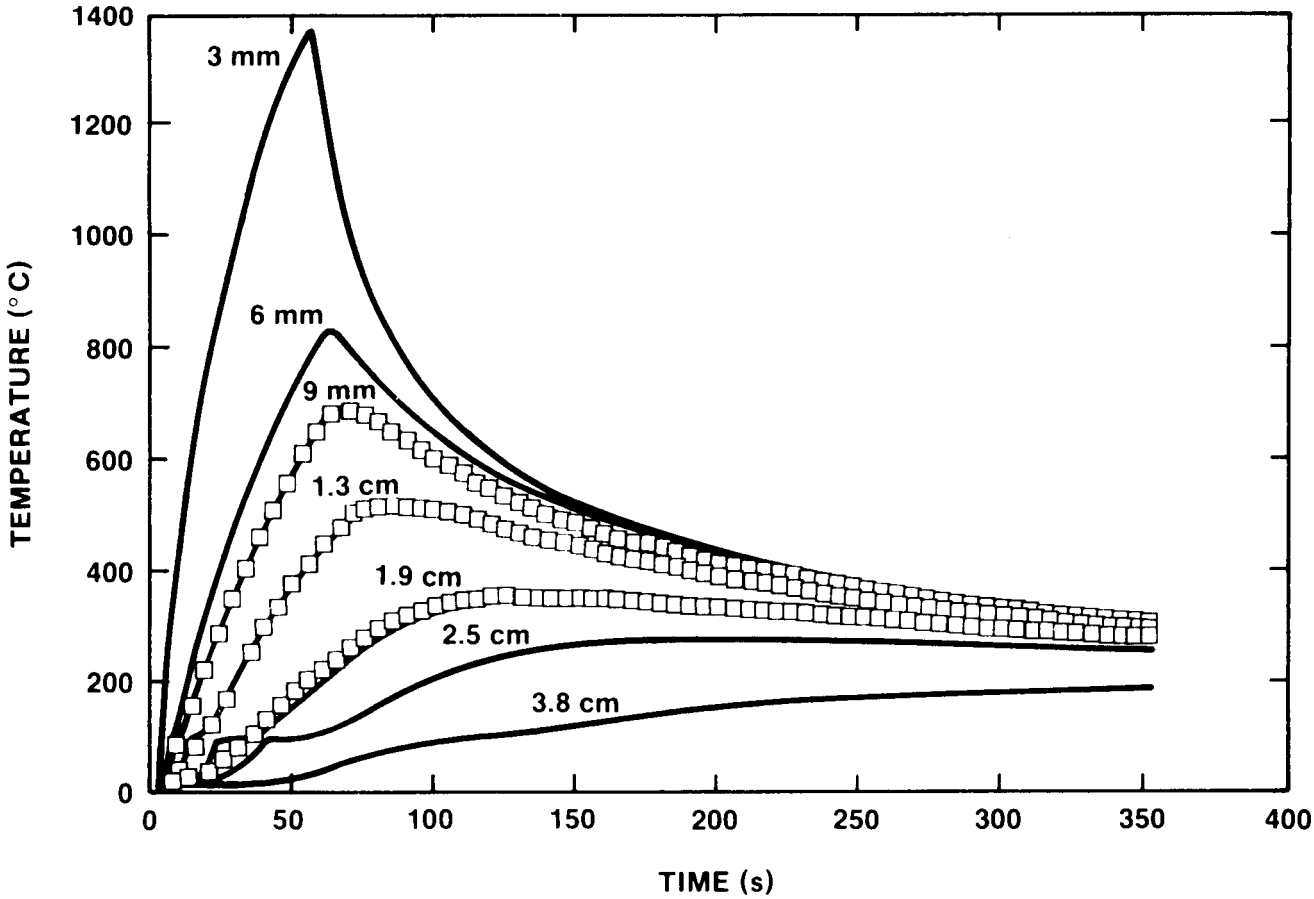

Figure 2.6 - Comparison of Experiment Thermal History and Predictions of the "PROPTY" Code. Curves are labelled according to the depth below the surface exposed to the incident heat flux. Data obtained in the experiment are shown as open squares. Results calculated with PROPTY code are shown as solid lines.

2.2 Concrete Material

The base of the interaction crucible was constructed of basaltic concrete. This concrete was used because it is typical of that used in the construction of nuclear power plants. Materials making up this type of siliceous concrete are found throughout the United States. This concrete melts over a range of 1350-1650 K and typically liberates 1.5 weight-percent CO_2 gas and 5 weight-percent H_2O vapor when heated to melting.

The casting of the concrete was performed by mixing the concrete constituents in a clean paddle mixer. Once a homogeneous mixture had been achieved, the mix was carefully placed into the casting forms and vibrated as previously described in Section 2.1.

Specifications for the concrete are listed in Table 2.2. Tables 2.3 and 2.4 summarize the engineering and chemical composition of the basaltic concrete. Tables 2.5 and 2.6 show comparisons of the size specifications and the distribution of sizes for the aggregate and sand actually used for the concrete.

Four 10.2 cm diameter x 20.3 cm long test cylinders were cast with the concrete slug to measure the compressive strength after 7, 14, 28 and 55 (day of the experiment) days. The concrete cylinder was cured at ambient temperature conditions-nominally 20° ± 10°C. Compressive strengths are plotted against cure time in Figure 2.7.

The thermal behavior of the concrete can be characterized by thermal gravimetric analysis (TGA), derivative thermogravimetric analysis (DTGA), and differential thermal analysis (DTA). Figure 2.8 shows the thermogram produced by TGA for the SURC 4 basaltic concrete.

2.3 Charge Material

The melt charge used in this experiment was a solid cylinder of 304 stainless steel having a mass of 200 kg. The cylinder was 35.6 cm in diameter and 25.4 cm high. The composition of the 304 stainless steel cylinder is shown in Table 2.7.

Twenty (20) kg of zirconium metal was added to the melt-concrete interaction after a constant rate of concrete erosion was observed. The zirconium was in the form of solid cylinders 3.3 cm in diameter and nominally 7.6 cm long. These cylinders were saw cut from a rod 3.0 meters long. The chemical composition of the zirconium is shown in Table 2.8. The elemental analysis is taken from the top, middle and bottom of the ingot from which the rod was fabricated.

Table 2.2

Concrete Specifications

1)	Compressive strength after 90 day cure = 27.5 MPa minimum
2)	Slump = 5 cm
3)	Cement = American Type II Portland Cement
4)	Air content = 3 to 5% by volume
5)	Air entraining agent per reference (a) below
6)	Composition per reference (b) below
7)	Aggregate size and size distribution per reference (c) below
8)	Water reducing agent per reference (a) below
9)	Mixing, forming, and placing per references (b,c,d,e) below

(a) ASTM C-494-71, Standard Specification for Chemical Admixtures for Concrete, American Society for Testing and Materials, Philadelphia, PA.

(b) ACTI 211. 1-74, Recommended Practices for Normal and Heavy Concrete, American Concrete Institute, Detroit, MI.

(c) ASTM 33-74., Standard Specifications for Concrete Aggregates, American Society for Testing and Materials, Philadelphia, PA.

(d) ACI 347-68, Recommended Practice for Working Concrete, American Concrete Institute, Detroit, MI.

(e) ACI 315-74, Detailing Manual, American Concrete Institute, Detroit, MI.

Table 2.3

Engineering Composition of Basaltic Concrete

Constituents[b]	Mass	Weight %
Aggregate[c]	42.3 kg	35.7
Sand	47.4 kg	40.1
Cement	19.4 kg	16.4
Water	9.3 kg	7.8
* AEA[a]	22.2 ml	-

* Air Entraining Agent

(a) ASTM C-494-71, Standard Specification for Chemical Admixtures for Concrete, American Society for Testing and Materials, Philadelphia, PA.

(b) ACTI 211. 1-74, Recommended Practices for Normal and Heavy Concrete, American Concrete Institute, Detroit, MI.

(c) ASTM 33-74., Standard Specifications for Concrete Aggregates, American Society for Testing and Materials, Philadelphia, PA.

Table 2.4

Chemical Composition of Basaltic Concrete Constitutents(a)(b)

Oxide	Type 1 and 2 Cement (%)	Sand (%)	Basalt Aggregate(c)
Fe_2O_3	4.11	2.15	7.78
Cr_2O_3	0.011	0.042	0.06
MnO	0.08	0.02	0.08
TiO_2	0.2	0.18	1.82
K_2O	0.54	2.7	7.2
Na_2O	0.27	1.74	1.85
CaO	63.5	1.52	6.54
MgO	1.53	0.34	9.7
SiO_2	20.1	82.8	54.9
Al_2O_3	4.2	7.24	9.51
CO_2	ND	ND	< 0.02
H_2O	ND	0.1	0.1
SO_2	1.0	ND	ND

ND = Not Determined

(a) ASTM C-494-71, Standard Specification for Chemical Admixtures for Concrete, American Society for Testing and Materials, Philadelphia, PA.

(b) ACTI 211. 1-74, Recommended Practices for Normal and Heavy Concrete, American Concrete Institute, Detroit, MI.

(c) ASTM 33-74., Standard Specifications for Concrete Aggregates, American Society for Testing and Materials, Philadelphia, PA.

Table 2.5

Comparison of Specified and Actual Size Distributions for the Fine and Coarse Aggregate

Through the Screen Opening		Observed Weight % Passing Through the Screen
Screen Opening (cm)	Specified Weight % Passing Through the Screen	
A) Coarse Aggregate		
2.5	95-100	100
1.9	90-100	96.3
1.3	25-60	54.7
0.95	20-55	not measured
0.48	0-10	not measured
0.23	0-5	not measured
B) Fine Aggregate		
1.3	100	100
0.95	85-100	98.9
0.48	10-30	96.8
0.23	0-10	not measured
0.12	0-5	not measured

Table 2.6

Comparison of Specified and Actual Size Distributions for the Sand

	Weight % Passing Through the Screen	
Screen Opening (cm)	Specified	Observed
0.95	100	99.85
0.48	95-100	97.85
0.23	80-90	85.14
0.12	55-75	60.93
0.058	30-60	33.92
0.030	12-30	16.50
0.015	2-10	7.11
0.0076	-	3.06

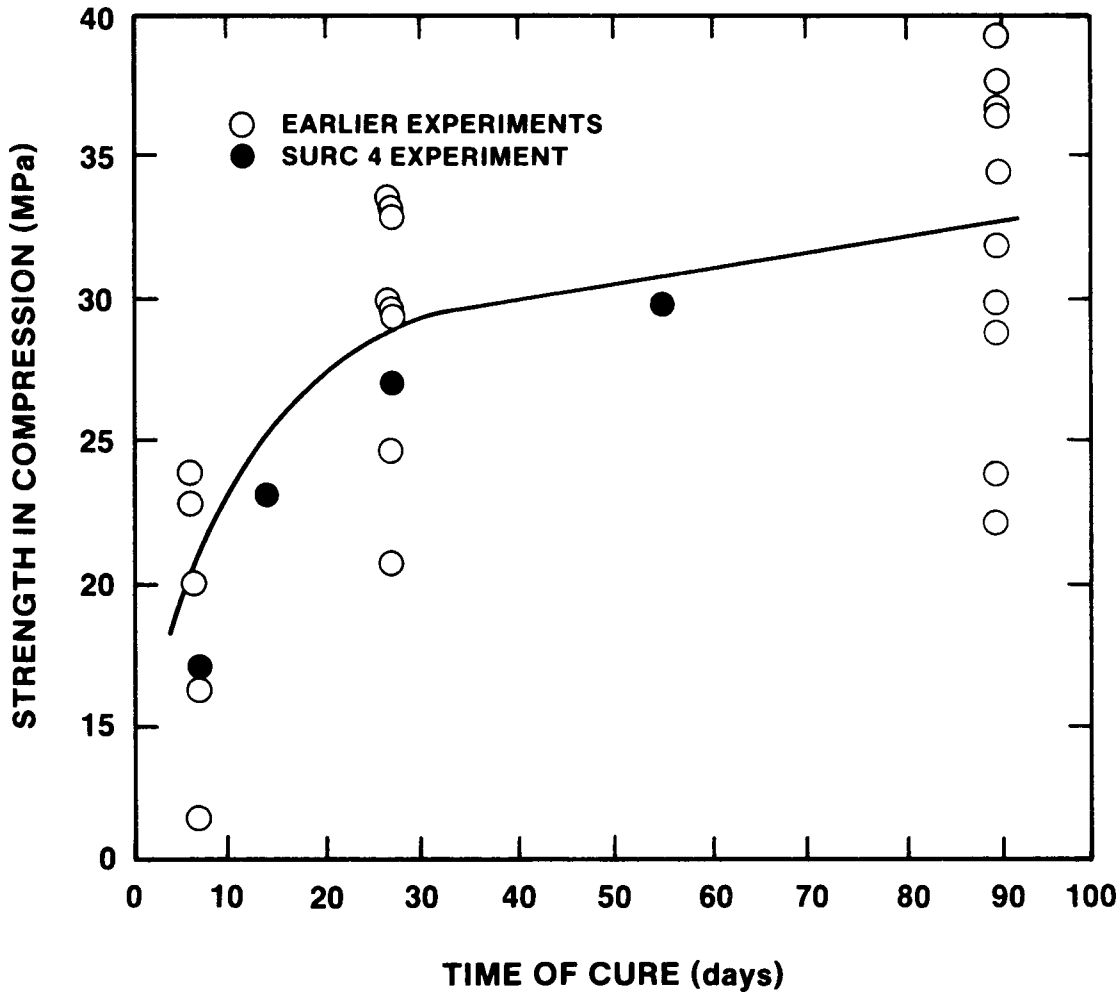

Figure 2.7 - Compressive Strength as a Function of Time for Basaltic Concrete. Data for concrete used in the SURC 4 test are shown as darkened circles. Data obtained from previous castings of basaltic concrete are shown as open circles.

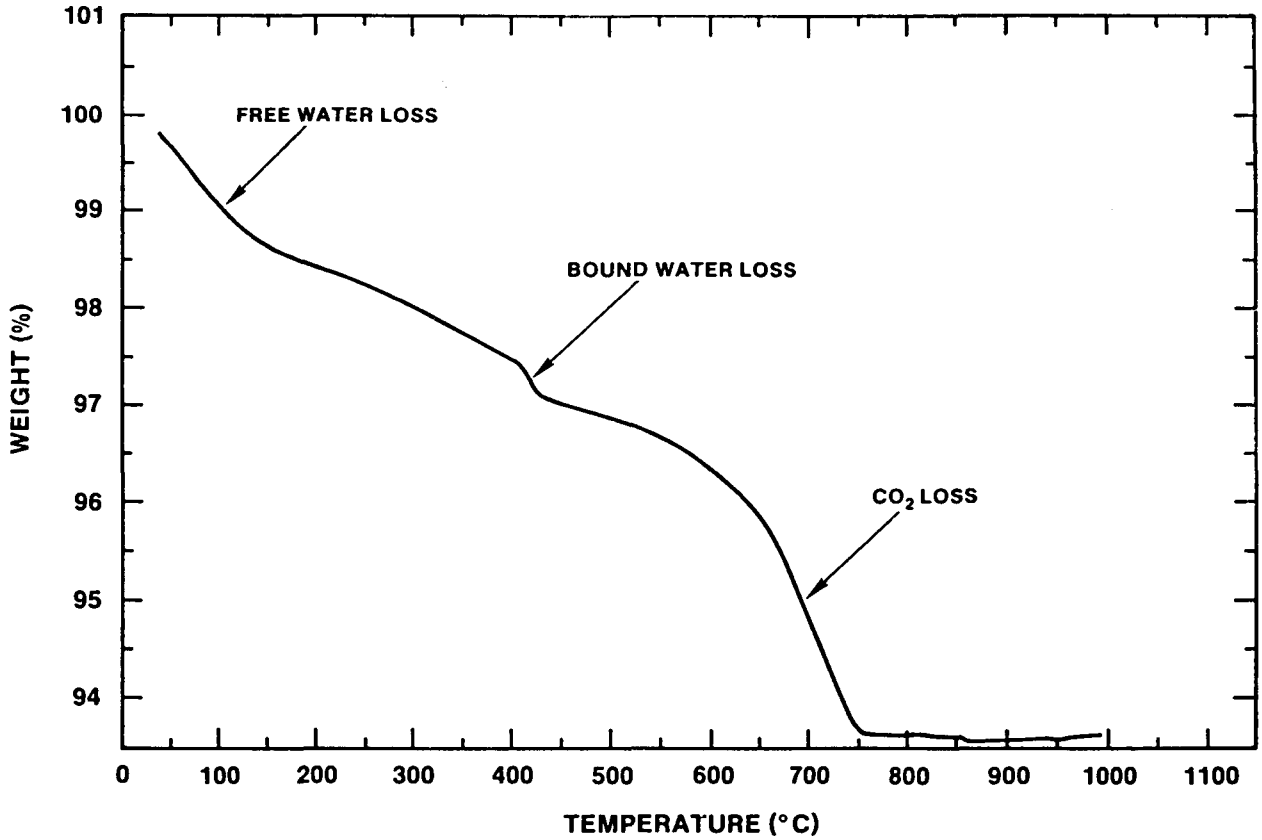

Figure 2.8 - Thermogram (TGA) of Basaltic Concrete

Table 2.7

Standard Composition Of
304 Stainless Steel

C Max.	Mn Max.	P Max.	S Max.	Si Max.	Cr	Ni Max.	Cu Max.	Mo Max.
.08	2.00	.040	.030	1.00	18.00/20.00	8.00/11.00	.50	.50

Table 2.8

Chemical Composition of the Zirconium Metal

Trace Element	Ingot Location Top (ppm)	Middle (ppm)	Bottom (ppm)
Al	150	135	125
C	150	150	150
Nb	71	76	120
Cr	110	79	62
Fe	1120	1140	1040
H	< 5	9	10
Hf*	0.079%	0.056%	0.055%
N	51	60	57
Ni	< 35	47	85
O	1360	1340	1300
P	10	8	10
Si	48	45	58
Sn	800	600	1100
Ta	< 100	< 100	< 100
Ti	34	27	27
W	< 25	< 25	< 25
Zr*	99.5	99.5	99.5

* Composition given in percent (%) rather than parts per million (ppm).

2.4 Fission Product Simulants

In order to evaluate the transport of fission products during the melt-concrete interaction, various chemical species, listed in Table 2.9, were added to the melt prior to heating. These were added to the charge prior to initial heating as a homogeneous powdered mixture. One third (approx. 2 cm) of the mixture was below the steel slug, one third was in the gap between the slug and the MgO wall, and one third was above the steel slug. Due to the porosity (50%), low conductivity, and high melting point of the mixture, the fission product simulants acted as an insulator to the stainless steel slug until the charge became molten.

Table 2.9

SURC-4 Fission Product Simulants

Fission Product	Quantity (kg)	Category
Molybdenum	2.0	Early Transition Element
Tellurium	0.5	Chaleognes
Lanthunum Oxide	1.17	Trivalents
Cerium Oxide	1.23	Tetravalents
Barium Oxide	1.1	Alkaline Earths
TOTAL	6.0	

3. EXPERIMENTAL APPARATUS

The major components of the SURC-4 experimental apparatus are shown in Figure 3.1 and include a sealed, water-cooled, containment vessel, interaction crucible, induction coil, and zirconium delivery tube. These components are described in the following sections. The remainder of the SURC 4 apparatus including the exit flow piping and the gravel bed filter are described in Section 4.3.

3.1 Containment Vessel

An aluminum containment vessel was used in SURC 4 to ensure that nearly all of the reaction products would pass through the instrumented exit flow piping. A sectional view of the water cooled containment vessel is shown in Figure 3.2. The vessel was fabricated in two sections using 2.5 cm thick, weldable 6061-T6 aluminum alloy. The two sections were assembled using 24, 1.4 cm diameter hex head bolts and nuts securing the mating flanges. The flange of the lower section incorporated a double O-ring for sealing. The vessel was supported by four 10 cm diameter x 45.7 cm long legs welded to the bottom of the lower section. Basic dimensions of the vessel are shown in Figure 3.2. The internal volume of the vessel was calculated to be approximately 2.0 m^3.

Aluminum (6061-T6) tubing 2.5 cm in diameter was welded to the outside and top of the vessel at a pitch of approximately 10 cm. This tubing was used to circulate a mixture of 50% by volume ethylene glycol in water used to cool the vessel during the experiment. The bottom of the vessel was cooled by means of three large reservoirs welded to the bottom of the vessel. The tubing and reservoirs were connected in series to form a single cooling circuit.

Bolted, flanged ports located in the lower section of the vessel were used to provide feedthroughs for power and instrumentation leads and for mounting fittings to connect a pressure transducer and tubing for supplying argon purge gas. Another port was fitted with a spring-loaded safety diaphragm calibrated to open at 15 psig to eliminate the potential for over-pressurization of the vessel. A three inch diameter flange port located in the base of the vessel was used as a feedthrough for all crucible thermocouple terminations. The sheaths and/or extension wires for all the thermocouples were pulled through a mating 90^{o} flanged elbow. The elbow was filled with epoxy and allowed to cure, encapsulating the instrumentation leads and thermocouple sheaths. The elbow was then bolted to the flanged port, sealing the instrumentation cabling. A flanged port in the top of the vessel was fitted with a 2 inch O.D. x .062 inch wall x 1 m long, 304 stainless steel tube. This tube connected the interaction crucible with the flow system instrumented for sampling evolved gas and aerosols and measuring gas flowrate.

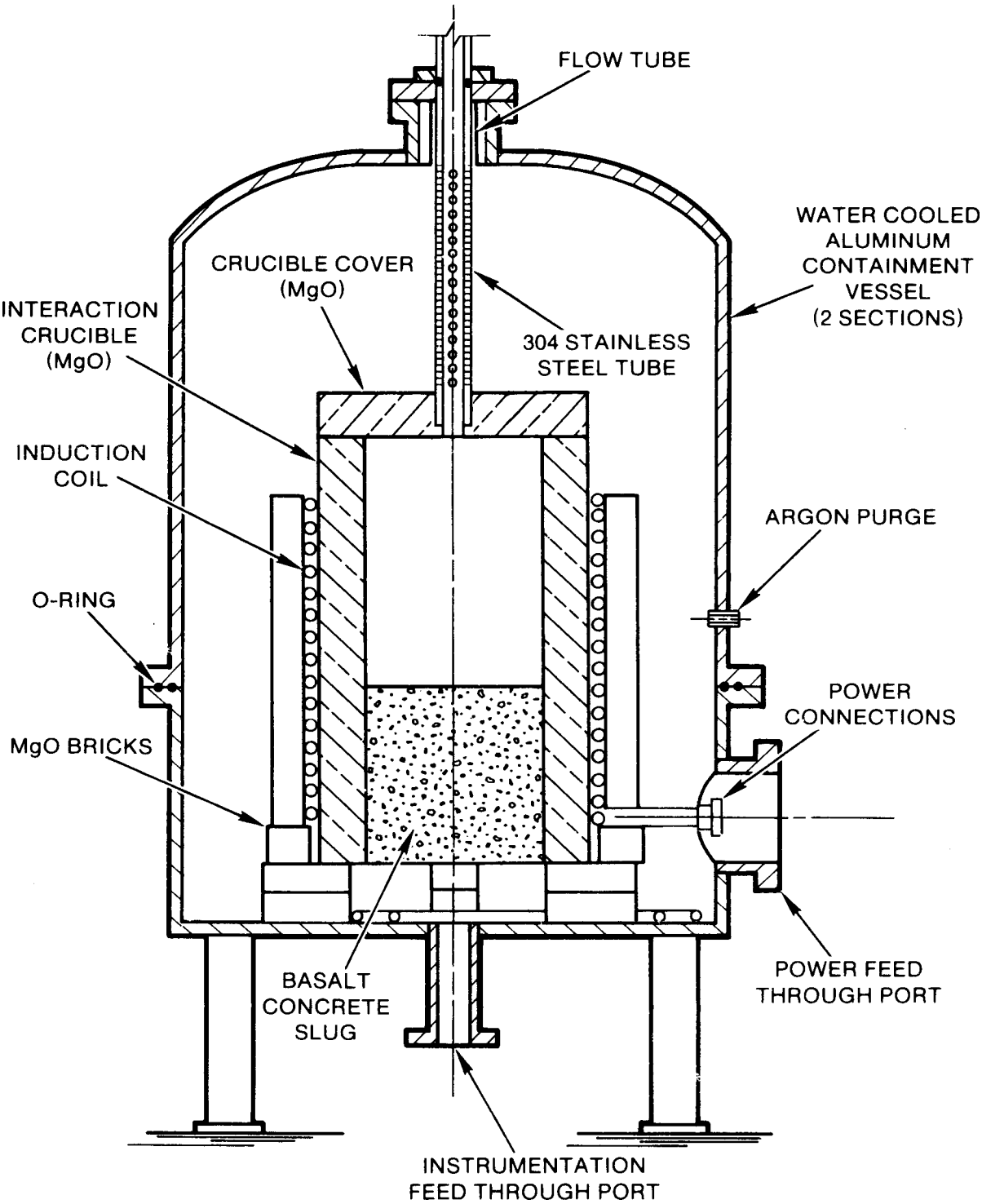

Figure 3.1 - SURC-4 Experimental Apparatus

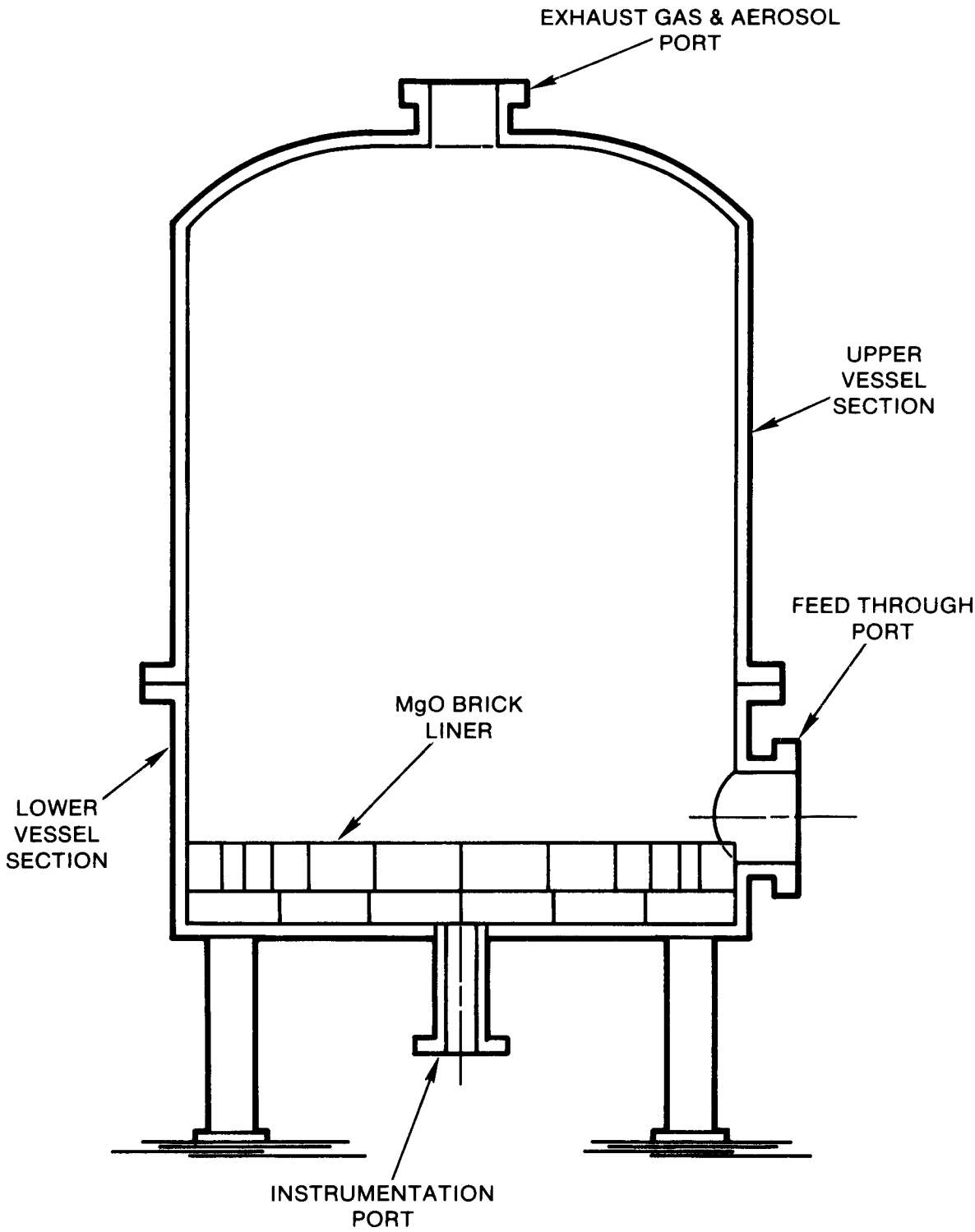

Figure 3.2 - Sealed, Water-Cooled, Containment Vessel

The inside floor of the lower vessel was lined with six inches of standard refractory MgO brick and back-filled with fine MgO powder. The perimeter of the floor was built-up with an extra layer of bricks six inches high and two inches thick. This was done to protect the vessel from melt attack should any molten material breach the interaction crucible during the experiment.

The vessel was pressure tested and certified to operate either in a partial vacuum or up to 20 psig.

3.2 Interaction Crucible

The interaction crucible for SURC 4 was designed to limit concrete erosion to the downward or axial direction. The materials used in the construction of the interaction crucible have been discussed in detail in Sections 2.1 and 2.2. The crucible used in SURC-4 was of cylindrical geometry and is shown in Figure 3.3. The main body of the crucible was cast in two sections--namely the upper and lower crucible. The overall dimensions of the crucible are 60 cm diameter x 100.0 cm high with a 40.0 cm diameter cavity 60.0 cm deep. Cast into the bottom of the lower crucible was an instrumented basaltic concrete cylinder 40.0 cm diameter x 40.0 cm thick. The upper crucible was cast with an annular step and the lower crucible with a mating annular recess. The two crucible sections were assembled and sealed with Saureisen Cement No. 31.

The annulus of the upper and lower crucible and cover were cast using a reusable steel casting form constructed in a clam shell arrangement. Bolts were placed through the crucible cover and threaded into brass anchors cast into the upper crucible securing the cover. A detailed description of the casting forms and fabrication procedures is presented in Appendix B.

Approximately 0.18 m^3 of MgO castable ceramic and 0.05 m^3 of basaltic concrete were required per crucible cast. The total estimated mass of the crucible was:

Annulus - MgO Castable
Volume - 0.15 m^3 @ 2680 kg/m^3 = 402 kg

Cover - MgO Castable
Volume - 0.03 m^3 @ 2680 kg/m^3 = 80 kg

Concrete Cylinder - Basaltic Concrete
Volume - 0.05 m^3 @ 2400 kg/m^3 = 120 kg

TOTAL MASS 602 kg

The annulus, concrete cylinder and crucible cover were instrumented with 95 type K thermocouples cast into the crucible

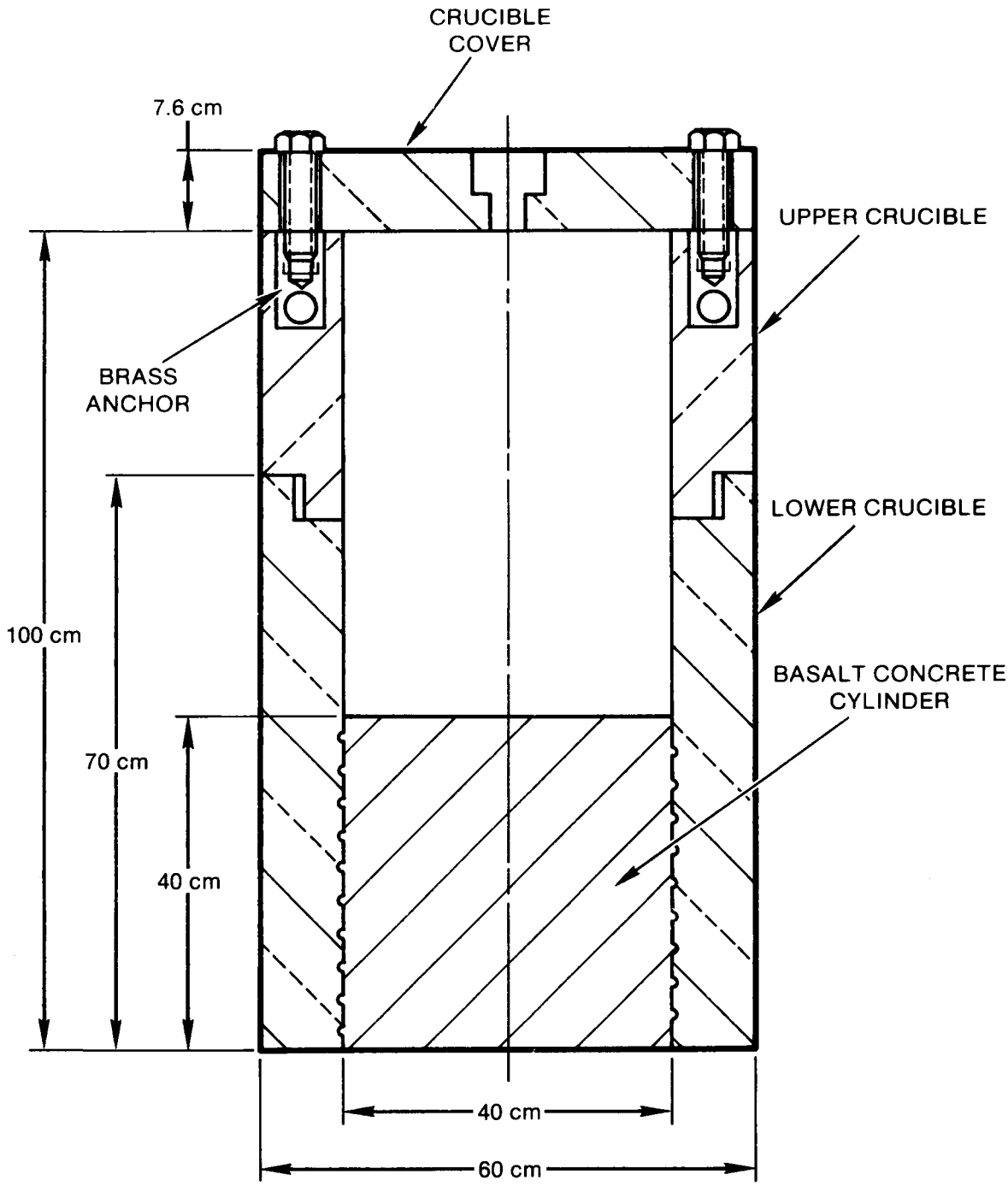

Figure 3.3 - Interaction Crucible, SURC-4

in 16 arrays to measure thermal response. Figure 3.4 shows the relative thermocouple locations and the various arrays cast into the crucible. This figure also shows the nomenclature used to describe the locations of the thermocouples in cylindrical coordinates, specifically r, θ, z and t. Additionally, six type S and six type C thermocouples installed into six alumina tubes were cast into the basaltic concrete cylinder to measure melt temperature.

Sixty thermocouples were cast into the concrete in three arrays. The array containing thermocouples designated C1 through C20 was located on the axial centerline at odd (1, 3, 5, etc.) centimeter depths. The array containing thermocouples designated C21 through C40 were located on a line parallel to the center axis at a radial distance of 10.0 cm. These thermocouples were located at even centimeter depths. The third array was identical to the center axis array except that it was located near the perimeter of the concrete cylinder at a radial distance of 18.0 cm. The locations of the thermocouples cast into the concrete cylinder are tabulated in Table 3.1. The sheath of each thermocouple was bent at an angle of 90 degrees ten sheath diameters from the tip. This was done to minimize the errors caused by heat conduction down the metal sheath. Installation of a typical thermocouple array is shown in Figure 3.5.

Six four-hole alumina tubes were cast into the concrete slug parallel to the axial centerline, 60 degrees apart at a radial distance of 14 cm. Installed in each tube were one type S and one type C thermocouple located at various depths from the surface of the concrete cylinder. These thermocouples were used to measure melt temperature and their locations are tabulated in Table 3.2. Figure 3.5 shows an installation of a typical alumina tube with the type S and type C thermocouples.

Thermocouples used to monitor sidewall temperatures in the MgO annulus of the crucible were installed into pre-cast MgO cylinders prior to casting as shown in Figure 3.6. The ends of the cylinders conformed to the curvature of the annulus of the casting forms providing a good fit. The cylinders were bolted to the inside diameter of the outer steel crucible form by threading a small hex head bolt into a small brass anchor cast into the MgO cylinders. This method for installation of sidewall thermocouples accurately positions the thermocouples which is critical for heat flux calculations. The thermocouple tips were oriented in a horizontal plane parallel to the base of the crucible and perpendicular to the thermal front. The specific locations of the sidewall thermocouples are tabulated in Table 3.3.

Two thermocouple arrays were cast into the crucible cover. Like the arrays cast into the annulus, the thermocouples were installed into pre-cast MgO cylinders. The locations of these thermocouples are listed in Table 3.4. The t dimension given in the table is referenced from the bottom face of the crucible cover.

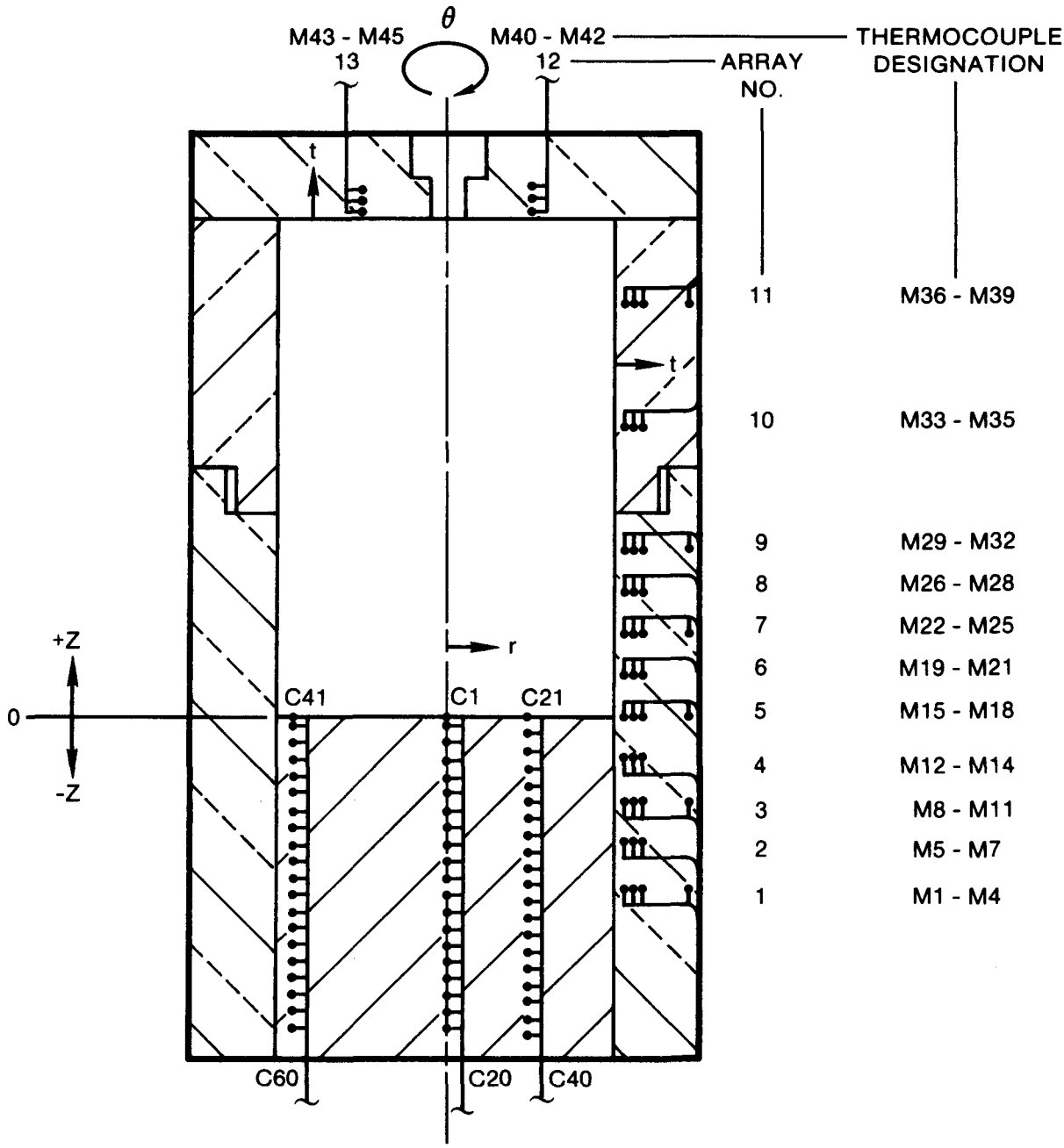

Figure 3.4 - Relative Sidewall Thermocouple Locations, SURC-4 Crucible.

Table 3.1

Location of Thermocouples Cast Within the Concrete Cylinder, SURC-4 (See Figure 3.4)

Thermocouple No.	r (cm)	θ (degree)	-z (cm)
C1	0	0	0
C2	0	0	1.0
C3	0	0	3.0
C4	0	0	5.0
C5	0	0	7.0
C6	0	0	9.0
C7	0	0	11.0
C8	0	0	13.0
C9	0	0	15.0
C10	0	0	17.0
C11	0	0	19.0
C12	0	0	21.0
C13	0	0	23.0
C14	0	0	25.0
C15	0	0	27.0
C16	0	0	29.0
C17	0	0	31.0
C18	0	0	33.0
C19	0	0	35.0
C20	0	0	37.0
C21	10.0	0	0.0
C22	10.0	0	2.0
C23	10.0	0	4.0
C24	10.0	0	6.0
C25	10.0	0	8.0
C26	10.0	0	10.0
C27	10.0	0	12.0
C28	10.0	0	14.0

Table 3.1 Cont'd.

Location of Thermocouples Cast Within the Concrete Cylinder, SURC-4 (See Figure 13)

Thermocouple No.	r (cm)	θ (degree)	-z (cm)
C29	10.0	0	16.0
C30	10.0	0	18.0
C31	10.0	0	20.0
C32	10.0	0	22.0
C33	10.0	0	24.0
C34	10.0	0	26.0
C35	10.0	0	28.0
C36	10.0	0	30.0
C37	10.0	0	32.0
C38	10.0	0	34.0
C39	10.0	0	36.0
C40	10.0	0	38.0
C41	18.0	180	0.0
C42	18.0	180	1.0
C43	18.0	180	3.0
C44	18.0	180	5.0
C45	18.0	180	7.0
C46	18.0	180	9.0
C47	18.0	180	11.0
C48	18.0	180	13.0
C49	18.0	180	15.0
C50	18.0	180	17.0
C51	18.0	180	19.0
C52	18.0	180	21.0
C53	18.0	180	23.0
C54	18.0	180	25.0
C55	18.0	180	27.0

Table 3.1 Cont'd

Location of Thermocouples Cast Within the Concrete Cylinder, SURC-4 (See Figure 3.4)

Thermocouple No.	r (cm)	θ (degree)	-z (cm)
C56	18.0	180	29.0
C57	18.0	180	31.0
C58	18.0	180	33.0
C59	18.0	180	35.0
C60	18.0	180	37.0

Table 3.2

Location of Thermocouples Installed in the Alumina Tubes and Cast Into the Concrete Cylinder, SURC-4

Tube Number	Thermocouple No.	Thermocouple Type	r (cm)	θ (degree)	-z (cm)
1	A1	S	14.0	30	1.0
4	A2	C	14.0	210	4.0
3	A3	S	14.0	150	7.0
6	A4	C	14.0	330	10.0
5	A5	S	14.0	270	13.0
2	A6	C	14.0	90	16.0
1	A7	S	14.0	30	19.0
4	A8	C	14.0	210	22.0
3	A9	S	14.0	150	25.0
6	A10	C	14.0	330	28.0
5	A11	S	14.0	270	31.0
2	A12	C	14.0	90	34.0

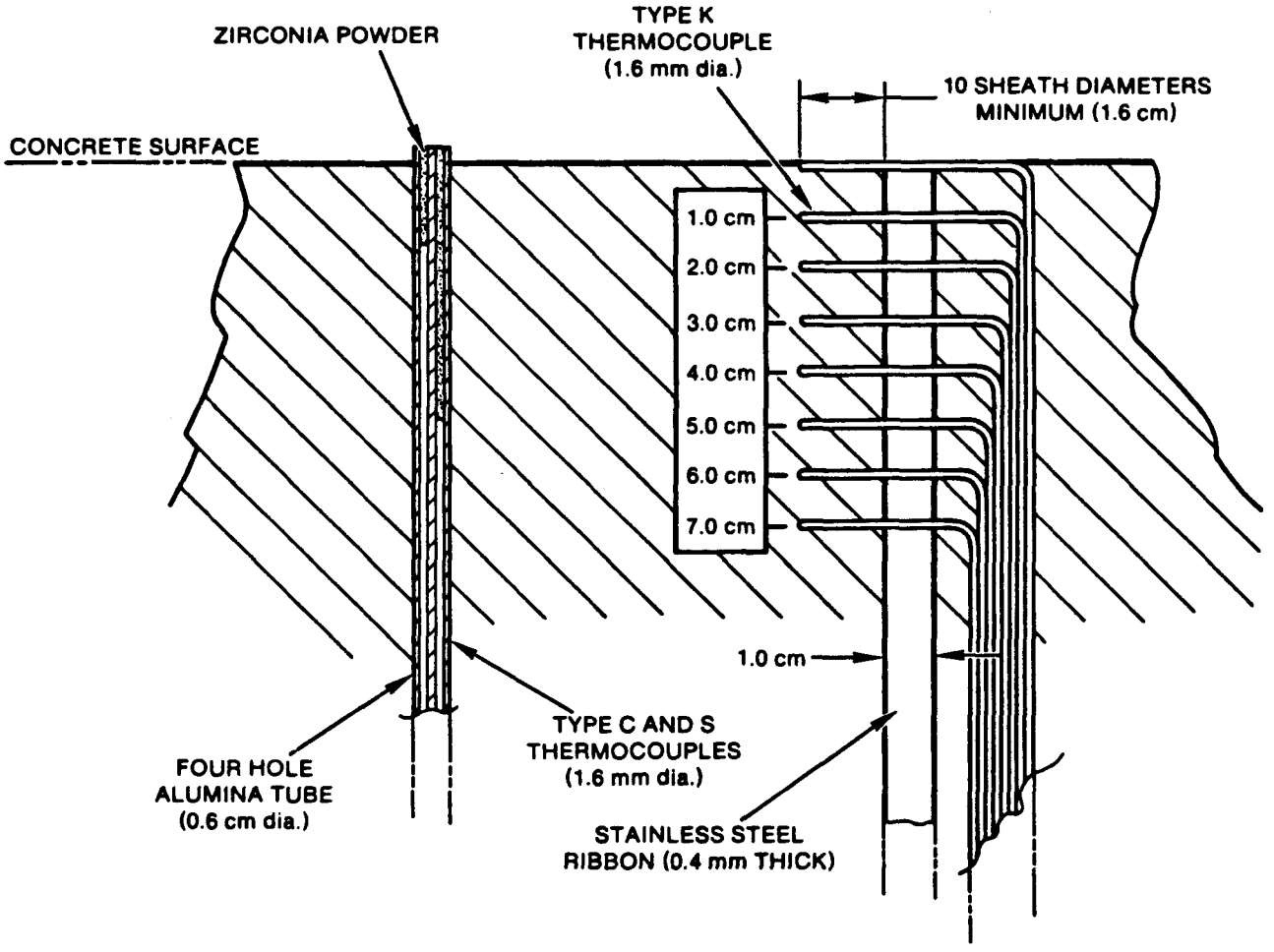

Figure 3.5 - Typical Thermocouple Arrays Cast into the Concrete.

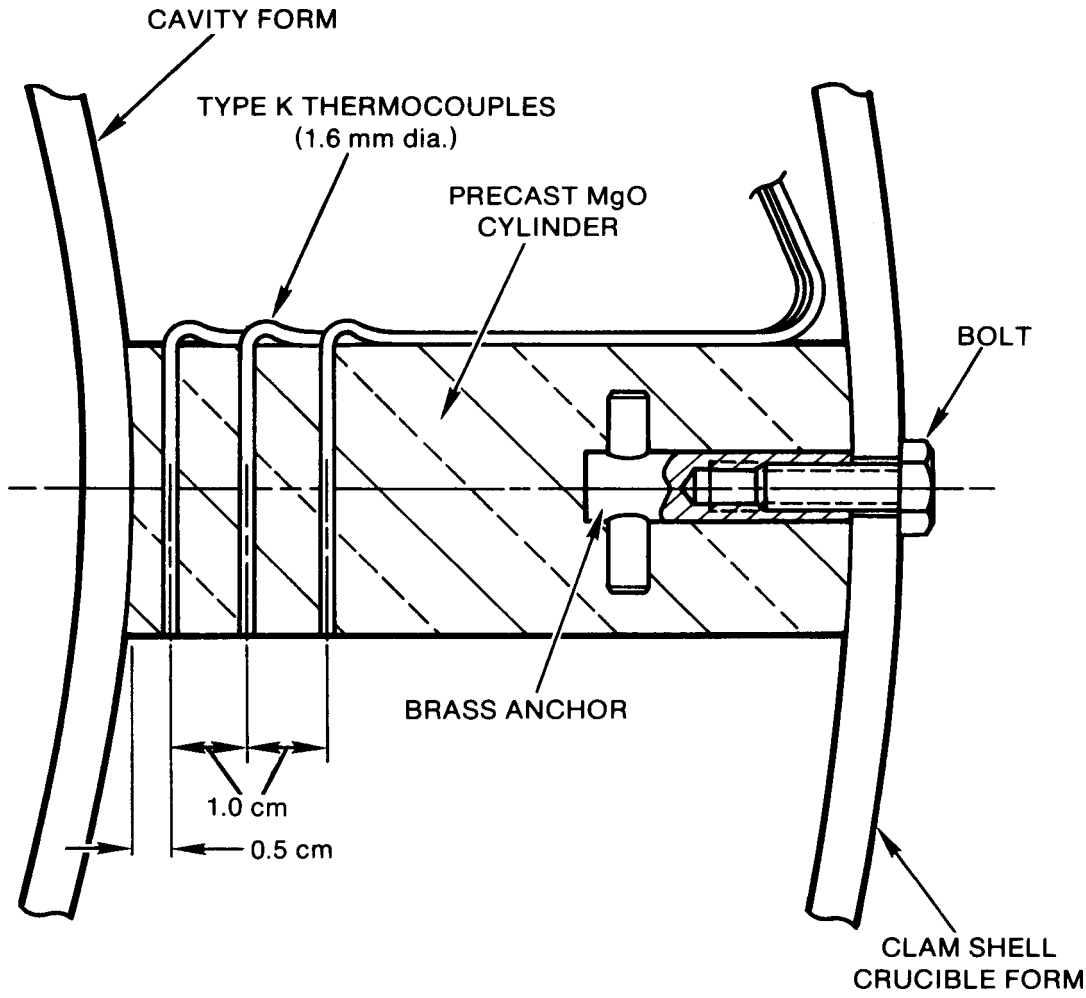

Figure 3.6 - Thermocouple Array Installation, MgO Annulus.

Table 3.3

Location of Thermocouples Cast Within the MgO Sidewall, SURC-4 (See Figure 3.4)

Array No.	Thermocouple No.	t (cm)	θ (degree)	z (cm)
1	M1	0.5	0	-20.0
	M2	1.5	0	-20.0
	M3	2.5	0	-20.0
	M4	9.0	0	-20.0
2	M5	0.5	0	-15.0
	M6	1.5	0	-15.0
	M7	2.5	0	-15.0
3	M8	0.5	0	-10.0
	M9	1.5	0	-10.0
	M10	2.5	0	-10.0
	M11	9.0	0	-10.0
4	M12	0.5	90	- 5.0
	M13	1.5	90	- 5.0
	M14	2.5	90	- 5.0
5	M15	0.5	90	0.0
	M16	1.5	90	0.0
	M17	2.5	90	0.0
	M18	9.0	90	0.0
6	M19	0.5	165	+ 5.0
	M20	1.5	165	+ 5.0
	M21	2.5	165	+ 5.0
7	M22	0.5	165	+10.0
	M23	1.5	165	+10.0
	M24	2.5	165	+10.0
	M25	9.0	165	+10.0
8	M26	0.5	270	+15.0
	M27	1.5	270	+15.0
	M28	2.5	270	+15.0
9	M29	0.5	270	+20.0
	M30	1.5	270	+20.0
	M31	2.5	270	+20.0
	M32	9.0	270	+20.0
10	M33	0.5	0	+35.0
	M34	1.5	0	+35.0
	M35	2.5	0	+35.0
11	M36	0.5	0	+50.0
	M37	1.5	0	+50.0
	M38	2.5	0	+50.0
	M39	9.0	0	+50.0

Table 3.4

Location of Thermocouples Cast Within the Crucible Cover, SURC-4 (See Figure 3.6)

Array No.	Thermocouple No.	t (cm)	θ (degree)	z (cm)
12	M40	10.0	0	0.5
	M41	10.0	0	1.5
	M42	10.0	0	2.5
13	M43	10.0	180	0.5
	M44	10.0	180	1.5
	M45	10.0	180	2.5

3.3 Introduction Coil

The induction coil used in the SURC-4 experiment was designed and built by Inductotherm Corporation. The coil was fabricated with 3.8 cm O.D. copper tubing having 20 turns with a pitch of 4.2 cm. The coil was supported by six equally spaced hard rock maple columns 7.5 cm x 5.5 cm x 100 cm long attached to the outside of the coil. The dimensions of the coil were 61 cm I.D. x 71 cm high. After the coil was placed around the crucible and centered on the stainless charge inside the aluminum containment vessel, fiberglass cloth was attached to the outside of the support columns. Fine MgO powder was placed between the crucible and coil and dry K/R Cast-98 was placed between the coil and fiberglass shroud. This was done to protect the coil from contact with debris, should the crucible fail.

3.4 Zirconium Delivery Tube System

The zirconium delivery tube was attached to the vertical leg of a stainless steel tee used to connect the gas and aerosol exhaust tube exiting the top of the containment vessel to the flow system. The delivery system is shown in Figure 3.7. Mounted to the top of the tee was a ball valve having a 3.8 cm diameter opening. Threaded to the inlet port of the ball valve was a 3.8 cm diameter black steel pipe 3 meters long. Fifty zirconium metal (3.3 cm diameter-7.6 cm long) cylinders were stacked end to end in the pipe. Each cylinder weighed 400 g. At the designated time in the experiment, the ball valve was opened, delivering 20 kg of zirconium to the molten stainless steel pool.

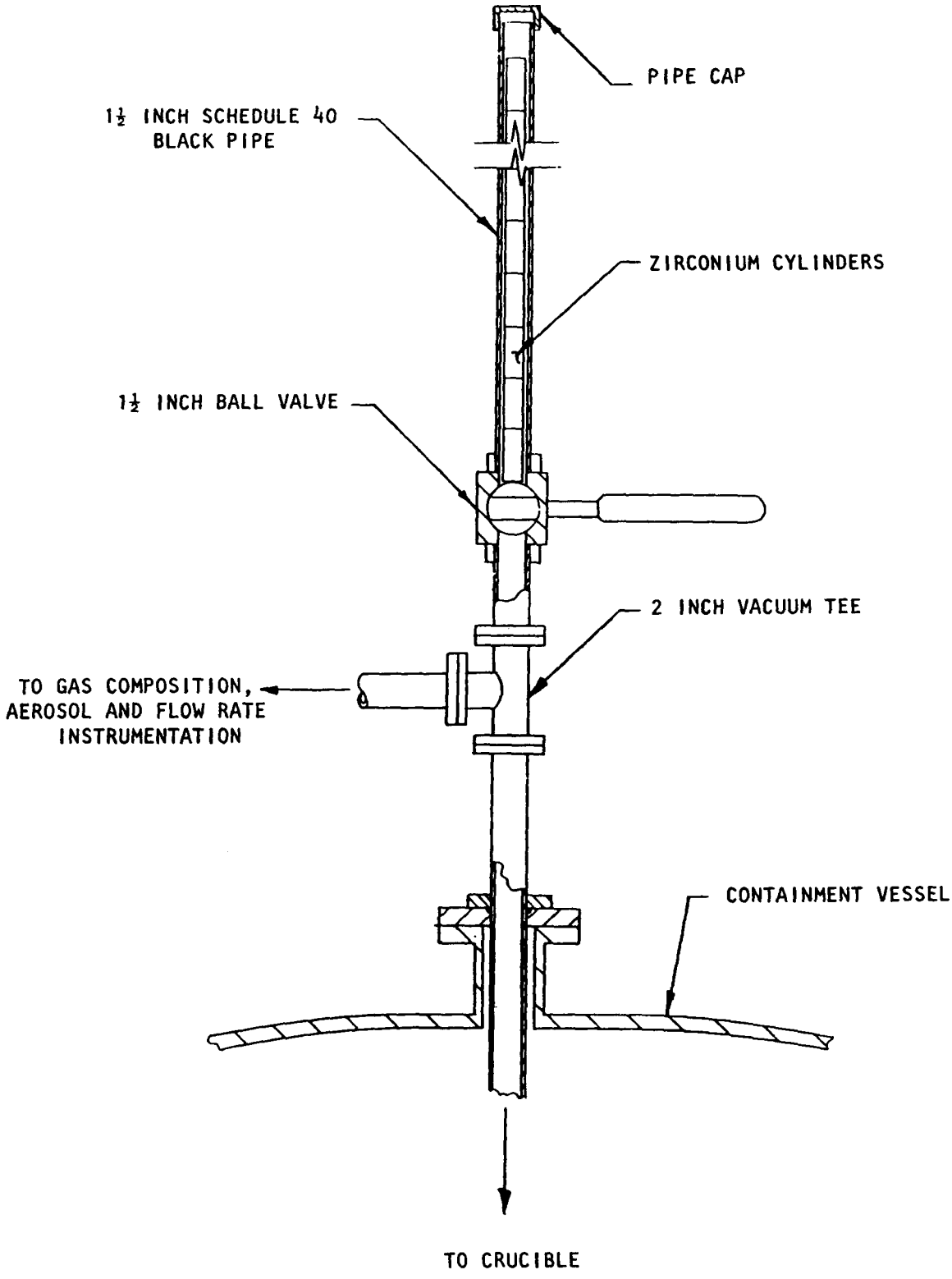

Figure 3.7 - Zirconium Delivery System

4. INSTRUMENTATION AND CALIBRATION

The HP 1000 acquisition system used 166 data channels to record the results of the SURC 4 test. Of these, 135 were thermocouple channels. Sixty thermocouple channels were used to monitor axial erosion in the concrete. An additional 45 thermocouple channels were used to record temperatures in the crucible sidewalls and lid. Eight thermocouples were located in the flow system to monitor the temperature of the effluent gases. Eight more thermocouples were used to monitor the temperature within the aerosol collection system, and the last fourteen thermocouple channels were used to record the meltpool temperature.

Thirty-one data channels were voltage channels. Ten of these were used to monitor pressure and flow through the system. One was used to record the relative opacity of the gas stream. Five more were used to measure the induction coil power and coolant flow levels. Four were used to monitor the composition of the effluent gas and the last 11 were used to record aerosol data. All of these instrument channels were recorded using the HP 1000 data acquisition system. Each channel was recorded every 10 seconds for the first 90 minutes of the test and every 3 seconds at times thereafter.

In addition to the HP 1000 data system, data were sampled and stored with the SEDS aerosol system (14 channels), the gas grab sample system (32 channels), the Infocon Mass Spectrometer (10 channels), and a video camera/recorder system.

4.1 Thermocouple Instrumentation

Sixty thermocouples divided into three groups were cast into the concrete slug of the interaction crucible. The relative locations of the thermocouples were discussed in Section 3.2. One typical array of 20 type K thermocouples was located on the axial centerline. Thermocouples in this array were spaced 1 cm apart. These thermocouples had a 0.16 cm diameter, 304 stainless steel, ungrounded sheathes. The sheath of each thermocouple in the axial array was bent at an angle of 90 degrees at a minimum of 10 sheath diameters from the tip. The bent tip of the thermocouple was located in a plane parallel to the concrete surface and thus parallel to the propagating isotherm. This was done to minimize the errors caused by heat conduction down the metal sheaths. Six sets of one type S and one type C (Tungsten - 5% Rhenium vs. Tungsten 26% Rhenium) thermocouples were mounted in alumina tubes and cast into the concrete. The alumina tubes were 0.64 cm in diameter and contained four 0.2 cm diameter holes in which the thermocouples were installed. The type S thermocouples installed in the alumina tubes were .16 cm diameter,and had ungrounded, tantalum sheathes. The type C thermocouples also had a 0.16 cm, ungrounded, tantalum sheath. These alumina tube arrays were cast into the concrete slug on a radius of 14 cm from the axis and at 60^{o} increments from an arbitrarily chosen 0 degree reference. The type S and the type C thermocouples were

installed for measuring melt temperatures. These thermocouples also provided some data on the concrete thermal response prior to ablation which complemented data from the arrays of type K thermocouples.

An additional 45 thermocoules were used to monitor the MgO sidewall and lid temperatures. Locations for these K-type devices are also described in Section 3.2. These type K thermocouples were similar in design to those cast in the concrete.

4.2 Gas Analysis Instrumentation

Gas composition analysis for the SURC 4 test was done using three techniques: An Infocon Model IQ200 mass spectrometer, an Infrared Industries Series 700 CO/CO_2 detector, and integral grab samples. The first two techniques yield real-time data which is viewed on-line and stored on computer disks. The grab samples are stored and analyzed post-test using both gas chromatography and mass spectrometry. A schematic layout of the SURC 4 gas composition sampling apparatus is shown in Figure 4.2.1.

Three different sampling locations were utilized. Location No. 1 was downstream of the main exhaustline gravel filter. Location No. 2 was between the containment vessel and the gravel filter and location No. 3 was inside the aluminum containment vessel. All sample lines for gas collection were 6.4 mm (.250 in) O.D. stainless steel with Swagelok stainless steel fittings and Nupro plug valves. The sample system manifold consisted of a normal and backup line and also a 40 psi argon source for backflushing filters. Inline filters used for SURC 4 were .3 micron Gelman HEPA filters with an element of acrylic copolymer.

Type K thermocouples were used to monitor sample gas temperatures in two different locations. A stainless steel cold trap with a volume of 75cc and cooled with liquid nitrogen was used to prevent condensibles from fouling the analysis equipment (Figure 4.2.2). A single Gast diaphragm-type air pump was used to provide flow for the gas analysis system. Flow indication for the system was measured by self-indicating rotameters. The CO/CO_2 supply was monitored with a Dwyer 0-10 scfh air rotameter and the grab sample line was monitored using a Sierra 0-15 lpm hot wire anemoneter.

Samples from the grab sample system were analyzed by gas chromatography/mass spectrometry using a Tracor MT-150g gas chromatograph and a Finnigan Mat 271/45 mass spectrometer. The samples were contained in 75cc stainless steel bottles with Nupro JB series regulating valves for closures. A Validyne absolute pressure transducer with a range of 1-1000 torr and a 0-10 volt output was used to mark the time of sampling events by monitoring manifold pressure. Vacuum in the bottles was maintained prior to sampling by a Welch two-stage belt drive vacuum pump with 175 lpm free air capacity. A remote control panel housed valve position

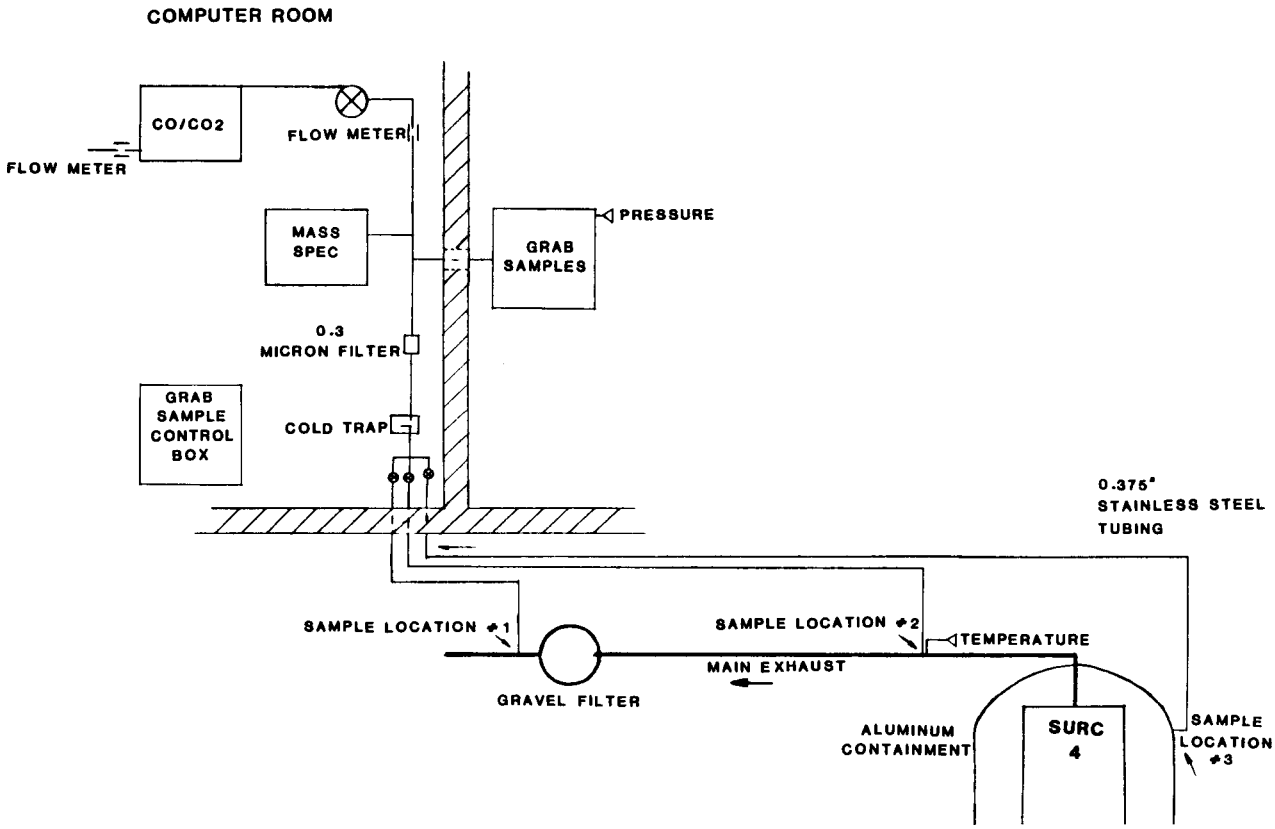

Figure 4.2.1 - SURC 4 Gas Sampling Schematic

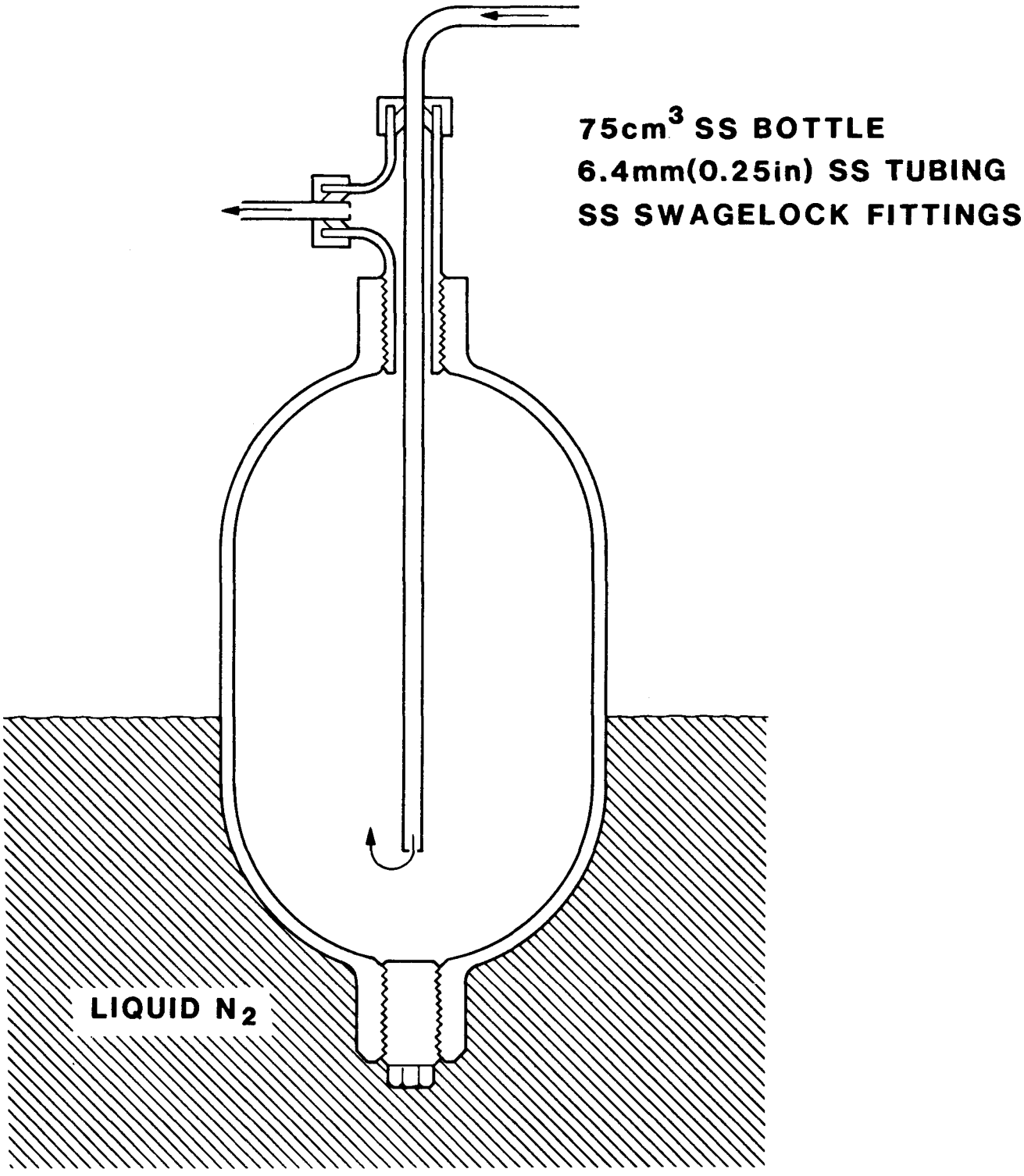

Figure 4.2.2 - Gas Analysis Cold Trap

indicator lights and four-position switches for controlling the multi-port valves used in acquiring grab samples (Figure 4.2.3).

The CO/CO_2 analyzer operates on an infrared absorption technique using Infrared Industries Models 702 and 703 detectors (Figure 4.2.4). Carbon monoxide is monitored over a range of 0-50% and carbon dioxide is monitored over a range of 0-20%. Response time is 5 seconds for 90% of the reading with a sensitivity of $\pm$ 2%. Output for the detectors to the data acquisition system is 0-5 volts.

Another diagnostic tool for gas data used for the SURC 4 test was a quadrupole residual gas analyzer, Inficon model IQ200 (Figure 4.2.5). This instrument was set up in the table display mode for scanning specifically selected masses corresponding to the gas species of interest: H_2, H_2O, CO, O_2, Ar, and CO_2. A pressure converter manifold with a 10 torr orifice, 27 lpm vacuum pump, and 0.5 mm (.020 in.) I.D. capillary tube provided the ability for continuous sampling from a pressure of up to 2 atmospheres at the sample source down to 10 torr at the analyzer supply where the associated 150 lps turbo pump could maintain 10^{-6} torr at the analyzer head. A Faraday cup detector was used to produce the currents for analysis.

For data acquisition, a Hewlett Packard 1000 (right side - Figure 4.2.4) series computer system was used with acquisition rates of 15 seconds for the test warm-up and 5 seconds for the majority of the run where test events necessitated a faster rate. Inputs from gas composition data were: temperature from the expansion chamber thermocouple; absolute pressure, 0-10 volts for 0-1000 torr; percent CO, 0-5 volts per 0-50%; and percent CO_2, 0-5 volts per 0-20%.

Layout and Location

The location of the various support components and analysis equipment can be seen in Figure 4.2.1. The stainless steel filters for the gas sample lines were mounted on the expansion chamber flange approximately 15 cm downstream from the end of the sample tube which was located inside the expansion chamber. The HEPA filter, cold trap, and argon backflush manifold were located just upstream of the grab sample line approximately 8.5 m from the test article. The diaphragm air pump and flowmeter were located at the CO/CO_2 monitor supply line. Temperature inside the expansion chamber was measured by one of the type K thermocouples while another type K thermocouple measured the gas temperature at the mass analyzer sample tee.

The grab sample system tied into the main gas line using a 6.4 mm (.250 in) O.D. stainless steel tube with a dead volume of 50cc. The grab sample equipment rack housed the sample bottles, multi-port valves, and pressure transducer and were located outside on the test pad approximately 7.6 m (25 ft.) from the SURC 4

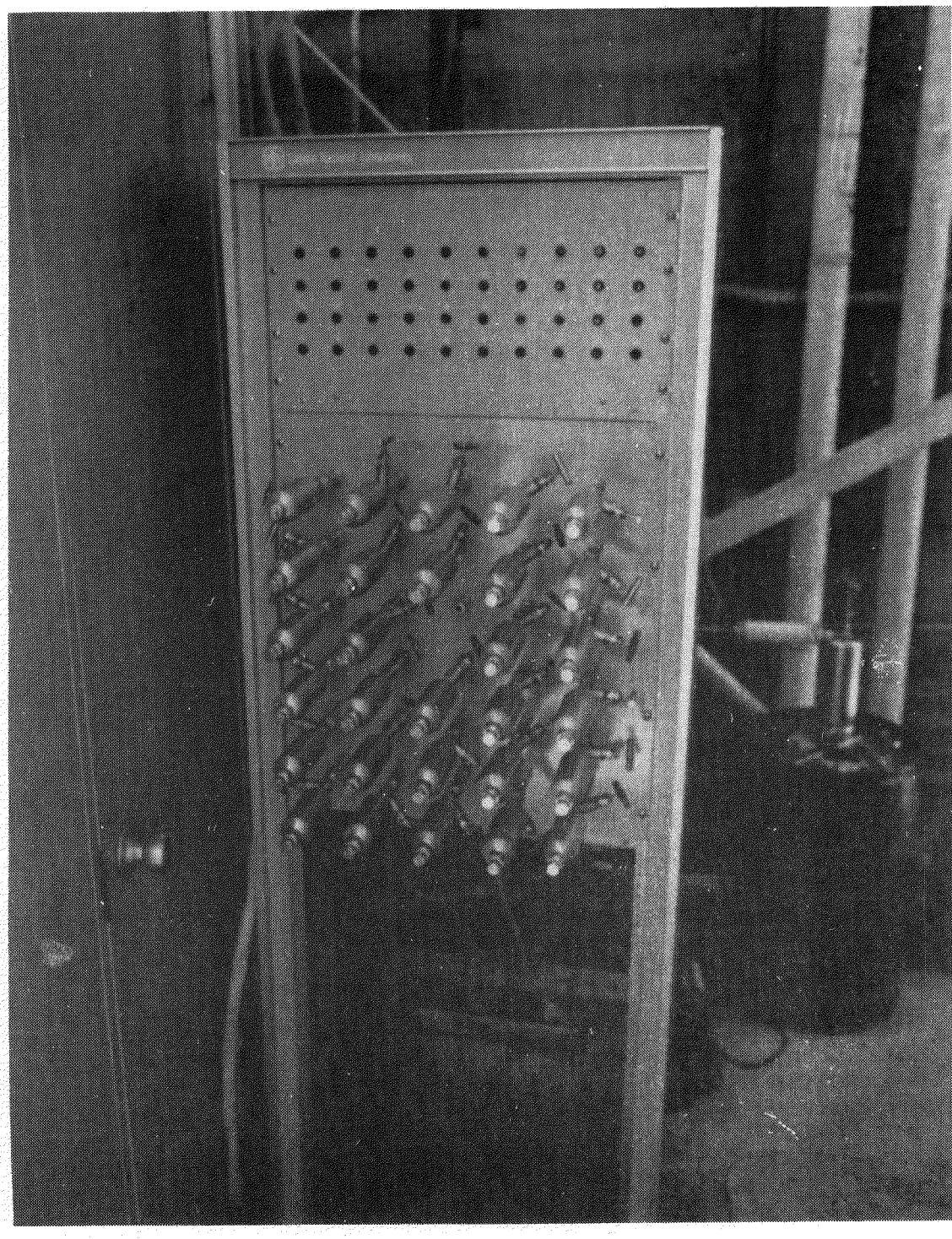

Figure 4.2.3 - Grab Sample Hardware

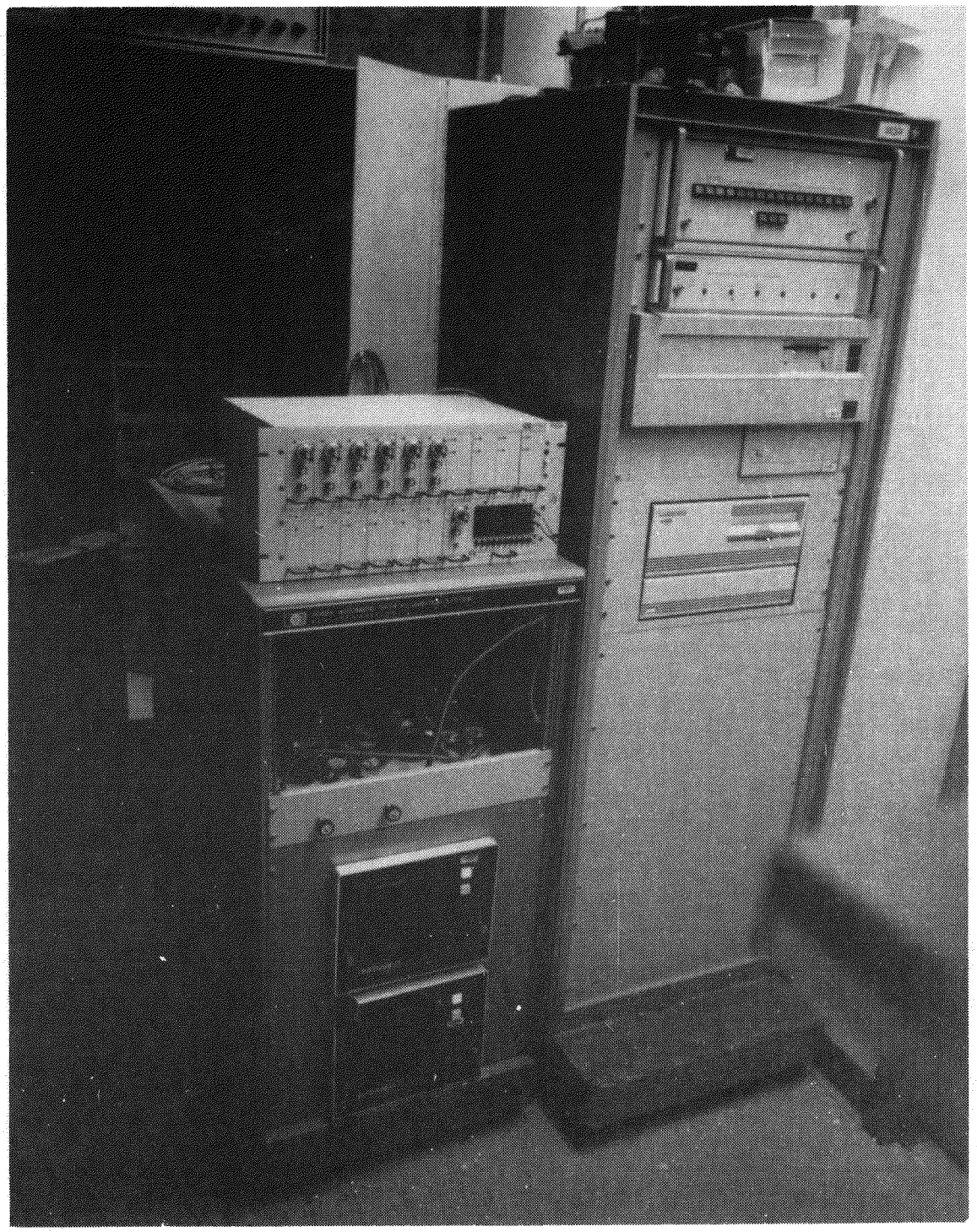

Figure 4.2.4 - CO/CO_2 Monitor Hardware

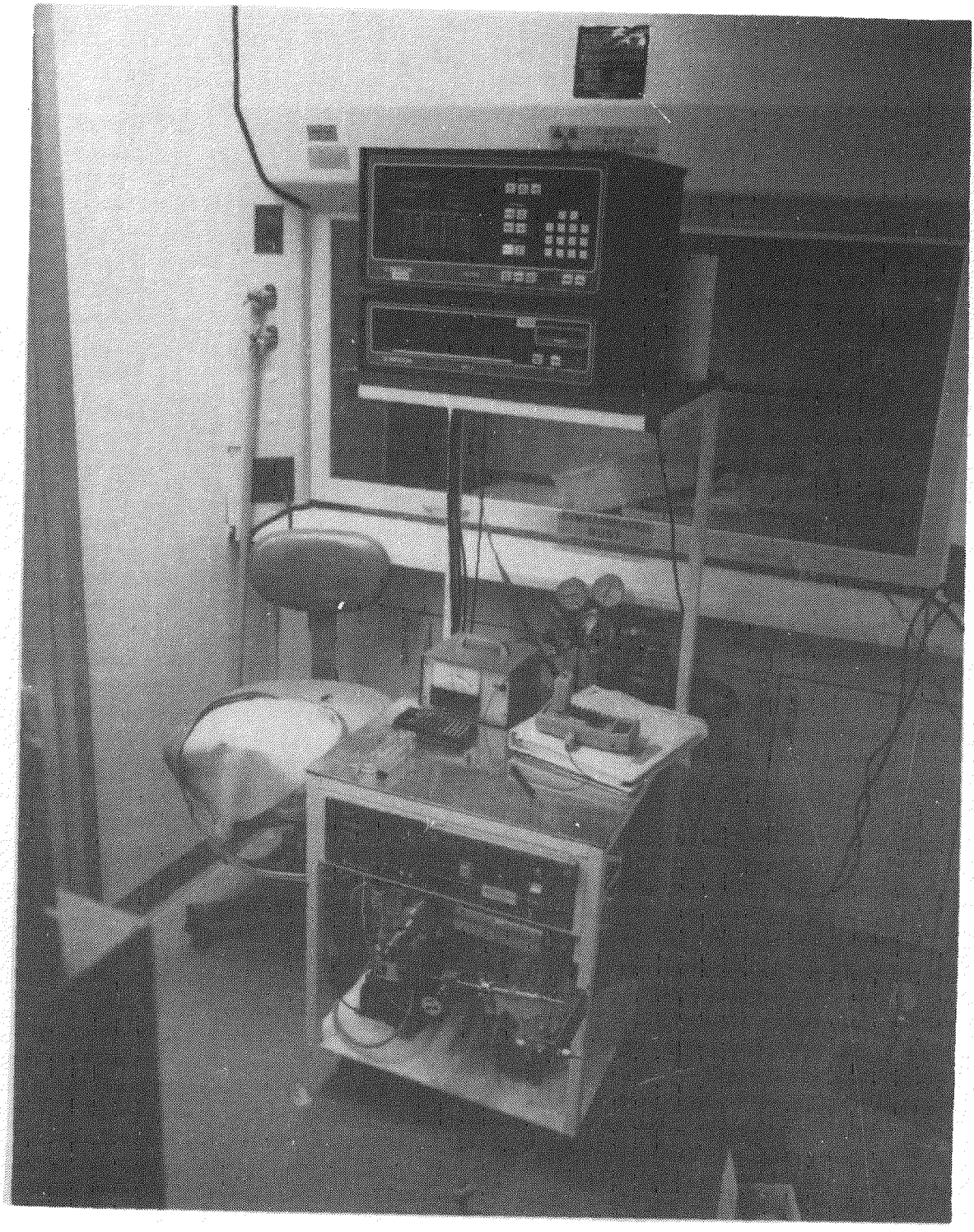

Figure 4.2.5 - Mass Spectrometer Hardware

containment vessel. The control panel was located in the shielded computer room along with other instrumentation.

The CO/CO_2 instrument was located in the shielded computer room where it was connected to the main gas line by a 6.4 mm (.250 in) O.D. stainless steel tube. A diaphragm pump and flowmeter supplied the sample gas from the main gas stream for the infrared detectors. The distance upstream to the SURC 4 test article was 9.5 m (31 ft).

The Inficon mass spectrometer was also located in the shielded computer room and was connected to the main gas stream by a .5 mm (.020 in) I.D. capillary tube and was situated approximately 10 m (33 ft) from the test vessel.

Calibrations

Calibrations for the different gas sampling equipment were accomplished with primary standard calibration gas mixtures from Alphagaz. For the grab sample analysis, mixtures of 2.0% CO, 10.0% CO_2, 88% Ar (Alphagaz Mix 1) and 45.0% CO, 15.0% CO_2, 40% N_2 (Alphagaz Mix 2) were analyzed in addition to the SURC 4 test samples. Results from these calibrations (grab samples 10A and 45N) are listed on Table 4.2.1.

The CO/CO_2 analyzer was calibrated according to the operating reference manual using a gas mixture of 2.0% CO, 10.0% CO_2, 88% Ar as well as pure nitrogen as a gas. This calibration procedure was accomplished pre-test. During the test (at time 150 minutes) and following the test completion, the zero and full range were again checked to ensure that there was no significant drift.

The calibration gas mixture of 2.0% CO, 10.0% CO_2, 88% Ar was used for the mass spectrometer.

Following the operational checks performed in the laboratory, the CO/CO_2 monitor and mass spectrometer were placed in their test locations in the sample system. Standard gas mixtures of 45.0% CO, 15.0% CO_2, balance N_2 and 2,0% CO, 10.0% CO_2, balance Ar, as well as a welding mixture of 25% CO_2 in Ar were introduced at different times into the expansion chamber as an operational check on these two instruments. After the test, the calibration procedure for the CO/CO_2 monitor and the mass spectrometer was completed again and showed no significant drift. Operational checks of the support components included response of the thermocouples from below ambient to above ambient as compared with other type K thermocouples in the same environment. Flow measurements through the self-indicating rotameters were matched with several other similar flowmeters. Output from the pressure transducer was monitored while changing the grab sample manifold configuration from pressure to vacuum conditions.

Table 4.2.1

RESULTS OF GRAB SAMPLE ANALYSIS
ON CALIBRATED GAS USING GAS CHROMOTOGRAPHY

SAMPLE #	CO(%)	CO_2(%)	N_2(%)	AR(%)
Alphagaz Mix 1	2.0	10.0	0.	88.0
Grab Sample 10A	2.03	9.85	N.D.*	87.90
Alphagaz Mix 2	45.0	15.0	40.0	0.
Grab Sample 45N	44.52	15.58	39.84	N.D.

*NOT DETECTED

Procedures

Gas flow through the sample line was established several minutes before the start of the test by energizing the diaphragm pumps. The flow was manually regulated to provide 6 lpm to the measurement devices. Plugging of the sample line filters was anticipated. The sample line flow was monitored every 2-5 minutes and, if a substantial decrease in flow was indicated, argon was introduced briefly into the sample line to backflush the stainless steel filters.

The grab sample bottles were evacuated before the test and then individually subjected to vacuum just prior to sample collection. Samples were taken manually. Times for the samples were recorded on computer disk as spikes in the pressure. Because of the dead volume in the grab sample line leading to the main gas stream, two grab samples were taken per sampling event. The first sample was presumed heavily contaminated with residual gases in the sampling line while the second sample more accurately reflected the composition of gases being produced at the time of the sampling event. After the test, two additional sample bottles were filled with calibration gas.

The CO/CO_2 monitor was warmed up for at least 30 minutes before the pre-test calibrations. The data acquisition recorded the output signals and the visible readout was monitored locally at the instrument and remotely in the control room. Following the test, another calibration check was performed on the instrument.

The mass spectrometer system was in operation under a low vacuum of 100 millitorr for one week prior to establishing a vacuum of 10^{-6} torr for three days before the test date. The analyzer display was continuously monitored locally and on-line data were recorded every few minutes during periods of low activity and almost every minute during more critical events.

The output from the type K thermocouple installed in the expansion chamber was continuously monitored and recorded by the data acquisition system while the output from the other thermocouple mounted in the sample stream was monitored about every 5 minutes with a portable temperature meter.

4.3 Flow Device Instrumentation

Five different devices were used to measure the gas flow rate in SURC 4: A 1.02 cm orifice plate, a laminar flow element, a turbine meter, a Rockwell 415 gas clock, and a Rockwell 750 gas clock. Figure 4.3.1 shows a flow train schematic of the hardware for SURC 4.

The flow system consisted of a series of piping, tubing, and a gravel filter instrumented with a variety of devices for measuring gas flow rates. The flow system starts with an exhaust tube that is mounted in the top part of the containment vessel and is fit into the crucible cover. The tube material was 304 stainless steel, having dimensions of 5.1 cm O.D. x 0.17 cm wall x 1.2 meters long. Several 0.32 cm diameter holes were drilled in the sidewall of the tubes in the section residing inside the containment vessel. These holes were used to provide a pathway for the argon gas used to purge the experimental chamber and provide background gas for gas composition measurements. A 5.1 cm diameter 304 stainless steel vacuum tee was mounted to the top of the exhaust tube. The vertical flange of the tee was fitted with a 5.1 cm diameter ball valve used to deliver the zirconium metal. The horizontal flange of the tee was connected to a 5.1 cm O.D. x 0.17 cm wall x 1.8 meter long length of 304 stainless steel tubing. The end of this tubing was fitted with a 5.1 cm O.D., 304 stainless steel flanged cross. The centerline of all the flange ports on the cross were positioned in a parallel plane. The cross was used to mount an opacity meter and a nozzle for sampling the aerosol. The cross was adapted to a 2.0 meter section of 5.1 cm diameter 150 pound schedule-40 black steel pipe via a 5.1 cm bolted flange. A 1.02 cm diameter, sharp-edge, concentric orifice was mounted between two flanges 1.0 meters from the stainless steel cross. Two Validyne pressure transducers were connected in parallel across pressure taps machined in the flanges. Another pressure transducer was connected to the flange upstream of the orifice to measure gas flow pressure.

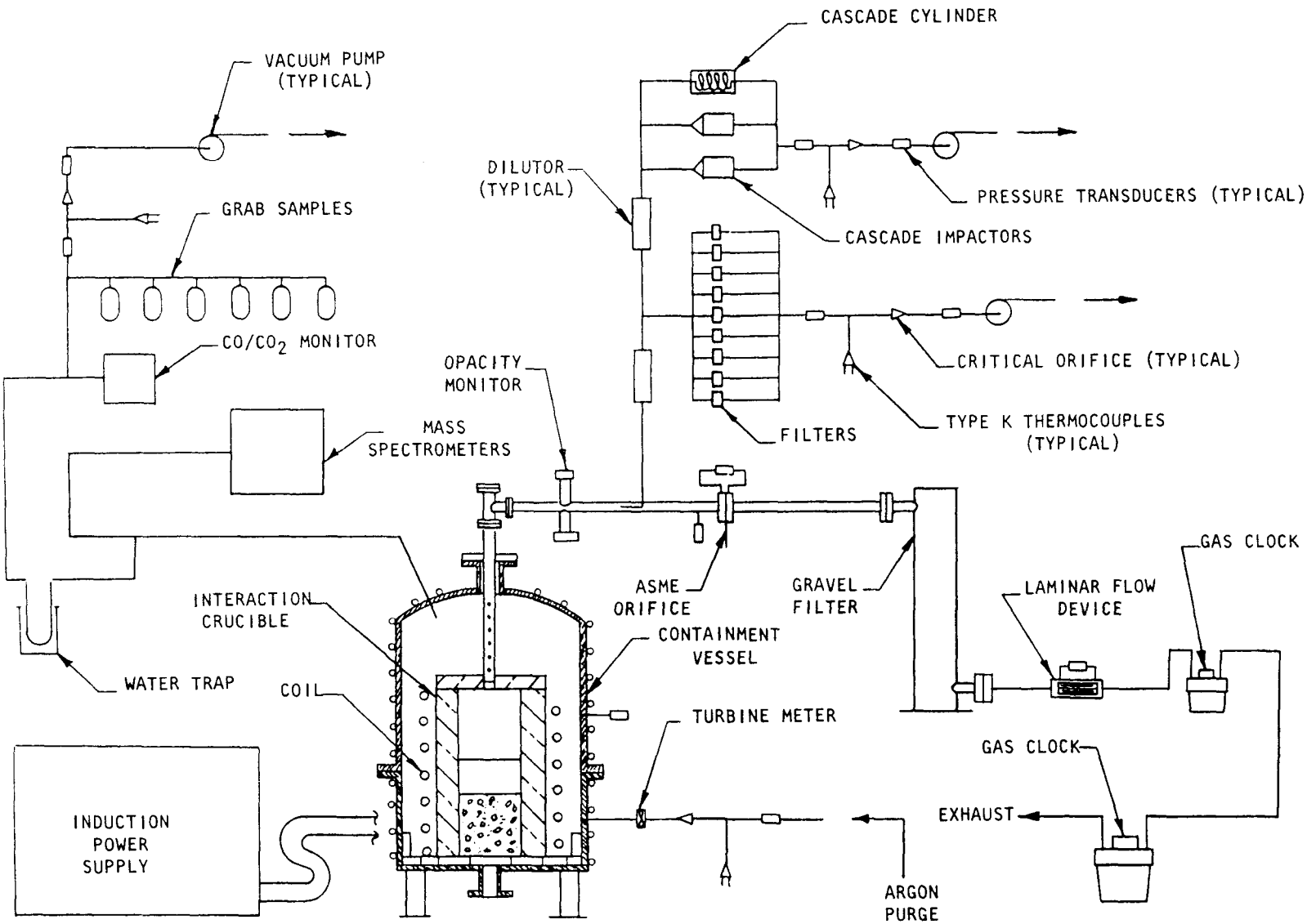

Figure 4.3.1 - Flow Train Schemmatic

The section of pipe containing the orifice was connected to the top of a gravel filter with a 1.1 meter length of 5.1 cm black steel pipe using a combination of flanges and fittings. The gravel filter had an inside diameter of 25.4 cm and was filled with sand to a depth of 1 meter. The gravel filter was used to filter aerosols, preventing them from entering the laminar flow device and the two gas clocks located downstream. The filter was designed (see Appendix D) and tested to remove 99% of the aerosols at flow rates of 300 slpm with a backpressure of less than .25 psig. Connected to the outlet of the gravel filter were two lengths of 2.54 cm schedule 40 black steel pipe, 50.8 cm long. A laminar flow element (LFE) was installed between the two pipe sections. The LFE was instrumented with a Validyne differential pressure transducer. The end of the flow train was terminated by two Rockwell gas clocks mounted in series. The gas clocks were connected using 2.5 cm schedule 40 black steel pipe fittings.

The principles of operation and pertinent equations for orifice plate flowmeters may be found in (Baker and Pouchot, 1983). The orifice plate flowmeter is probably the most widely used flowmeter in service today. It is found mostly in field use and is simple, rugged, reliable, accurate, and inexpensive. Orifice plates used for gas measurement are considered to be accurate to 1-2% based on physical dimensions and published correction factors. It should be noted, however, that uncertainties in differential pressure (the measured parameter), temperature, line pressure, and gas density can easily overwhelm the uncertainty from the laboratory calibration. One disadvantage of the orifice plate is that a 10:1 change in differential pressure results from only a 3:1 change in flow due to the square root relationship between differential pressure and flow. Hence, 50% of expected full flow is measured in 20% of expected differential pressure. This makes low flow rates difficult to measure accurately.

The orifice flowmeter used in the SURC 4 experiment had an opening of 1.02 cm and was mounted between flanges in a 5 cm I.D. pipe. This pipe was mounted to the SURC 4 expansion chamber so that 80 cm of straight pipe preceded the flow device and at least 50 cm of straight pipe followed the device. Three Valdyne pressure transducers were used in conjunction with the orifice plate. Two of these were used to record the differential pressures across the plate and had operational ranges of 0-2 psia and 0-5 psia. The third pressure transducer was used to measure the system pressure and had a range of 0-10 psig. All of these devices were calibrated as a set--both in the laboratory and at the test site--using several different gases and a range of flow rates. Results of the laboratory calibration are shown graphically in Figure 4.3.2.

The laminar flow element (LFE) is a group of capillary tubes bundled together to form a matrix such that the flow through each passage is laminar, even though the total flow upstream of the device may be turbulent. The LFE is not as sensitive to piping

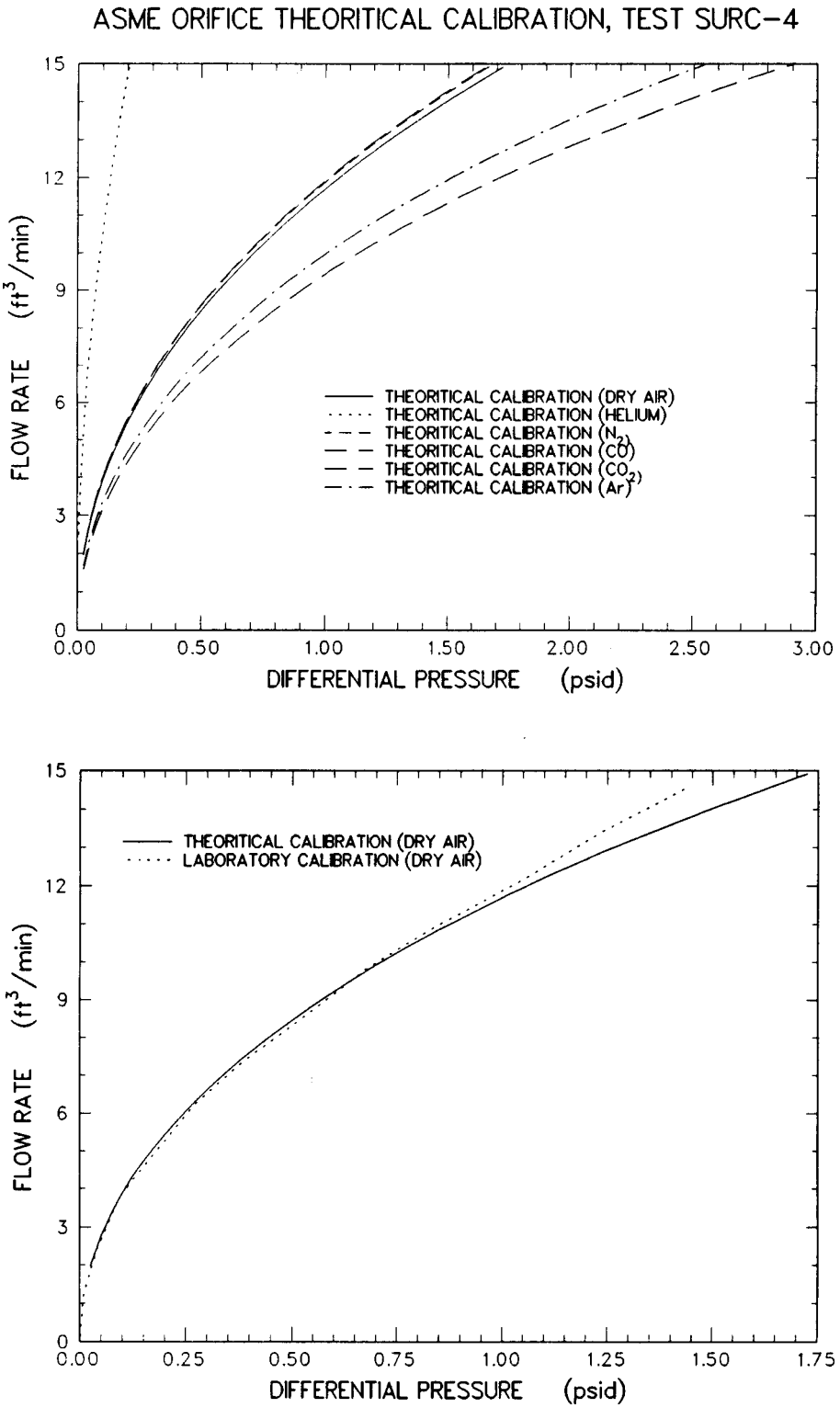

Figure 4.3.2 - Orifice Flowmeter Calibration

configuration as an orifice plate so that an inlet pipe length of one or two pipe diameters (instead of 5 or 10) is usually sufficient to provide a satisfactory flow pattern. The equations governing the operation of LFE devices are given in (Baker and Pouchot, 83). One advantage of an LFE is that the relationship between differential pressure (the measured parameter) and flow is linear for the range of flows for which it is designed. Calibration of the device should be done against a primary standard and is a function of gas viscosity which is itself a function of gas composition. A potential disadvantage is that the small passages in the flow matrix are susceptible to plugging when the gas contains aerosols or water vapor.

The LFE used in the SURC 4 experiment was designed and built by Calibrating and Measuring Equipment (CME) and has a nameplate flow range of 0-300 slpm for air at standard conditions. The LFE is contained in a 50 cm pipe with an I.D. of 3.6 cm. Differential pressure is measured using a Valdyne differential transducer with a range of 0-2 psia. The device was calibrated both in the laboratory and at the test site. Laboratory calibration (Figure 4.3.3) was done using a variety of gases with NBS-traceable critical orifices as the primary standard.

The turbine flow meter (Baker and Pouchot, 1983) consists of a freely rotating propeller mounted concentrically in a pipe. The force of the gas striking the propeller blades causes them to rotate at an angular velocity proportional to the gas velocity so that the volumetric gas flow is directly proportional to the rotational speed of the propeller. A magnetic pickup in the rotor causes a voltage to be generated in an external electrical coil. The magnitude of the voltage is then directly proportional to the volumetric flow rate for the designated flow range of the device. The output of the device is in actual liters per minute (ALPM) and must be corrected to standard conditions. Turbine flow meters must be calibrated to determine the coefficient of discharge but once this is done are considered to be accurate to about 1%. Some advantages of the turbine flowmeter are that it is insensitive to gas composition and that it produces a linear response over its design flow range. Some disadvantages are that it is susceptible to drag if the gas contains aerosols or water and that the magnetic pickup can be affected by an induction or electrical field.

The turbine meter used in SURC 4 was made by Flow Technology, Inc., and was contained in a 50 cm long pipe with an I.D. of 1.3 cm. The operating range of the device is 0-280 slpm as indicated by a voltage output of 0-10 volts dc. The turbine meter was calibrated in the laboratory and at the test site using argon, He, air, and CO_2. Results of the laboratory calibration are shown in Fig. 4.3.4.

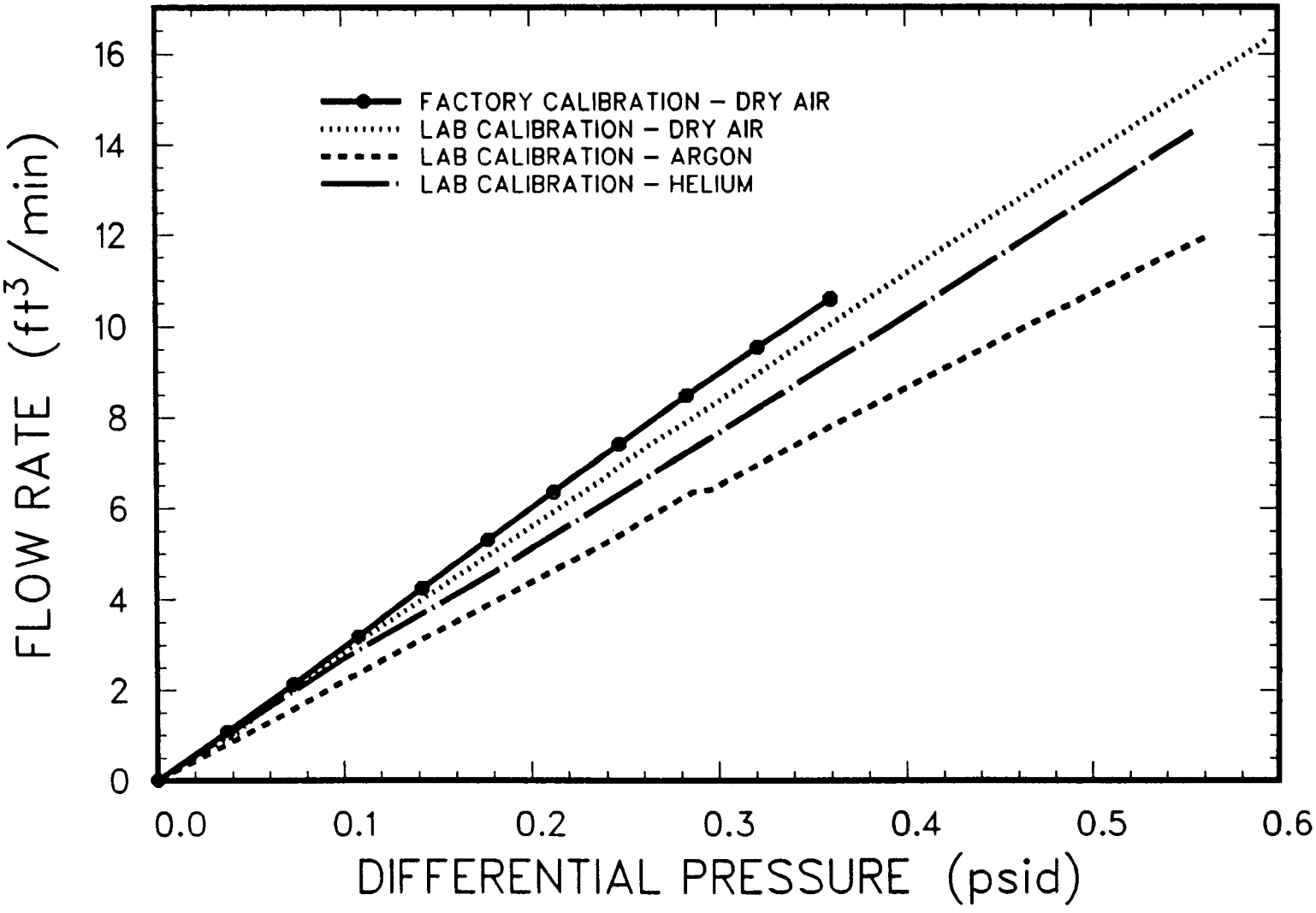

Figure 4.3.3 - LFE Flow Rate Calibration

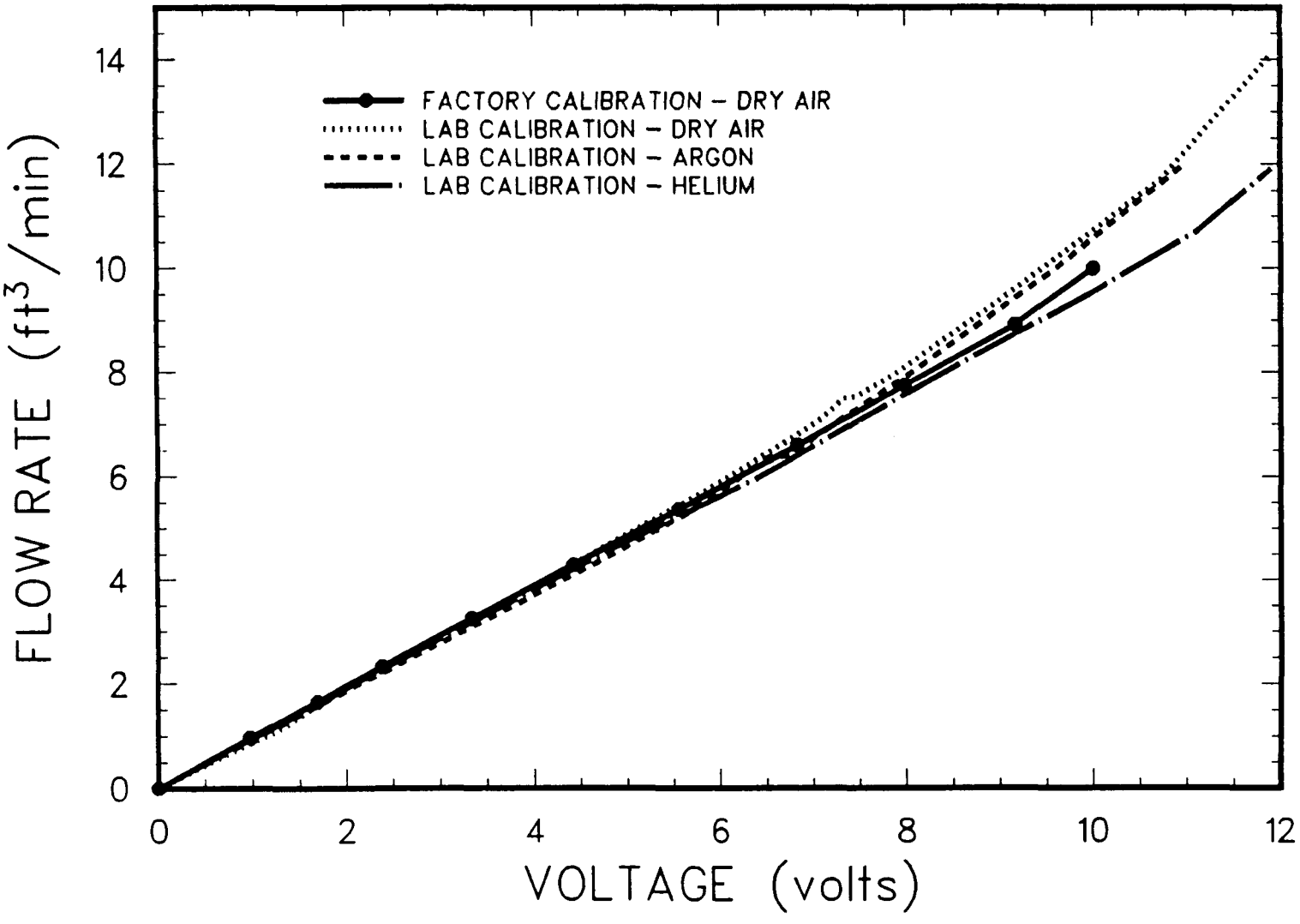

Figure 4.3.4 - Turbine Meter Calibration

The Rockwell gas clocks used in SURC 4 are dry gas meters. These devices have four bellows-type chambers that alternately fill and empty known volumes of gas. The slide valves that control the cycle are attached to mechanical counters that totalize the volume of gas that passes through the meter. These devices are very rugged and bulky and register the total volume in actual liters per minute (ALPM). They are impervious to the aerosol or water content in the gas and measure total volume independently without corrections for density or viscosity. Once the volume of the bellows is known, the accuracy of the gas clocks is within 1%. The major disadvantages of the dry gas meter are its size and lack of sensitivity to transient flow perturbations.

The Rockwell 415 gas clock has a stated operational range of 0-200 LPM at STP. The device has a sensitivity of 28.3 liters per cycle. The Rockwell 750 was also manufactured by Rockwell and has an operational range of 0-350 LPM at STP. The Rockwell 750 gas clock has a sensitivity of 283 liters per cycle. Both devices were calibrated in the laboratory and at the test site with different gases and a range of flow rates. The laboratory calibrations are shown in Figures 4.3.5 and 4.3.6.

After the experimental setup was completed for the SURC 4 test, an in-situ calibration was performed using N_2 and Ar. This was done to insure that the laboratory calibrations were still valid, to evaluate the entire flow system, and to determine the system pressure as a function of flow rate. Results of the in-situ calibration for the orifice flowmeter, LFE, turbine meter, and system pressure are given in Table 4.3.1. In addition, a systems leak test was performed by valving off the flow train and pressurizing the crucible and expansion chamber. A pressure decay chart for this procedure is given in Table 4.3.2. Based on the in-situ checks, the initial leak rate from the crucible was calculated to be 8.5 slpm at a system pressure of 1.0 psig or 5% of the 165 slpm flow rate.

Table 4.3.1

In-Situ Calibration* for SURC 4 Flow Devices

750 Gas Clock Flow (SLPM)	Inlet Turbine Flow (SLPM)	Orifice Plate Flow (SLPM)	LFE Flow (SLPM)	System Pressure (psig)
227	237	222	217	1.8
182	199	184	177	1.4
148	158	144	141	1.0
106	118	108	107	.7
80	90	78	74	.4
50	60	50	47	.1
-	37	30	30	.1

*Calibration done with argon gas

Table 4.3.2

Pressure Decay and Leakrate for SURC 4A

Expansion Crucible/Flowtrain*

Time (min)	Pressure (psig)
0.	2.25
1.0	2.05
3.0	1.68
5.0	1.38
10.0	.82
15.0	.47

*Calibration with argon gas

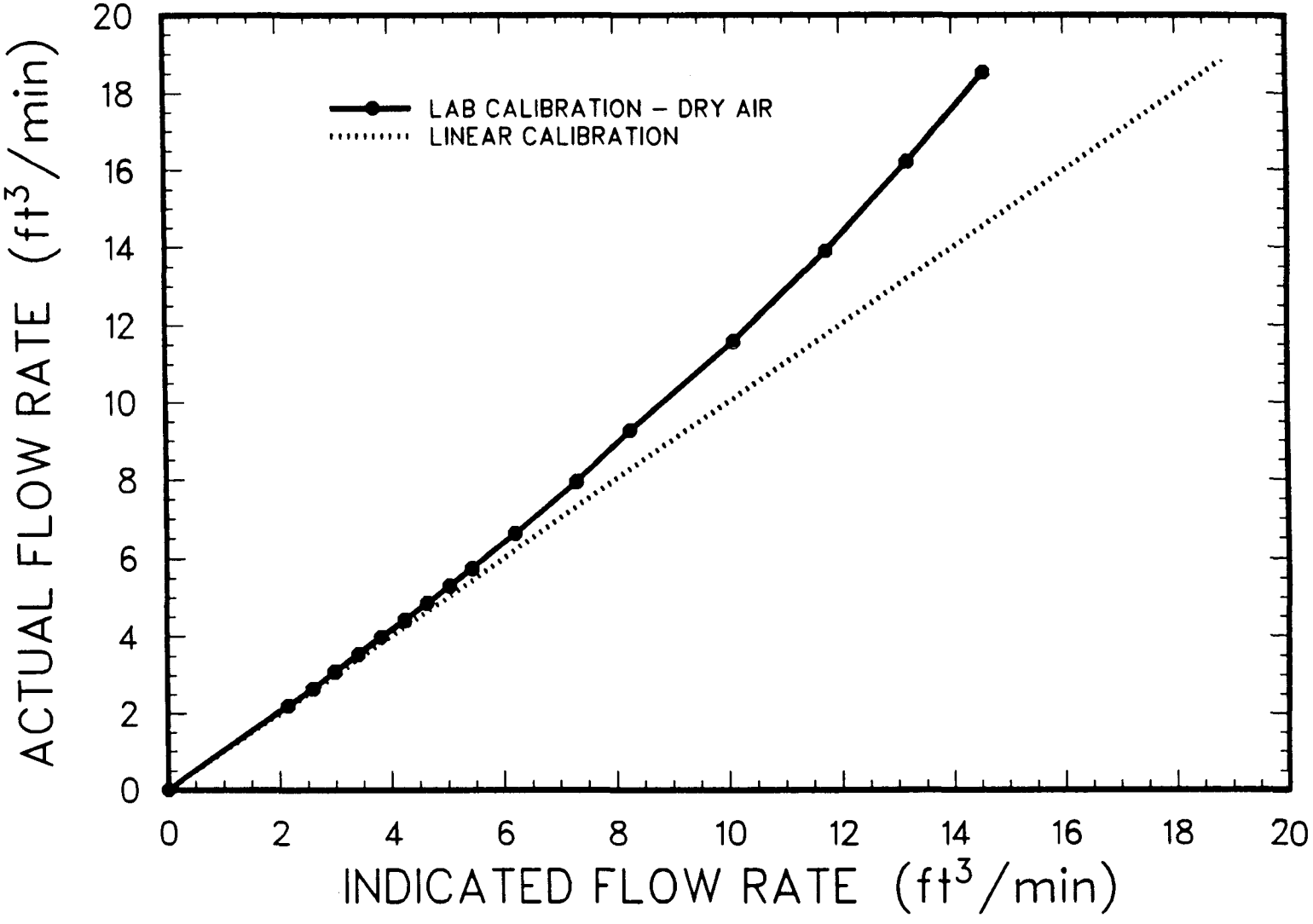

Figure 4.3.5 - Rockwell 415 Calibration

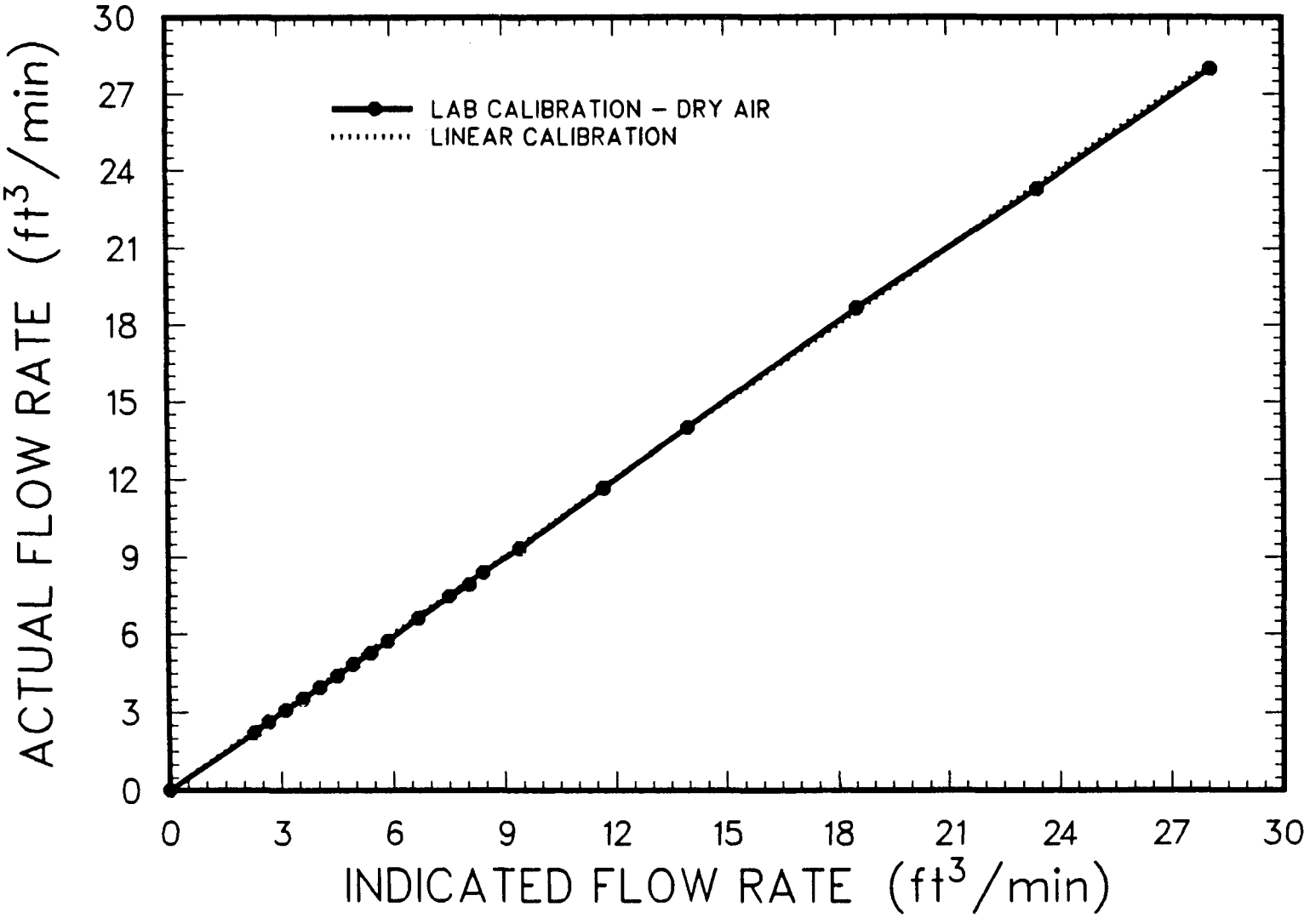

Figure 4.3.6 - Rockwell 750 Calibration

4.4 Aerosol Instrumentation

The interaction of molten material with concrete produces an aerosol. In the context of nuclear reactor accidents, the aerosol produced by the interaction of molten core debris with concrete basemat material is a potential source of radionuclide release (Brockmann, 1987).

It is, therefore, important to characterize this aerosol with respect to its mass source rate, concentration, composition, and transport properties. The aerosol source term is defined as the mass source rate of aerosol generation, its composition, and its size distribution, as well as additional parameters such as the dynamic shape factor which aids in the description of the aerosol's transport behavior and the agglomeration shape factor which aids in the description of the aerosol's coagulation behavior. Measurements of the aerosol source term resulting from the melt/concrete interaction experiments provide a data base against which to test predictive models of aerosol release and formation (Powers, et. al, 1986).

The SURC-4 test contained aerosol instrumentation designed to provide data which would allow calculation of the aerosol source term. Specific measurements were made in order to determine the aerosol mass generation rate, aerosol size distribution, and aerosol composition. Figure 4.4.1 is a flow chart illustrating how each of the three source term parameters mentioned above is determined. The aerosol mass generation source rate is the product of the melt/concrete gas evolution rate and the aerosol mass concentration in the evolved gas. The gas flow train described in Section 4.3 measures the gas evolution rate. The aerosol mass concentration is measured primarily by filter samples; however, impactor samples and an opacity meter provide additional means of aerosol mass concentration measurement. The size distribution of the sampled aerosol is primarily determined by cascade impactor samples. The cascade cyclone gives an additional means of determining the integral aerosol size distribution over an extended sampling time.

Aerosol composition is determined from elemental analysis of the aerosol collected on the filters. A size dependent aerosol composition is obtained from analysis of the aerosol collected by the cascade cyclone.

Brockmann, et al. (1987) are developing a technique for measurement of aerosol dynamic shape factors. Dynamic shape factor determination can be made by inclusion of additional instrumentation on future tests.

The sample extraction dilution system (SEDS) comprised of the filters, cascade impactors, cascade cyclone, and the necessary dilution systems and flow control is shown schematically in Figure 4.4.2. An aerosol sample is drawn into the SEDS through

a gooseneck sample probe (from Andersen, Inc.). The probe has a nozzle with a 1/8" inside diameter opening located coaxially in the center of the exhaust line. The nozzle expands into a 5/8" inside diameter tube. The cyclone samples the undiluted aerosol. The primary dilution is performed on the sample and this is sampled by the filters. A secondary dilution is performed and this aerosol is sampled by the impactors.

SURC-4 AEROSOL INSTRUMENTATION/
AEROSOL SOURCE TERM FLOW CHART

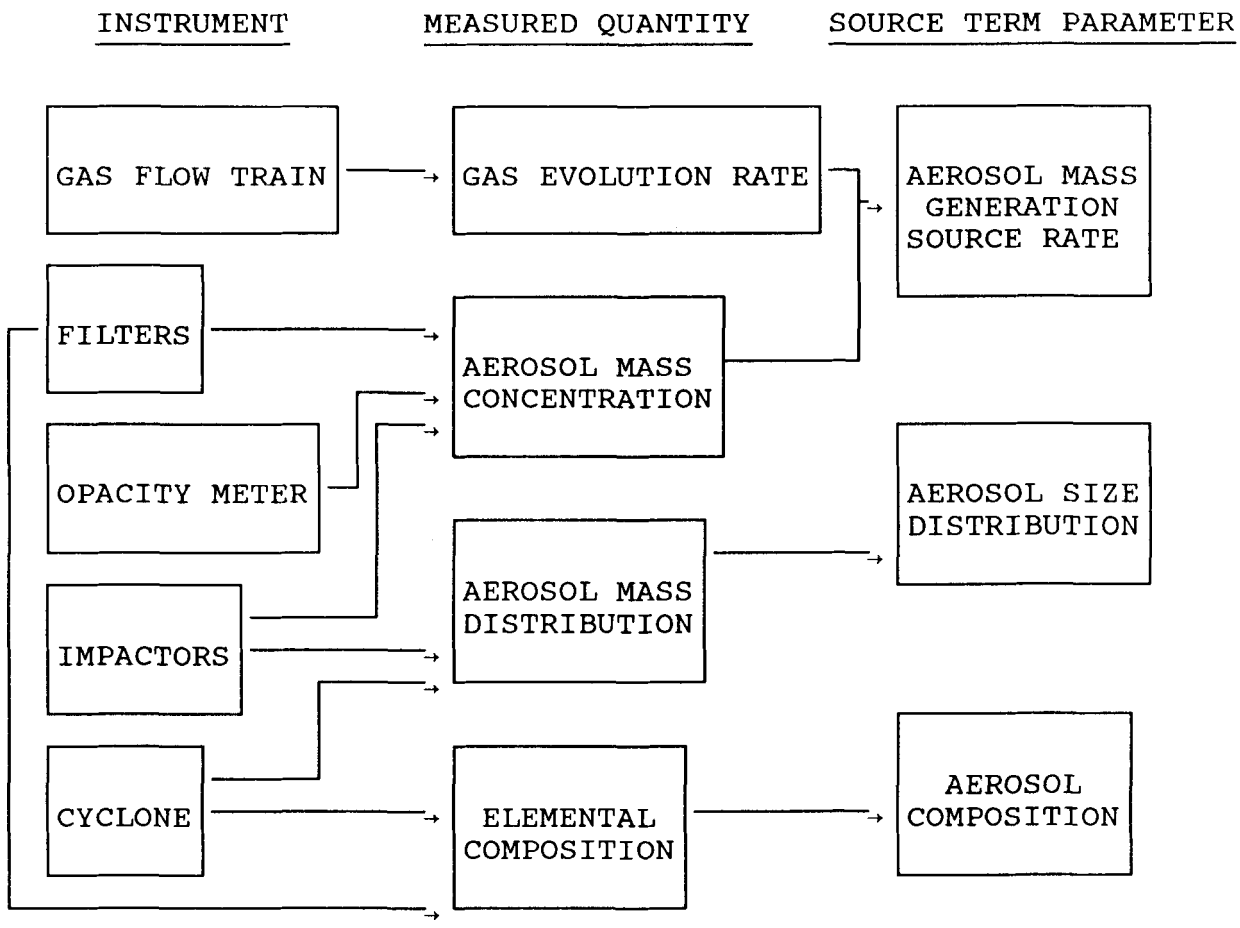

Figure 4.4.1. Flow chart illustrating how the source term parameters are determined from measurements made in the SURC-4 melt/concrete interaction test.

SAMPLE EXTRACTION DILUTION SYSTEM

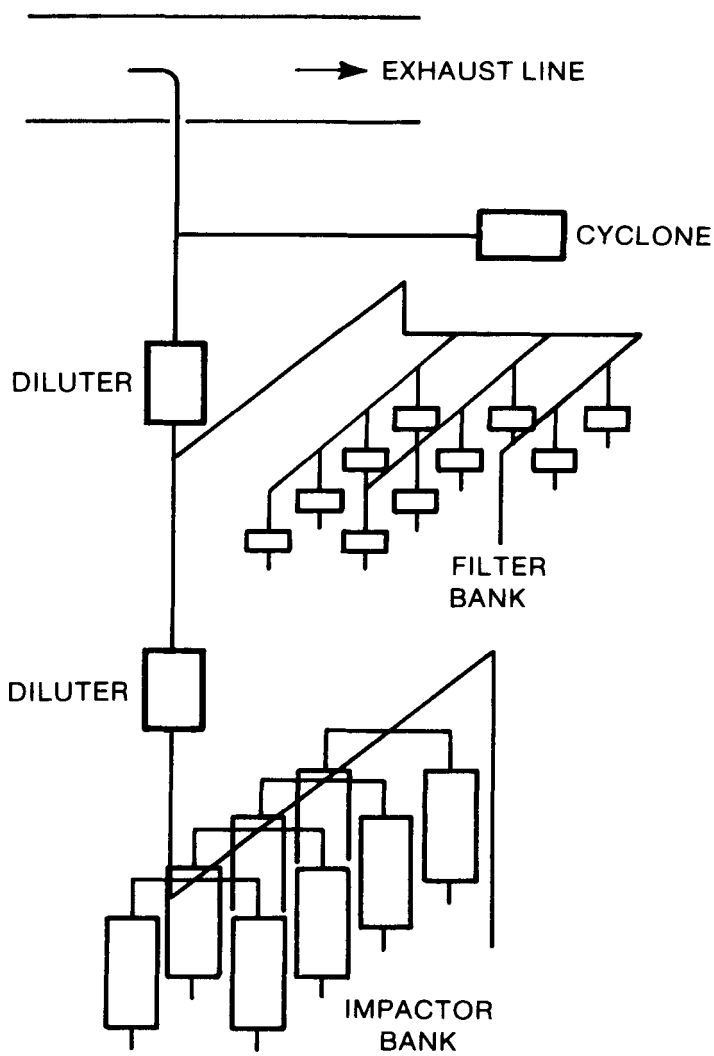

Figure 4.4.2 - Schematic diagram of the sample extraction dilu-dilution system showing the configuration of the filter, impactor, and cyclone samples with respect to the diluters and the aerosol sampling point.

Figure 4.4.3 is a more detailed schematic diagram of the SEDS showing the locations and connections of the dilution and gas flow control systems. The locations of the flow controlling orifices, pressure transducers, and thermocouples are shown. Their alpha-numeric identifications are also listed on the figure.

The flows are controlled by critical orifices manufactured by Millipore and calibrated at Sandia's Primary Standards Laboratory. Critical flow occurs when the ratio of upstream to downstream absolute pressure exceeds two. The equations governing flow through a critical orifice are (Holman, 1966):

$$Q = Q_c\left[\frac{T}{T_c} \cdot \frac{MW_c}{MW}\right]^{1/2}$$

$$\dot{n} = \frac{PQ}{RT}$$

$$= \frac{PQ_c}{RT_c^{1/2}T^{1/2}}\left[\frac{MW_c}{MW}\right]^{1/2}$$

where Q is the volumetric flow rate of gas upstream of the orifice, T is the upstream temperature, P is the upstream pressure, MW is the molecular weight of the gas, $\dot{n}$ is the molar flow rate, R is the universal gas constant, and the subscript c refers to the calibration conditions.

As shown in Figure 4.4.3 temperature and pressure upstream of the orifices are measured. Where the critical orifices are located away from any heated sections of the test apparatus, such as the cyclone and dilution gas supply system, ambient temperature is assumed.

Figure 4.4.4 shows photographs of the Millipore critical orifices and how they are mounted in a 3/8" swagelok male to male connector.

The dilution flows and sample flows are turned on and off by remotely actuated valves manufactured by ASCO. The remotely actuated valves for the samplers are operated by the Modicon Micro 84 programmable controller shown in Figure 4.4.5.

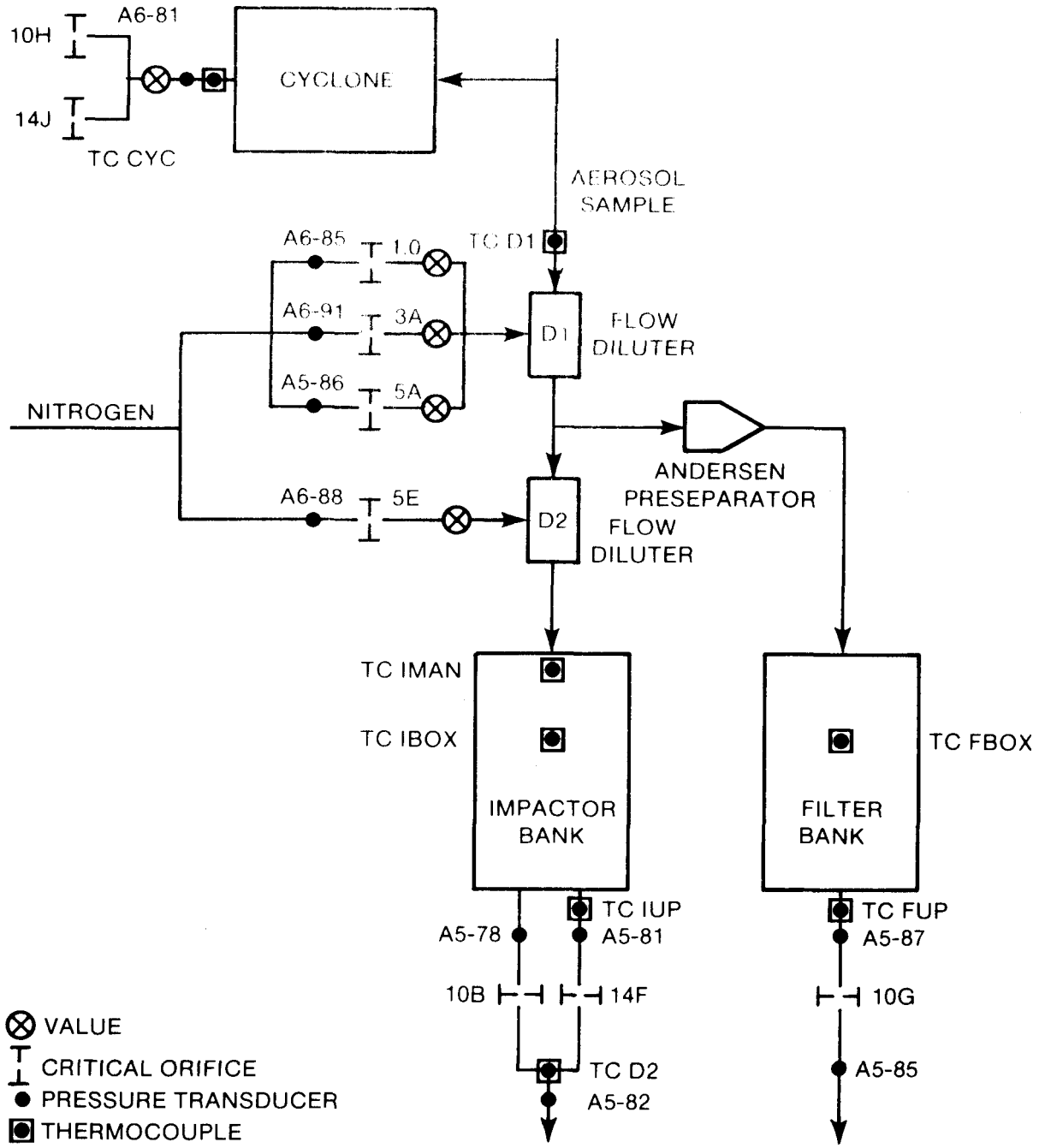

Figure 4.4.3 - Schematic diagram of the sample extration dilution system (SEDS) showing the locations of pressure transducers, thermocouples, and flow controlling orifices. The identifying designations of the orifices and thermocouples are also shown.

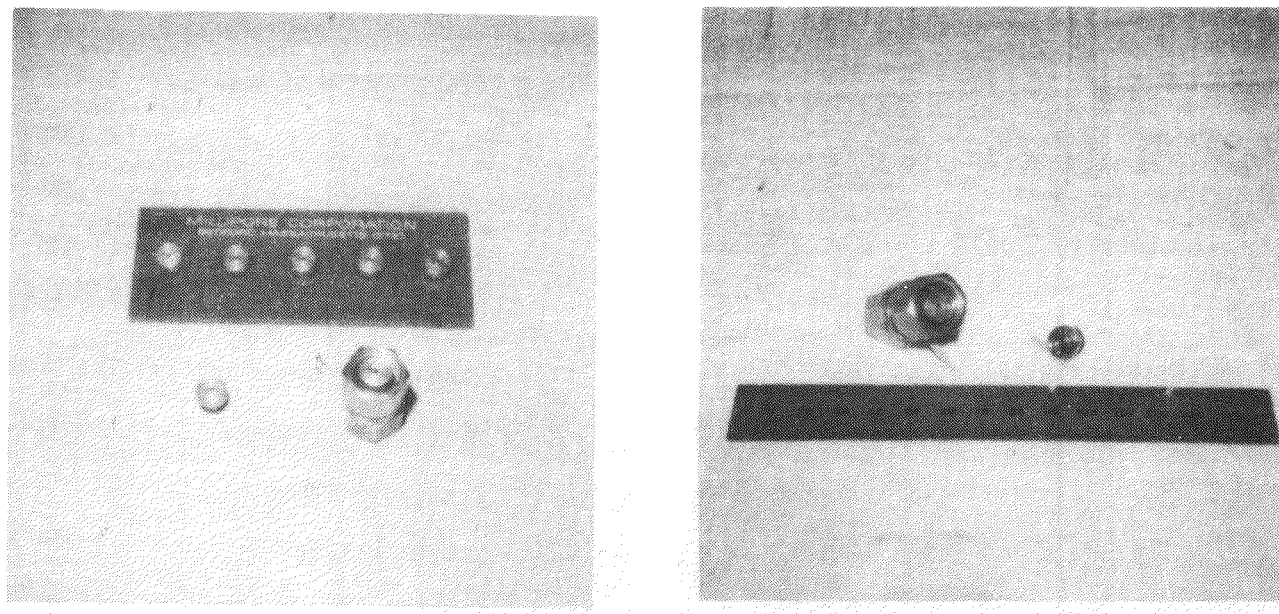

Figure 4.4.4 - Millipore critical orifices used to control the sample flows and dilution gas flows.

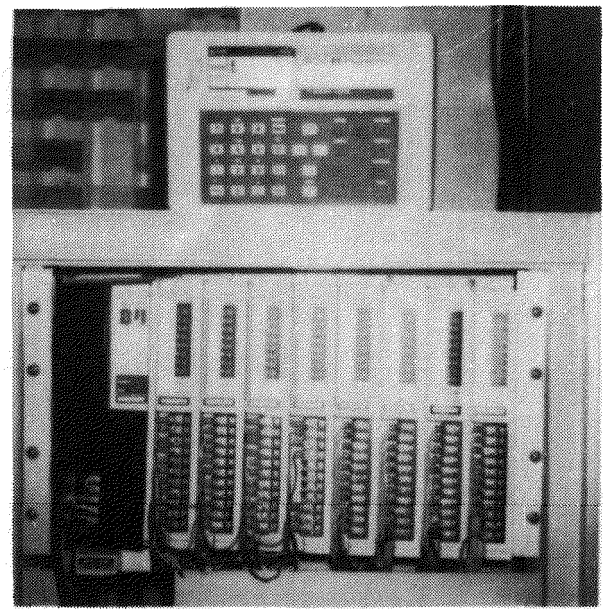

Figure 4.4.5 - Modicon Micro 84 Programmable Controller shown with the control/programming unit sitting atop the switching section.

Dilution of the sample by the diluters D1 and D2 serves three purposes. The first is to reduce the high aerosol concentration to a level that is within the measurement range of the instrumentation (less than about 20 g/m^3 for the filters and less than about 5 g/m^3 for the impactors). The second is to cool the flow and to reduce the temperature variation of gas passing through the SEDS by the addition of the cooler dilution gas. The third is to reduce the variation in gas properties by the addition of a known dilution gas in high enough amounts to dominate the gas properties. Dilution can be used to inhibit further evolution of an aerosol size distribution resulting from coagulation and condensation (Brockmann, et al., 1984). In this application, however, the aerosol size distribution has evolved during transport through the crucible and exhaust line and is likely to have reached a point where the time scale of evolution is large compared to that of transport through the SEDS.

Figure 4.4.6 is a schematic diagram of the flow diluter designed for this test series. Figure 4.4.7 shows photographs of the assembled and disassembled diluter. The diluter consists of an aluminum outer tube 15 cm long and 6.35 cm in outside diameter and a 1.9 cm outside diameter sintered stainless steel inner tube. End caps hold the tubes in place. Dry dilution gas passed through a 1/4" swagelok fitting in the outer tube to the annular plenum region between the two tubes. Gas passes through the porous walls of the inner tube diluting the aerosol sample flowing through it.

The total flow out of the diluter, Q_T, was measured and the dilution flow into the diluter, Q_D, was measured. The dilution ratio DR is then defined as Q_T divided by the difference between Q_T and Q_D. Some care in the magnitude of the dilution is necessary. The dilution ratio is calculated using the difference between two numbers and when those numbers are close, the error in the difference can become large. For example, if the uncertainty in the flows Q_T and Q_D is $\pm$ 5% for each, the resulting uncertainty in dilution ratio is $\pm$ 36% for a nominal dilution ratio of 5. This magnefication of the flow uncertainties in the calculation of the dilution ratio places a practical upper limit on dilution ratio of about 5. For this test, nominal dilution ratios were about three for each of the two diluters.

Because the system pressure in the SEDS is the same as that of the experimental apparatus, the SEDS can become pressurized (at higher gas evolution rates, the evolution gas flow train causes some back pressure in the apparatus). Each orifice controlling the dilution gas flow delivers a fixed molar flow of dilution gas by virtue of its fixed upstream temperature and pressure. The orfices controlling the sample flow draw at a fixed volumetric flow rate. The fixed volumetric flow rate yields a molar flow rate directly proportional to the system pressure. Consequently, if the dilution flow is unchanged, the dilution ratio will decrease with increasing system pressure. To maintain a consistent level of dilution in the face of a pressurizing

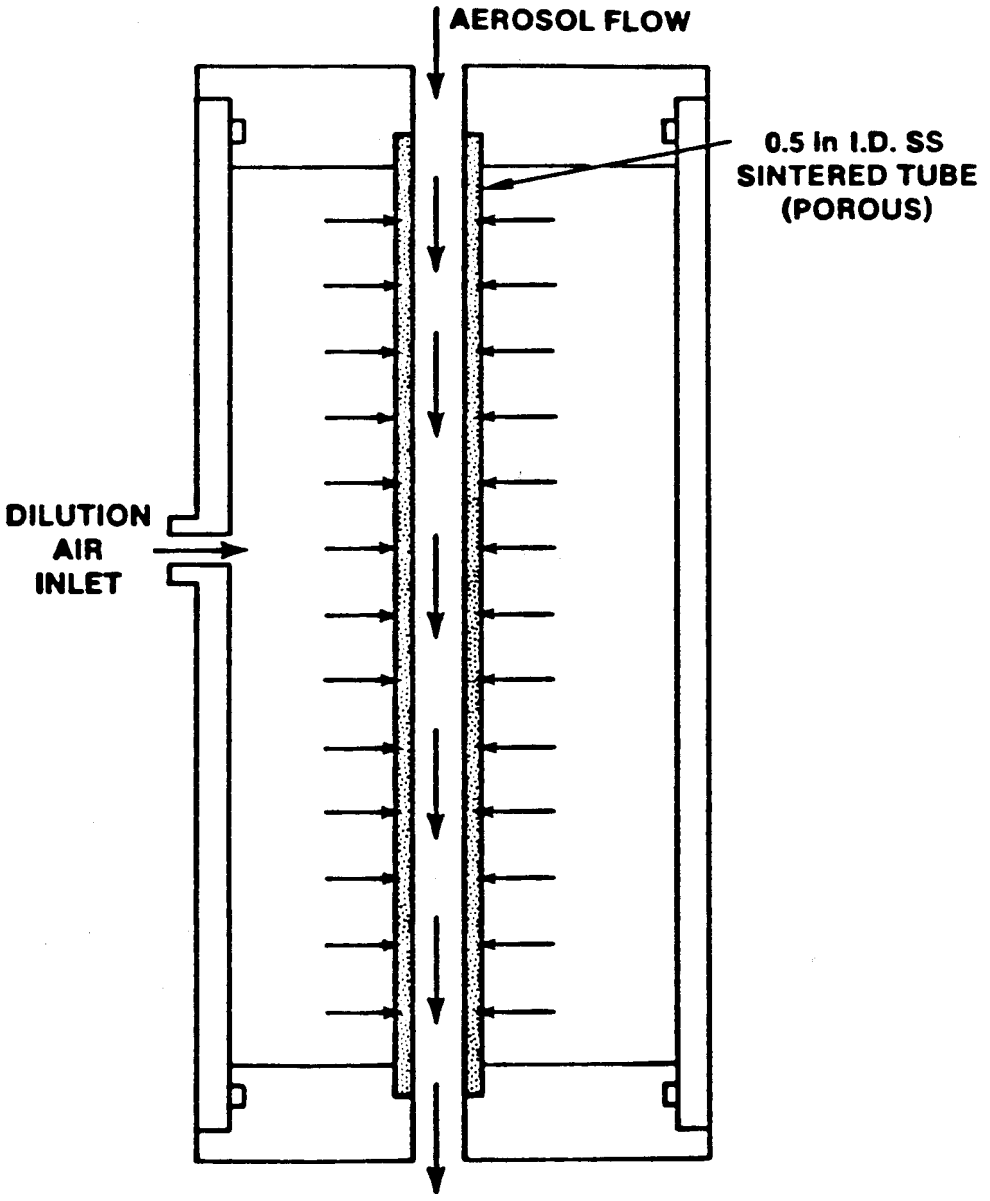

Figure 4.4.6 - Schematic diagram of flow diluter used in the sample extraction dilution system.

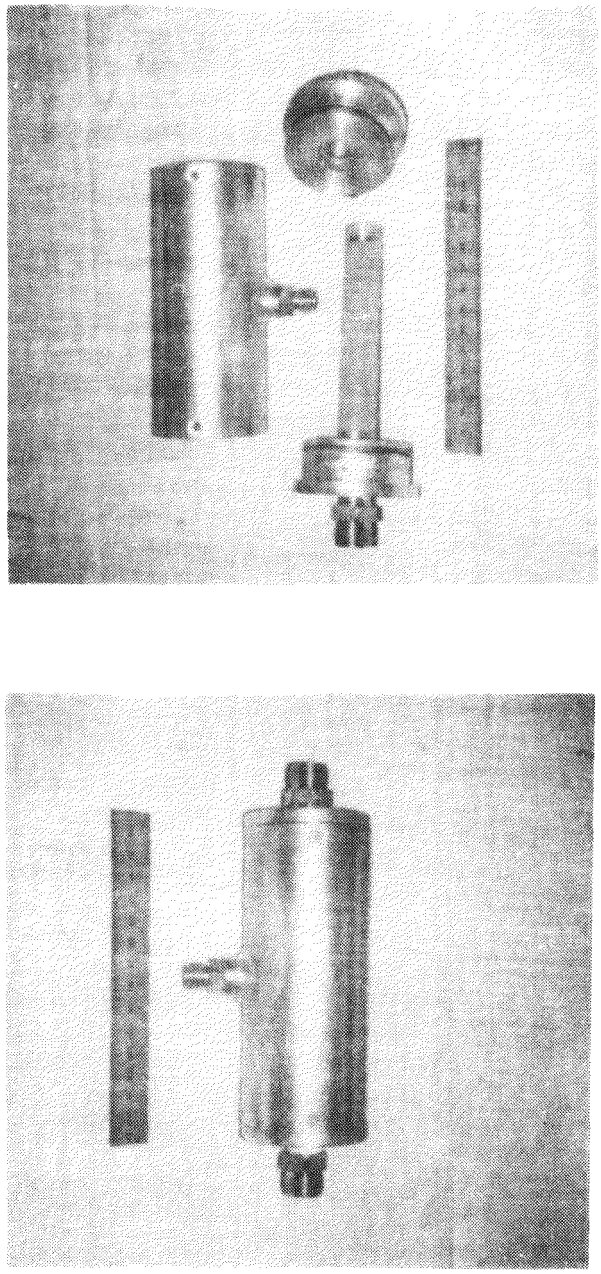

Figure 4.4.7 - Photographs of the assembled and disasembled flow diluter used in the SURC 4 tests showing the diluter body, sintered inner tube and end caps.

system, the molar flow of dilution gas must be increased in proportion to the increase in molar flow of the sample produced by the increase in system pressure. This increase in dilution molar flow was accomplished in diluter 1 by selecting combinations of three orifices as shown in Figure 4.4.3. These orifices were switched in and out by actuating remotely controlled valves controlling each orifice. This feature was not included in diluter 2.

Figure 4.4.8 is a schematic diagram of the filter bank of 12 filter samples on the SEDS. The flow through each filter was controlled by a remotely actuated valve. The 12 valves were plumbed to a single critical orifice giving a nominal filter sample flow rate of 10 liters per minute. The filter bank consists of 12 Gelman in-line stainless steel filter holders. These stainless steel, 5.9 cm diameter, 5.7 cm long filter holders (Gelman catalog number 2220) are designed for pressure applications of up to 200 psig. They use 47 mm diameter Durapore Membrane filtration media from Millipore (catalog designation HVLP 047). The effective filtration area is 9.67 cm^2 for each filter sample. Figure 4.4.9 shows photographs of one Gelman high pressure filter holder.

The inlet to the filter sample section was connected to a preseparator which removes particles larger than 10 to 15 micrometers aerodynamic equivalent diameter. This preseparator is manufactured by Andersen and is of stainless steel construction, 8.2 cm in diameter and 12.8 cm long. The preseparator collects coarse material in an impaction cup, passing on the finer aerosol to the filter sample section.

Each filter sample provides a collected mass of aerosol with aerodynamic equivalent particle diameter less than 10 to 15 micrometers. This sample allows calculation of the aerosol mass concentration of these smaller particles. The collected material can also be chemically analyzed. The filter sample is the principal measurement in determining aerosol mass source rate and elemental composition.

The filter sample section was mounted in an insulated box and electrically heated to avoid water condensation. The heaters were controlled by an Omega Model 920 temperature controller with a type K thermocouple.

Figure 4.4.10 is a schematic diagram of the impactor sample section. Andersen Mk III cascade impactors were used. An Andersen Mk III cascade impactor intertially classifies aerosol particles into nine size bins. This inertial classification is accomplished by accelerating the particles through successively smaller holes (and higher velocity jets) in a stack of orifice plates. Under the jets of each plate is a glass fiber collection substrate. Particles are collected by impaction on the substrates. Those small enough to follow the gas stream lines in

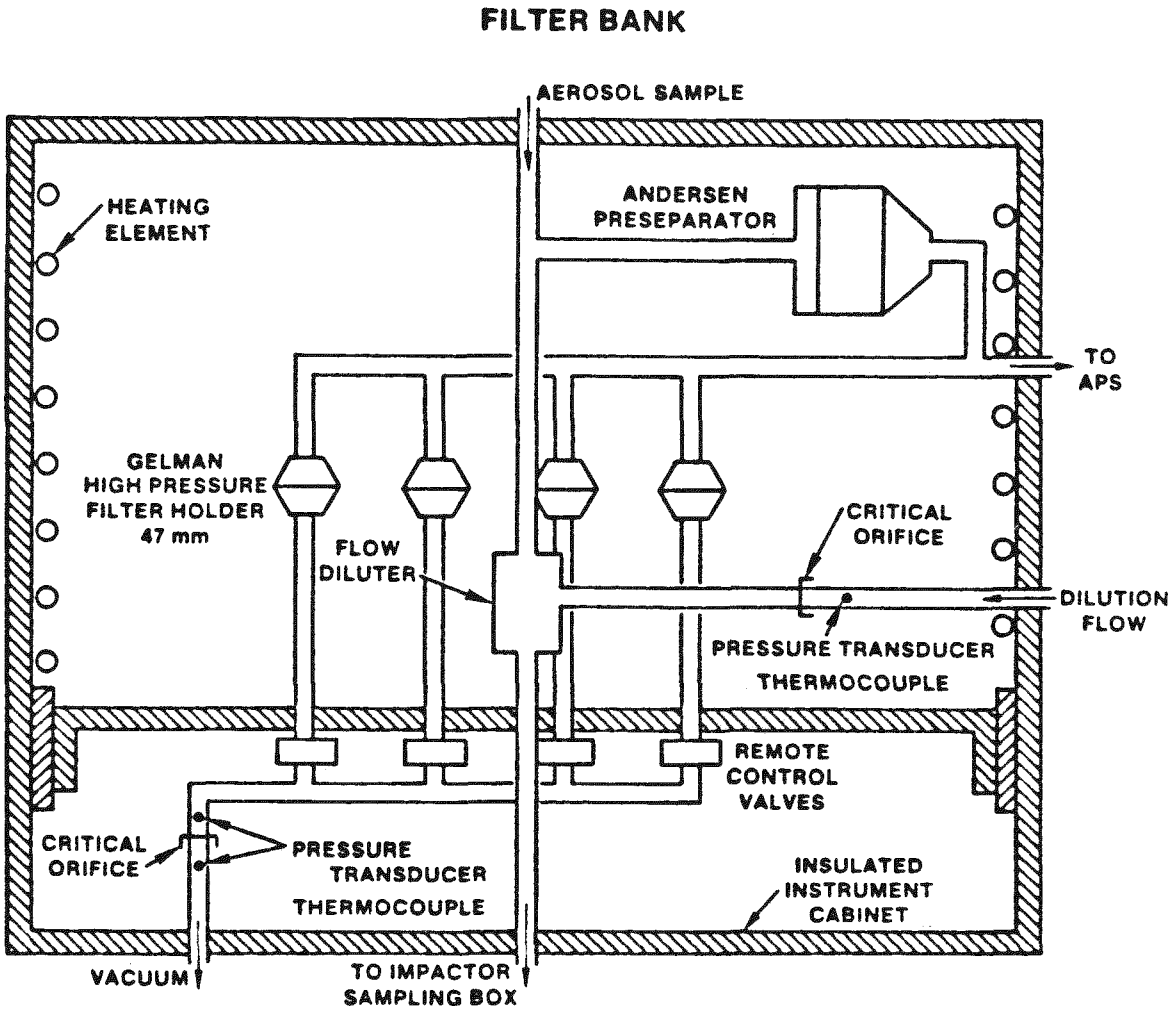

Figure 4.4.8 - Schematic diagram of the filter bank in the sample extraction dilution system showing the locations of the preseparator, filter holders, heating elements. Remotely actuated valves and flow controlling orifice. The diluter diluting the sample flow going on to the impactor bank is also shown.

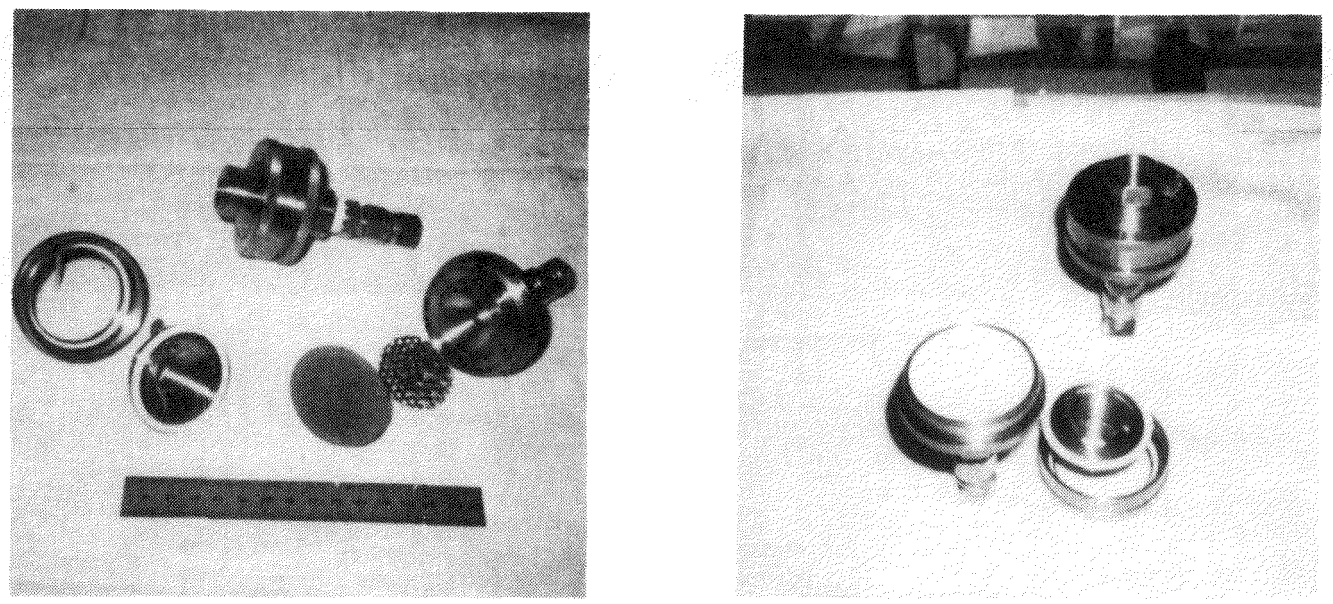

Figure 4.4.9 - The Gelman high pressure filter holder shown disassembled with filter substrate support (left) and filter substrate and supports in place (right). The assembled filter holder is shown at the top in each photograph.

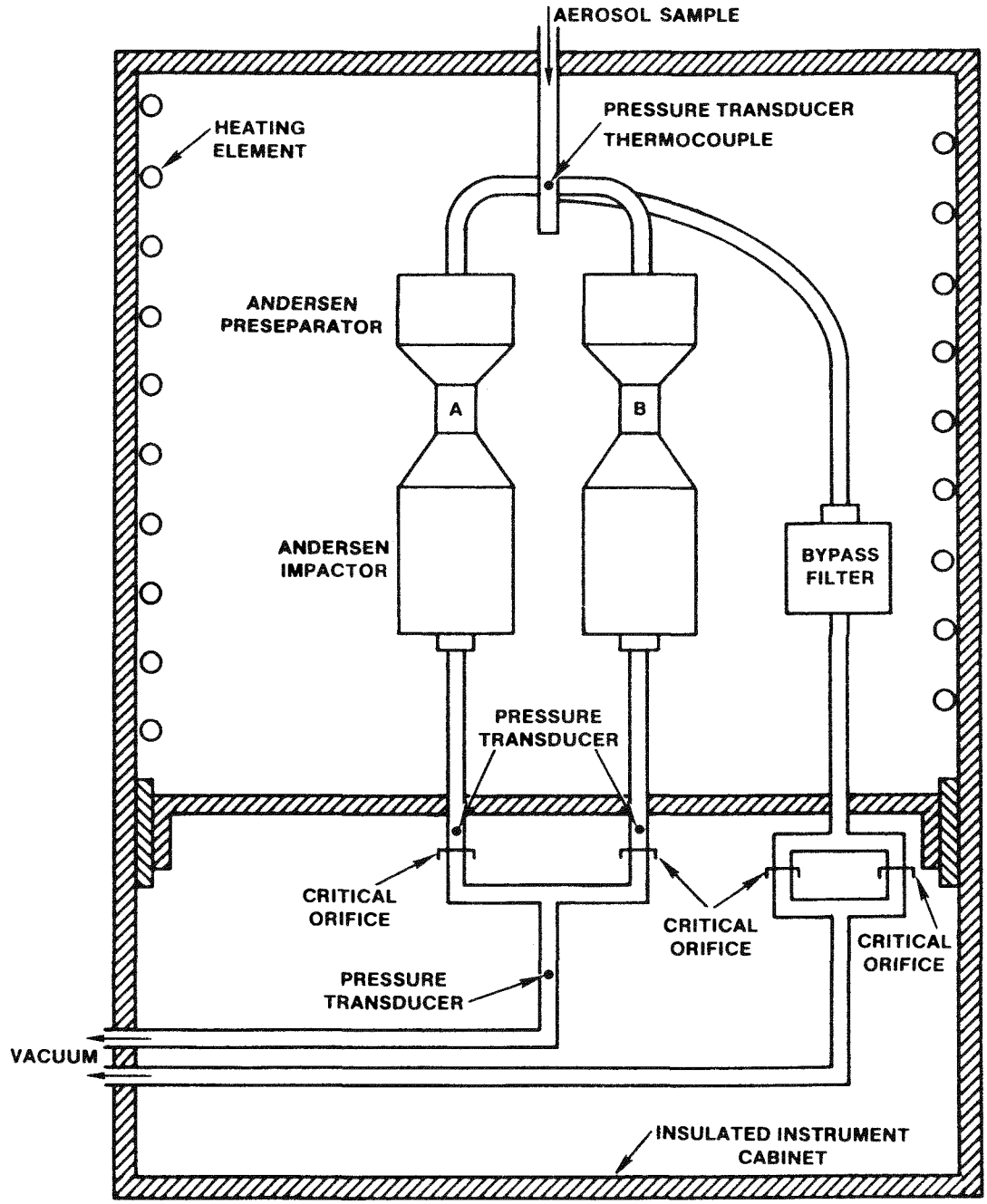

Figure 4.4.10 - Schematic diagram of the impactor bank showing the impactors and by-pass filter.

one stage pass on to subsequent orifice plates or stages where they may be collected. The impactor consists of eight stages and a backup filter to collect any unimpacted particles. It yields a mass distribution of aerosol with respect to aerodynamic equivalent particle diameter. The Anderson Mk III cascade impactor is 8.2 cm in diameter and 18 cm long and is constructed of stainless steel.

A preseparator (shown in Figure 4.4.11), which removes particles nominally larger than 10 to 15 micrometers aerodynamic diameter, was used to avoid overloading (more than ~25 mg of material on any one stage) of the impactor by these larger particles. It effectively collects material which would otherwise be collected on the first two stages of the impactor. The preseparator collects material in an impaction cup, which is brushed out to retrieve the collected sample. The preseparator is of stainless steel construction, 8.2 cm in diameter and 12.8 cm long. It threads into the front of the impactor. The assembled preseparator-impactor is 8.2 cm in diameter and 29.8 cm long.

Two impactor samples were taken simultaneously, one at a nominal 10 liters per minute and the other at a nominal 15 liters per minute. This provides a more detailed measurement of the aerosol size distribution and will be discussed further in the section on impactor calibration. The box containing the impactor bank is heated in the same way as the filter sample box.

Figure 4.4.11 shows photographs of the assembled and disassembled Andersen Mark III impactor and preseparator. Also shown are the jet plates and glass fiber collection substrates.

Figure 4.4.12 shows photographs of the filter bank and impactor bank.

Figure 4.4.3 shows how the cascade cyclone is plumbed into the SEDS. Sample flow was controlled by two Millipore critical orifices in parallel to give a nominal sample flow of 24 liters per minute. A remotely actuated valve manufactured by ASCO was used to take the sample.

The cascade cyclone is manufactured by Sierra. This device intertially classifies aerosol particles and yields a mass distribution with respect to aerodynamic equivalent particle diameter. This classification is accomplished by flowing the aerosol sample through a succession of smaller cyclones. The flow is introduced tangentially into the circular body of the cyclone where the circulating swirling flow causes larger particles to move by centrifugal force to the walls where they are collected. The smaller particles are withdrawn through the center and passed on to subsequent cyclones where they may be collected. Particles too small to be collected by the cyclones are collected by a backup filter. A cyclone is capable of collecting much more material than an impactor and can be used to collect size classified material for bulk analyses.

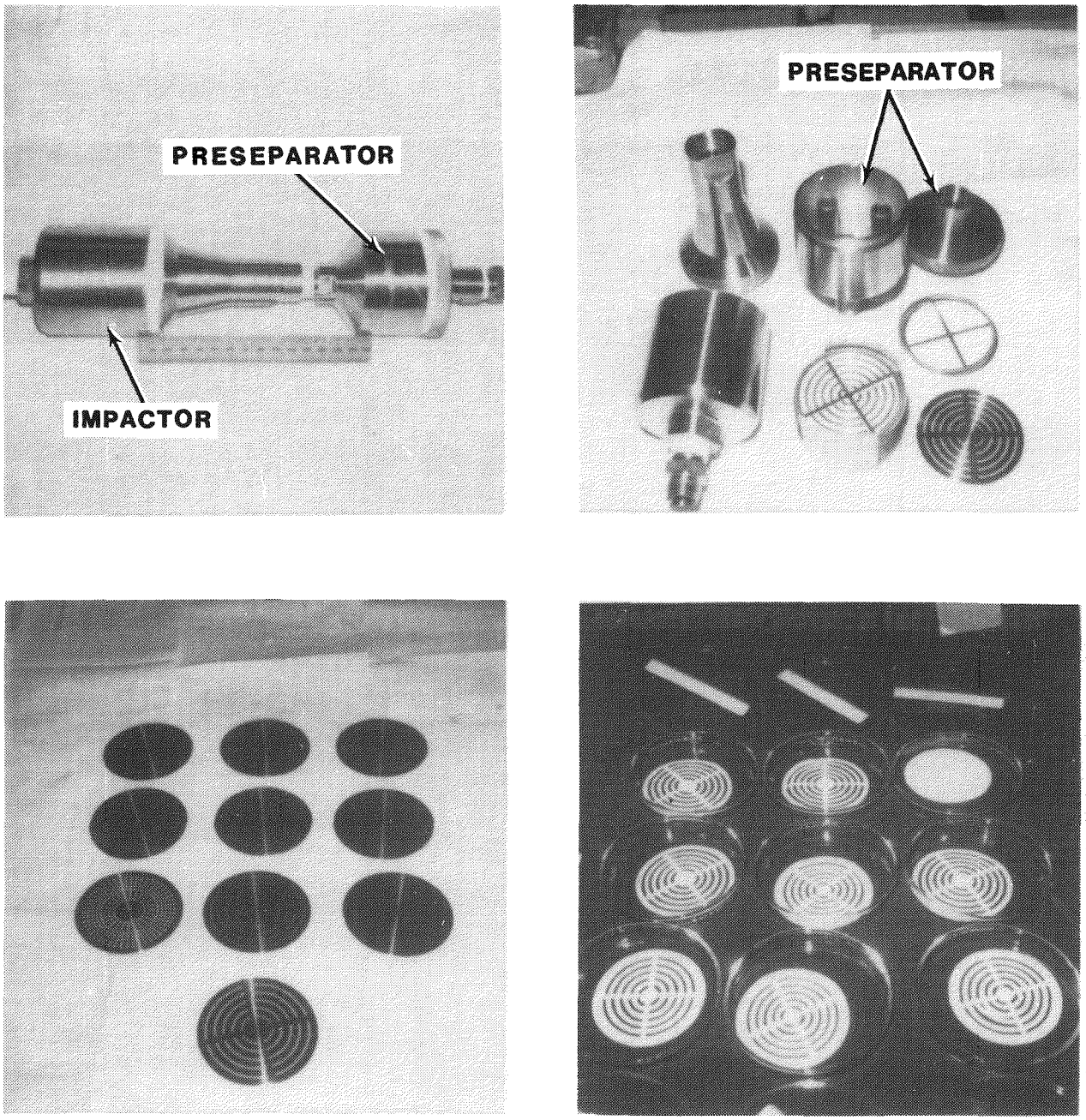

Figure 4.4.11 - Photographs showing the assembled Anderson Mark III impactor-preseparator assembly (top left), the disassembled preseparator and impactor with the stack of orfice plates and collection substrates (top right) and the separate orifice plates (bottom left) and glass fiber collection substrates (bottom right).

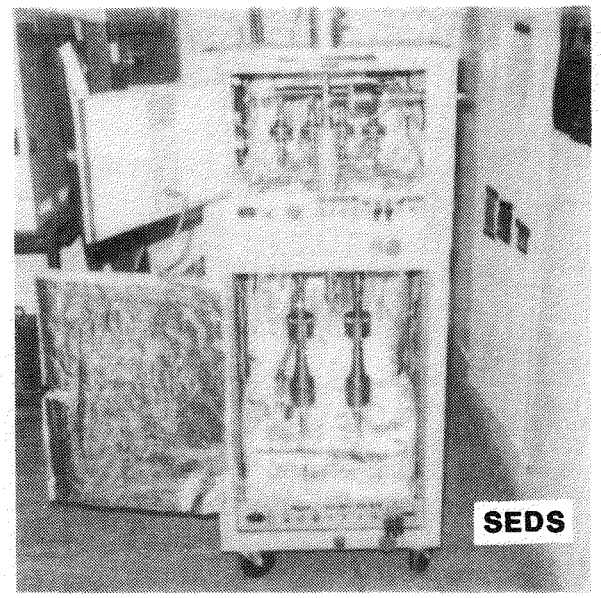

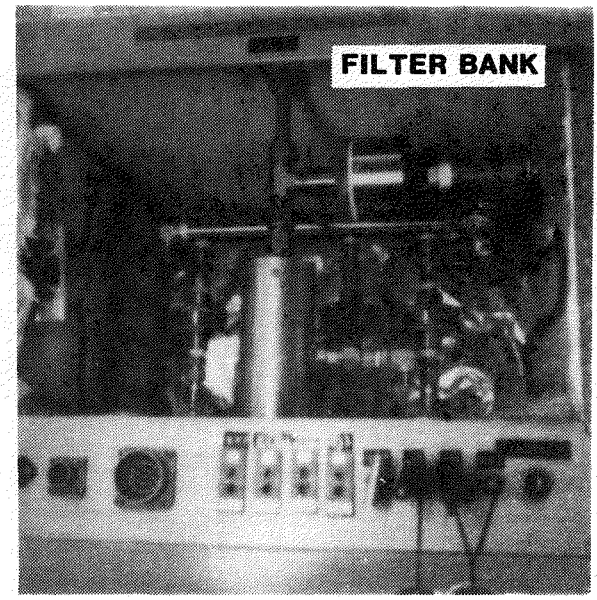

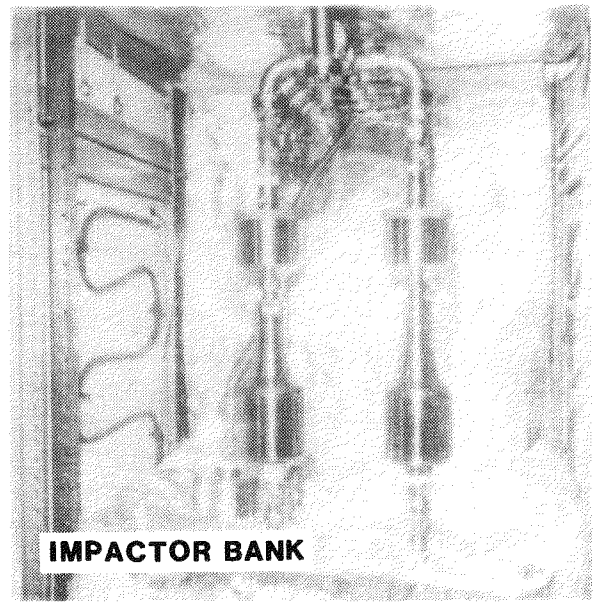

Figure 4.4.12 - Photographs of the filter bank and impactor bank of the sample extraction dilution system showing the banks joined together with diluter 1 on top, and diluter 2 in the filter bank heated box as well as close ups of each of the two banks showing the samplers.

The Sierra cascade cyclone is a series of six cyclones of increasing capability to collect smaller particles followed by a glass fiber backup filter. The aerosol sample was brushed out of the collection cup of each cyclone for weighing. The cascade cyclone is of stainless steel construction and when assembled is 12.7 cm in diameter at the widest point and about 60 cm in length.

Figure 4.4.13 shows two views of the Sierra cascade cyclone: assembled and disassembled into its component six cyclones and the backup filter. The assembled unit is actually more compact than shown in the photograph because the cyclones were rotated about their connection points to nest together in a more compact cylindrical configuration.

Figure 4.4.14 is a schematic diagram of the Dynatron Model 301 opacity meter placed in the exhaust line of the test article upstream of the gravel filter and flow measurement devices. This device measures the attenuation of a light beam as it travels through an aerosol. Light attenuation correlates with aerosol mass concentration. Correlation of the opacity meter output with the mass measured by the filter samples provided a continuous record of mass concentration in the 3-inch pipe exhausting gas and aerosol from the interaction crucible in the SURC test. The windows allowing light transmission were kept clean and free of aerosol deposition by a purge gas flow.

Figure 4.4.15 shows the light source module, the photo detector module and the on-line output of the Dynatron Opacity Monitor.

Pressure Transducer Calibration

Kulite 0 to 100 psia pressure transducers were used to monitor the pressure of the gas upstream of the orifices in the diluters and the pressures in the sample extraction-dilution system. The calibration data for the pressure transducers are given in Tables 4.4.1 through 4.4.9. The locations of the pressure transducers and the flow controlling critical orifices in the SEDS are shown in Figure 4.4.3.

From the pressure transducers located upstream and downstream of the flow controlling orifices, critical flow determination is made.

Orifice Calibration

The sample flows are controlled by critical orifices from Millipore. These orifices have been calibrated in Sandia Laboratories' primary standards lab. The orifice calibration flow rates are given in Table 4.4.10. The orifice location and designation are shown in Figure 4.4.3 of the SEDS.

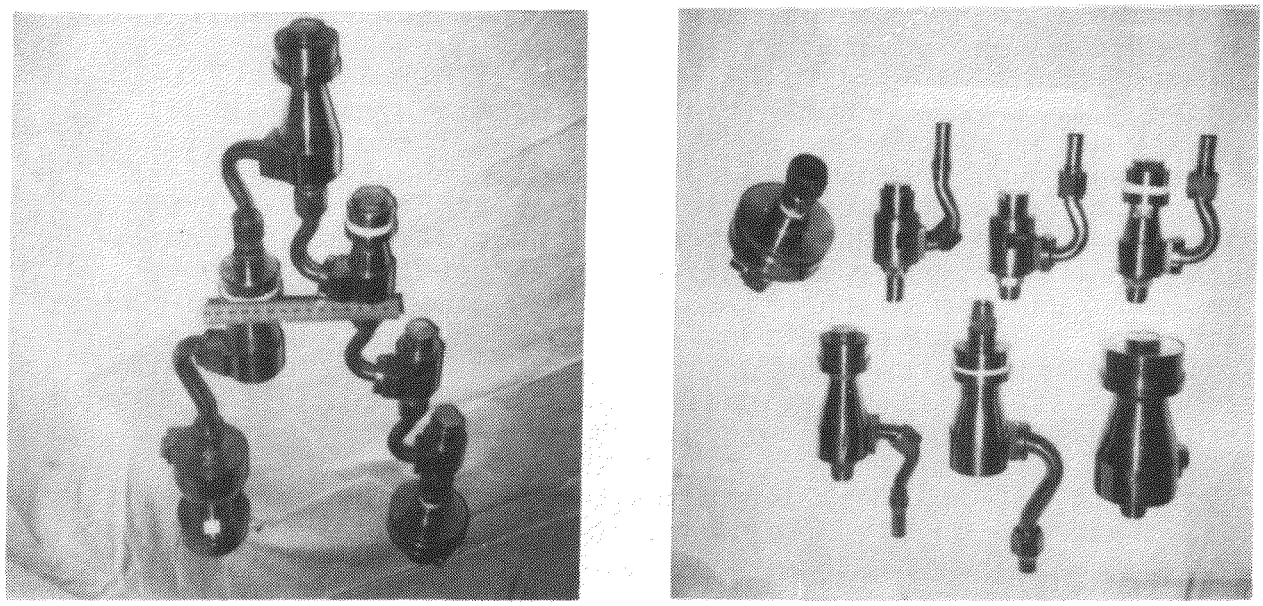

Figure 4.4.13 - Sierra Cascade Cyclone shown assembled (left) and disassembled (right) into its six constituent cyclones and backup filter.

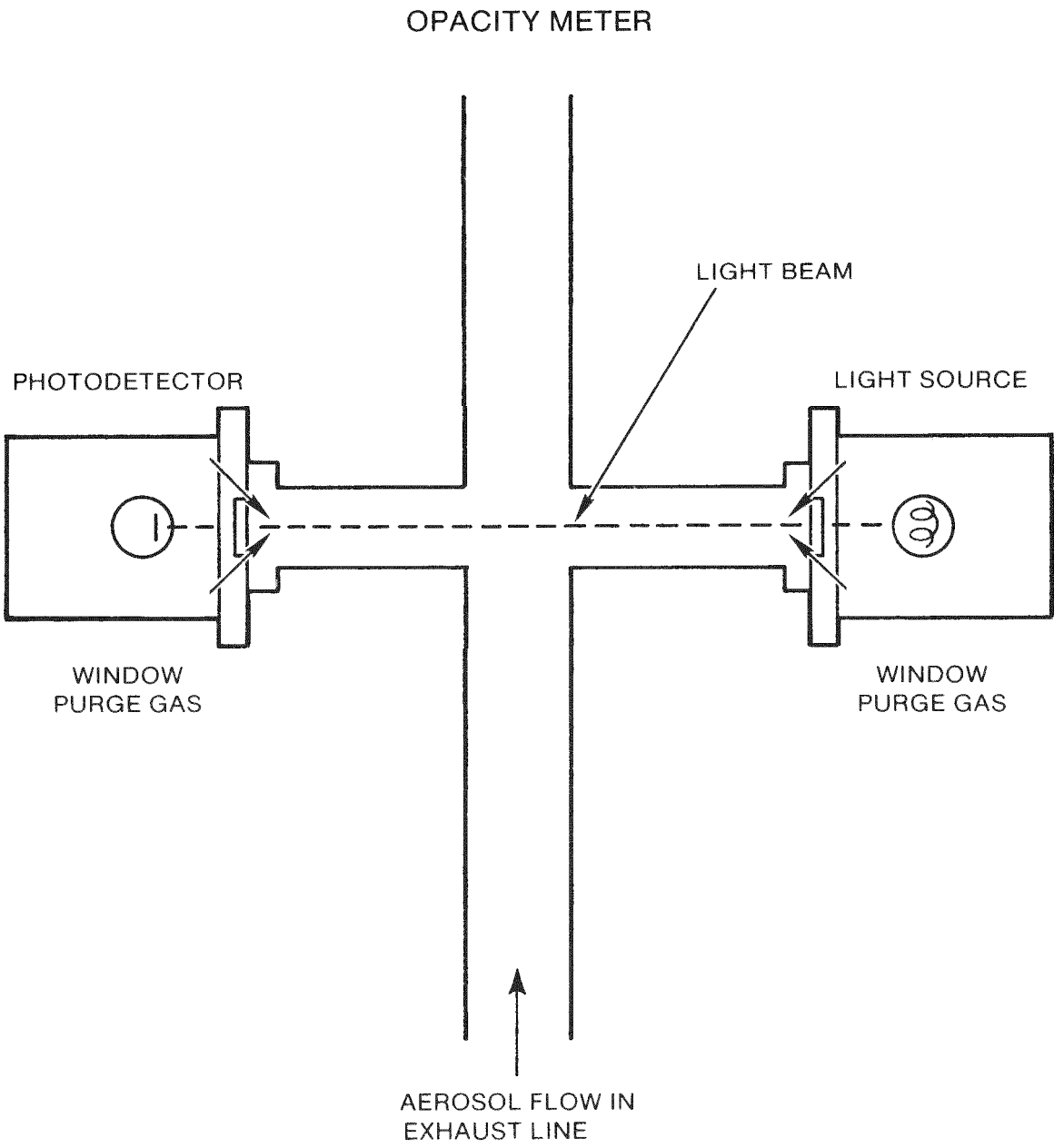

Figure 4.4.14 - Schematic diagram of the opacity meter used on the SURC 4 test showing how it was installed behind gas purged windows in the exhaust gas line.

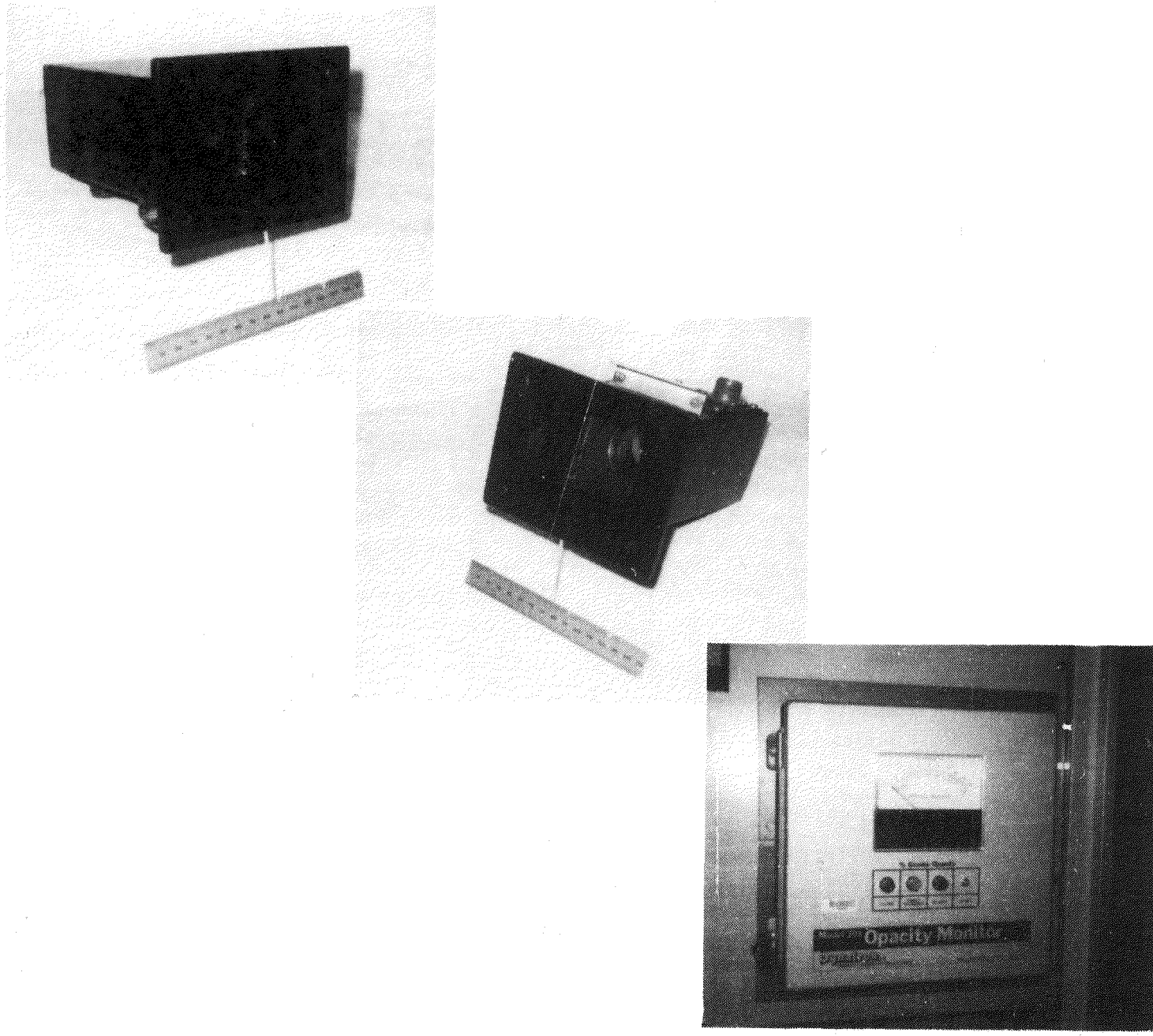

Figure 4.4.15 - Photographs of the light source (left) and photo-detector (center) modules and the on-line output of the Dynatron opacity meter (right).

Table 4.4.1

Pressure Transducer Calibration
ID No. A6-85
0 - 100 psia
Diluter D1
Critical Orifice 1.0

Pressure (psia)	mV Output
12.2	13.85
112.2	93.07
102.2	85.39
92.2	77.51
82.2	69.45
72.2	61.64
62.2	53.69
52.2	45.75
47.2	41.74
42.2	37.75
37.2	33.75
32.2	29.77
27.2	25.82
22.2	21.83
17.2	17.88
12.2	13.87

Table 4.4.2

Pressure Transducer Calibration
ID No. A6-91
0 - 100 psia
Diluter D1
Critical Orifice 3A

Pressure (psia)	mV Output
12.2	9.38
112.2	103.73
102.2	94.29
92.2	84.94
82.2	75.48
72.2	66.11
62.2	56.70
52.2	47.27
42.2	37.80
37.2	33.09
32.2	28.31
27.2	23.56
22.2	18.84
17.2	14.11
12.2	9.37

Table 4.4.3

Pressure Transducer Calibration
ID No. A5-86
0 - 100 psia
Diluter D1
Critical Orifice 5A

Pressure (psia)	mV Output
12.2	21.77
112.2	157.41
102.2	143.89
92.2	130.37
82.2	116.81
72.2	103.34
62.2	89.70
52.2	76.12
47.2	69.26
42.2	62.60
37.2	55.70
32.2	48.91
27.2	42.12
22.2	35.33
17.2	28.58
12.2	21.77

Table 4.4.4

Pressure Transducer Calibration
ID No. A6-88
0 - 100 psia
Diluter D2
Critical Orifice 5E

Pressure (psia)	mV Output
12.2	10.02
112.2	87.49
102.2	79.76
92.2	72.09
82.2	64.33
72.2	56.63
62.2	48.86
52.2	41.12
47.2	37.25
42.2	33.36
37.2	29.47
32.2	25.54
27.2	21.67
22.2	17.78
17.2	13.92
12.2	10.05

Table 4.4.5

Pressure Transducer Calibration
ID No. A5-87
0 - 100 psia
Upstream Filter Orifice
Critical Orifice 10G

Pressure (psia)	mV Output
12.2	3.18
112.2	139.22
102.2	125.71
92.2	112.04
82.2	98.58
72.2	84.98
62.2	71.38
52.2	57.75
42.2	44.09
32.2	30.43
22.2	16.74
12.2	3.18

Table 4.4.6

Pressure Transducer Calibration
ID No. A5-85
0 - 100 psia
Downstream Filter Orifice
Critical Orifice 10G

Pressure (psia)	mV Output
12.2	0.64
112.2	121.14
102.2	109.13
92.2	96.99
82.2	85.06
72.2	73.02
62.2	60.97
52.2	48.89
42.2	36.82
32.2	24.74
22.2	12.60
12.2	0.64

Table 4.4.7

Pressure Transducer Calibration
ID No. A5-78
0 - 100 psia
Upstream Impactor Orifice
Critical Orifice 10B

Pressure (psia)	mV Output
12.2	3.18
112.2	152.41
92.2	122.74
72.2	122.74
52.2	85.06
32.2	73.02
12.2	3.18

Table 4.4.8

Pressure Transducer Calibration
ID No. A5-81
0 - 100 psia
Upstream Impactor Orifice
Critical Orifice 14F

Pressure (psia)	mV Output
12.2	2.15
112.2	139.84
92.2	112.48
72.2	85.16
52.2	57.43
32.2	29.97
12.2	2.15

Table 4.4.9

Pressure Transducer Calibration
ID No. A5-82
0 - 100 psia
Downstream Impactor Orifice

Pressure (psia)	mV Output
12.2	3.73
112.2	121.39
92.2	97.96
72.2	74.59
52.2	50.89
32.2	27.43
12.2	3.73

Table 4.4.10

Calibrated Flows for Critical Orifices
Used in SURC-4 Test

Orifice Designation	Critical Calibration Flow (cm^3/sec)
10B	174.8
10G	170.8
10H	171.1
14F	241.5
14J	252.3
5A	75.3
5E	72.8
3A	46.0

Impactor Calibration

The Andersen Mark III cascade impactor has been calibrated by Cushing et al. (1976). We have employed their experimentally-determined calibration in the reduction of data taken with the Andersen Mark III impactors.

Each impactor stage is assumed to collect all particles larger than some characteristic size and pass along all particles smaller than that size. This characteristic size is called the cut point. Thus, in a cascade impactor (an impactor composed of a series of stages with successively smaller cut points) each stage collects particles of a size between the cut point of that stage and that of the previous stage. The impactor yields a distribution of aerosol mass as mass between successive cut points.

The cut point of an impactor can be expressed as a Stokes number:

$$Stk = \frac{\rho_o D_{ae}^2 U}{18 L \mu}$$

where ρ_o is the density of 1 g/cm^3, D_{ae} is the aerodynamic equivalent diameter, U is the velocity through the orifice, μ is the absolute viscosity of the gas, and L is the diameter of the orifice. Impactor theory holds that for a given stage, the characteristic Stokes number is constant (Marple and Willeke, 1979). Thus, changing the flow (or U) through the impactor changes the cut point for that stage. The aerodynamic equivalent diameter corresponding to the cut point for each stage for impactors operating at 10 and 15 liters per minute are given in Table 4.4.11.

The preseparator used on the impactors has been calibrated by McFarland et al. (1978) and their calibration is used in the work presented here. Table 4.4.11 gives the cut points for the preseparator-impactor combination at the two nominal flow rates of 10 and 15 liters per minute.

The cut points for the two flow rates were staggered. A simultaneous sample taken by two such impactors will give the same distribution but with different cut points. Combination of the two distribution measurements gives a distribution with a finer definition than either measurement alone.

Cyclone Calibration

The cyclone exhibits the same general cut point behavior as an impactor, but there is no corresponding theory of cyclones as there is for impactors. The cyclone must be calibrated and operated at the same conditions. The manufacturers calibration (Table 4.4.12) is used in the work presented here pending subsequent calibration at Sandia.

Table 4.4.11

Andersen Mark III Impactor Cut Points

50% Cut Points (Particle diameter in micrometers) for Two Flow Rates

Stage	10 LPM	15 LPM
Preseparator	10.5	10.0
1	-	-
2	-	-
3	7.6	6.3
4	5.1	4.3
5	2.8	2.4
6	1.3	1.1
7	.84	.70
8	.49	.41

Table 4.4.12

SIERRA CASCADE CYCLONE CUT POINTS SUPPLIED BY MANUFACTURER. FLOW NOMINALLY AT 0.8 SCFM AND TEMPERATURE AT 23°C.

CYCLONE STAGE	CUT POINT (μm)
1	Not supplied at these conditions
2	6.2
3	2.65
4	1.55
5	0.84
6	0.54

Since the cyclone was used to collect bulk aerosol material over an extended period of the test, the calibration employed is deemed adequate. Should an obvious size dependent composition be observed, post test laboratory calibration of the cyclone could be used to provide a more quantitative analysis of the size distribution data.

Aerosol Transport Calibration

The relationship between the sampled aerosol and the aerosol actually evolved from the test crucible must be understood. This relationship is defined by the efficiencies of aerosol extraction and transport. These efficiencies are calculated with an aerosol sampling efficiency model and an aerosol penetration model of the sampling system.

The extraction of the aerosol sample from the exhaust line through the gooseneck sampling probe is subject to the inefficiencies of anisokinetic sampling. Models describing the sampling efficiency exist in the literature (Davies and Subari, 1982; Jayasekera and Davies, 1980) and are used to calculate the probe performance.

The aerosol penetration model employed is described more fully in Gronager, et al. (1986). In this model, particle losses have been estimated for inertial deposition, diffusive deposition, and particle settling. The source term at the sampling point and sampling times can be adjusted for estimated loss and delay time.

Aerosol transport through the sample extraction and dilution system (SEDS) is not universally efficient. It is dependent upon particle size and flow conditions. Transport data for the SEDS system have been taken to test the transport model. These data are highly limited comprising only a portion of the desired calibration work. Exacting test schedules and limited resources prevented the in-depth testing desired. Further calibration of the system is under way.

The aerosol mass source rates are calculated by multiplying the measured aerosol concentration by the exhaust gas flow rates. Delay times for the aerosol to flow from the crucible volume to the sampling point are taken into account by calculating the time to flow through the intervening volume.

Experimental measurements of penetration through a series of 90° bends and through the SEDS plumbing from inlet to filter sample point and to impactor sample point have been made. The calibration aerosol was monodisperse oleic acid particles generated with the vibrating orifice generator manufactured by TSI, Inc. (Berglund and Liu, 1973). Measurements of the aerosol concentration were made with a TSI aerodynamic particle sizer (APS-33). Aerosol concentration measurements were made upstream and

downstream of the test section to obtain the penetration efficiency. Table 4.4.13 gives the results for the 90# bend and Figure 4.4.16 shows these results as penetration efficiency plotted against Stokes number along with the theoretical curve. For these high levels of penetration, the theory and data match well; however, for larger particles or higher flows resulting in lower penetration, the theory may be in some error.

Figure 4.4.17 is the room temperature penetration of a 4.56 micrometer diameter particle through the SEDS plumbing to the filter sample point. The curve is the theoretical penetration calculated by the model discussed above. Figure 4.4.18 is the penetration of a 4.56 micrometer particle through the plumbing to the impactor sample point along with the theoretical penetration.

In both cases, the experiment gave lower penetration than the model calculated: about 30% low for the filters and 15% low for the impactors. The cause of these differences is not known and further calibration and verification of models are required.

Aerosol data from previous tests (Brockmann, 1987) have indicated that aerosols produced during melt interactions with concrete are typically on the order of one micrometer aerodynamic equivalent diameter. Penetration of this size to the samplers is seen from Figures 4.4.17 and 4.4.18 to be high.

Procedures

Twelve filter holders were loaded with 12 preweighed filters and installed into the SEDS filter sample box. Eight impactors were loaded with preweighed collection substrates and installed into the SEDS impactor sample box.

Each substrate and filter was placed in a desiccator for approximately two days before weighing. This was done to prevent erroneous weights of samples due to water absorption.

The Dynatron opacity meter was adjusted and the zero set according to the manufacturer's specifications.

The pressures determined for the desired dilution ratios were set by adjusting pressure regulators upstream of the diluter orifices. The remote valves opening and closing flow to the diluters were cycled to check that the pressures returned to their set values.

The Modicon 84 programmer was programmed to take four data sets, each at the determination of the operator. A data set consisted of a 1 minute filter sample followed by a 1 minute sample taken with two impactors and a filter together and concluded by a 1 minute filter sample. During the first and third minutes, a bypass filter in the impactor bank was used to maintain constant flow through the SEDS while impactor samples were not being taken.

Table 4.4.13

Particle Penetration Through a 90° Bend

D_p (μm)	Q (cm^3/sec)	Tube I.D. (cm)	Stk	Experimental Penetration	Model Predicted Penetration
4.56	136	1.092	$8.3 \cdot 10^{-3}$	.978-.987	.987
4.56	208	1.092	$1.26 \cdot 10^{-2}$	.961-.972	.980
4.56	136	1.727	$2.1 \cdot 10^{-3}$	.972-1.00	.997
4.56	208	1.727	$3.2 \cdot 10^{-3}$	.981-1.00	.995
7.24	136	1.727	$5.2 \cdot 10^{-3}$	.945-.985	.992
9.12	136	1.727	$8.3 \cdot 10^{-3}$	.942-.967	.987

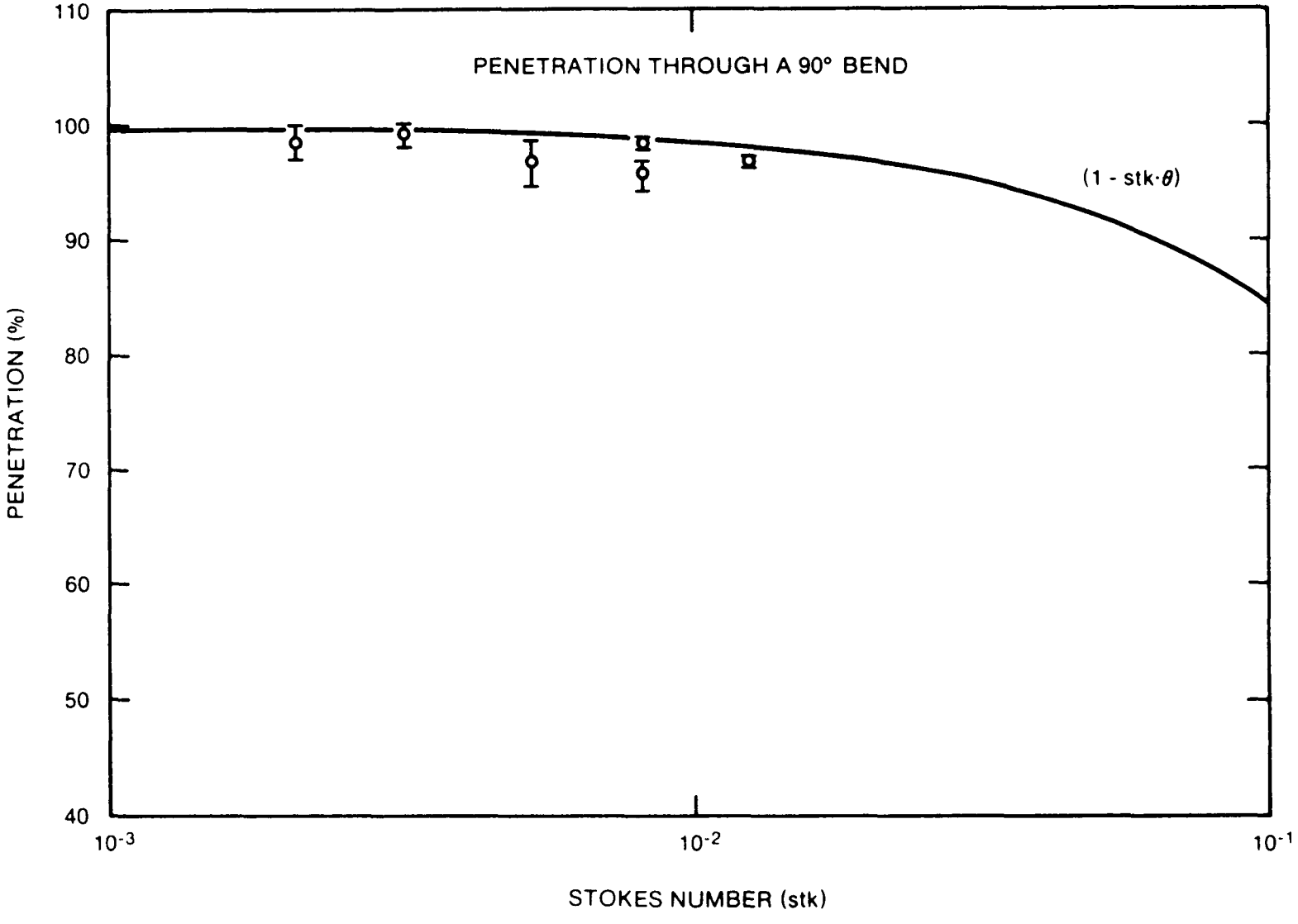

Figure 4.4.16 - Experimental results and theory for particle penetration through a 90° bend as a function of stokes number.

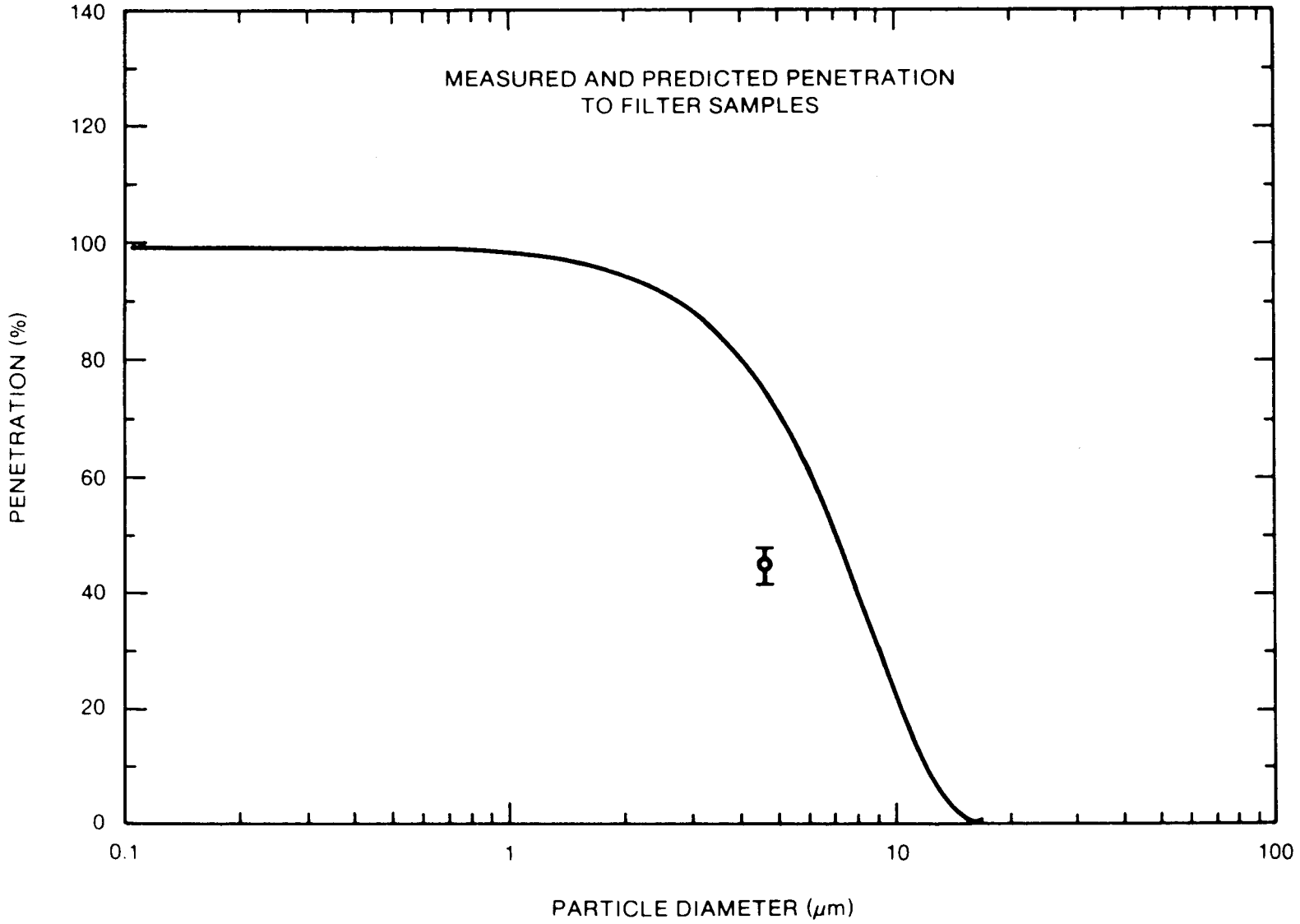

Figure 4.4.17 - Penetration efficiency as a function of particle aerodynamic diameter predicted by theory and measured for a 4.56 μm particle from the SEDS inlet at diluter 1 to the filter sample point.

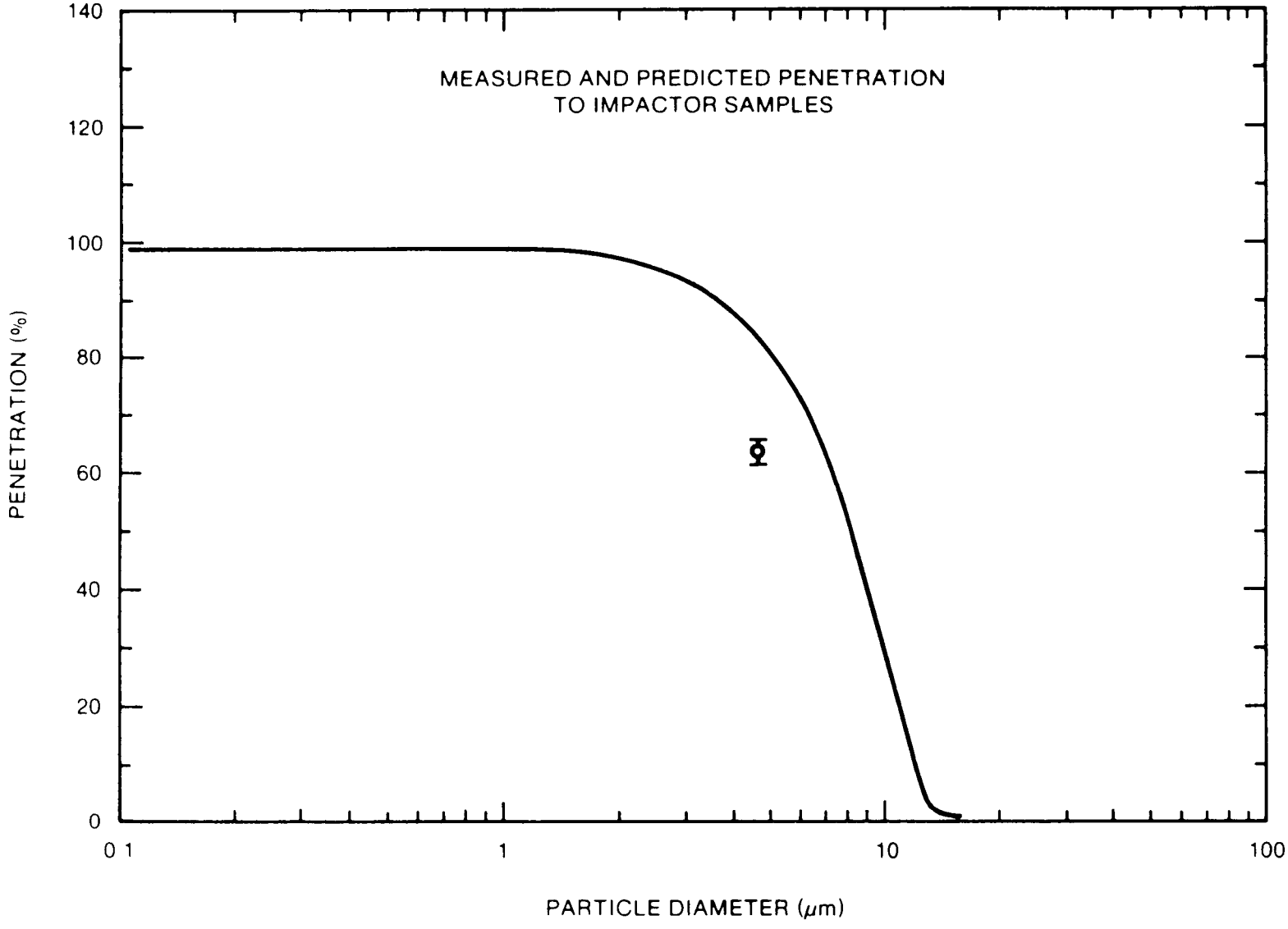

Figure 4.4.18 - Pentration efficiency as a function of particle aerodynamic diameter predicted by theory and measured for a 4.56 μm particle from the SEDS inlet at diluter 1 to the impactor sample point.

Table 4.4.14 indicates the times during the SURC-4 test that aerosol samples were taken.

The Gelman filter holders were disassembled and the filters were placed into pre-weighed dishes which were returned to the desiccator for two days. The filters were then weighed and weights recorded. The difference in weights were used to calculate mass concentration data.

The impactors were disassembled and the collection substrates and filters placed in pre-weighed dishes and placed in the desiccator similarly to the filters. Slight overloading was observed in stages 5, 6, and 7 which corresponds to approximately 1 micrometer aerodynamic size.

There was no significant amount of material recovered from the preseparators.

The cascade cyclone was disassembled similarly to the impactors, but the material was brushed into pre-weighed dishes and then weighed. The differences in weights were recorded.

Filter samplers A, B, C, D, E, F, H, and cyclone stages 1, 2, 3, 4, 5, 6, and 7 were analyzed using inductively coupled plasma (ICP) atomic emission spectrometry for a quantitative elemental analysis.

Impactor sample A stages 1, 2, 3, 4, 5, 6, 7, 8, and backup filter were analyzed using scanning electron microscopy (SEM).

Table 4.4.14

Aerosol Samples Taken in SURC-4

Sample	Time
Cyclone	135 min to 163 min
Set 1	113 min to 116 min
Set 2	124 min to 127 min
Set 3	155 min to 158 min
Set 4	Not Taken
Opacity Meter	100 min to 165 min

4.5 Induction Power Instrumentation

The 200 kg of stainless steel was melted and sustained using an Inductotherm 250 kW, 1 kHz induction power supply, shown in Figure 4.5.1. Power was delivered to the coils via remote control using a pair of No. 16 high current, water-cooled, flexible leads. During the melting process, the induction power supply automatically controlled voltage and frequency to deliver the desired power. Maximum efficiency was maintained throughout the experiment without the need to switch capacitors or voltage taps. The power delivered to the crucible coil was measured using a power transducer built by Inductotherm Corporation. The transducer measured coil voltage and current and converted it into a voltage equivalent of the power delivered. This transducer does not calculate the phase angle between the current and voltage and therefore only measures gross input power.

The temperature of the cooling water was measured across the inlet and exit of each of the coils with two Omega ON-970-44008, 30,000 ohm thermistors arranged in half bridge circuit. The flow of water through the crucible coil was regulated manually with a 19.1 mm diameter ball valve and measured using a Brooks Model 1110 rotameter.

4.6 Data Acquisition System

All 166 instrument channels were recorded every 15 seconds for the first 105 minutes of the test and every 5 seconds thereafter using an HP 1000 data acquisition system. Two-hundred-ten channels of data may be acquired during an experiment. Of the 210 channels, 150 are for type K thermocouples, 20 are for either type S or type C thermocouples and the remaining 40 are DC voltage channels. A patch panel routes all the analog data channels from the test location to the Hewlett-Packard Model 2250 Measurement and Control Unit. This unit houses an analog to digital converter capable of multiplexing the 210 data channels. The voltage range of the data acquisition unit is ± 10 volts DC, with a programmable gain to increase sensitivity if the expected signal is small. A Hewlett-Packard Model 1000 series A-600 minicomputer is used to control all remote devices and manipulate the data received from the Measurement and Control Unit. Data are stored on a Hewlett-Packard Model 7946, 15 Megabyte hard disk. A Hewlett-Packard Model 2623 terminal is used to command the minicomputer during test and to display real time data in a tabular format as data acquisition progresses. A desk top terminal Hewlett-Packard Model 9836 is used to display real time data in both graphic and numeric format as well as to provide interrupt control over the minicomputer during a test. A Hewlett-Packard Model 9872 four color plotter and nine track magnetic tape are used for post-test data plotting and transfer. The measurement accuracy of the 14-bit analog to digital converter is 1.56 microvolts in the most sensitive range and 1.25 millivolts at the highest range (-10 to +10 volts). With the

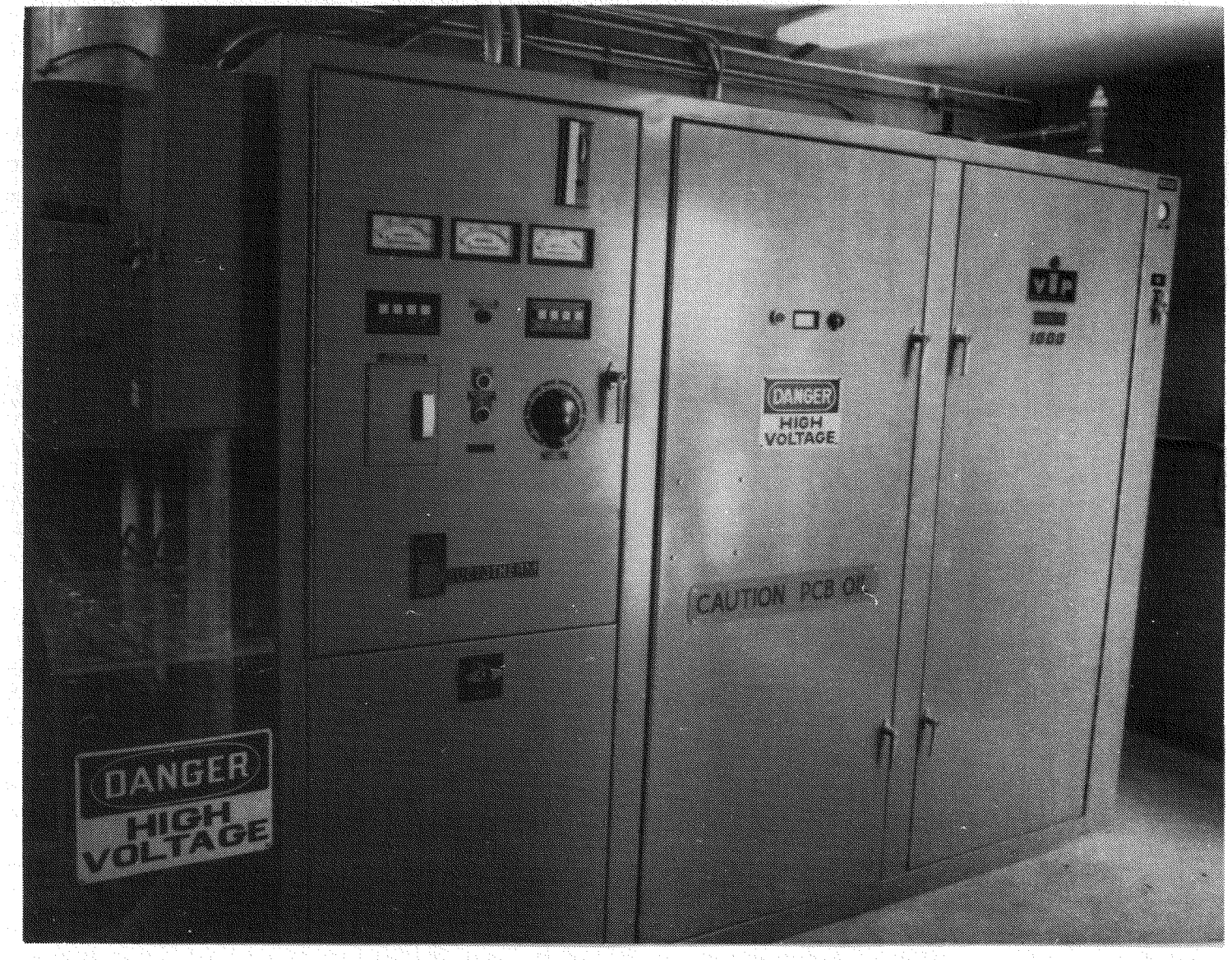

Figure 4.5.1 - Inductotherm Power Supply

appropriate range setting, the resolution for a K type thermocouple is ± 1°C, and for a type S or a type C thermocouple, the resolution is ± 1.1°C.

The data acquisition speed can be selected from 1.25 seconds per point upward for 210 channels. The sample rate can be increased by reducing the number of channels sampled. For the SURC 4 test, data for the channels were sampled initially at 15 second intervals.

4.7 Video Monitoring Instrumentation

The experiment was monitored remotely using a Sony Beta Model HVC 2200 video camera connected to a Sony Model SL 2000 portable Beta recorder and Model TT 2000 Tuner/Timer. The real time camera image was displayed on a 19-inch Sony model CVM 1900 color monitor. The image was passed between the video recorder and color monitor via a RG-59 coax cable.

5. PROCEDURE

Initial calibration runs (complete results shown in Appendix B) with the 250 kw power supply were performed using a 200 kg stainless steel slug in order to determine the coupling efficiency and overall losses for the SURC 4 geometry. Thermocouples placed in the slug indicated a temperature rise of 800°C in 38 minutes followed by losses of 90°C in fifty minutes after power shutdown. Power to the coil was set at 175 kw. These results indicated a net efficiency of 25.5 ± 2 percent (45 kw total to the slug) with overall losses of 3.5 kw. Following these power calibration tests, the SURC 4 apparatus was assembled and leak tested. Results of the leak tests using argon gas as the flow medium indicated a cold leak rate of 8.5 slpm at an inlet flow rate of 165 slpm (5% losses) and an overpressure of 1 psig in the SURC 4 containment vessel.

After the final calibration and pretest checkouts were performed, power was applied to the coil (Figure 5.1) at a rate of 98 kw. This constituted the start of SURC 4 at time = 10.7 minutes. A summary of the major events in the SURC 4 test is presented in Table 5.1. The temperature at the outer edge of the steel slug was monitored (Fig. 6.1) to confirm that 25.5% of the power was being transmitted to the metallic slug. After 33.3 minutes of heating, the power to the coil was increased to 200 kw at time = 44 minutes. A second power increase to the maximum allowable rate of 244 kw was accomplished at time = 80.5. This resulted in a net power of 62.2 kw to the slug. At time = 86 minutes, the steel slug reached the meltpoint of 1703 K. After nearly twenty minutes at the meltpoint, the steel became fully molten and concrete attack began. The centerline concrete thermocouple at the concrete surface minutes failed at time 105.4 minutes. The meltpool temperature at 105.4 minutes was 1746 K. Shortly after erosion began, the initial aerosol samples were taken. Aerosol filter sample "A" was taken at 113 minutes and filter sample B was taken at 114 minutes. The durations of both samples were 1 minute. Impactor samples A and B were also taken at these times. A third filter sample (sample C) was taken at time = 115 minutes, again for 1 minute. After nearly fifteen minutes of concrete ablation, the ball valve on top of the SURC 4 containment vessel was opened to deposit the Zr metal. A cursory inspection indicated that the pool was molten with no overlying crusts. The Zr delivery tube was actuated and the full 20 kg charge of Zr entered the melt at time = 119 minutes. The ball valve was then closed, having been open a total of 96 seconds. The power supply shut off at 124.1 minutes due to the failure of an auxiliary cooling line to the containment vessel. Field repairs quickly replaced the line and power was resumed at 245 kw to the coil at time = 131.7 minutes. During the power outage, three aerosol filter samples (D, E, and F) and two impactor samples (C & D) were taken at times 124.1 125, and 126 minutes. Each sample had a duration of 1 minute. Power to the meltpool was held constant at 245 kw for the remainder of the test except for a 30 second excursion at 144.8 minutes. The final aerosol samples were taken

Table 5.1

EVENTS OF TEST SURC-4

Time (min)	Events
0.0	Start of data acquisition system, 15 second intervals
10.7	Power supply on power meter reading 98 kw
18.3	Gas grab sample 10-1 taken from location #3 (inside containment vessel)
44.0	Power increased to 200 kw (power meter)
58.5	Gas grab sample 10-2 taken from location #2 (upstream of gravel filter)
80.5	Power increased to 245 kw (power meter)
102.8	Concrete surface perimeter thermocouple C41 failed (r = 18.0 cm)
104.3	Gas grab sample 10-3 taken from location #1 (down stream of gravel filter)
105.4	Concrete surface axial centerline thermocouple C1 failed (r = 0.0 cm)
108.8	Data acquisition changed to 5 second intervals
111.9	Concrete surface midradius thermocouple C21 failed (r = 10.0 cm)
113 - 114	Filter sample "A" taken
114 - 115	Filter sample "B" taken Impactor sample "A" taken Impactor sample "B" taken
115 - 116	Filter sample "C" taken
117.6	Ball valve opened to inspect melt
118.0	Ball valve closed - zirconium delivery tube installed
119.0	Zirconium metal delivered to the melt (20 kg)
119.2	Ball valve closed
123.1	Gas grab sample 9-2 taken at location #2
124 - 125	Filter sample "D" taken

Table 5.1 Cont'd

EVENTS OF TEST SURC-4

124.1	Power supply off
125 - 126	Filter Sample "E" taken Impactor sample "C" taken Impactor sample "D" taken
125.2	Gas grab sample 9-4 taken at location #2
126 - 127	Filter sample "F" taken
131.7	Power supply on power meter reading 245 kw
133.2	Gas grab sample 8-2 taken at location #1
135.2	Gas grab sample 8-3 taken at location #2
137.1	Gas grab sample 8-4 taken at location #2
139.3	Gas grab sample 7-2 taken at location #2
141.2	Gas grab sample 7-3 taken at location #2
144.8	Power supply off
145.1	Power supply on power meter reading 245 kw
150.3	Gas grab sample 6-3 taken at location #1
155 - 156	Filter sample "G" taken
156 - 157	Filter sample "H" taken Impactor sample "G" taken Impactor sample "H" taken
156.1	Gas grab sample 6-4 taken at location #2
157 - 158	Filter sample "I" taken
158.1	Gas grab sample 5-2 taken at location #2
161.9	Pressure spike inside containment vessel
162.5	Melt flowing from bottom of containment vessel Power supply turned off Test terminated
165.0	Data acquisition changed to 15 second intervals
169.1	Gas grab sample 5-4 taken at location #1

Table 5.1 Cont'd

EVENTS OF TEST SURC-4

175.6	Gas grab sample 4-3 taken at location #2
177.0	Gas grab sample 4-4 taken at location #3
177.6	Data acquisition terminated
185.0	Gas grab sample 3-2 taken at location #3
190.0	Gas grab sample 3-3 taken at location #2

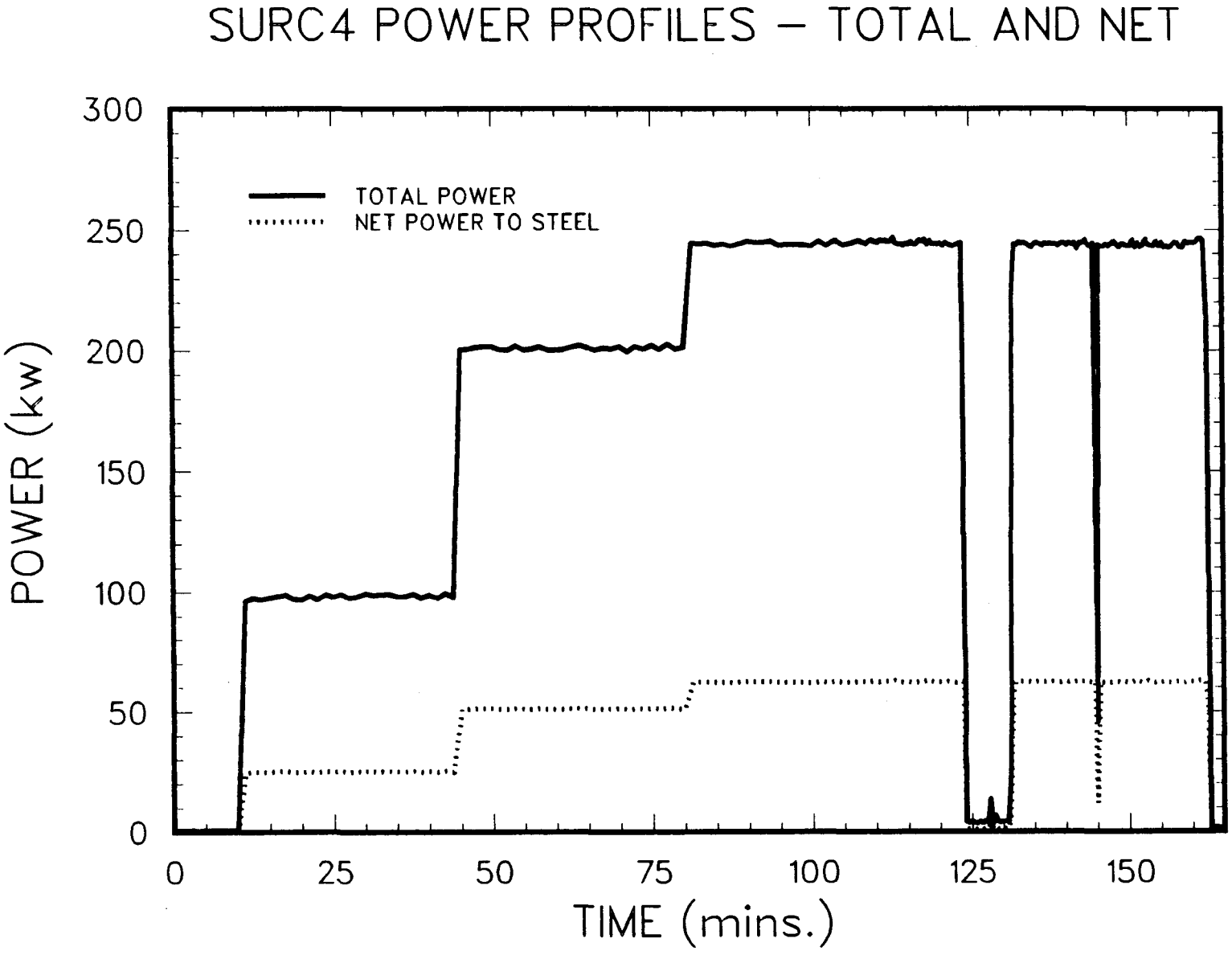

Figure 5.1 - Power History for SURC 4

at 155, 156, and 157 minutes. These were filter samples G, H, and I and impactor samples G and H--these again had durations of 1 minute. At time = 161.9 there was a pressure spike exceeding 7 psig inside the containment vessel--thirty seconds later, melt was observed flowing out the bottom of the apparatus. The power supply automatically shut off and the SURC 4 experiment was terminated at 162.5 minutes. Grab samples of gas were taken for the next 28 minutes.

6. INITIAL CONDITIONS, BOUNDARY CONDITIONS, AND POSTTEST OBSERVATIONS

The SURC 4 test met all of its established pre-test goals and was successful in observing and recording all the effects associated with both steady state concrete erosion as well as the additional effects of Zr addition on steel-concrete attack. These effects were evident in the measured meltpool temperatures, erosion rates, heat losses, gas flow rate, gas composition, and aerosol characterization. A total of nine aerosol filter samples and six impactor samples were taken for posttest analysis. Eighteen grab samples were taken for gas composition analysis and 70 mass spectrometer data points were recorded. Only three of the 166 data channels failed to record properly. The detective channels were M39 and M42 in the MgO sidewall and the meltpool thermocouple at a depth of 10 cm. All of these were redundant measurements so that essentially no information was lost.

6.1 Initial Conditions

Initial conditions for the SURC 4 test up to the onset of concrete ablation are shown in Figures 6.1 through 6.3. Figure 6.1 shows the heatup and melting of the steel slug. Complete melting of the slug required approximately 13 minutes. At the onset of ablation (105 minutes into the test) the temperature recorded by the thermocouple in the molten steel was 1750 K. Figure 6.2 shows the temperature profile in the basaltic concrete substrate prior to concrete ablation. Based on this figure, it is estimated that prior to the onset of concrete ablation evaporable water was released from the first 3-4 cm of concrete, bound water was released from the first 1-2 cm, and carbon dioxide was released from less than 1 cm. Figure 6.3 shows the thermal response of the MgO sidewall at a position adjacent to the steel charge and 10 cm above the initial concrete interface. When concrete attack started, the MgO sidewall was at a temperature of 1610 K at a depth of 0.5 cm, 1420 K at 1.5 cm, 1200 K at 2.5 cm, and 690 K at 9.0 cm.

6.2 Boundary Conditions

Figures 6.4 and 6.5 show the thermal response of the MgO walls in the upper region of the crucible - at 35 cm and 50 cm above the original concrete interface. Figure 6.6 shows the thermal response of the thermocouples embedded in the MgO cover. Substantial heating of the MgO is evident at each of these locations.

Based on the response of the thermocouples in the MgO walls adjacent to the molten steel during the experiment, the heat flux from the steel melt to the MgO has been calculated. These values are shown in Figures 7.1.9-7.1.11. Although minor fluctuations in the heat flux were calculated, a constant heat flux of 1.0×10^5 W/m^2 can generally be assumed.

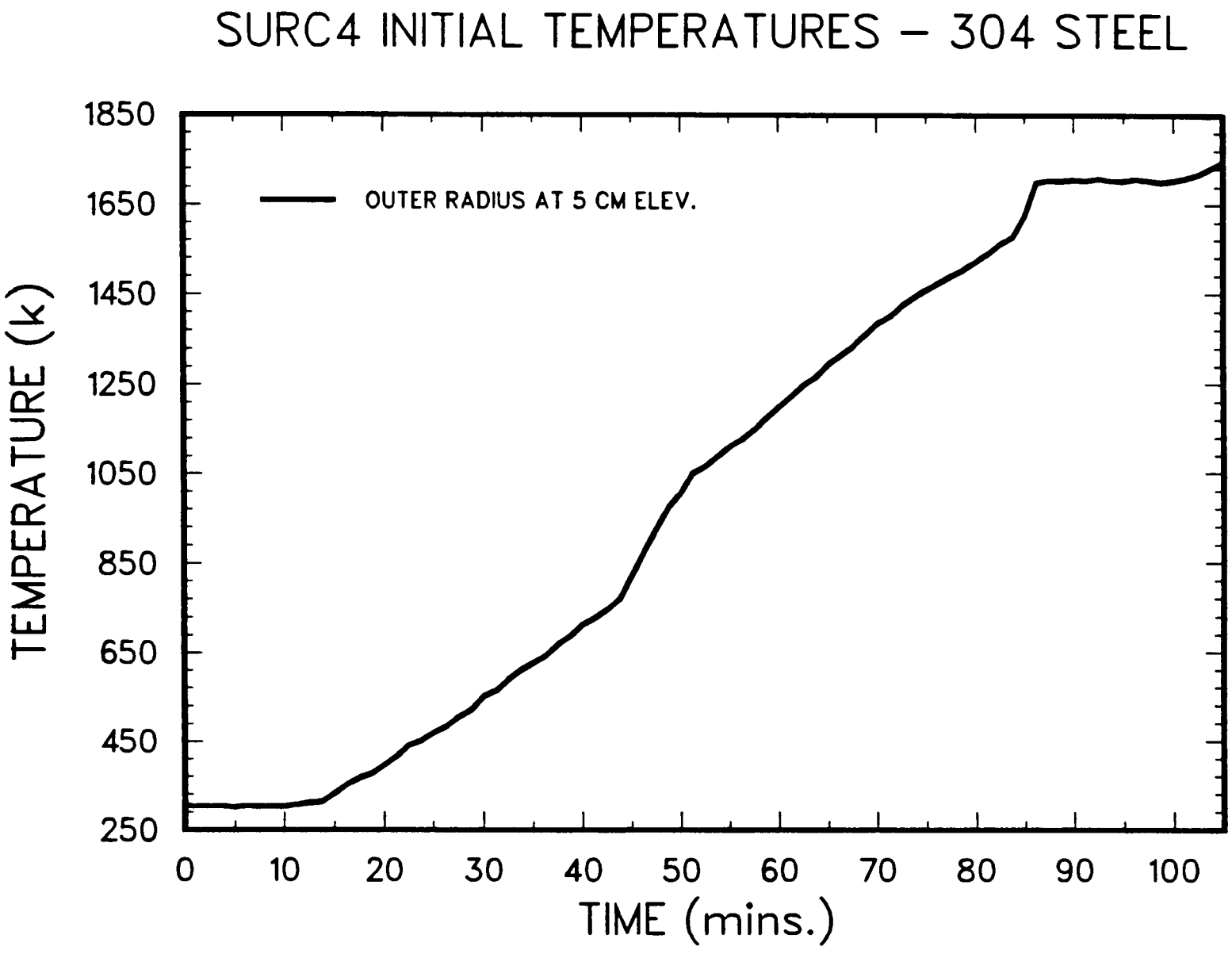

Figure 6.1 - SURC 4 Initial Steel Temperature

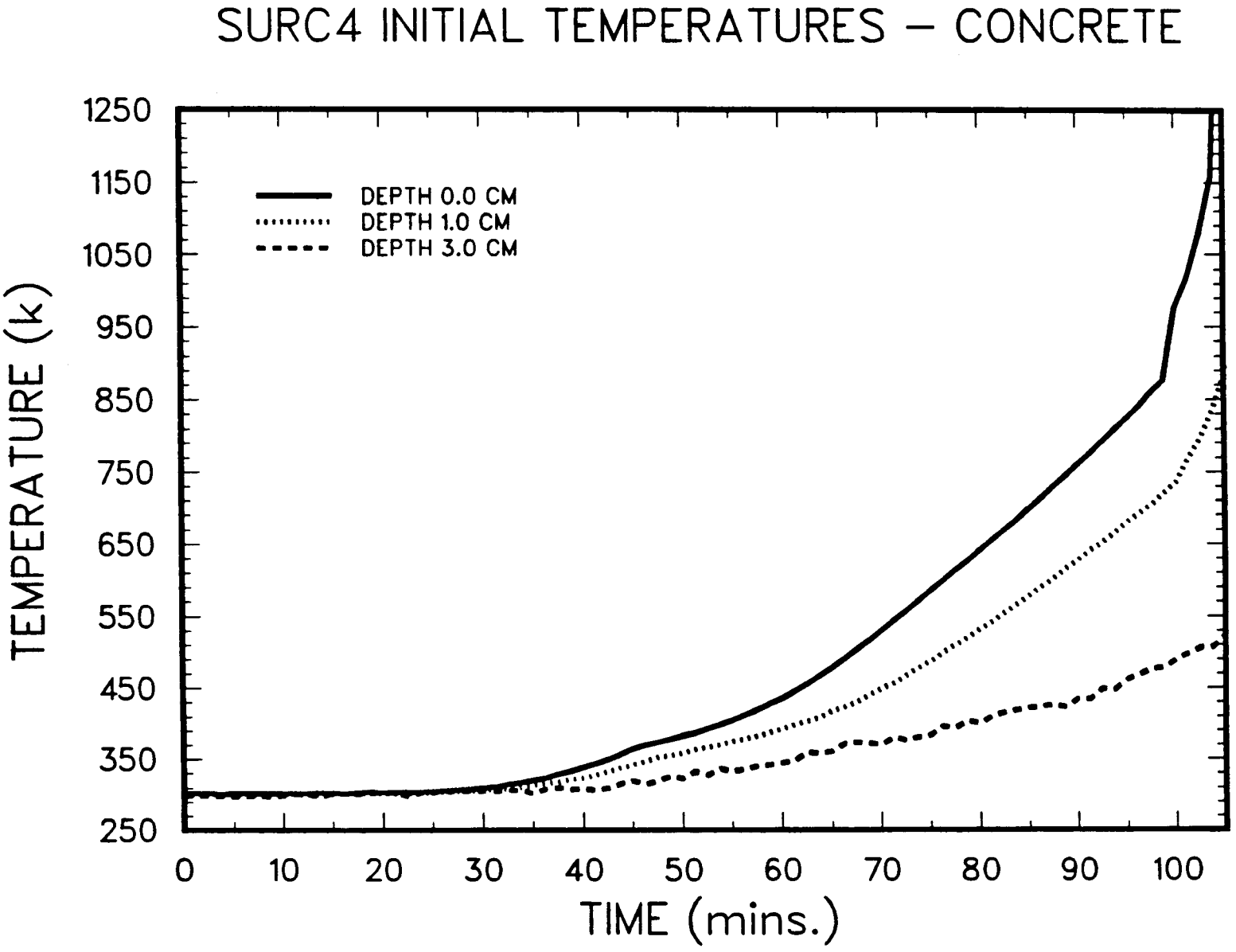

Figure 6.2 - SURC 4 Initial Concrete Temperatures

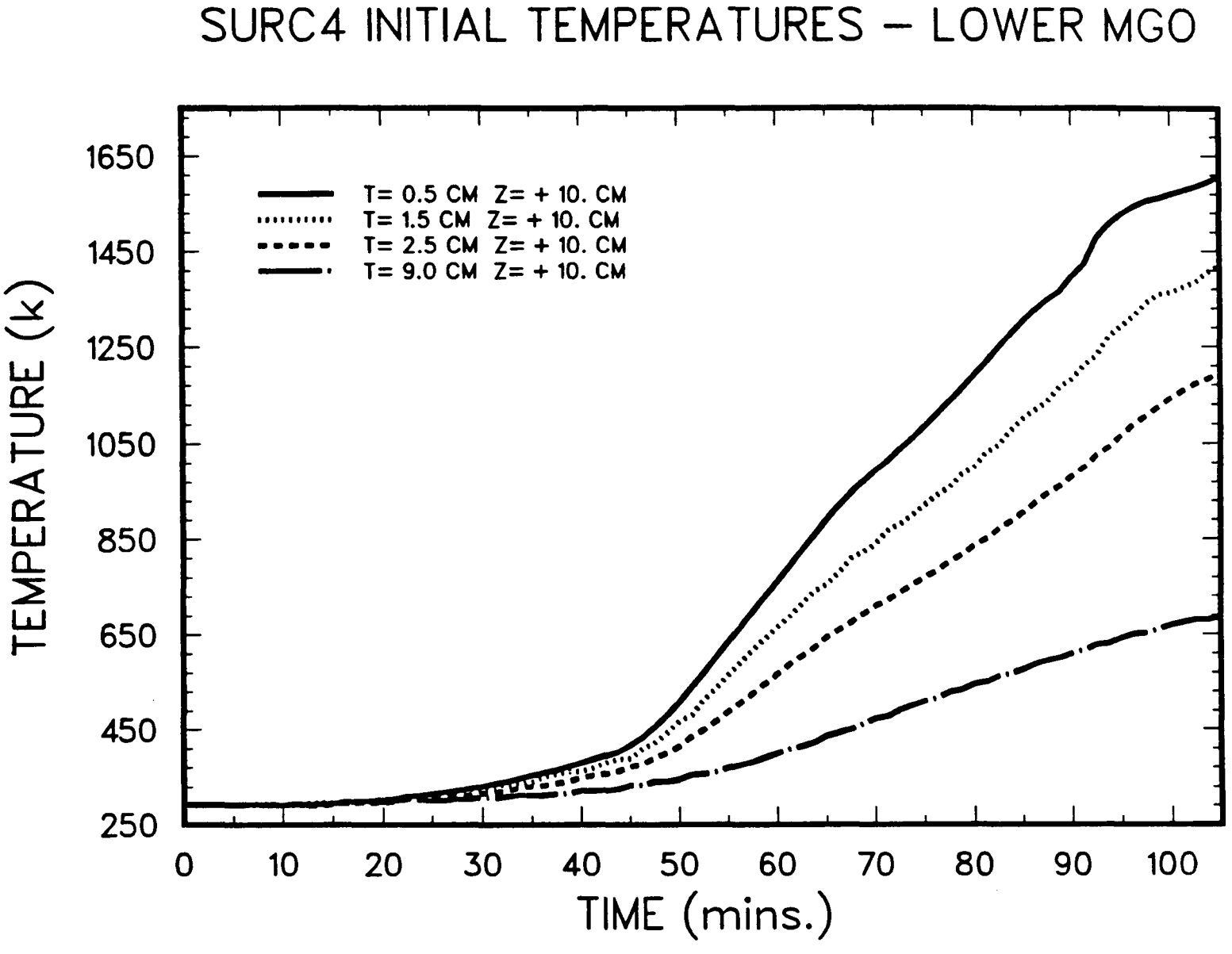

Figure 6.3 - SURC 4 MgO sidewall temperatures

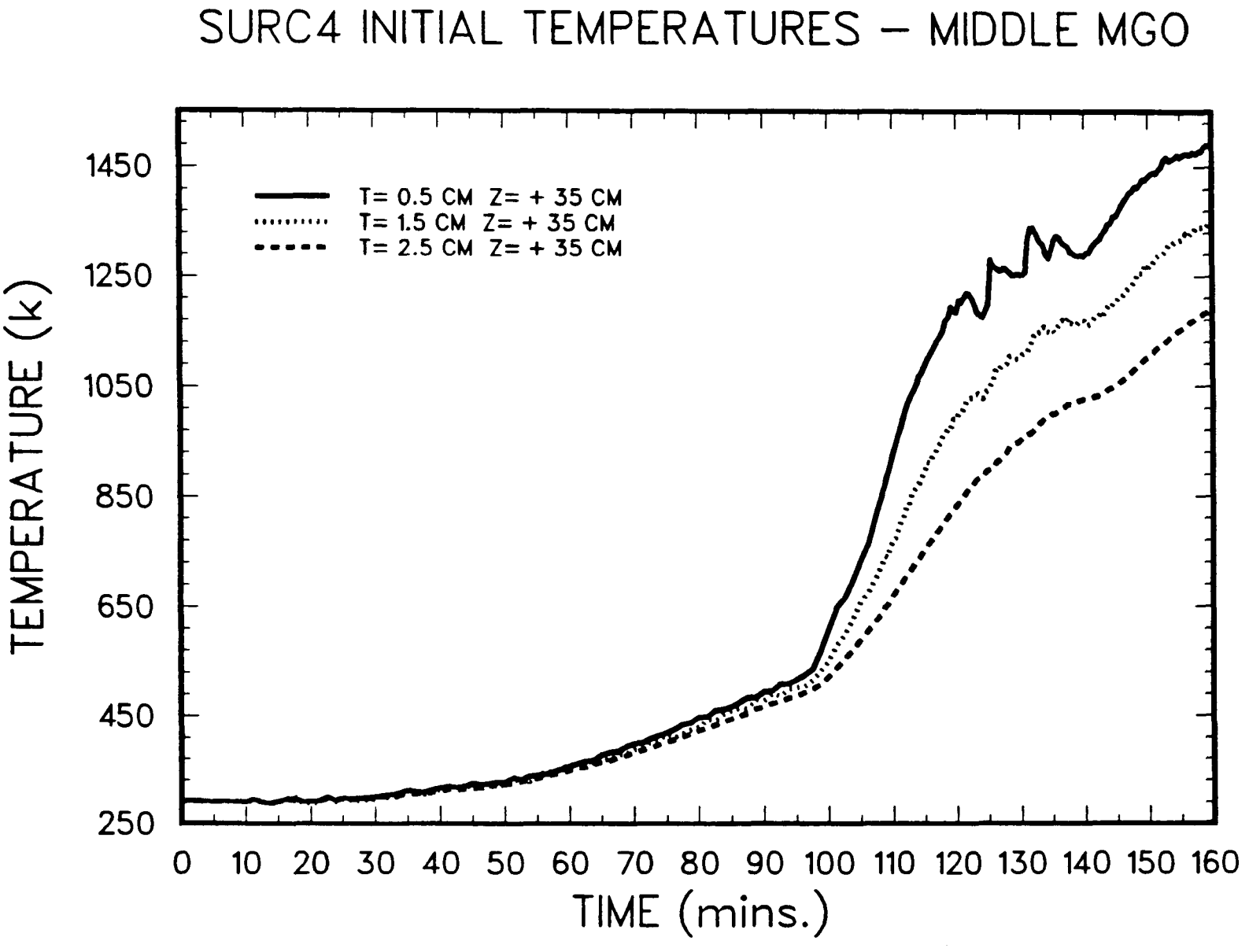

Figure 6.4 - SURC 4 Middle MgO Temperatures

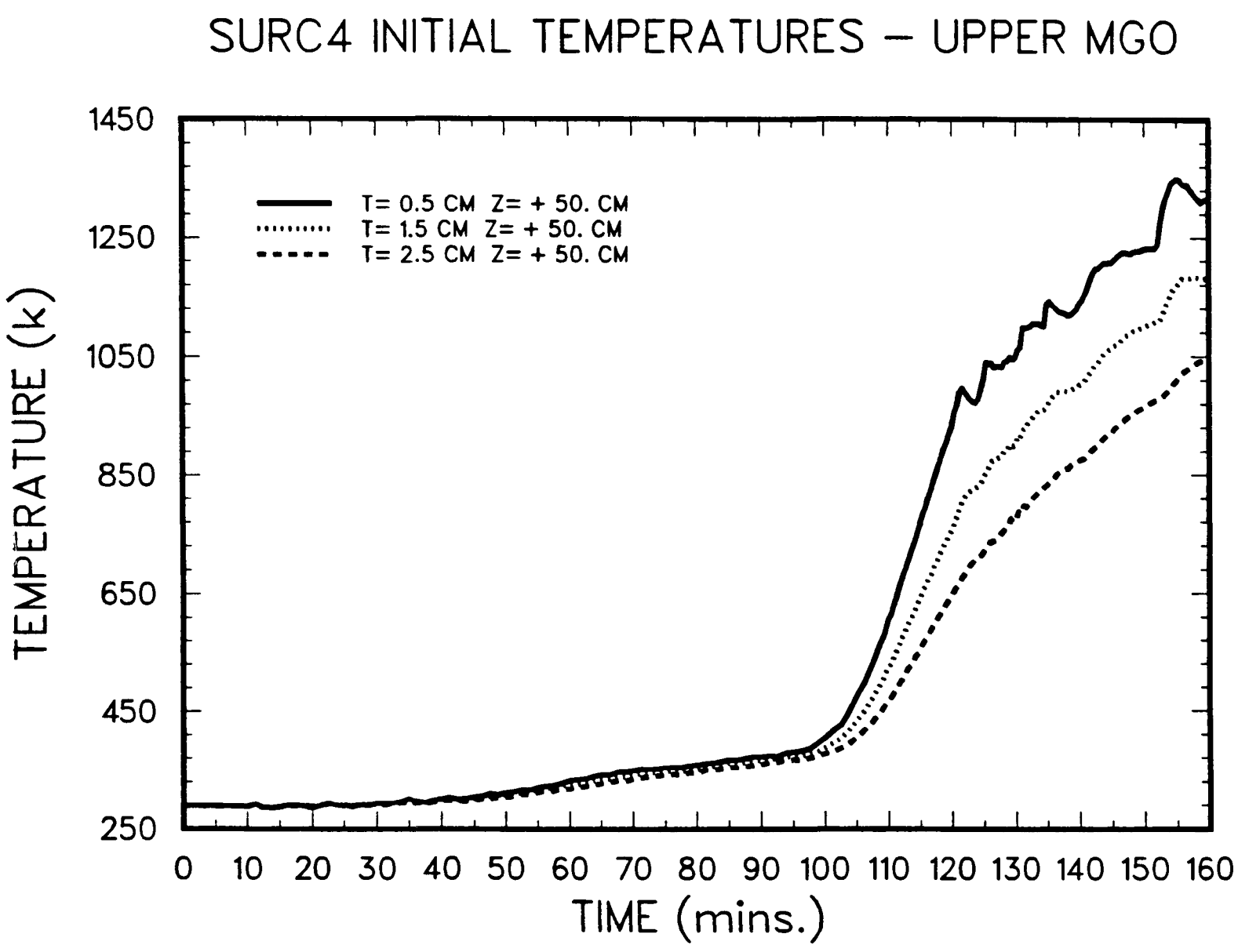

Figure 6.5 - SURC 4 Upper MgO Temperatures

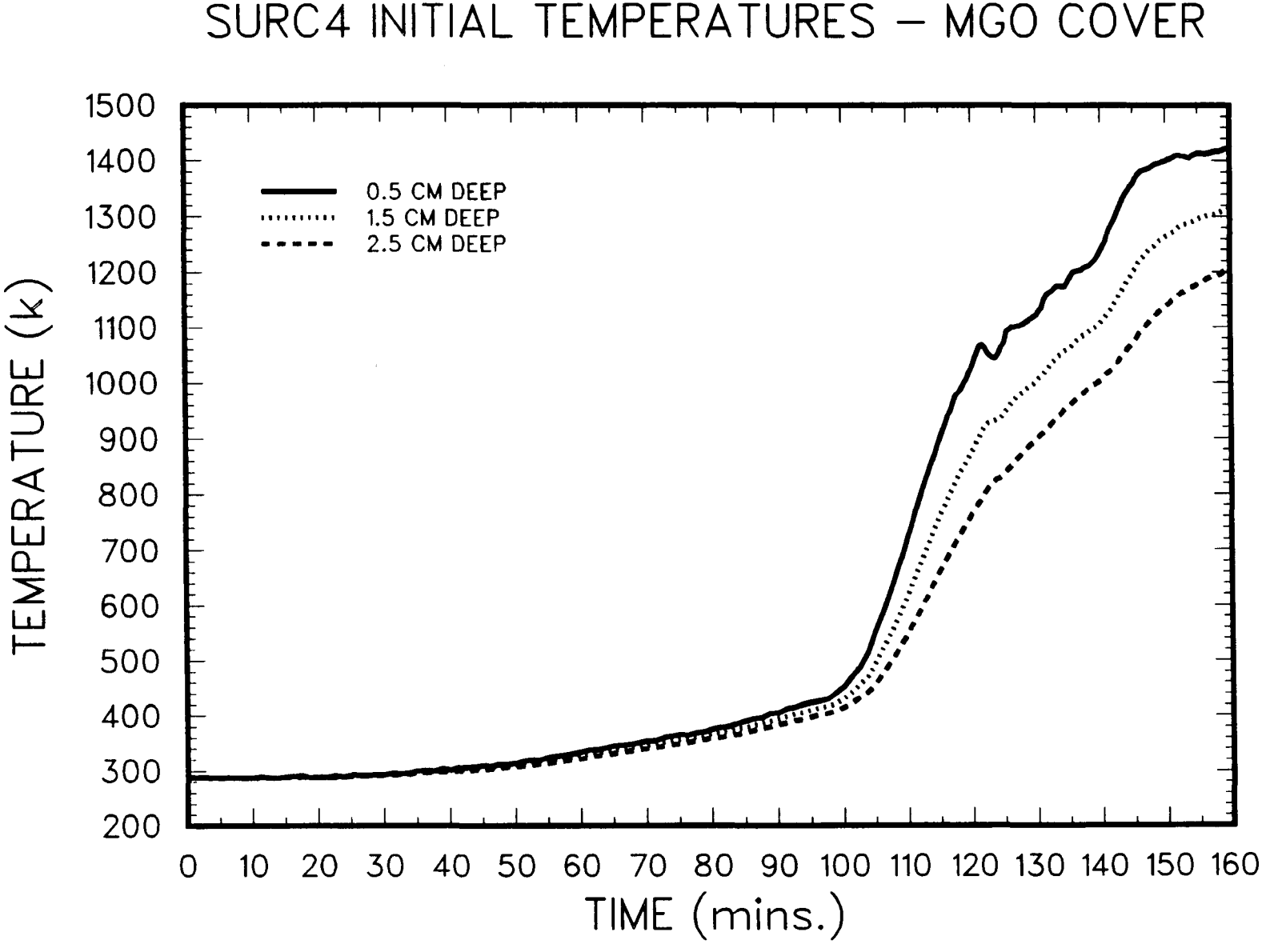

Figure 6.6 - SURC 4 MgO Cover Temperatures

6.3 Posttest Observations

The SURC 4 containment vessel was opened after the test in order to remove and section the interaction crucible. This inspection showed that the MgO sidewalls were intact and that there was no evidence of melt pool-sidewall interaction other than thermal dehydration. The molten steel charge had completely penetrated the bottom of the interaction crucible through a gap between the MgO annulus and the remainder of the concrete basemat. The remainder of the basemat was not cracked and showed no signs of asymmetric erosion. Further inspection of the steel charge and the slag material remaining in the crucible showed that 100% of the zirconium metal had been incorporated into the melt.

A posttest x-ray was taken prior to disassembly of the test article. The x-ray showed that several cracks were present in the MgO sidewalls of the inner crucible and that the central cavity of the crucible was filled with a material having an apparent density less than either MgO or concrete. No signs of steel, zirconium or other metallic materials were detected. The concrete interface was easily distinguishable and was slightly higher (2-3cm) in the center of the cavity than at the edges. A crack in the MgO sidewall appeared at the top of the crucible and extended roughly 20 cm downward. Another crack appeared at a distance 40 cm from the top of the crucible which extended at least 150° around the circumference. Aside from these cracks (~ 0.5 cm wide) there was no evidence of mechanical or chemical decomposition of the MgO sidewalls.

Following x-ray examination, the SURC 4 test articles were dissasembled. The aluminum containment vessel was unbolted and lifted to reveal the coil and crucible. Examination of the upper containment bell showed a thin layer of black aerosol deposition throughout the structure. The coil and crucible from SURC 4 are shown in Figure 6.7. The upper lid to the crucible had been lifted and broken during the test. A green and black lava-like substance was found frozen in the cracks, on the sides, and around the bottom of the crucible. A large circumferential crack was observed roughly 40 cm below the top of the crucible and level with the top of the induction coil. This crack was also penetrated by the green and black lava-like substance. Approximately 18,000 cubic centimeters of the lava-like substance were found in the gap between the coil and the pressure vessel. The material was black to green in color, very porus, and glass-like in nature with a density ranging from 0.7 to 1.2 g/cm^3.

The coil was removed and the lower crucible was sectioned so that the internals could be examined. The result is illustrated in Figure 6.8. The interior of the crucible was filled with black to green porus material similar to that found on the exterior. The MgO walls were discolored to a depth of 1 or 2 cm but were otherwise unaffected mechanically or chemically. There was no evidence of metal in the crucible. All indications were that, at

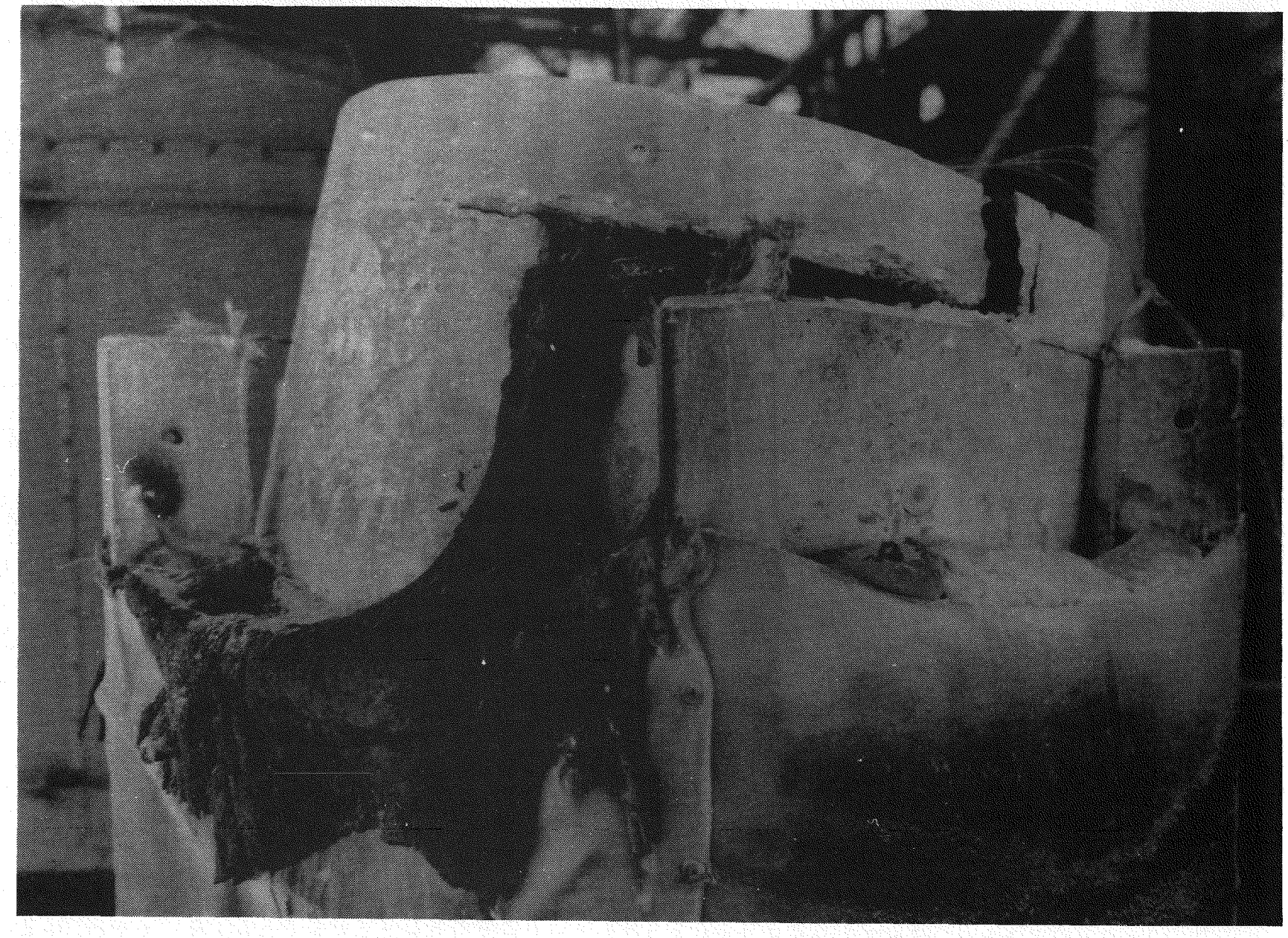

Figure 6.7 - Posttest Examination of the SURC 4 Crucible

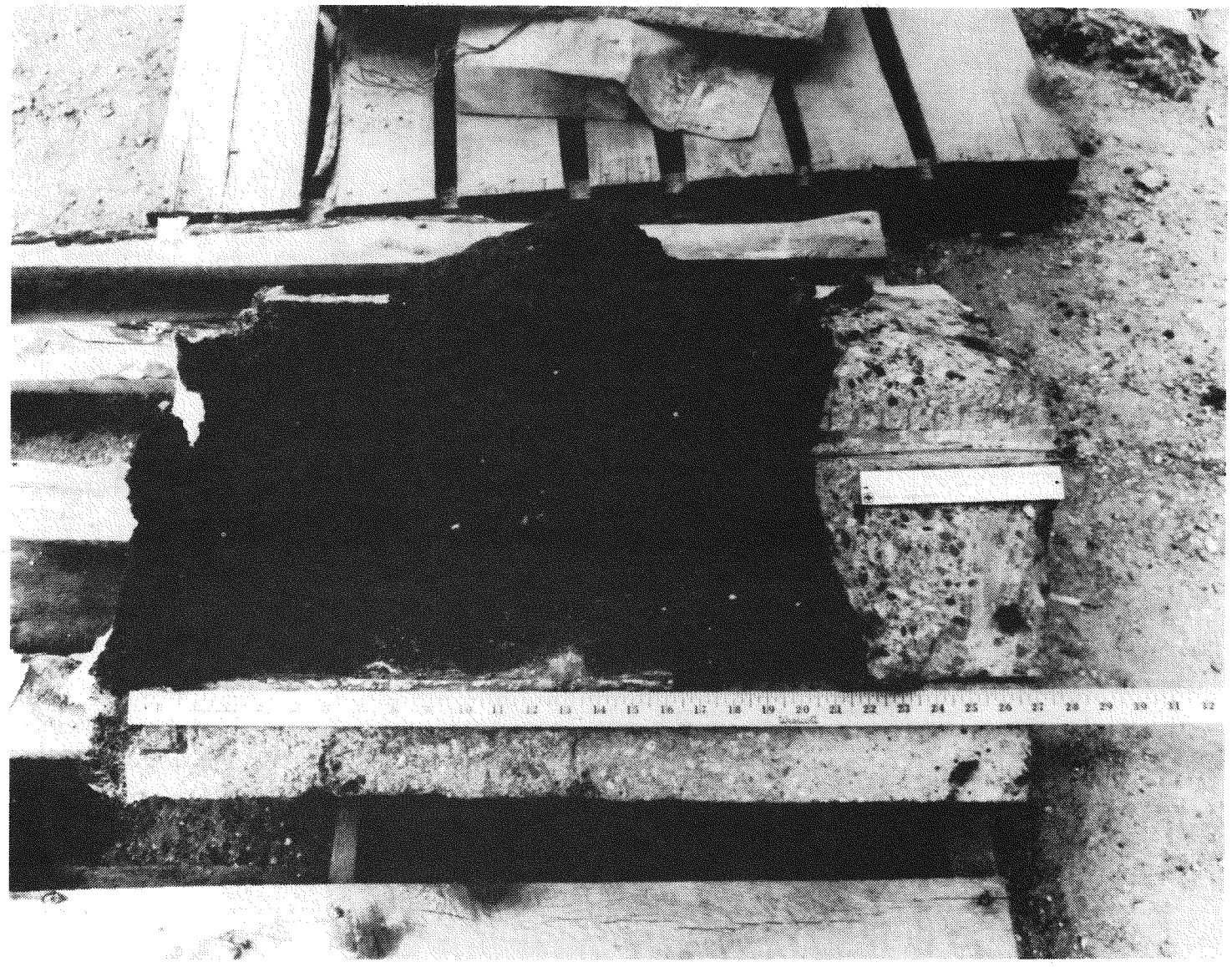

Figure 6.8 - SURC 4 Crucible Section

the conclusion of the SURC 4 test, the melt escaped through the bottom of the crucible via a 1 cm separation between the concrete and the MgO annulus located adjacent to the far radial thermocouple bundle. The interface between the concrete and the overlying black-green material was sharp and well defined, indicating that material had slumped back to the interface after the exit of the steel. In addition there was a voided area in the upper third of the crucible which roughly approximated the volume of steel in the SURC 4 test. This void probably formed when the crucible failed and the steel was discharged. Inspection of the remnant concrete plug showed that the concrete near the melt interface was discolored and chalky in texture to a depth of .5 to 1 cm. The remnant plug had a height of 12.5 cm along the outer radius and 15.5 cm in the center indicating a total erosion distance between 24.5 to 27.5 cm.

The flow pipe from the crucible to the aerosol and flow instrumentation was also disassembled and inspected. Green and black material similar to that found in the crucible was found to be forced along the flow path for a distance of 190 cm. A 2 cm opening remained on the crucible side of the flow pipe. This opening narrowed to roughly 1 cm at the outlet but was continuous and provided a constricted but unobstructed flow path to the aerosol, gas analysis, and flow instrumentation. The aerosol, gas analysis, and flow orfices were inspected and were found to be covered with a fine black powder but were otherwise unobstructed.

The molten steel that escaped from the SURC 4 crucible at the conclusion of the test ran down through the MgO bricks in the bottom of the containment vessel then melted out the bottom of the vessel and poured out onto the concrete pad at Sandia's Large Melt Facility Test site. A footprint of the frozen steel runout is shown in Figure 6.9. This runout weighed approximately 180 kg. It was 180 cm long and 40 to 90 cm in width. The thickness of the runout was measured in eight locations along the footprint and was found to vary between 1.6 and 3.4 cm with a mean value of 2.7 cm.

Material swipes were taken from the inside of the aluminum containment bell and the aerosol sampling port. These samples were analyzed using Inductively Coupled Plasma (ICP) atomic emission spectrometry to determine their elemental composition. Additional samples were taken from the metallic steel runout and the black to green lava-like material found outside the crucible and in the flow tube. These were also analyzed using the ICP technique. Results for eight samples are shown in Table 6.1 along with an analysis of the original 304 stainless steel material. These results indicate that the aerosols within the containment bell were rich in MgO and steel while those taken from the aerosol sampling port were rich in tellurium.

The foamy black-green by-product of the Zr-steel attack on the final 20 cm of basaltic concrete had an approximate total volume

Figure 6.9 - Melt Runout Footprint

Table 6.1 - SURC 4 Posttest Chemical Analysis

Elemental Composition in Weight Percent*

Sample Descriptor	Fe	Ni	Cr	Mn	Mg	Ba	Na	K	Si	Ca	Te	La	Ce	Zr
4.0 Containment Aerosol Grey-Green Powder	.4	.05	.07	.05	26.6	.07	.14	.3	1.3	.85	6.3	--	.15	--
4.2 Containment Aerosol Darker Residue	.15	.03	.02	--	32.2	--	.08	--	.4	.6	.4	--	.25	--
4.3 Containment Aerosol Light Residue	15.2	.09	1.9	.1	30.7	--	.1	--	.4	.6	.1	.03	.3	--
4.4 Flow Tube Aerosol Black Fine Powder	.6	.07	.4	.9	10.2	--	4.8	6.0	1.2	.14	41.	--	.1	--
4.5 Flow Tube Material Black-Green Lava	.73	.05	3.8	2.6	2.8	.75	.1	.1	12.2	7.9	.4	.9	1.7	17.2
4.6 Inner Crucible Black-Green Lava	1.9	.18	3.8	2.7	2.8	1.0	2.1	.21	15.3	7.7	.6	.9	1.2	17.8
4.8 Outer Crucible Black-Green Lava	.6	.03	3.9	2.7	3.0	.8	1.2	.12	15.9	8.3	.3	.9	1.1	17.3
4.10 304 Stainless Steel Pre-test Solid	68.0	9.64	18.2	1.67	.1	.26	--	--	.86	--	--	--	--	--
4.7 304 Stainless Steel Posttest Runout	69.5	9.85	16.1	.33	.11	1.2	--	--	.92	--	.1	--	--	--

* Balance of material is noble gas, halogen, H, O, or S.

of 100,000 cm^3. This lava-like substance was comprised of 17-18% Zr in addition to concrete and steel component oxides as indicated in Table 6.1. Additional analyses of the foamy material were performed using x-ray diffraction and microcombustion techniques. The x-ray diffraction analysis identified the major phases of the foamy material as calcium iron magnesium silicate (Augite) and zirconium oxide (Baddeleyite). The microcombustion analysis indicated that trace amounts of hydrogen, carbon and nitrogen were present in the foam with carbon having the largest abundance at .1 weight percent. By comparison, the metallic meltpool material at the end of the SURC 4 test was devoid of Zr metal and showed reduced amounts of chromium and manganese. For a density of 1 g/cm^3, the zirconium content of the foamy by-product is 17-18 kg so that at least 85% and perhaps all of the 20 kg of zirconium metal which was added to the meltpool is now located in this foamy lava-like material. Similarly, the by-product material has 3.5 to 4 kg of chromium metal in it whereas the metal residue is missing 4.2 kg of chromium.

7.0 DATA PRESENTATION AND RESULTS

The 200 kg, 304 stainless steel charge, doped with fission product simulants was inductively heated for approximately 100 minutes prior to the onset of melting and concrete erosion. At t = 119 min, after eroding between 4 to 7 cm of concrete, and establishing a steady ablation rate, 20 kg of zirconium metal was released to the melt pool. At t = 162 min, after ablating between 24 and 27 cm of concrete, melt escaped the crucible by flowing down the interface between the concrete slug and MgO annulus, thus terminating the test.

7.1 Temperature Data

The temperature data from SURC 4 are used to determine concrete erosion and the crucible thermal response. Three regions of the melt/concrete interaction are shown in Figure 7.1.1. The pool consists primarily of stainless steel, but it may also contain zirconium metal and condensed products of concrete decomposition and fission product compounds. The "dry" region consists of the concrete that is dehydrated, decomposing, and beginning to melt. The "wet" region is the concrete that still contains water of hydration and water in the concrete pores. The transition between the "wet" and the "dry" region is taken here to be the point at which hydration and pore water undergo the phase change to vapor.

Surrounding the three important regions of the melt/concrete interaction in the SURC 4 test, is the magnesium oxide annulus. In an ideal circumstance, the confining annulus of the test would be totally inert. That is, it would neither conduct heat nor mechanically degrade or chemically interact. Clearly, no such totally inert material exists and it is necessary to consider how the magnesia annulus affects the melt/concrete interaction.

In this section, the temperature data obtained in the SURC 4 experiment will be used to describe the thermal response of the three regions of melt/concrete interactions, the magnesium oxide annulus and crucible cover.

Concrete Response

Some typical temperatures plotted as a function of time, indicated by thermocouples embedded in the concrete slug, during a period of steady ablation, are shown in Figure 7.1.2. The temperature histories for other thermocouples cast into the concrete slug in various arrays are presented in Appendix E. Temperatures rise slowly between 400 and 600 K as the concrete dehydrates followed by a rapid increase to failure caused by contact with the melt pool. The failure temperature for type K thermocouples is approximately 1645 K.

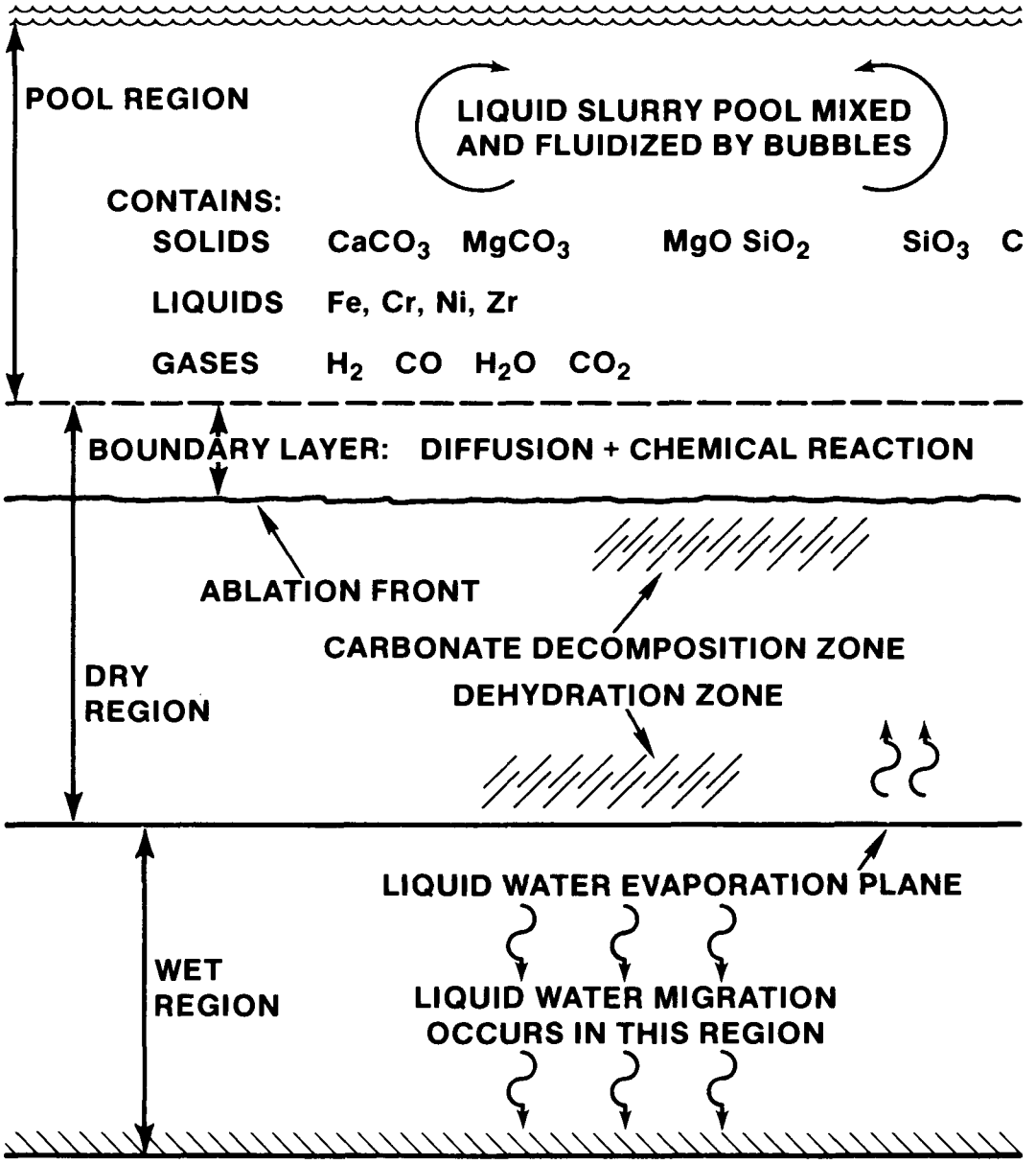

Figure 7.1.1 - Three regions for analyzing melt concrete interactions

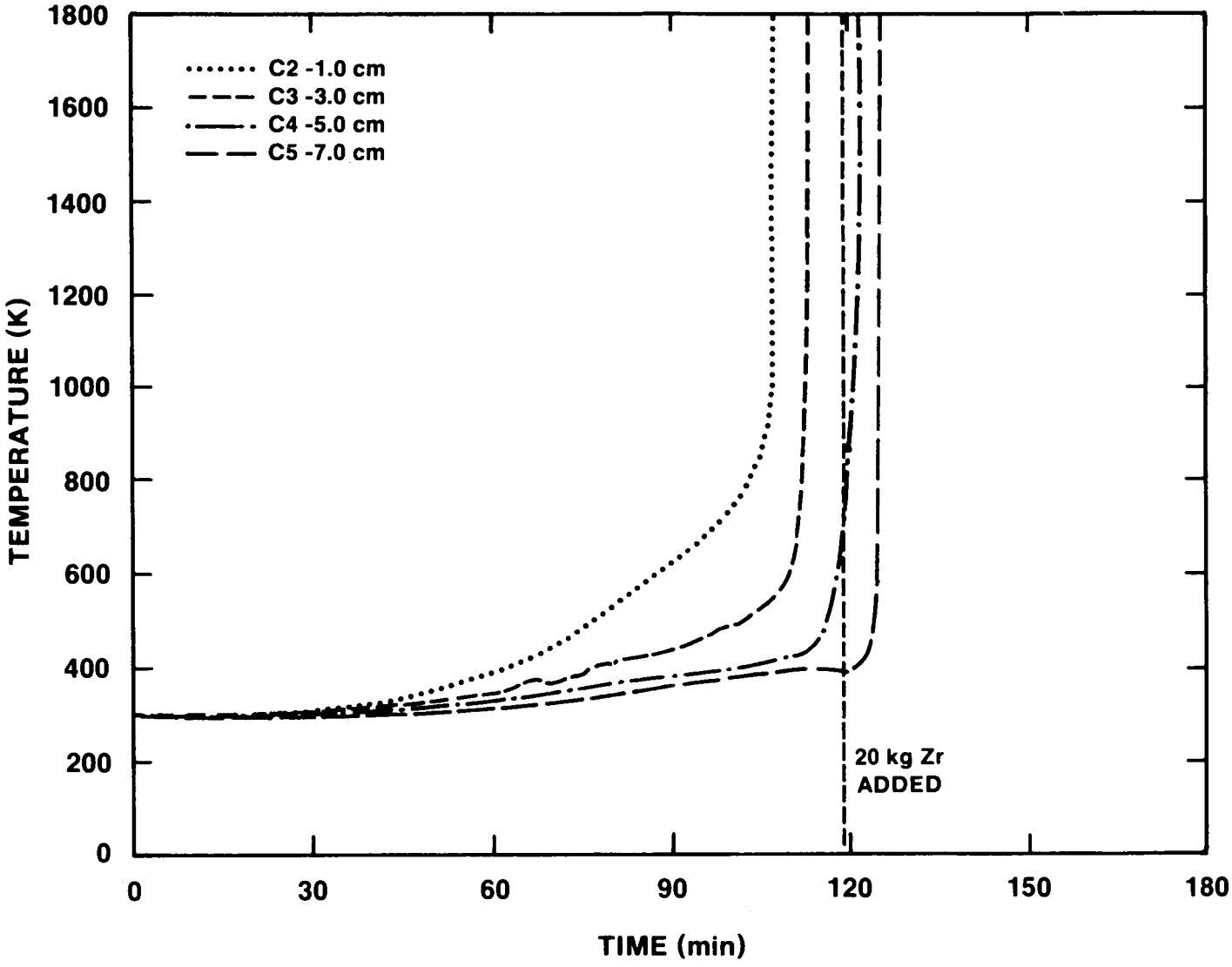

Figure 7.1.2 - Typical SURC 4 concrete thermal response

The propagation of the interface between the "wet" and the "dry" zones may be characterized in the SURC-4 test by the motion of the 400 K isotherm. The location of this isotherm is shown plotted as a function of time in Figure 7.1.3. The isotherm begins to move through the concrete slug during the initial heating of the stainless steel cylinder and assumes a steady rate between t = 35 and t = 100 min. The propagation rate of the isotherm increases during the steady ablation period between t = 100 and t = 119 minutes. After the addition of 20 kg of zirconium at t = 119 the propagation rate of this isotherm increased significantly and remained nearly constant for the duration of the test. The power supply was turned off between t = 124 and 132 to repair a hose that supplied cooling water to the aluminum containment vessel. This period of power loss did not appear to have any effect on the propagation rate of the 400 K isotherm.

During the initial heating period of the stainless steel cylinder, the velocity of the interface was calculated to be 6 ± 1 cm/hr. The velocity of this isotherm for the steady ablation period between t = 100 and t = 119 min was calculated to be 12 ± 1.5 cm/hr. This is twice the initial rate. After the zirconium addition at t = 119 and for the remainder of the test to t = 162, the velocity was calculated to be 30 ± 3 cm/hr. This final propagation rate is over two and one half times the steady state ablation rate and almost five times the initial rate.

The basaltic concrete used in the SURC-4 experiment melts over the temperature range of 1350 to 1650 K. The temperature at which physical ablation of the melting concrete occurs is not precisely known. Here it is assumed ablation occurs at 1600 K for the purpose of measuring the propagation of the erosion front. The position of the 1600 K isotherm plotted as a function of time is shown in Figure 7.1.4. Based on the data shown in the figure, concrete ablation began at approximately t = 102 min. and continued until the melt escaped the crucible terminating the test at t = 162. There were two interesting observations made based on the erosion data. First, the addition of the zirconium significantly increased the ablation rate of the concrete. Secondly, the eight minute loss of power between t = 124 and 132, did not effect the ablation rate. During the initial period of ablation prior to zirconium addition between t = 102 and t = 119 min. the velocity of the ablation front was calculated to be 16 ± 2 cm/hr. The propagation rate after the zirconium addition between t = 119 and t = 162 was calculated to be 29 ± 2 cm/hr. Based on these calculations, the ablation rate after the zirconium addition nearly doubles and increases 15 cm/hr compared to the initial rate. The data in Figure 7.1.4 show an offset when comparing individual arrays. Posttest observations indicated that the erosion front of the outer radius array preceeded the center array by about 3 cm. This data confirms this fact and shows that the erosion pattern developed early and was maintained throughout the test.

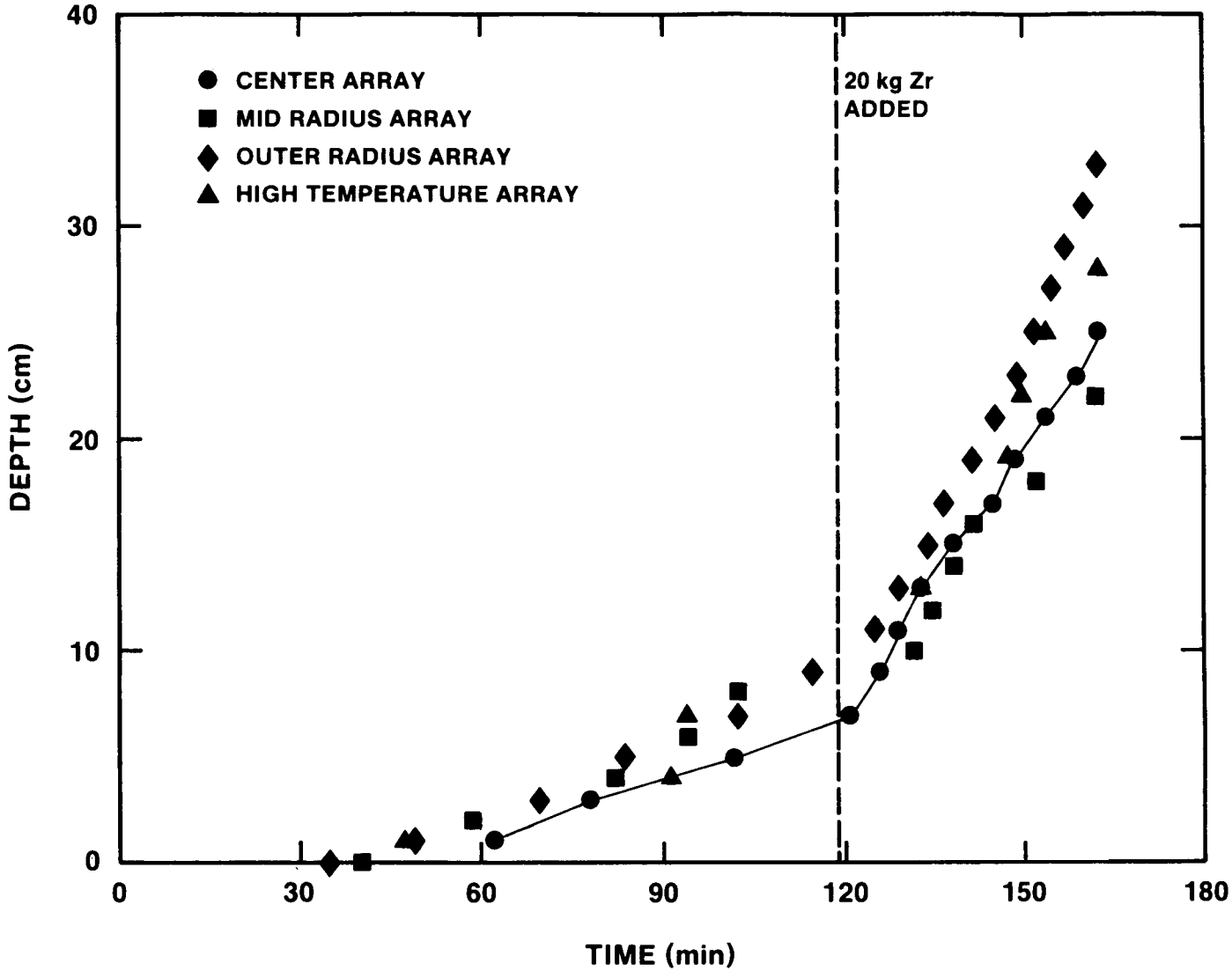

Figure 7.1.3 - Propagation Rate of the SURC 4 400°K Isotherm

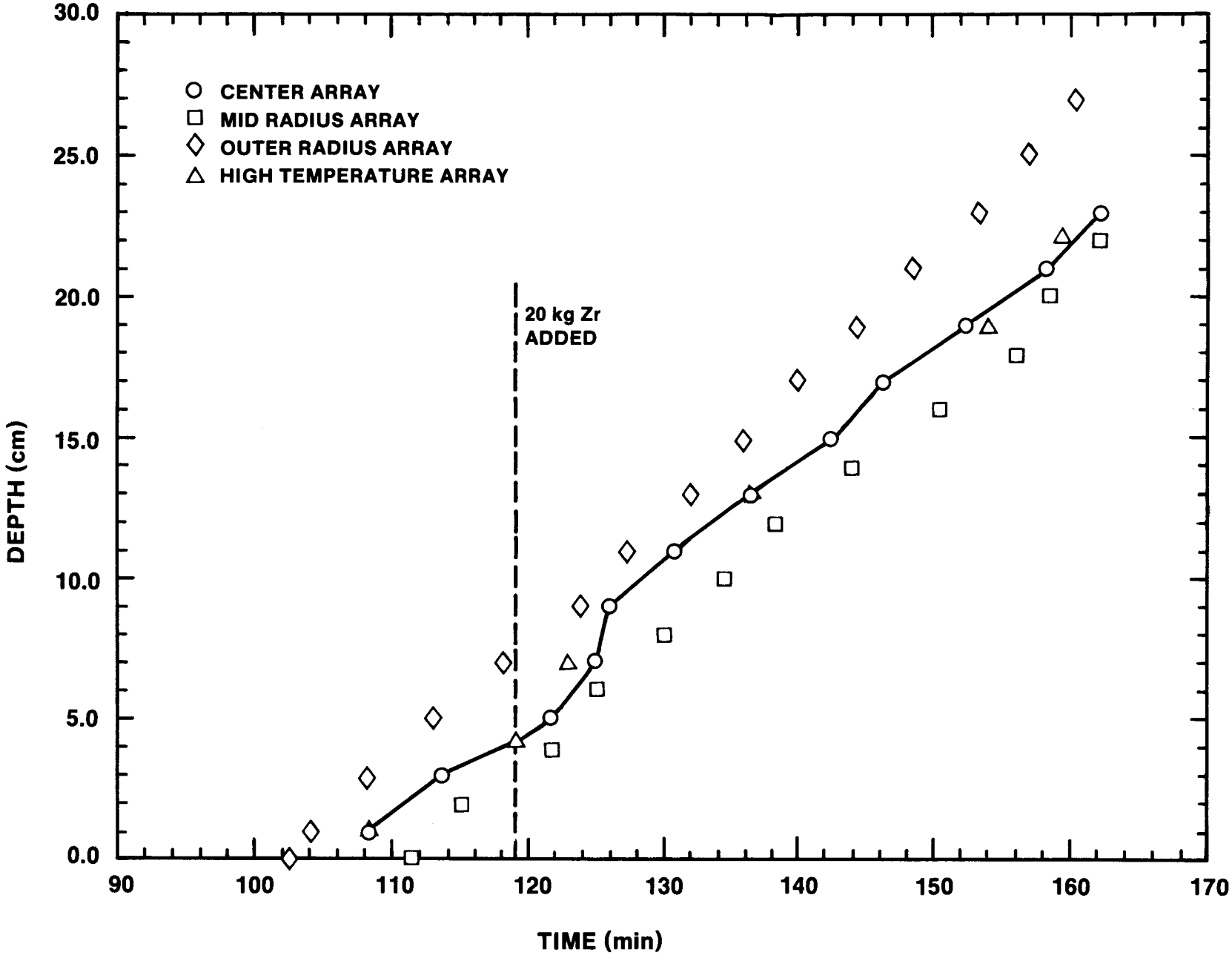

Figure 7.1.4 - Propagation of the SURC 4 Erosion Front

The depth to which the concrete was dehydrated (Note that the dehydration temperature increases as test proceeds) can be determined by comparing the position of the 400 K (wet/dry interface) and 1600 K (ablation front) isotherm at a specific time. Figure 7.1.5 shows a plot comparing data representing the 400 and 1600 K isotherms. The depth of the dehydrated concrete at the onset of ablation is initially 4 cm at t = 102 min. The 1600 K isotherm converges to within 3 cm of the 400 K isotherm near t = 125 min. After this time the 400 K isotherm precedes the ablation front by approximately 2 cm on the average for the remainder of the test.

Meltpool Temperature

Melt temperatures were measured during the experiment with six type C and six type S thermocouples installed in alumina tubes and cast at various depths within the concrete slug. A typical temperature response of these thermocouples plotted against time is shown in Figure 7.1.6. Other individual plots of melt temperature can be found in Appendix E. The figure shows that for each thermocouple the temperature increases slowly between 400 and 1000 K. Upon contact with the advancing melt front, the temperature then rises rapidly to a plateau usually lasting several minutes. These plateaus closely match the failure times of the type K thermocouples from the center array. Figure 7.1.7 shows a plot of the peak temperature prior to failures during the test. The melt temperature ranged between 1785 and 1925 K. This amounted to a superheat in the steel of between 85 and 225 K. The results show that the 304 stainless steel reached its melt point of 1700 K at 86 minutes into the test. After 100 minutes, concrete erosion began along with a meltpool temperature increase from 1700 to 1785 K, indicating a superheat of 85 degrees. This temperature was maintained for twenty minutes during which 4-6 cm of concrete were eroded. Zirconium was then added to the melt at time 120. Immediately after Zr addition, the melt temperature began to rise and five minutes later reached a peak temperature of 1925 K. This increase represents a superheat of 225 K and was sustained despite the fact that the power to the melt was temporarily lost for eight minutes between times 124 and 132. The meltpool temperature during the remainder of the test decreased to 1835 K at time 140 and then to 1790 K at time 160.

MgO Sidewalls

The heat transfer to the MgO sidewalls during the interaction has a global effect on the energy balance and therefore, the heat transfer to the concrete. As discussed in Section 3.2 thermocouple arrays were installed at various locations within the MgO annulus to determine the thermal response of the sidewalls. A typical temperature history is shown in Figure 7.1.8 for the sidewall array located adjacent to the melt at an elevation of z = +10 cm. Thermocouple M22 located at a depth of 0.5 cm rises gradually and fails at approximately t = 108 min. Thermocouples M23 and M24 located at depths of 1.5 and 2.5 cm

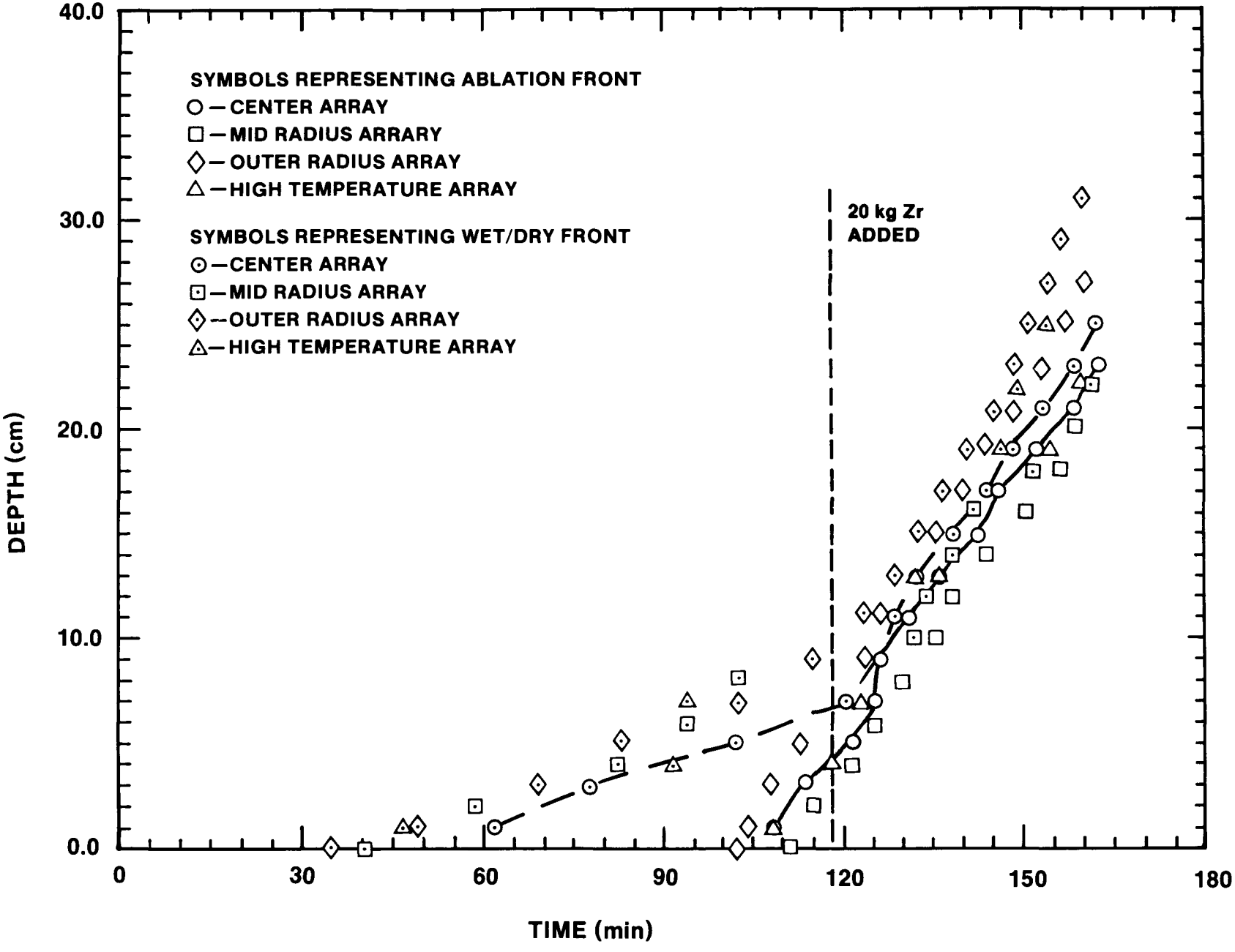

Figure 7.1.5 - Comparison of 400 K and 1600 K Isotherms in SURC 4

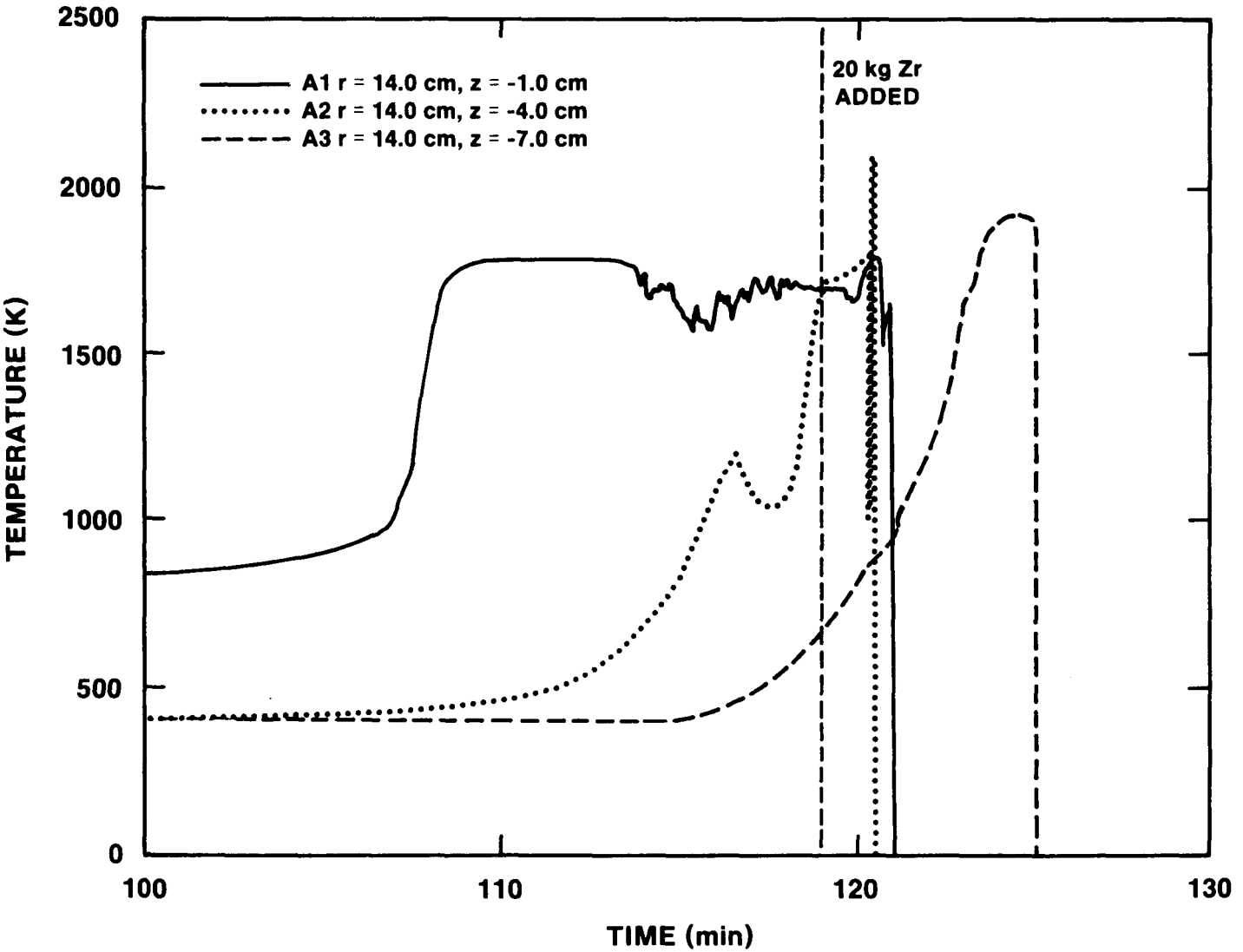

Figure 7.1.6 - Typical SURC 4 Meltpool Thermocouple Response

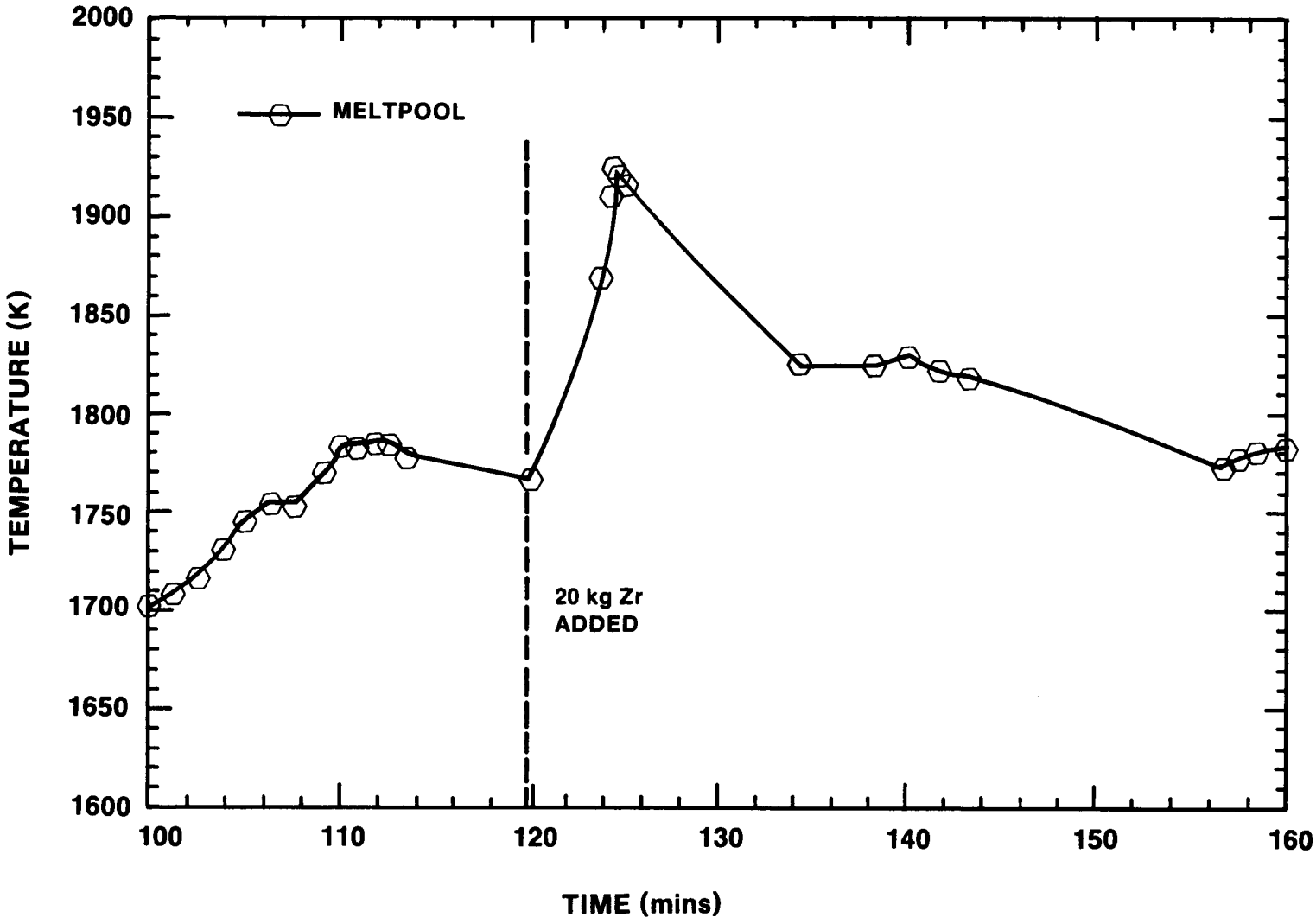

Figure 7.1.7 - SURC 4 Meltpool Temperature as a function of time

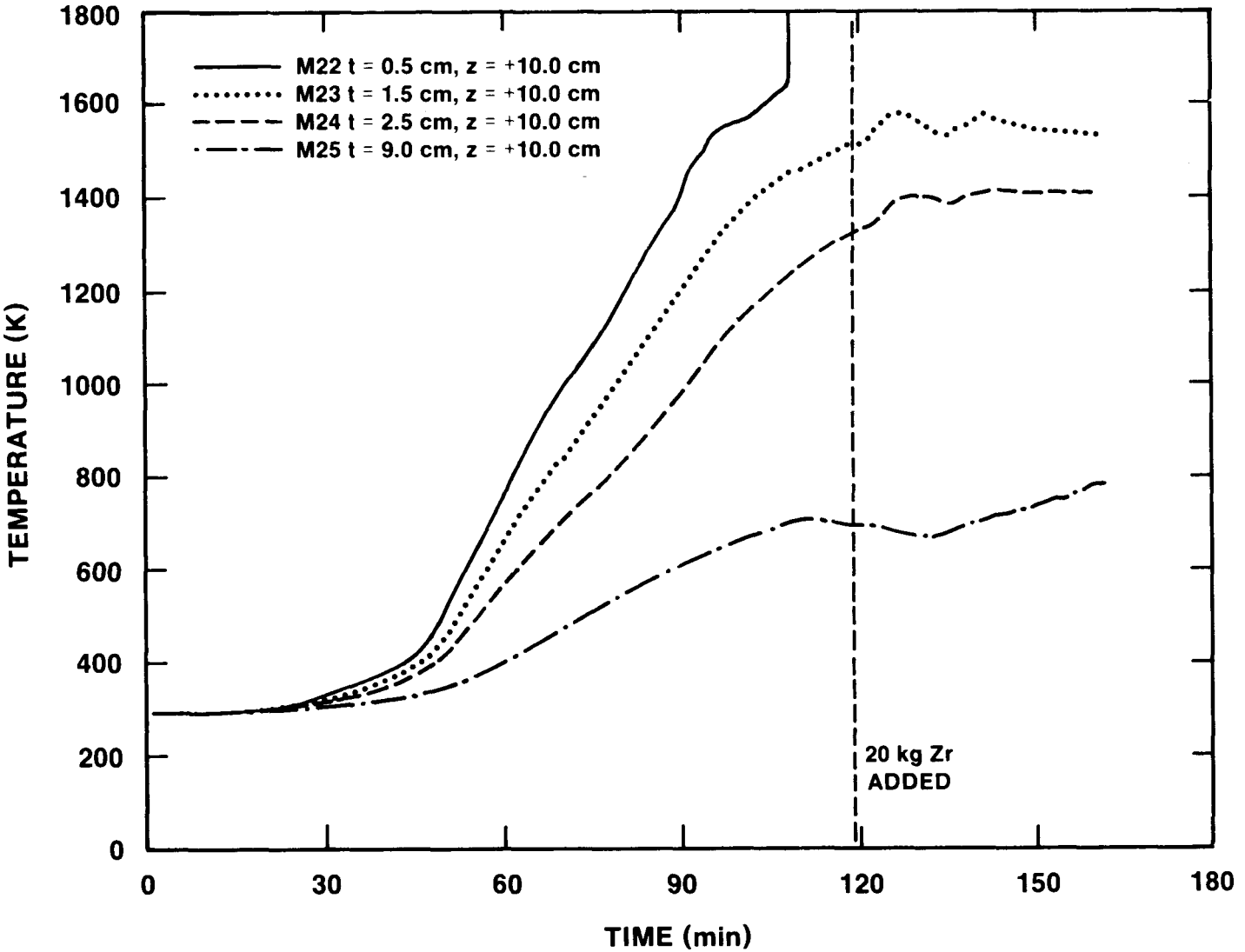

Figure 7.1.8 - Typical SURC 4 MgO Thermocouple Response

respectively, peaked at temperatures of 1580 and 1420 K and remain near this value until the test was terminated. Thermocouple M23 indicates a 70 K increase in temperature shortly after the zirconium was delivered to the melt pool. This temperature increase is also detected by thermocouple M24. The thermocouple located at a depth of 9 cm near the perimeter of the annulus rises gradually and peaks at a temperature of 800 K at test termination. The temperature histories measured by thermocouples in other arrays, cast into the MgO sidewall, are presented in Appendix E.

The calculation of heat flux to the MgO walls is a classic example of an "inverse" heat conduction problem (IHCP) where the boundary condition (e.g., heat flux) is determined from known interior temperatures. Of the available methods for solving the IHCP, one that appears to be successful for a wide variety of applications is a non-linear estimation technique. In this method, the value of the calculated heat flux minimizes the square of the difference between the calculated and the experimental temperatures. A computer code, IHCP, has been written by Bradley based on Beck's methods (Beck, 1985). The code was tested using a variety of exact solution problems and was found to perform excellently. In general, it was found that the greater the number of thermocouples utilized in the analysis, the greater the accuracy of the solution. However, Bradley found that beyond three thermocouples, the improvement in accuracy was not sufficient to justify additional instrumentation. The experimental data utilized in the IHCP consisted of at least two thermocouples at depths from the surface of 0.5 to 2.5 cm into the MgO sidewall. A typical IHCP solution was calculated for each array of the thermocouples that was imbedded in the MgO sidewall at various locations above and below 0 cm. Here the 0 cm location is taken as the original location of the concrete surface.

The thermal properties for the MgO used to calculate the sidewall heat fluxes are listed below:

Density (kg/m^3)	26640
Specific Heat (J/kg K)	1250
Thermal Conductivity (W/m K)	$k = aT + b$

where:

$a = -5.0 \times 10^{-3}$

$b = 8.193$

Minimal Thermal Conductivity (W/m K) = 1.955

Shown in Figure 7.1.9, 7.1.10 and 7.1.11 are the heat flux histories for the sidewall arrays initially below the melt, adjacent to the melt, and above the melt, respectively. Heat flux histories for other sidewall arrays are shown in Appendix E. Figure 7.1.9 shows the heat flux at z = -20.0 cm. The heat flux shown slowly increases to a value 9×10^3 W/m^2 at t = 120 min and

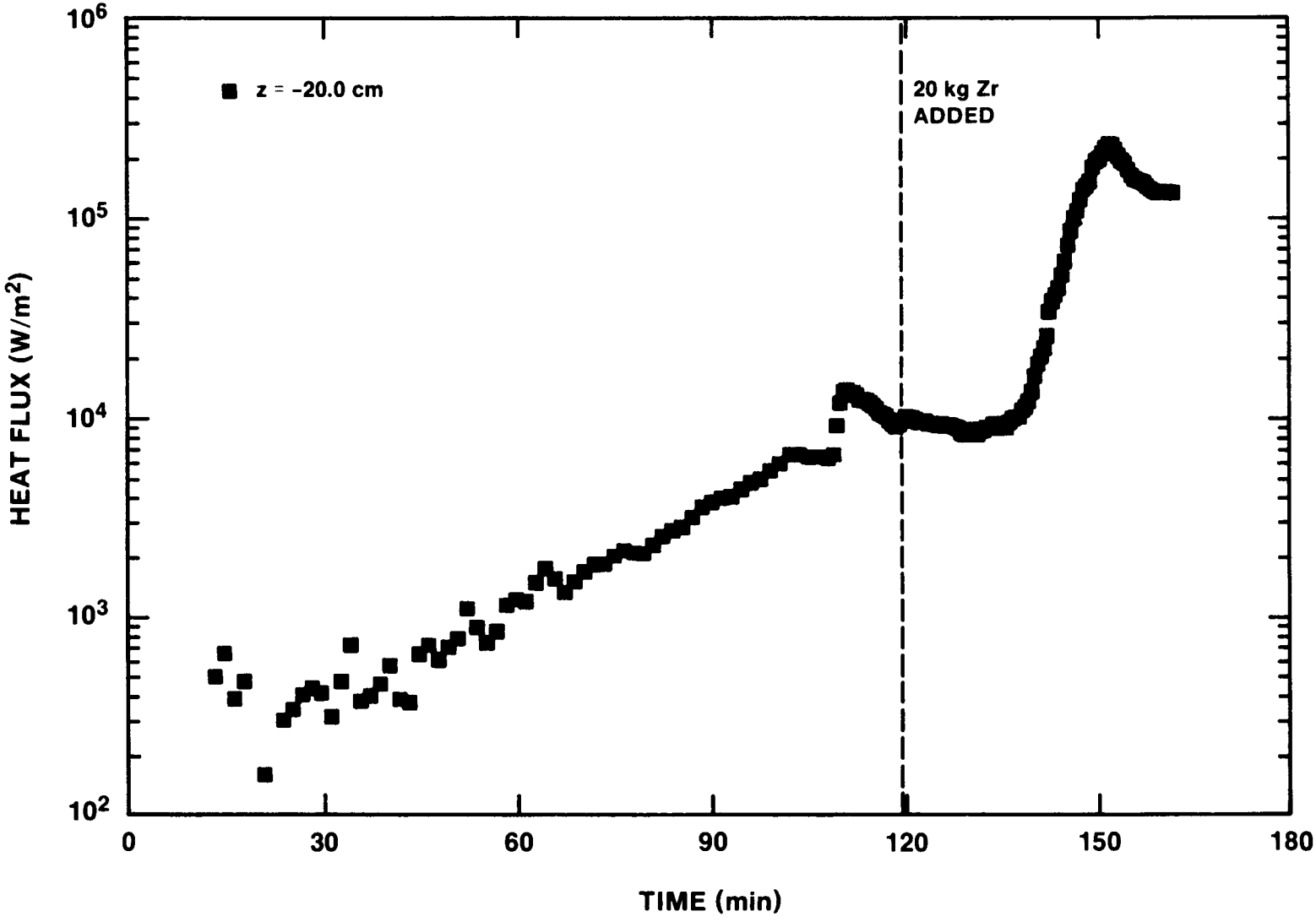

Figure 7.1.9 - SURC 4 Sidewall Heat Flux - Below the Melt

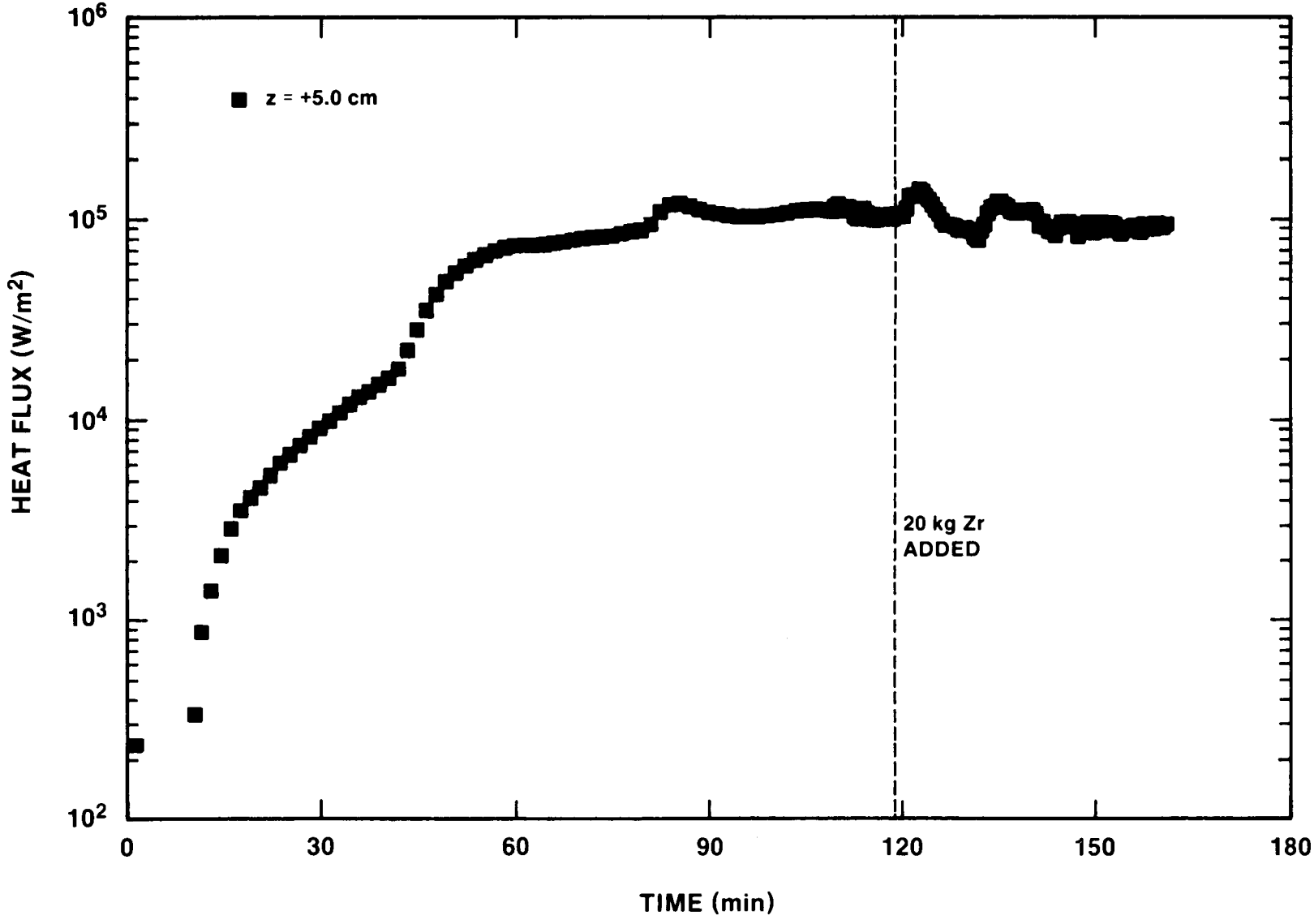

Figure 7.1.10 - SURC 4 Sidewall Heat Flux - Adjacent to Melt

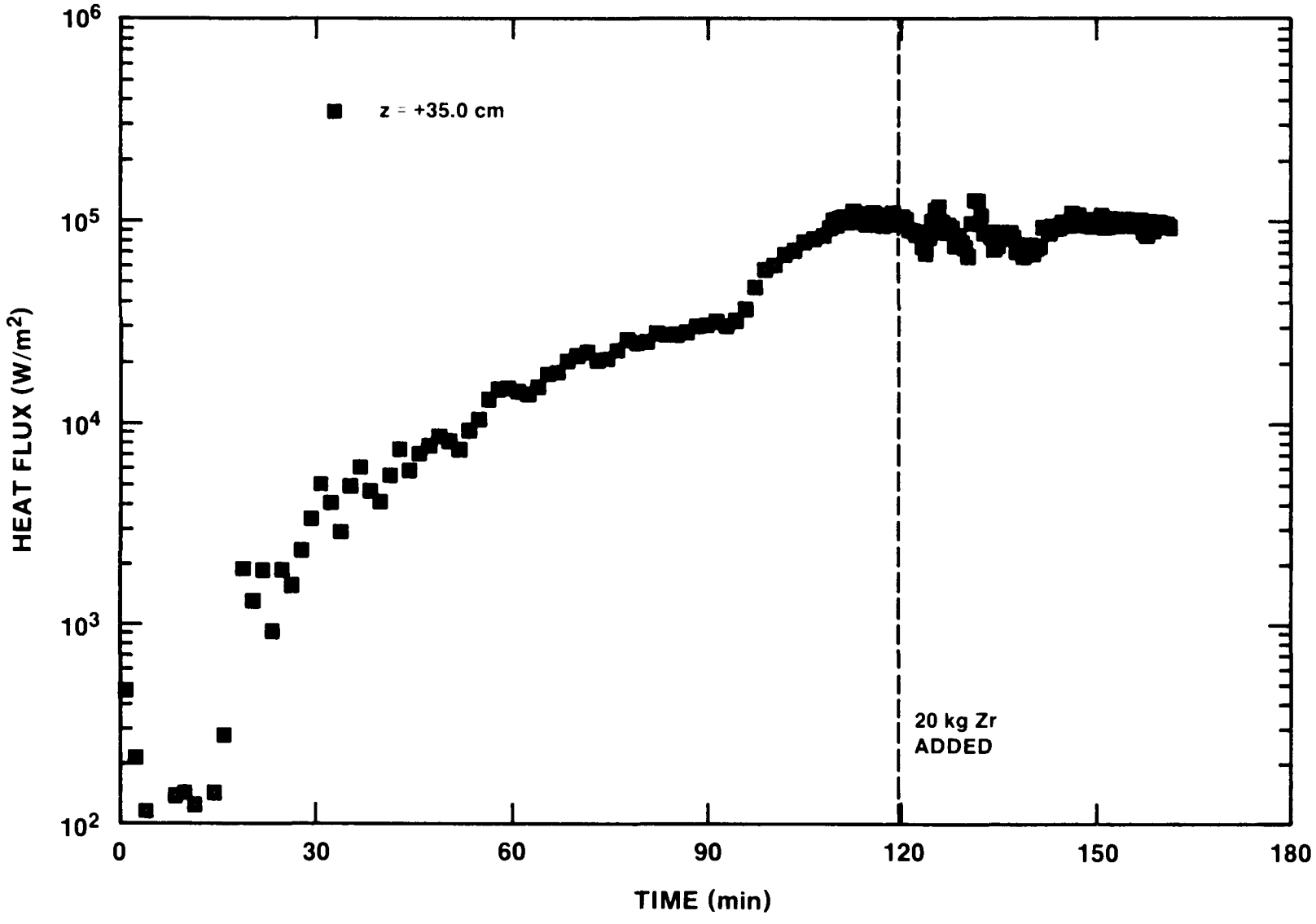

Figure 7.1.11 - SURC 4 Sidewall Heat Flux - Above the Melt

remains constant until t = 138. The heat flux then sharply increases as the melt penetrates downward, peaking at a value of 2.5×10^5 W/m^2 at t = 152 min. This peak occurs as the melt becomes adjacent to the thermocouple array. The heat flux then decreases to 1.2×10^5 W/m^2 at t = 162 min as the MgO wall is heated.

The thermocouples in the array located at z = +5.0 cm (Figure 7.1.10) were directly adjacent to the stainless steel during initial heating, melting and the early period of erosion. The heat flux history at this elevation is sensitive to fluctuations in the power delivered to the melt. After the melt reaches a temperature of 1700 K at time = 85, the heat flux maintains a value between 8.0×10^4 W/m^2 and 1.03×10^5 W/m^2 for the remainder of the test. An increase in heat flux is noted just after the zirconium was added to the melt pool followed by a decrease in heat flux between t = 124 and t = 132 min when the power supply was temporarily shut down.

Thermocouples in the sidewall array at z = +35.0 cm (Figure 7.1.11) were always above the metallic phase of the melt during the experiment. The heat flux history at this elevation also responds to the temperature of the melt but here the response is delayed. The heat flux reaches a peak value at this elevation of 1.0×10^5 W/m^2 at t = 110 min. This value was maintained throughout the remainder of the test except for fluctuations due to the addition of the zirconium and the temporary power shutdown.

In summary, the heat flux when the melt was adjacent to the MgO sidewall arrays was calculated to average 1.0×10^5 W/m^2. The array located above the melt inferred heat fluxes in the range of 7.0×10^4 to 1.0×10^5 W/m^2. Heat fluxes indicated by the array embedded in the sidewalls below the concrete surface increased to a value near 2.0×10^5 W/m^2 when the melt was directly adjacent to the array. This value decreased to a value 1.2×10^5 W/m^2 as the melt continued to penetrate the concrete and pass the array.

Crucible Cover

Two duplicate arrays of three thermocouples each were cast into the MgO cover to infer upward heat flux. The temperatures indicated by type K thermocouples cast in one of the arrays is shown in Figure 7.1.12. The temperature response of the second array is virtually identical as seen in Appendix E. The specific location of these thermocouples with respect to the crucible geometry can be found in Table 3.4. Figure 7.1.12 shows the temperature profile of the three type K thermocouples cast at depths of 0.5, 1.5, and 2.5 cm in the crucible cover. The temperature increased from 280 to 425 K in the first 98 minutes of the test. After t = 100 the steel slug becomes molten and thetemperatures increase rapidly due initially to radiation off the meltpool and later to contact with the foamy material produced during the zirconium reaction. Figure 7.1.13 shows the

heat flux calculated from the temperatures measured by the thermocouples.

The figure indicates that the heat flux steadily increased to a value of 9.0×10^4 W/m^2 at t = 110 min. The heat flux remains constant for the remainder of the test with only minor flucations caused by the loss of induction power and the addition of zirconium.

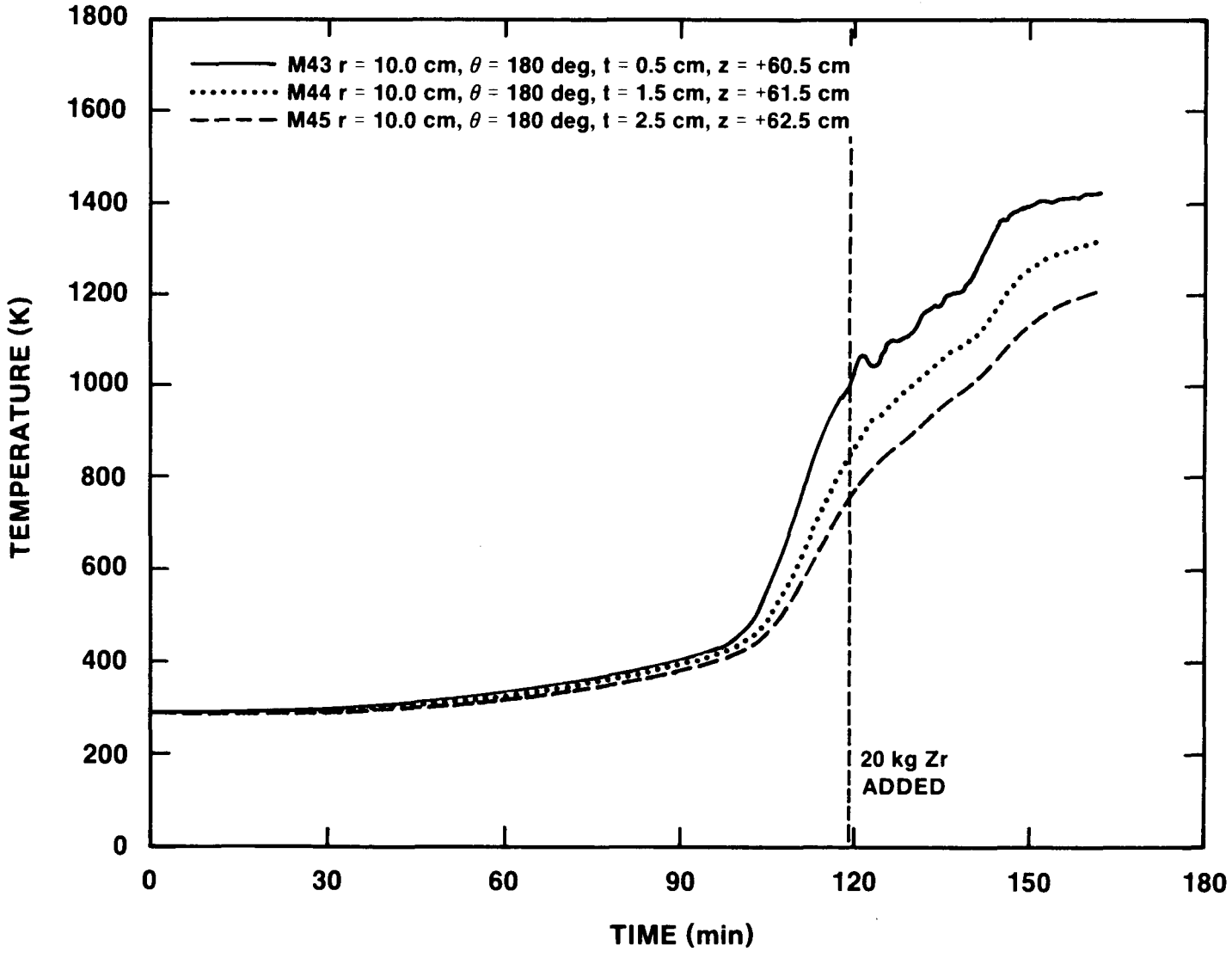

Figure 7.1.12 - Typical SURC 4 MgO Cover Thermocouple Response

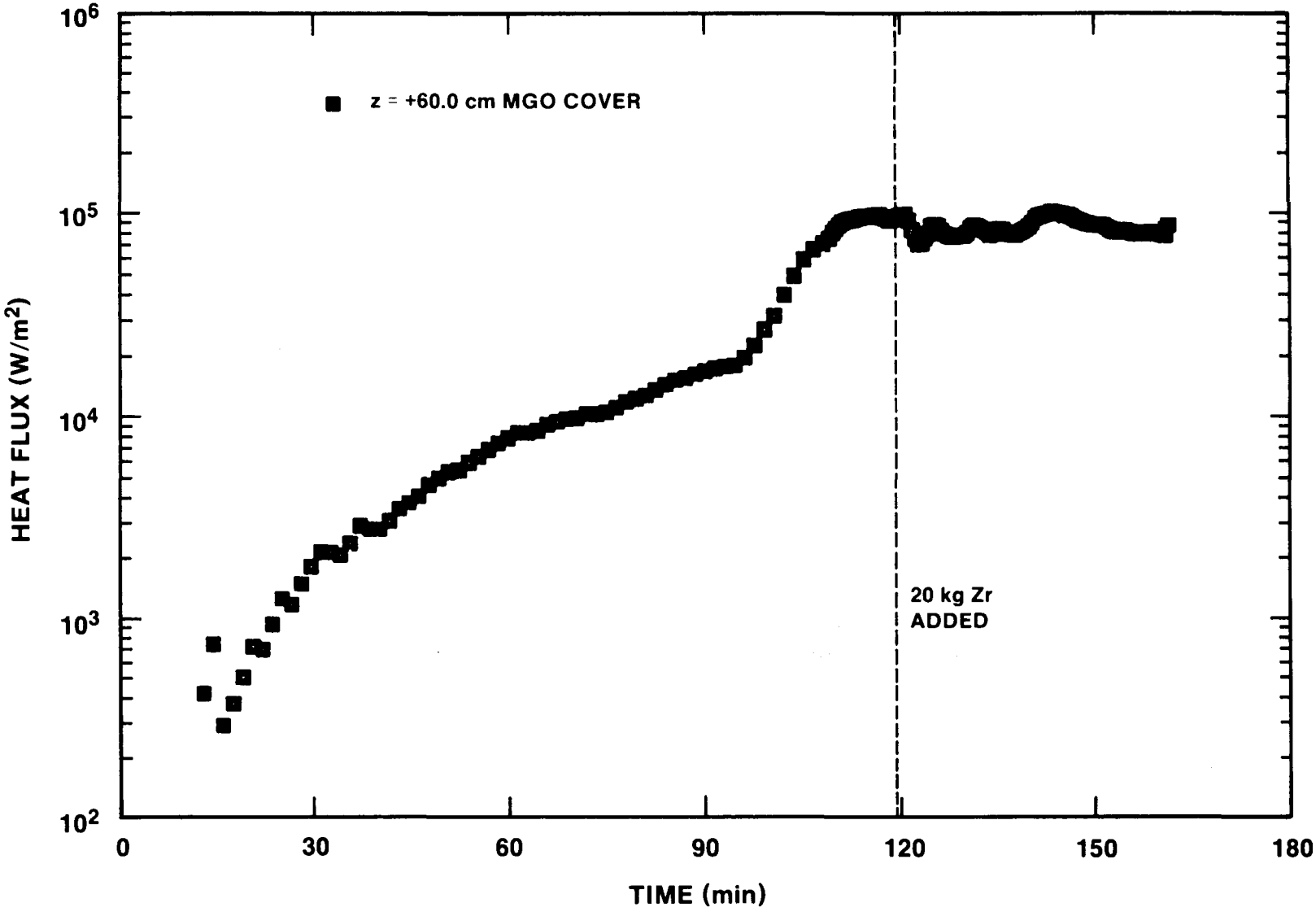

Figure 7.1.13 - SURC 4 Upward Heat Flux - MgO Cover

7.2 Gas Composition Data Presentation

Gas sampling for the SURC 4 test was done using three techniques: an Infocon Model IQ200 mass spectrometer, an Infrared Industries Model 700 CO/CO_2 detector, and integral grab samples. The first two techniques yield real-time data which is viewed on-line and stored on computer disks. The grab samples are stored and analyzed posttest using both gas chromotography and mass spectrometry. Additional information on these systems is detailed in section 4.2.

Test Procedures

Operational procedures for the gas analysis equipment and support components were accomplished in the following manner:

The output from the K-type thermocouple installed in the flow stream 3 meters downstream from the crucible was continously monitored and recorded by the data acquisition system while output from the other K-type thermocouple mounted at the actual sampling location was monitored manually every five minutes with a portable temperature monitor. Although the temperature in the flow line ranged from 300 to 650 K, the conditions at the actual sampling point were very constant at 285±3 K throughout the test.

Gas flow through the sample line was established 30 minutes before the test by energizing the diaphram pump. The flow was manually regulated to provide a 6 lpm flow rate. Monitoring of the sample line flow rate was done every 2-5 minutes and no substantial fluctuations were indicated.

The grab sample bottles were evacuacted before the test and then individually subjected to vacuum just prior to sample collection. Eighteen samples were taken manually. Times for the samples were recorded on computer disk as pressure spikes shown in Figure F-6 in Appendix F. One grab sample bottle was utilized at each sampling event and each sample was completed in approximately 1 second.

The CO/CO_2 monitor was warmed up at least 30 minutes before the test. A pretest calibration was performed prior to start-up of the data acquisition system and no irregularities were noted. The CO/CO_2 data were automatically recorded by the data acquisition system throughout the test. In addition, a visible readout was monitored locally at the instrument and remotely in the control room. Following the test, another calibration run was performed, again indicating no irregularities.

The mass spectrometer system was in operation under a low vacuum of 100 m torr for one week prior to establishing a vacuum of 10^{-6} torr for three days before the test date. The analysis display was continously monitored and a total of 70 discrete samples were recorded during the test. On-line data were recorded every five minutes before time = 100 and almost every minute after that time.

Results

Three periods of time are of interest for the SURC 4 gas composition data: the onset of gas production between 60 and 100 minutes, steady erosion between 100 and 118 minutes, and the ensuing reaction due to the Zr metal addition from 120 to 160 minutes. Notable events during the test which affected the gas composition data were the additon of Zr metal at time 119 and switching the gas sampling location in the flow line from a point after the gravel filter to a point before the gravel filter at times 56.5, 121.5, 133.5 and 154 minutes.

Although water vapor is present in the reaction gas, it cannot be measured by the gas analysis systems without ruining the equipment. Consequently, water vapor traps are installed in the gas analysis flow lines. A total of 4 ml of water was recovered from the gas analysis lines. Three ml of this total was recovered from the sample line condensate traps and one ml was recovered from the liquid nitrogen cold trap. This would have added 6.2 l of H_2O vapor to the 240 l of collected H_2, CO, and CO_2 yielding an estimated water content of 3-5% in addition to the reported gas compositions for H_2, CO, and CO_2.

The results from the mass spectrometer are shown in Table 7.2.1. This table lists the raw data as volume (mole) percent along with the time and sampling location for the sampled gas species. The mass spectrometer data indicate the onset of gas release at 52 minutes followed by the establishment of steady erosion between 104 and 120 minutes. The change in gas composition after the introduction of Zr metal at time 119 minutes is marked by high percentages of H_2 gas production from time 123 until time 162 when the lower crucible failed. The reaction gas (H_2, CO, and CO_2) is separated from the argon carrier gas and normalized in Table 7.2.2. Here the H_2O content is omitted but can be assumed to have an average value of 4% based on the volume of water collected in the condensate traps. An examination of the normalized data from the mass spectrometer shows that the onset of gas production between times 52 and 100 is characterized by a gas composition which is 40 to 50% H_2, 20 to 30% CO and 20-30% CO_2. When concrete erosion began at around 100 minutes, the hydrogen concentration in the effluent gas increased and the CO_2 concentration decreased. A typical composition during this period (100-120 minutes) is 65% H_2 - 20% CO-15% CO_2. After the addition of Zr metal at time = 119 minutes the gas composition changed dramatically to a mixture rich in hydrogen and practically devoid of CO_2. This composition averaged 83.3% H_2 - 14.3% CO - 1.4% CO_2 from the time Zr was added at 119 minutes until the crucible failed at time 162.

The results from the CO/CO_2 monitor are shown in Figure 7.2.1. The raw data, shown here as percent CO and percent CO_2 in the sampling flowline, indicate the onset of gas release between 55-60 minutes into the test. Both CO and CO_2 content rise from the onset of gas release until erosion begins at around time =

100 with the CO content being lower than the CO_2 content by a ratio of 2:3. When concrete erosion begins at time = 100, the CO concentration increases and the CO_2 concentration decreases so that between times 110 and 120 minutes the CO/CO_2 ratio steadily decreases from 3:2 to 4:1. After Zr metal was added at time 119, the concentration of both CO and CO_2 dropped rapidly to zero for a period of 5-10 minutes after which the CO concentration recovered to a level above the value indicated before Zr addition while the CO_2 concentration recovered to levels at or below those values. The CO/CO_2 ratio for the remaining period (133-162 minutes) of Zr interaction averaged 8:1.

The grab sample results for SURC 4 are shown in Table 7.2.3. The carrier gas for these samples included air as well as argon in total amounts ranging from 30 - 95%. A total of 21 samples were taken in which no other gases besides H_2, O_2, CO_2, N_2, or Ar were detected. Three samples contained traces of methane. Normalized results for the eleven samples taken during the Zr interaction phase of the test between times 123 and 158 are also shown in Table 7.2.3. These samples have an average H_2 concentration of 97.8% with 2.0% CO and .2% CO_2. As with the mass spectrometer results, these concentrations do not include H_2O vapor which averaged 4% over the entire test.

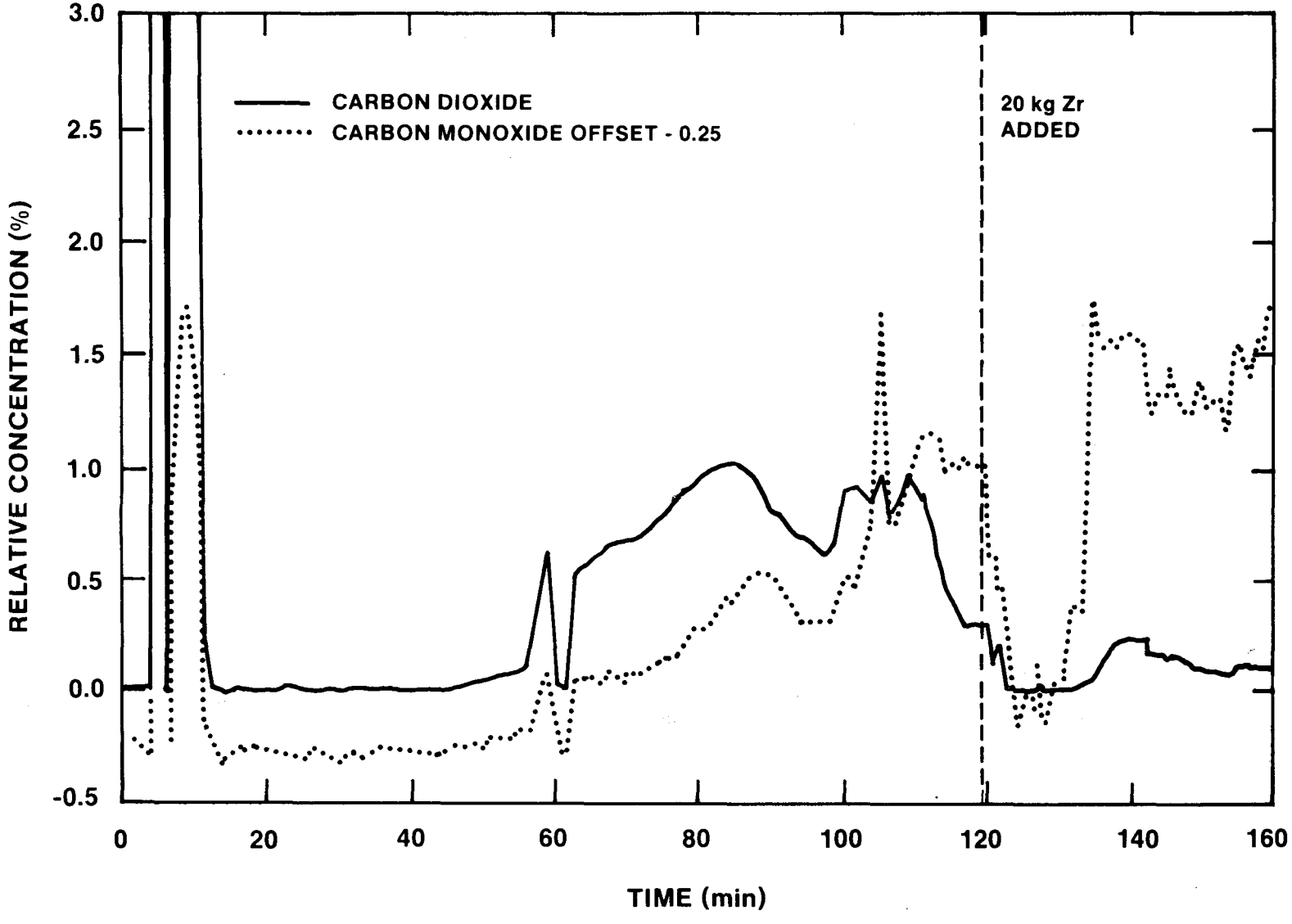

Figure 7.2.1 - SURC 4 CO/CO_2 Monitor Data

Table 7.2.1 - SURC 4 Mass Spectrometer Data

Raw Data - Volume Percent

Run Time (min)	Sample Location*	H_2	CO	Ar	CO_2	Notes
30	1	--	--	100.	---	
46	1	--	--	100.	---	
52	1	1.7	5.1	91.2	2.0	Start of
54	1	2.0	1.7	94.1	2.1	gas release
56	1	2.3	1.7	93.9	2.1	
57	2	4.3	2.3	93.4	---	
58	2	5.0	3.3	89.7	2.0	
65	1	3.4	3.4	93.0	---	
75	1	4.8	4.5	90.6	---	
80	1	6.3	4.5	89.3	---	
85	1	5.8	4.4	87.3	2.6	
91	1	5.7	2.3	92.0	---	
100	1	6.3	2.2	88.8	2.7	
104	1	12.9	3.2	83.9	---	Erosion starts
106	1	16.1	3.0	77.4	3.6	
107	1	18.4	5.6	72.6	3.4	
110	1	19.3	8.0	69.5	3.2	
116	1	20.6	2.8	73.2	3.4	
119						Zr addition
121	1	18.5	27.8	53.7	---	
123	2	82.8	17.2	--	---	
124	2	93.7	6.3	--	---	
125	2	78.5	21.5	--	---	
126	2	90.3	9.7	--	---	
130	1	35.4	5.0	59.6	---	
133	1	39.4	4.7	55.9	---	
135	2	86.1	13.9	--	---	
137	2	86.1	13.9	--	---	
139	2	74.5	18.2	--	---	
141	2	75.9	24.1	--	---	
144	1	42.0	8.3	49.8	---	
146	1	39.6	7.9	47.7	4.8	
150	1	83.9	16.1	--	---	
153	1	37.9	8.2	49.0	4.9	
155	2	46.0	7.7	46.3		
156	2	41.3	13.7	41.0	4.1	
158	2	85.8	14.2	--	---	
160	2	84.9	15.1	--	---	
162	2	84.0	16.0	--	---	Crucible failure

* location 1 was downstream from the general filter
location 2 was upstream of the orifice plate

Table 7.2.2 - SURC 4 Mass Spectrometer Results

Normalized Data - Volume Percent

Run Time(min)	H_2	CO	CO_2	Notes
Before 52	--	--	--	Ar only
52	19.3	58.	22.7	
54	33.9	28.8	35.6	
56	37.7	27.9	34.4	
57	65.1	34.8	--	Gas Release Before
58	48.5	32.0	19.4	Ablation
65	50.0	50.0	--	
75	51.0	49.0	--	
80	58.0	42.0	--	
85	45.7	34.6	20.5	
91	71.2	28.8		
100	56.3	19.6	24.1	Erosion Begins
106	71.2	13.3	15.9	
107	67.2	20.4	12.4	
110	61.2	25.4	10.1	
116	76.9	10.4	12.7	
				Zr drop at 119
123	82.8	17.2		
124	93.7	6.3		
125	78.5	21.5		Zr Reaction in
126	90.3	9.7		Progress
130	87.6	12.4		
133	89.3	10.7		
135	86.1	13.9	--	
137	86.1	13.9	--	
139	74.5	18.2	--	
141	75.9	24.1	--	
144	83.6	16.4	--	
146	75.7	15.1	9.2	Zr Reaction Continues
150	83.9	16.1	--	
153	74.3	16.1	9.6	
155	85.7	14.3	--	
156	79.6	23.2	6.9	
158	85.8	14.2	--	
160	84.9	15.1	--	
162	84.0	16.0	--	Crucible Breach -
				Melt Escapes

Table 7.2.3 - SURC 4 Grab Sample Analysis

RAW DATA IN VOLUME (MOLE) PERCENT

SAMPLE #	H_2	N_2	O_2	CO	Ar	CO_2	TIME(min)
3-2*	17.54	39.98	11.93	0.98	28.73	0.83	185
3-3*	4.56	41.38	12.38	0.28	41.20	0.20	190
4-2	No sample gas in bottle						
4-3	0.40	27.11	8.07	---	64.40	0.02	175
4-4*	17.59	27.05	8.07	0.94	45.58	0.77	177
5-2	71.29	9.51	2.70	1.69	14.71	0.09	158
5-3**	---	76.11	22.81	---	1.05	0.04	
5-4	18.50	37.53	11.15	0.66	32.11	0.06	169
6-3	52.68	23.20	6.75	1.08	16.23	0.06	153
6-4	69.76	9.61	2.60	1.13	16.81	0.09	156
7-2	67.72	15.05	4.19	1.10	11.76	0.19	139
7-3	70.24	13.62	3.91	1.59	10.42	0.22	141
7-4	44.50	34.42	10.16	0.93	9.90	0.08	150
8-2	49.44	29.28	8.63	0.49	12.13	0.03	133
8-3	64.07	17.49	5.03	1.23	12.14	0.05	135
8-4	24.22	48.76	14.59	1.44	10.84	0.14	137
9-2	47.15	31.74	9.14	0.35	11.51	0.10	123
9-3**	---	76.11	22.86	---	0.98	0.04	
9-4	69.59	15.92	4.61	0.20	9.66	0.01	126
10-1	---	30.64	9.00	---	60.33	0.02	18
10-2	13.47	33.87	10.06	0.25	42.00	0.34	58
10-3	23.49	34.01	10.13	1.03	30.83	0.50	104
10-4**	---	75.81	22.72	---	1.42	0.06	
10A	---	0.62	0.07	2.07	87.59	9.63	

* Trace amounts (not quantified) of methane (CH_4) were detected.
**Valves were not tightly closed.

NORMALIZED DATA IN VOLUME (MOLE) PERCENT

H_2	CO	CO_2	Time(min)
99.0	.7	.2	123
99.0	1.0	--	126
98.9	1.1	--	133
98.0	2.0	--	135
93.9	5.6	.5	137
98.1	1.6	.3	139
97.5	2.2	.3	141
97.8	2.0	.2	150
97.9	2.0	.1	153
98.3	1.6	.1	156
97.6	2.3	.1	158

7.3 Flow Data Presentation

Four different devices were used to measure the reaction gas flow rate in SURC 4: A 1.02 cm orifice plate, a laminar flow element, a Rockwell 450 gas clock, and a Rockwell 750 gas clock. A flow train schematic for these devices is shown in Figure 4.3.1 and information regarding the description, operation, and calibration of the flow equipment is detailed in Section 4.3.

Procedures

All of the flow devices were operated continously throughout the the test. Data from the devices in the form of voltage outputs from either pressure transducers or a summing transmitter were recorded at 15 second intervals on computer disk using the HP1000 data acquisition system. Initial flow for the system was established and maintained using argon carrier gas. Argon was introduced into the appartus at two locations. The first location was into the water cooled aluminum containment vessel. The flow rate of argon at this position was monitored using a turbine meter. Argon was also used to purge a window protecting the opacity meter. The opacity meter was located in the flow tube approximately 3 meters downstream from the crucible. The flow of argon at this position was monitored using a kulite 100 psi pressure transducer upstream of a Milipore 1.1 mm diameter criticle orifice. The turbine meter registered a flow rate of 26±1 liters per minute throughout the test. The pressure transducer recorded a constant gauge pressure of 16±1 psi. The flow rate at this location based on the pressure and orifice calibration was calculated to be 27±1 liters per minute. The combined flow rate of argon into the experimental apparatus considering both locations was 50±2 slpm.

The temperature of the gas in the flow system was measured at three locations: 3 meters downstream from the crucible at the second gas sampling pickoff point; four meters downstream from the crucible at the orifice plate flow device; and 7 meters downstream from the crucible at the flow system exhaust. A plot of the flow system temperatures at these locations is shown in Figure 7.3.1. Although the reaction gases generated in the crucible can have initial temperatures in excess of 1600 K, these gases cool quickly and were mixed with argon at ambient conditions so that the temperatures at the flow measurement devices were generally less than 400 K. The system pressure was also monitored and is shown in Figure 7.3.2. This pressure was recorded at a position 4 meters downstream from the crucible and 10 cm upstream from the orifice flow meter. This location represents the highest pressures achieved in the flow system during the SURC 4 test at which the measured values were very modest and ranged from .1 to 1.4 psi.

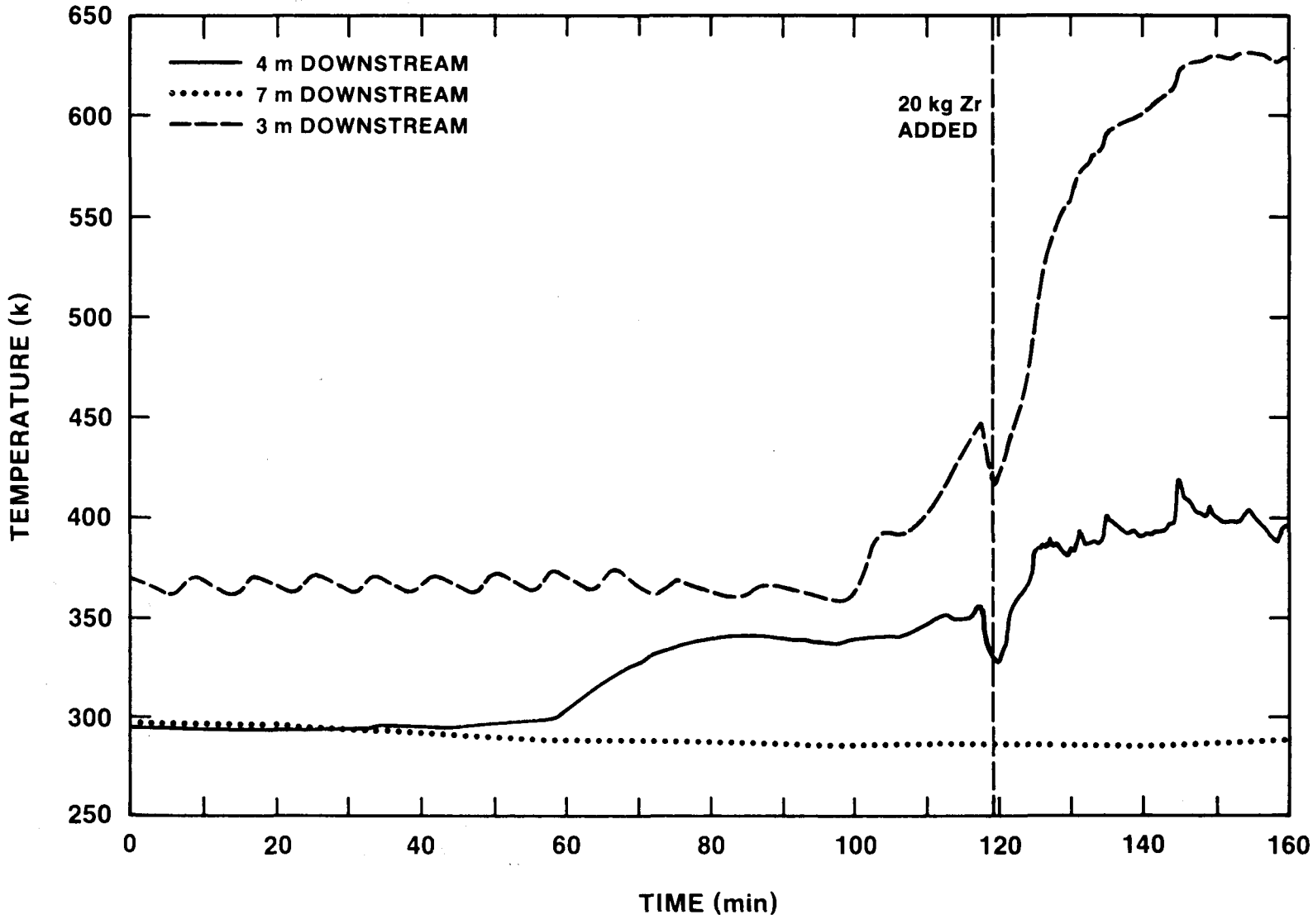

Figure 7.3.1 - Temperature Distribution in the SURC 4 Flow System

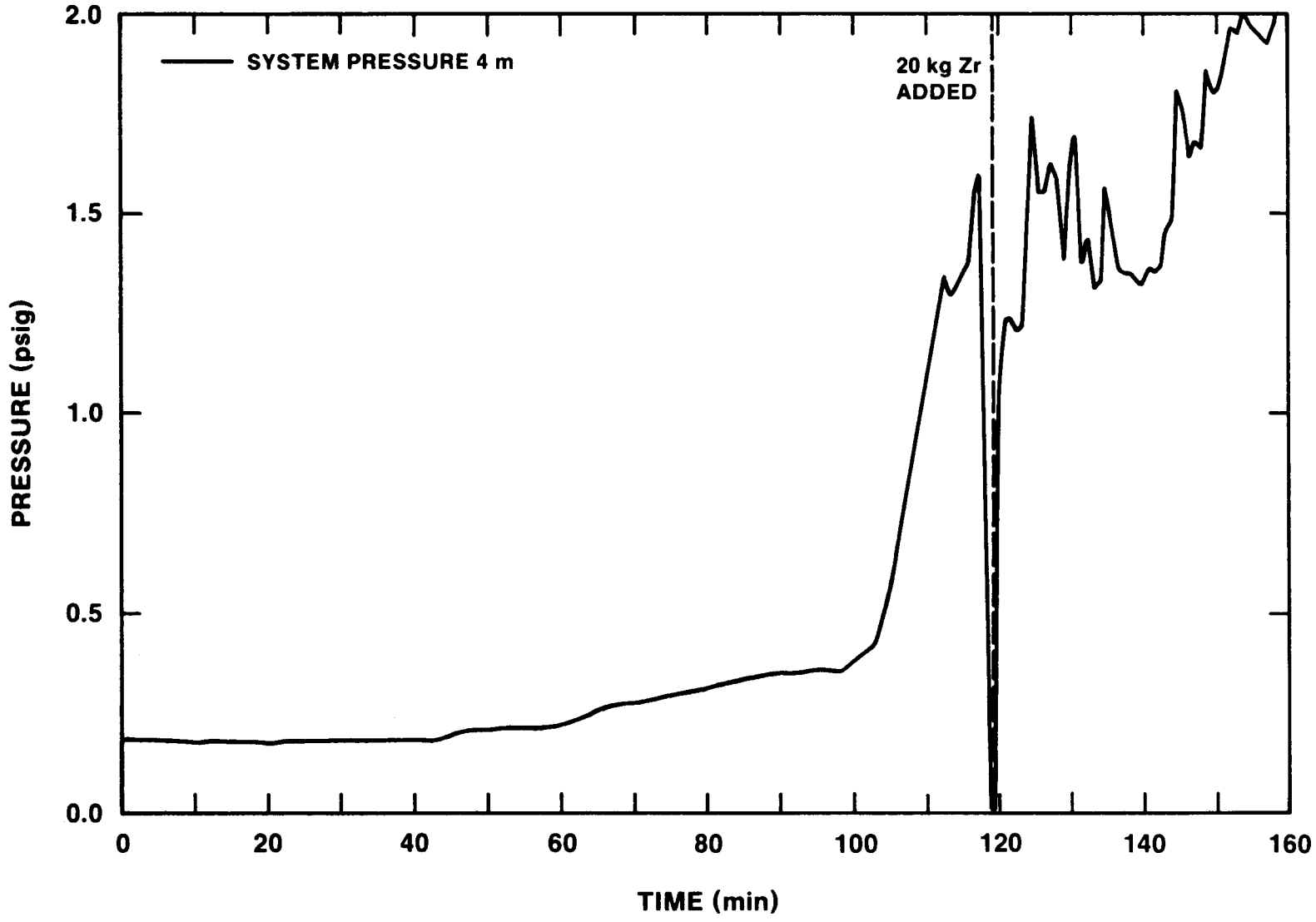

Figure 7.3.2 - Pressure History in the SURC 4 Flow System

Results

As with the crucible temperature and gas composition data, three time periods are of interest for the SURC 4 flow data. These are the onset of gas release from concrete between 50 to 100 minutes, the gas release associated with steady state concrete erosion between 100 and 119 minutes, and the increase in gas evolution due to the effect of Zr interactions at times after 120 minutes and lasting until crucible failure at 162 minutes. Events during the SURC 4 test which caused fluctuations in the data are limited to times 118-120 during which the flow pipe was opened in order to add the Zr metal.

The raw data for the gas clocks are shown in Figure 7.3.3. Here the total volume is in actual cubic meters of gas collected at the ambient conditions of 12.2 psia and 284 K. As seen by Figure 7.3.3, the two gas clocks measured virtually identical volumes of gas throughout the experiment. A total of 17,650 liters of gas were collected before the crucible failed in SURC 4. Based on a constant argon input flow of 50 slpm and the temperature profiles for the crucible materials, approximately 8800 liters of this total were due to the argon carrier gas, 3500 liters were due to the dehydration of the MgO, and 5400 liters were due to the decomposition of the basaltic concrete basemat. Average flow rates for discrete periods of time during the test have been calculated using the gas clock data and are presented in Table 7.3.1.

Table 7.3.1 - SURC 4 Flow rates from Gas Clock Data

Time (min)	Total Flow (Actual Liters)	Avg. Flow Rate (ALPM)	Corrected Flow Rate (SLPM)
0	2,150	---	---
12.5	2,830	54	49
63.3	5,650	55	50
100.0	8,480	77	69
123.0	11,300	123	110
134.2	14,200	260	233
145.8	17,000	240	216
159.2	19,800	210	189

The actual flow rate has been corrected in the final column of Table 7.3.1 to account for leakage from the system (5%) and STP conditions. These data indicate that the initial argon flow was 50 slpm. When the initial argon flow of 50 slpm is subtracted from the values shown in the final column of Table 7.3.1, it can been seen that significant offgassing of the concrete basemat began between 60 and 100 minutes at an average rate of 19 slpm. During the period from 100 to 120 minutes, the reaction gas

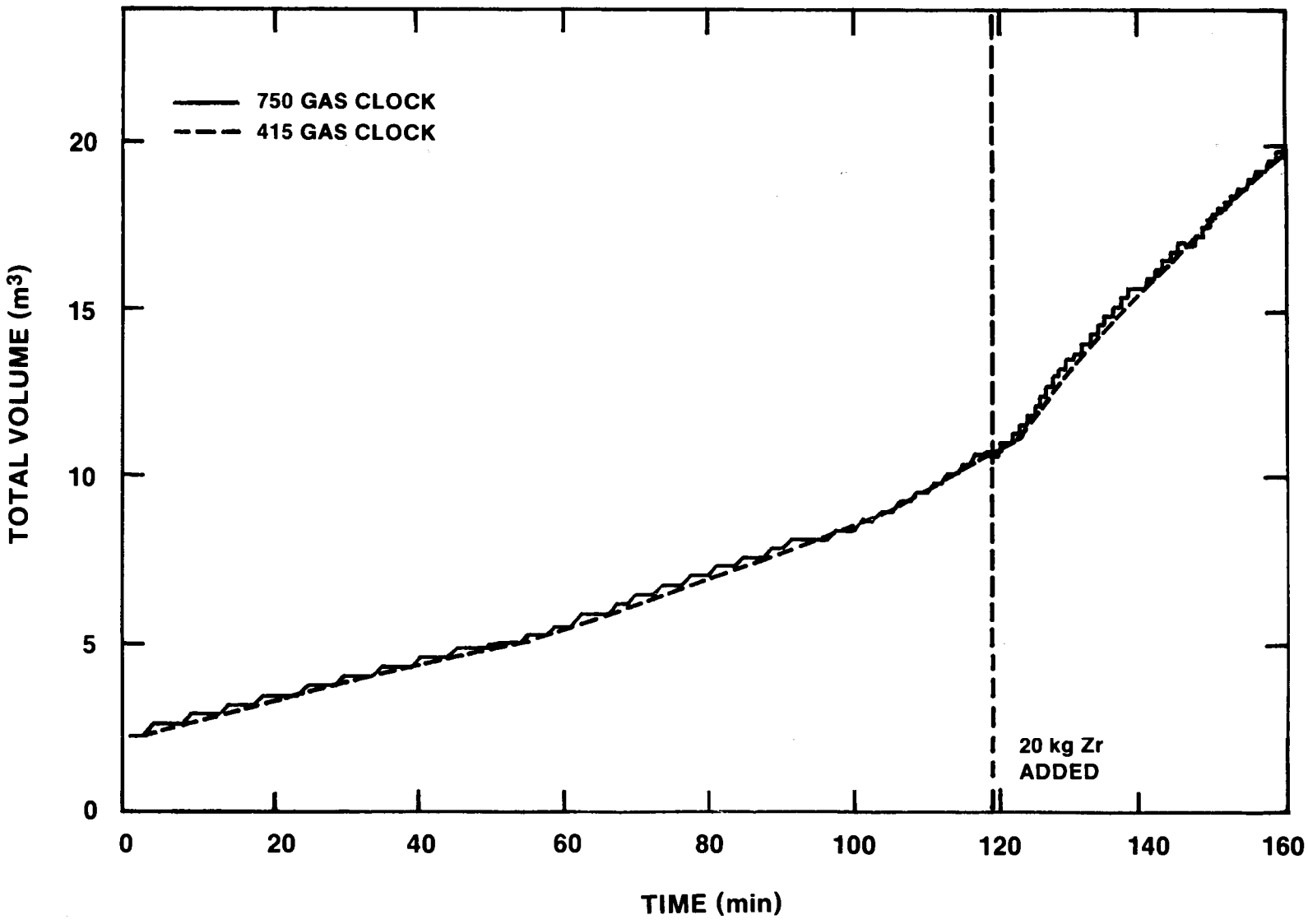

Figure 7.3.3 - SURC 4 Total Flow - Gas Clock Data

flow rate averaged 60 slpm. This is the characteristic flow rate for the period of steady concrete ablation prior to the addition of Zr. After the Zr was added the flow rate increased to 183 slpm between 123 and 134 minutes and then gradually decreased to a final rate of 139 slpm at 160 minutes.

The reduced data for the orifice plate flowmeter are shown in figures 7.3.4 and 7.3.5. Figure 7.3.4 is a plot of the total flow rate including the argon inlet flow for the period identical to that for the gas clocks. Argon and nitrogen were used to calibrate the flow devices thus two results are calculated from the pressure transducer data. The first is derived assuming that the flow has the standard density of argon (40 g/mole) and the second is derived assuming that the flow has the standard density of nitrogen (28 g/mole). Both plots were computed from the original temperature, systems pressure, and differential pressure data shown in Appendix F. A summation of the "argon" flow rate yields a total volume of 15,600 liters of gas as compared to a total of 17,650 liters measured by the gas clocks. A summation of the "nitrogen" flow rate yields a total of 19,500 liters of gas. As discussed in section 4.3, the actual flow rate measured by the orifice plate device is strongly dependent on the density of the reaction gas and is highly affected by the large quantities of H_2 produced in the SURC 4 test. The "argon" result represents a lower bound on the SURC 4 flow rate while the "nitrogen" result represents the approximate flow rate for an arbitrary SURC 4 gas mixture of 50% argon - 5% CO - 5% CO_2 - 5% H_2O - 35% H_2. Examination of the total flow rate at the orifice plate from figure 7.3.2 shows that the initial argon input flow was 50-60 lpm. Initial offgassing begins between 40-50 minutes and the total flow rate increases to a plateau of 100-125 lpm during the steady ablation period before Zr metal is added to the melt. Flow levels drop to nearly zero at 119 minutes, corresponding to the time that the ball valve was open so that the Zr delivery tube could be mounted. After 120 minutes, the total flow jumps to 200-240 lpm and averages between 170-200 lpm for the duration of the test. During the final period of the test between 120-160 minutes the flow rate was observed to rise and fall at regular intervals so that seven distinct peaks occurred at times 128, 131, 135, 145, 149, 154 and 156 minutes. These peaks show an average increase in magnitude of 35-50 lpm and a duration of 2-5 minutes. Figure 7.3.3 shows the reduced orifice plate flow rate data after corrections for non-STP conditions, leakage, and carrier gas flow have been made. These results show that the initial offgassing started at 44 minutes with low flow rates of 5 slpm. Significant offgassing began after 60 minutes as the flow rate increased from 5 slpm to 40-50 slpm at 88 minutes. After concrete erosion began at 100 minutes, the flow rate increased to 75-100 slpm prior to the addition of Zr metal at 119 minutes. After 120 minutes the reaction gas flow rate increases to 140-170 slpm and averages 110-130 slpm for the remainder of the test.

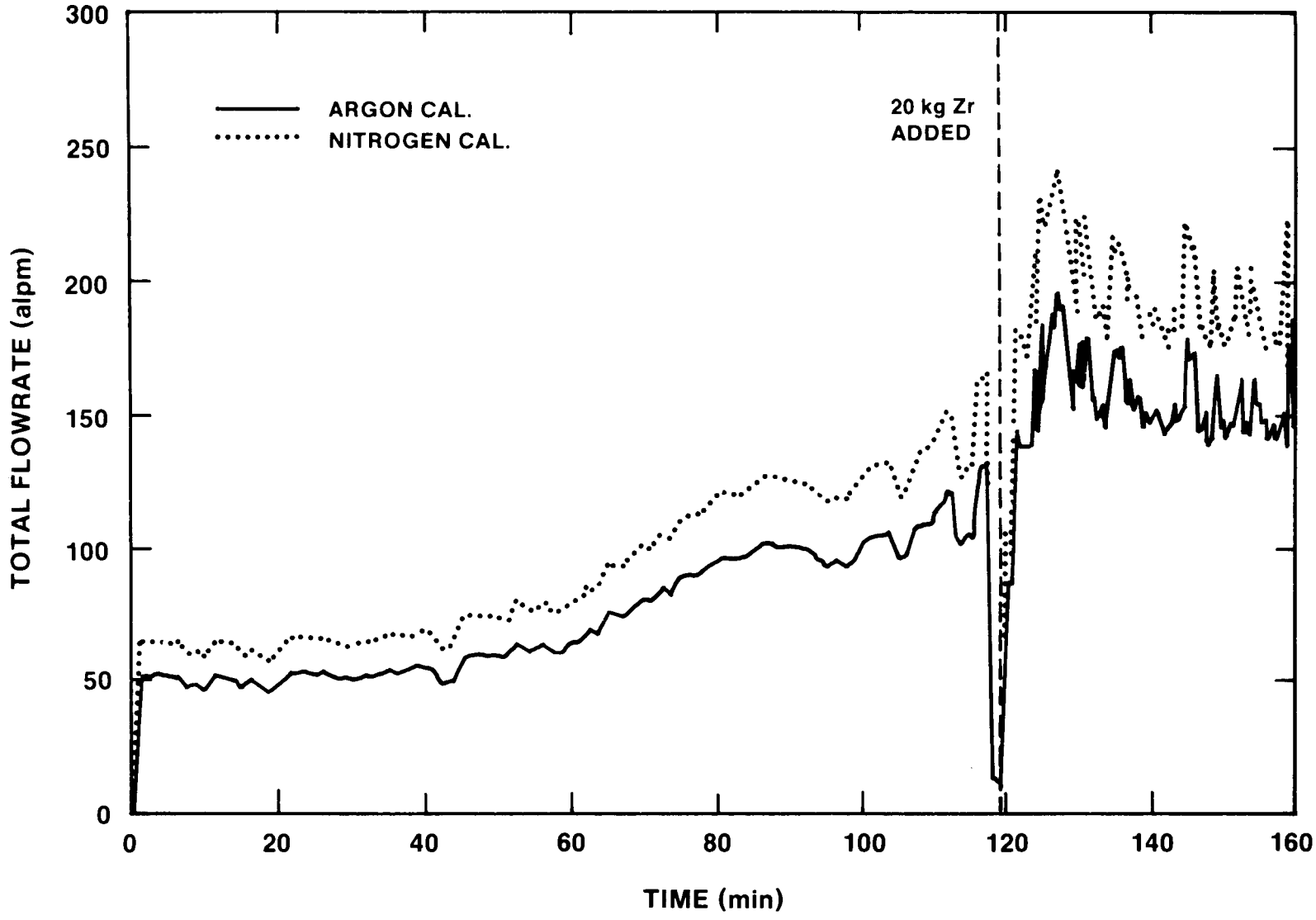

Figure 7.3.4 - SURC 4 Total Flow - Orifice Plate Data

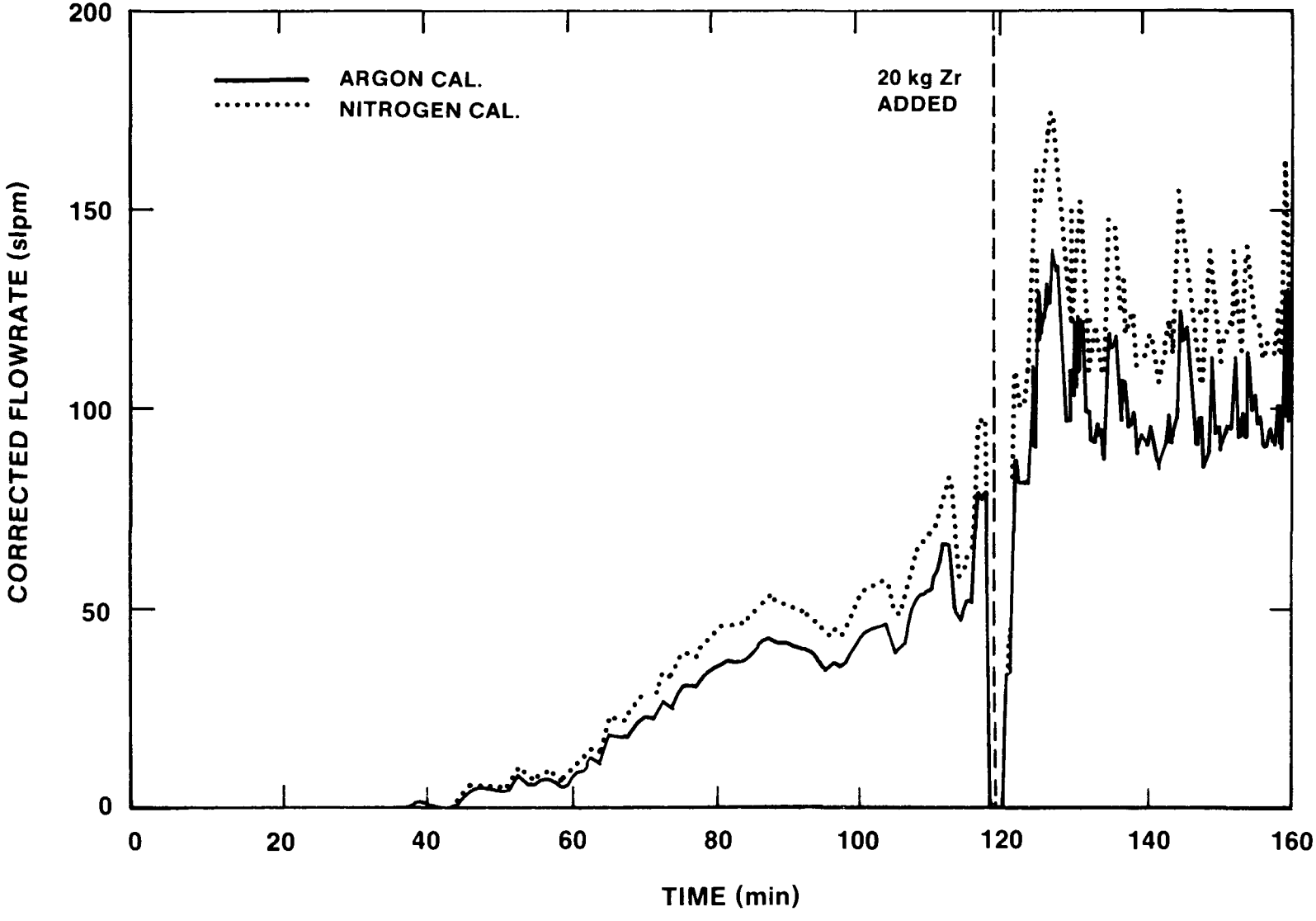

Figure 7.3.5 - SURC 4 Reaction Gas Flow - Orifice Plate

Similar results are shown in Figure 7.3.6 and 7.3.7 for the laminar flow element. This device also is sensitive to gas composition, hence, a range of output is shown using either argon or nitrogen as a basis for data reduction. Figure 7.3.6 illustrates the total flow rate during the SURC 4 test for the period identical to that for the orifice plate and the gas clocks. The argon inlet flow is established at 55-60 lpm between 0 and 40 minutes. Offgassing begins between 40 and 50 minutes and the flow rate increases to a plateam of 85-105 lpm between 85 and 100 minutes. After concrete erosion begins at 100 minutes the flow rate increases to a rate of 145-180 lpm. Flow is then interrupted at 119 minutes followed by a sharp increase to 240-290 lpm after Zr metal was added to the melt and averaged between 180-220 lpm for the duration of the test. At least five distinct peaks in flow rate are noted between 120 and 160 minutes at times 125, 131, 135, 145, and 155. The summed total volume for the argon flow rate was 16,500 liters and was 20,500 liters for the nitrogen flow rate as compared to 17,650 liters for the gas clocks. Figure 7.3.7 shows the reaction gas flow rate after corrections were made for leakage, temperature, pressure, and the argon carrier gas flow. The initial flow begins at 45 minutes, and increases gradually to 25-30 slpm at 85 minutes. After concrete ablation begins at 100 minutes the flow rate increases to 85-100 slpm just prior to Zr addition at 119 minutes. After the Zr addition the reaction gas flow rate jumps to 150-195 slpm and averages 115 to 135 slpm for the duration of the test.

The results from the orifice plate and laminar flow element compare well with the results of the gas clocks with regard to the timing and relative magnitudes of the initial gas release, the gas release associated with steady state concrete erosion, and the increased release associated with the addition of Zr metal to the melt. In addition, both the orifice plate and the laminar flow device provide details with regards to the pulsating nature of the flow rate during the forty minutes after Zr addition. The absolute flow rates for these events, however, are most accurately represented by the gas clocks (Table 7.3.1) since no corrections are required to account for significant fluctuations in gas density or gas viscosity as are required for the orifice plate and laminar flow element. A detailed listing of the gas clock results is included in Appendix F.

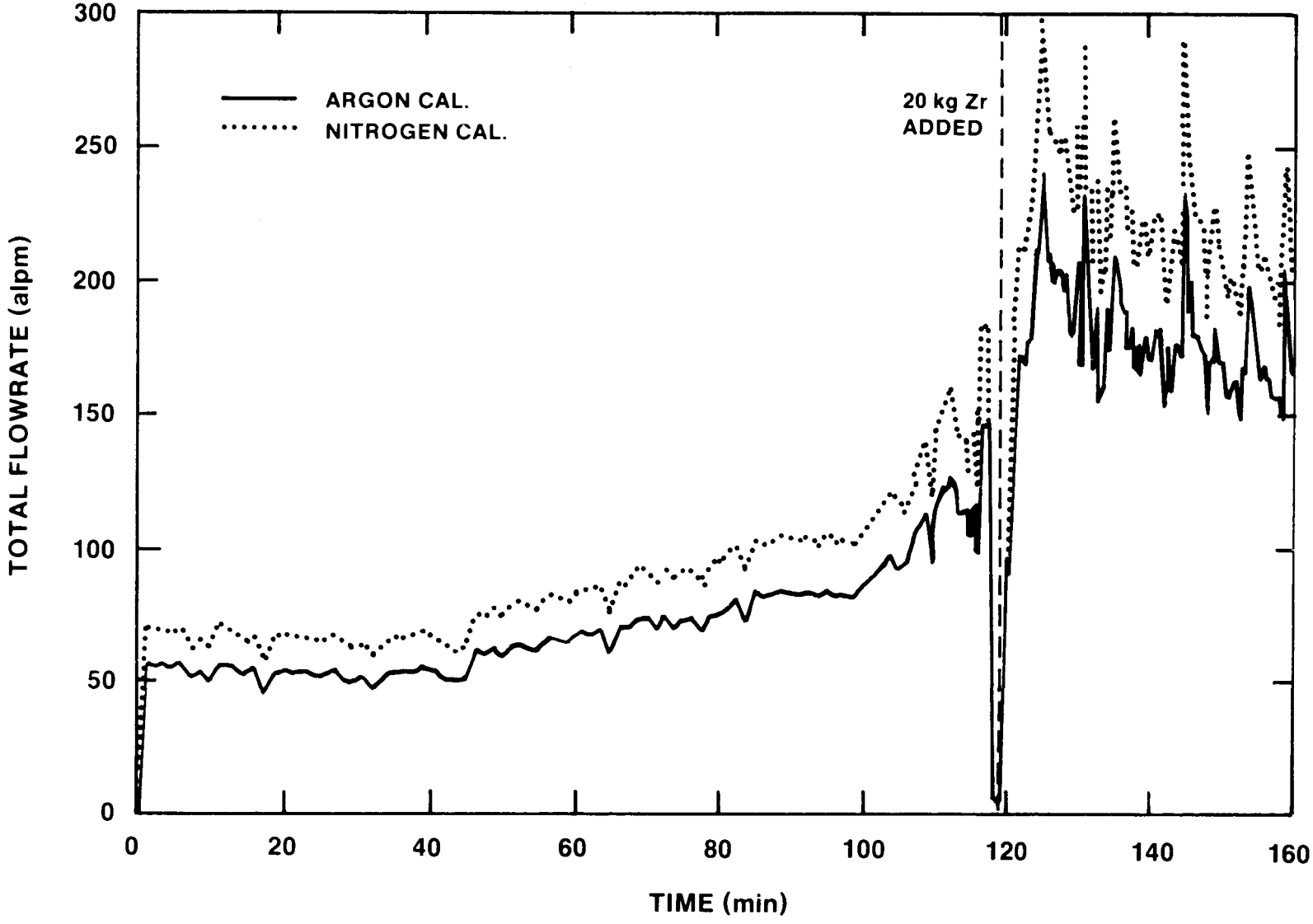

Figure 7.3.6 - SURC 4 Total Flow - Laminar Flow Element

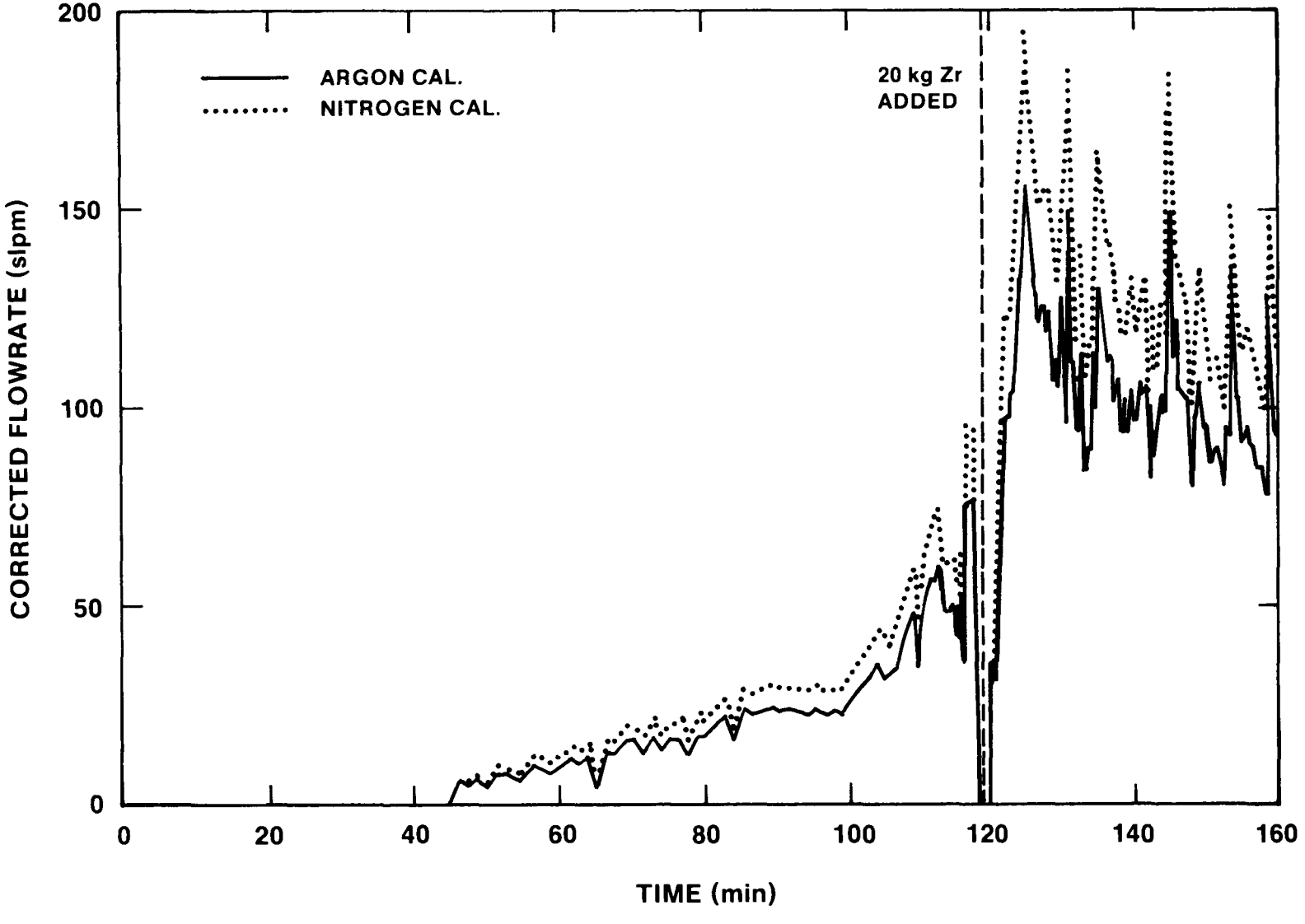

Figure 7.3.7 - SURC 4 Reaction Gas Flow - LFE

7.4 Aerosol Data

Aerosols were collected and measured using Gelman filters, Anderson Impactors, cyclones, and an opacity meter. These instruments are described in Section 4.4. The SURC 4 aerosol was found to be broadly distributed between about 0.1 to 10 micrometers aerodynamic particle diameter with a peak ranging from .7 to 2 micrometer. Its composition was dominated by tellurium with the next highest contributions coming from sodium, potassium, and silicon from the concrete along with chromium and manganese from the steel. Electron micrographs showed the particles to have the agglomerate morphology expected of a vapor condensation aerosol. There was also evidence of spherical particles likely produced by liquid entrainment of melt. The aerosol concentrations measured during SURC 4 ranged from on the order of one-tenth to one hundred g/m^3 STP.

Events during the test which affected the aerosol results include foaming of the melt as indicated by the presence of black-green lava material found posttest and the incursion of the foam into the exhaust line. Approximately 100,000 cubic centimeters of this material was produced during the test as discussed in Section 6.3. This material prevented a continuous examination of the aerosol generation and produced unknown transport characteristics to the sample point and perhaps additional generation mechanisms.

Procedure

Sample gangs were initiated manually at the Modicon controller prior to erosion at 113 minutes, during the concrete attack at 127 minutes and near the end of the test at 155 minutes. Each sample gang consisted of three sequential 1 minute filter samples along with two 1 minute impactor samples (one at 10 LPM and one at 15 LPM nominal flows) beginning at the second minute of the sequence. The output of the pressure transducers giving flow indication was monitored at the control site and recorded on the data acquisition system. A cyclone sample was taken for a total of 22.5 minutes from 134 to 137.5, 139 to 154, and 158 to 162 minutes.

The opacity meter operated for the duration of the test. Its output was monitored on the meter at the control site and recorded on the data acquisition system.

Pressure transducer outputs and thermocouple readings were recorded on the data acquisition system. The instrumentation and its calibration and operation has been discussed in Section 4.4. The aerosol mass was collected on filters, on impactor collection surfaces and in the cyclone. These masses were recovered and weighed after the test using procedures described in section 4.4.

Selected filter, impactor, and cyclone samples were submitted for elemental analysis using inductively coupled plasma spectroscopy.

Electron micrographs were taken of some of the samples for morphological analysis.

Results

The sample times, sample flows, collected masses, dilution rates and calculated concentrations for the filter samples are given in Table 7.4.1. The same information for the impactors is given in Table 7.4.2. This information for the cyclone is given in Table 7.4.3. The flow was calculated from the system temperature and pressure and the flow control orifice calibration.

The voltage output from the opacity meter is plotted as a function of time in Figure 7.4.1. Here voltage is used as an indicator of relative aerosol density. The higher the voltage, the greater the opacity and the higher the aerosol concentration.

The filter samples A, B and C (113-116 minutes) give good agreement on an aerosol concentration between 6 and 7 g/m^3 STP. The opacity meter does not register during this time since the concentration is below the instrument's threshold. The impactor samples taken at this time (A and B, 114-115 minutes) are in close agreement with each other at about 16 g/m^3 STP but are higher than the filter sample concentrations. This may be attributed to differences in sampling or transport efficiency. An average concentration of 10.6 g/m^3 STP with a standard deviation of 5.2 g/m^3 STP is calculated using all five results.

The filter samples D, E and F (124-127 minutes) show collected mass but the pressure records indicate no measurable flow for these samples. The transducer outputs monitored at the control site indicated flow initially for each sample but the readings dropped to a no flow condition within a few seconds. The high concentrations indicated by the impactor samples (C and D, 125-126 minutes) could account for the mass present on the filters for even a short period (a few seconds) of normal sampling flow. The data has been reduced assuming no flow. This no flow condition caused the dilution ratio for the impactors to be unacceptably high at 1:18. This introduces a high level of uncertainty in the 100 to 170 g/m^3 STP concentrations indicated by the impactors. The concentration is in the range of about 40 g/m^3 STP to over 200 g/m^3 STP based on the uncertainty in dilution ratio. The opacity meter registered very high opacity during this sampling period and when viewed with the mass collection on the filters during an apparently very curtailed period of operation, a concentration on the order 100 g/m^3 is not unreasonable.

Spurrious indications that filter D had failed and allowed aerosol to pass to the filter control orifice, clogging it, led to the implementation of the following procedure. All diluters were turned on purging the system and producing excess dilution air flow so that no aerosol would be drawn through the sample inlet when samplers were activated. The filter H and

Table 7.4.1

FILTER SAMPLE DATA FOR SURC 4

Filter Sample	Time (min.)	Sample Flow (SLPM)	Dilution Ratio	Collected Mass (mg)	Mass Concentration (g/m^3 STP)
A	113-114	8.93	1:1	64.7	7.2
B	114-115	8.93	1:1	63.1	7.1
C	115-116	8.93	1:1	54.3	6.1
D*	124-125	--	--	4.09	--
E*	125-126	--	--	3.50	--
F*	126-127	--	--	4.41	--
G	154-155	9.39	1:2.76	0.15	0.12
H**	155-156	9.39	1:2.76	6.32	1.86
I	156-157	9.39	1:2.76	0.14	0.11

* Critical orifice pressure records indicate no flow (or very little flow) for these samples

** Filter H was turned on manually from 137.5 to 138.5 with no sample flow (excess dilution flow) to check the pressure readings on the filter flow orifice.

Table 7.4.2

IMPACTOR SAMPLE DATA FOR SURC 4

Impactor Sample	Time (min.)	Sample Flow (SLPM)	Dilution Ratio	Collected Mass (mg)	Mass Concentration (g/m^3 STP)
A	114-115	9.28	1:1	153.4	16.5
B	114-115	12.82	1:1	207.5	16.2
C*	125-126	10.2	1:17.7*	59.6	103*
D*	125-126	14.10	1.17.7*	138.8	174*
G**	155-156	10.13	1:4.59	6.88	3.1
H**	155-156	14.0	1:4.59	15.33	5.0

* The results are based on an indicated zero flow for the concurrent filter sample E.

** Impactors G and H were turned on manually from 137.5 to 138.5 with no sample flow (excess dilution flow) to check the pressure readings on the flow orifices.

Table 7.4.3

CYCLONE SAMPLE DATA FOR SURC 4

Cyclone Sample	Time (min)	Sample Flow (SLPM)	Dilution Ratio	Collected Mass (mg)	Mass Concentration (g/m^3 STP)
1	134-137.5 139-154 158-162	23.8	1:1	463.4	0.76

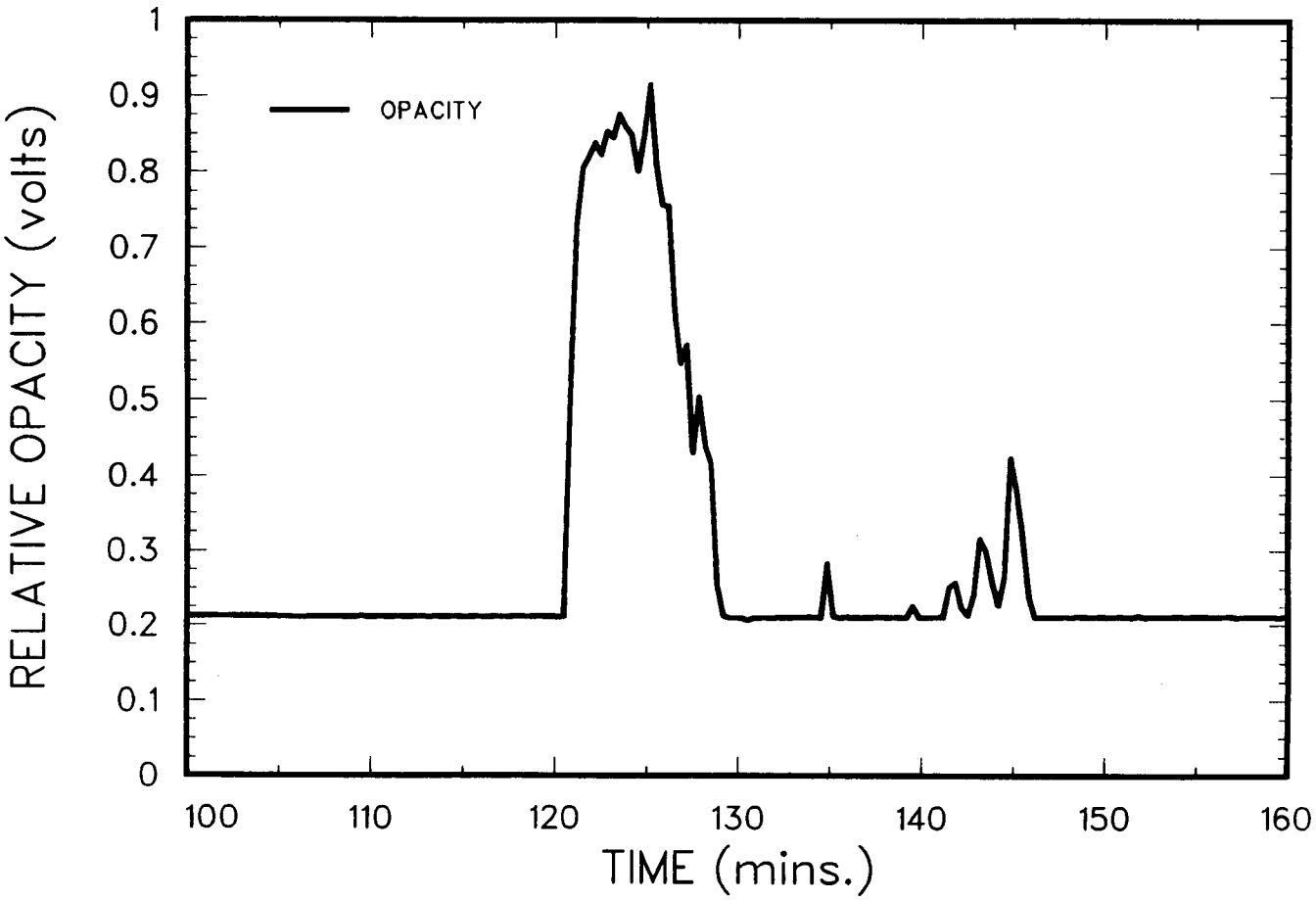

Figure 7.4.1 - Opacity Meter Output for SURC 4 Test as a Function of Time. Voltage Level is Directly Proportional to Aerosol Concentration.

impactors G and H were manually activated for a period of 1 minute at 137.5 minutes. The pressure signals indicated normal flow conditions. Posttest examination indicated no filter failure and no orifice clogging. However, activating these samplers, even with excess dilution flow, still cleared the dead volumes in the aerosol sampling lines between the samplers and diluters. These dead volumes are about 500 cm^3 for the filter lines and 300 cm^3 for the impactor lines.

The filter samples G, H, and I (154 to 157 minutes) show a discrepancy. Filters G and I show good agreement with each other at 0.1 g/m^3 STP but are lower than the 1.86 g/m^3 STP indicated by filter H. The pressure records indicate that the SEDS was fully operational as were the filters during this sampling period. The impactors G and H (155-156 minutes) indicate concentrations of 3 and 5 g/m^3 STP, respectively. The opacity meter does not indicate a reading above the baseline during this time period. A possible explanation for this discrepancy is that in clearing the dead volume the filter sampler H and impactors G and H collected the mass shown in Tables 7.4.1 and 7.4.2. This would require a local aerosol concentration in the filter line dead volume of at least 12 g per actual m^3 and in the impactor line dead volume of at least 74 g per actual m^3. This is unlikely as the actual mass concentration in the previous sample at 124 to 127 minutes was only on the order of 10 g/m^3. It is also unlikely that a sample would clear the entire dead volume requiring even higher dead volume aerosol loading to collect these masses of material. The possibility of sampler leakage is not ruled out but the pressure records do not indicate this. The filter samples G and I are accepted as indication of the aerosol concentration at this point of the test. Filter H and impactors G and H are disregarded and are not considered to be representative samples of the aerosol concentration.

The cyclone gives an average aerosol concentration of 0.76 g/m^3 STP over a period of time from 134 to 162 minutes. This includes the period of activity on the opacity monitor from about 141 to 146 minutes as well as the sampling times for filter samples G and I. The cyclone concentration, opacity monitor record and filters G and I are consistent. Figure 7.4.2 shows the opacity record with the measured aerosol concentrations from impactors, filters and cyclones. This gives a consistent representation, albeit a somewhat qualitative one, of the aerosol concentration in the exhaust gas during the test.

Figure 7.4.3 shows the normalized mass distributions from impactors A and B. A substantial fraction of mass is contained on the filter in the submicron sizes. A distinct peak occurs at about 2 micrometers. There is additional mass up to 10 μm. The two impactors give good agreement on this size distribution.

Figure 7.4.4 shows the normalized mass distributions from impactors C and D. There is a peak at about 0.7 μm with substantial mass below 1 μm. This distribution is different than

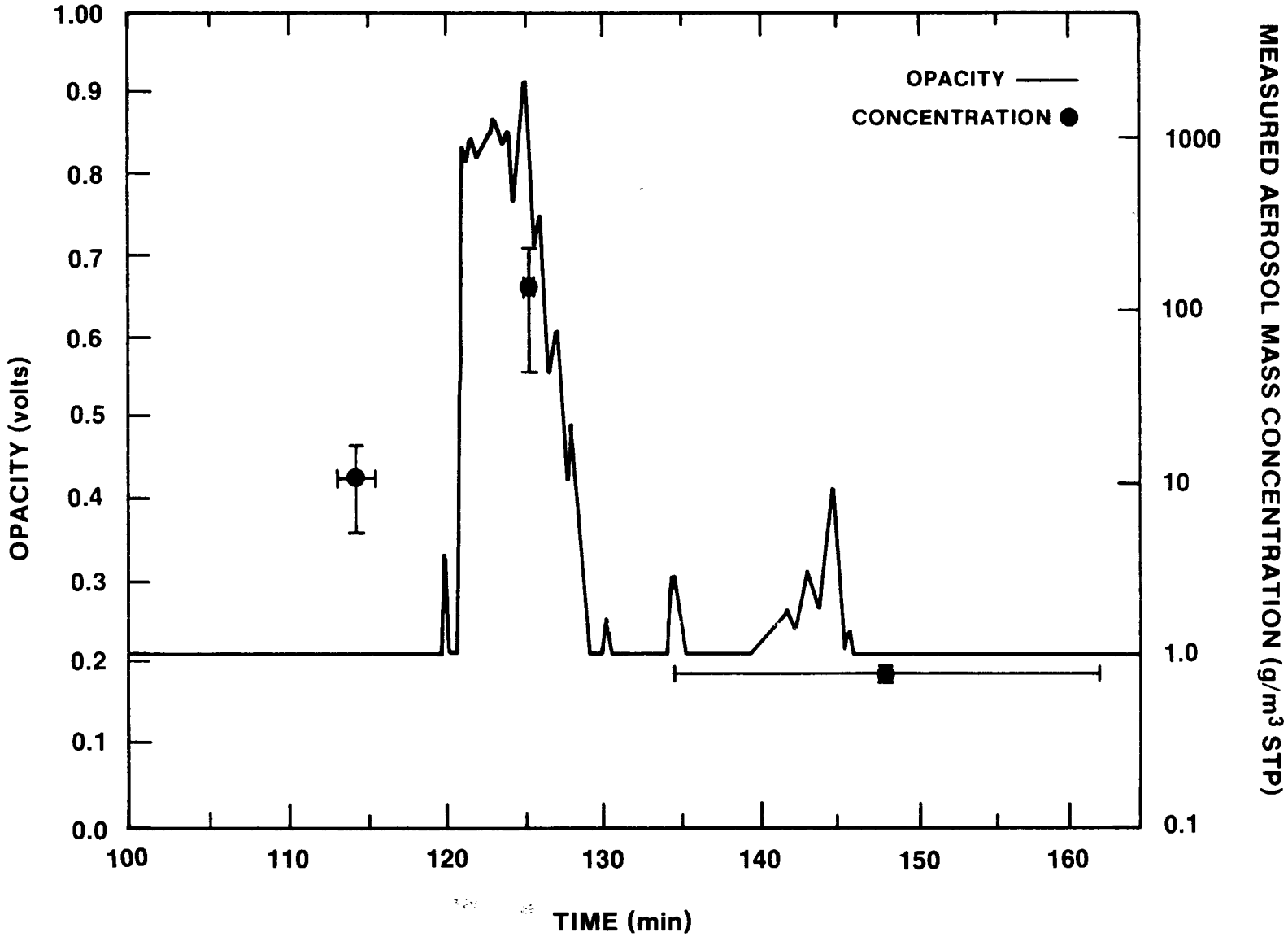

Figure 7.4.2 - Measured Aerosol Concentrations for SURC 4 Test Compared to Opacity Meter Output as a Function of Time.

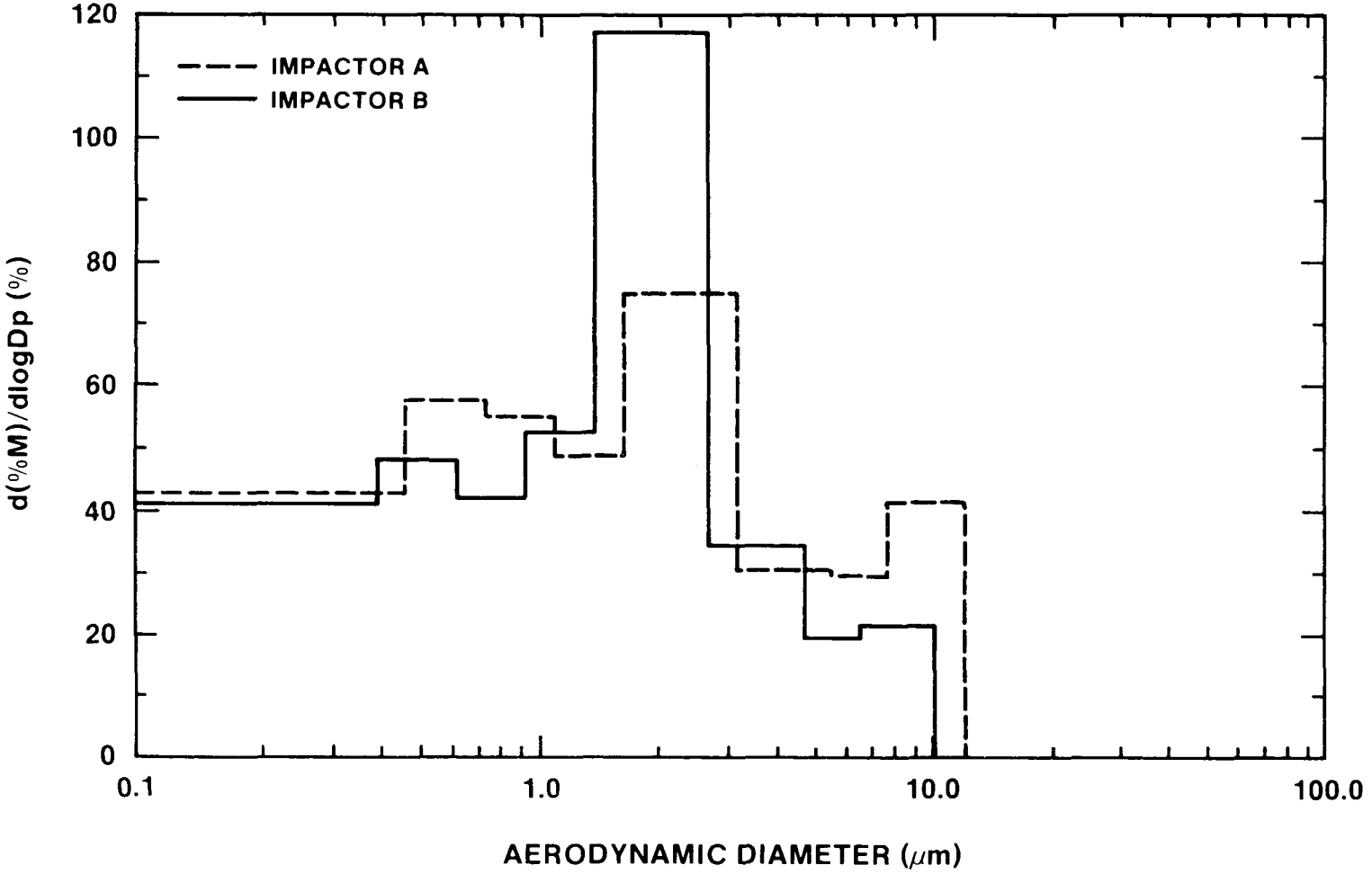

Figure 7.4.3 - Normalized Aerosol Mass Distributions from Impactors A and B Taken at 114 to 115 Minutes.

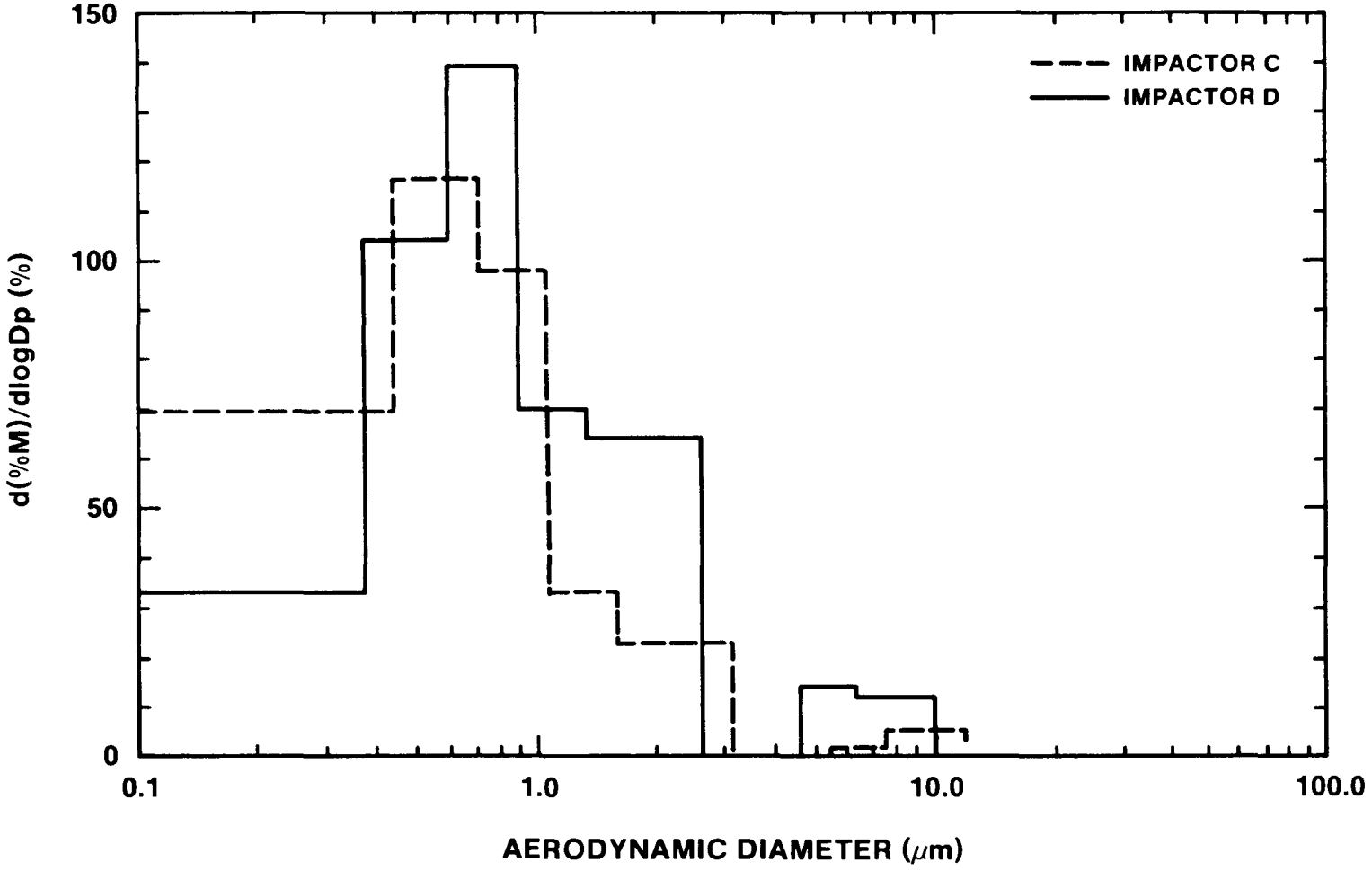

Figure 7.4.4 - Normalized Aerosol Mass Distributions from Impactors C and D Taken at 125 to 126 Minutes.

that measured by impactors A and B. This sample was taken after the addition of Zr and, consequently after the onset of considerable melt foaming as discussed in section 6.3. The presence of foam could effectively remove larger particles seen in the A and B sample while providing a generation mechanism for the particles seen at 10 μm in the C and D samples.

Figure 7.4.5 shows the normalized mass distributions for impactors G and H. The broad distribution indicated by both impactors is different than that seen in the other samples. These samples are not considered for analysis.

Figure 7.4.6 shows the normalized mass distribution from the cyclone. It shows a narrowly distributed aerosol with a peak in the distribution at 2 μm.

Figure 7.4.7 is an electron micrograph of the aerosol collected on Stage 8 of impactor A. The particles appear as agglomerates collected on the substrate. This morphology is consistent with a vapor condensation aerosol.

Figure 7.4.8 is an electron-micrograph of the aerosol collected on Stage 1 of impactor A. Some of the particles are spherical, suggesting a liquid entertainment generation mechanism.

Selected filter samples, A, B, C and H and the cyclone samples were analyzed by inductively coupled plasma spectroscopy. Table 7.4.4 gives the results for these samples. Where no element was detected, the result is given as less than the detectable threshold for the element on that sample. The cyclone samples were combined by stages to give three samples. Cyclones 1 and 2 combined stages 1 and 2 (>3.2 μm aerodynamic diameter), cyclones 3 and 4 combined stages 3 and 4 (1.44 to 3.2 μm aerodynamic diameter) and cyclones 5 and 6 combined stages 5 and 6 (0.6 to 1.44 μm aerodynamic diameter).

The filter sample H is the only filter sample taken after Zr addition with enough material for quantitative analysis. Its analysis is in good agreement with the analysis of the cyclone samples. The filters A, B, and C were taken before Zr addition. They show good agreement in composition among themselves. In all cases, tellurium is a major constituent of the collected mass. Chromium and manganese constituents from the steel are present as a few weight percent. The concrete constituents of sodium, potassium, and silicon are present at the 1 to 5 weight percent level. Molybdenum, calcium, and cerium were detected at low levels and lanthanum, niobium, and zirconium were not detected.

Filter sample H was similar to the samples A, B and C in the steel constituents. It had a lower weight fraction of Te and a higher fraction of Na, K and Ca. The Ce fraction was higher as well.

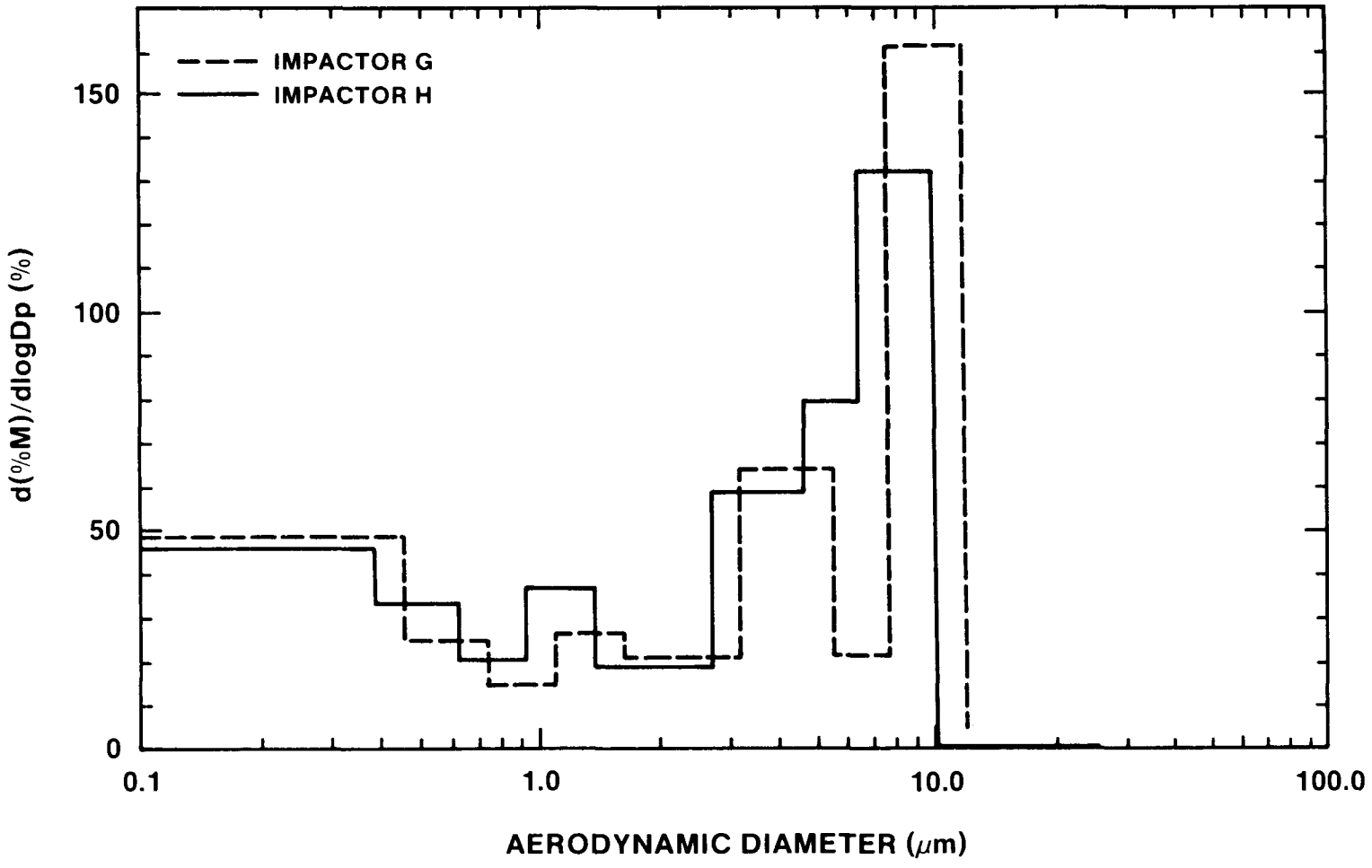

Figure 7.4.5 - Normalized Aerosol Mass Distributions from Impactors G and H Taken at 155 to 156 Minutes.

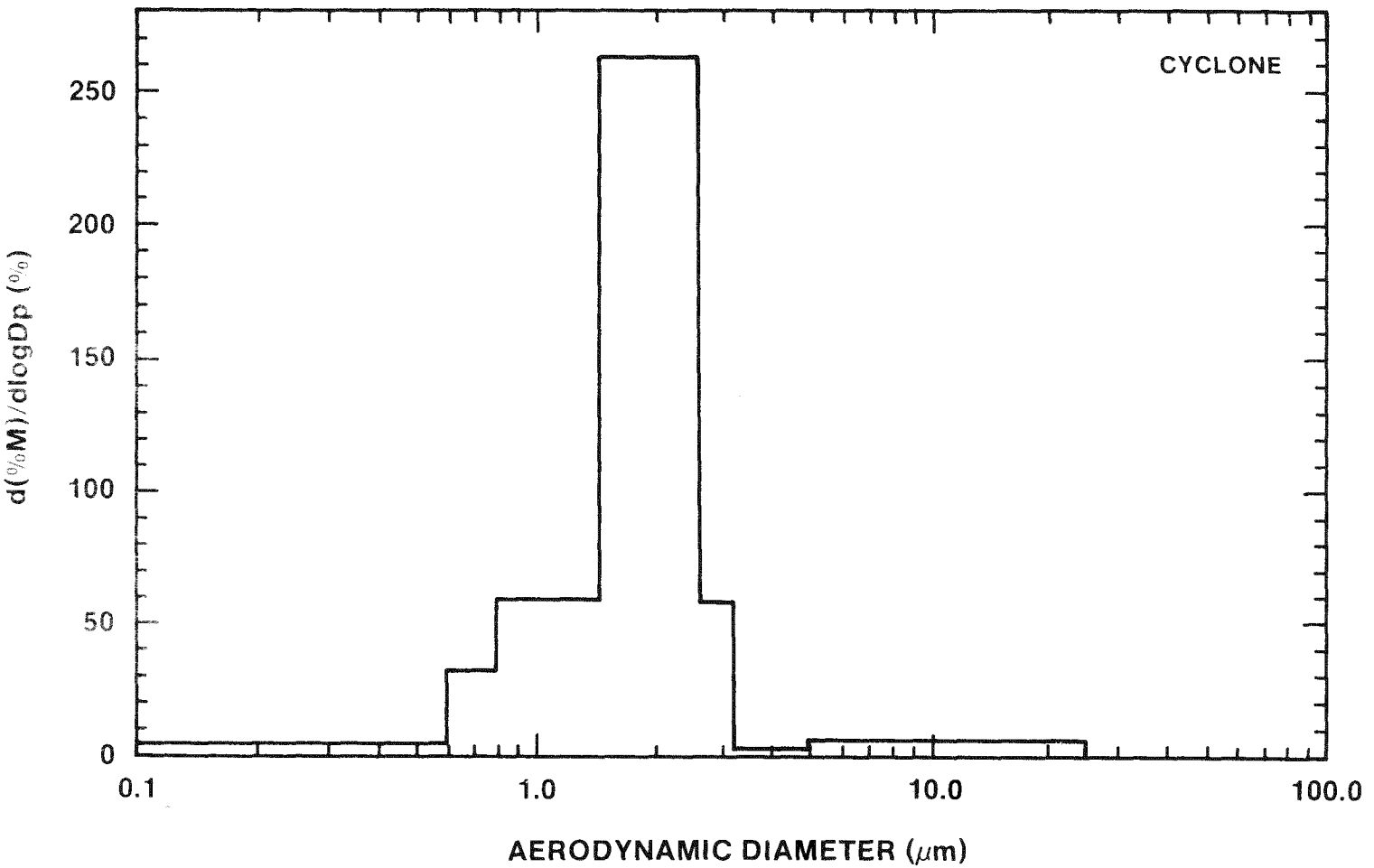

Figure 7.4.6 - Normalized Aerosol Mass Distribution from Cyclone Taken from 134 to 137.5, 139 to 154, and 158 to 162 Minutes.

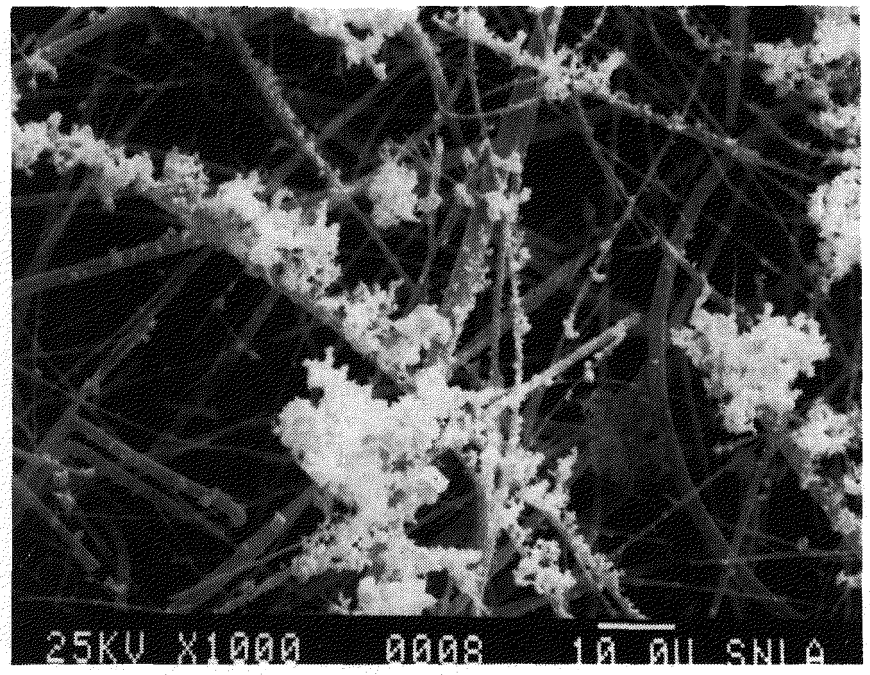

Figure 7.4.7 - Electron Micrograph of Aerosol Collected on Stage 8 of Impactor A. Agglomerate Morphology is Consistent with a Vapor Condensation Aerosol.

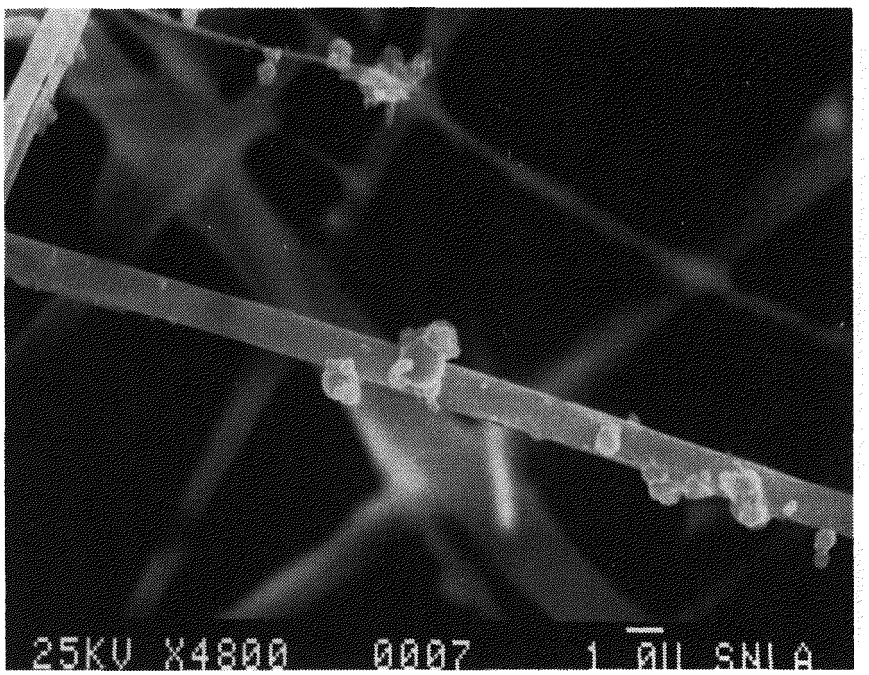

Figure 7.4.8 - Electron Micrograph of Aerosol Collected on Stage 1 of Impactor A. The Spherical Particles Suggest a Melt Entrainment Formation Mechanism.

Table 7.4.4

ELEMENTAL ANALYSIS OF SURC 4 AEROSOL
WEIGHT PERCENT OF ELEMENT IN SAMPLE

Element	Filter A	Filter B	Filter C	Filter H	Cyc 1&2	Cyc 3&4	Cyc 5&6
Fe	.265	.650	.276	.328	3.10	.306	.295
Ni	<.02	.101	.020	<.16	.368	.030	.026
Cr	1.18	1.11	1.27	.861	1.13	.585	.483
Mn	3.33	3.03	3.33	3.50	2.95	3.91	3.20
Mg	.130	.126	.101	1.45	.859	.306	.252
Ba	<.02	<.02	<.02	0.44	<.047	<.026	<.017
Na	2.89	2.88	3.27	10.9	10.2	12.3	12.2
K	4.16	3.96	4.37	8.61	7.03	10.7	10.9
Si	1.55	1.40	1.52	1.02	1.69	1.40	1.30
Ca	<.02	.025	.022	.195	.166	.036	.040
Te	65.2	67.8	70.6	47.8	33.2	31.5	32.7
La	<.02	<.02	<.02	<.16	<.047	<.026	<.017
Mo	.029	.029	<.02	<.16	.087	<.026	.021
Ce	.063	.093	.095	.972	.218	.180	.136
Nb	<.02	<.02	<.02	<.16	<.047	<.027	<.017
Zr	<.02	<.02	<.02	<.16	<.047	<.027	<.017

The cyclone samples were close to the filter H sample in composition. Sodium and potassium were comparable, tellurium was lower as was cerium. An interesting result is the significantly higher iron and nickel content in the cyclones 1 and 2 sample. This could indicate the presence of larger particles produced by the physical fragmentation of melt material containing iron and nickel.

8. TEST SUMMARY AND CONCLUSIONS

The SURC 4 experiment used 200 kg of 304 stainless steel and 20 kg of Zr metal as reactor core debris simulant materials. It was designed to be a comprehensive test examining the additional effects of zirconium metal addition to molten steel interacting with basaltic concrete. The goals of the experiment were to measure in detail the gas evolution, aerosol generation, and erosion characteristics associated with steel-zirconium-concrete interactions.

The SURC 4 experiment was conducted in a 60 cm diameter interaction crucible constructed with a 40 cm diameter basaltic concrete cylinder in the base of a magnesium oxide (MgO) annulus. A 10 cm thick, circular cover of MgO was fabricated and placed on top of the crucible. The interaction crucible and an induction coil were housed in a sealed, water cooled, aluminum containment vessel. The vessel was 180 cm high, 120 cm in diameter and contained feedthroughs for the induction power leads, instrumentation leads, and an exhaust gas port connected to the flow and aerosol sampling instrumentation. The interaction crucible was instrumented with thermocouple arrays cast into the concrete cylinder, MgO annulus and MgO cover. A 280 kw induction power supply and coil were used to heat and melt the 200 kg stainless charge within the test article and to sustain the interaction for the duration of the experiment. Additionally, 6 kg of fission product simulants were added to the melt to study fission product release. Flow rates of generated gases were measured using a sharp edge concentric orifice, a laminar flow device and two dry gas clocks. Gaseous effluents produced during the experiment were monitored and sampled using an infrared gas analyzer, mass spectrometer, and by an integral grab sample technique. Aerosols were captured on filters, cascade impactors and a cascade cyclone. Erosion characteristics were measured using type K, S, and C thermocouples in order to define the meltpool temperature and overall heat balance as well as the axial erosion rate. The apparatus was sealed and purged with argon gas in order to direct the majority of the reaction gas and aerosol effluents through a 5 cm diameter flow pipe. The SURC 4 test was run at local atmospheric pressure (.83 atm) and at an ambient temperature of 25°C.

The zirconium metal was added to the meltpool after steady-state concrete erosion was established via a single tube, manually actuated, delivery system attached vertically to the containment vessel. The tube contained 50 Zr cylinders each with a diameter of 3.3 cm and a length of 7.6 cm. Each cylinder weighed 400 g and the total charge weighed 20 kg. Deposition into the meltpool was accomplished by opening a ball valve to the gas flow line, dropping the Zr metal, and closing the ball valve to re-establish flow through the exit port.

The SURC 4 test ran for a total of 162 minutes. During this time, a net power of 63±6 kw was applied to the 200 kg stainless

steel charge to sustain the melt-concrete interaction. A total of 25 cm of basaltic concrete were eroded in the final 62 minutes of the experiment.

Three time periods during the test are of particular interest. These are the onset of gas release from the concrete between 50 to 100 minutes, steady state concrete erosion due to molten steel attack between 100 and 119 minutes, and the increased attack resulting from Zr addition to the melt at times after 120 minutes and lasting until crucible failure at 162 minutes.

During the initial heatup period between 50 and 100 minutes, the temperature of the steel charge increased from 970 K to 1700 K and began to melt. The concrete basemat started to dehydrate during this time at an average rate of 3 cm/hr producing a reaction gas flow rate of 19 slpm. The composition of this initial effluent gas was 40 to 50% H_2, 20 to 30% CO and 20-30% CO_2 with an average H_2O content of 4%. No aerosol samples were taken during this period and the opacity meter did not register an aerosol density greater than 10 g/m^3.

Concrete erosion began after 100 minutes when the stainless steel became completely molten. The 6 kg of fission product simulants which had been used to insulate the steel were incorporated into the melt between 102-105 minutes, thus initiating the attack. The steel temperature at 105 minutes was 1750 K. Molten steel-concrete attack was allowed to proceed until 119 minutes into the test when 20 kg of Zr metal was added to the melt pool. During the time between 105 and 110 minutes the steel melt pool temperature increased from 1750 to 1800 K then held constant at 1800 K until the Zr was added at 119 minutes. A total of 6 cm of concrete was eroded during this period at a steady rate of 15-18 cm/hr. The reaction gas flow rate between 100-120 minutes averaged 60 slpm and had a typical composition of 65% H_2 - 20% CO - 10% CO_2 - 5% H_2O. Five aerosol samples were taken during the steel-concrete ablation period. These samples indicated aerosol densities ranging from 6-16 g/m^3 and were rich in tellurium, manganese, sodium, potassium, chromium and silicon. The size distribution of these aerosols ranged from .1 to 10 microns with a mass mean diameter at 2.0 microns.

At time = 119 minutes, the Zr metal was added to the meltpool resulting in a dramatic increase in every single measured parameter. The melt pool temperature increased from 1800 K to 1950 K at 125 minutes followed by a gradual decrease in melt temperature to 1800 K at 162 minutes. The ablation rate increased from 18 to 30 cm/hr as an additional 19-21 cm of concrete eroded during the final 40 minutes of the SURC 4 test. The reaction gas flow rate increased from 60 to 183 slpm for the period from 123 to 134 minutes followed by a gradual decrease to a rate of 139 slpm at 160 minutes. The gas composition of the flow was 83% H_2 - 14% CO - 1% CO_2 - 1% H_2O from the time Zr was added until the test was terminated at time = 162. Eleven aerosol samples were taken during this period yielding aerosol

densities ranging from 200 g/m^3 at 125 minutes to .1 g/m^3 at 155 minutes. These aerosols were predominantly in the 1-2 micron size range but indicated some larger species in the 8-15 micron range. Traces of cerium and calcium were found in these later samples in addition to abundant amounts of tellurium, sodium, chromium, iron, and potassium.

Posttest analysis of the SURC 4 crucible revealed that in the process of ablating 24-27 cm of basaltic concrete the Zr-steel attack created a foamy black-green by-product which had a volume of approximately 100,000 cm^3. The major phases of this material were identified as calcium iron magnesium silicate and zirconium oxide. This lava-like substance readily flowed out of cracks in the upper crucible and into the flow piping. The material was very porous, had a composition which was 17-18% Zr in addition to steel and concrete constituents, and had a density of .7 to 1.2 g/cm^3. In addition, the metallic melt pool material at the conclusion of the SURC 4 test was devoid of Zr metal and showed reduced amounts of chromium and manganese when compared to the pretest composition of 304 steel. This implies that most if not all of the zirconium and manganese had been oxidized and incorporated into the SURC 4 by-product material whereas chromium had just begun to oxidize before the test was terminated.

The results of the SURC 4 test show that zirconium reactions have two major impacts on core-concrete interactions. First is the dramatic increase in temperature and gas release. Second is the extensive production of low density oxide foam. Neither of these two phenomena are accounted for using current computer models (Bradley, 1986).

The increase in meltpool temperature and gas release are most indicative of the type of reaction observed in the SURC 4 test. These increases cannot be accounted for using gaseous concrete by-products as the sole source of oxidation as is the case in nearly all of the current computer models. Apparently there are exothermic condensed phase reactions between zirconium and concrete oxides which supercede the gas phase reactions. This means that CORCON and its companion codes are omitting a significant chemistry model if they do not include condensed phase oxidation during the core-concrete interaction. The inclusion of such a model is essential and when properly implemented could lead to greatly enhanced predictions of radionuclide release during ex-vessel severe accidents.

The second phenomena of major importance is the extensive production of low density oxide foam. This process is also not accounted for in current computer models and could significantly affect the aerosol release and upward heat transfer during core-concrete interactions. The low density foam might serve to enhance core-concrete interactions by acting as an impervious upper insulator. The foam might also have some potential mitigating features. One mitigating quality of the foam or of any overlying material is that it has the potential to reduce the

aerosol source term by scrubbing as described in Appendix D. It is important to note, however, that the aerosol scrubbing potential for the overlying oxide foam found in SURC 4 may be seriously limited since aerosol source terms were continuously measured during the test despite an overburden which was 75 cm thick.

All in all, the SURC 4 test provides comprehensive, redundant, and well-characterized information on steel-zirconium interactions with basaltic concrete which are well-suited for code validation efforts. The data return was excellent and all of the test goals were successully met. Consequently, the information from SURC 4 was used as input to an OECD code comparison exercise designed by the NRC to test the applicability of current reactor accident analysis computer models.

APPENDIX A

THERMOPHYSICAL PROPERTIES OF CAST MgO

Introduction

Samples of cast MgO were submitted by R. Acton, Sandia National Laboratories (SNLA) for thermophysical property testing at Purdue University. R. E. Taylor and H. Groot of Purdue measured the bulk density (d), thermal diffusivity (α) and specific heat (C_p). The thermal conductivity (λ) is the product of these quantities, i.e. $\lambda = \alpha C_p d$. The results of this study have been summarized in a Purdue University Report, TPRL 447 and issued to SNLA and the data are presented in this appendix.

A Perkin-Elmer Model DSC-II Differential Scanning Calorimeter was used to measure specific heat. A reference and a sample holder in this apparatus are equipped with heaters and temperature sensors. These sensors detect fluctuations of the sample holder temperature. A closed-loop electronic system provides differential electrical power to the heater to compensate for fluctuations. This differential power is read out directly in millicalories per second and is equivalent to the rate of energy absorption or evolution of the sample. By comparing this rate with the rate measured during the heating of a known mass of sapphire, the specific heat could be calculated. The experiments are performed under computer control and the specific heat is automatically calculated at equal temperature intervals.

The flash method, in which the front face of a small disc-shaped sample was subjected to a short laser burst and the resulting rear face temperature rise was recorded, is used in over 80% of the present thermal diffusivity measurements throughout the world. A highly developed apparatus exists at TPRL and Purdue University has been involved in an extensive program to evaluate the technique and broaden its uses. The apparatus consists of a Korad K2 laser, a high vacuum system including a bell jar window for viewing the sample, a tantalum tube heater surrounding a sample holding assembly, a spring-loaded thermocouple or an infrared detector, appropriate biasing circuits, amplifiers, A-D converters, crystal clocks and a minicomputer-based digital data acquisition system capable of accurately taking data in the 40 microsecond and longer time domain. The computer controls the experiment, collects the data, calculates the results and compares the raw data with the theoretical model.

Results and Discussion

Sample dimensions, masses and bulk density values are given in Table A-1. The densities ranged from 2.68 to 2.81 gm cm^3 for the samples used in the diffusivity measurements.

TABLE A-1

SAMPLE DIMENSIONS, MASSES AND BULK DENSITY VALUES

Sample Designation	Thick (in.)	Diameter (in.)	Mass (gms)	Density (gm cm^{-3})
51-6323-1	0.2016	0.5005	1.8045	2.776
51-6323-2	0.2015	0.5005	1.8252	2.810
51-6323-3	0.2025	0.5007	1.8234	2.791
51-6323-4	0.1990	0.5007	1.7236	2.684

Specific heat results are given in Table A-2 and are plotted in Figure A-1. Four runs were made. During Run 1, the specific heat of the as-received materials was measured to 227°C. A peak near 100°C was noted. Run 2 was a duplicate of Run 1 and no peak was observed. Thus, the peak observed in Run was undoubtedly due to the evaporation of moisture. Run 3 covered the range up to 527°C. During this run, a large peak was noted around 430°C. The total weight decrease from the as-received sample of Run 3 to the conclusion of Run 3 was from 0.12990 to 0.11643 gms. No peaks was observed. Thus, the peak observed in Run 3 was probably due to the release of bound water. The results of Run 4 were extrapolared to 1200°C for purposes of calculating thermal conductivity values.

Previous diffusivity measurements on thinner samples were 0.0316, 0.0244, and 0.0815 cm^2 sec^{-1}. The thin sample with the relatively large value was composed mainly of one grain which extended through the entire thickness of the sample. Therefore, thicker samples were obtained. Thermal diffusivity results on the thicker samples are given in Table A-3 and are plotted in Figure A-2. The diffusivity values for the four samples ranged from 0.0279 to 0.0352 cm^2 sec^{-1} at room temperature. Measurements made on Sample 51-6323-1 during cooling agreed with the heating curve to 800°C but were substantially lower at lower temperatures, indicating microcracking. Data were obtained on Sample 51-6323-3 to 600°C and then the sample was cooled to room temperature. The room temperature value was significantly lower than that of the as-received sample. The value at 600°C obtained during re-heating was lower by about the same amount. Diffusivity values at higher temperatures approached the values which would be obtained by extrapolating the first run data. This behavior is typical of that observed in heating of microcracked materials.

Thermal conductivity calculations are given in Table A-4. The results are plotted in Figure A-3. Thermal conductivity values for Sample 51-6323-3 are divided into two parts - one obtained during heating to 600°C and the other obtained after cooling to room temperature and re-heating to higher temperatures. The results for Sample 51-6323-1 and for Sample 51-6323-3 up to 600°C are for as-received samples. Conductivity values decreased during thermal cycling.

Table A-2

SPECIFIC HEAT RESULTS*

Temperature (C)	Run 1	Run 2	Run 3	Run 4
42.0	0.9971	0.9504		
62.0	1.0442	0.9783	0.9867	0.9671
77.0	1.0971	0.9970	1.0132	0.9907
102.0	1.2029	1.0269	1.0601	1.0203
127.0	1.2731	1.0552	1.0983	1.0496
152.0	1.2578	1.0815	1.1036	1.0778
177.0	1.2246	1.1069	1.0959	1.1035
202.0	1.2054	1.1322	1.0891	1.1257
227.0	1.2032	1.1579	1.0831	1.1447
252.0			1.0809	1.1605
277.0			1.0841	1.1742
302.0			1.0882	1.1847
327.0			1.0939	1.1924
352.0			1.1169	1.1987
377.0			1.2007	1.2049
402.0			1.4802	1.2112
427.0			1.9173	1.2162
452.0			1.8922	1.2200
477.0			1.4146	1.2251
502.0			1.2454	1.2296
527.0			1.2329	1.2340
552.0				1.2430
557.0				1.2543
602.0				1.2681
627.0				1.2740
652.0				1.2800

* W s $gm^{-1}K^{-1}$

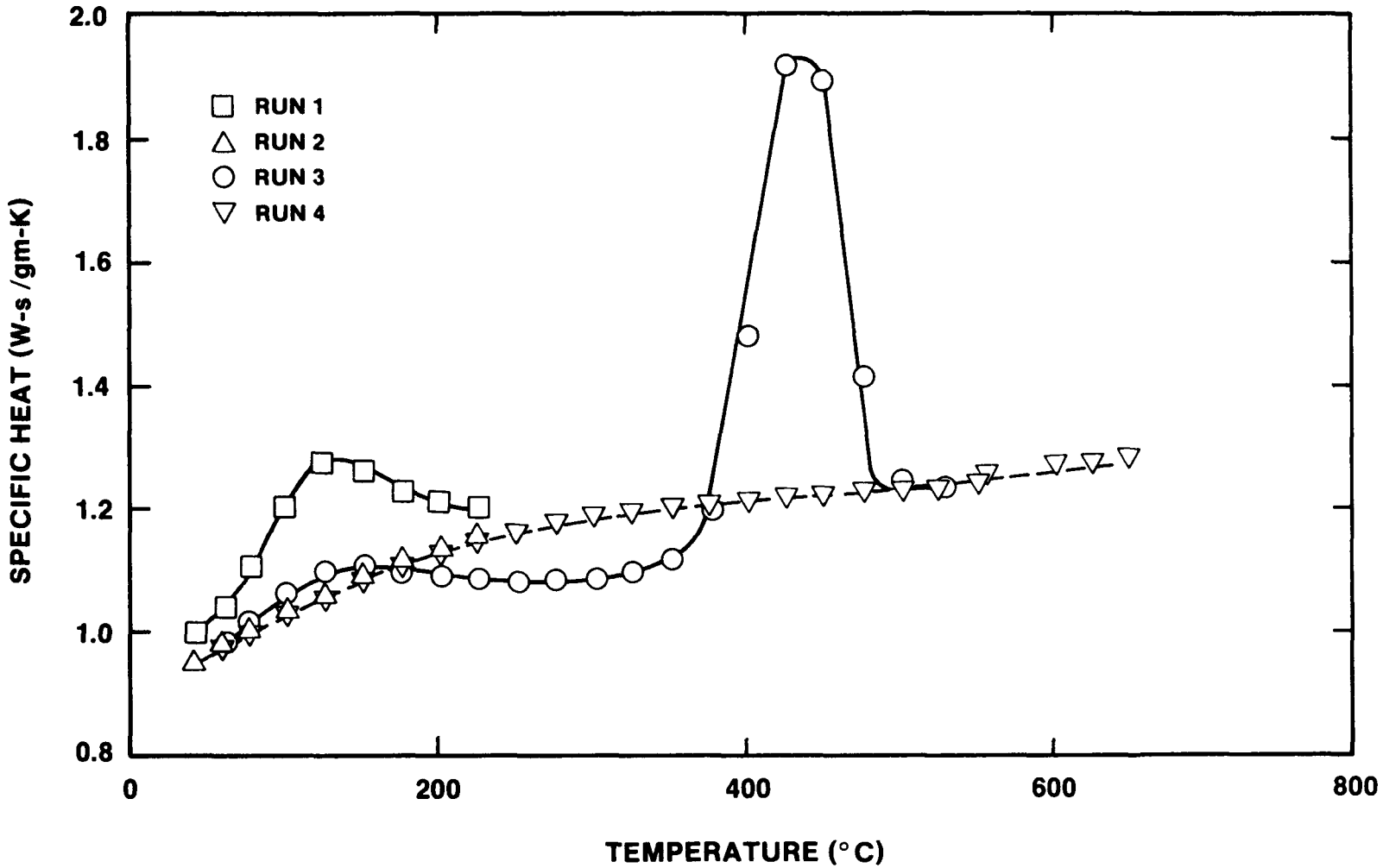

Figure A-1 - Specific Heat

Table A-3

THERMAL DIFFISIVITY RESULTS

Sample Designation	Temperature (°C)	Diffusivity (cm^2 sec^{-1})	Remarks
51-6323-1	23	0.0318	
	100	0.0298	
	200	0.0241	
	300	0.0202	
	400	0.0176	
	500	0.0143	
	600	0.0158	
	800	0.0105	
	900	0.00988	
	1000	0.00966	
	1200	0.00886	
	800	0.0107	Cooling
	500	0.0124	Cooling
	300	0.0148	Cooling
51-6323-2	23	0.0342	
51-6323-3	23	0.0352	
	100	0.0311	
	200	0.0268	
	300	0.0222	
	400	0.0195	
	500	0.0162	
	600	0.0139	
	23	0.0285	Cooling
	600	0.00910	Reheat
	700	0.00844	Reheat
	800	0.00827	Reheat
	900	0.00766	Reheat
	1000	0.00811	Reheat
	1200	0.00810	Reheat
51-6323-4	23	0.02789	

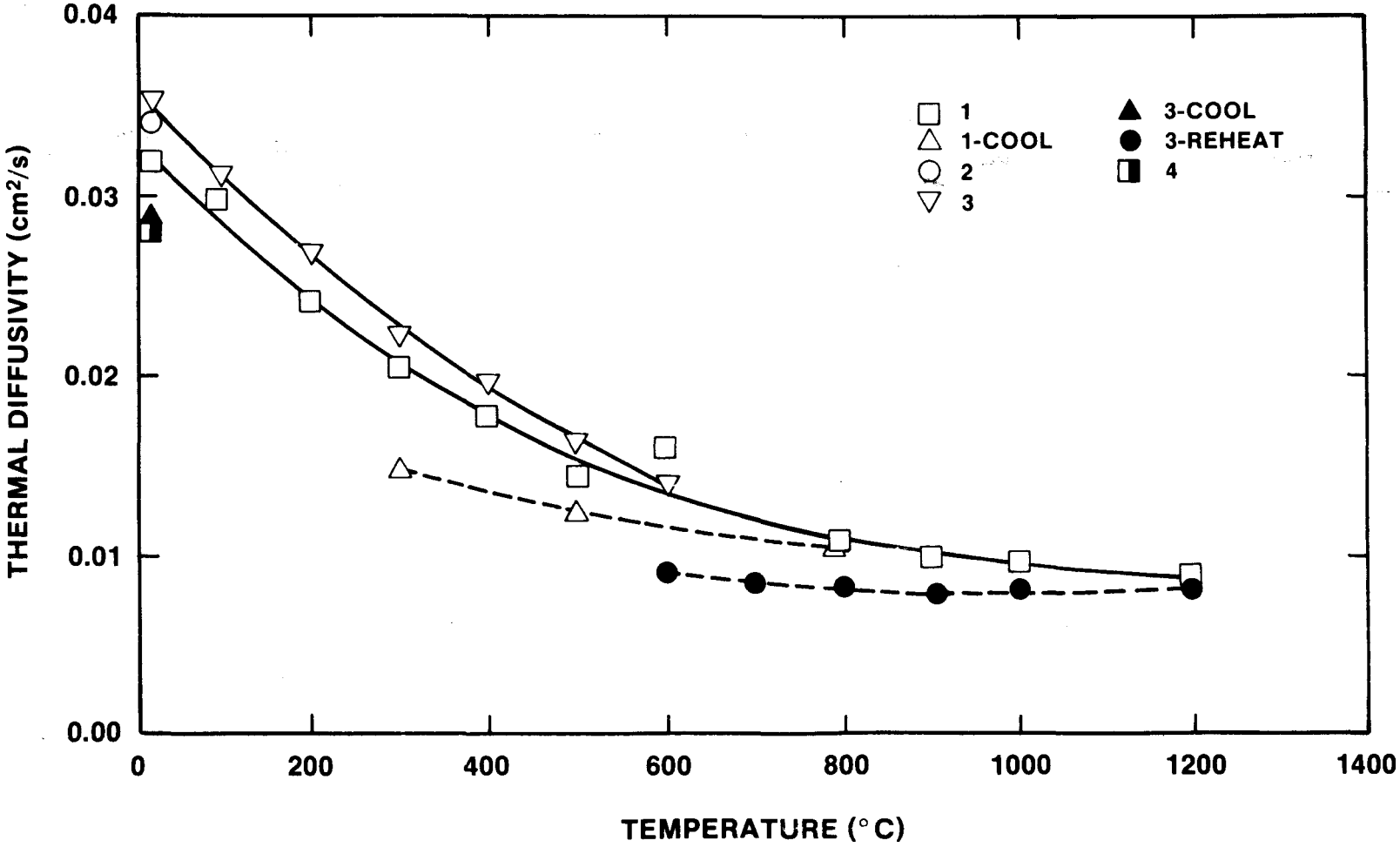

Figure A-2 - Thermal Diffusivity

Table A-4

THERMAL CONDUCTIVITY CALCULATIONS

Sample (No.)	Temp. (C)	Density ($gm\ cm^{-3}$)	Specific Heat ($W\ s\ gm^{-1}K^{-1}$)	Diffusivity (cm^2sec^{-1})	Conductivity ($W\ cm^{-1}K^{-1}$)	Conductivity (BTU units*)	Temp. (F)
51-6323-1	22.0	2.776	0.8850	0.03260	0.08009	55.53	71.6
51-6323-1	100.0	2.776	1.0180	0.02860	0.08082	56.04	212.0
51-6323-1	200.0	2.776	1.1230	0.02420	0.07544	52.31	392.0
51-6323-1	300.0	2.776	1.1840	0.02090	0.06869	47.63	572.0
51-6323-1	400.0	2.776	1.2110	0.01790	0.06018	41.72	752.0
51-6323-1	500.0	2.776	1.2420	0.01560	0.05379	37.29	932.0
51-6323-1	600.0	2.776	1.2680	0.01240	0.04365	30.26	1112.0
51-6323-1	700.0	2.776	1.2850	0.01200	0.04281	29.68	1292.0
51-6323-1	800.0	2.776	1.3000	0.01080	0.03898	27.02	1472.0
51-6323-1	900.0	2.776	1.3070	0.01010	0.3665	25.41	1652.0
51-6323-1	1000.0	2.776	1.3140	0.00950	0.03465	24.03	1832.0
51-6323-1	1100.0	2.776	1.3250	0.00910	0.03347	23.21	2012.0
51-6323-1	1200.0	2.776	1.3300	1.00880	0.03249	22.53	2192.0
51-6323-3	22.0	2.791	0.8850	0.03510	0.08670	60.11	71.6
51-6323-3	100.0	2.791	1.0180	0.03070	0.08723	60.48	212.0
51-6323-3	200.0	2.791	1.1230	0.02600	0.08149	56.50	392.0
51-6323-3	300.0	2.791	1.1840	0.02240	0.07402	51.32	572.0
51-6323-3	400.0	2.791	1.2150	0.01950	0.06613	45.85	752.0
51-6323-3	500.0	2.791	1.2420	0.01670	0.05789	40.14	932.0
51-6323-3	600.0	2.791	1.2680	0.01440	0.05096	35.33	1112.0
51-6323-3	700.0	2.791	1.2850	0.00910**	0.3264	22.63	1292.0
51-6323-3	800.0	2.791	1.3000	0.00860**	0.03120	21.63	1472.0
51-6323-3	900.0	2.791	1.3070	0.00820**	0.02991	20.74	1652.0
51-6323-3	1000.0	2.791	1.3140	0.00800**	0.02934	20.34	1832.0
51-6323-3	1100.0	2.791	1.3250	0.00800**	0.02958	20.51	2012.0
51-6323-3	1200.0	2.791	1.3300	0.00810**	0.03007	20.85	2192.0

* (BTU in $hr^{-1}ft^{-2}F^{-1}$)
** After Cooling

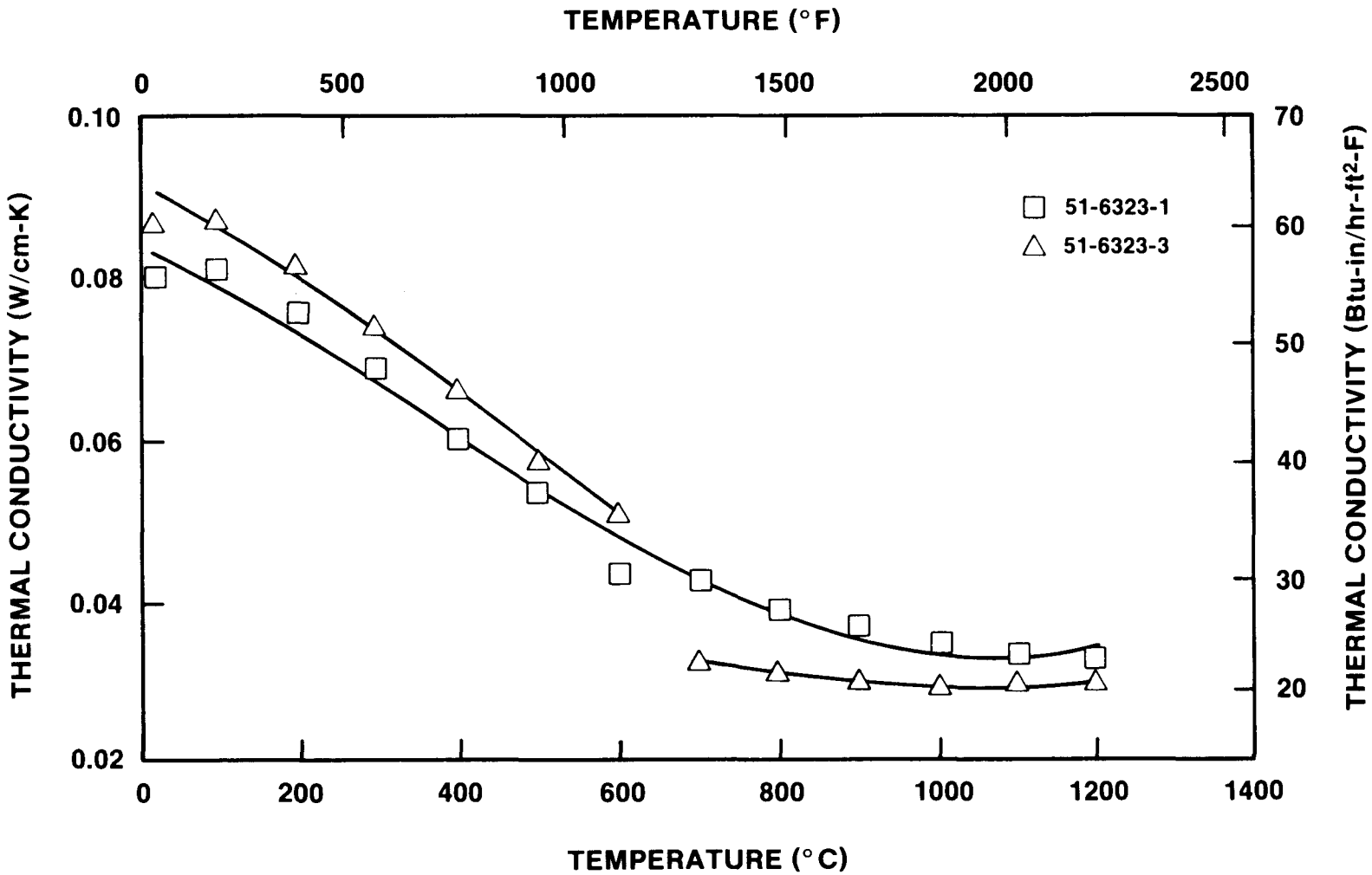

Figure A-3 - Thermal Conductivity

APPENDIX B

DESCRIPTION OF TEST ARTICLE FABRICATION

This appendix presents a detailed description of the casting forms, installation of thermocouples and casting of the components making up the interaction crucible.

Lower Crucible Form

The crucible used in the SURC 4 test is similar in design to those used in the past Transient Uranium Concrete (TURC) (Gronager et al., 1986) experiments. The crucible, shown schematically in Figure B-1, consists of an instrumented concrete cylinder 40.6 cm in diameter and 40.6 cm in height, cast at the base of an MgO annulus 60.0 cm outside diameter and 100.0 cm in height. The "1-D" interaction crucible was cast using four (4) different steel casting forms--namely, the lower crucible form, upper crucible form, cover form, and sidewall thermocouple form. The main body of the crucible, consisting of the upper and lower crucible forms, was cast in two sections. This was done to facilitate the installation of instrumentation and melt charge.

An assembly of the lower crucible form is shown in Figure B-2. Figures B-3 through B-7 show photographs of the components of the lower casting form in progressive stages of assembly. This form was prepared and cast inverted to its test orientation. The concrete slug was cast into the annulus of this section of the crucible. The inside diameter of the crucible was formed using a mild steel pipe having dimensions 40.6 cm outside diameter, 0.6 cm wall thickness and 70.0 cm length. The pipe was mounted to a 1.3 cm thick, steel, casting base using six (6) 3.8 cm x 3.8 cm x 0.6 cm thick steel angle sections, 2.5 cm wide. The outside diameter of the pipe was wrapped with 0.6 cm diameter cable having a pitch of 4.0 in the region where the concrete slug was cast. The cable was removed after the MgO had cured leaving grooves for improving the bond between the concrete and MgO annulus.

The outside diameter of the crucible was formed using another mild steel pipe configured in a bolted clam shell arrangement. This outer form had dimensions of 61.0 cm outside diameter, 0.6 cm wall thickness and 70.0 cm length. After assembly, the clam shell was bolted to the casting base using steel angles. A mild steel ring having an outside diameter of 50.2 cm, an inside diameter of 40.9 cm and a thickness of 5.1 cm was bolted to the casting base adjacent to the 40.6 cm diameter pipe forming the cavity. This ring forms an annular recess that mates to an annular step cast into the upper casting crucible assembly and sealing. Brass anchors were bolted to the inner diameter of the clam shell. These anchors were installed for handling and securing the upper and lower crucible sections at assembly.

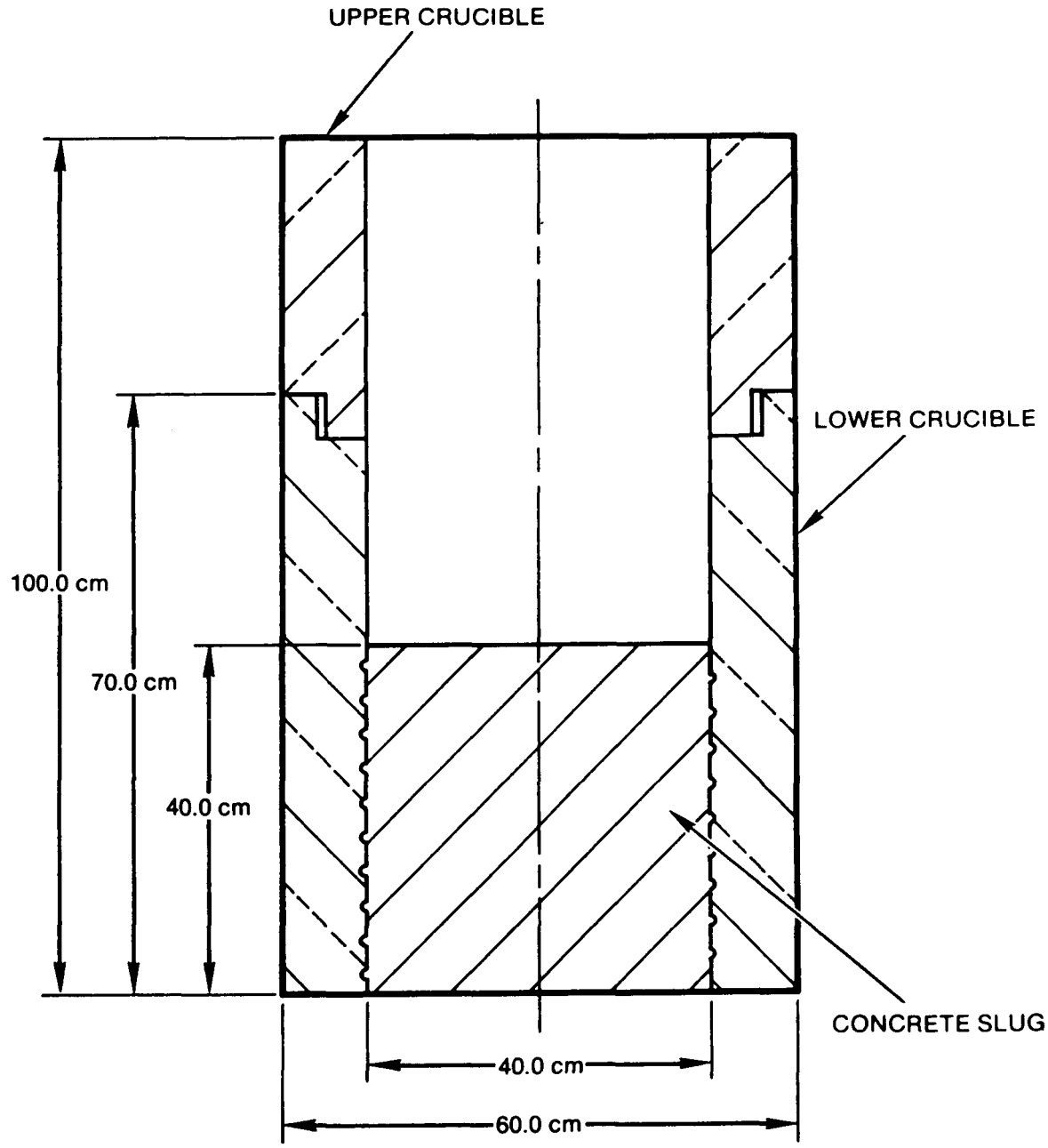

Figure B-1 - Interaction Crucible, SURC-4

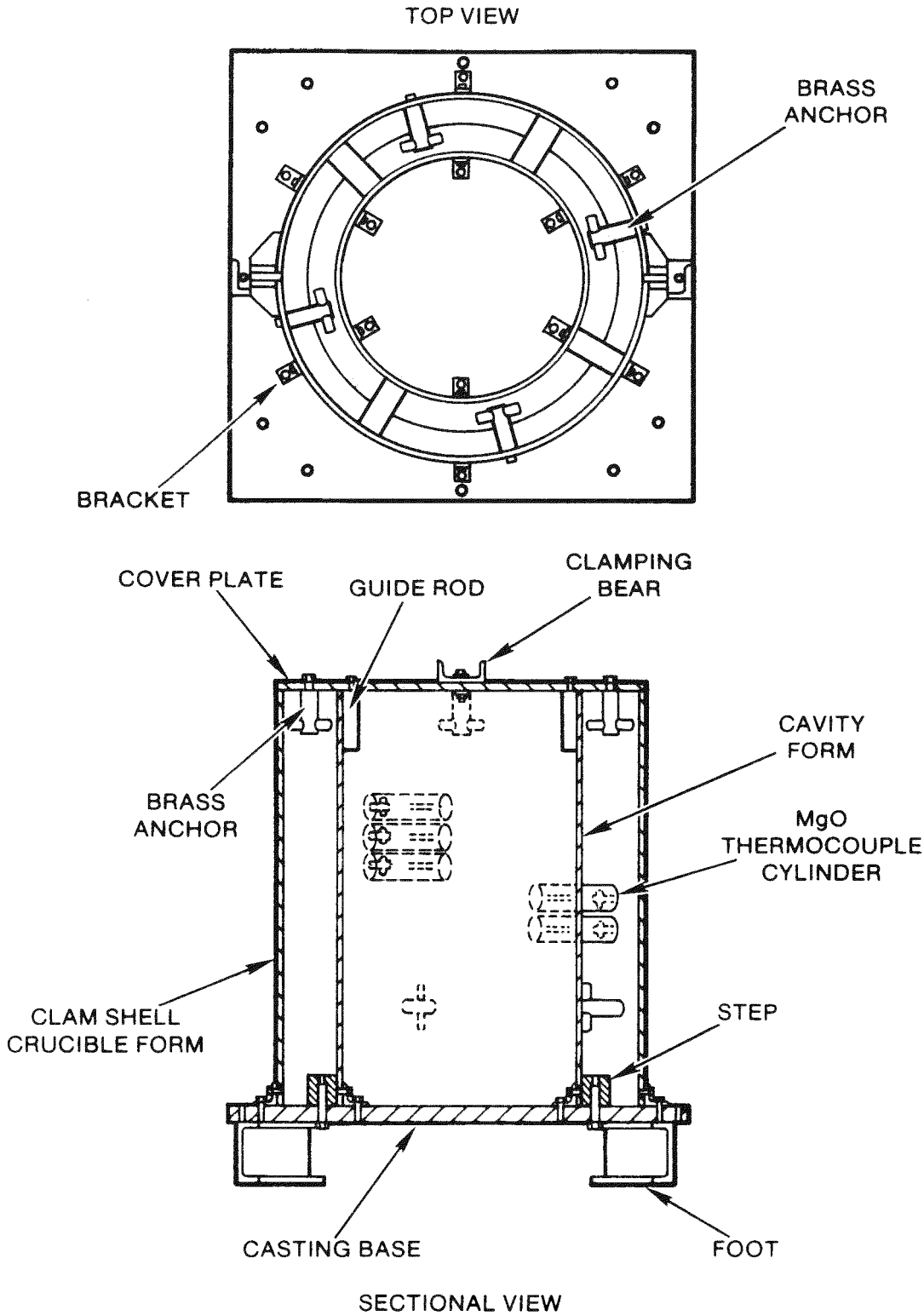

Figure B-2 - Casting Form, Lower Crucible, SURC-4

Figure B-3 - Steel Casting Form Components, Annular Ring Installed, Lower Crucible

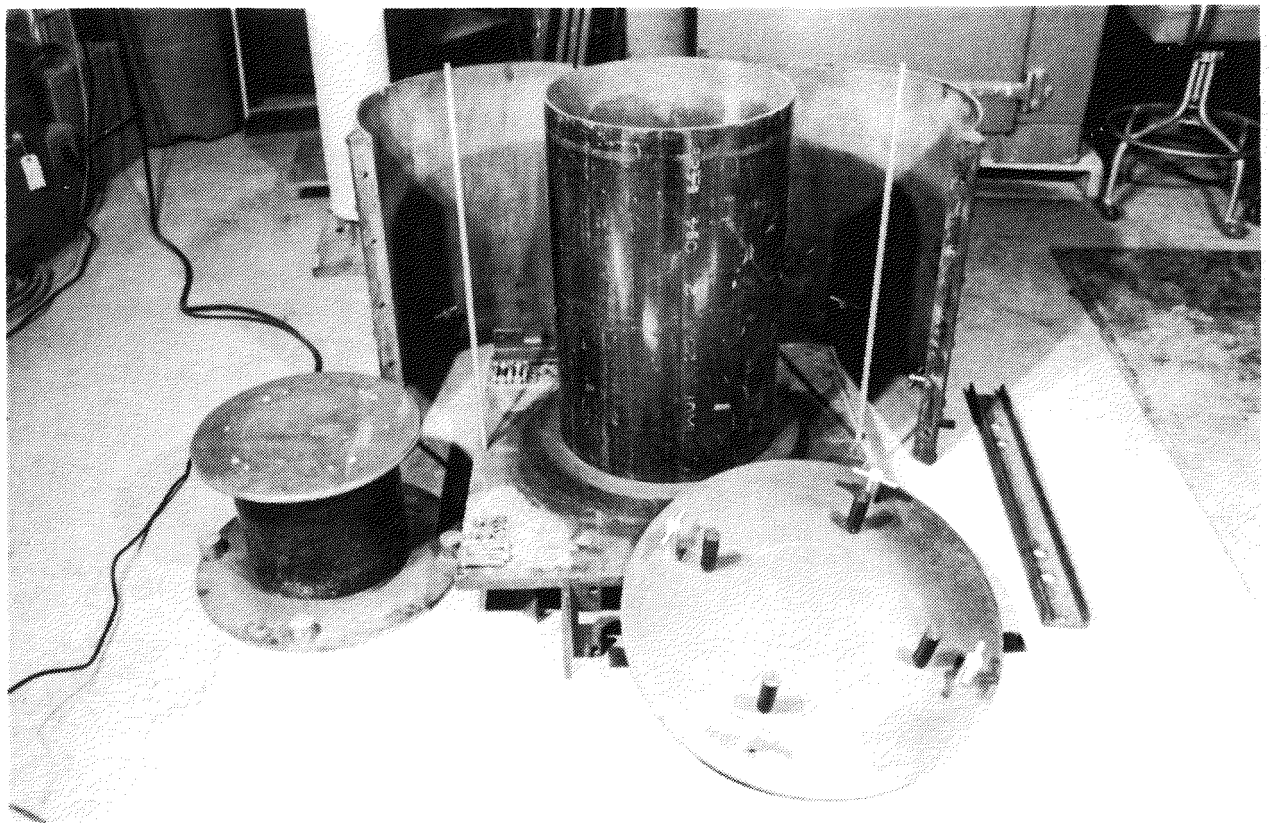

Figure B-4 - Steel Casting Form Components, Cavity Form Installed, Lower Crucible

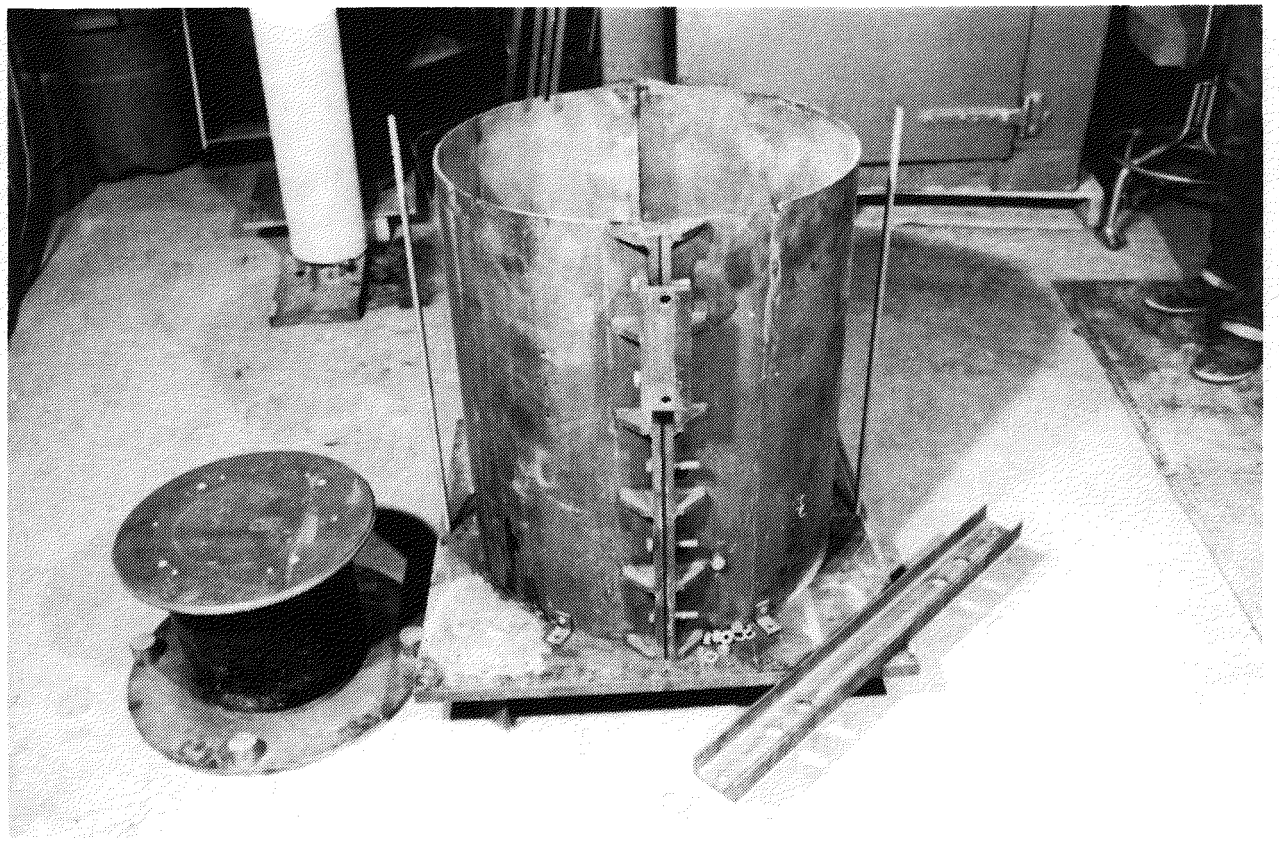

Figure B-5 - Steel Casting Form Components, Clam Shell Assembly, Lower Crucible

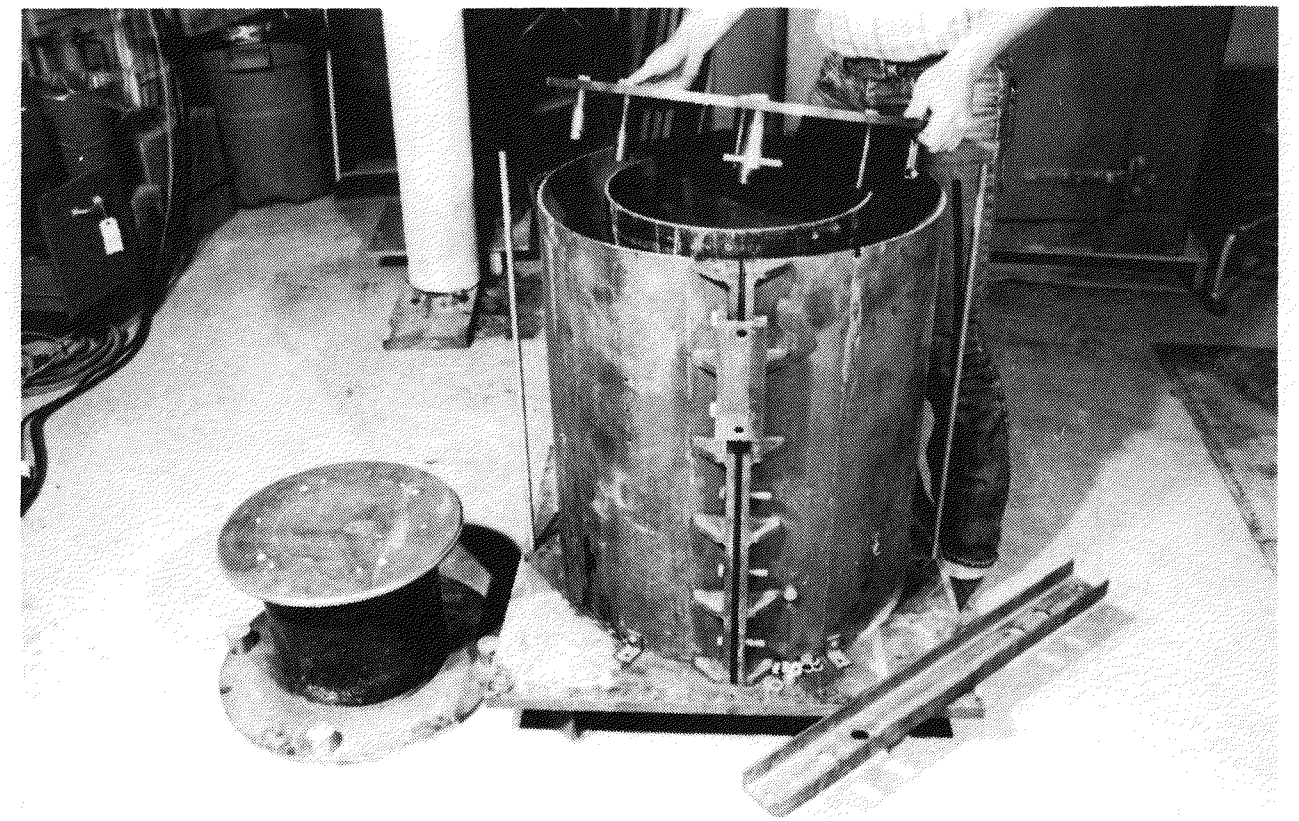

Figure B-6 - Steel Casting Form Components, Cover Plate Installation, Lower Crucible

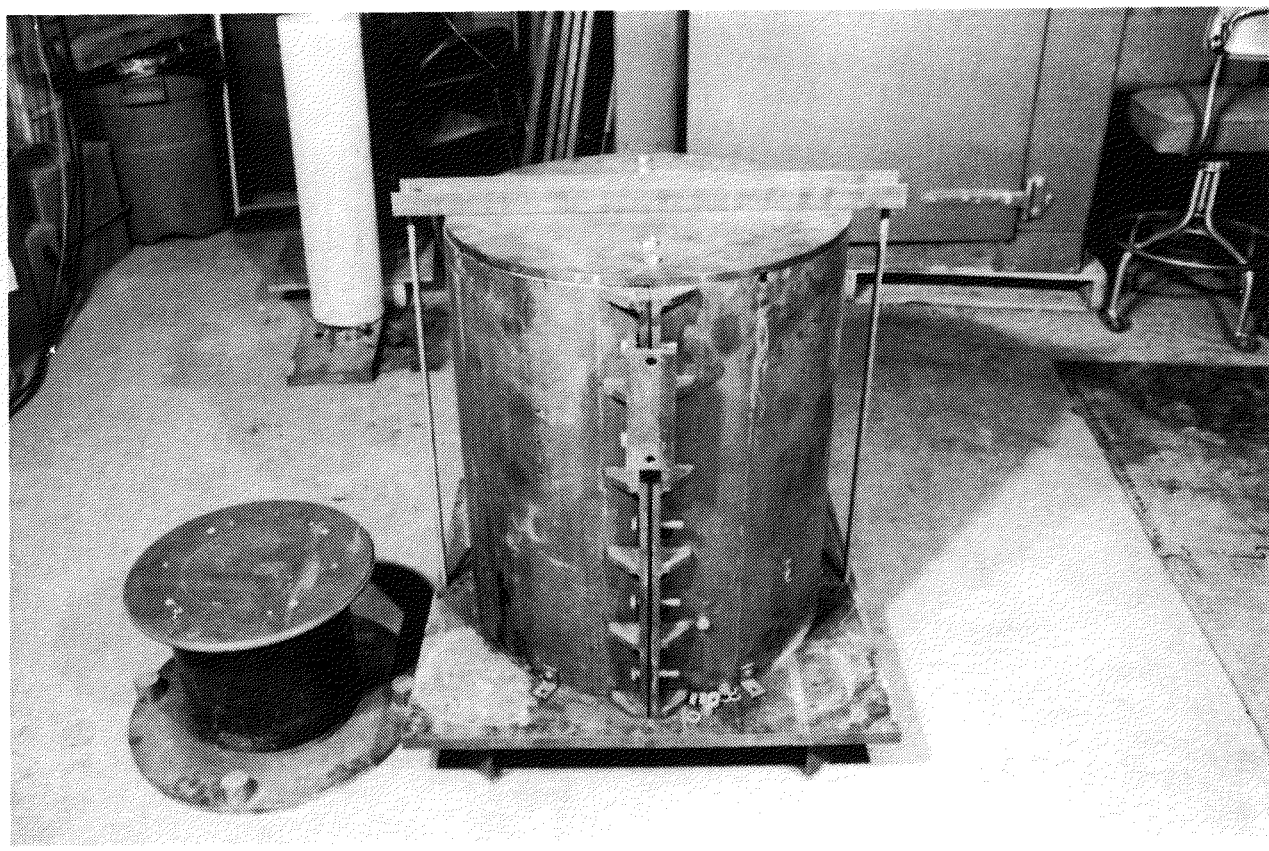

Figure B-7 - Steel Casting Form Assembly, MgO Annulus Bake Out, Lower Crucible

Prior to casting the lower form, Teflon releasing agent was sprayed on all steel surfaces in contact with the casting material to serve as mold release for ease of disassembly after curing was complete. One pneumatically operated eccentric vibrator was attached to brackets mounted to the clam shell. Another vibrator was inserted into the mix. These vibrators were operated while the castable was being placed into the forms to densify the mix and to remove entrained air. After the mix was in place and vibrated, a 1.3 cm thick steel plate installed with four (4) brass anchors was placed on top of the casting form to accurately locate brass anchors within the mix in the base of the crucible (See Figure B-6). These anchors were used to support and locate mounting hardware for supporting thermocouple arrays cast into the concrete slug. After the annulus was cured, the forms were disassembled and the cable was removed leaving grooves to improve surface bonding of the concrete cylinder. The lower form was then prepared for casting the concrete cylinder.

Sidewall thermocouples were installed into pre-cast MgO cylinders and these cylinders were accurately bolted to the inner diameter of the clam shell. The sidewall casting form is shown in Figure B-8. A photograph of the forms is shown in Figure B-9. The steel form was configured in a clam shell arrangement for ease of assembly and disassembly. The form was assembled except for the cap containing the small brass anchor. Camie #1000 dry lubricant release agent was sprayed on all the steel surfaces in contact with the casting material to serve as mold release for ease of disassembly after the castable has cured. Four (4) 0.17 cm diameter piano wires were placed through the small holes in the form and span both sides of the casting. MgO castable was mixed and placed into the casting form. The cap, with the brass anchor installed, was bolted to the body of the form and vibrated on a vibration table to densify and remove entrained air. After the castable was cured, the form was disassembled and the piano wires removed leaving a hole for inserting the type K (chromel vs. alumel) thermocouples, as shown in the photo, Figure B-10. The thermocouples had a 304 stainless steel sheath 0.16 cm in diameter. The thermocouples were installed into the holes left by removal of the piano wires, as shown in Figure B-11. The tips of the thermocouples were accurately located on the axial centerline of the pre-cast cylinder using a pin gauge, (see Figure B-12). After all the thermocouples were installed, their sheaths were bent along the length of the cylinder and wrapped with copper wire to secure the thermocouples, Figure B-13.

The ends of the MgO cylinders conformed to the curvature of the annulus providing a good fit. The cylinders were bolted to the inside diameter of the clam shell by threading a bolt through the form and into a small brass tee anchor cast into the cylinders, Figure B-14. This method for installation of the sidewall thermocouples is reliable for accurate positioning which is important for heat flux calculations. Figure B-15a shows the installation of a typical sidewall thermocouple array using the pre-cast MgO cylinders. The thermocouple tips were located in a

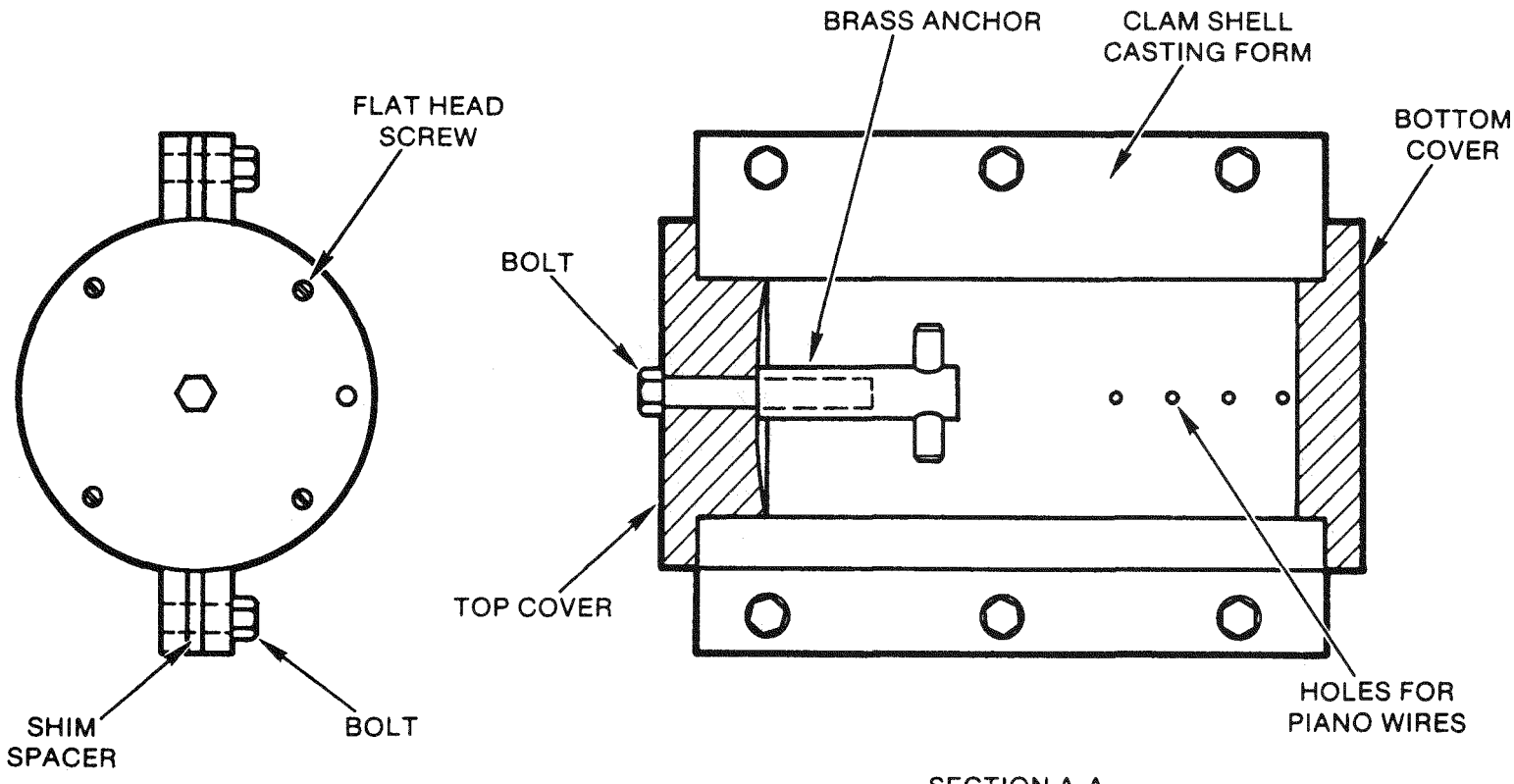

Figure B-8 - Casting Form, Pre-Cast MgO Sidewall
Thermocouple Cylinder

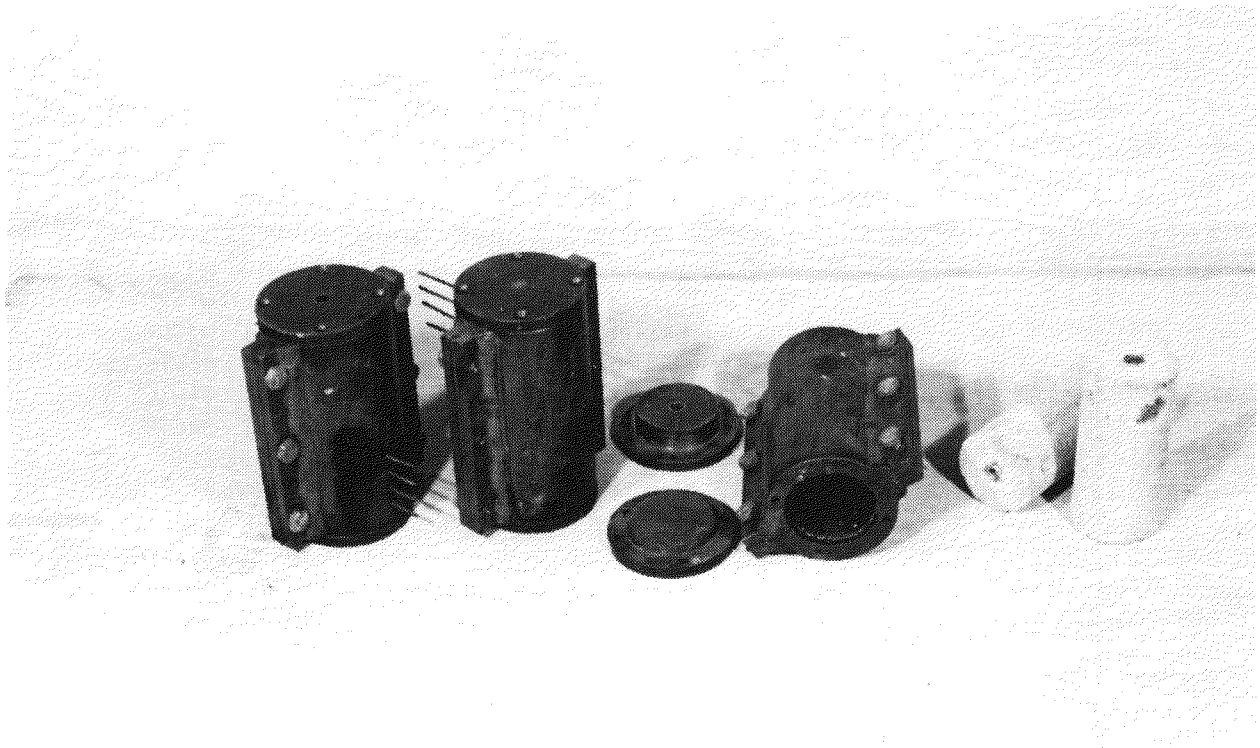

Figure B-9 - Casting Form Components and Pre-Cast MgO Sidewall Thermocouple Cylinders

horizontal plane parallel to the base of the crucible and to the direction of the isotherms propagating through the MgO annulus. General locations of all the sidewall thermocouples for the SURC-4 experiment are shown in Figure B-15b.

The assembly for casting the thermocouples into the concrete cylinder is shown in Figure B-17. A steel pedestal was installed into the cavity of the crucible using the recessed annulus for accurate orientation and alignment. Pre-assembled thermocouple arrays were configured by accurately spot welding the sheaths, made of 304 stainless steel, to a 304 stainless band 1.0 cm wide and 0.04 cm thick. Photographs of a typical array are shown in Figures B-18 and B-19. The tips of the thermocouples were bent parallel to the anticipated front of the propagating isotherms no less than ten (10) sheath diameters (1.6 cm) from the stainless steel band. The stainless bands with the welded thermocouples were secured to the bottom side of the steel pedestal using small clamps, as shown in Figures B-20 and B-21. The other end of each band was similarly clamped to a thermocouple support mounted above the cavity on four (4) 1.3 cm diameter threaded rods, as shown in the photo in Figure B-22. The stainless steel bands were made taunt by adjusting the elevation of the thermocouple support, shown in Figure B-23, thus, accurately positioning the arrays in both the vertical and radial directions. The installation of a typical thermocouple array in the concrete cavity is shown graphically in Figure B-24.

Six (6), four-hole, alumina tubes 0.6 cm in diameter were installed into counter-bored holes drilled in the top of the steel pedestal at a radial distance of 14.0 cm and 60 degrees apart as shown in Figure B-25. Each tube was fitted with both type C (tungsten-5% rhenium vs tungsten-26% rhenium) and type S (platinum vs platinum 10% rhodium) thermocouples having a 0.16 cm diameter tantalum sheaths. After the thermocouples were installed, the holes in the alumina tubes were back-filled with zirconium powder. The opposite end of each tube was supported by a 'Y-shaped' bracket attached to the threaded rods holding the thermocouple support, shown in Figure B-26. These thermocouples were installed to measure melt temperature. The alumina tubes served to hold and protect the high temperature thermocouples for a short period after melt contact. The final installation of the alumina tubes and type K thermocouple arrays cast into the concrete is shown in Figure B-27. Figure B-28 shows the general elevation location of the thermocouples cast into the concrete cylinder rotated into the same plane. Figure B-29 shows a top view of the concrete cylinder showing the orientation of the three type K thermocouple arrays and six alumina tubes. Figure B-30 shows a photo of the lower crucible (inverted) ready for testing.

Upper Crucible Form

The assembly of upper crucible form is shown in Figure B-31 in its test orientation. The form was cast entirely of MgO

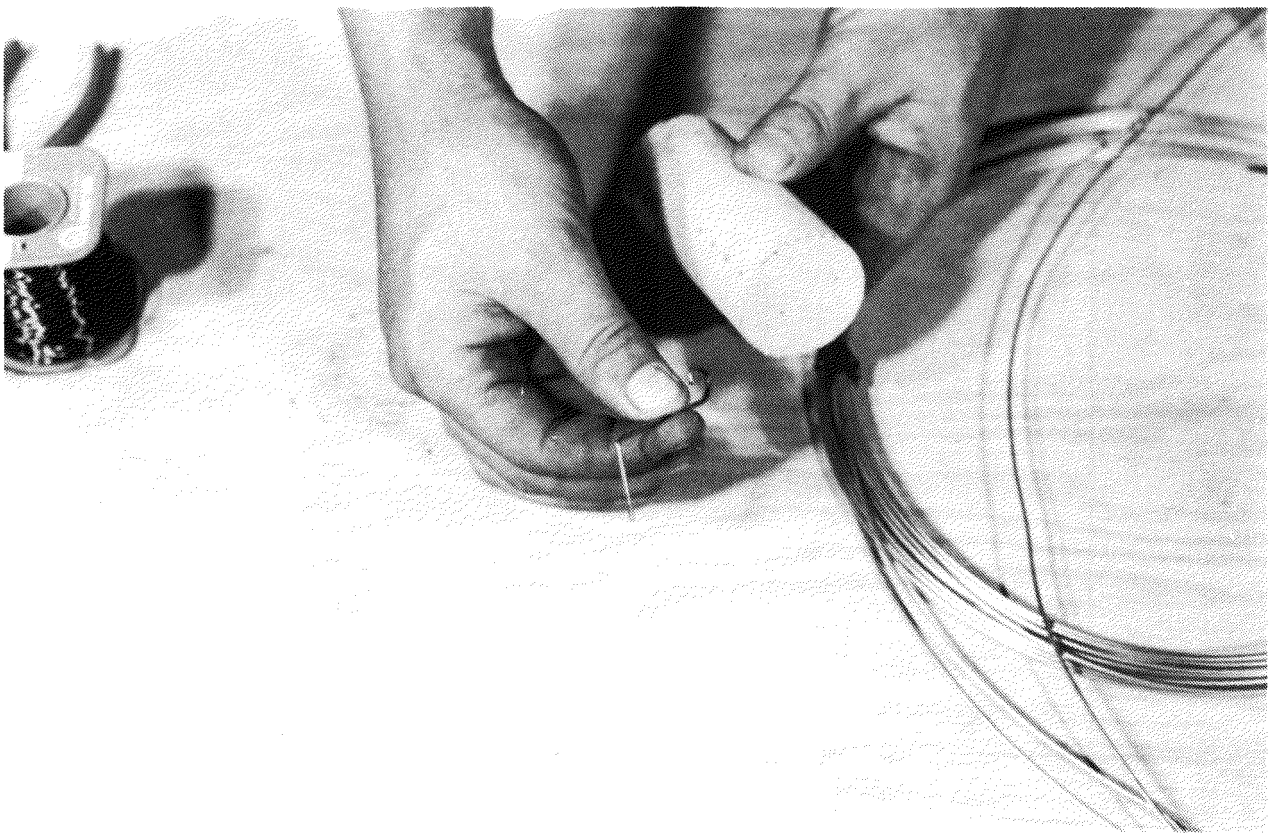

Figure B-10 - Pre-Cast MgO Sidewqll Thermocouple Cylinder
Showing Holes Left by Removal of Piano Wire

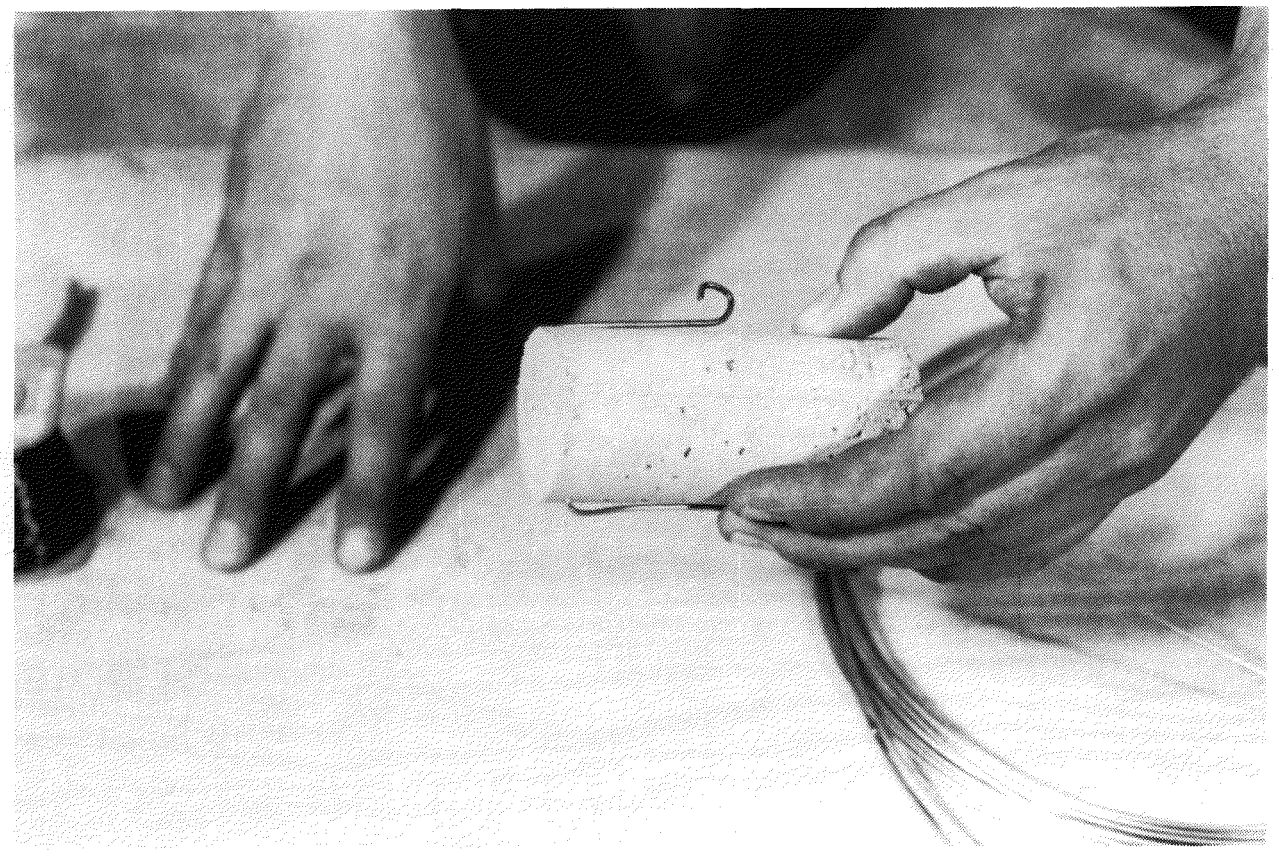

Figure B-11 - Thermocouple Installation, Pre-Cast MgO Sidewall Cylinder

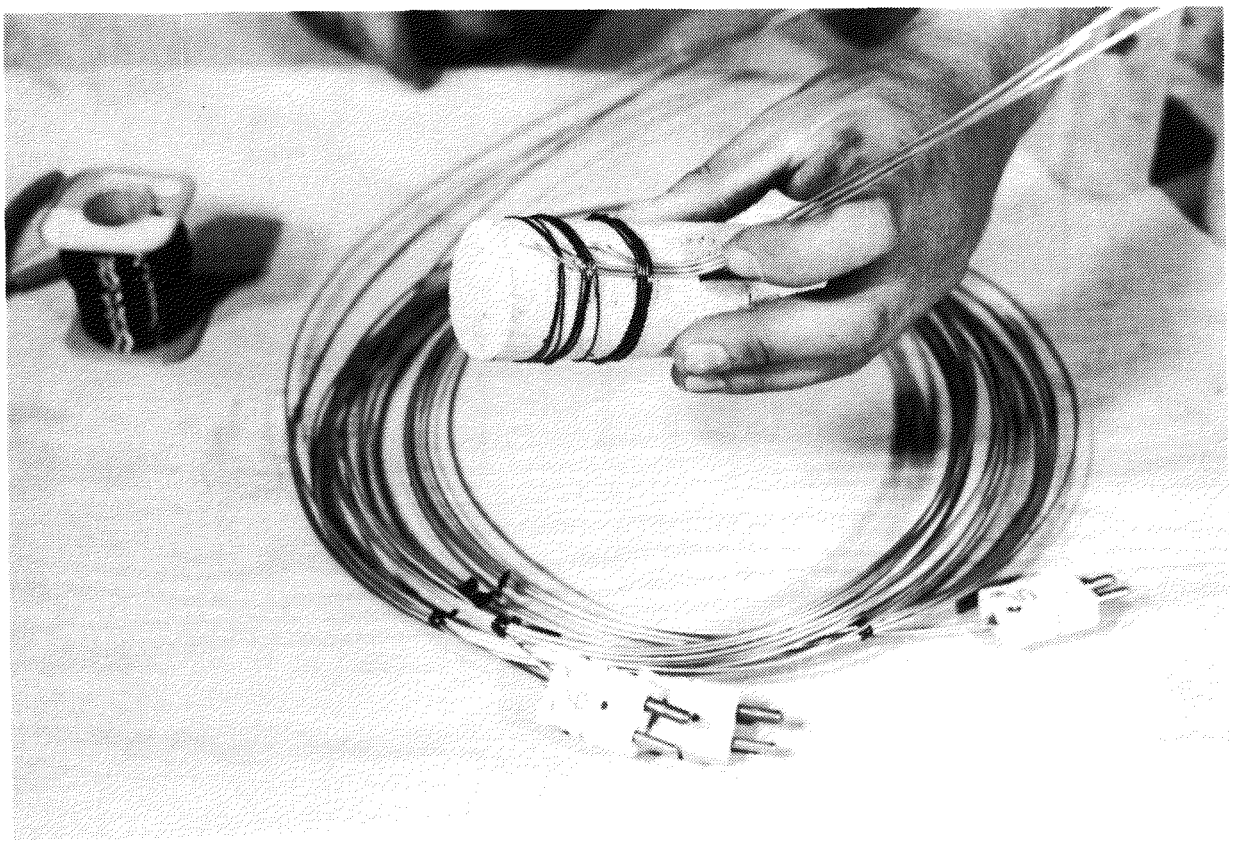

Figure B-12 - Final Assembly of Three Thermocouples Installed into a Pre-Cast Mgo Sidewall Cylinder

Figure B-13 - Final Assembly of Four Thermocouples Installed into a Pre-Cast MgO Sidewall Cylinder

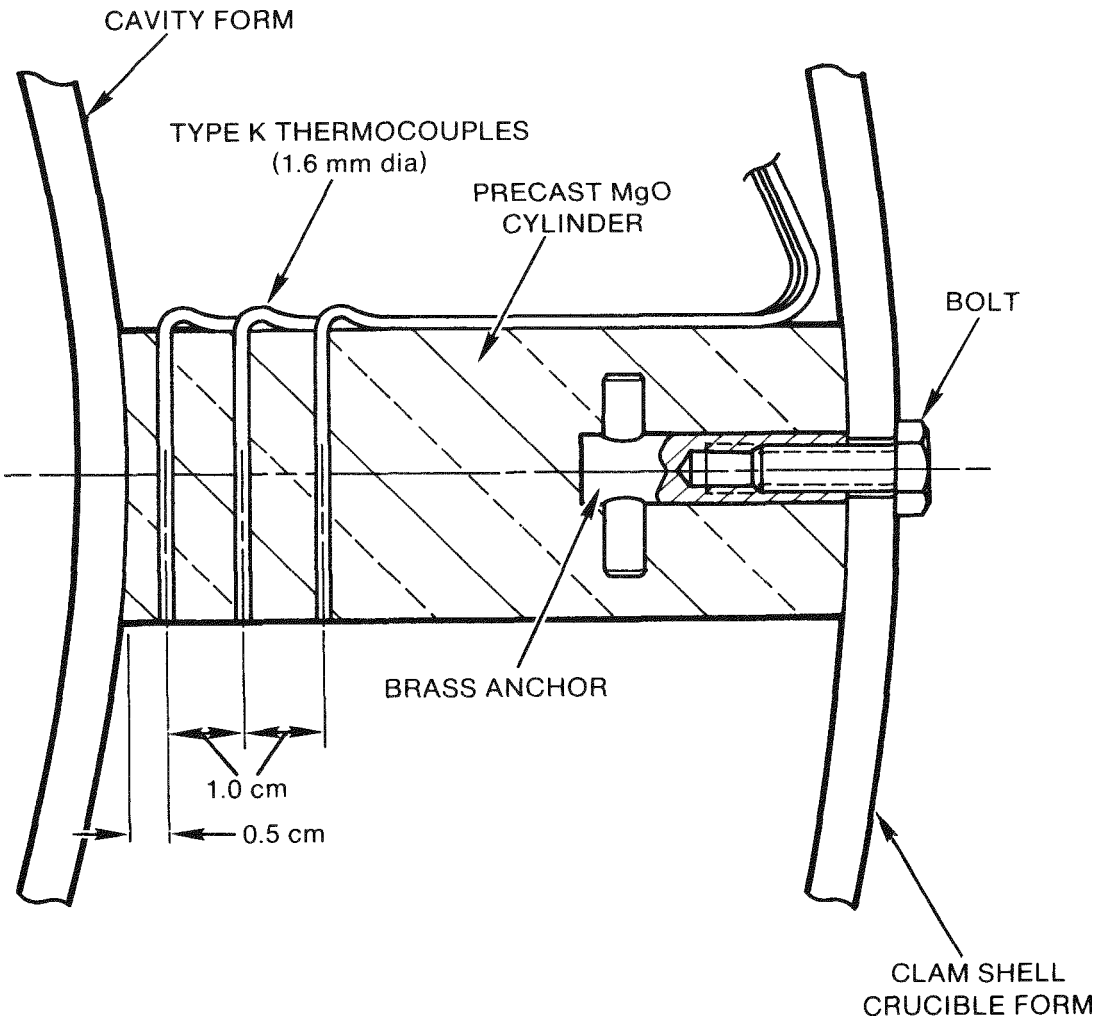

Figure B-14 - MgO Annulus Thermocouple Arrays, SURC-4

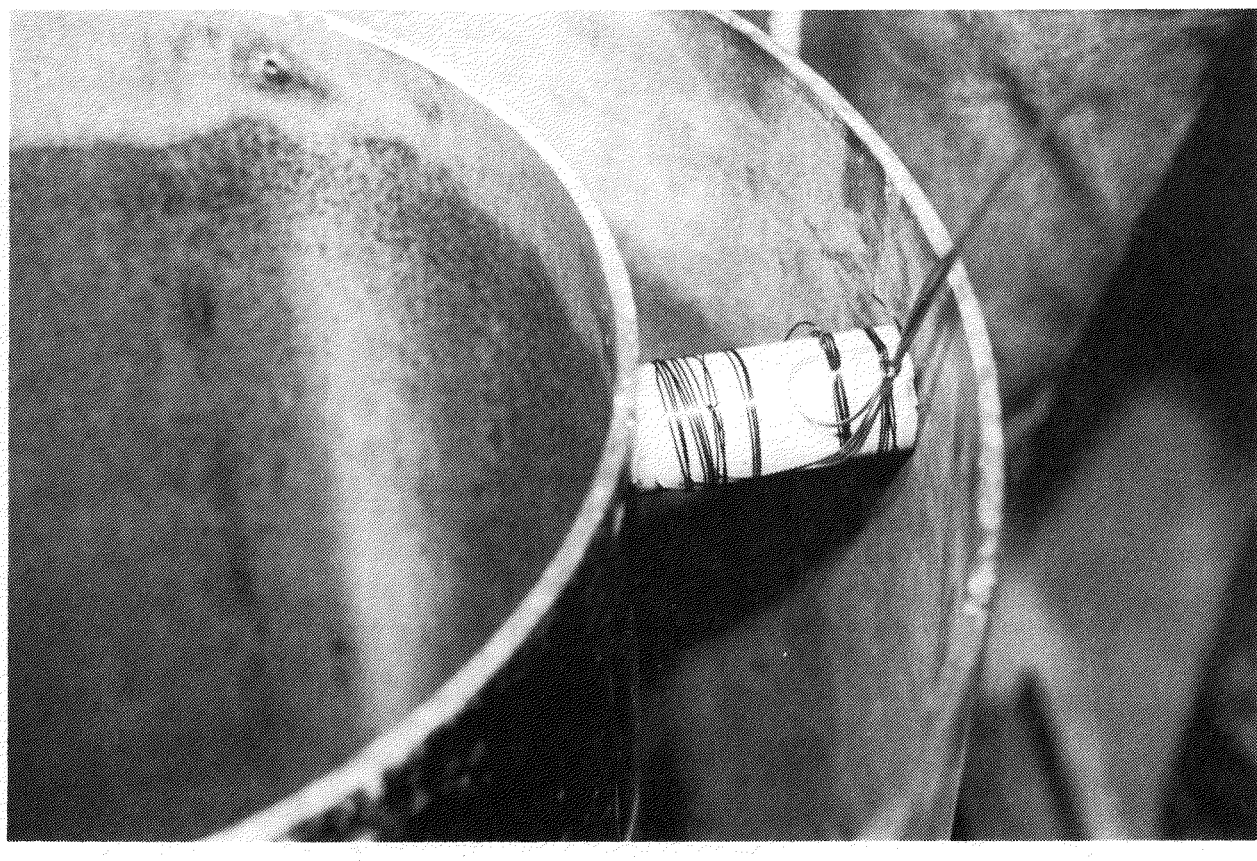

Figure B-15 - Typical Installation of MgO Sidewall Thermocouple Cylinder

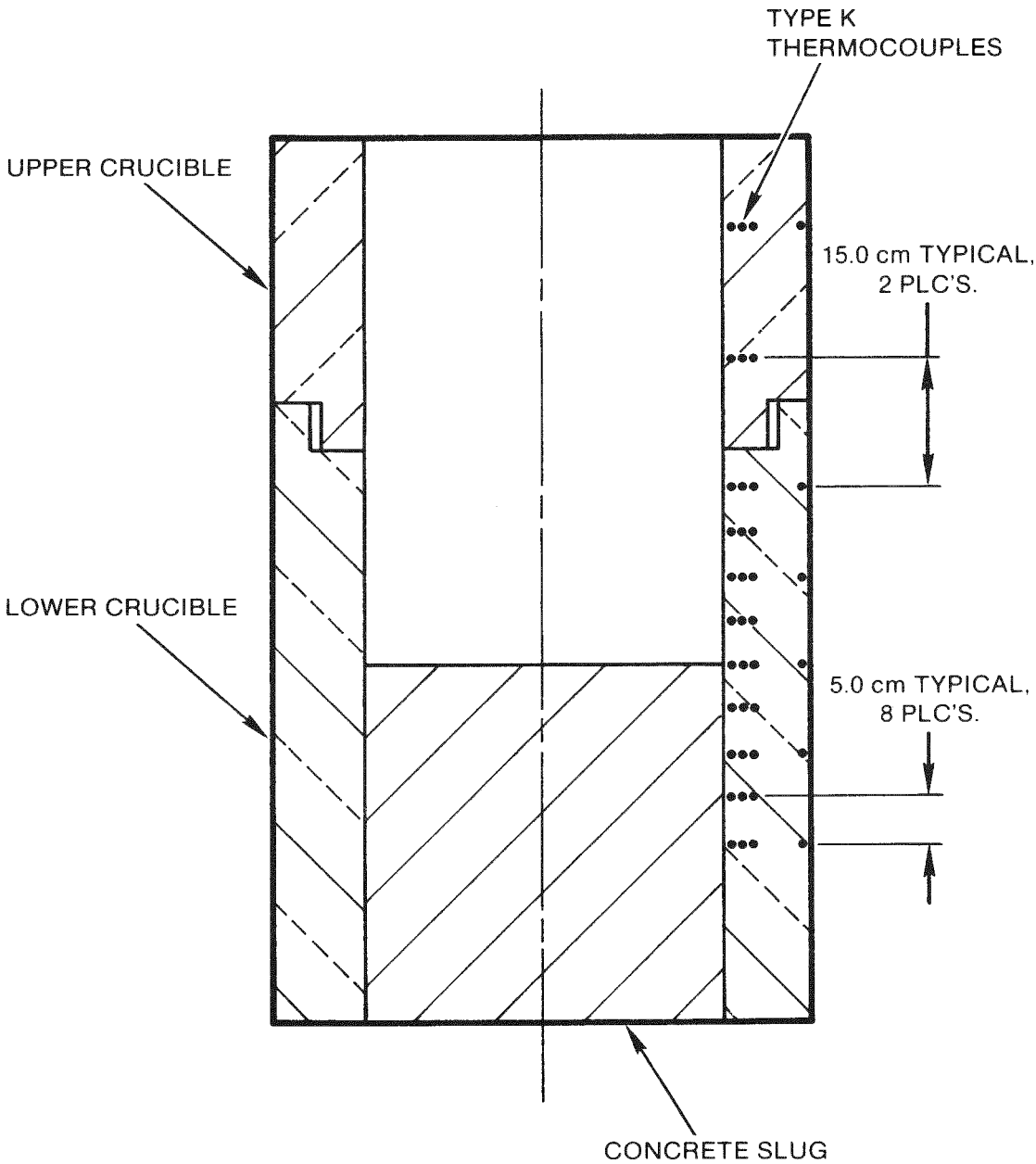

Figure B-16 - Relative Sidewall Thermocouple Locations, SURC-4

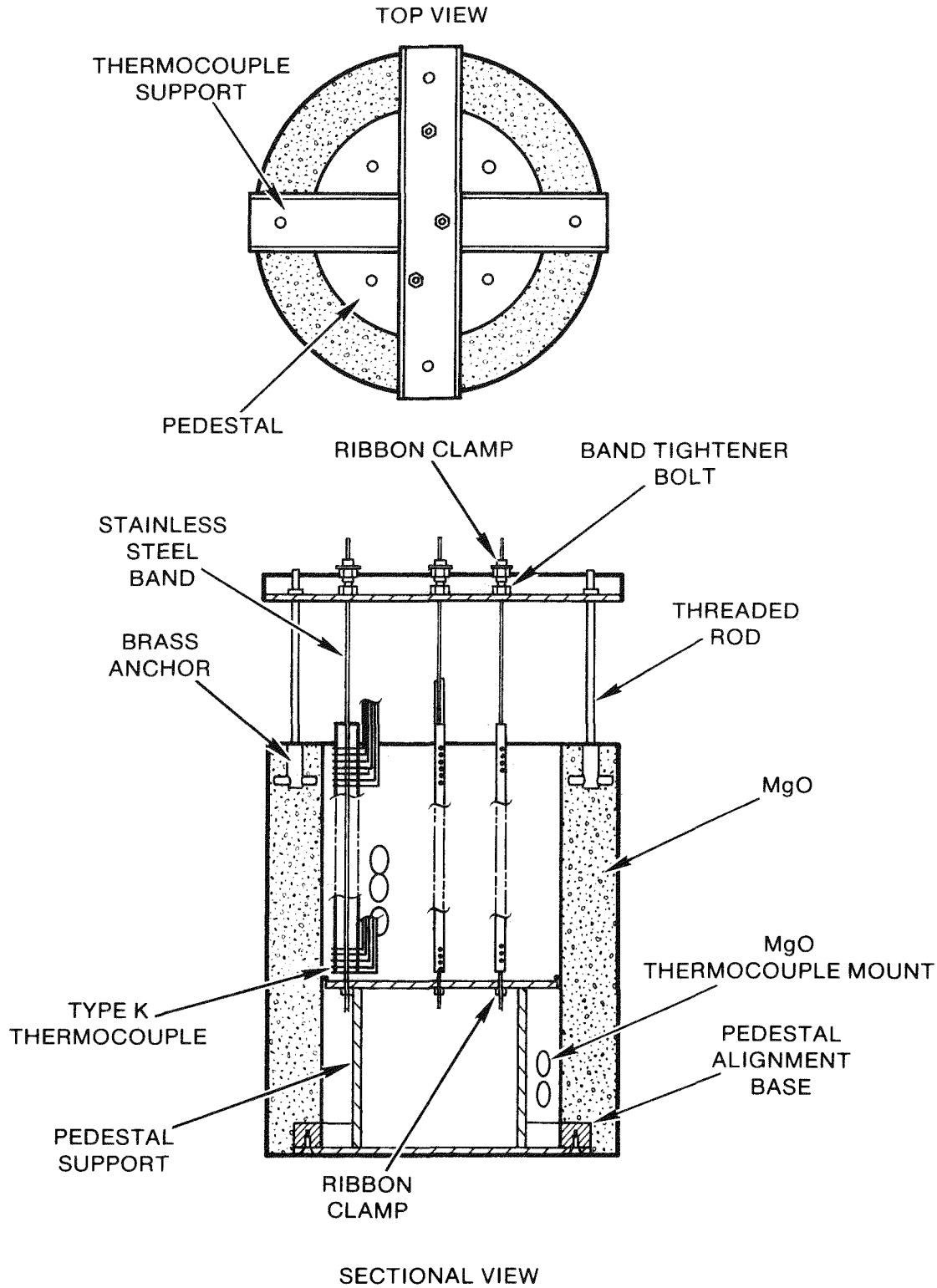

Figure B-17 - Thermocouple Casting Assermbly, Lower Crucible, SURC-4

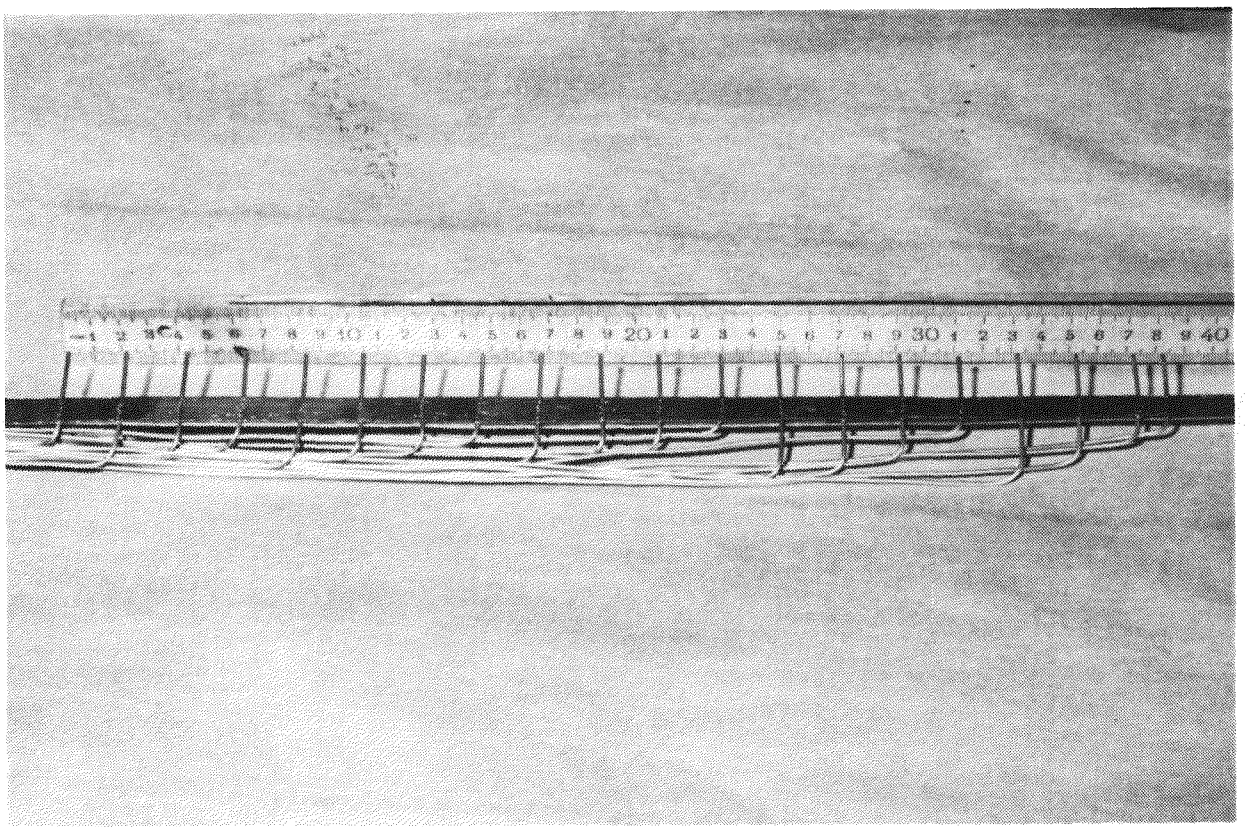

Figure B-18 - Typical Thermocouple Array Assembly
(Profile View) Cast into the Concrete Cylinder

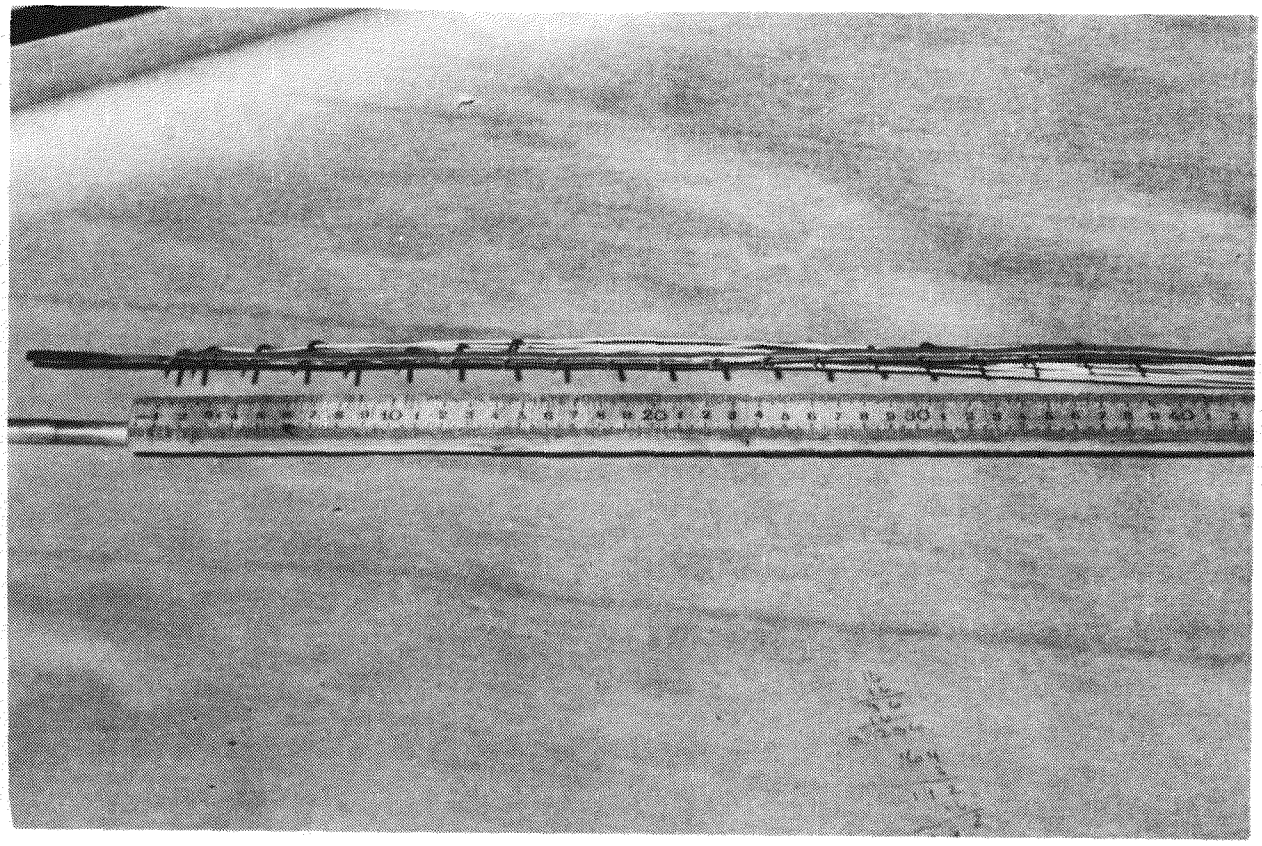

Figure B-19 - Typical Thermocouple Array Assembly
(Side View) Cast into the Concrete Cylinder

Figure B-20 - Installation of Thermocouple Arrays into the Pedestal Casting Base

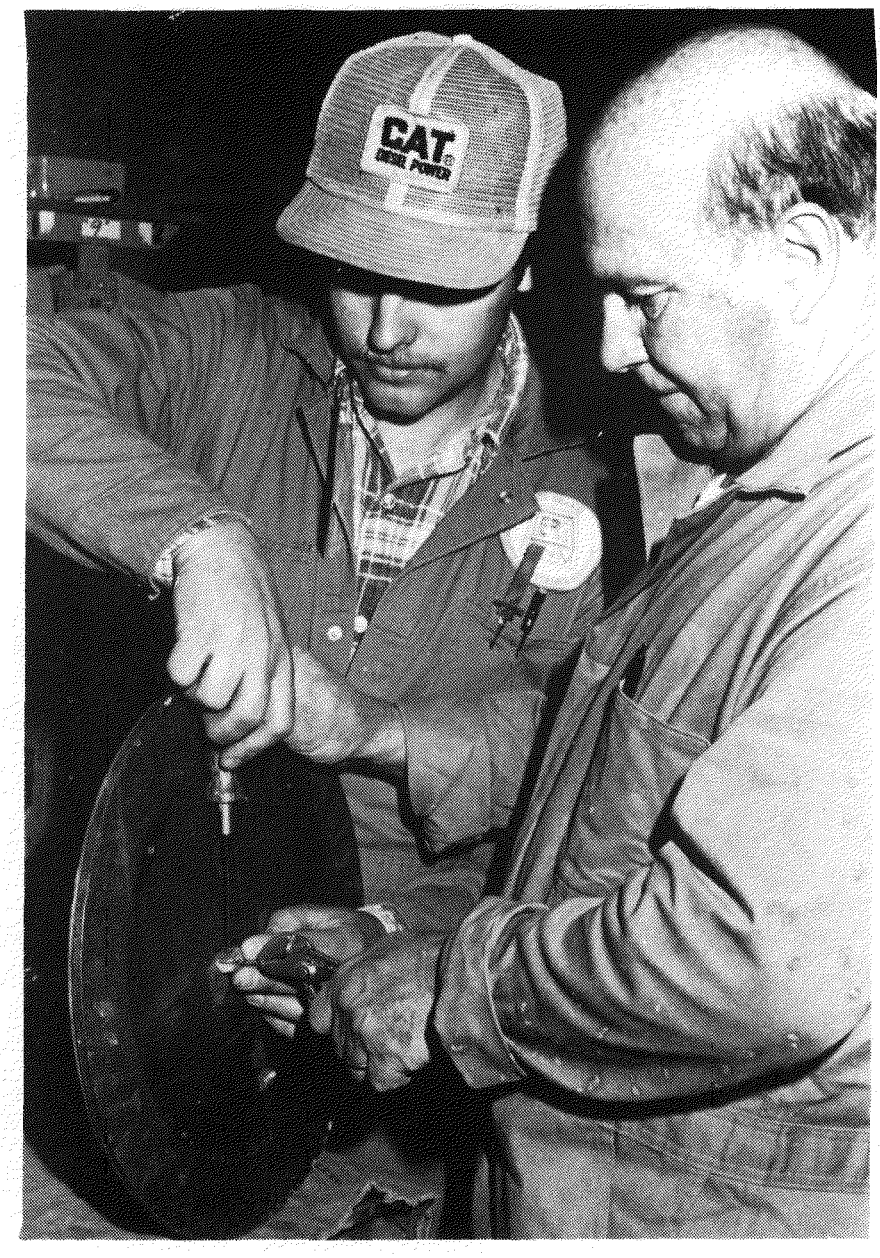

Figure B-21 - Securing the Stainless Steel Bands Supporting the Thermocouple Arrays to the Pedestal Casting Base

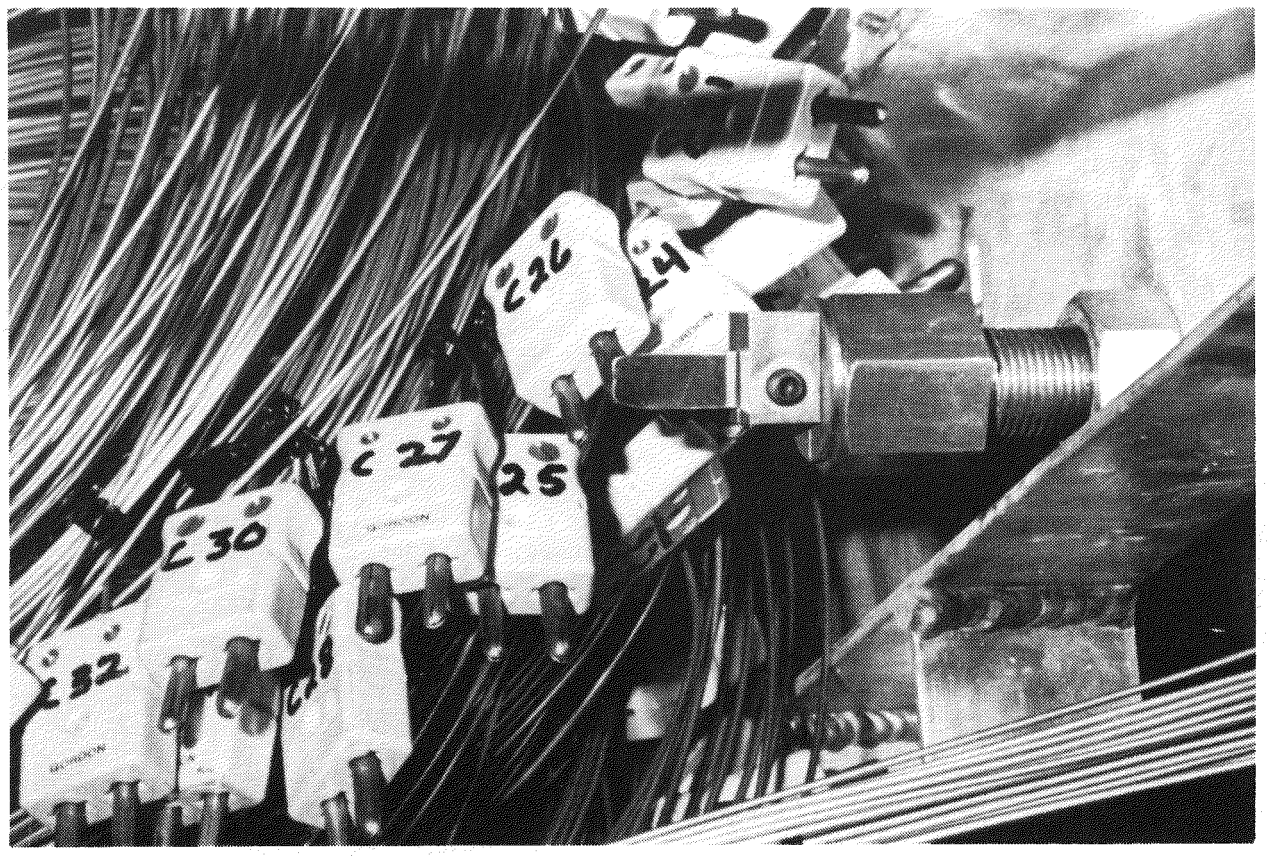

Figure B-22 - Stainless Steel Band Clamping Assembly, Thermocouple Support

Figure B-23 - Final Adjustment of the Thermocouple Arrays Welded to the Stainless Steel Bands

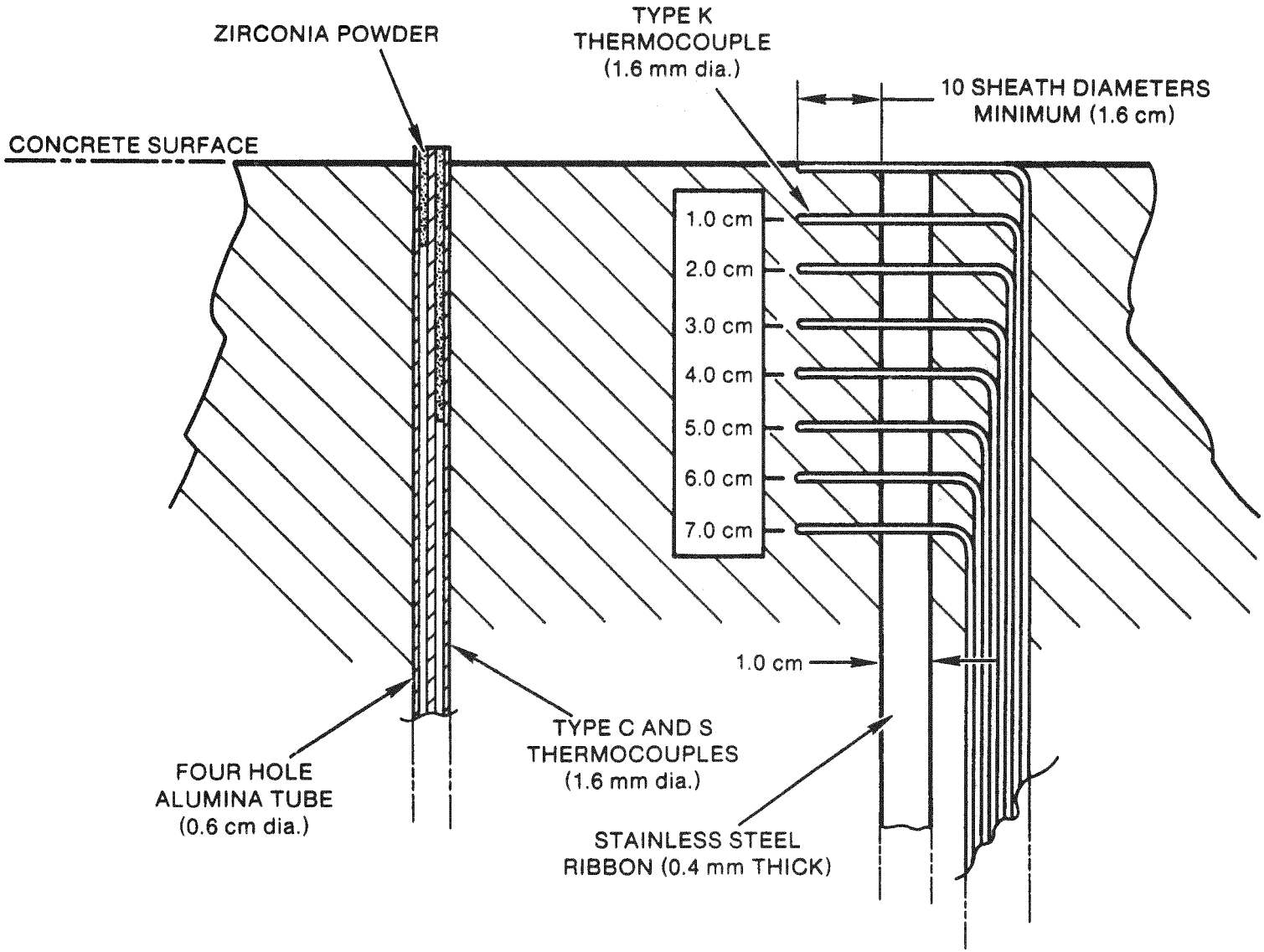

Figure B-24 - Typical Concrete Thermocouple Array, SURC-4

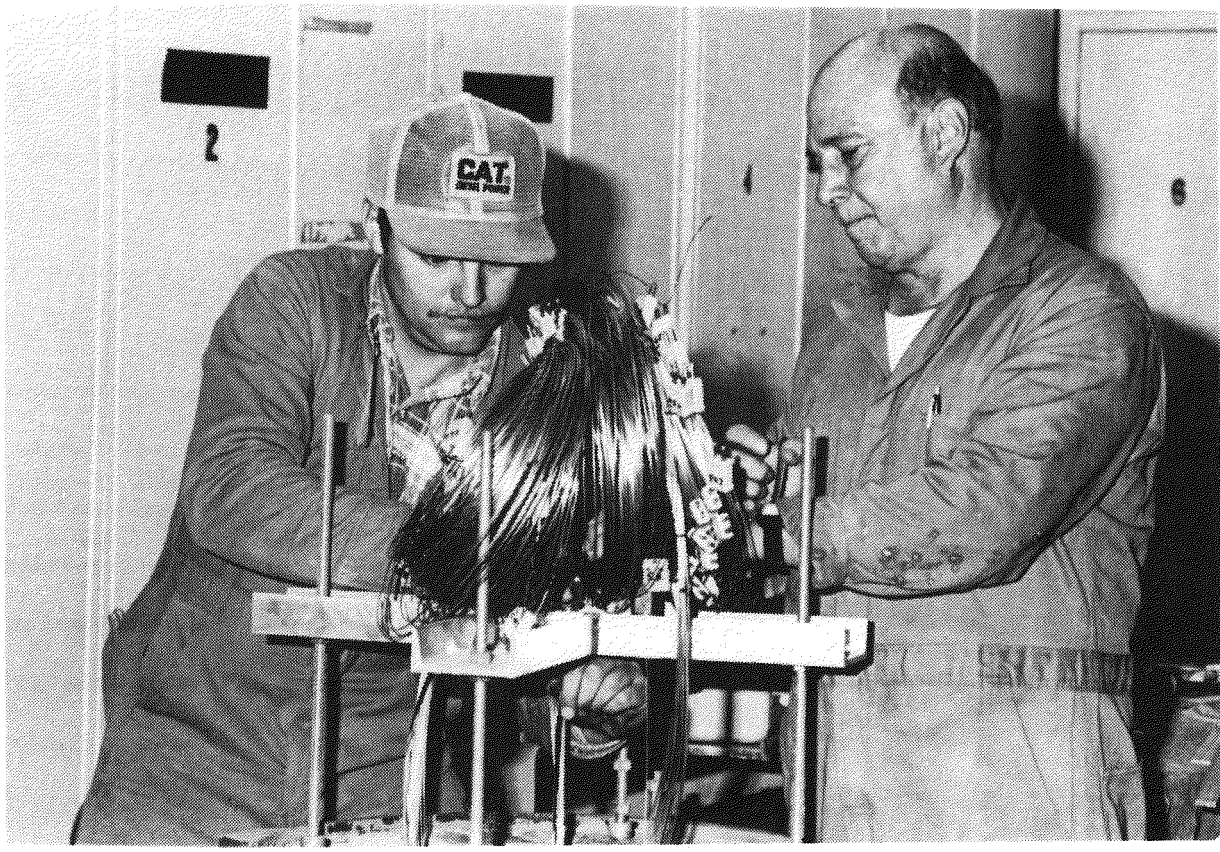

Figure B-25 - Installation of Four Hole Alumina Tubes for Installation of Type S and Type C Thermocouples

Figure B-26 - Alumina Tubes being Installed and Secured to "Y" Bracket Prior to Casting the Concrete Cylinder

castable. The geometry of this form is similar to the lower casting form except that it is 35.0 cm high. The casting forms, sidewall thermocouple forms, and brass anchors are installed as previously described. All thermocouple terminations were routed exiting the side of the crucible form near the top, surface. A steel ring having dimensions 59.4 cm outside diameter, 50.8 cm inside diameter and 5.1 cm thick was bolted to the casting base adjacent to the outer clam shell form. This provided an annular step for assembling and sealing the upper and lower crucible sections. Brass anchors were cast into the top surface of the form for mounting the crucible cover. The anchors attached to the side of the clam shell were used to assemble the upper and lower crucible sections. Figures B-32 through B-34 show different stages of assembly and casting the lower crucible form. Releasing agent was sprayed on all steel surfaces in contact with the casting material for ease of disassembly. The castable was mixed, placed, cured and the forms were removed following procedures previously described. Figures B-35 and B-36 show the cast and baked upper crucible section ready for assembly and test.

Crucible Cover

The casting assembly for the crucible cover is shown in Figure B-37. The cover was cast entirely of MgO castable. The steel clam shell form has dimensions of 61.0 cm outside diameter, 60.0 cm inside diameter, and 10.2 cm high. The cover was cast on a 1.3 cm thick casting base like the other forms. Void forms fabricated from mild steel and sprayed with releasing agent, were bolted to the center of the casting base to provide penetrations for the exhaust gas and aerosol flow tube. Brass anchors were cast into the side of the cover to facilitate lifting and assembly. Four (4), 6.5 cm inside diameter, copper tubes 10.2 cm long were cast into the cover to provide holes for bolting the cover to the top crucible form. Releasing agent spray was used as necessary to coat steel areas in contact with the castable for easy disassembly. Two type K thermocouple arrays were cast into the cover to measure upward heat flux. These type K thermocouples were installed in pre-cast MgO cylinders as described earlier. The procedures for mixing, installing, vibrating, and curing the MgO castable were performed as previously described. The cast and baked crucible cover is shown in Figure B-38, ready for assembly and test.

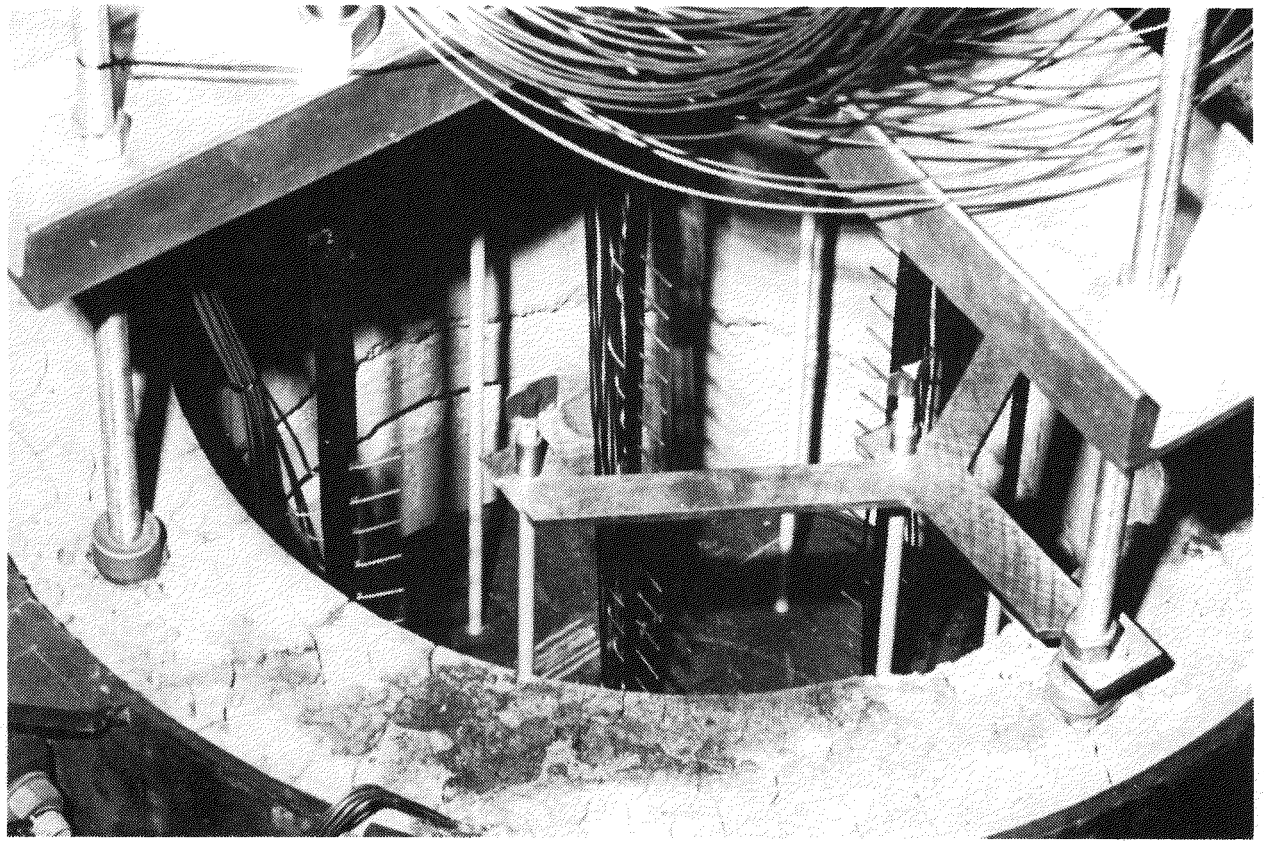

Figure B-27 - Final Installation of Array Thermocouples and Alumina Tubes Prior to Casting the Concrete Cylinder

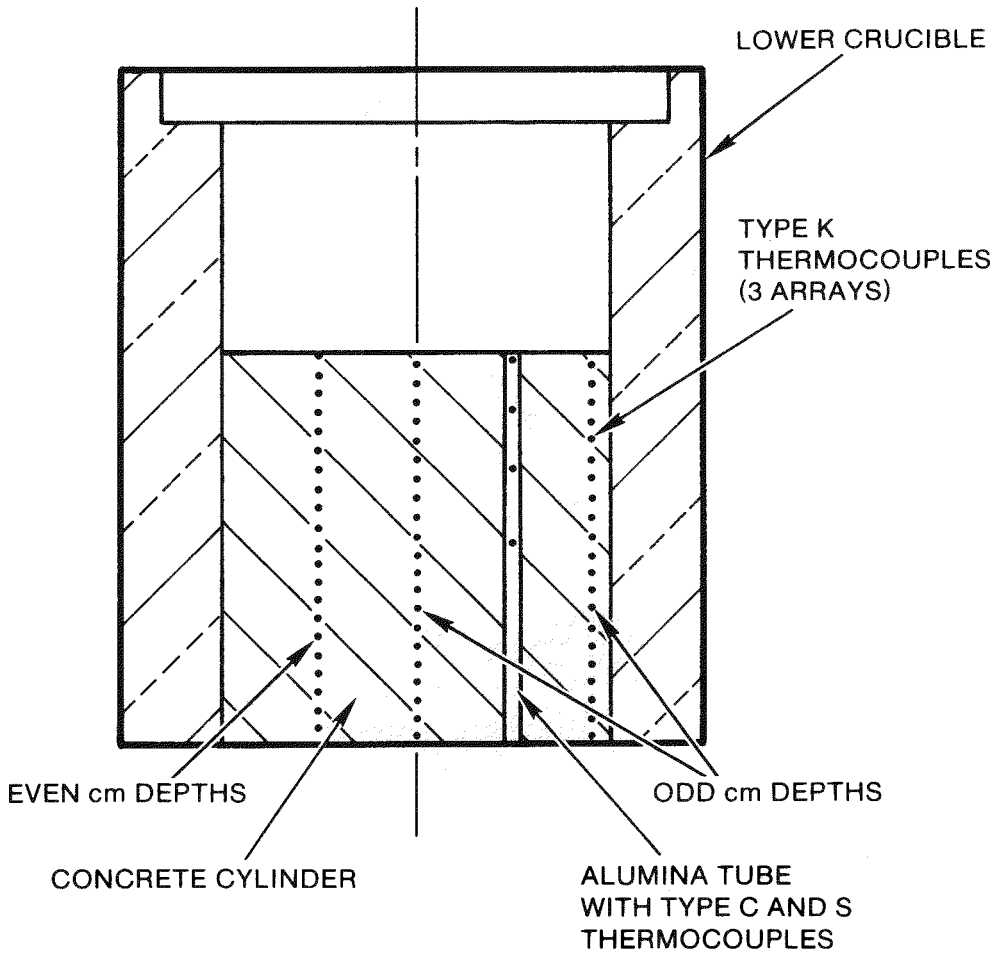

Figure B-28 - Relative Thermocouple Locations in the Concrete Cylinder, SURC-4

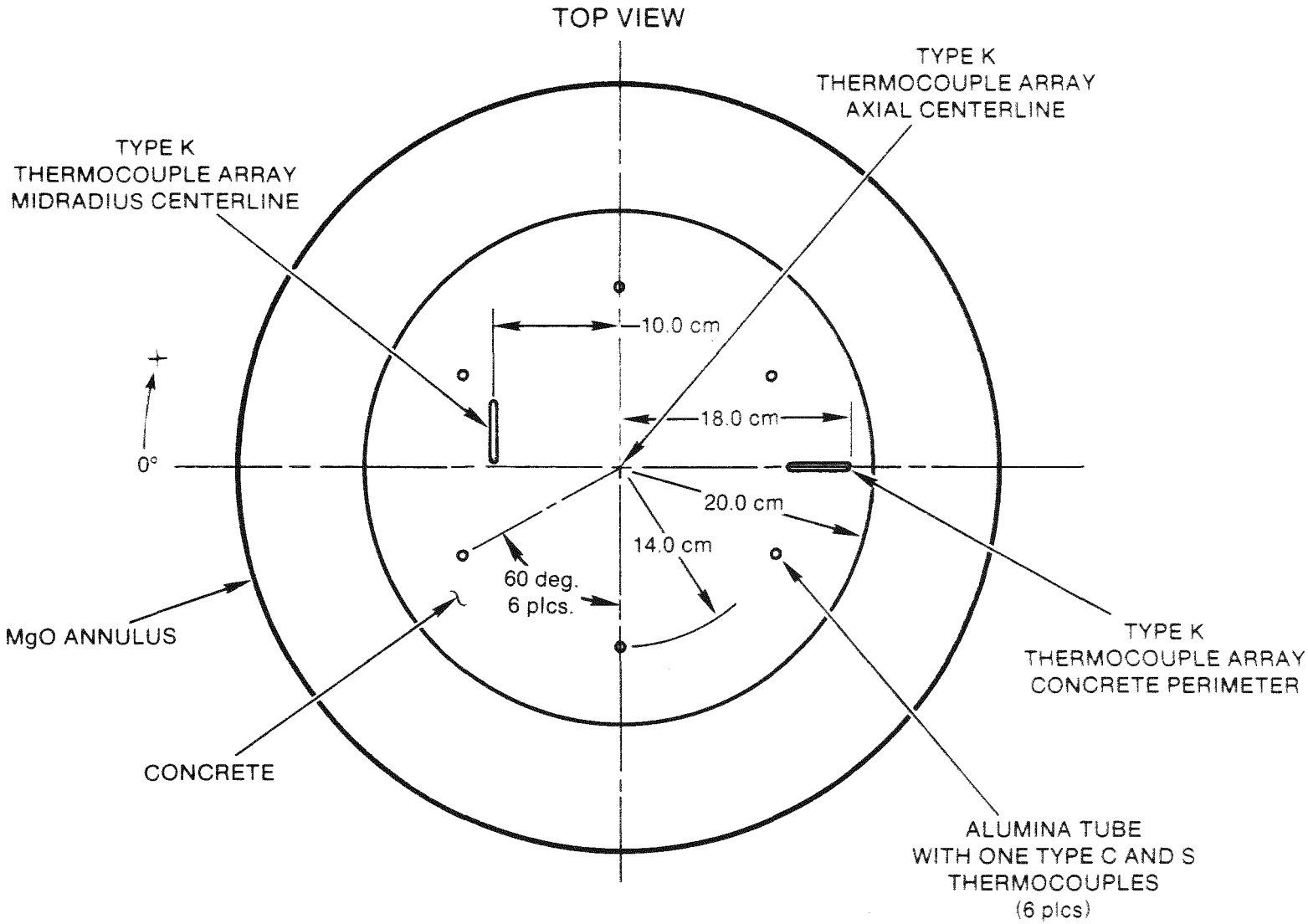

Figure B-29 - Thermocouple Orientation, Concrete Cylinder, SURC-4

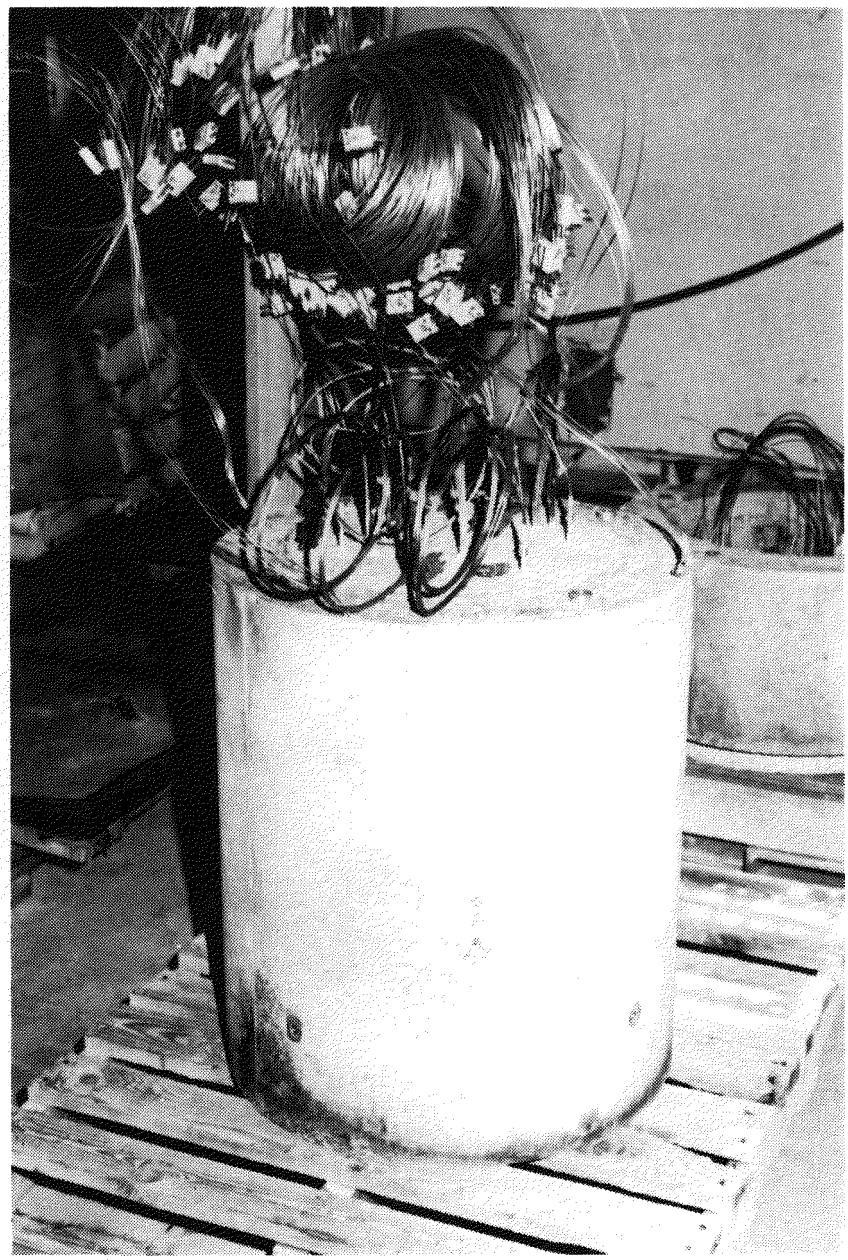

Figure B-30 - Final Assembly of the Lower Crucible

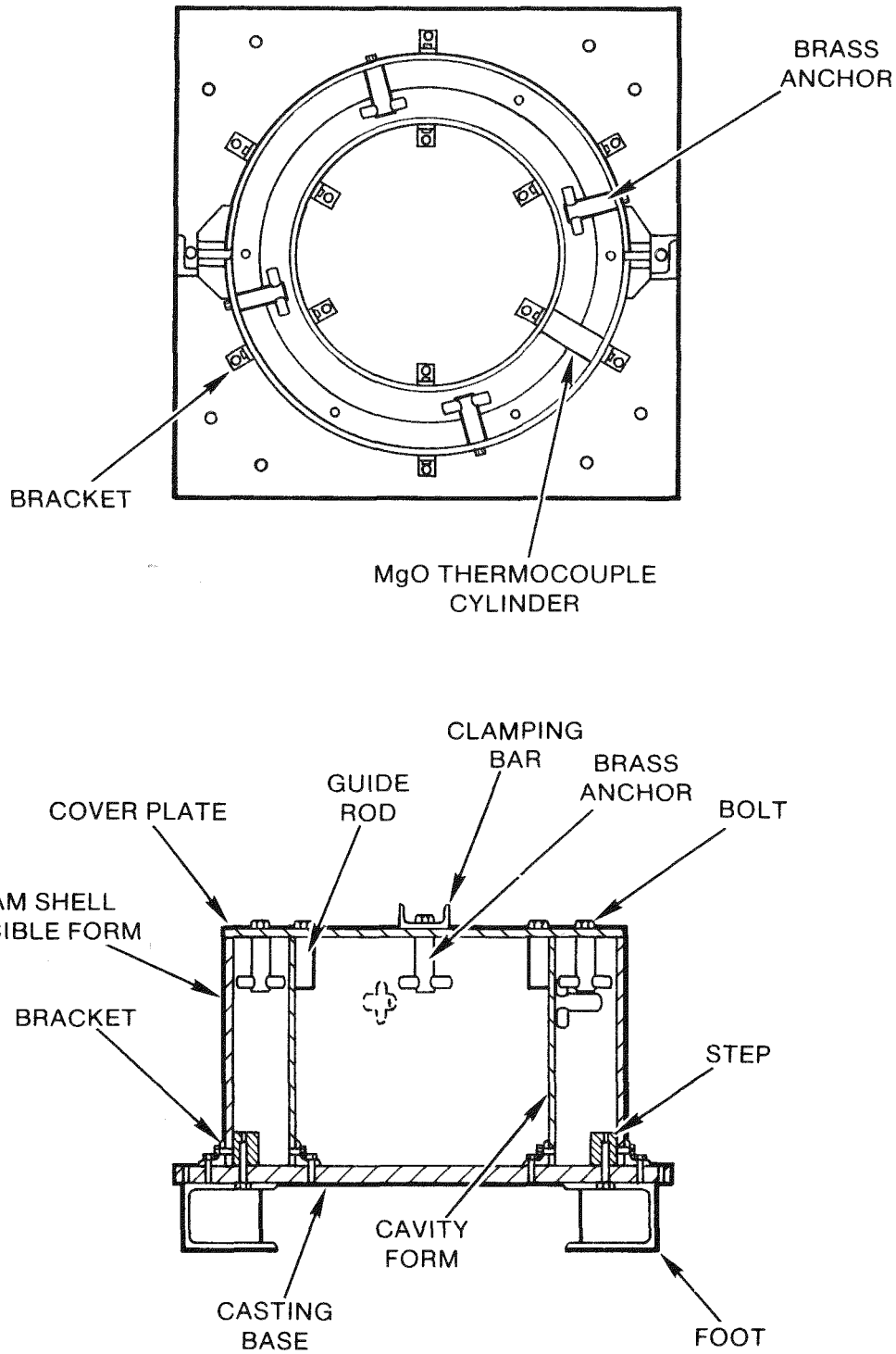

Figure B-31 - Casting Form, Upper Crucible, SURC-4

Figure B-32 - Steel Casting Form Components, Cover Plate Installation, Upper Crucible

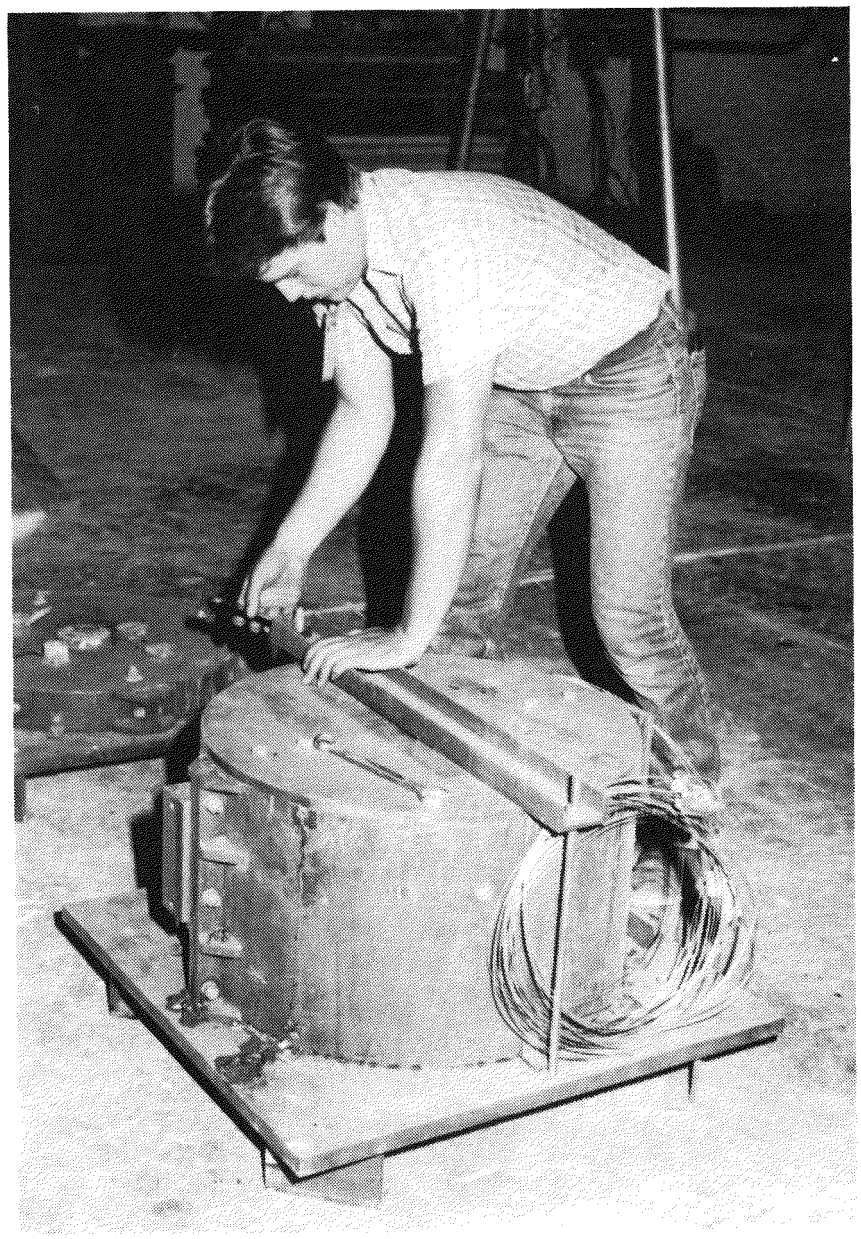

Figure B-33 - Steel Casting Form Assembly, MgO Annulus Bake Out, Upper Crucible

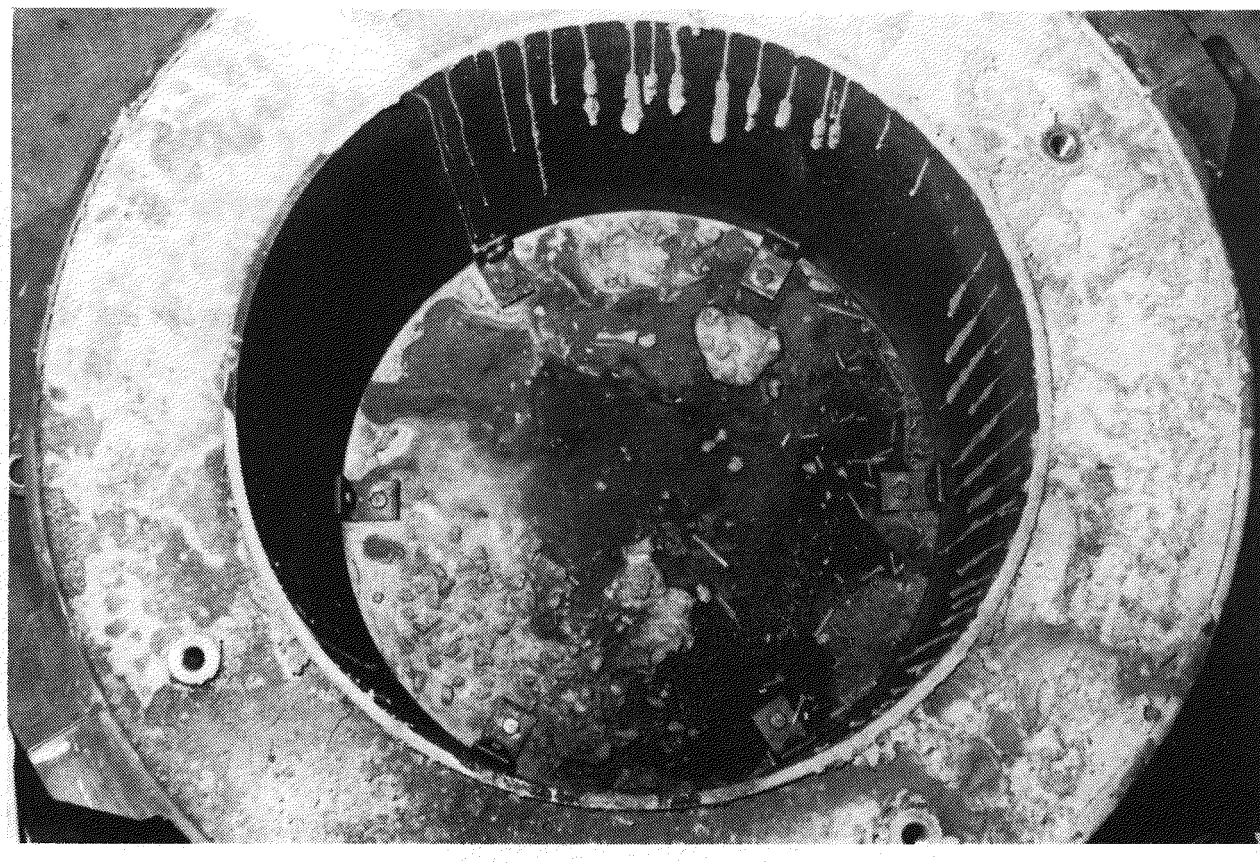

Figure B-34 - Top View, Post-Baked Assembly, Upper Crucible

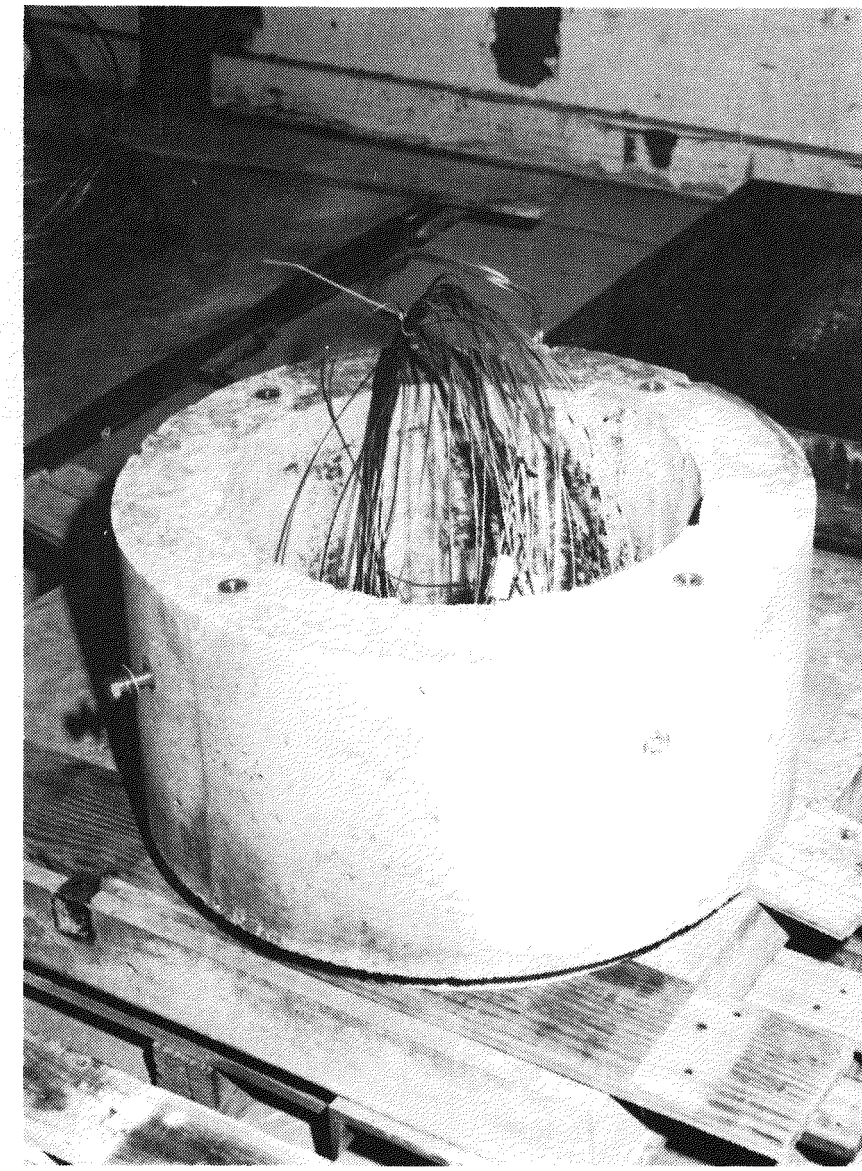

Figure B-35 - Final Baked Assembly of the Upper Crucible

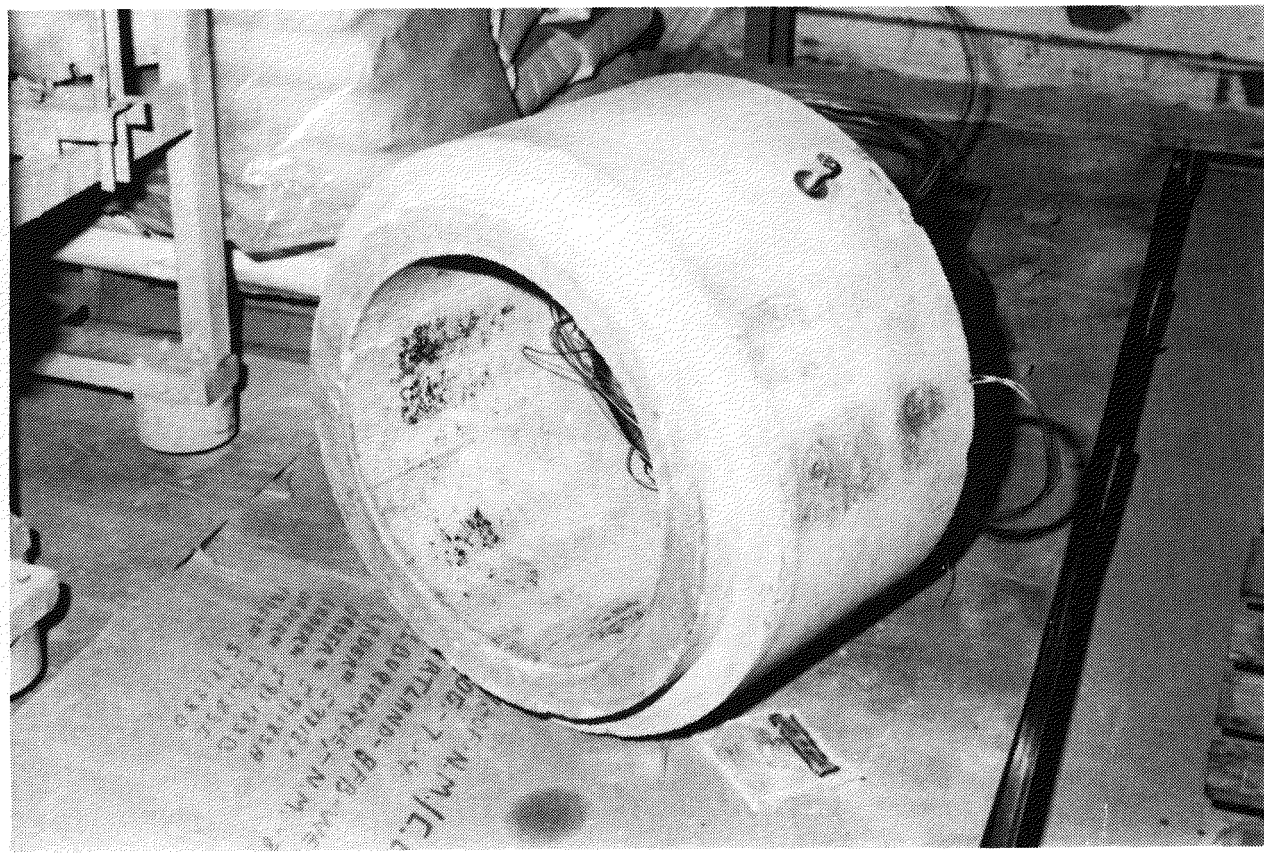

Figure B-36 - Final Assembly of the Upper Crucible Showing the Annular Step

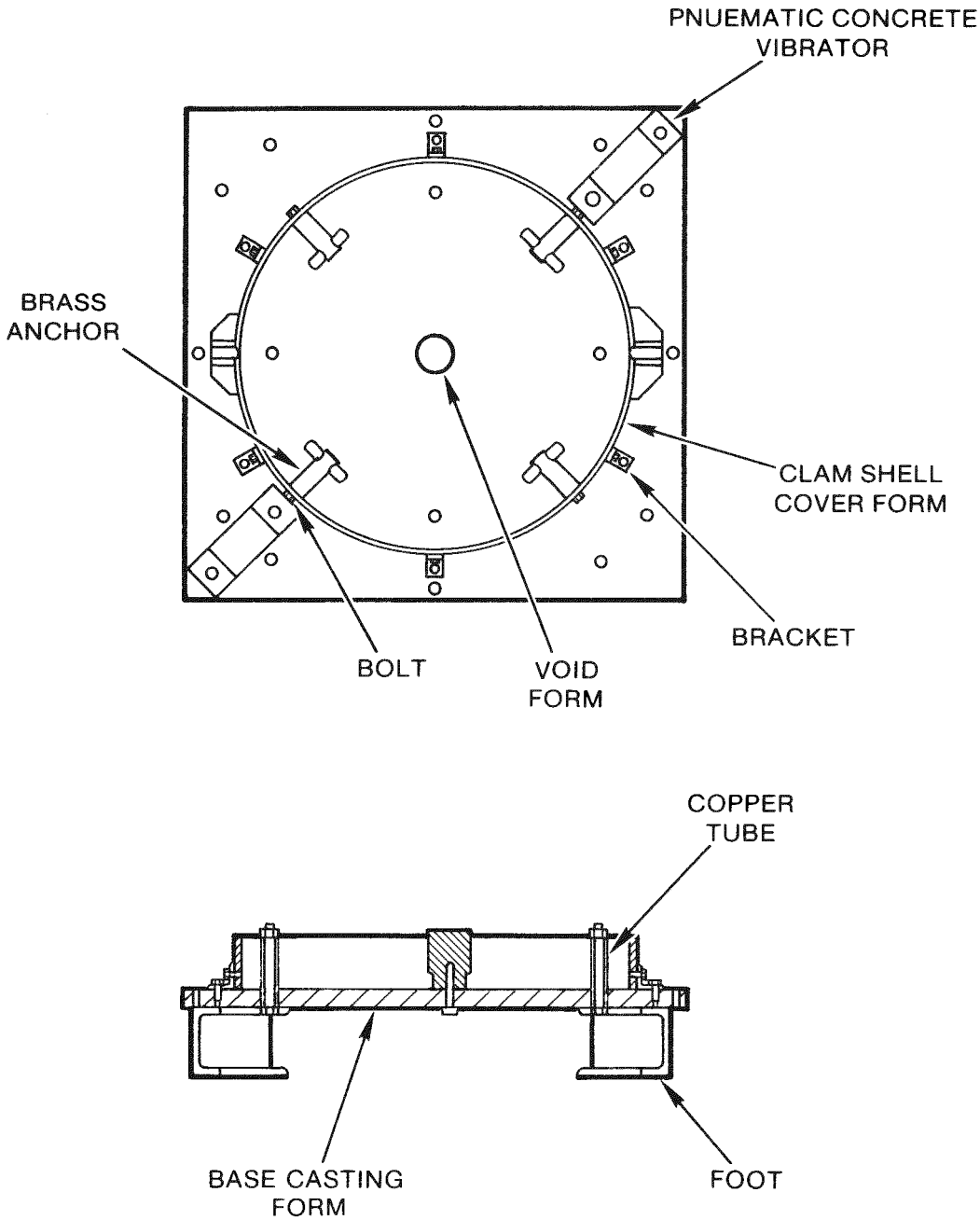

Figure B-37 - Casting Form, Crucible Cover, SURC-4

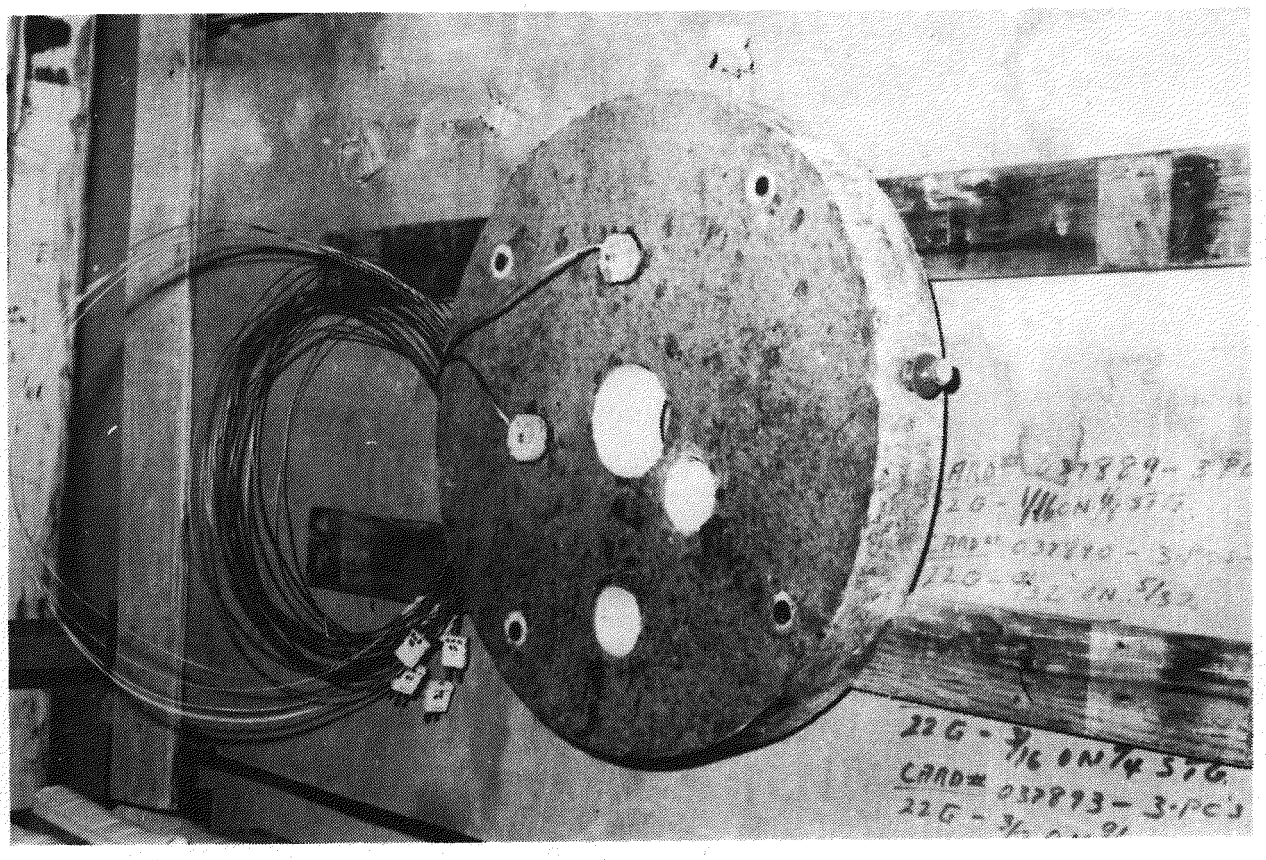

Figure B-38 - Final Baked Assembly of the Crucible Cover

APPENDIX C

Calorimetric Test Data and Equations

Experimental Apparatus

Data obtained in the calorimetric test of the induction power supply are shown in this appendix. Calorimetric tests were conducted to verify the calibration of the coil power transducer, on a well characterized stainless steel cylinder. A 200 kg cylinder of 304 stainless steel 35.6 cm in diameter and 25.4 cm high was used as the heat sink for the induction power. The cylinder was instrumented with type K thermocouples installed into the cylinder at radial distances of 0.0, 8.9 and 17.8 cm from the axis and approximately 6.2 cm deep. The outputs of the thermocouples were recorded on a data acquisition system. The instrumented cylinder was wrapped completely with a minimum of 2.5 cm thick Fiber Frax spun glass insulation. This was done to minimize any heat losses during the heating period. This assembly was placed into a crucible cast of MgO having the same radial dimensions as the test article used in the SURC 4 test. The induction coil was placed around the MgO crucible and vertically centered with respect to the stainless steel cylinder.

Energy Based on Calorimetry Calculations

Four calibration tests were performed at input powers of 100, 175, 250 and 280 kW, based on power meter readings on the control console of the power supply. The outputs of the power transducer connected to the buss bars and the thermocouple were connected to a Hewlett-Packard HP-1000 data acquisition system for collection and posttest plotting and analysis.

The calorimeter test was initiated by starting the data acquisition system, establishing baseline data for the power transducer, and stainless cylinder temperature. After taking approximately 4 minutes of baseline data, the induction power supply was started and a constant input power was applied to the stainless steel cylinder. For the initial test the input power was 100 kW. The power supply was turned off when the thermocouple closest to the perimeter (radius = 17.8 cm) reached 1473 K. The cylinder heating profile for the various thermocouple locations is shown in Figure C-2. The cylinder does not heat uniformly. The perimeter heats more rapidly than the center. The output from the power transducer is shown in Figure C-1.

The stainless steel cyliner was allowed to come into thermal equilibrium. This occurred 91.3 minutes after the power supply was started and the equilibrium temperature was measured to be 1283 K. The amount of energy deposited into the stainless steel cylinder for the heating period is given by:

$$E_S = m\ C_p\ (T_{eq} - T_I) \qquad (C\text{-}1)$$

where

E_s = energy deposited (MJ),

m = mass of stainless steel cylinder (kg),

C_p = specific heat of stainless (J/kg·K),

T_{eq} = equilibrium temperature of cylinder (K),

T_I = initial temperature of the cylinder (K).

Thermal properties for 304 stainless steel are listed in Table C-2. The value of the specific heat was selected using the mean temperature ($(T_{eq} - T_I)/2$) of the stainless steel cylinder during the heatup phase. The value selected was 581.9 J/kg K. The initial temperature T_I was measured to be 384 K. Substituting into equation C-1 and solving yields a value of 104.6 MJ of energy deposited into the stainless steel.

For the calorimetric test to be accurate, thermal heat losses, even though small, had to be accounted for. Figure C-1 also shows the cooling history of the stainless cylinder. The thermal energy lost during the 91.3 minute period required for the cylinder to reach thermal equilibrium is characterized by the slope of the temperature versus time curve after the point the equilibrium temperature was reached. The energy lost during this period is approximated by:

$$E_t = 1/2 \left[m\ C_p\ (\Delta T/\Delta t)\ t_{eq} \right] \qquad \text{(C-2)}$$

where

E_t = cylinder thermal losses (J),
ΔT = temperature difference (K),
Δt = time difference (s), and
t_{eq} = time to reach thermal equilibrium (s).

The mass (m) of the stainless cylinder and the specific heat (C_p) were defined in equation C-1. The slope of the cooling profile at the equilibrium temperature was measured to be 2.15 K/min. The time (t_{eq}) for the cylinder to reach an equilibrium temperature from the start of the power supply was measured to be 91.3 minutes. Substituting the appropriate values into equation C-2, and solving results in a total energy loss of 12.6 MJ over the period considered. Based on these calculations the total energy input to the stainless steel cylinder was equal to the energy deposited E_S = 104.6 MJ (Eqn. A-1) plus the energy lost E_t = 12.6 MJ, (Eqn. C-2) or 117.2 MJ. The deposited energy calculated from calorimetry will be used as the standard for comparison with the energy measured by the power transducer.

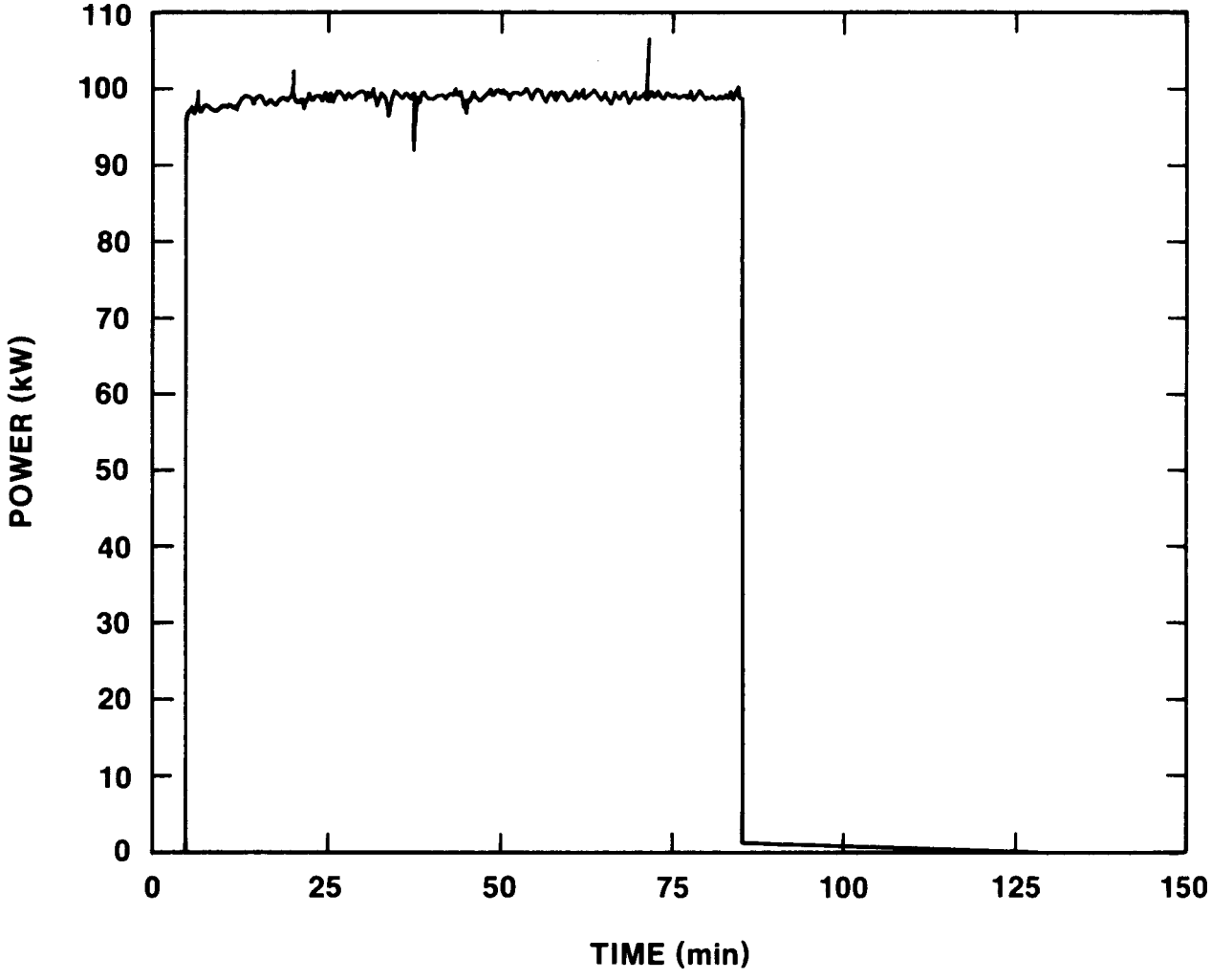

Figure C-1 - Plot of Effective Power vs. Time, 100 kW Calorimetric Test.

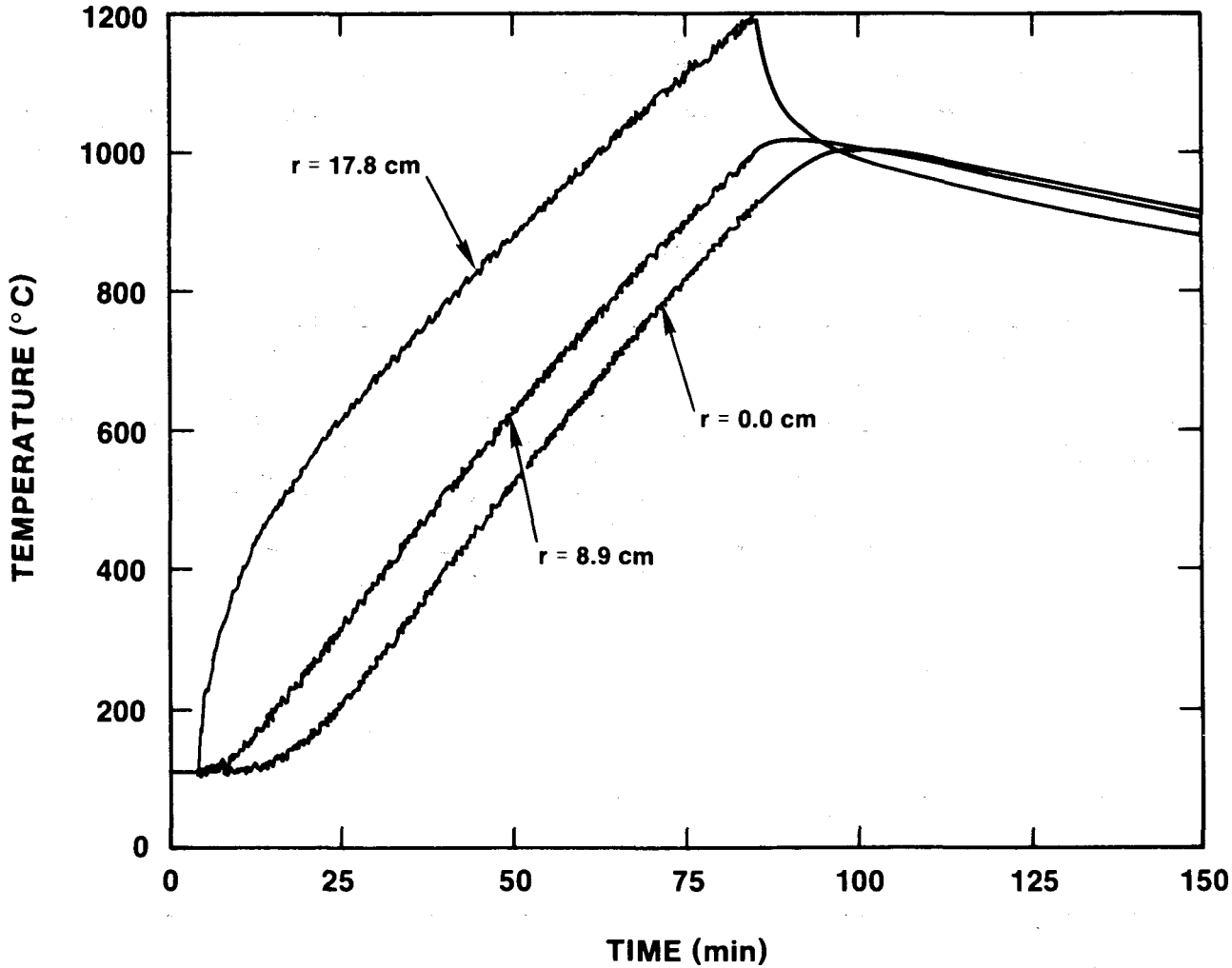

Figure C-2 - Thermocouple Response vs. Time, Stainless Steel Cylinder, 100 Calorimetric Test.

Table C-1

Specific Heat[1] for 304L Stainless Steel

Temperature (K)	Specific Heat (J/kg K)
300	510.0
400	523.4
500	536.8
600	550.2
700	564.0
800	577.4
900	590.8
1000	604.2
1100	617.6
1200	631.4
1300	644.8
1400	658.1
1500	671.5
1600	685.3
1700(s)	698.7
1700(l)to 3000	795.0

(1) Choong, S. Kim, Thermophysical Properties of Stainless Steels, Argon National Laboratory, Argon, IL 60439, Report ANL-75-55, September 1975.

Energy Measured by the Power Transducer

The total energy measured at the buss bars by the power transducer is found by integrating the power curve shown in Figure C-2 and is mathematically represented by the equation shown below.

$$E_b = \int_{t_1}^{t_2} P \, dt \qquad \text{(C-3)}$$

where

E_b = energy measured at the buss bars,

$\int_{t_1}^{t_2} P \, dt$ = Area under the power versus time curve between the limits of t_1 and t_2 (J) (See Figure C-2).

The total energy at the buss bars was calculated to be 479.9 MJ.

The coupling efficiency of the system is defined by

$$\text{Efficiency} = E_s/E_b \times 100 \qquad \text{(C-4)}$$

where

Efficiency = coupling efficiency (%)
E_s = Energy deposited into the stainless steel cylinder (MJ), and
E_b = Energy measured by the power transducer (MJ)

Substituting into equation (C-4), for the 100 kW test the coupling efficiency is found to be 24.4.

Temperature profiles for the stainless steel cyliner and corresponding input power profiles for the 175, 250 and 280 kW calorimetry test are shown in Figures C-3 through C-8. Based on these results, the coupling efficiency for the 175, 250, and 280 kW power levels were calculated. The calculated coupling efficiency for the 100, 175, 250, and 280 kW tests are presented in Table C-2. The efficiencies range between 22.9 and 24.4 for input powers between 97.8 and 285.9 kW. The net power delivered to the stainless cylinder is taken to be the input power measured at the buss bars times the efficiency derived from the calorimetric tests.

Table C-2

System Coupling Efficiency

Method 1

Input Power Console Power Meter	Energy Measured at Buss Bars (MJ)	Energy Deposited in Stainless Cylinder (MJ)	Coupling Efficiency (%)
97.5	479.9	117.2	24.4
175.0	374.8	86.0	22.9
253.5	339.4	78.6	23.2
285.9	288.6	67.9	23.5

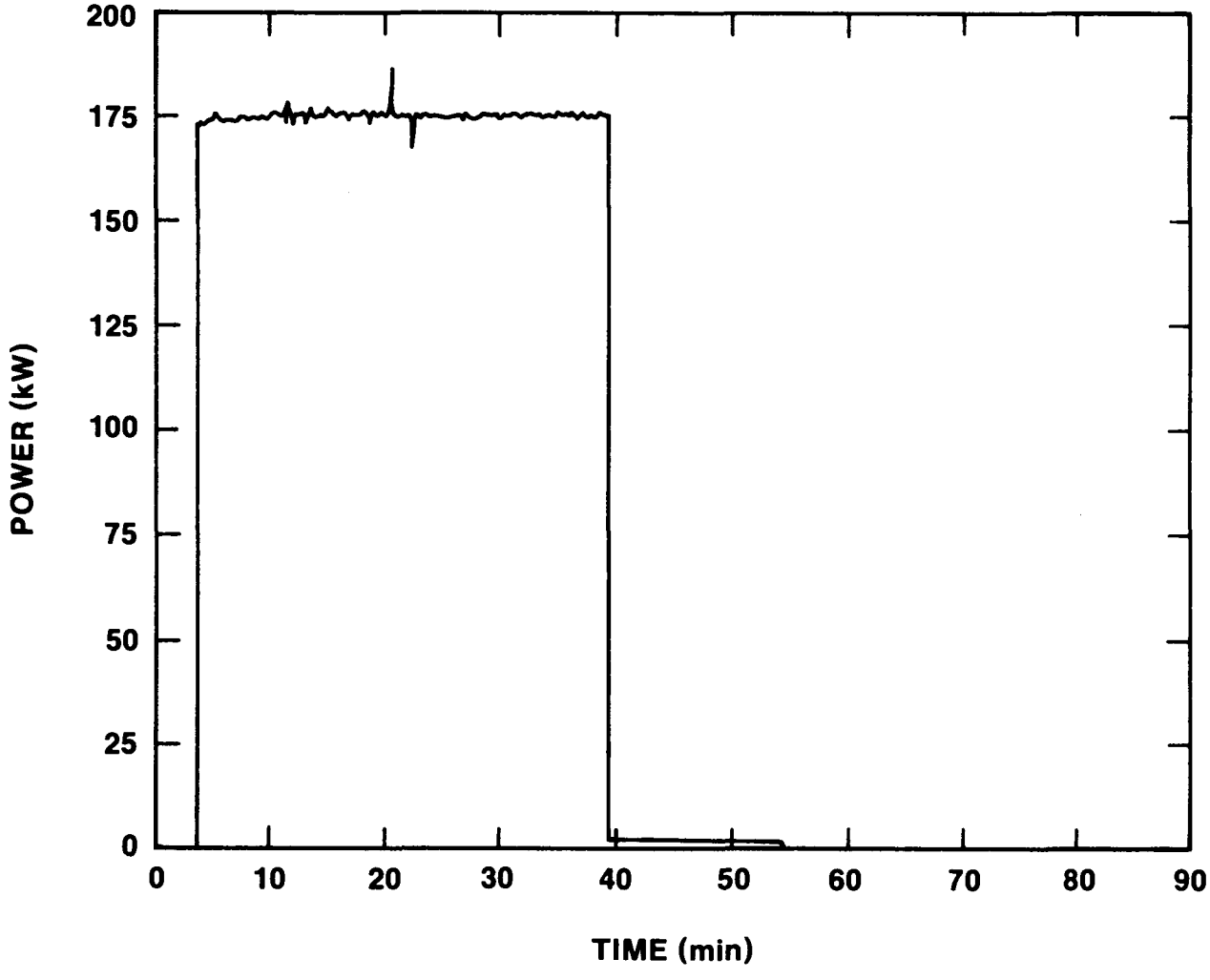

Figure C-3 - Plot of Effective Power vs. Time, 175 Kw Calorimetric Test.

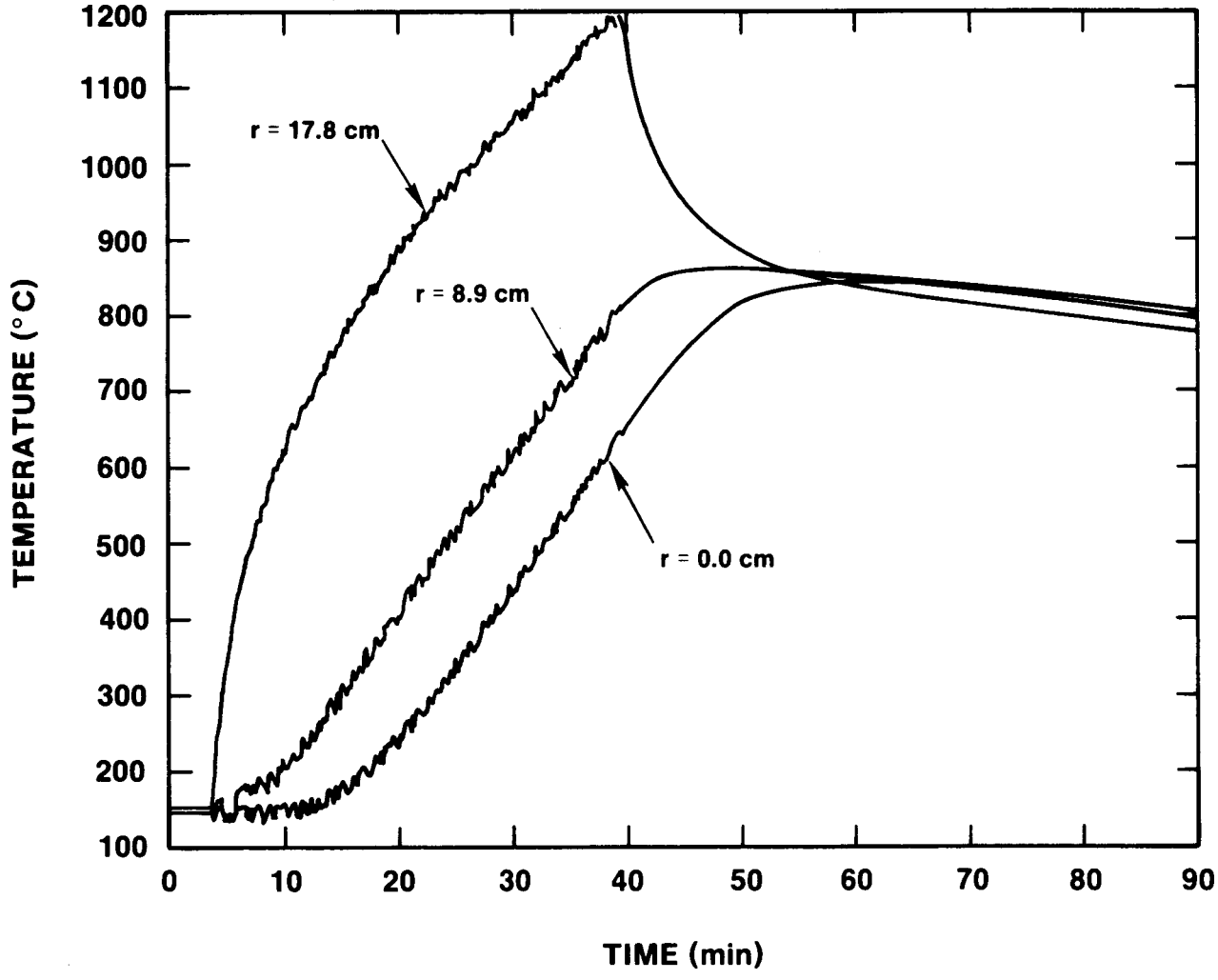

Figure C-4 - Thermocouple Response vs Time Stainless Steel Cylinder, 175 kw Calorimetric Test.

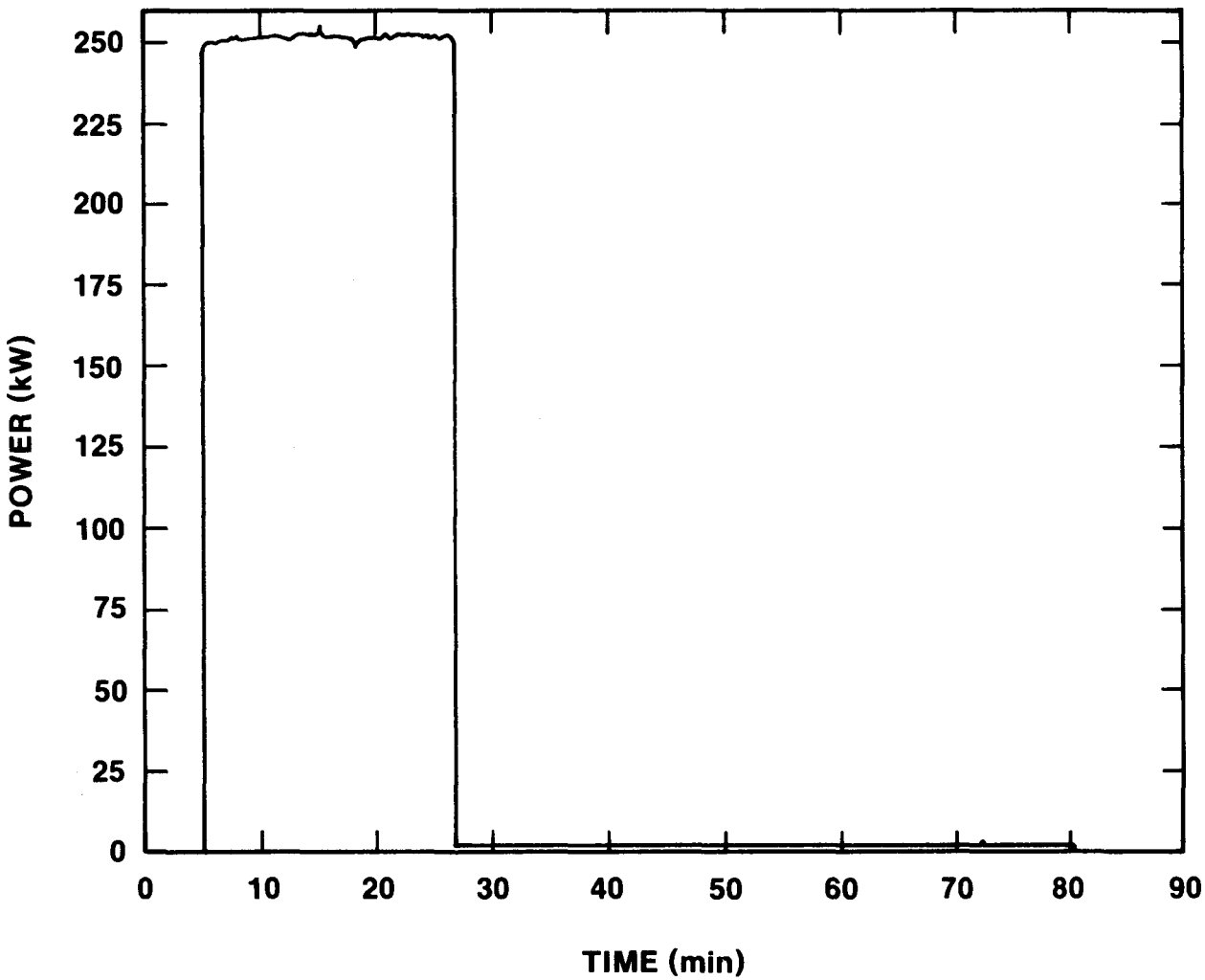

Figure C-5 - Plot of Effective Power vs. Time 250 KW Calorimetric Test.

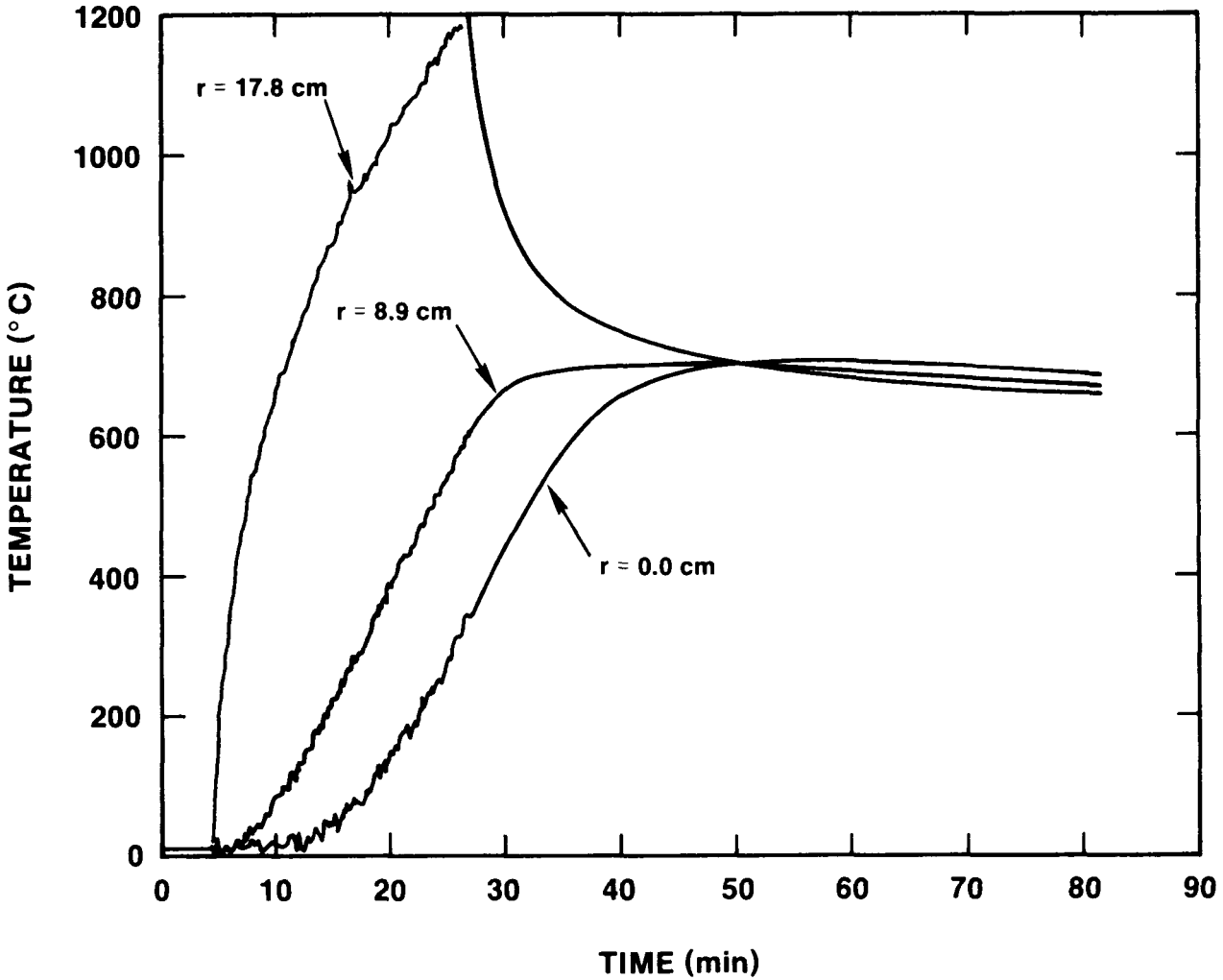

Figure C-6 - Thermocouple Response vs Time Stainless Steel Cylinder, 250 kw Calorimetric Test.

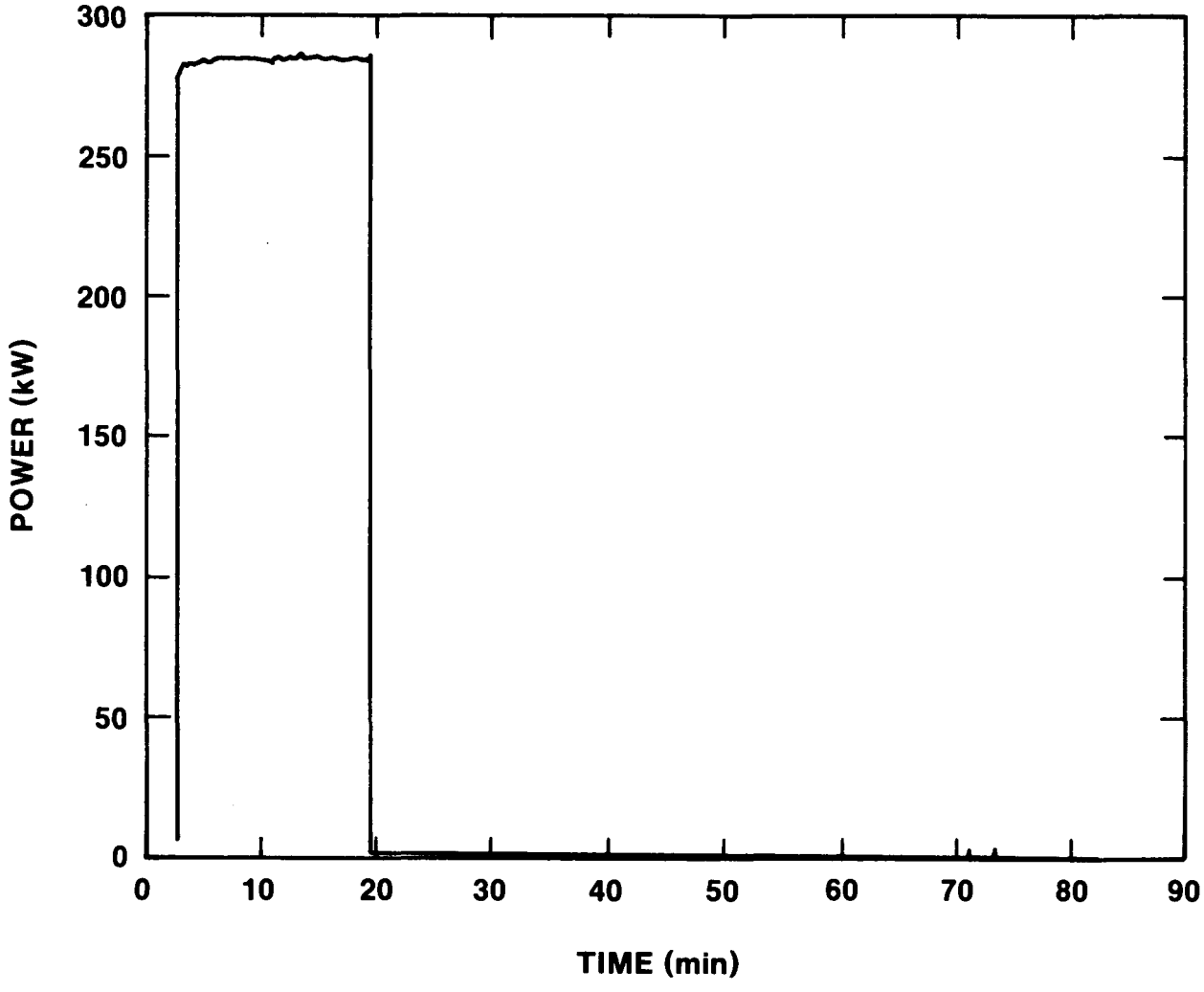

Figure C-7 - Plot of Effective Power vs. Time 280 Kw Calorimetric Test.

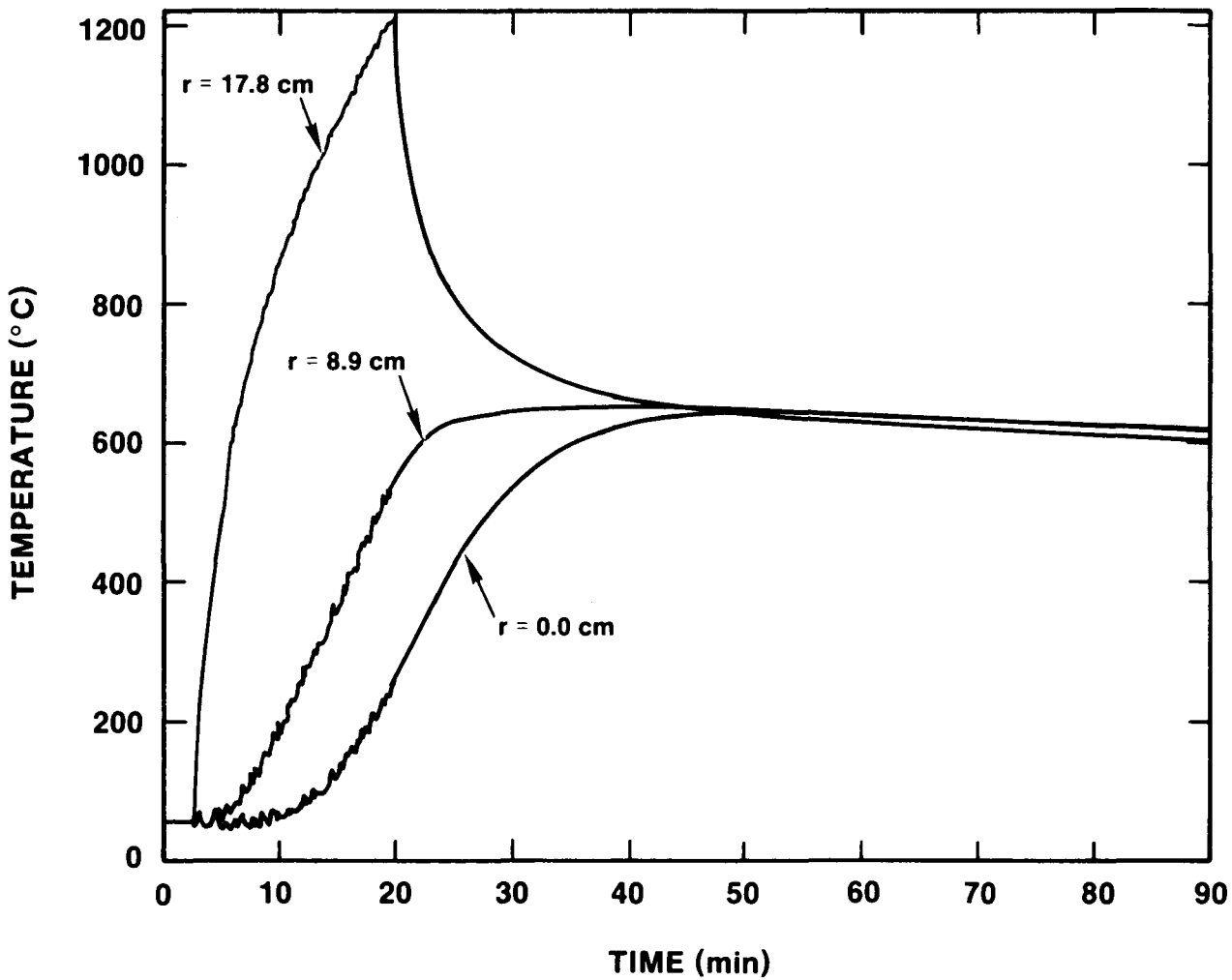

Figure C-8 - Thermocouple Response vs Time Stainless Steel Cylinder, 280 Kw Calorimetric Test.

An alternate approach to the calculation of net power to the slug and coupling efficiency is to consider that the thermal response of the three thermocouples embedded in the slug can be used to characterize the rates of energy addition and loss for three segments of the slug. The center thermocouple is assumed to represent the interior segment from radius r =0.0 to 4.45 cm; the thermocouple at 8.9 cm is assumed to represent the middle segment from r = 4.45 to 13.34 cm; and the thermocouple at 17.8 cm is assumed to represent the outer segment from r = 13.34 to 17.78 cm. The masses of the three segments of the slug are 12.5, 100.0 and 87.5 kg, respectively.

The rate of energy addition to each segment is determined from the slope of the thermocouple plots (see Figs. C-1, C-3, C-5, and C-7) during the last 10 to 15 minutes of the heating period. The energy addition rate is calculated by

$$P_{add} = \sum_{i=1,3} m_i \, c_{pi} \, (\Delta T/\Delta t)_i \qquad \text{(C-5)}$$

Where m_i is the mass of segment i, c_{pi} is the average specific heat of segment i during the time period, and $(\Delta T/\Delta t)_i$ are the slopes taken from the temperature plots.

Similarly, the rate of energy loss can be calculated from the slopes of the temperature plots during the cooldown phase. Once the steel slug has reached thermal equilibrium, each segment of the slug cools at approximately the same rate. It is this rate that is used in the loss calculation. Here,

$$P_{loss} = m \, c_p \, (\Delta T/\Delta t) \qquad \text{(C-6)}$$

where m is the total mass of the slug, c_p is the specific heat evaluated at the equilibrium temperature, and $\Delta T/\Delta t$ is the slope taken from the thermocouple plot.

The total power input to the slug is the sum of P_{add} and P_{loss}. Comparing the total power input calculated in this maner to the power measured at the buss bar gives the efficiency of inductive coupling. The results calculated for the 100 kW, 175 kW, 250 kW, and 280 kW power levels are shown in Table C-3.

The different methods were used to calculate the coupling efficiency of the system based on data produced from calorimetric tests. The energy method of determining the coupling efficiency resulted in a slightly lower value for efficiency compared to the mass segment method. The average efficiency for the four power runs using the energy method averaged 23.5%. The average coupling efficiency calculated for the mass segment method was 25.4%, 1.9% greater than the energy method. Based on these independent calculations the efficiency was determined to be 25% with a calculated uncertainty of ± 2%.

Table C-3

System Coupling Efficiency

Method 2

Input Power Console Power Meter	Energy Addition Rate (kW)	Energy Loss Rate (kW)	Coupling Efficiency (%)
97.5	21.1	3.9	25.6
175.0	38.1	3.7	23.9
253.5	61.5	2.2	25.1
285.9	75.7	1.7	27.1

APPENDIX D

Granular Bed Aerosol Filter for SURC Tests

Experience with the high aerosol source term of previous melt/concentrate tests has focused our attention on the necessity of removing aerosol particulate from the exhaust gas stream before it enters the flow measurement devices.

We outline a model here for granular bed filter performance and propose a laboratory test matrix for model validation or development or our own models should the ones presented here prove inadequate.

The design parameters for our bed are aerosol penetration through the bed and pressure drop across the bed. The target figures are a penetration of less than 10 percent and a pressure drop of less than 2 psi for an operating face velocity of 10 cm/sec. The granule size of the material is stated by the manufacturer to be between 0.5 and 1.0 mm in diameter.

Models for pressure drop (Eckert and Drake, 1972) and aerosol penetration (Lee, 1981) found in the literature indicate that the design target may be met. Experimental verification is required and the test matrix outlined.

Pressure drop through a bed of packed spheres can be estimated by the Ergun Equation (Eckert and Drake, 1972):

$$\Delta P = \rho V_o^2 \frac{L}{D} \left[\frac{1-\varepsilon}{\varepsilon^3}\right] \left[\frac{150\mu}{3V_o D} + 1.75\right]$$

where

ΔP = Pressure drop
L = Length of flow through bed
ρ = Gas density
μ = Gas viscosity
o = Gas face velocity
D = Granule diameter, and
ε = Porosity of bed.

Aerosol penetration is estimated using the granular bed penetration model of Lee (1981). This model includes three removal mechanisms--interception, diffusion, and gravitational settling--for particles directed downward through the bed. Inertial impaction is not included in this model because there are no analytical expressions for this mechanism--numerical solutions must be used. This presents no problem in the analysis since impaction does not play an important role in particle removal until the Stokes number of the particle is on the order of 1 and does not contribute at all for particle Stokes numbers less than 0.1 (Gutfinger and Tardos, 1979; Tardos, et al., 1979).

$$E = \exp\left[\frac{-3(1-\varepsilon)\ L\ (\eta R + \eta D + \eta G)}{2\varepsilon D}\right]$$

E = Particle penetration efficiency
ηR = Single particle interception efficiency
ηD = Single particle diffusion efficiency
ηG = Single particle gravitational settling efficiency

$$\eta R = 1.5\,\frac{\varepsilon}{K}\,\frac{R^2}{(I+R)^S}$$

$$\eta D = 3.5\left[\frac{\varepsilon}{K}\right]^{1/3} Pe^{-2/3}$$

$$\eta G = \frac{G \cdot St}{1 + G \cdot St}$$

where

R = interception parameter
= Dp/D
Dp = particle diameter
$K = 1 - 1.8(1-\varepsilon)^{1/3} + (1-\varepsilon) - 0.2(1-\varepsilon)^2$

$$S = \frac{(3-2\varepsilon)}{3\varepsilon}$$

Pe = Peclet number

$$= \frac{3\pi\mu\ V_o\ Dp\ D}{kT}$$

k = Boltzmann's constant
T = Temperature

$$G = \frac{gD}{2V_o^{\,2}}$$

g = gravitational acceleration
St = Stokes number

$$= \frac{\rho_p\ Dp^2}{18\mu}\quad\frac{V_o}{D}$$

The results of these approximations have been calculated for grain sizes of 1 mm and 0.5 mm, bed depths of 100 cm and 200 cm, and face velocities of 5 cm/sec, 10 cm/sec, and 20 cm/sec. These results are presented below.

A 200 cm deep bed of 1 mm particles has the following performance:

Face Velocity (cm/sec)	ΔP(psi)	Penetration of 1μ particle (%)
5.	0.18	16
10.	0.37	30
15.	0.57	39

Decreasing the particles to 0.5 mm diameter gives

Face Velocity (cm/sec)	ΔP(psi)	Penetration of 1μ particle (%)
5	0.71	0.2
10	1.4	1.3
15	2.2	3.1

This matrix may be filled out if necessary. The data will be fit to the relationship for aerosol penetration and pressure drop in order to identify the porosity and effective grain size so that the model may be applied to the granular bed employed in the tests.

Pressure drop across a 100 cm long column of the granule material used in the granular bed filter was measured for various flow velocities. These results and extrapolations to a 200 cm long column are given below:

Face Velocity (actual cm/sec)	Pressure Drop (psi)	
	100 cm	200 cm
3.5	0.145	0.29
6.75	0.40	0.80
10.0	0.70	1.40
13.0	1.10	2.20

The extrapolation to 200 cm is close to the prediction for the 200 cm bed of 0.5 mm granules. The bench top test indicate satisfactory pressure drop performance for the granular bed.

Time constraints prohibited aerosol penetration tests. However, the pressure drop data suggest that the bed acts as if the granule site is 0.5 mm. This granule size gives low aerosol penetration predictions through the bed.

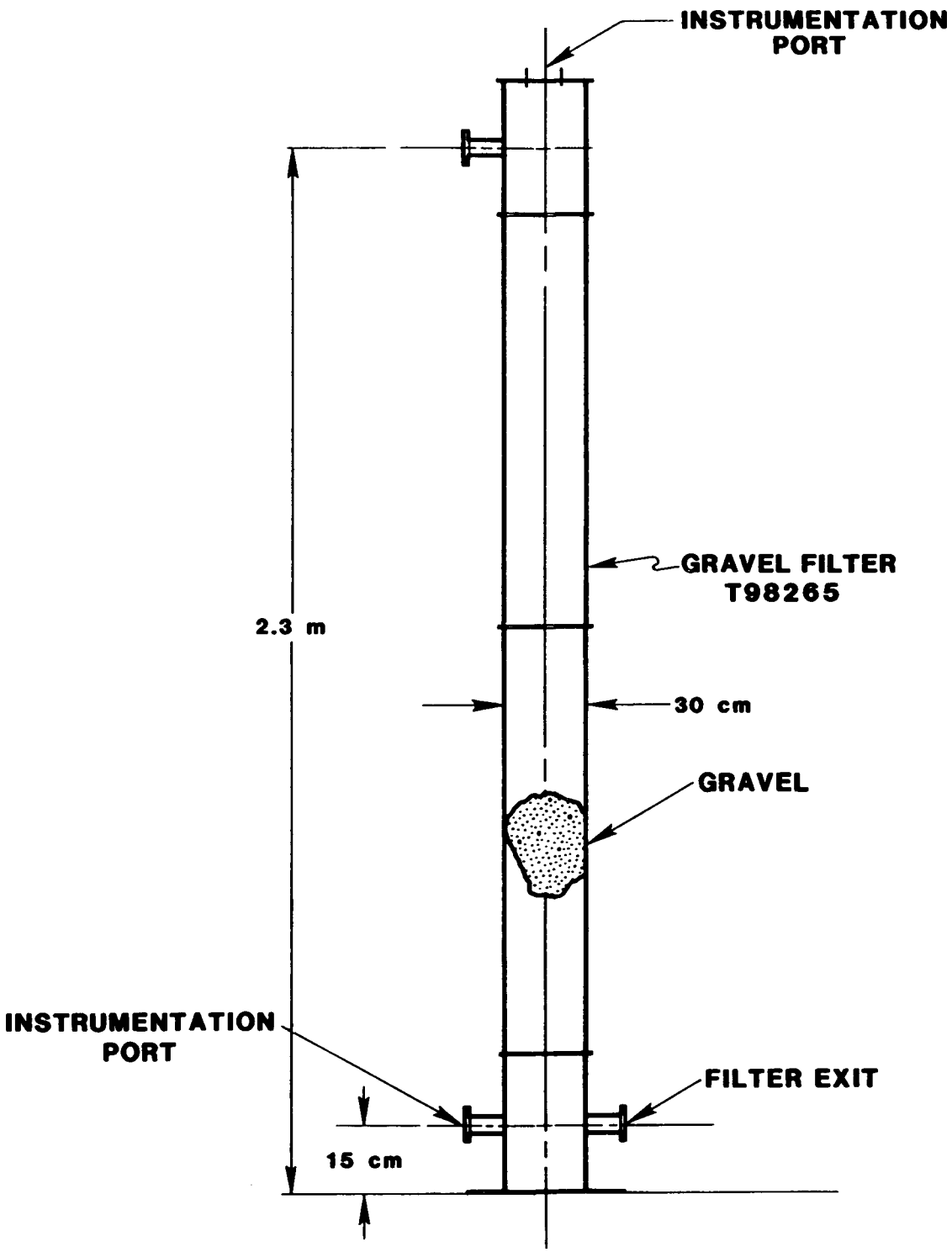

Figure D-1 - Grannular Bed Aerosol Filter

APPENDIX E

SURC 4 THERMOCOUPLE PROFILES

In this appendix are the type K, S and C thermocouple calibration data, concrete thermocouple data, MgO sidewall thermocouple data, sidewall and upward heat flux data calculated from the thermocouples imbedded in the MgO annulus and cover, comparison of sidewall temperature data measured during the experiment and calculated from the inverse heat flux code, gas temperature data, and differential temperature data of the cooling fluid measured at the induction power supply and coil.

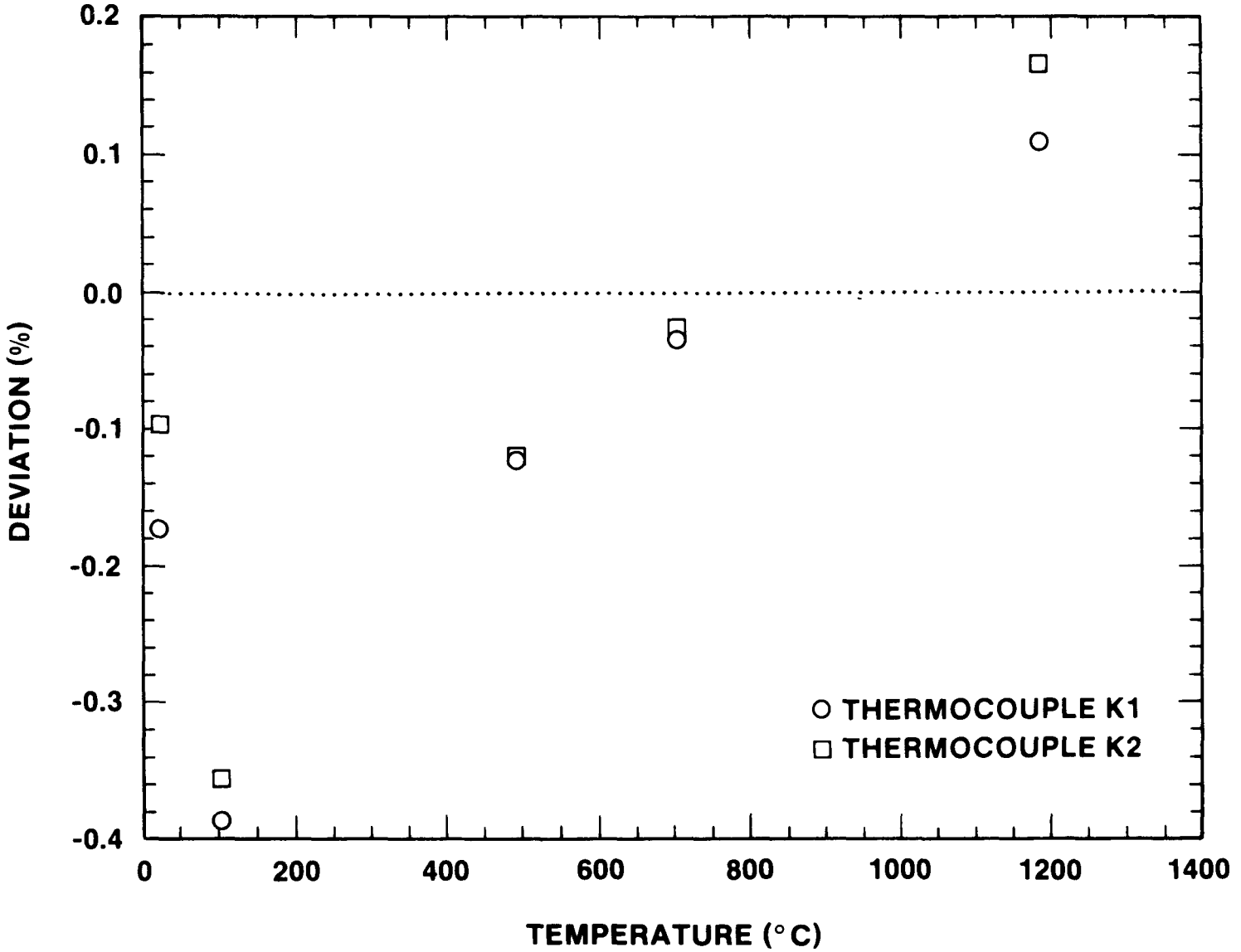

Figure E-1 - Type K Thermocouple Calibration Plot

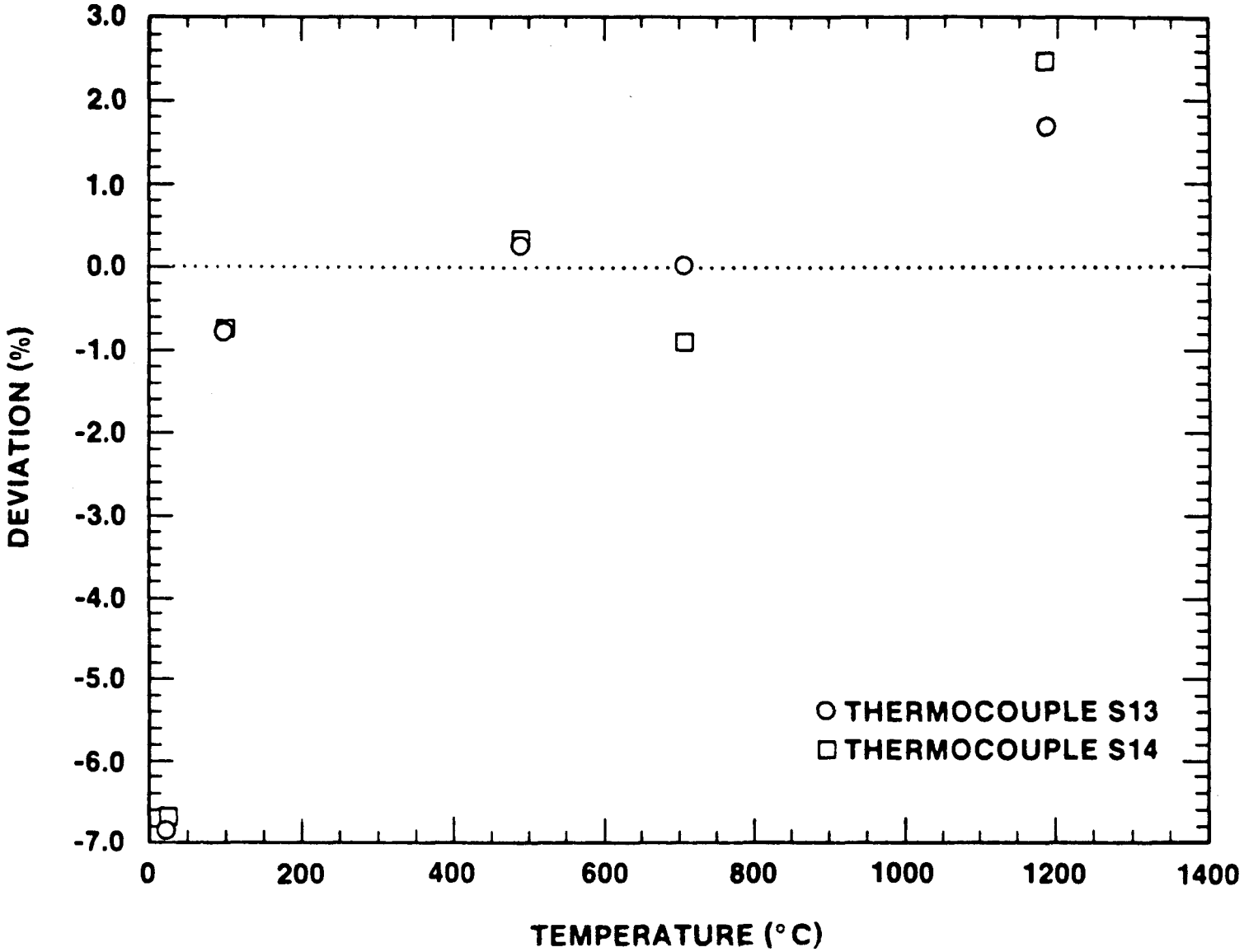

Figure E-2 - Type S Thermocouple Calibration Plot

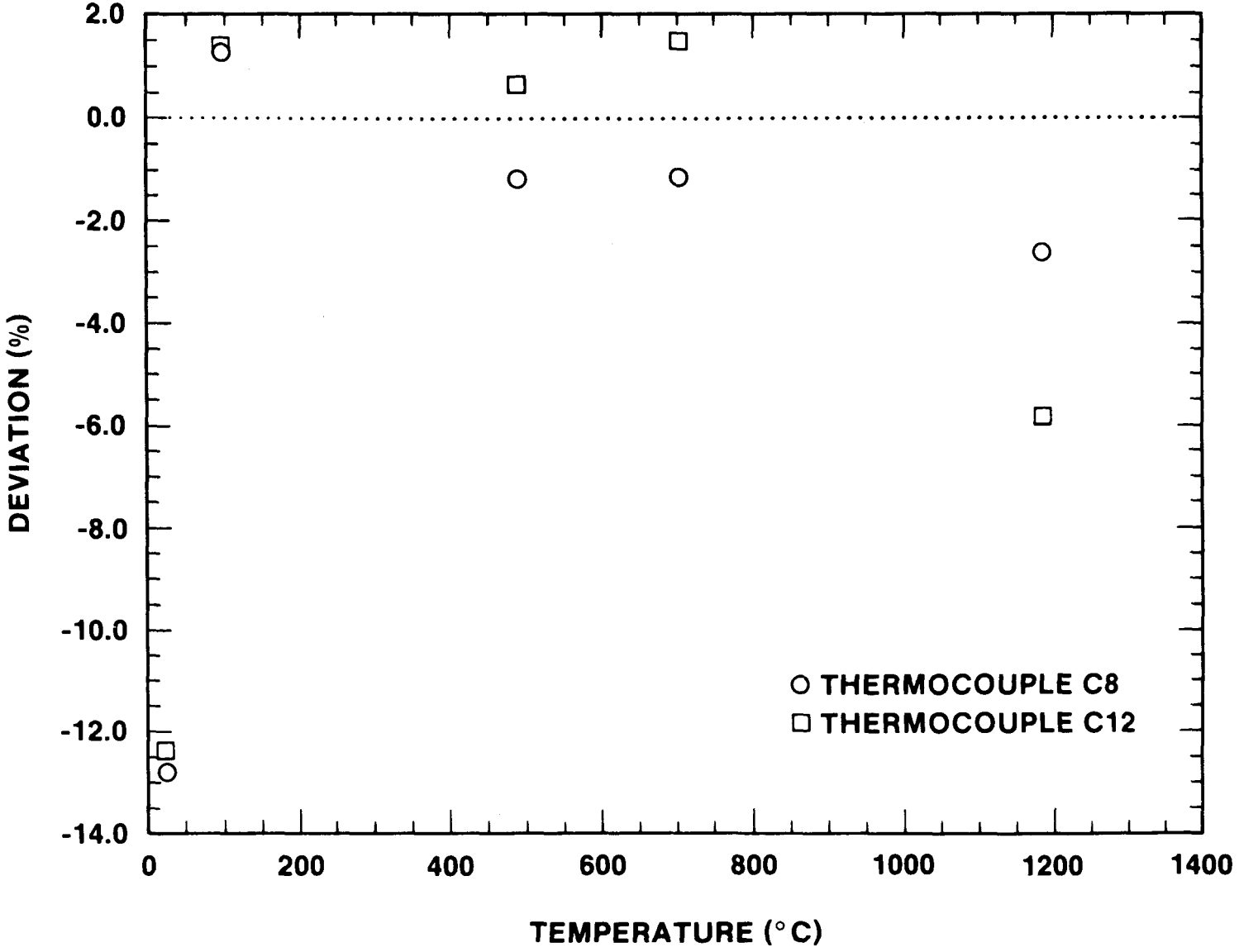

Figure E-3 - Type C Thermocouple Calibration Plot

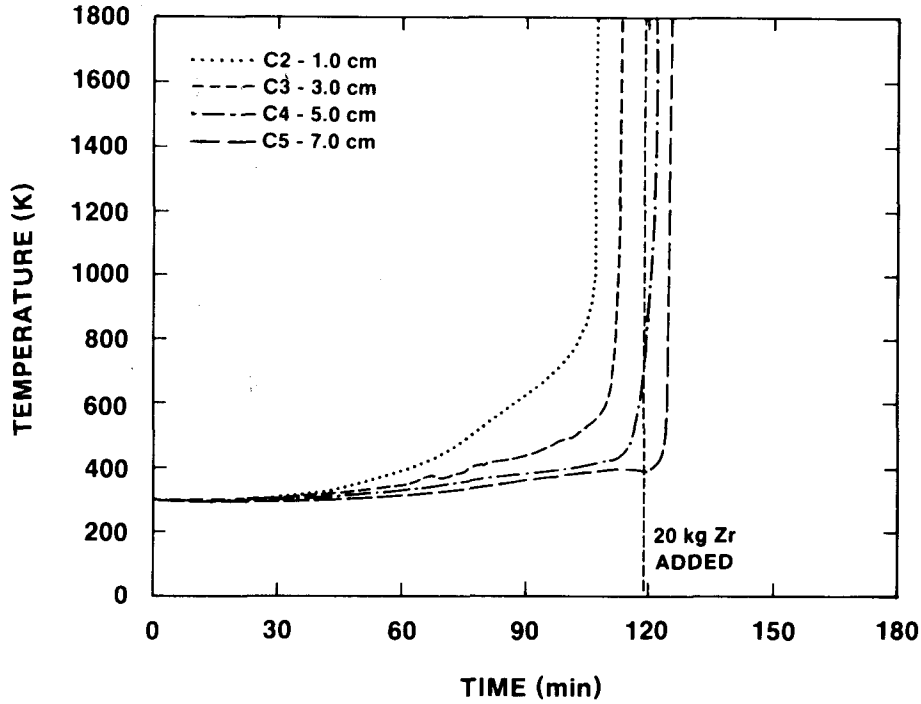

Figure E-4 - Concrete Temperature Data Measured by Thermocouples Located in the Axial Centerline Array Between z = -1.0 and -7.0 cm.

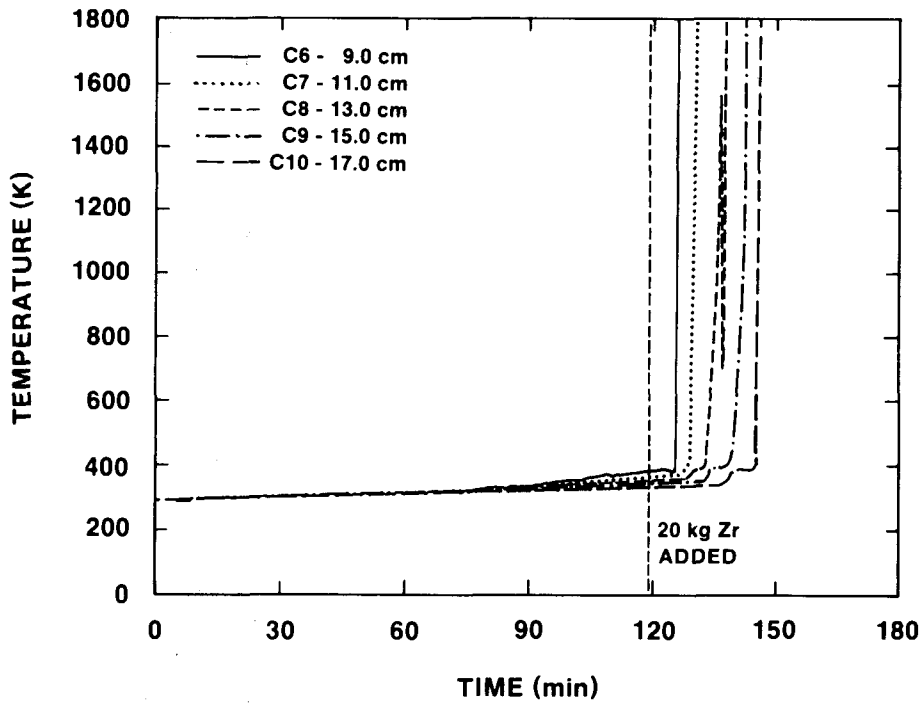

Figure E-5 - Concrete Temperature Data Measured by Thermocouples Located in the Axial Centerline Array Between z = -9.0 and -17.0 cm.

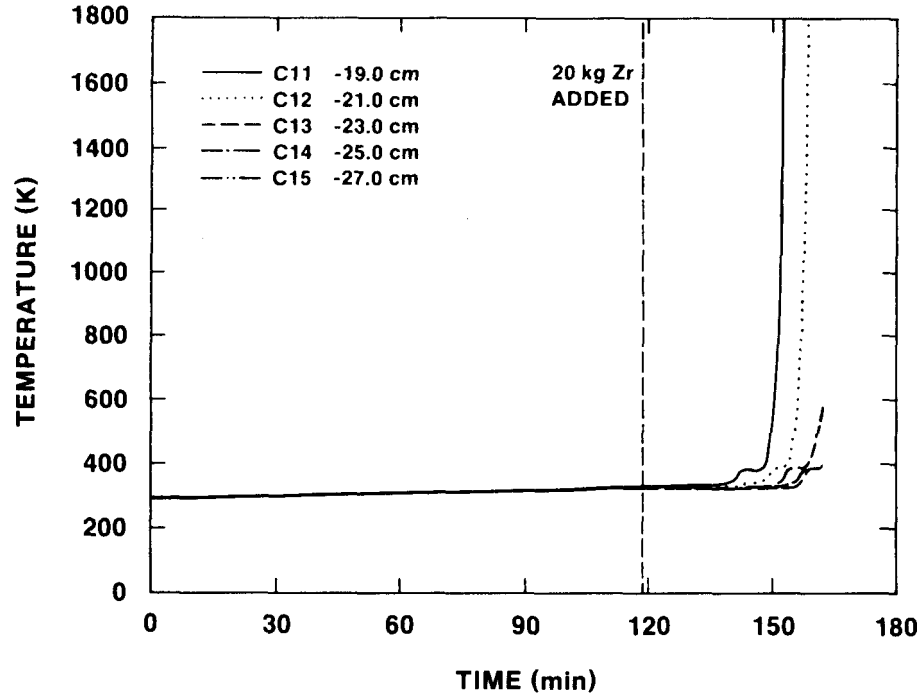

Figure E-6 - Concrete Temperature Data Measured by Thermocouples Located in the Axial Centerline Array Between z = -19.0 and -27.0 cm.

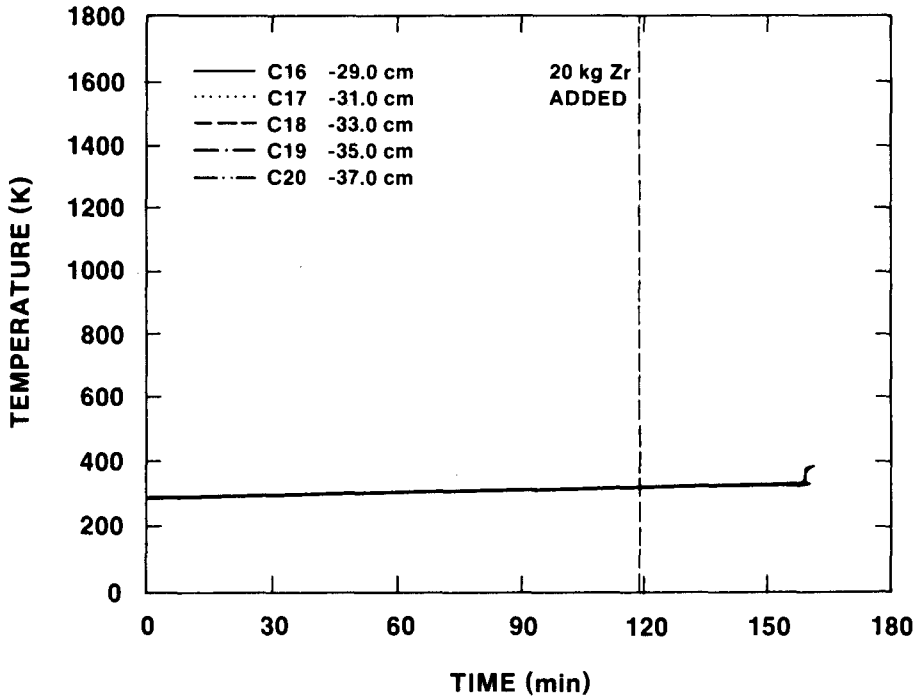

Figure E-7 - Concrete Temperature Data Measured by Thermocouples Located in the Axial Centerline Array Between z = -29.0 and -37.0 cm.

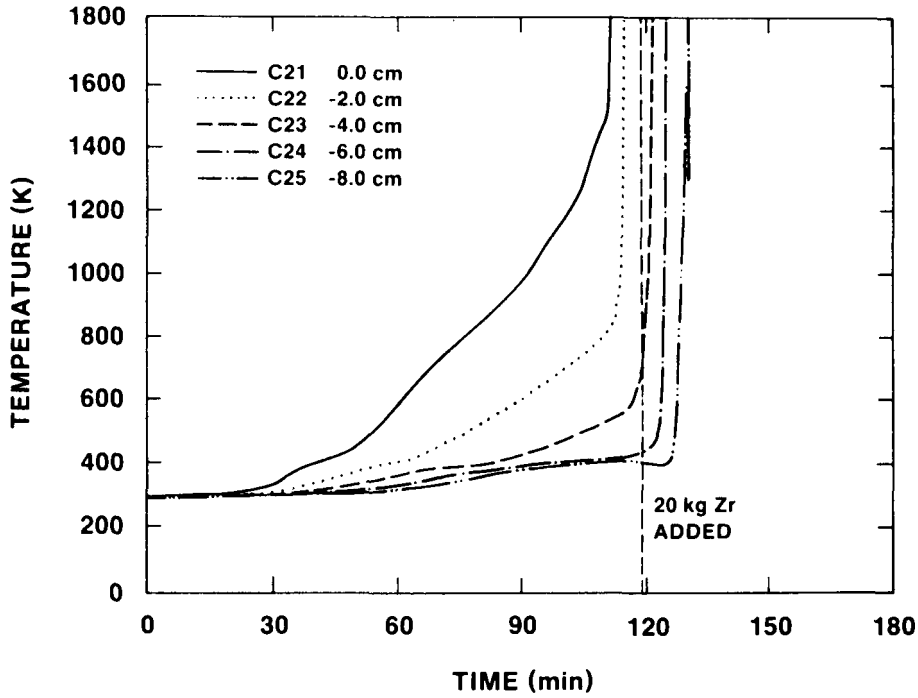

Figure E-8 - Concrete Temperature Data Measured by Thermocouples Located in the Midradius Array Between z = -0.0 and -8.0 cm.

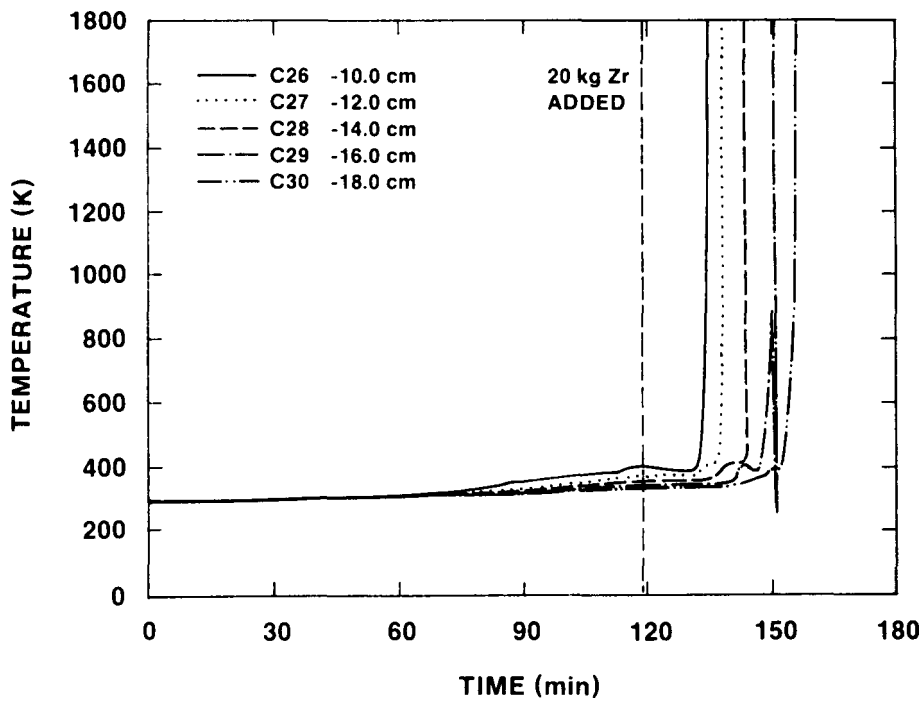

Figure E-9 - Concrete Temperature Data Measured by Thermocouples Located in the Midradius Array Between z = -10.0 and -18.0 cm.

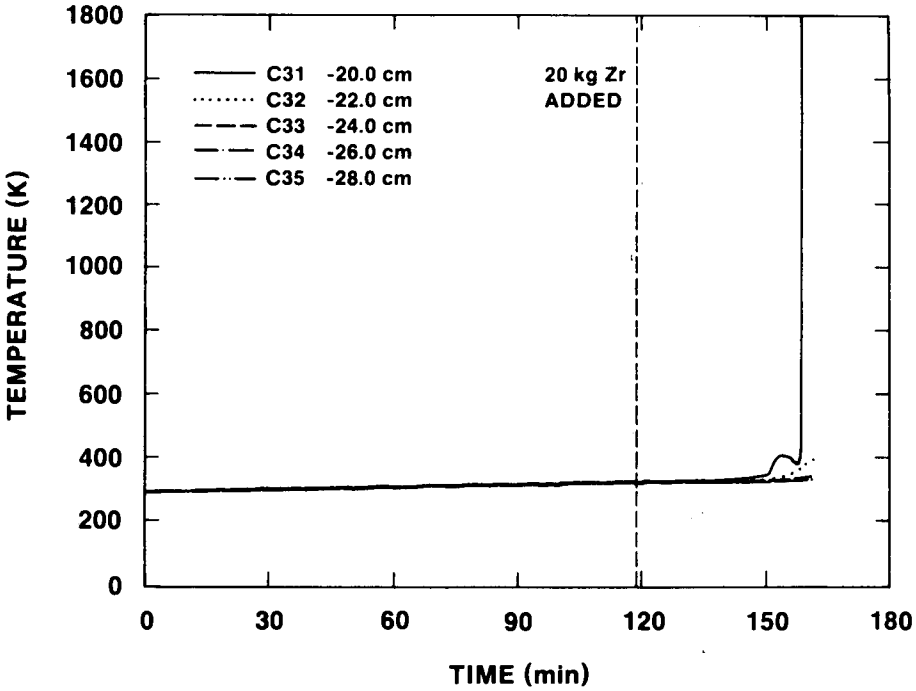

Figure E-10 - Concrete Temperature Data Measured by Thermocouples Located in the Midradius Array Between z = -20.0 and -28.0 cm.

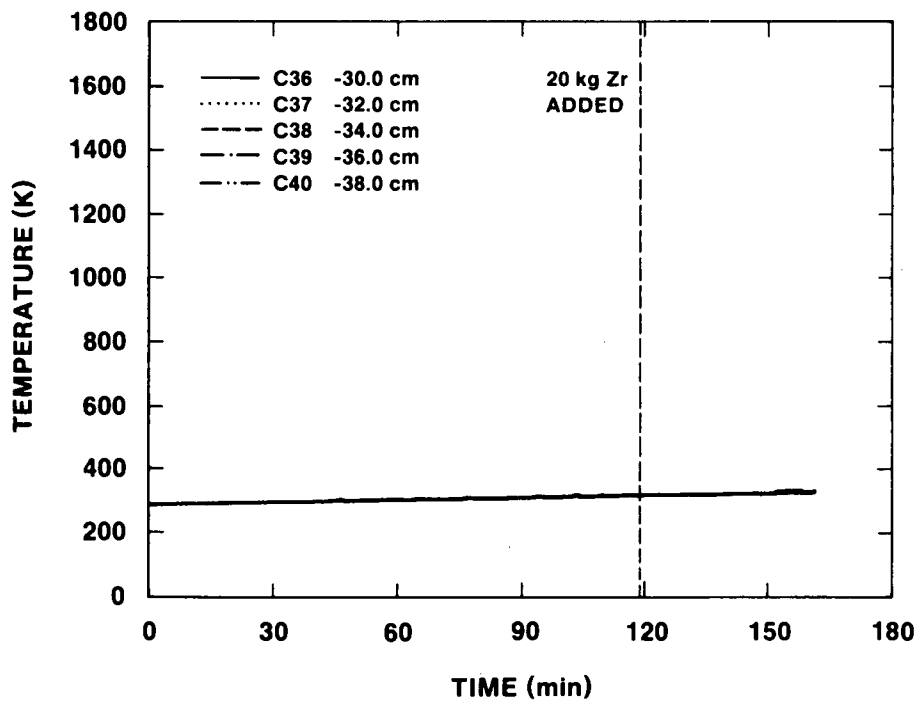

Figure E-11 - Concrete Temperature Data Measured by Thermocouples Located in the Midradius Array Between z = -30.0 and -38.0 cm.

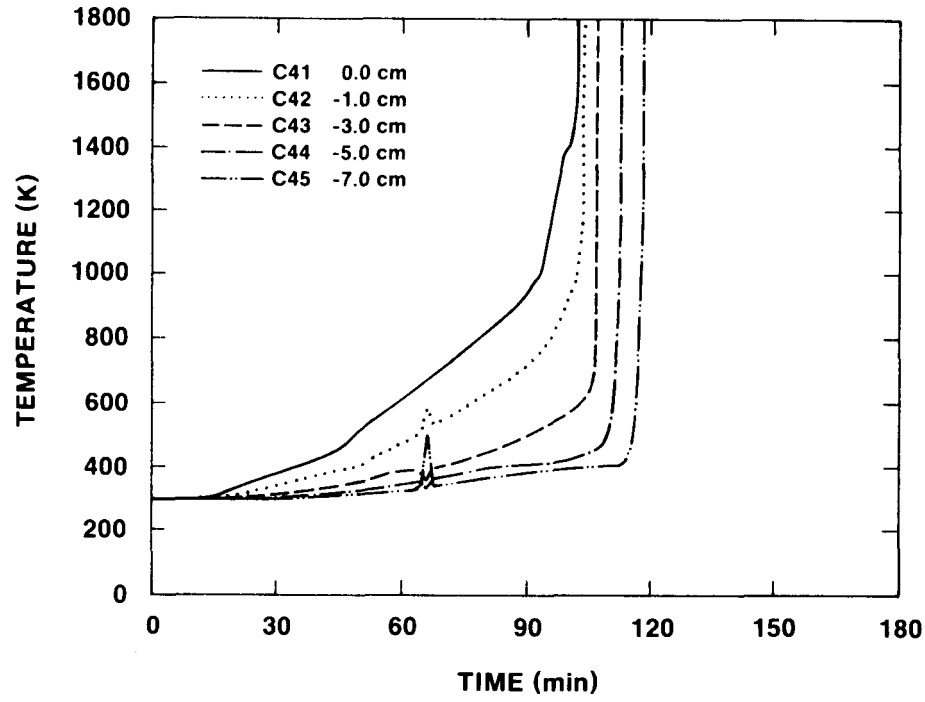

Figure E-12 - Concrete Temperature Data Measured by Thermocouples Located in the Perimeter Array Between z = 0.0 and -7.0 cm.

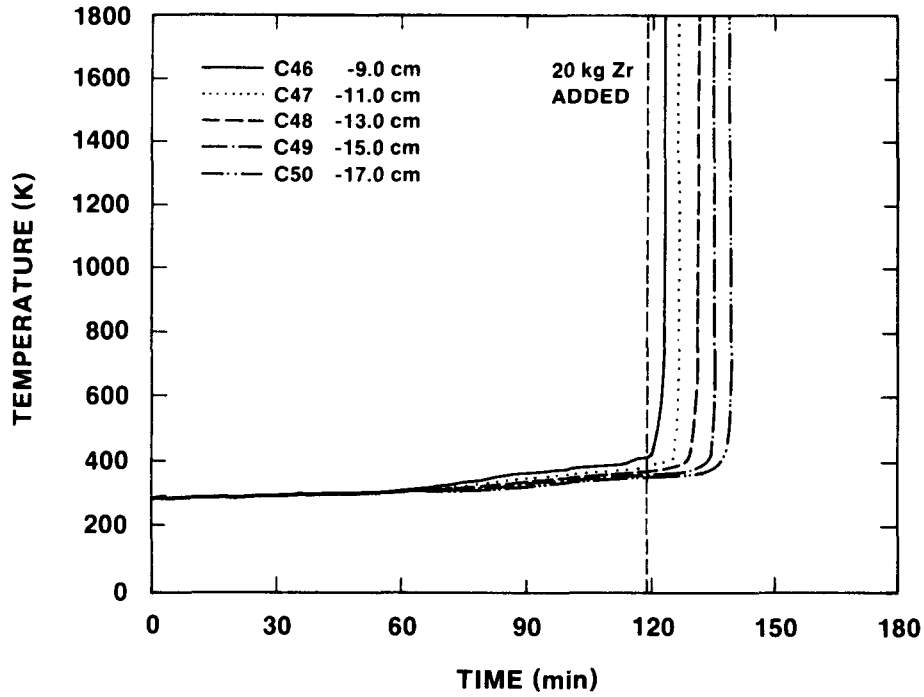

Figure E-13 - Concrete Temperature Data Measured by Thermocouples Located in the Perimeter Array Between z = -9.0 and -17.0 cm.

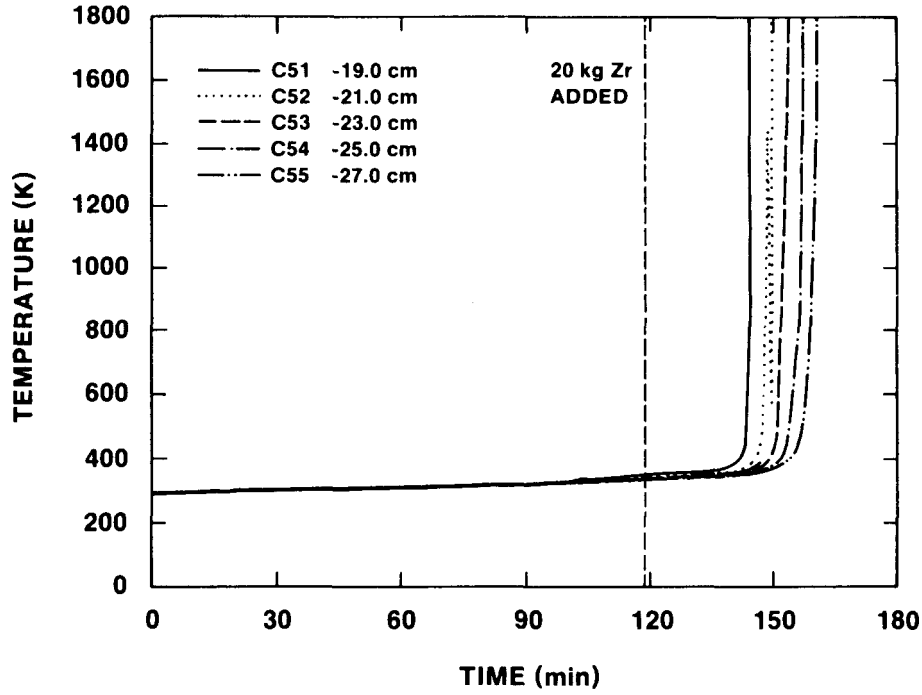

Figure E-14 - Concrete Temperature Data Measured by Thermocouples Located in the Perimeter Array Between z = -19.0 and -27.0 cm.

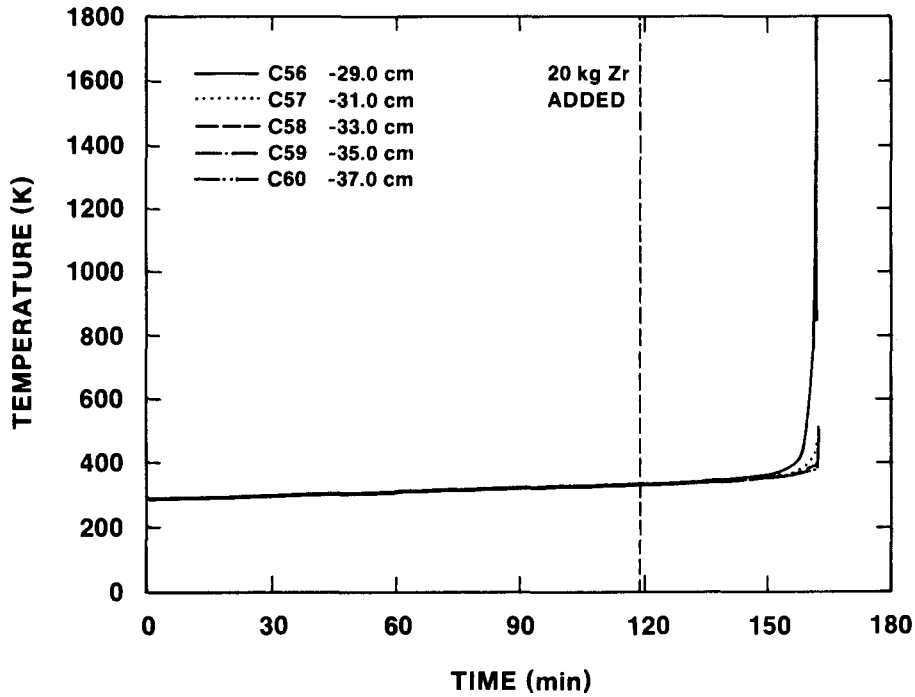

Figure E-15 - Concrete Temperature Data Measured by Thermocouples Located in the Perimeter Array Between z = -29.0 and -37.0 cm.

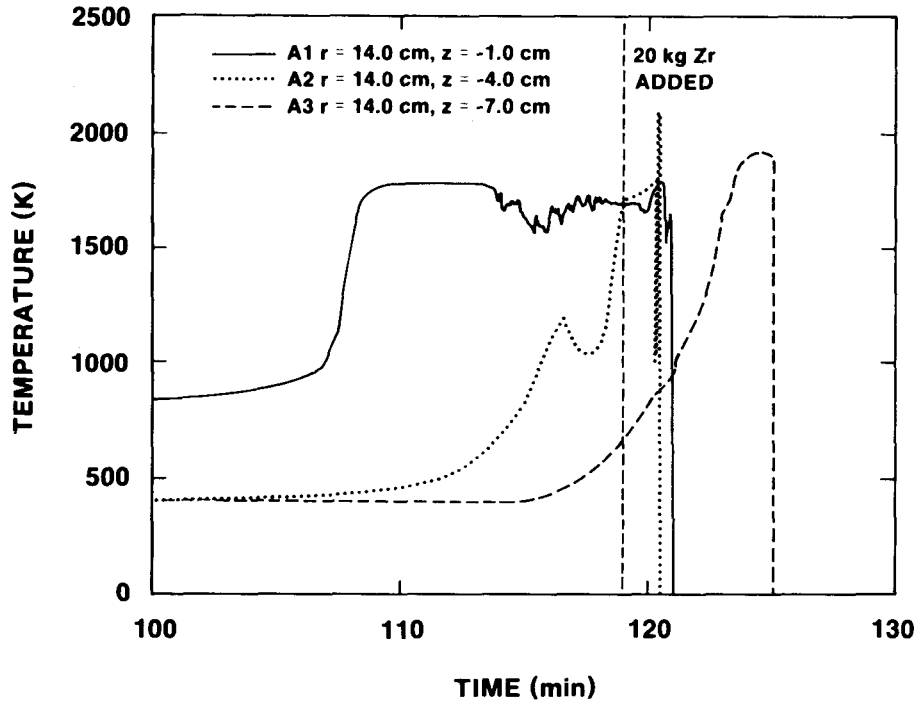

Figure E-16 - Melt Temperatures Measured by Type S Thermocouples Installed into the Alumina Tubes Between z = -1.0 and -7.0 cm.

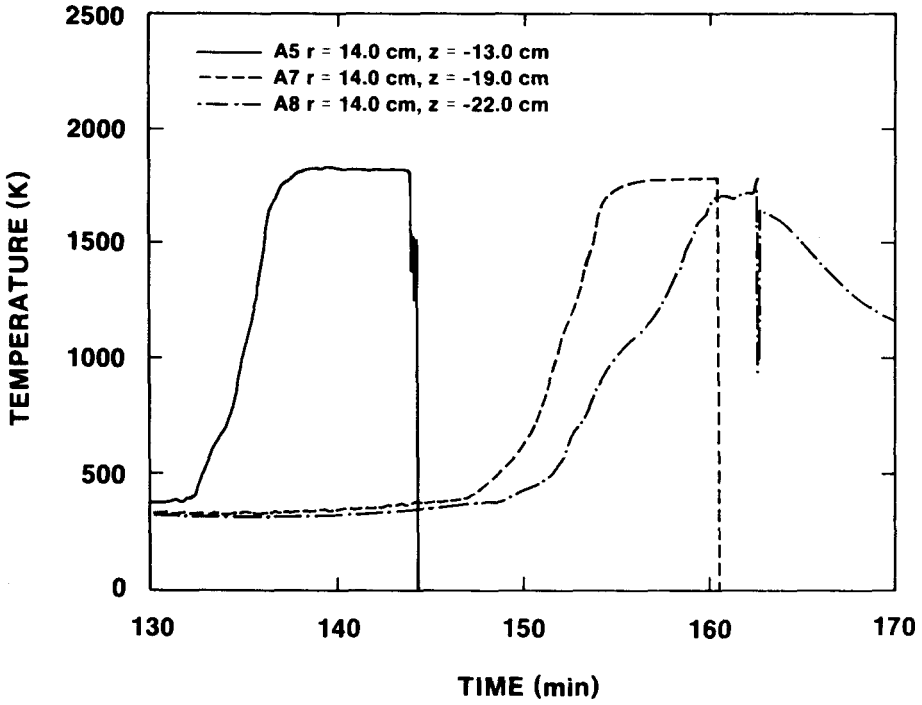

Figure E-17 - Melt Temperatures Measured by Type S and C Thermocouples Installed into the Alumina Tubes Between z = -13.0 and -22.0 cm.

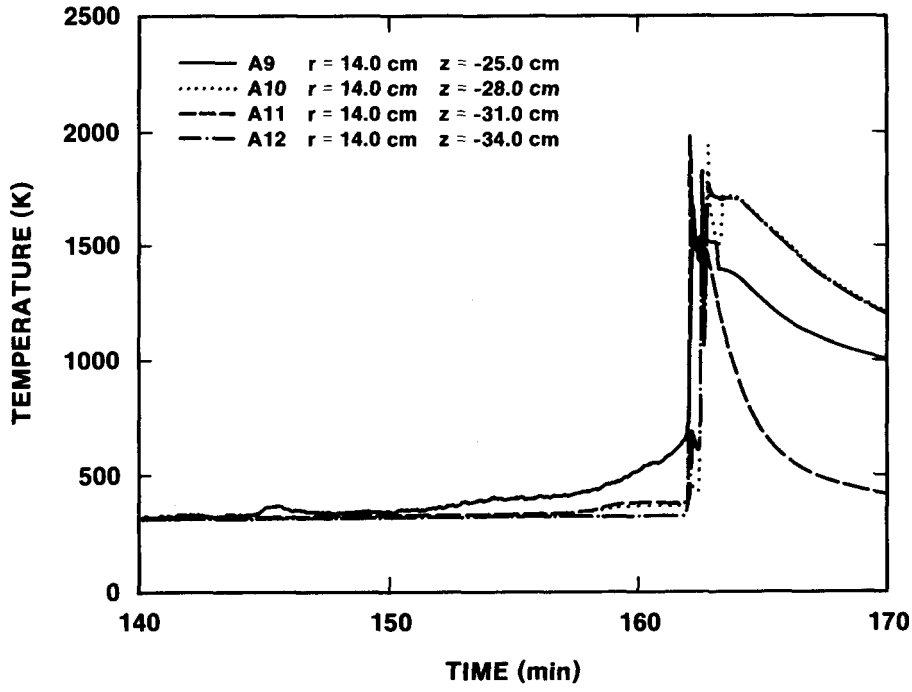

Figure E-18 - Melt Temperatures Measured by Type C Thermocouples Installed into the Alumina Tubes Between z = -25.0 and -34.0 cm.

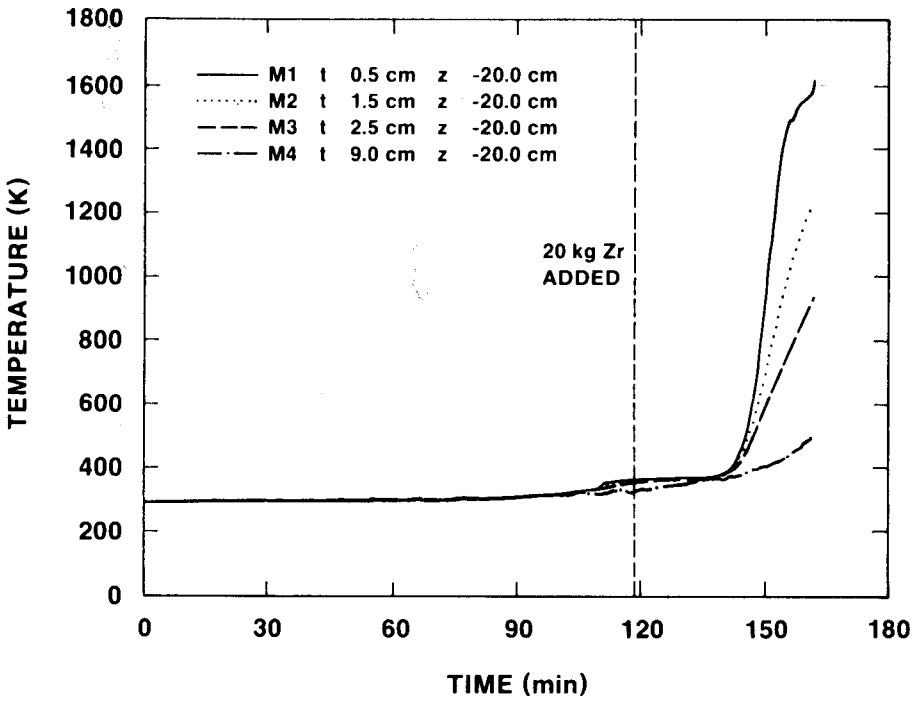

Figure E-19 - MgO Sidewall Temperature Data Measured by Thermocouples in the Array Located at z = -20.0 cm.

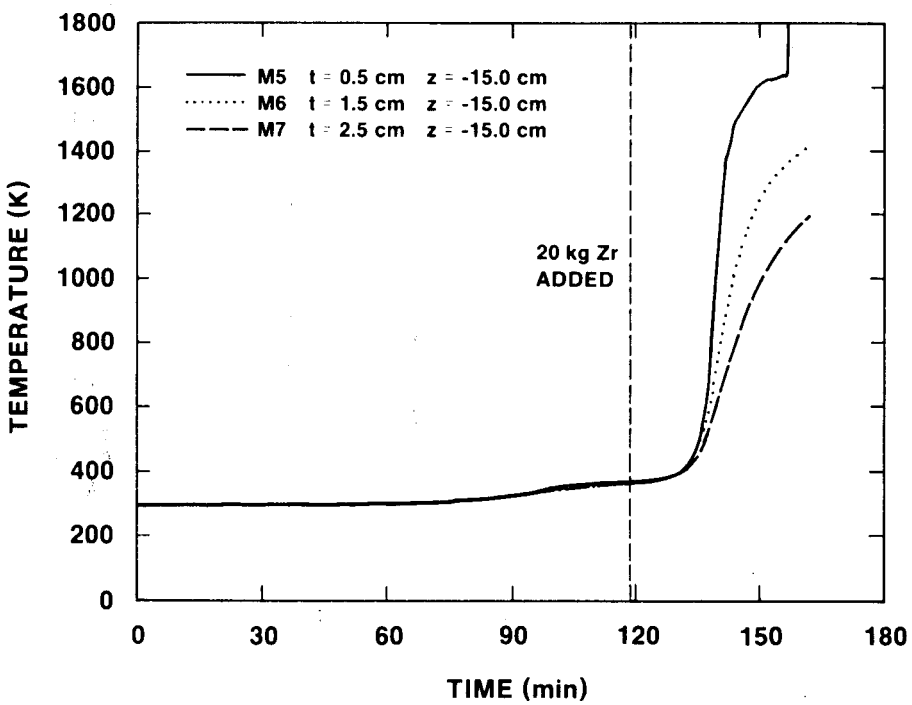

Figure E-20 - MgO Sidewall Temperature Data Measured by Thermocouples in the Array Located at z = -15.0 cm.

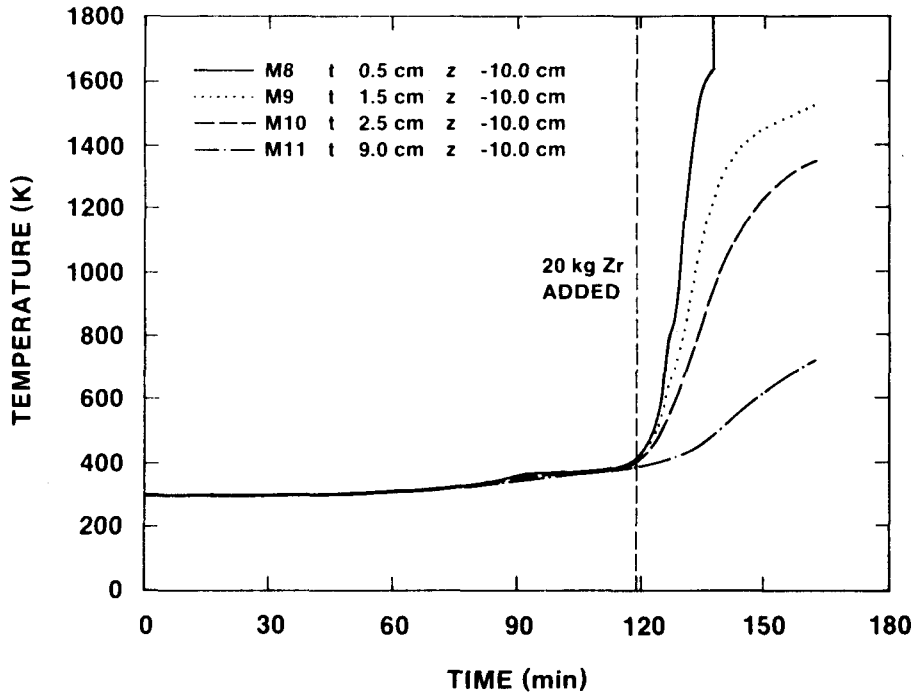

Figure E-21 - MgO Sidewall Temperature Data Measured by Thermocouples in the Array Located at z =-10.0 cm.

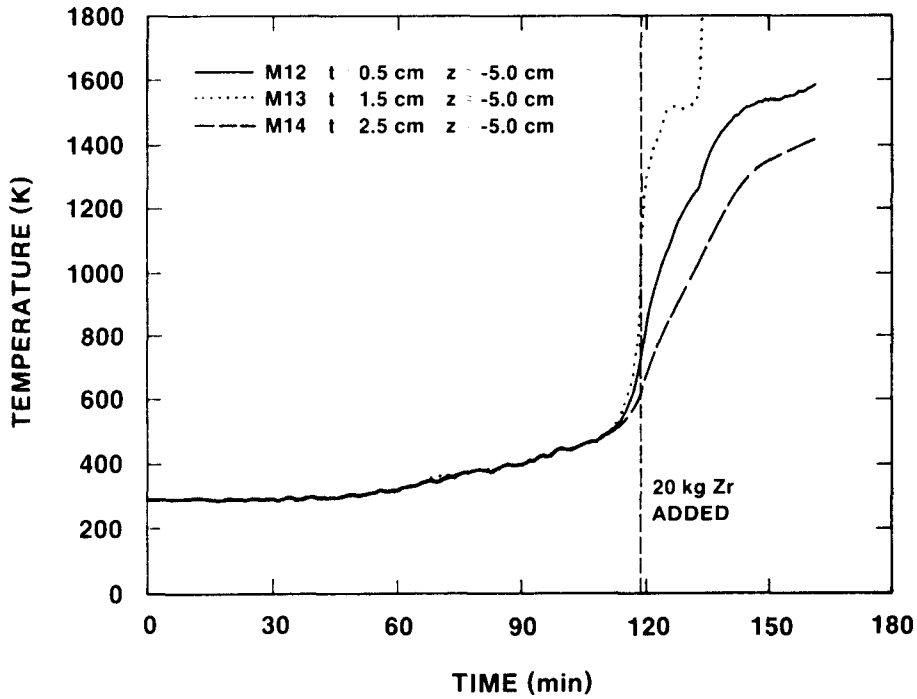

Figure E-22 - MgO Sidewall Temperature Data Measured by Thermocouples in the Array Locatd at z = -5.0 cm.

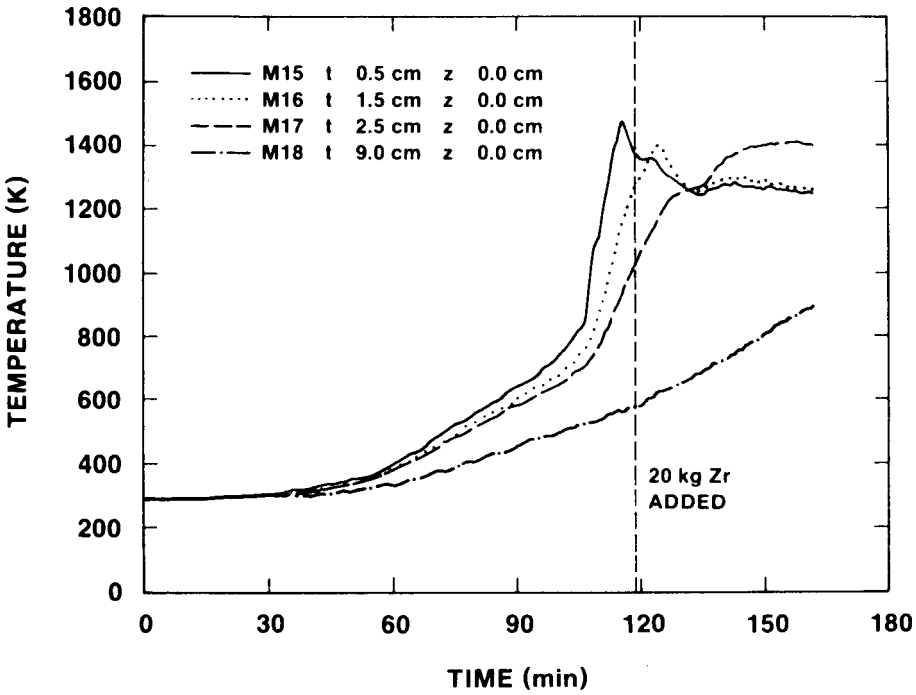

Figure E-23 - MgO Sidewall Temperature Data Measured by Thermocouples in the Array Located at z = 0.00 cm.

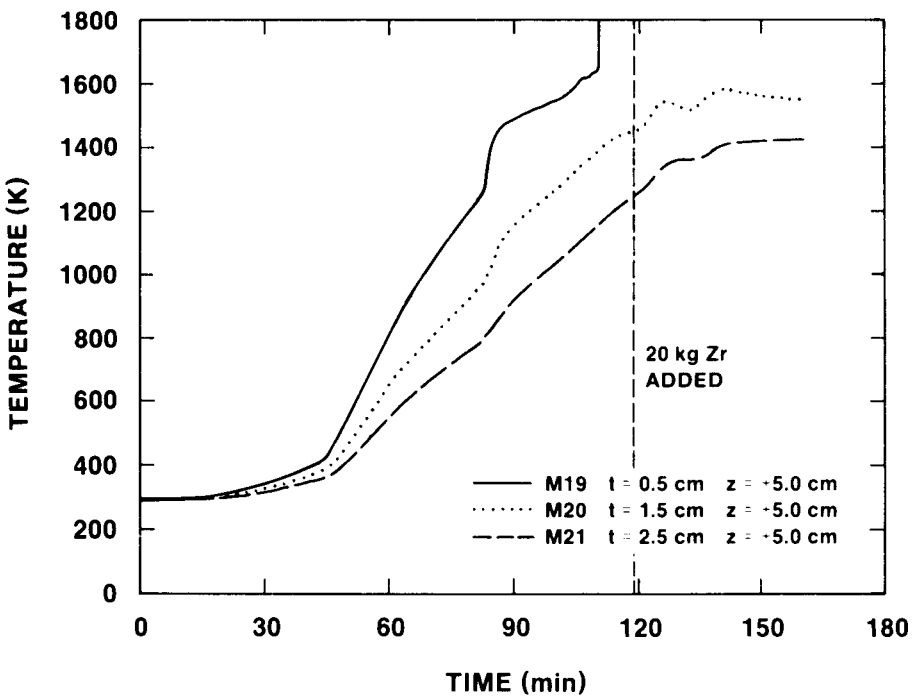

Figure E-24 - MgO Sidewall Temperature Data Measured by Thermocouples in the Array Located at z = +5.0 cm.

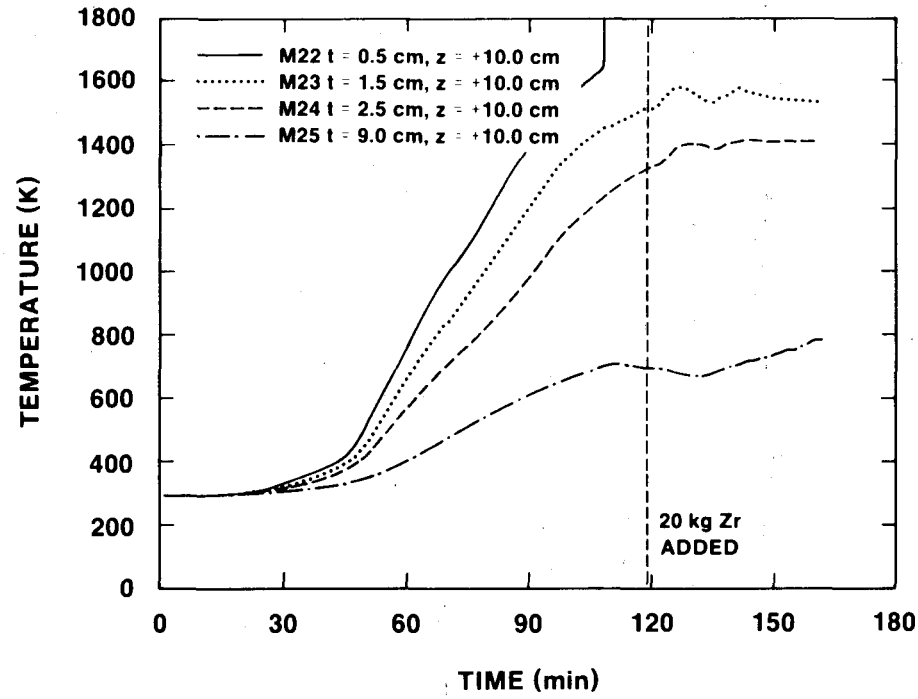

Figure E-25 - MgO Sidewall Temperature Data Measured by Thermocouples in the Array Located at z = +10.0 cm.

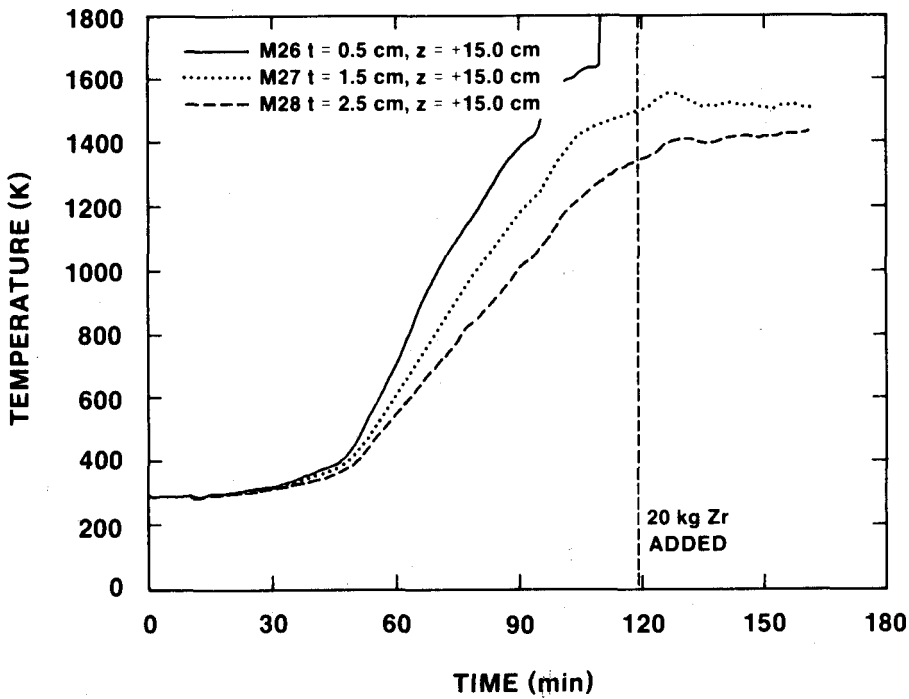

Figure E-26 - MgO Sidewall Temperature Data Measured by Thermocouples in the Array Located at z = +15.0 cm.

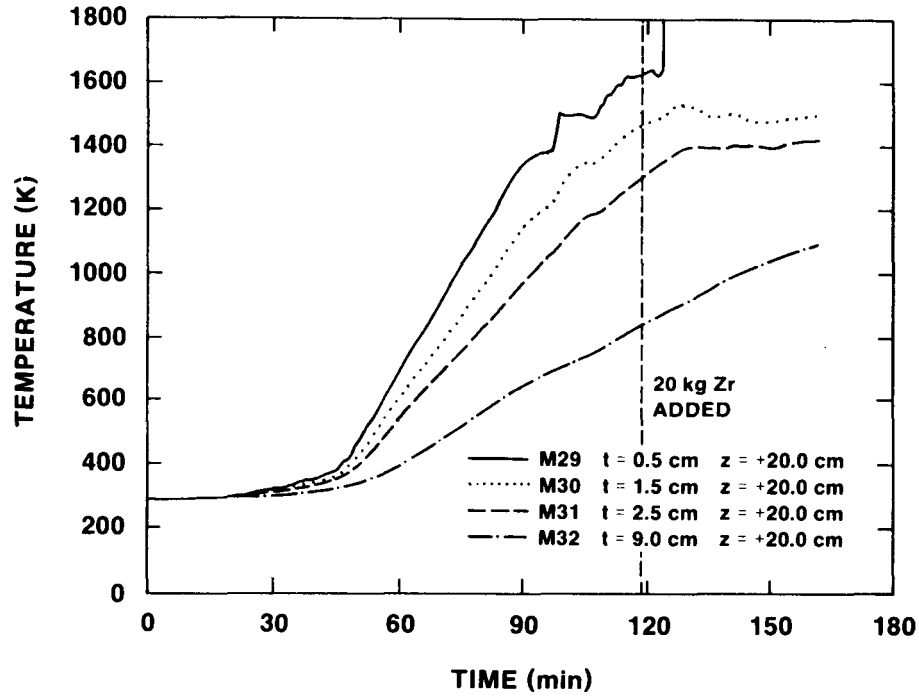

Figure E-27 - MgO Sidewall Temperature Data Measured by Thermocouples in the Array Located at z = +20.0 cm.

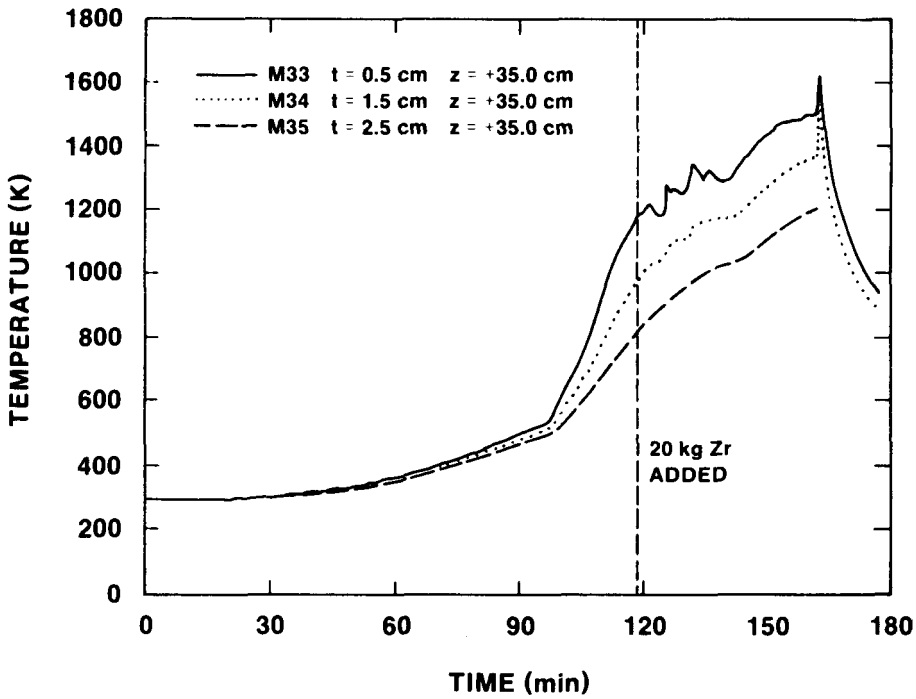

Figure E-28 - MgO Sidewall Temperature Data Measured by Thermocouples in the Array Located at z = -35.0 cm.

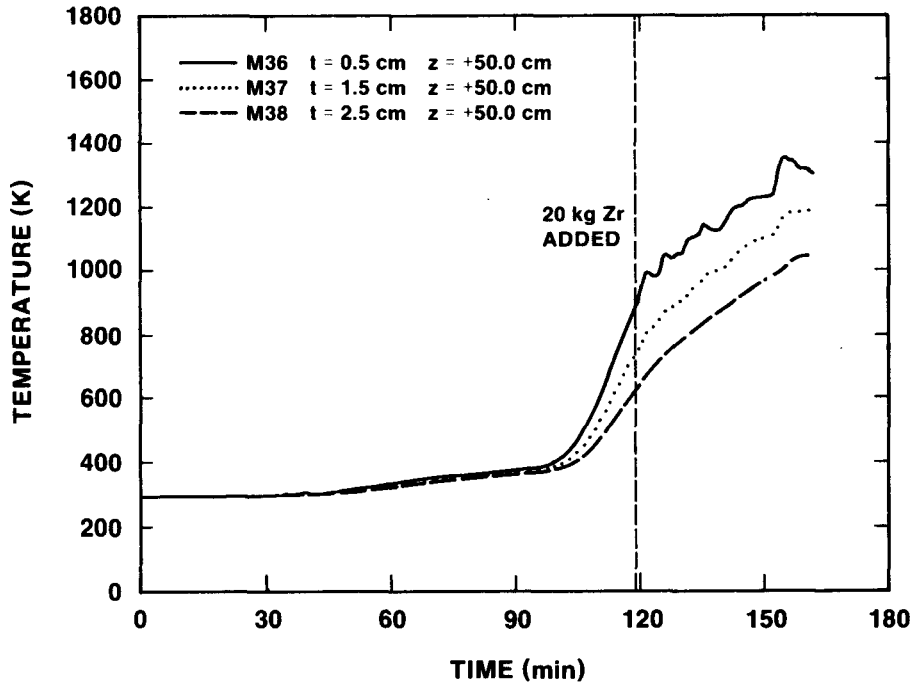

Figure E-29 - MgO Sidewall Temperature Data Measured by Thermocouples in the Array Located at z = -50.0 cm.

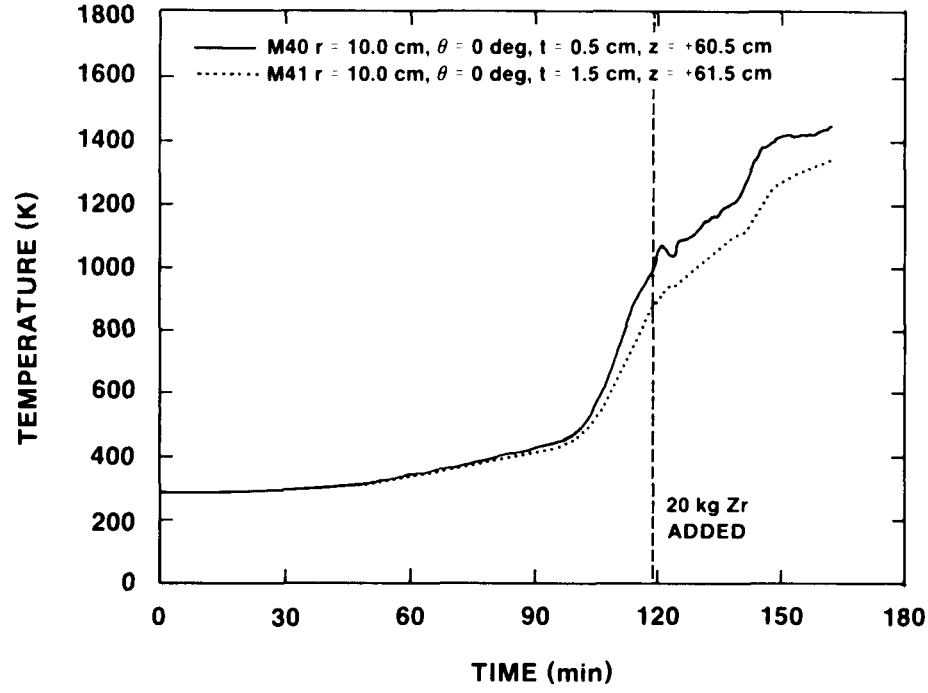

Figure E-30 - MgO Cover Temperature Data Measured by Thermocouples in the Array Located at r = 10.0 cm, θ = 0, and z = -60.0 cm.

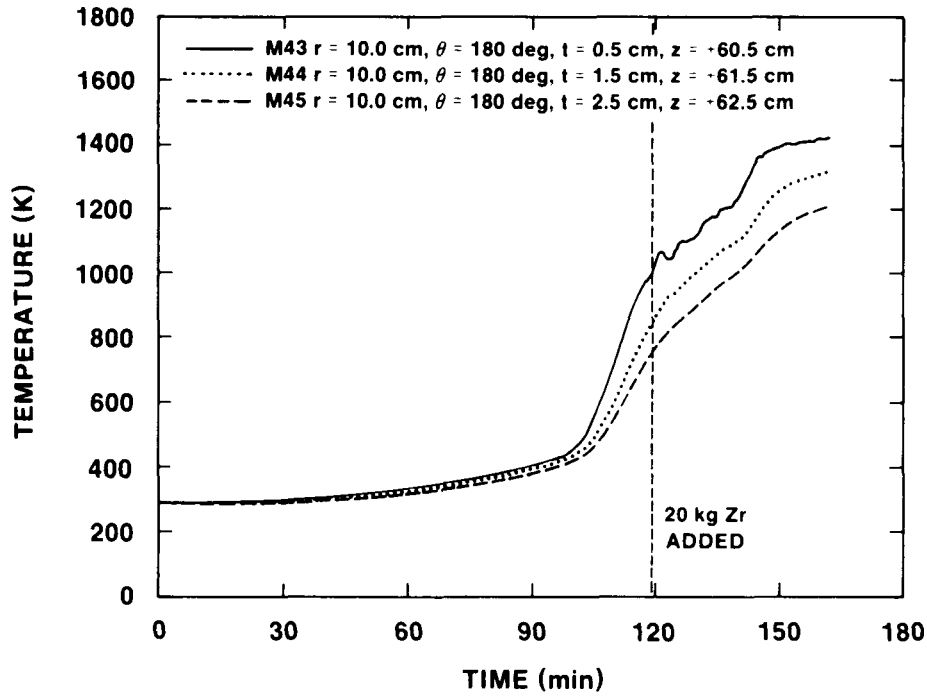

Figure E-31 - MgO Cover Temperature Data Measured by Thermocouples in the Array Located at r = 10.0 cm, θ = 180, and z = -60.0 cm.

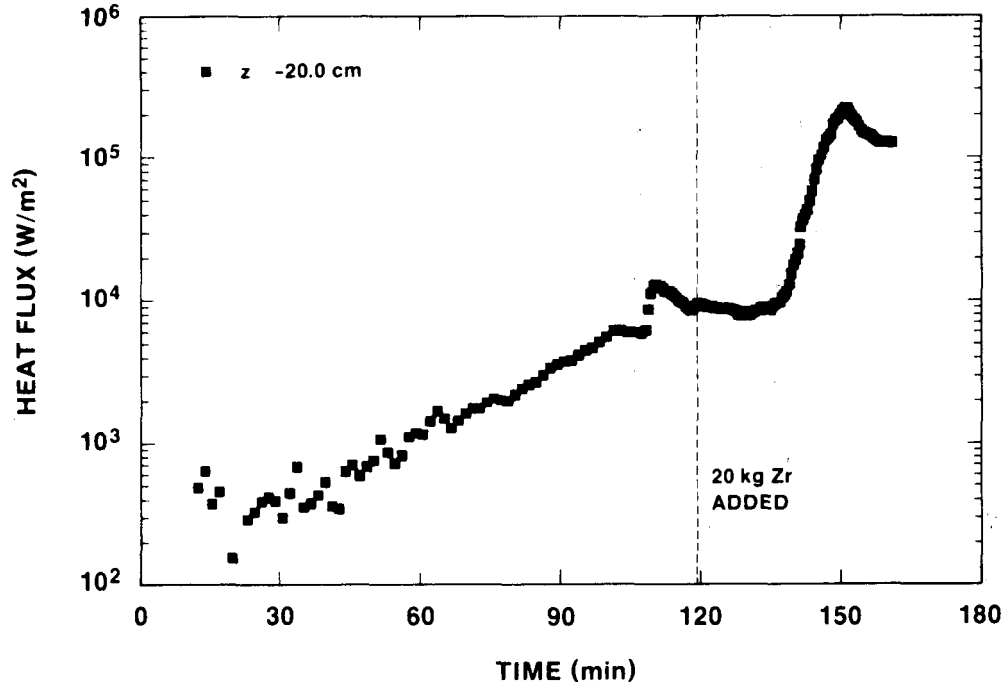

Figure E-32 - MgO Sidewall Heat Flux Calculatd from Thermocouple Data for the Array Located at z = -20.0 cm.

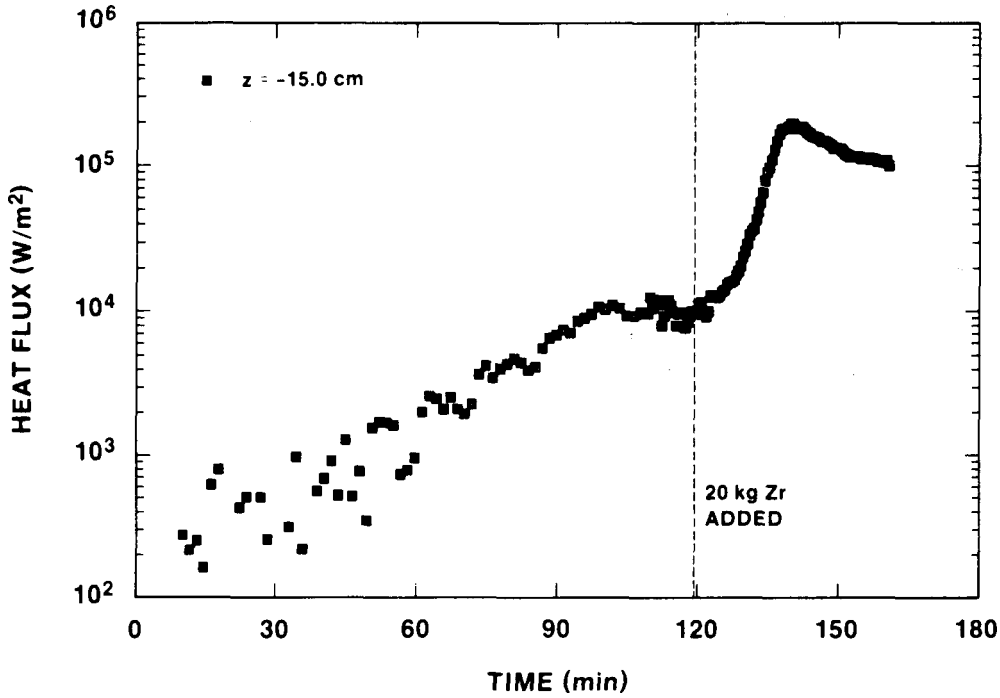

Figure E-33 - MgO Sidewall Heat Flux Calculated from Thermocouple Data for the Array Located at z = -15.0 cm.

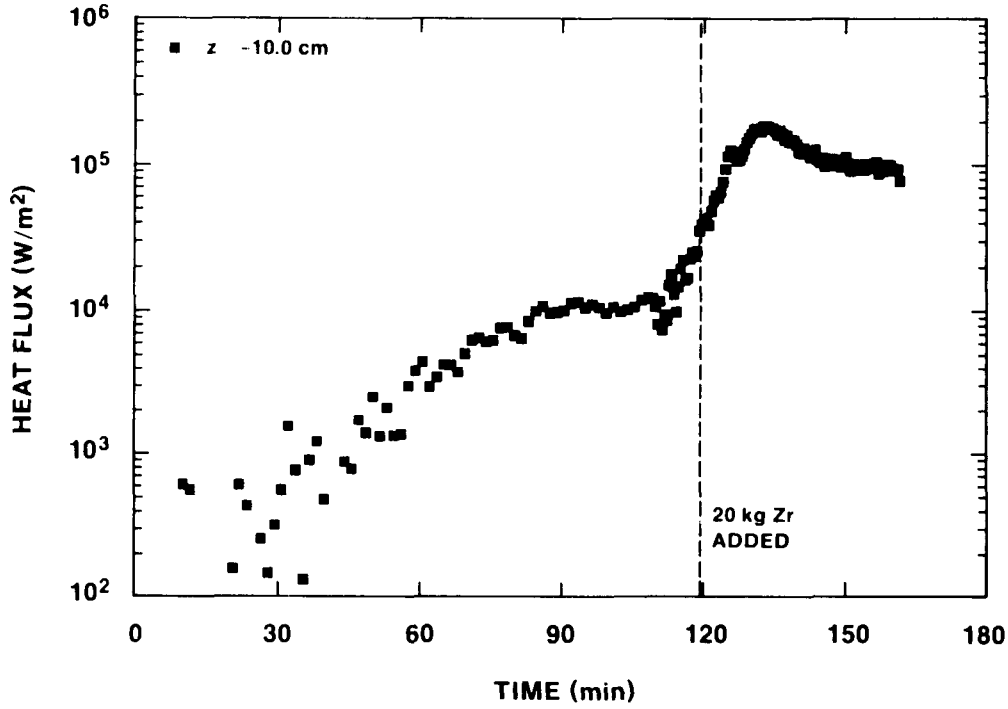

Figure E-34 - MgO Sidewall Heat Flux Calculated from Thermocouple Data for the Array Located at z = -10.0 cm.

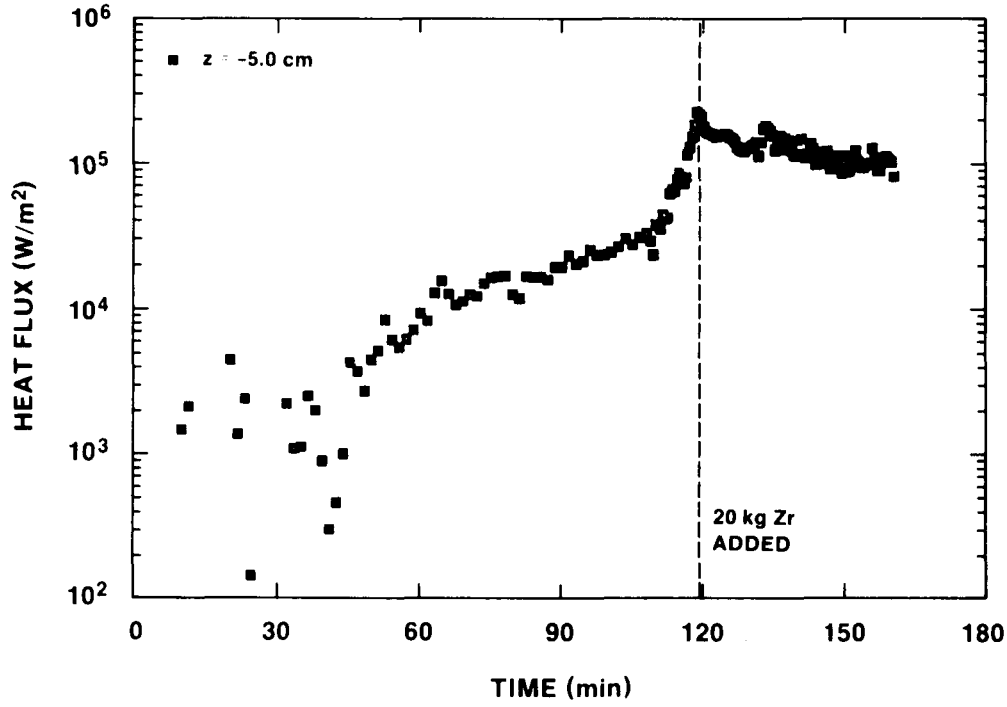

Figure E-35 - MgO Sidewall Heat Flux Calculated from Thermocouple Data for the Array Located at z = -5.0 cm

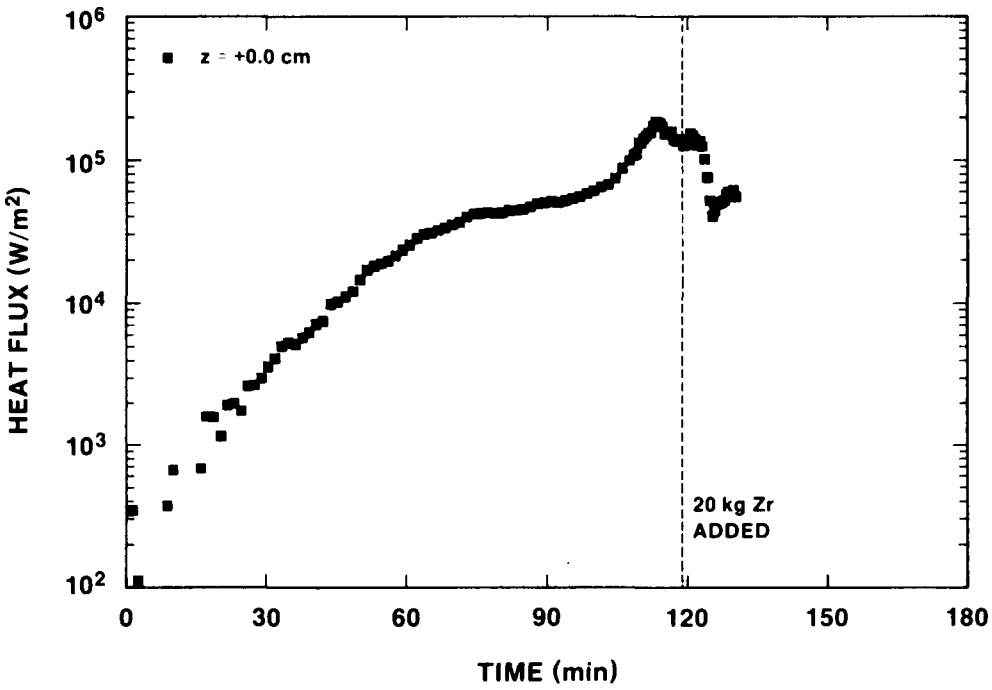

Figure E-36 - MgO Sidewall Heat Flux Calculated from Thermocouple Data for the Array Located at z = 0.0 cm.

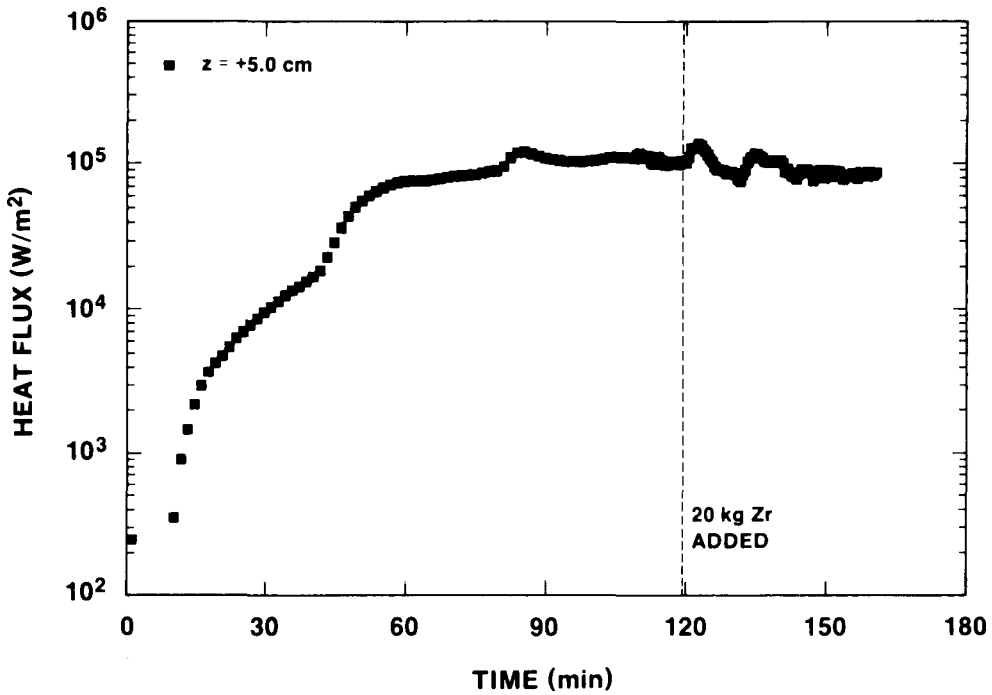

Figure E-37 - MgO Sidewall Heat Flux Calculated from Thermocouple Data for the Array Located at z = +5.0 cm.

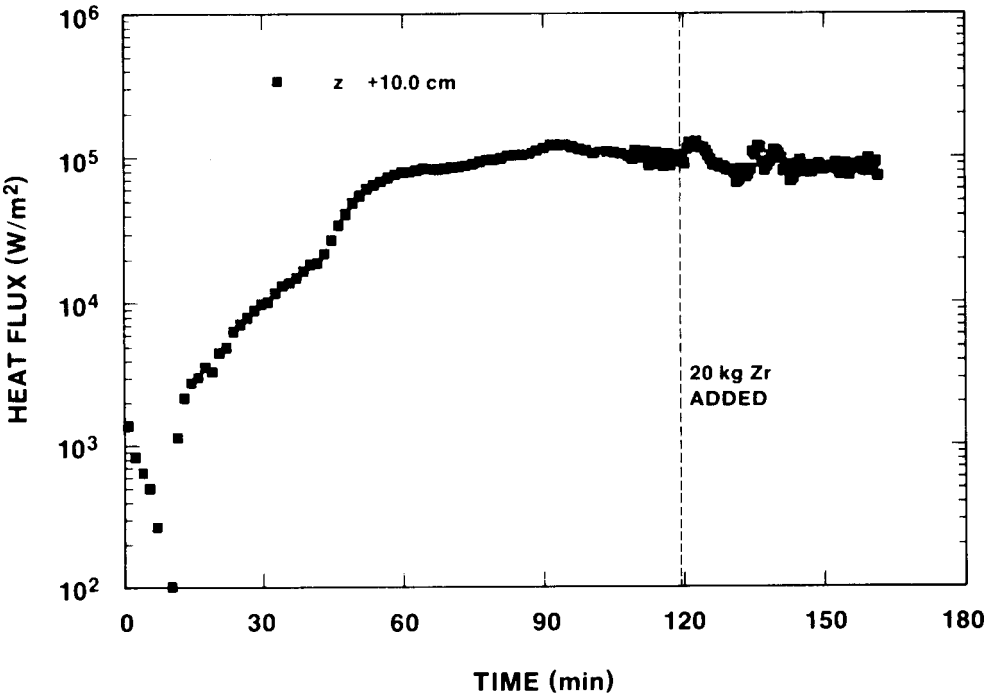

Figure E-38 - MgO Sidewall Heat Flux Calculated from Thermocouple Data for the Array Located at z = +10.0 cm.

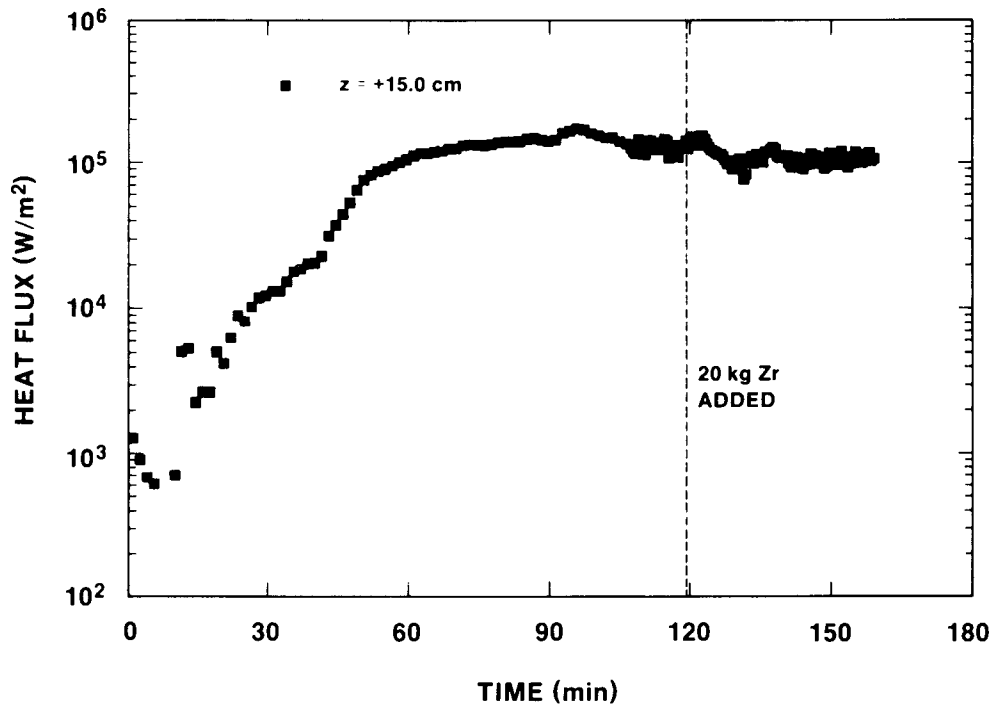

Figure E-39 - MgO Sidewall Heat Flux Calculated from Thermocouple Data for the Array Located at z = +15.0 cm.

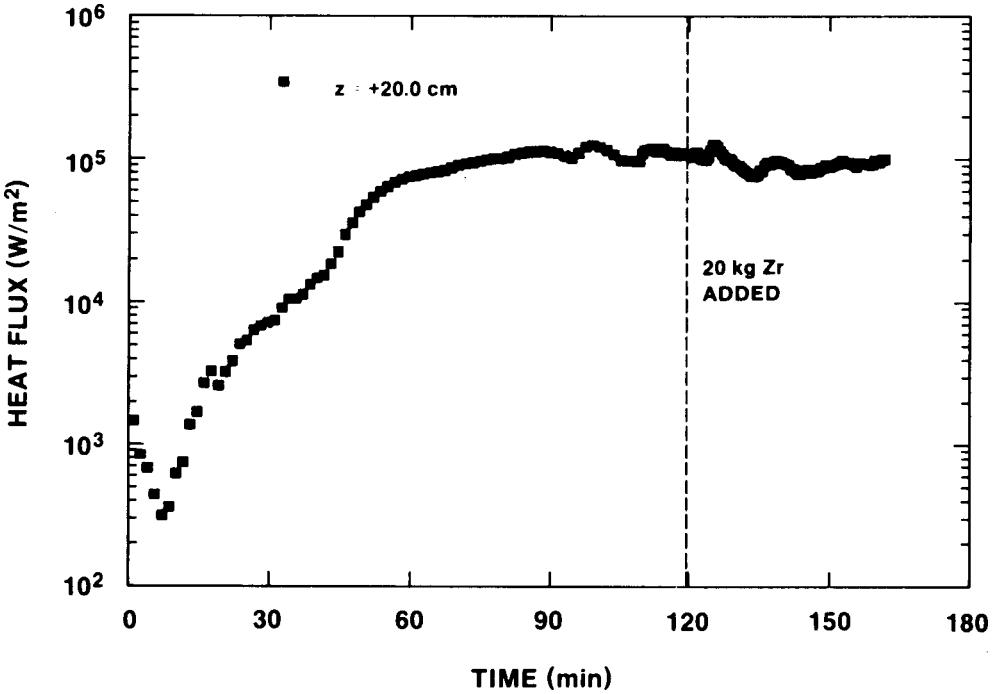

Figure E-40 - MgO Sidewall Heat Flux Calculated from Thermocouple Data for the Array Located at z = +20.0 cm.

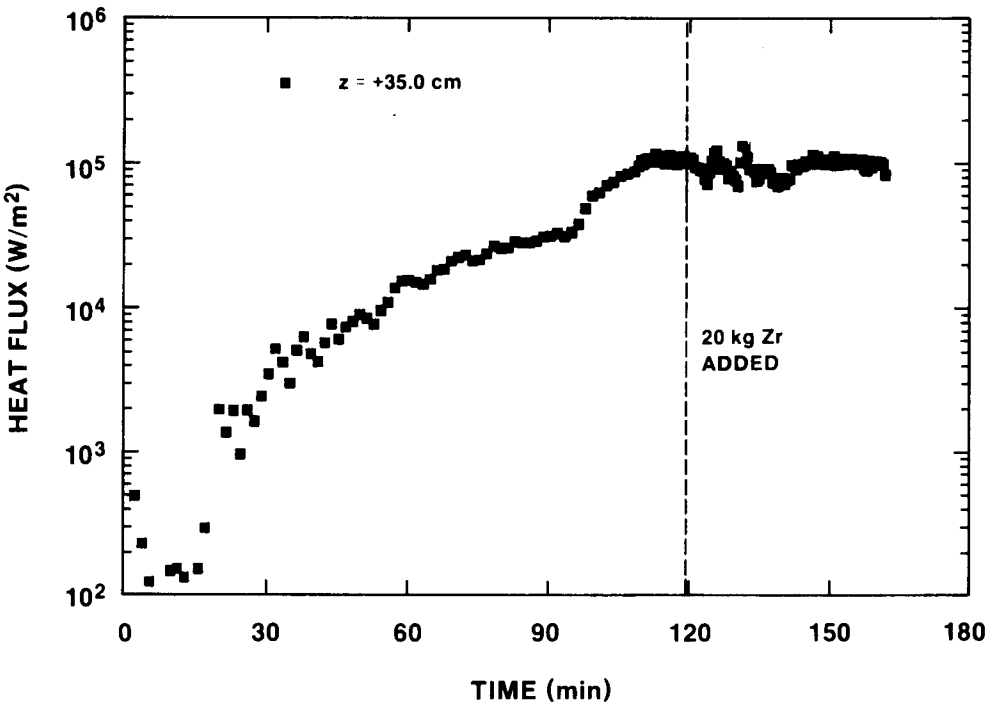

Figure E-41 - MgO Sidewall Heat Flux Calculated from Thermocouple Data for the Array Located at z = +35.0 cm.

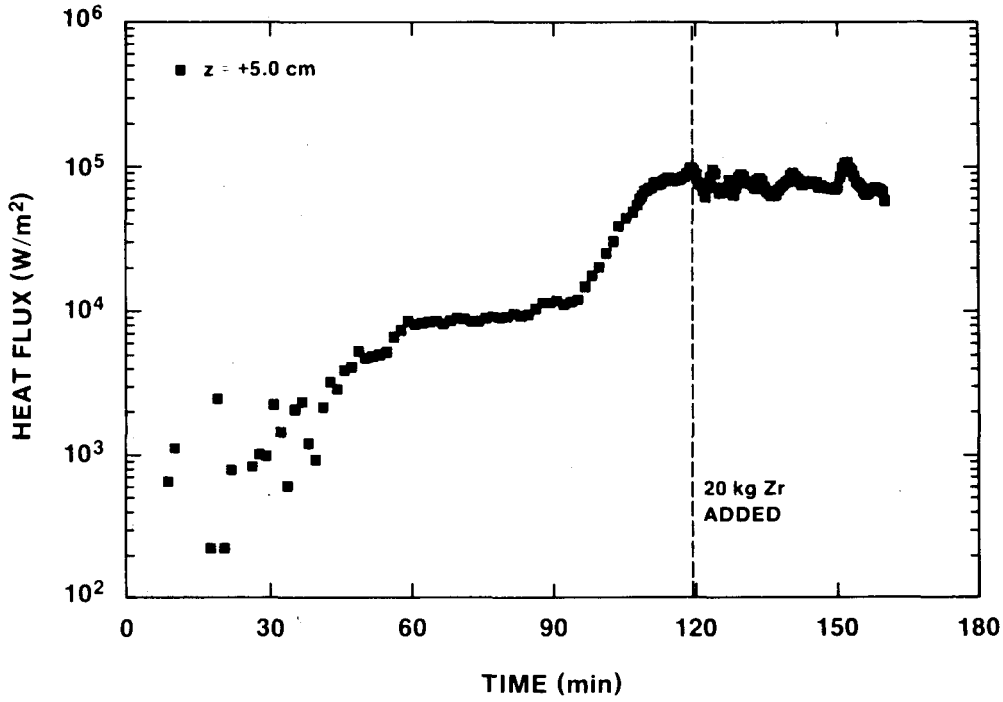

Figure E-42 - MgO Sidewall Heat Flux Calculated from Thermocouple Data for the Array Located at z = +50.0 cm.

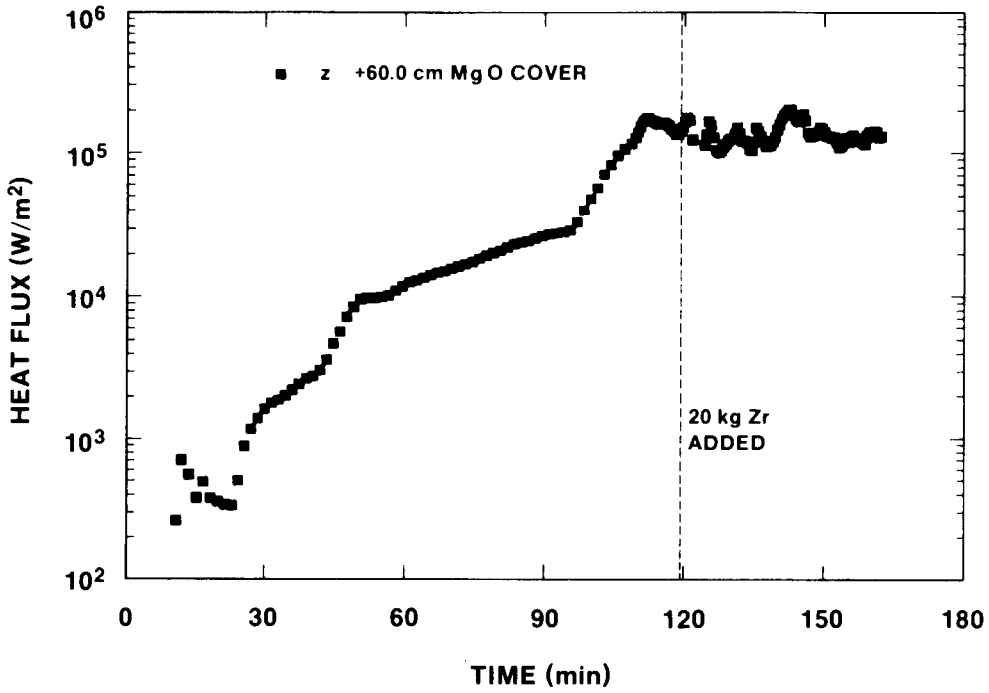

Figure E-43 - MgO Cover Heat Flux Calculated from Thermocouple Data for the Array Located at r = 10.0 cm, θ = 0, and Z = +60.0 cm.

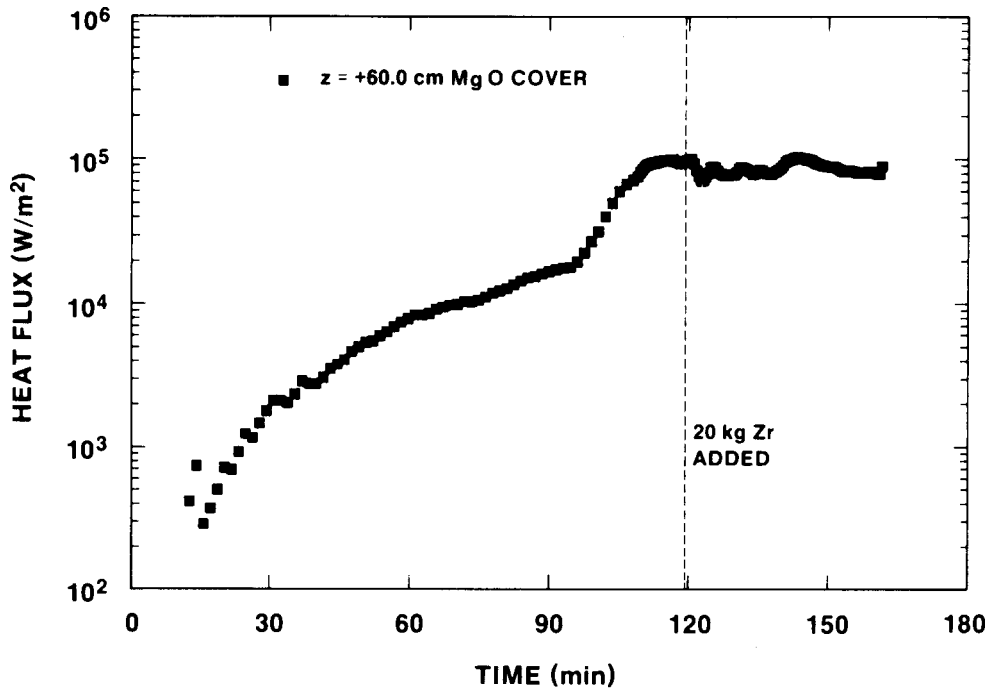

Figure E-44 - MgO Cover Heat Flux Calculated from Thermocouple Data for the Array Located at r = 10.0 cm, θ = 180, znd z = +60.0 cm.

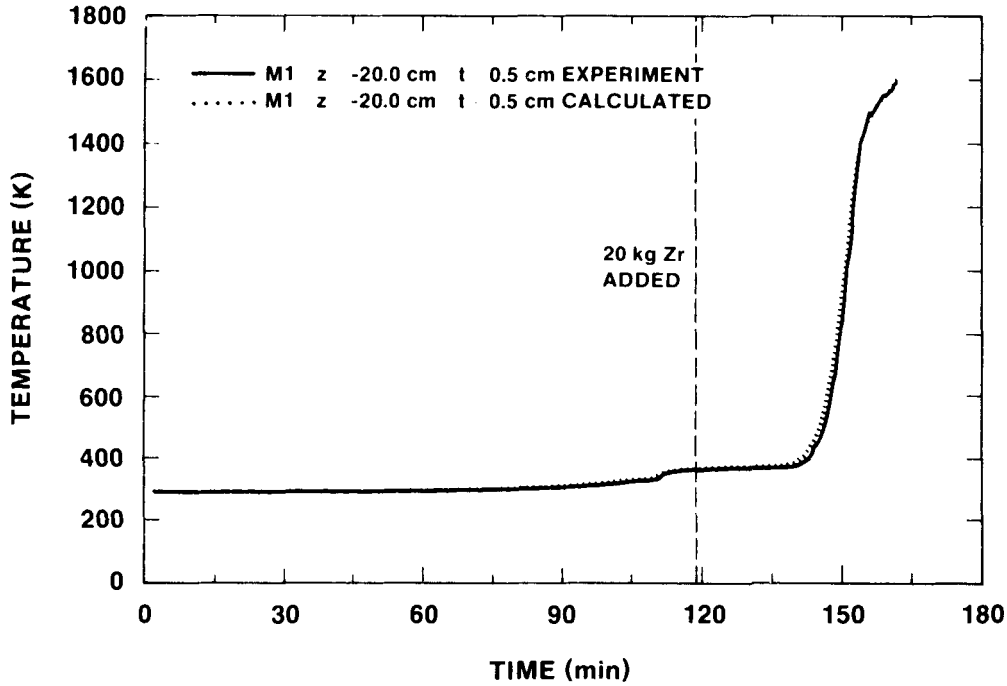

Figure E-45 - Comparison of Sidewall Temperatures Measured during the Experiment and Calculated from the Heat Flux Code for the Thermocouple Located at z = -20.0 cm and t = 0.5 cm.

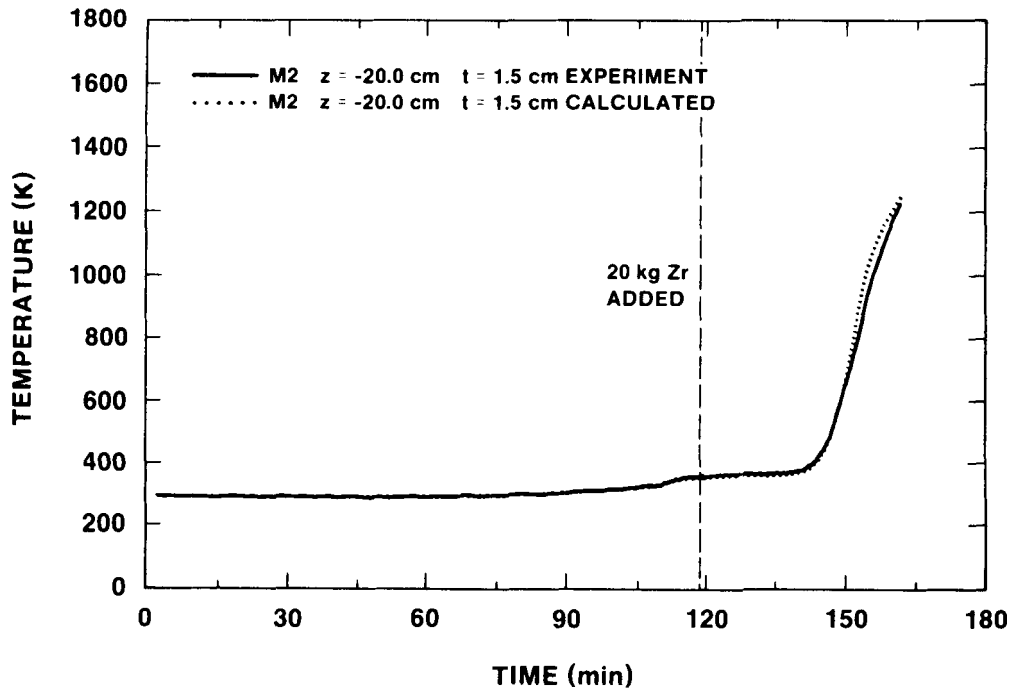

Figure E-46 - Comparison of Sidewall Temperatures Measured during the Experiment and Calculated from the Heat Flux Code for the Thermocouple Located at z = -20.0 cm and t = 1.5 cm.

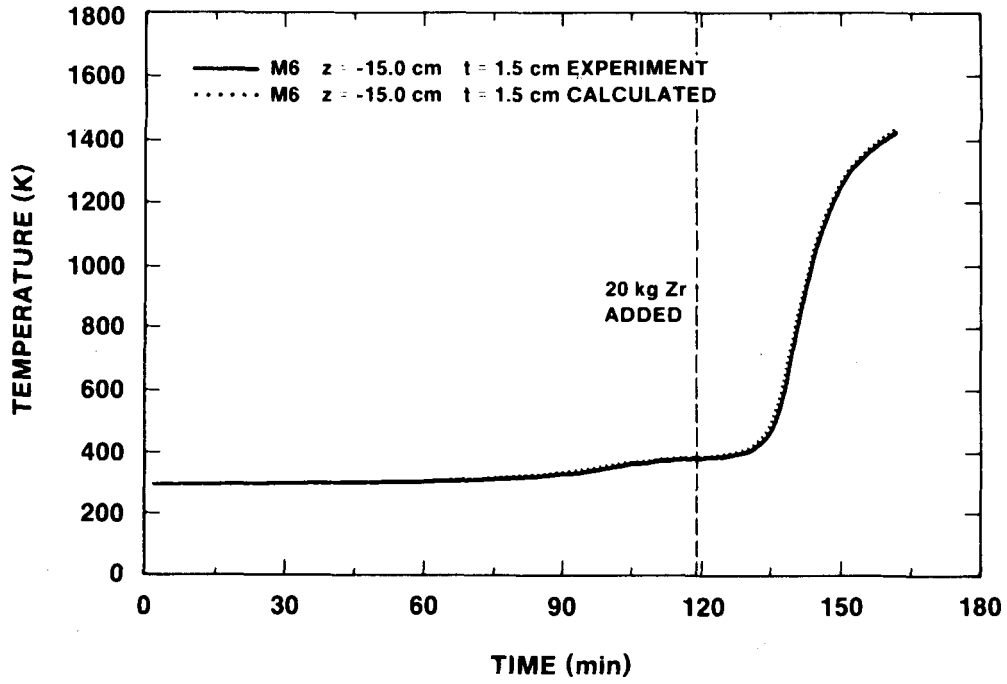

Figure E-47 - Comparison of Sidewall Temperatures Measured during the Experiment and Calculated from the Heat Flux Code for the Thermocouple Located at z = -15.0 cm and t = 1.5 cm.

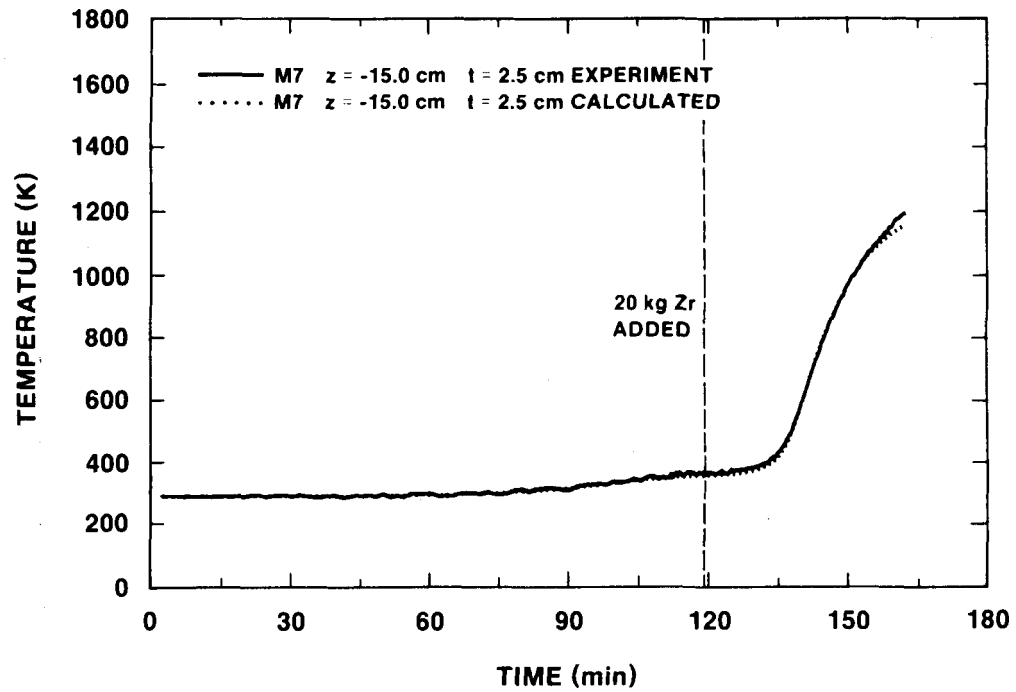

Figure E-48 - Comparison of Sidewall Temperatures Measured during the Experiment and Calculated from the Heat Flux Code for the Thermocouple Located at z = -15.0 cm and t = 2.5 cm.

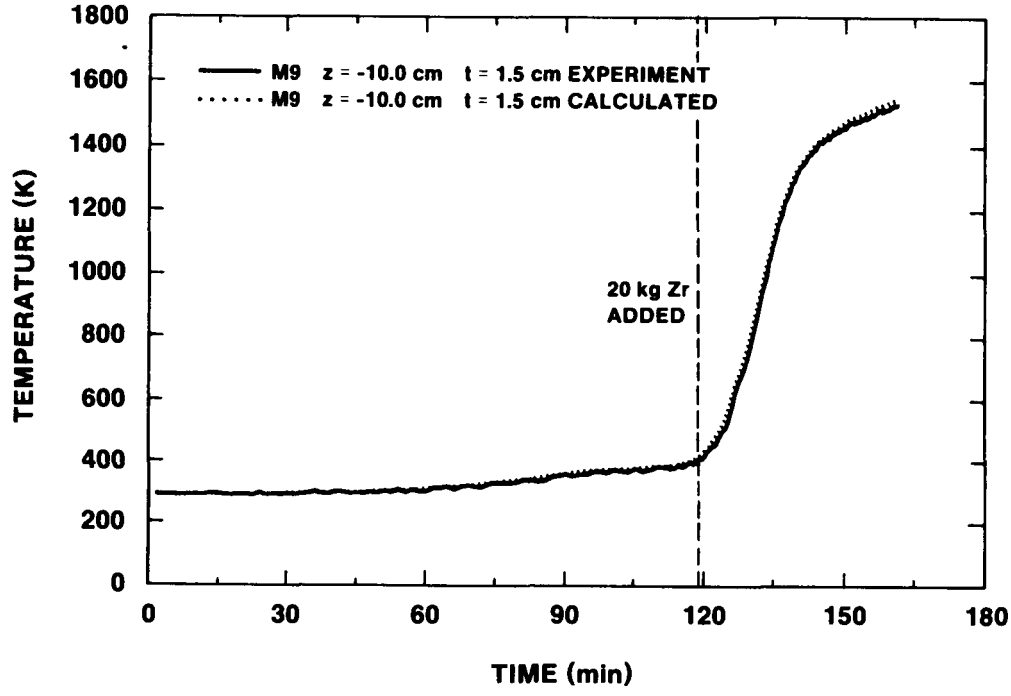

Figure E-49 - Comparison of Sidewall Temperatures Measured during the Experiment and Calculated from the Heat Flux Code for the Thermocouple Located at z = -10.0 cm and t = 1.5 cm.

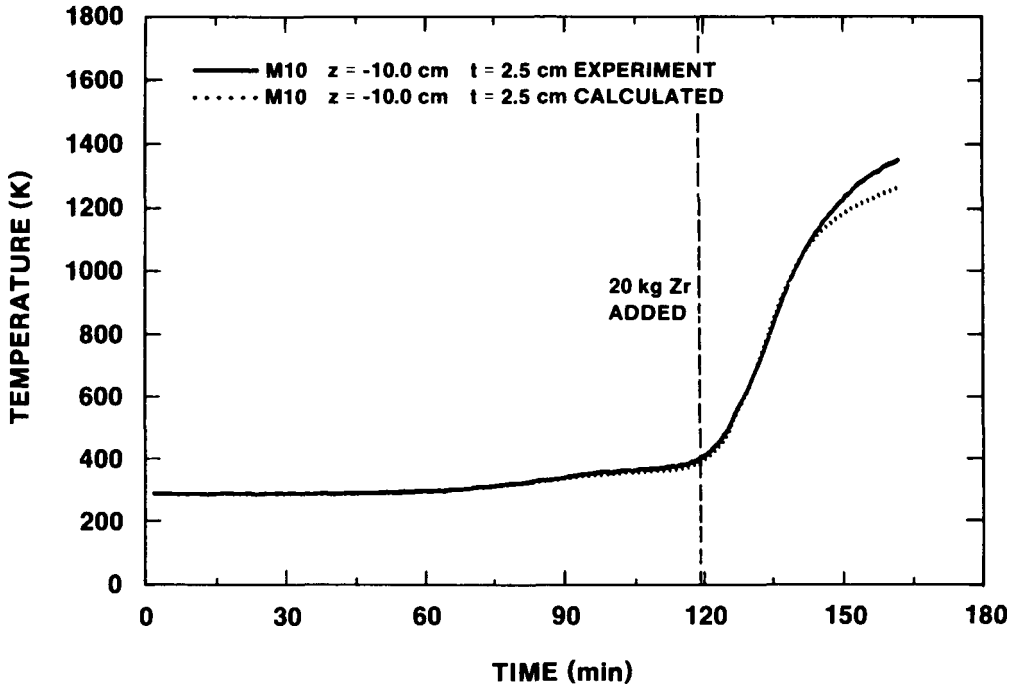

Figure E-50 - Comparison of Sidewall Temperatures Measured during the Experiment and Calculated from the Heat Flux Code for the Thermocouple Located at z = -10.0 cm and t = 2.5 cm.

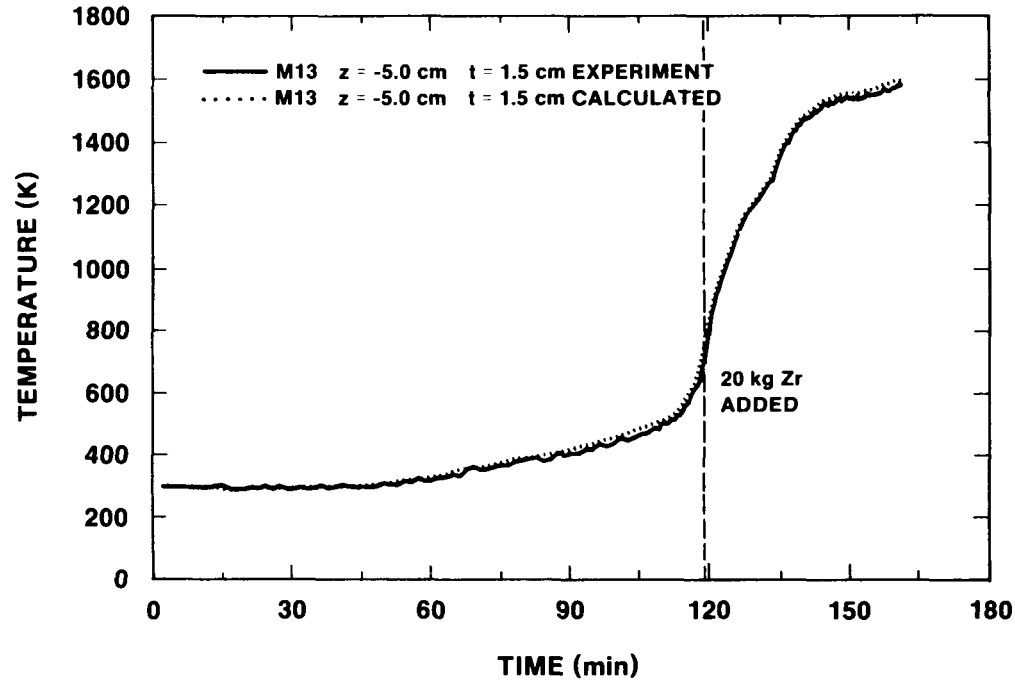

Figure E-51 - Comparison of Sidewall Temperatures Measured during the Experiment and Calculated from the Heat Flux Code for the Thermocouple Located at z = -5.0 cm and t = 1.5 cm.

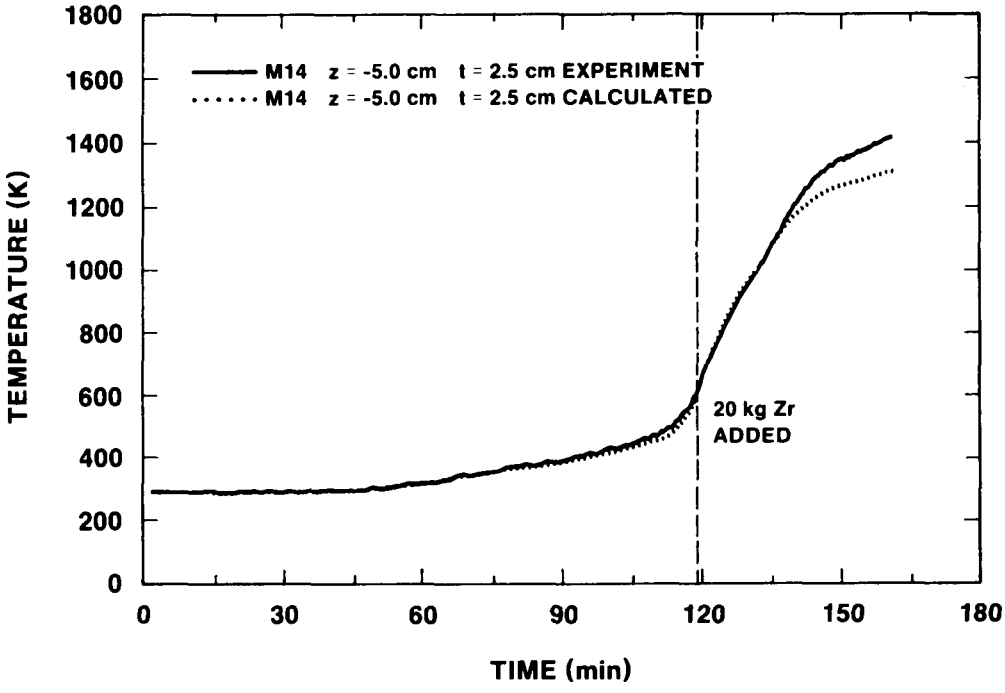

Figure E-52 - Comparison of Sidewall Temperatures Measured during the Experiment and Calculated from the Heat Flux Code for the Thermocouple Located at z = -50.0 cm and t = 2.5 cm.

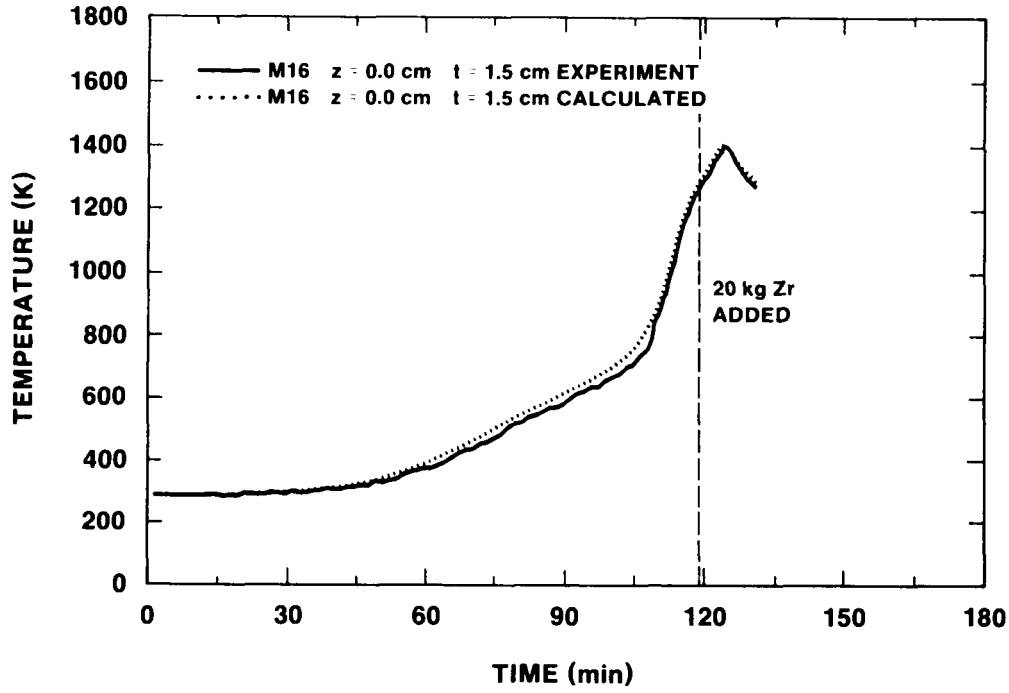

Figure E-53 - Comparison of Sidewall Temperatures Measured during the Experiment and Calculated from the Heat Flux Code for the Thermocouple Located at z = 0.0 cm and t = 1.5 cm.

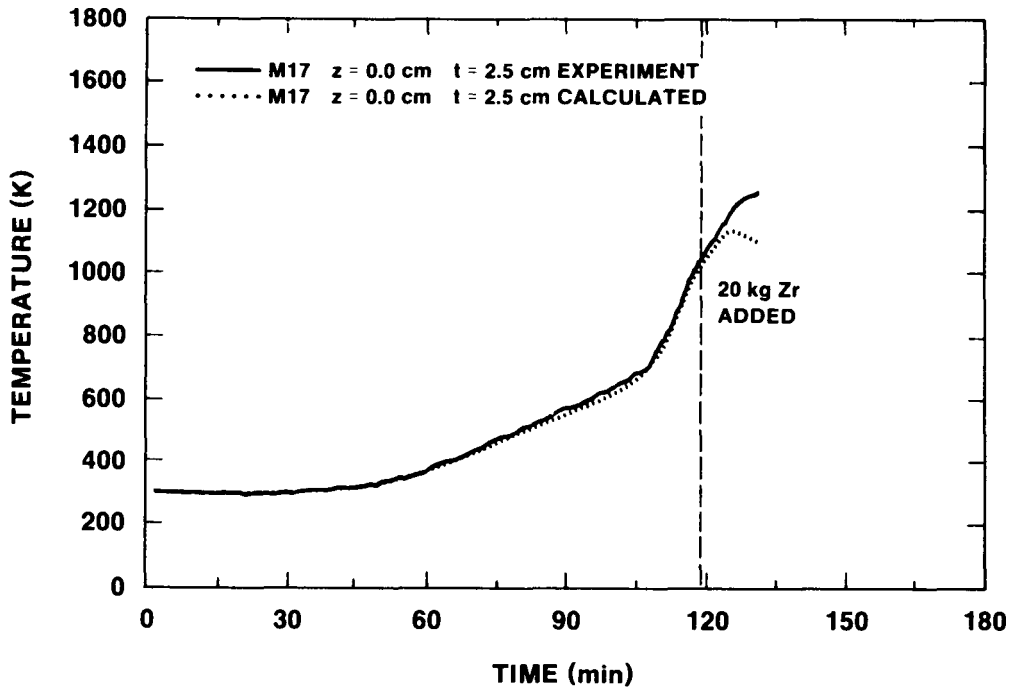

Figure E-54 - Comparison of Sidewall Temperatures Measured during the Experiment and Calculated from the Heat Flux Code for the Thermocouple Located at z = 0.0 cm and t = 2.5 cm.

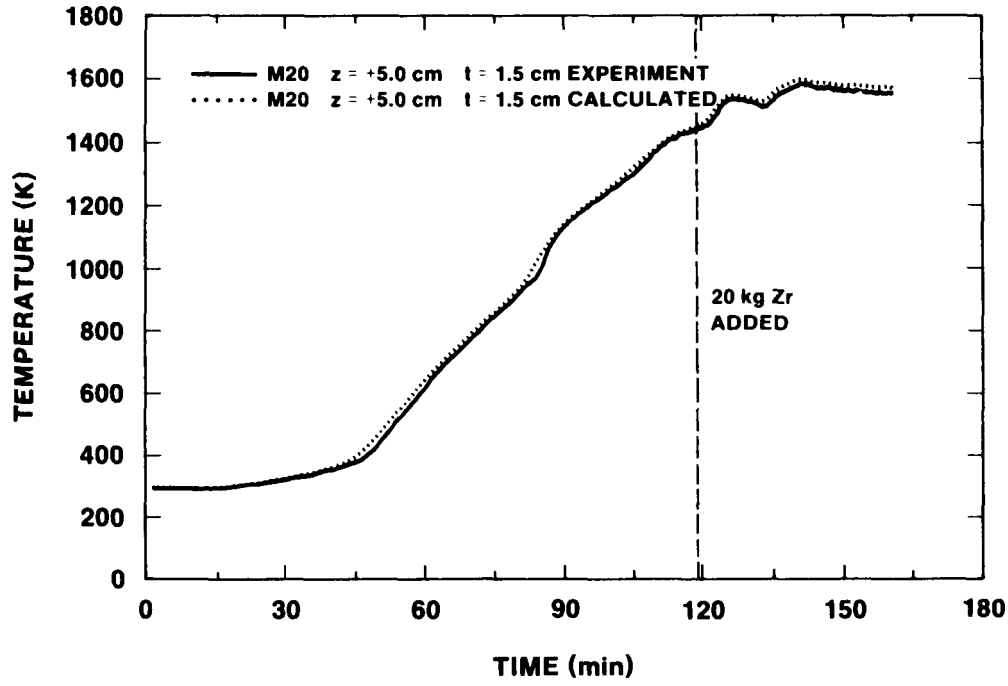

Figure E-55 - Comparison of Sidewall Temperatures Measured during the Experiment and Calculated from the Heat Flux Code for the Thermocouple Located at z = +5.0 cm and t = 1.5 cm.

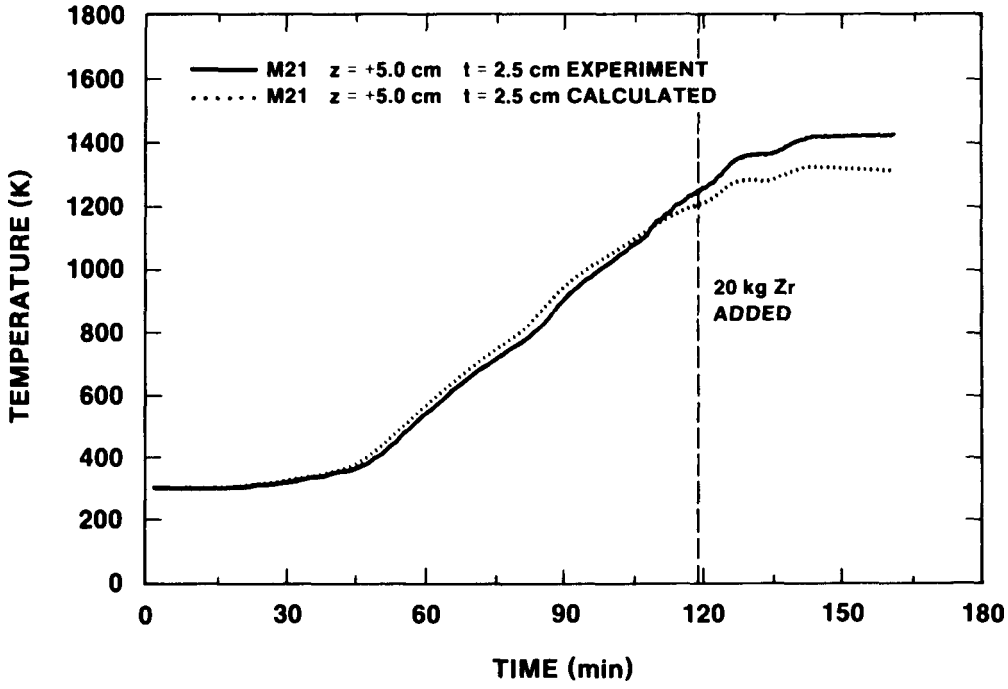

Figure E-56 - Comparison of Sidewall Temperatures Measured during the Experiment and Calculated from the Heat Flux Code for the Thermocouple Located at z = +5.0 cm and t = 2.5 cm.

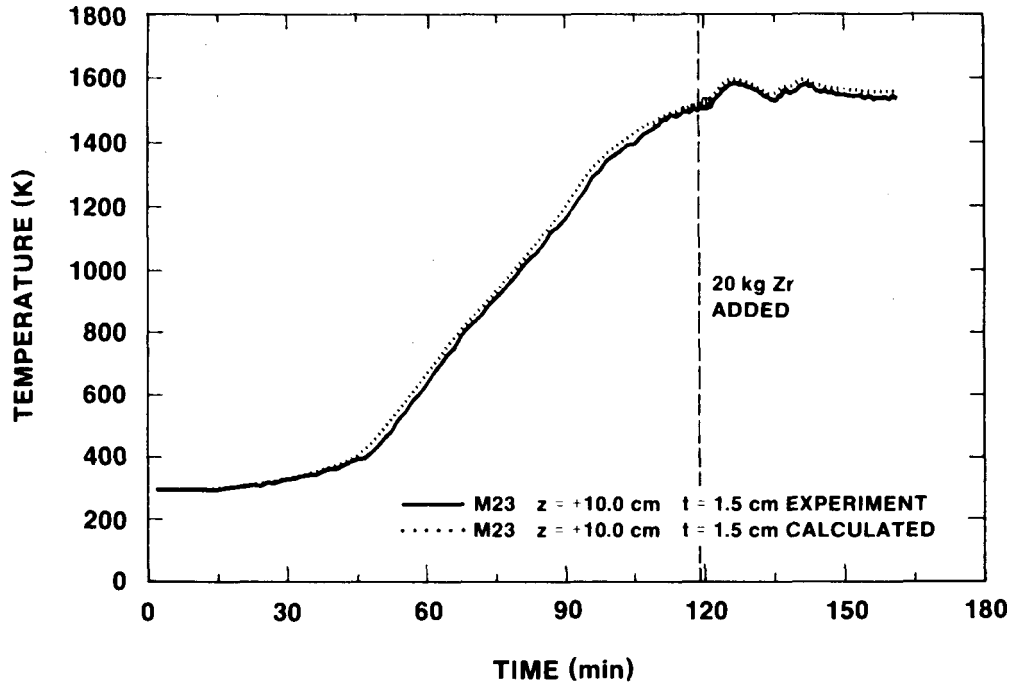

Figure E-57 - Comparison of Sidewall Temperatures Measured during the Experiment and Calculated from the Heat Flux Code for the Thermocouple Located at z = +10.0 cm and t = 1.5 cm.

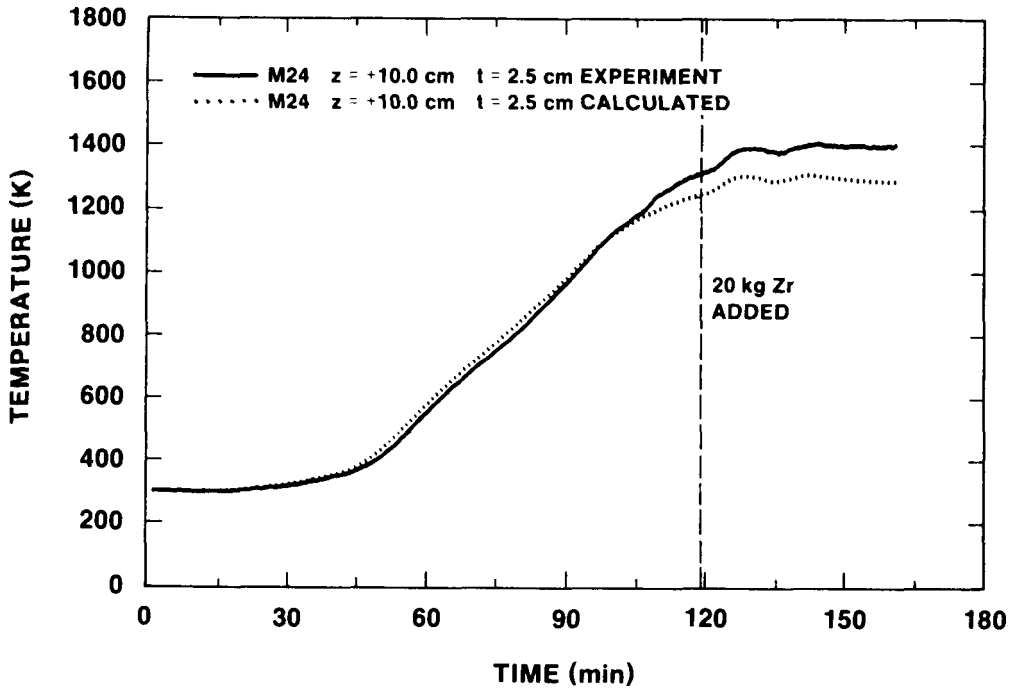

Figure E-58 - Comparison of Sidewall Temperatures Measured during the Experiment and Calculated from the Heat Flux Code for the Thermocouple Located at z = +10.0 cm and t = 2.5 cm.

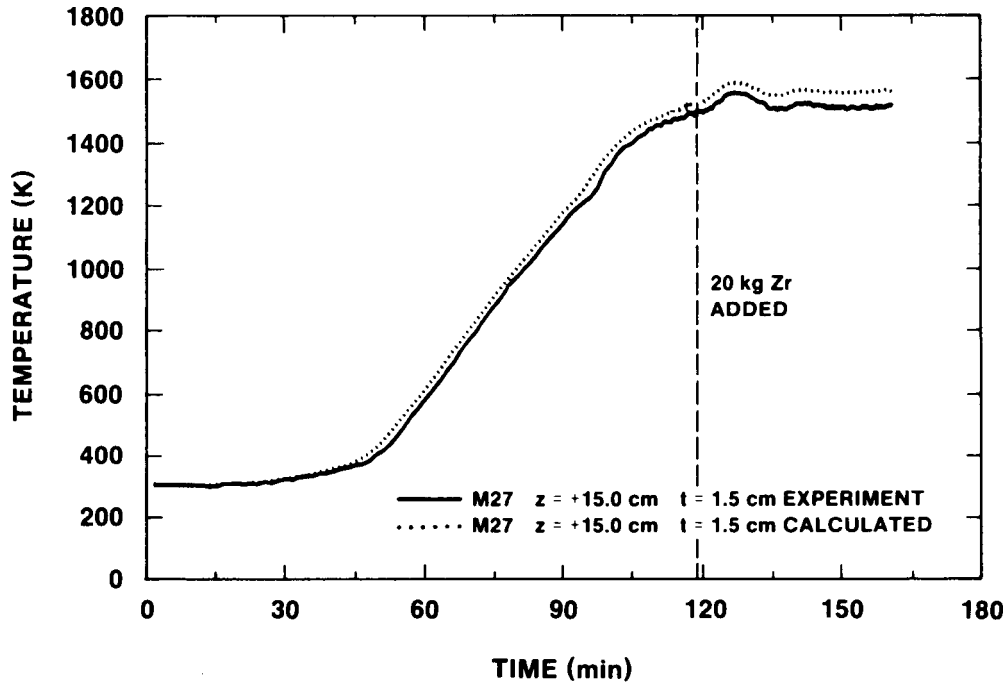

Figure E-59 - Comparison of Sidewall Temperatures Measured during the Experiment and Calculated from the Heat Flux Code for the Thermocouple Located at z = +15.0 cm and t = 1.5 cm.

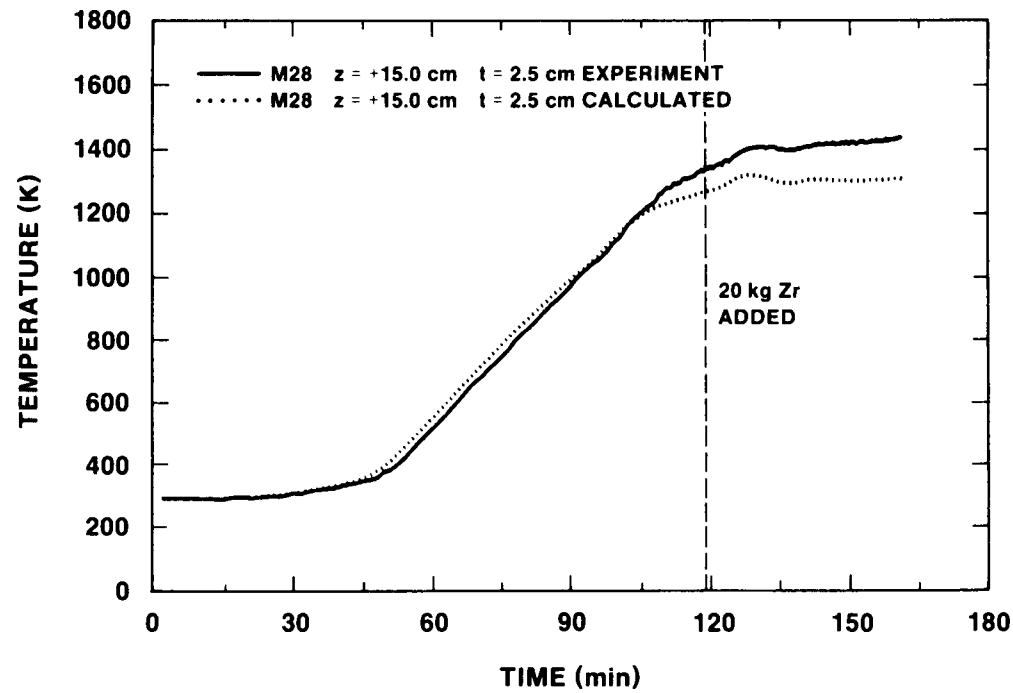

Figure E-60 - Comparison of Sidewall Temperatures Measured during the Experiment and Calculated from the Heat Flux Code for the Thermocouple Located at z = +15.0 cm and t = 2.5 cm.

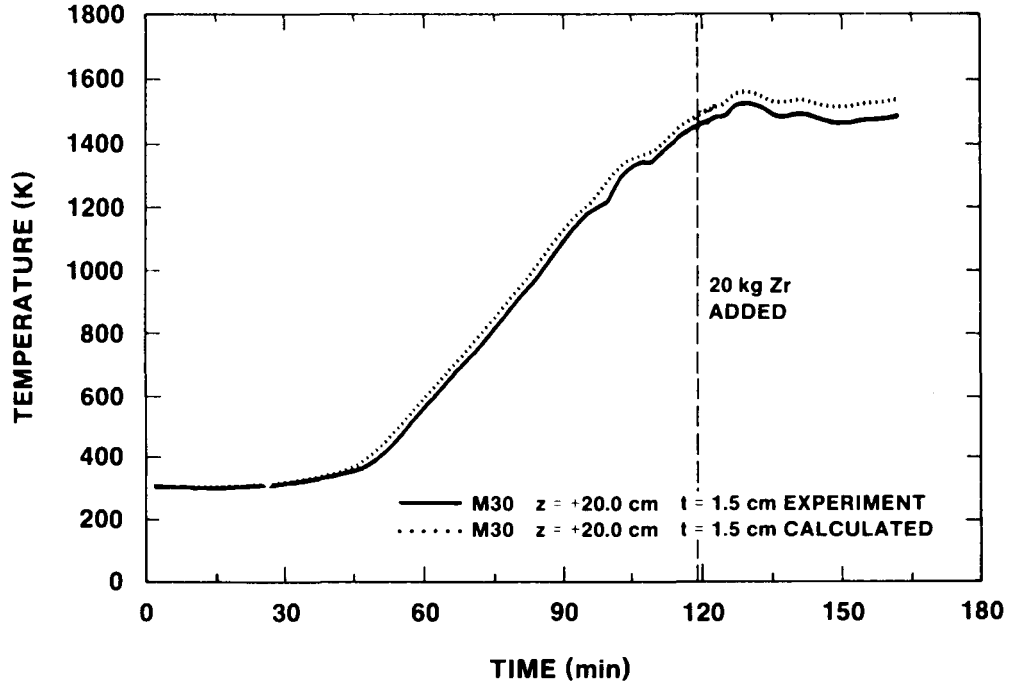

Figure E-61 - Comparison of Sidewall Temperatures Measured during the Experiment and Calculated from the Heat Flux Code for the Thermocouple Located at z = +20.0 cm and t = 1.5 cm.

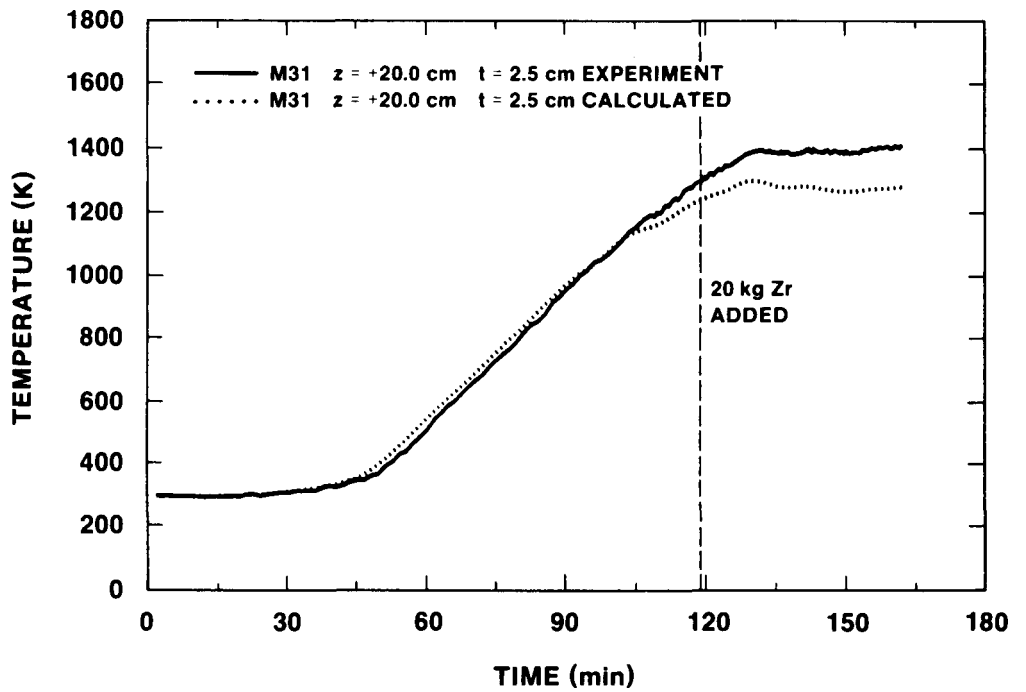

Figure E-62 - Comparison of Sidewall Temperatures Measured during the Experiment and Calculated from the Heat Flux Code for the Thermocouple Located at z = +20.0 cm and t = 2.5 cm.

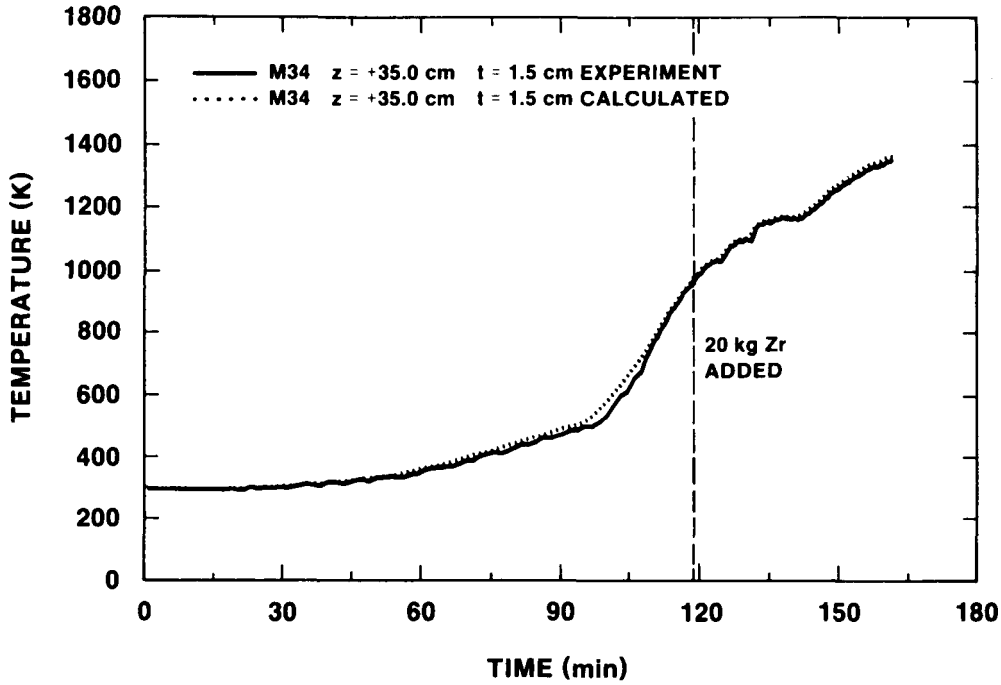

Figure E-63 - Comparison of Sidewall Temperatures Measured during the Experiment and Calculated from the Heat Flux Code for the Thermocouple Located at z = +35.0 cm and t = 1.5 cm.

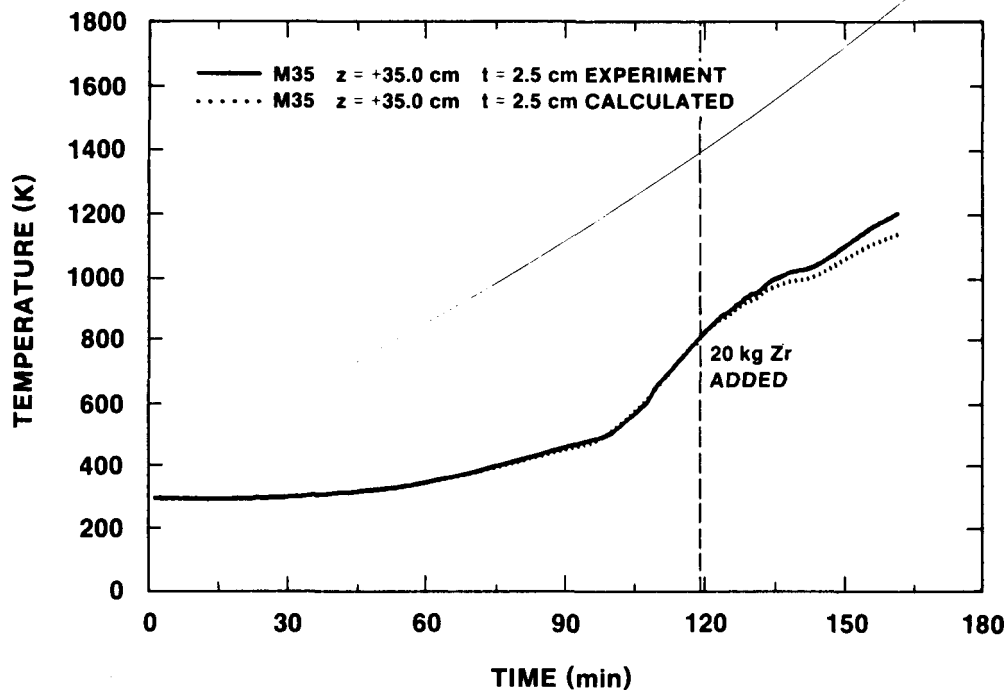

Figure E-64 - Comparison of Sidewall Temperatures Measured during the Experiment and Calculated from the Heat Flux Code for the Thermocouple Located at z = +35.0 cm and t = 2.5 cm.

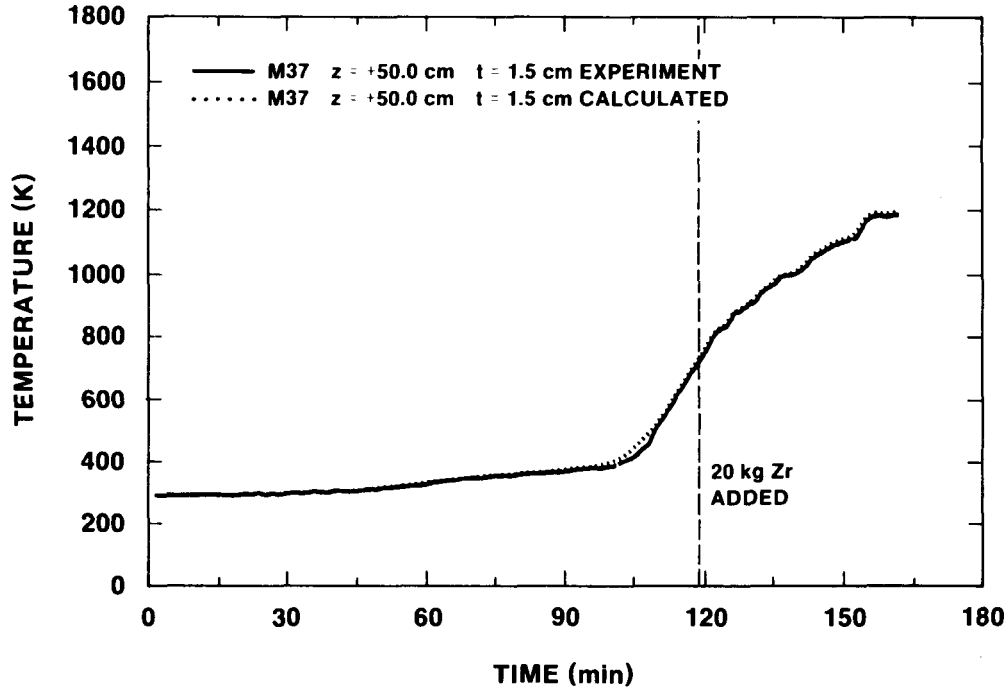

Figure E-65 - Comparison of Sidewall Temperatures Measured during the Experiment and Calculated from the Heat Flux Code for the Thermocouple Located at z = +50.0 cm and t = 1.5 cm.

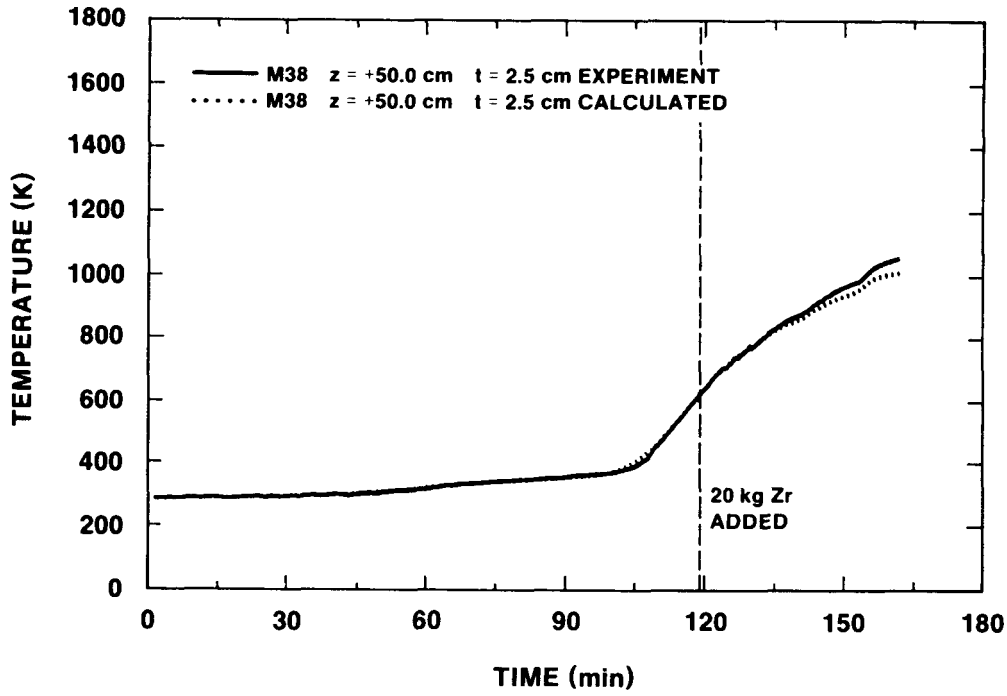

Figure E-66 - Comparison of Sidewall Temperatures Measured during the Experiment and Calculated from the Heat Flux Code for the Thermocouple Located at z = +50.0 cm and t = 2.5 cm.

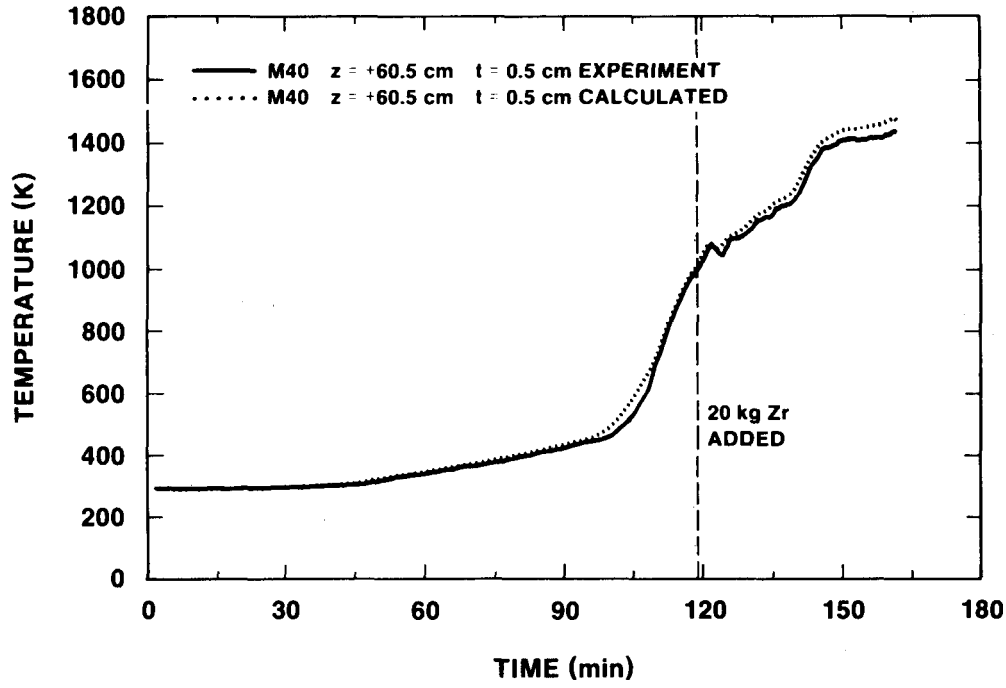

Figure E-67 - Comparison of Cover Temperatures Measured during the Experiment and Calculated from the Heat Flux Code for the Thermocouple Located at r = 10.0 cm, θ = 0, z = +60.0 cm and t = 0.5 cm.

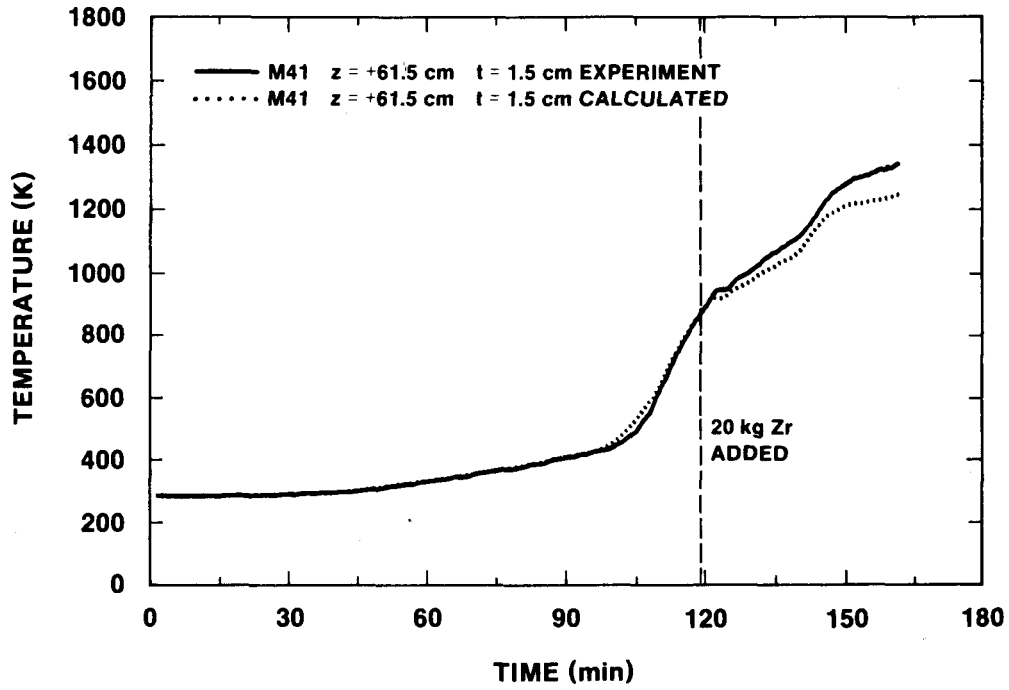

Figure E-68 - Comparison of Cover Temperatures Measured during the Experiment and Calculated from the Heat Flux Code for the Thermocouple Located at r = 10.0 cm, θ = 0, z = +60.0 cm and t = 1.5 cm.

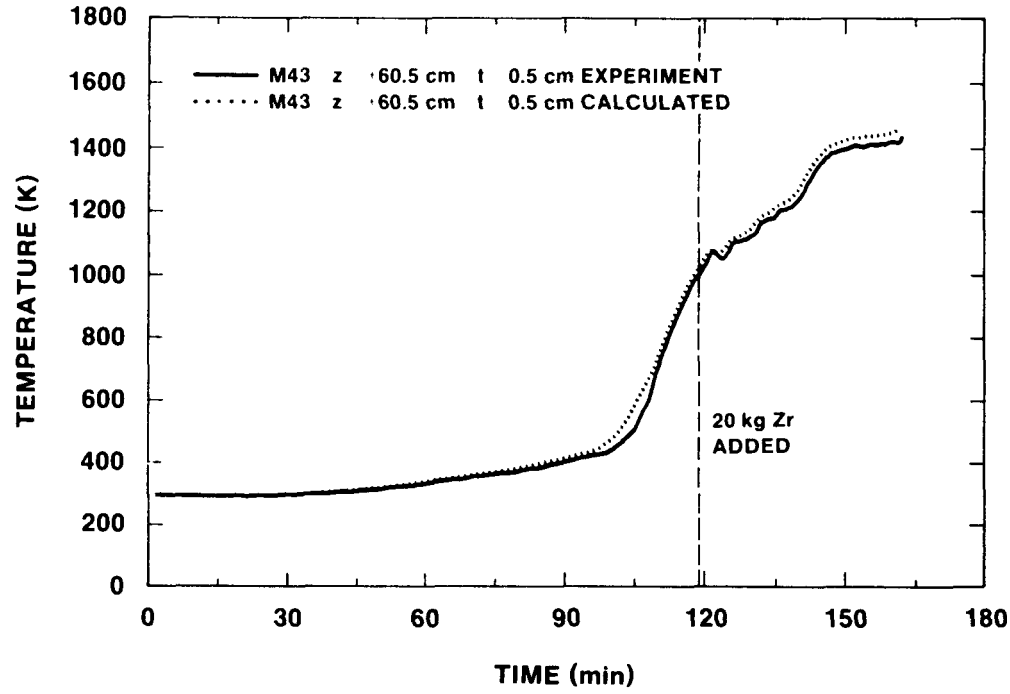

Figure E-69 - Comparison of Cover Temperatures Measured during the Experiment and Calculated from the Heat Flux Code for the Thermocouple

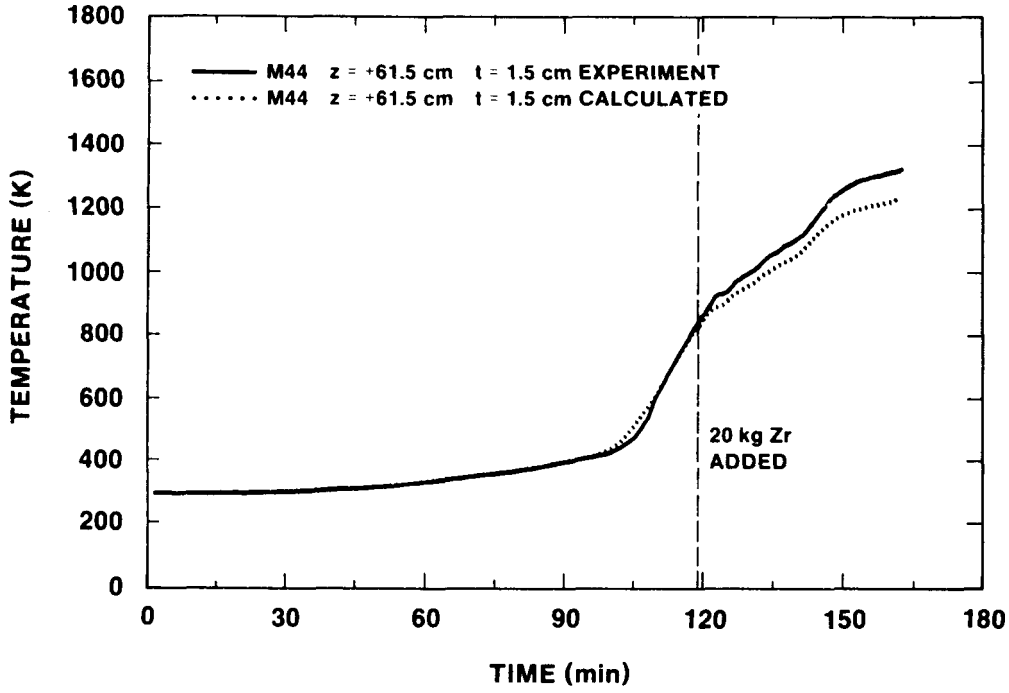

Figure E-70 - Comparison of Cover Temperatures Measured during the Experiment and Calculated from the Heat Flux Code for the Thermocouple Located at r = 10.0 cm, θ = 180, z = +60.0 cm and t = 1.5 cm.

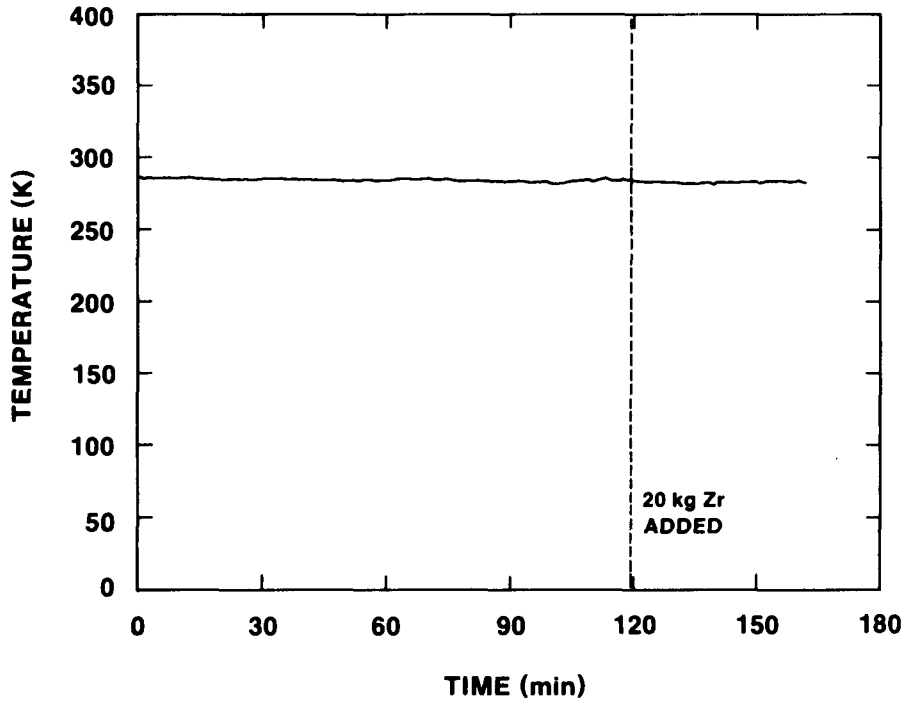

Figure E-71 - Argon Gas Purge Inlet Temperature

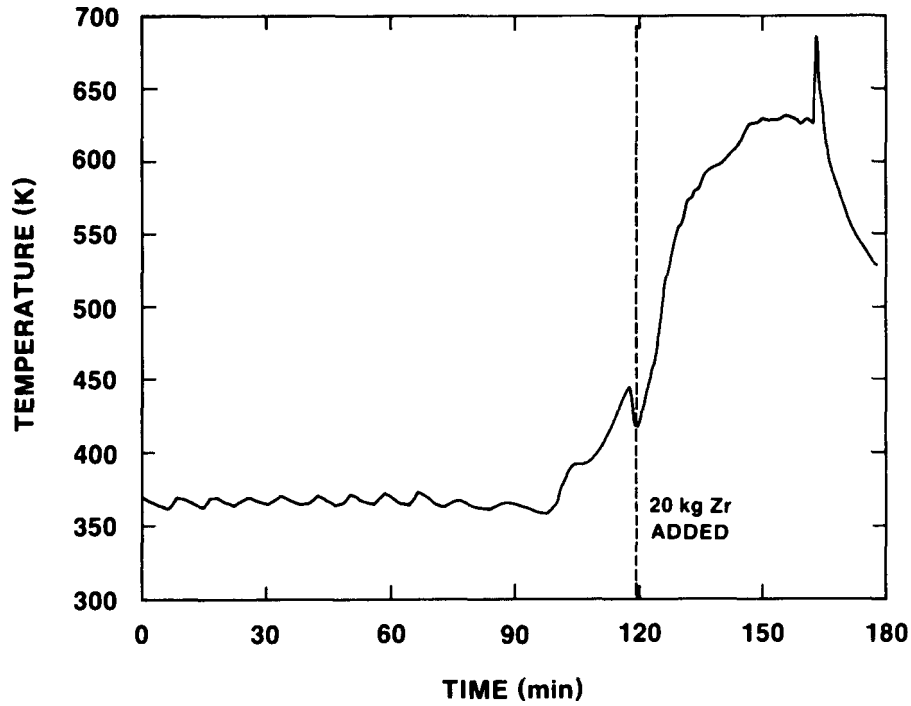

Figure E-72 - Gas Sample Temperature Three Meters Downstream from the Crucible

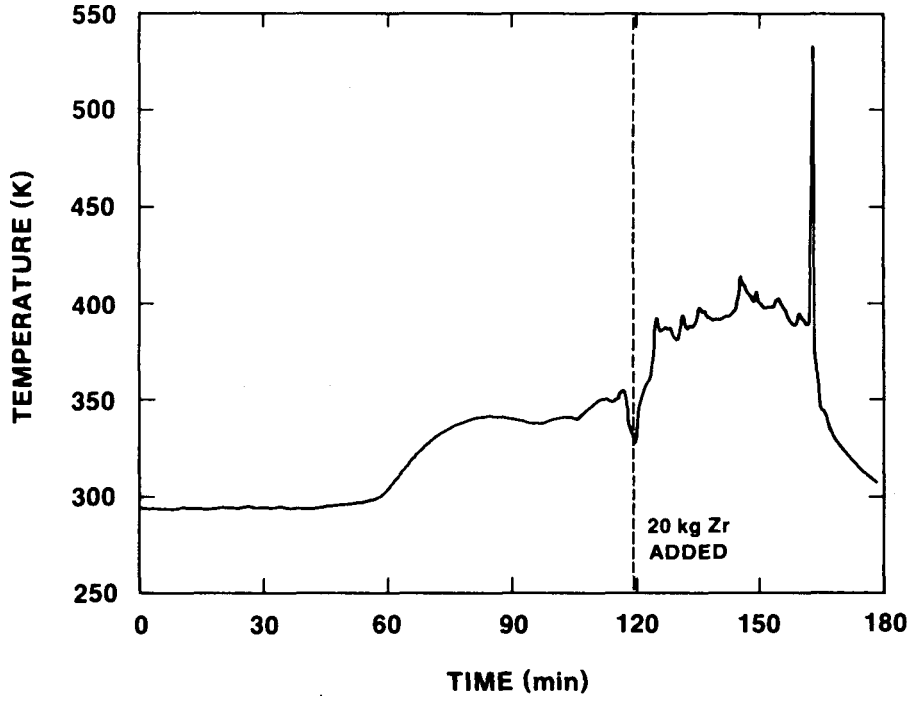

Figure E-73 - Gas Temperature at the ASME Orifice Four Meters Downstream from the Crucible

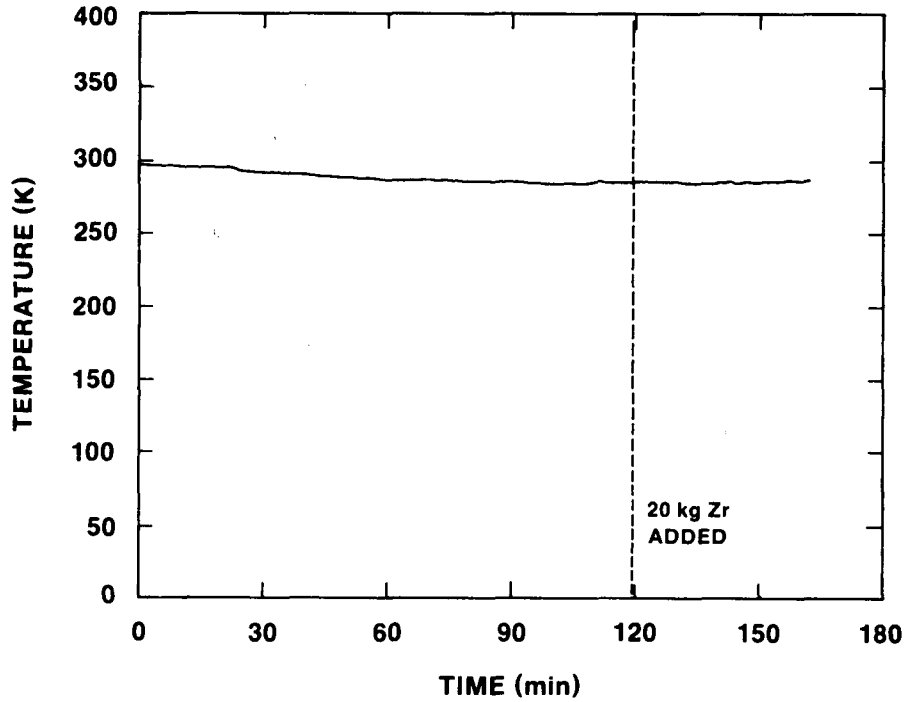

Figure E-74 - Gas Temperature at the Exit of the Flow System Downstream from the Gas Clocks

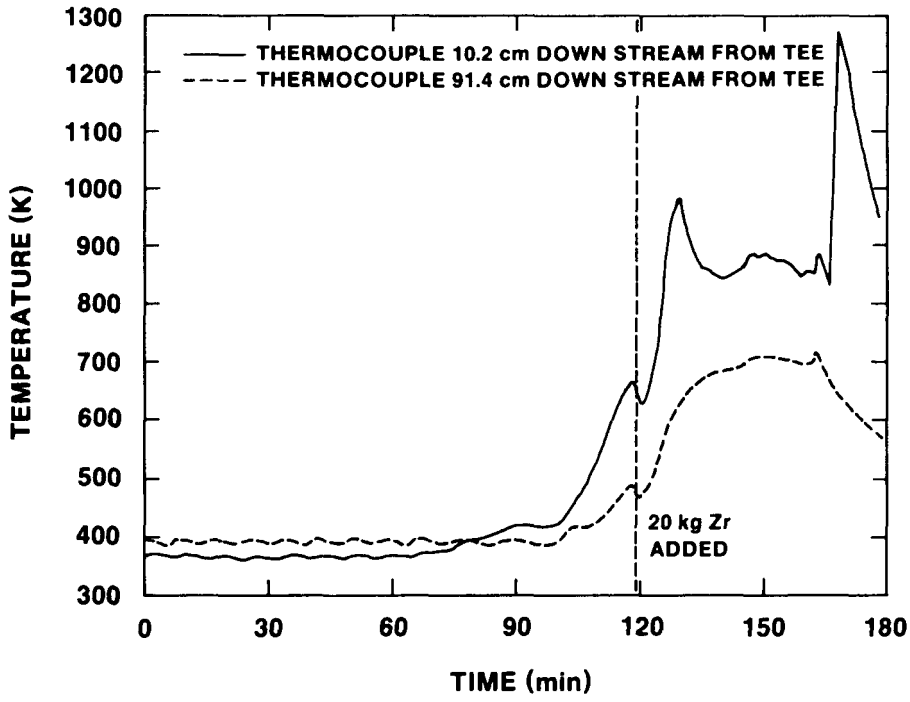

Figure E-75 - Flow Tube Temperature 10.2 cm and 91.4 Downstream from the Tee

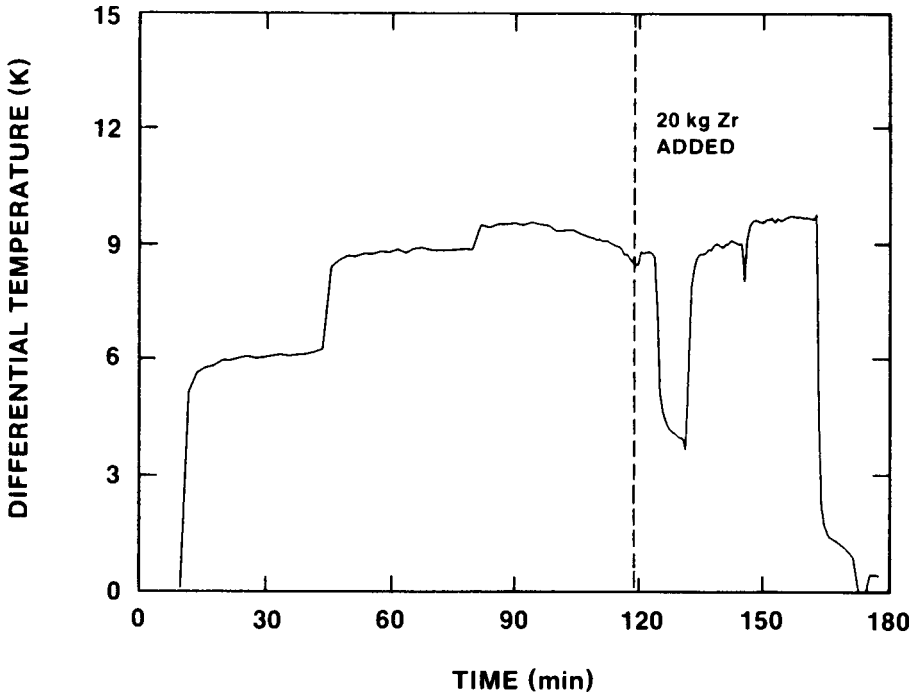

Figure E-76 - Temperature of the Cooling Fluid Flowing Through the Induction Power Supply

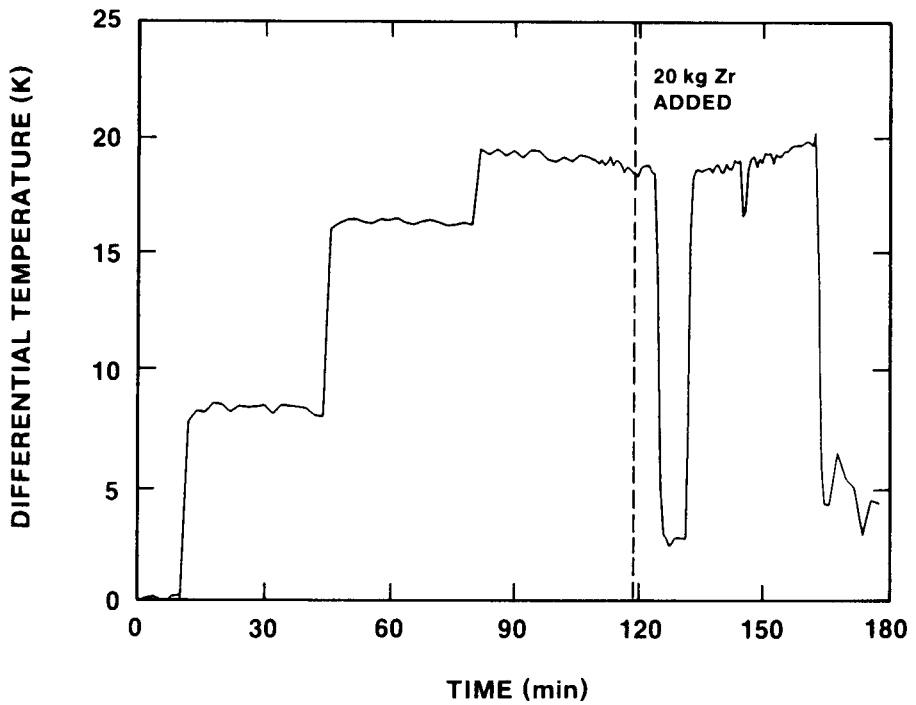

Figure E-77 - Temperature of the Cooling Fluid Flowing Through the Induction Coil

APPENDIX F

SURC 4 PRESSURE AND FLOW PROFILES

Enclosed in this appendix are the calibration data for the pressure transducers used in the flow system, calibration plots of the flow devices used in the experiment, pressure and flow data taken during the experiment, and finally flow rate data for the cooling fluid flowing through the induction power supply and coil.

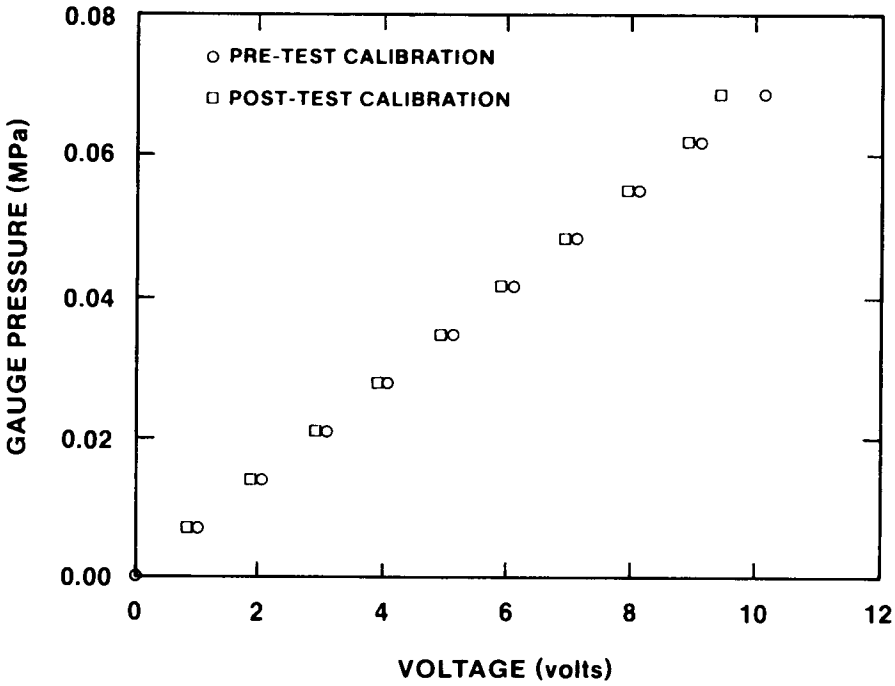

Figure F-1 - Gauge Pressure Transducer Calibration Located at the Containment Vessel

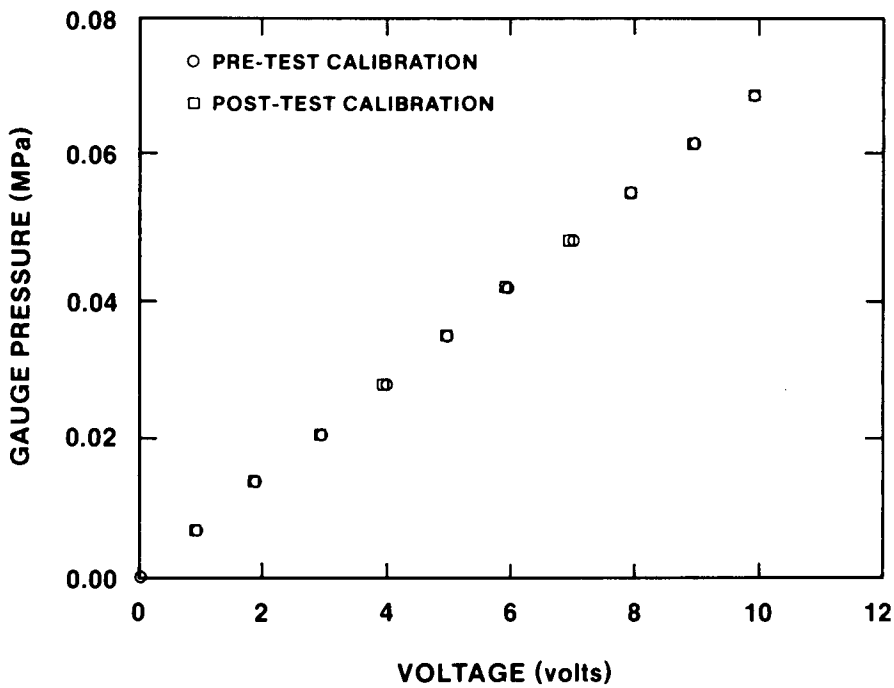

Figure F-2 - Gauge Pressure Transducer Calibration Located Upstream of the ASME Orifice

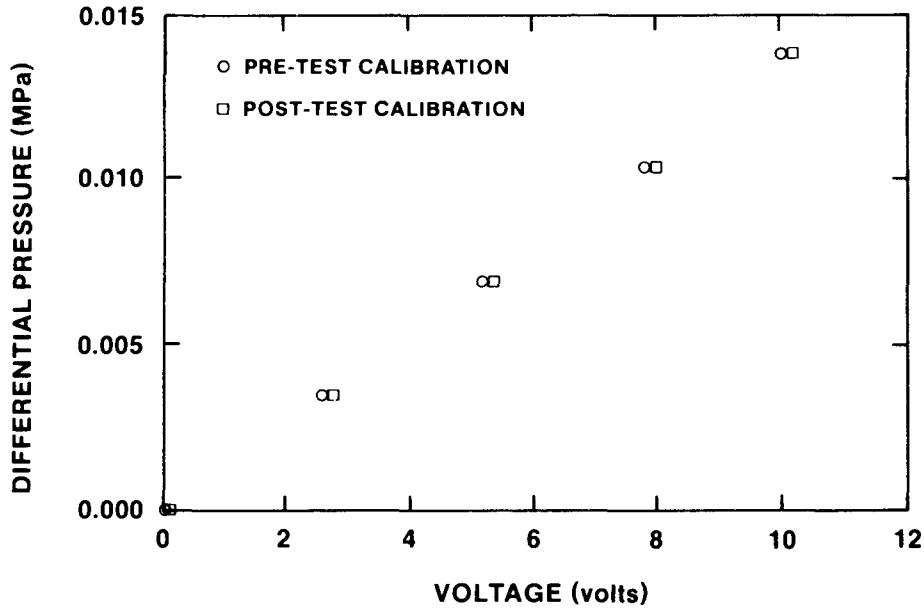

Figure F-3 - Differential Pressure Transducer Calibration Located Across AME Orifice

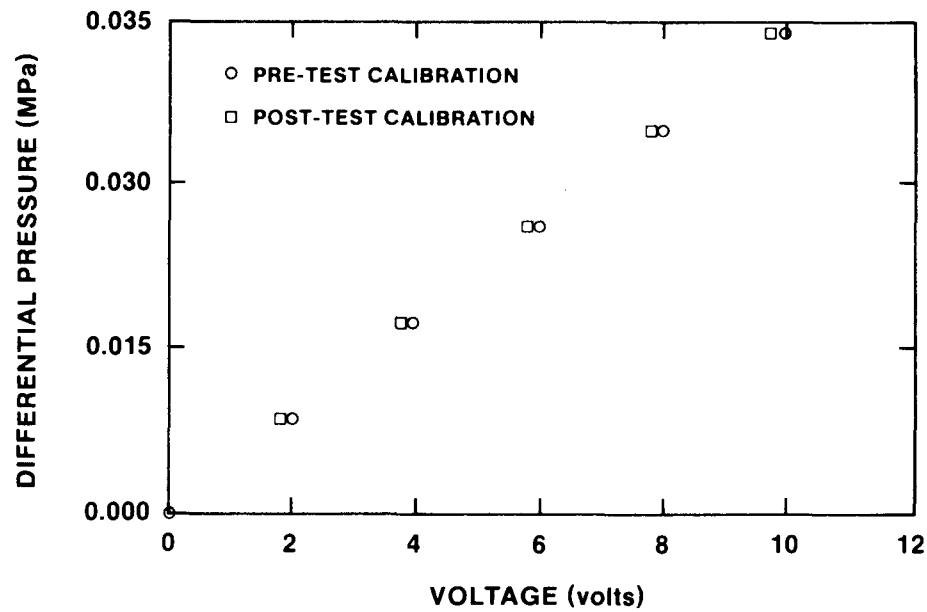

Figure F-4 - Differential Pressure Transducer Calibration Located Across ASME Orifice

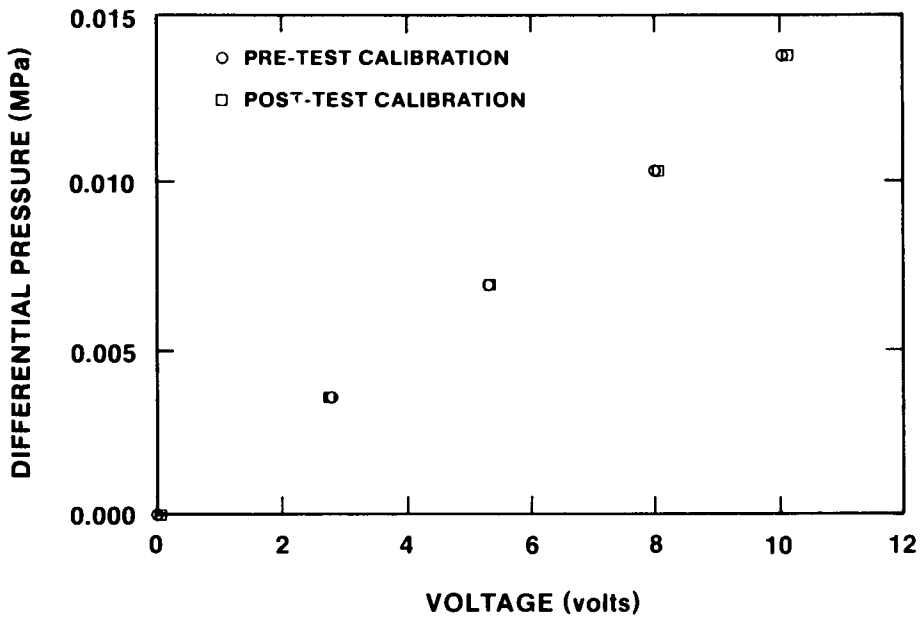

Figure F-5 - Differential Pressure Transducer Calibration Located Across the Laminar Flow Device

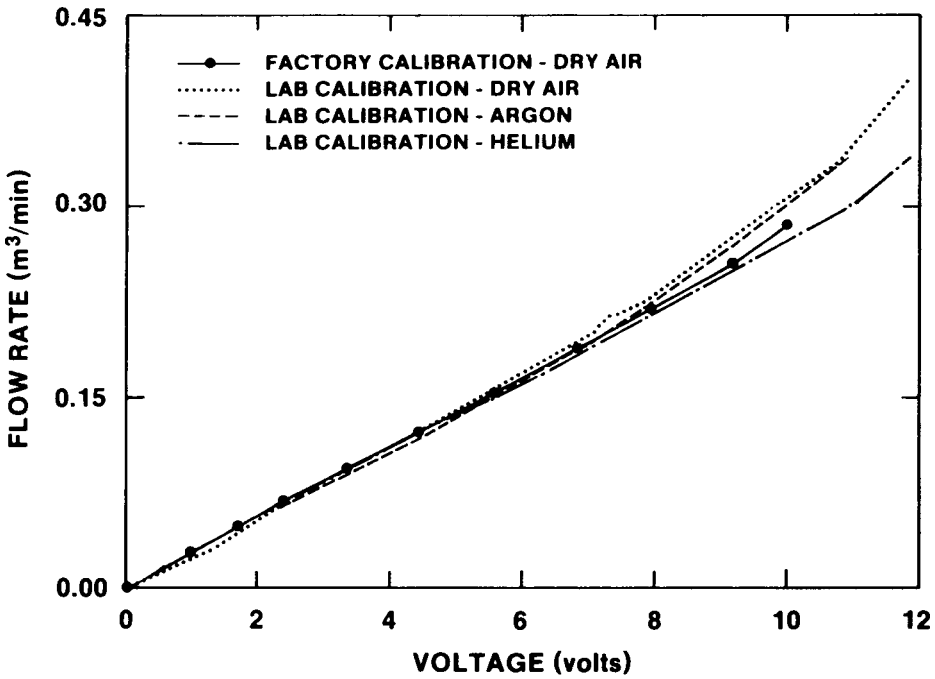

Figure F-6 - Tubine Meter Calibration

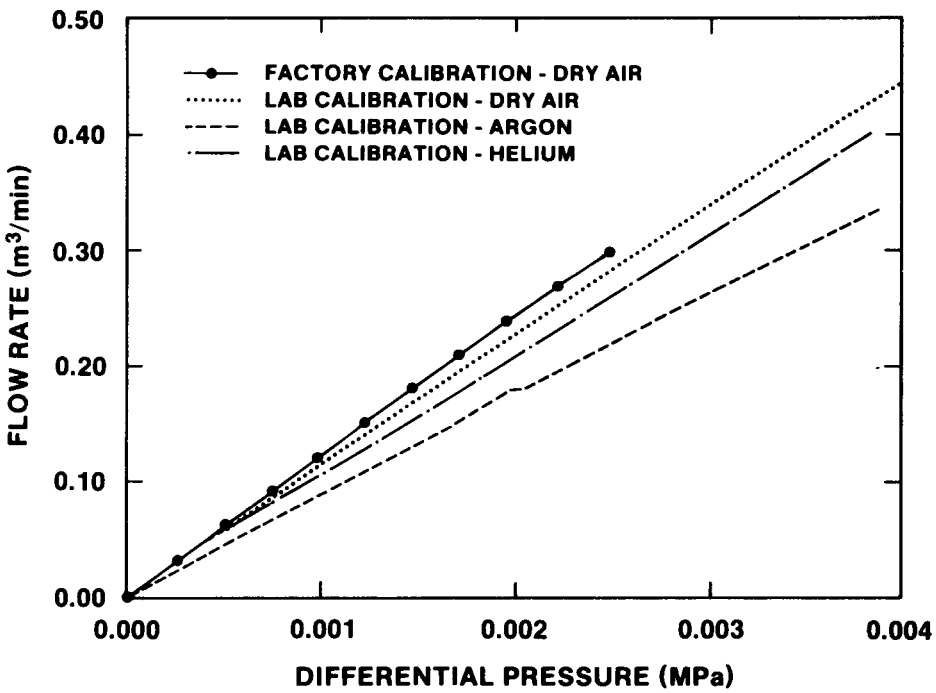

Figure F-7 - Laminar Flow Element Calibration

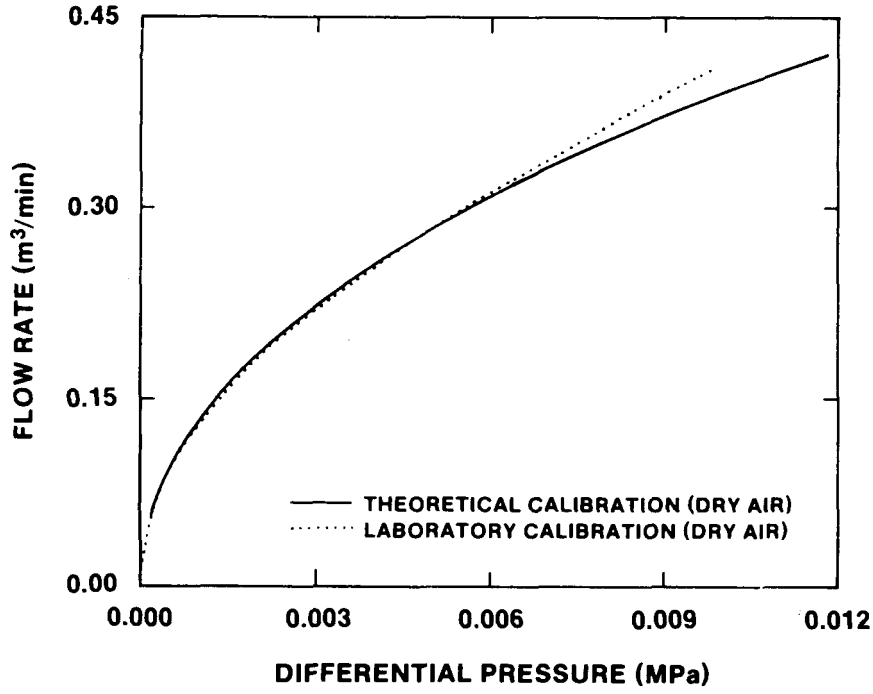

Figure F-8 - ASME Sharp Edge Concentric Orifice Calibration (Dry Air)

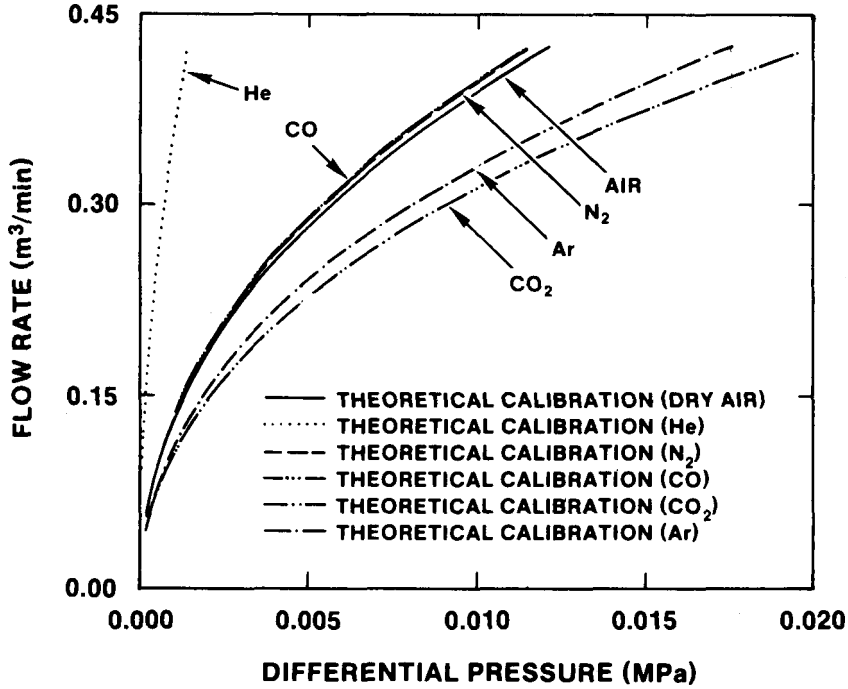

Figure F-9 - Theoretical Calibration ASME Sharp Edge Concentric Orifice

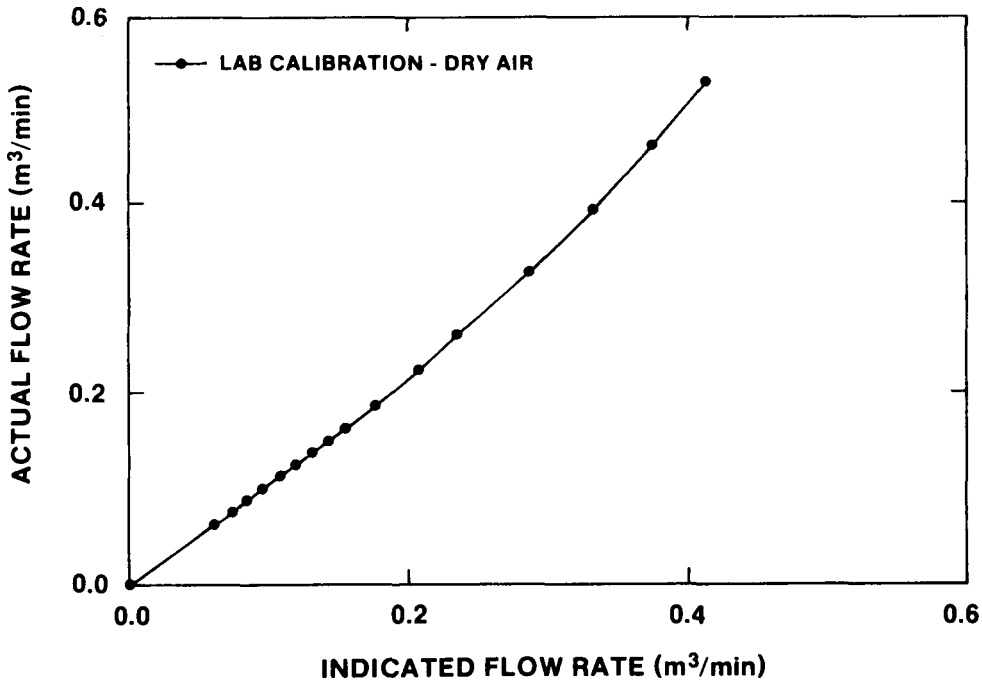

Figure F-10 - Rockwell 415 Gas Clock Calibration

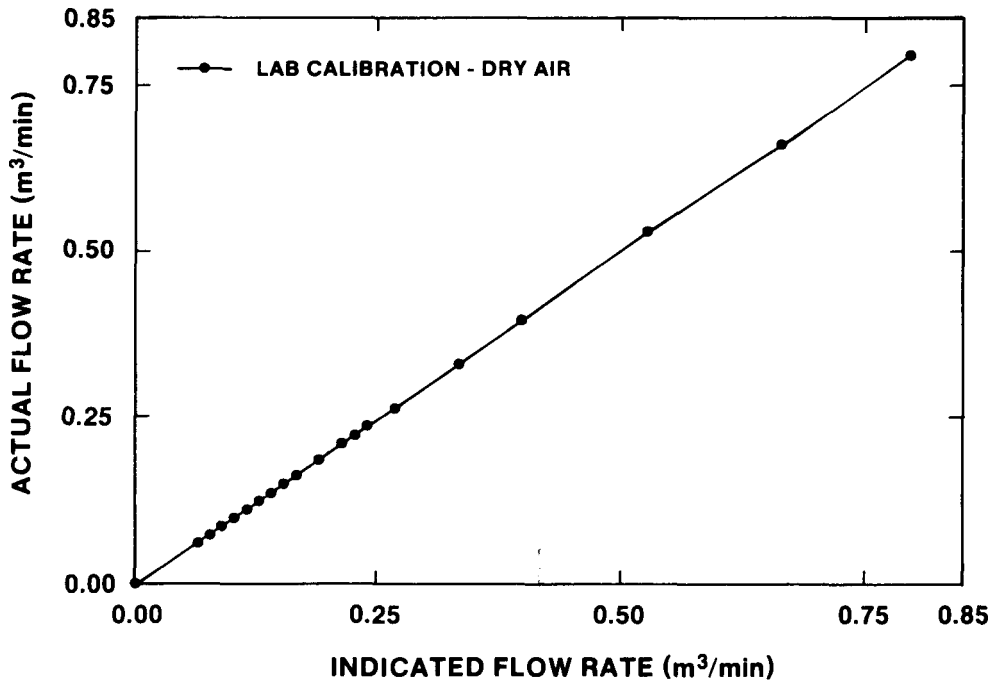

Figure F-11 - Rockwell 750 Gas Clock Calibration

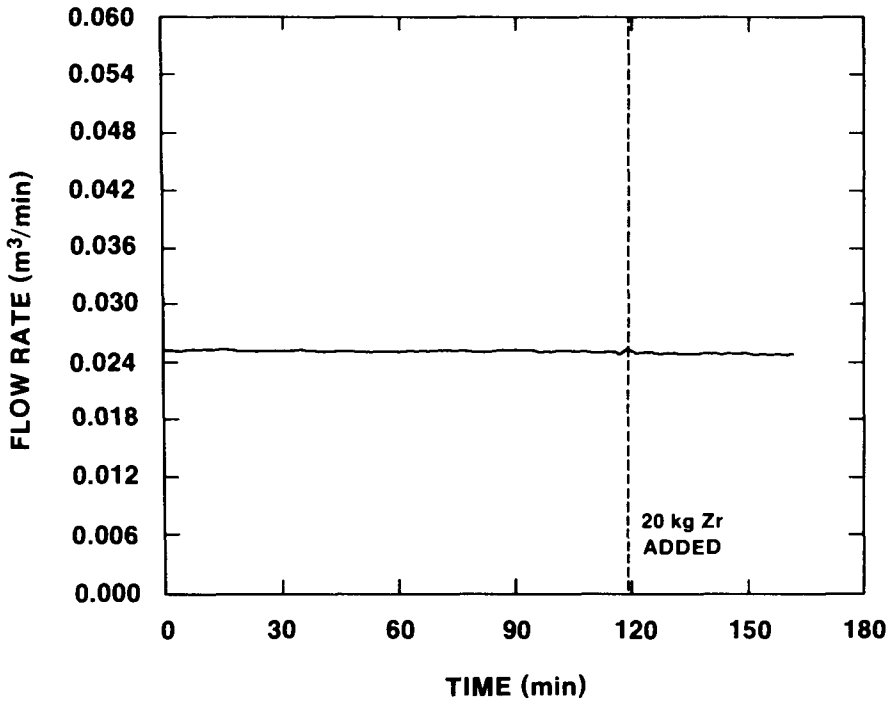

Figure F-12 - Flow Rate of Argon Purge Gas Measured by the Turbine Meter at the Containment Vessel

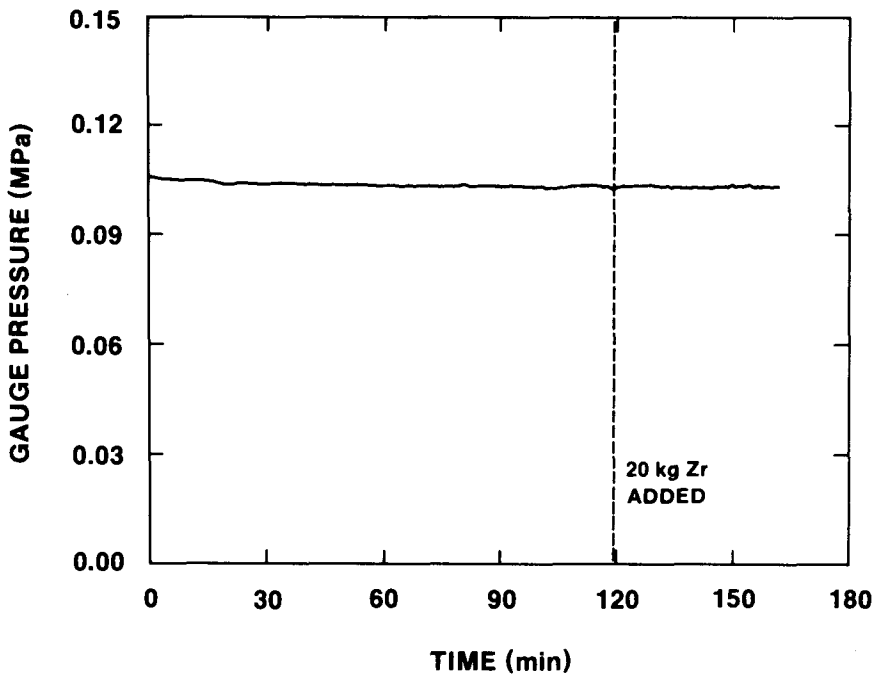

Figure F-13 - Gauge Pressure Upstream from the Critical Orifice Used to Measure the Volume of Argon Gas Used to Purge the Windows of the Opacity Meter

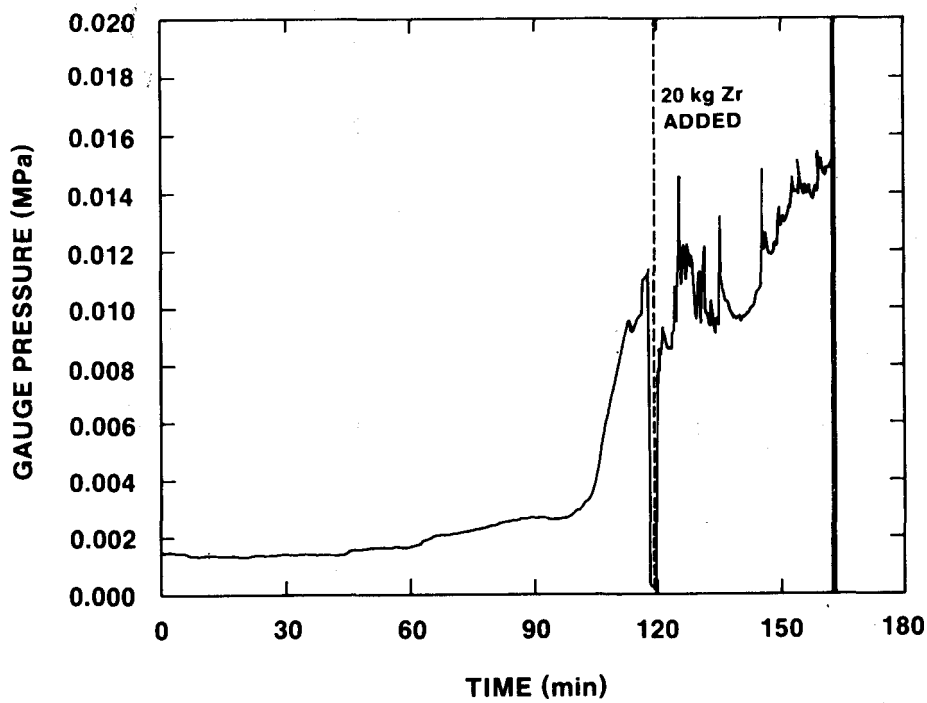

Figure F-14 - Gauge Pressure Measured Inside the Containment Vessel

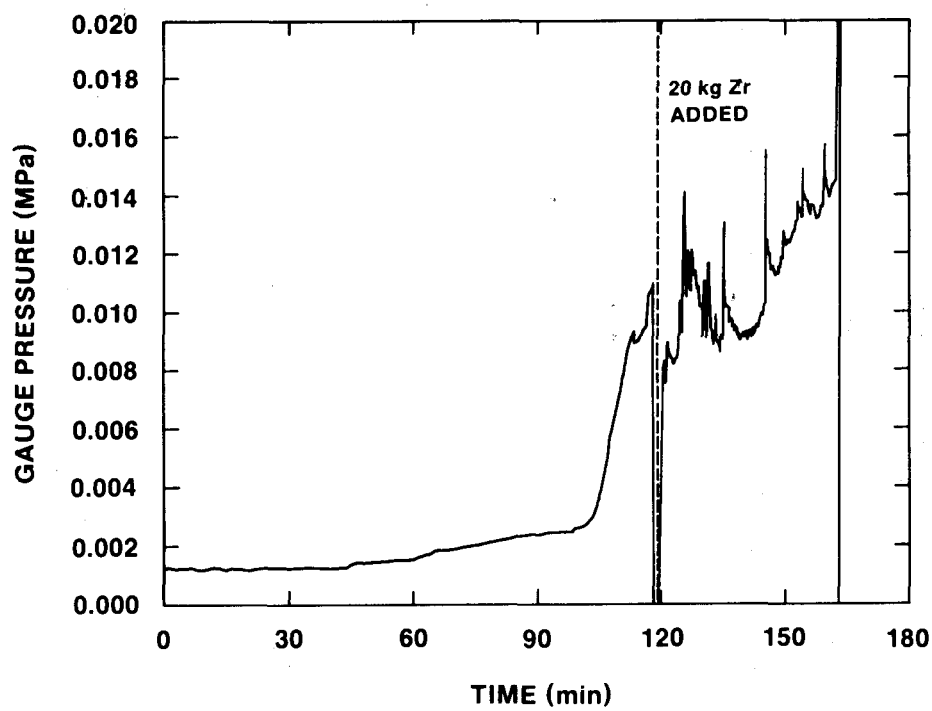

Figure F-15 - Gauge Presure Measured 5 cm Upstream of the ASME Orifice

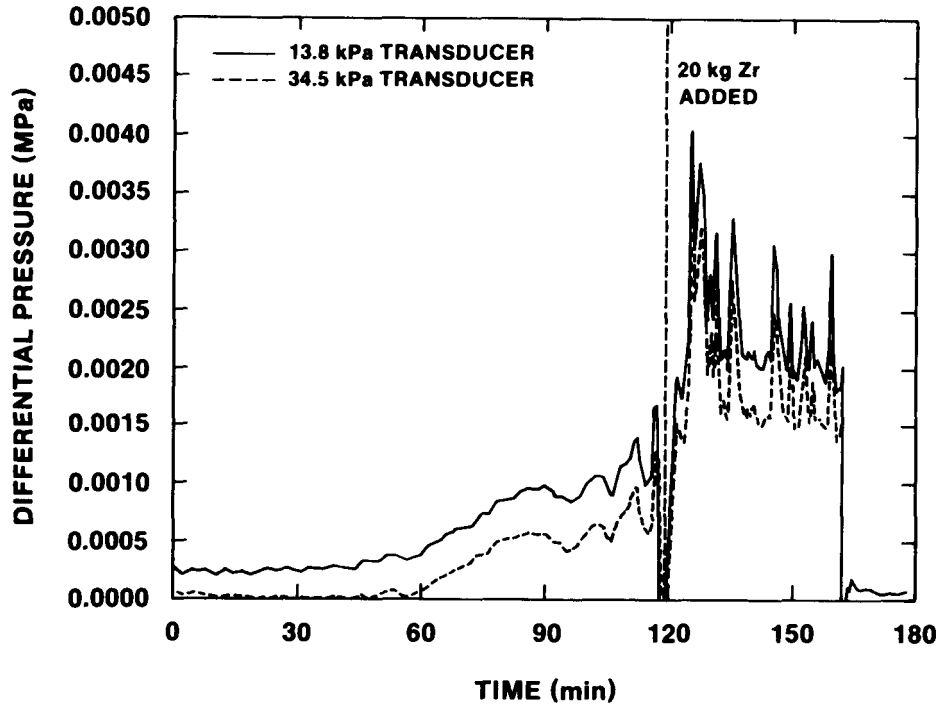

Figure F-16 - Differential Pressure Measured by Two Pressure Transducers Located Across the ASME Orifice

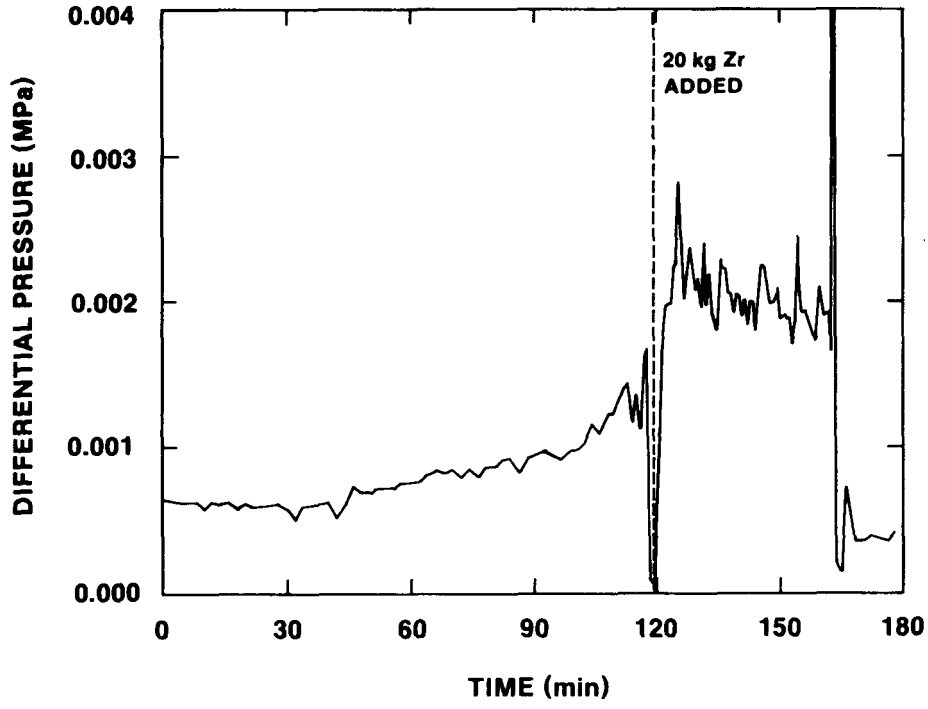

Figure F-17 - Differential Pressure Measured Across the Laminar Flow Element

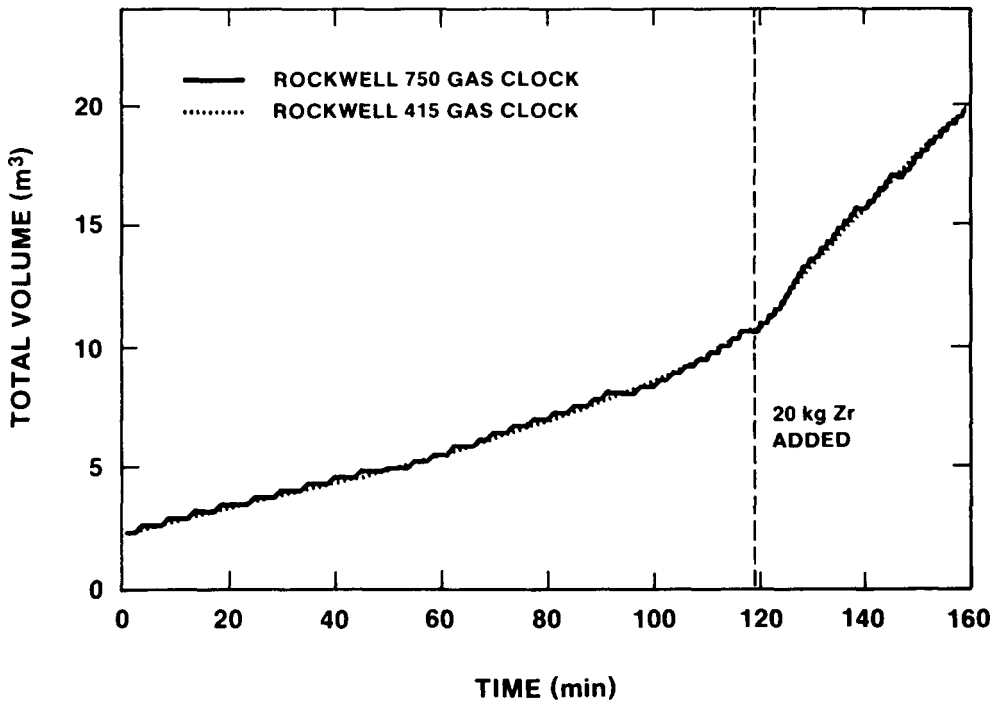

Figure F-18 - Volume of Gas Generated During the Experiment Measured by the Rockwell 415 and 750 Gas Clocks

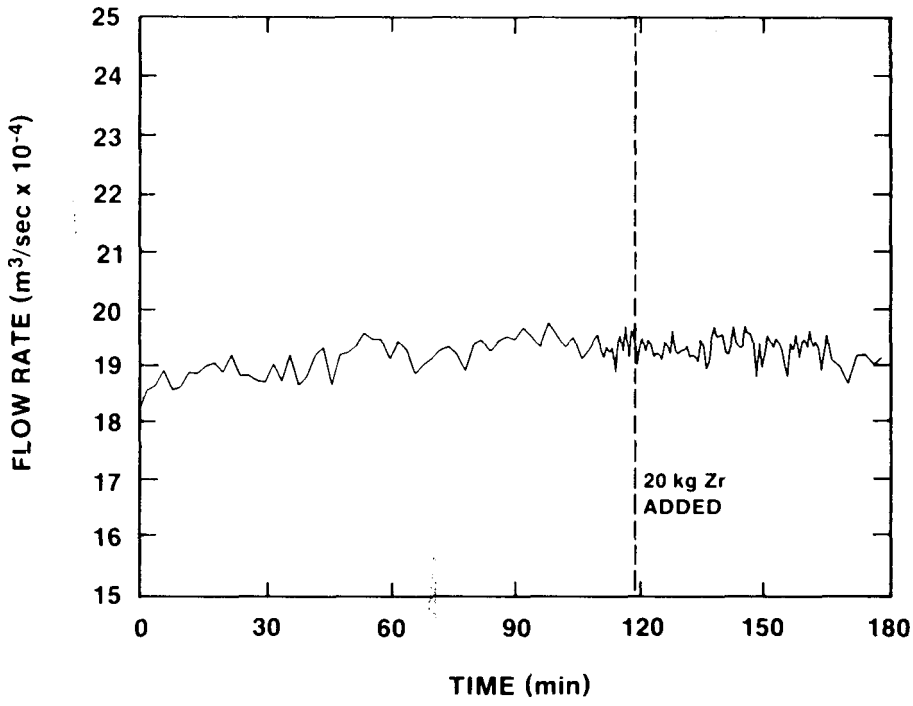

Figure F-19 - Flow Rate of Cooling Fluid Through the Induction Power Supply

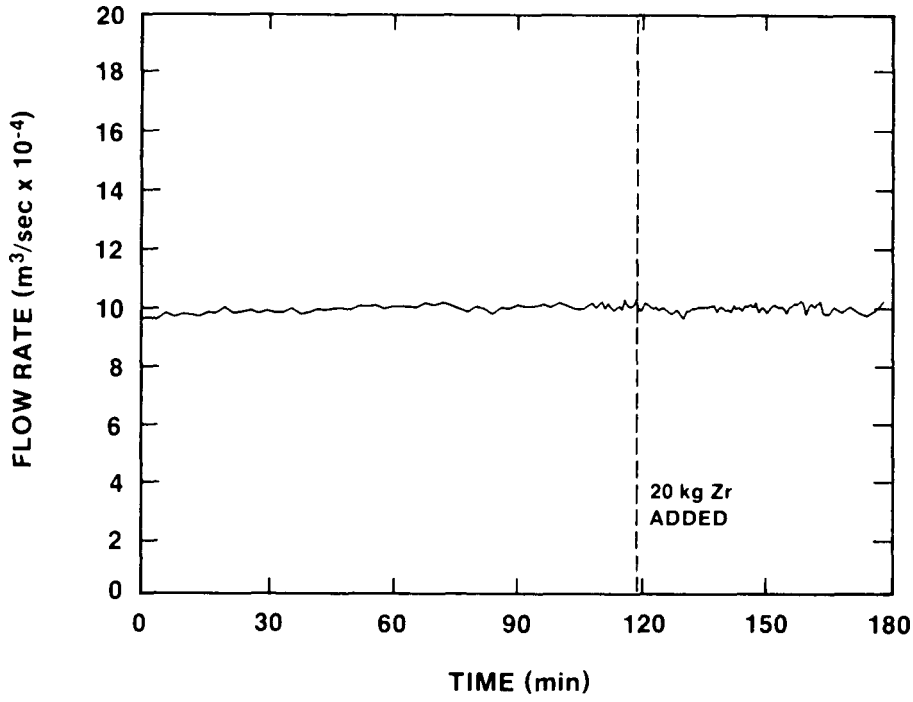

Figure F-20 - Flow Rate of Cooling Fluid Through the Induction Coil

GAS CLOCK DATA

TIME(SEC)	760 CLOCK	415 CLOCK
0.10000E+01	0.2234E+02	0.2150E+02
0.76000E+02	0.2241E+02	0.2208E+02
0.15100E+03	0.2241E+02	0.2264E+02
0.22600E+03	0.2527E+02	0.2350E+02
0.30100E+03	0.2527E+02	0.2406E+02
0.37600E+03	0.2527E+02	0.2491E+02
0.45100E+03	0.2527E+02	0.2548E+02
0.52600E+03	0.2810E+02	0.2630E+02
0.60100E+03	0.2810E+02	0.2685E+02
0.67600E+03	0.2810E+02	0.2741E+02
0.75100E+03	0.2810E+02	0.2832E+02
0.82600E+03	0.3101E+02	0.2889E+02
0.90100E+03	0.3101E+02	0.2974E+02
0.97600E+03	0.3097E+02	0.3031E+02
0.10511E+04	0.3101E+02	0.3088E+02
0.11261E+04	0.3373E+02	0.3173E+02
0.12011E+04	0.3373E+02	0.3229E+02
0.12761E+04	0.3377E+02	0.3285E+02
0.13511E+04	0.3377E+02	0.3372E+02
0.14261E+04	0.3377E+02	0.3430E+02
0.15011E+04	0.3667E+02	0.3487E+02
0.15761E+04	0.3667E+02	0.3572E+02
0.16511E+04	0.3667E+02	0.3629E+02
0.17261E+04	0.3667E+02	0.3691E+02
0.18011E+04	0.3947E+02	0.3776E+02
0.18761E+04	0.3950E+02	0.3832E+02
0.19511E+04	0.3950E+02	0.3888E+02
0.20261E+04	0.3950E+02	0.3946E+02
0.21011E+04	0.4240E+02	0.4014E+02
0.21761E+04	0.4240E+02	0.4071E+02
0.22511E+04	0.4240E+02	0.4127E+02
0.23261E+04	0.4240E+02	0.4212E+02
0.24011E+04	0.4510E+02	0.4273E+02
0.24761E+04	0.4510E+02	0.4330E+02
0.25511E+04	0.4510E+02	0.4414E+02
0.26261E+04	0.4510E+02	0.4472E+02
0.27011E+04	0.4803E+02	0.4522E+02
0.27761E+04	0.4800E+02	0.4606E+02
0.28511E+04	0.4800E+02	0.4690E+02
0.29261E+04	0.4800E+02	0.4747E+02
0.30011E+04	0.4900E+02	0.4840E+02
0.30761E+04	0.4910E+02	0.4924E+02
0.31511E+04	0.4920E+02	0.4980E+02
0.32261E+04	0.4920E+02	0.5066E+02
0.33011E+04	0.5200E+02	0.5152E+02
0.33761E+04	0.5200E+02	0.5208E+02
0.34511E+04	0.5210E+02	0.5292E+02
0.35261E+04	0.5470E+02	0.5377E+02
0.36011E+04	0.5470E+02	0.5461E+02
0.36761E+04	0.5470E+02	0.5544E+02
0.37511E+04	0.5869E+02	0.5636E+02
0.38261E+04	0.5865E+02	0.5719E+02
0.39011E+04	0.5865E+02	0.5804E+02
0.39761E+04	0.5865E+02	0.5890E+02
0.40511E+04	0.6142E+02	0.6003E+02
0.41261E+04	0.6142E+02	0.6088E+02
0.42011E+04	0.6436E+02	0.6174E+02
0.42761E+04	0.6436E+02	0.6288E+02
0.43511E+04	0.6436E+02	0.6374E+02
0.44261E+04	0.6711E+02	0.6459E+02
0.45011E+04	0.6711E+02	0.6549E+02
0.45761E+04	0.6715E+02	0.6662E+02
0.46511E+04	0.7005E+02	0.6748E+02
0.47261E+04	0.7005E+02	0.6844E+02
0.48011E+04	0.7002E+02	0.6929E+02
0.48761E+04	0.7271E+02	0.7014E+02
0.49511E+04	0.7271E+02	0.7131E+02
0.50261E+04	0.7274E+02	0.7215E+02
0.51011E+04	0.7565E+02	0.7329E+02
0.51761E+04	0.7568E+02	0.7408E+02
0.52511E+04	0.7565E+02	0.7520E+02
0.53261E+04	0.7848E+02	0.7642E+02
0.54011E+04	0.7848E+02	0.7761E+02
0.54761E+04	0.8134E+02	0.7838E+02
0.55511E+04	0.8134E+02	0.7952E+02
0.56261E+04	0.8134E+02	0.8066E+02
0.57011E+04	0.8070E+02	0.8152E+02
0.57761E+04	0.8070E+02	0.8262E+02
0.58511E+04	0.8367E+02	0.8346E+02
0.59261E+04	0.8354E+02	0.8465E+02
0.60011E+04	0.8354E+02	0.8578E+02
0.60761E+04	0.8630E+02	0.8691E+02
0.61511E+04	0.8630E+02	0.8804E+02
0.62261E+04	0.8920E+02	0.8946E+02
0.63011E+04	0.8920E+02	0.9062E+02
0.63761E+04	0.9203E+02	0.9204E+02
0.64511E+04	0.9203E+02	0.9318E+02
0.65261E+04	0.9493E+02	0.9492E+02
0.65472E+04	0.9493E+02	0.9520E+02
0.65722E+04	0.9493E+02	0.9579E+02
0.65972E+04	0.9493E+02	0.9616E+02
0.66222E+04	0.9493E+02	0.9674E+02
0.66472E+04	0.9762E+02	0.9730E+02
0.66722E+04	0.9762E+02	0.9787E+02
0.66972E+04	0.9762E+02	0.9843E+02
0.67222E+04	0.9762E+02	0.9904E+02
0.67472E+04	0.9762E+02	0.9961E+02
0.67722E+04	0.1005E+03	0.1002E+03
0.67972E+04	0.1005E+03	0.1007E+03
0.68222E+04	0.1005E+03	0.1013E+03
0.68472E+04	0.1005E+03	0.1018E+03
0.68722E+04	0.1005E+03	0.1024E+03
0.68972E+04	0.1034E+03	0.1029E+03
0.69222E+04	0.1035E+03	0.1032E+03
0.69472E+04	0.1035E+03	0.1038E+03
0.69722E+04	0.1035E+03	0.1047E+03
0.69972E+04	0.1063E+03	0.1053E+03
0.70222E+04	0.1063E+03	0.1061E+03
0.70472E+04	0.1063E+03	0.1067E+03
0.70722E+04	0.1063E+03	0.1070E+03
0.70972E+04	0.1063E+03	0.1070E+03
0.71222E+04	0.1063E+03	0.1070E+03
0.71472E+04	0.1063E+03	0.1070E+03
0.71722E+04	0.1063E+03	0.1070E+03
0.71972E+04	0.1063E+03	0.1076E+03
0.72222E+04	0.1097E+03	0.1078E+03
0.72472E+04	0.1097E+03	0.1084E+03
0.72722E+04	0.1097E+03	0.1092E+03
0.72972E+04	0.1097E+03	0.1101E+03
0.73222E+04	0.1126E+03	0.1109E+03
0.73472E+04	0.1126E+03	0.1118E+03
0.73722E+04	0.1126E+03	0.1127E+03
0.73972E+04	0.1163E+03	0.1135E+03
0.74222E+04	0.1163E+03	0.1146E+03
0.74472E+04	0.1153E+03	0.1155E+03
0.74722E+04	0.1102E+03	0.1166E+03
0.74972E+04	0.1182E+03	0.1180E+03
0.75222E+04	0.1210E+03	0.1195E+03
0.75472E+04	0.1210E+03	0.1209E+03
0.75722E+04	0.1239E+03	0.1221E+03
0.75972E+04	0.1239E+03	0.1232E+03
0.76222E+04	0.1266E+03	0.1245E+03
0.76472E+04	0.1266E+03	0.1256E+03
0.76722E+04	0.1295E+03	0.1267E+03
0.76972E+04	0.1295E+03	0.1279E+03
0.77222E+04	0.1324E+03	0.1290E+03
0.77472E+04	0.1324E+03	0.1299E+03
0.77722E+04	0.1325E+03	0.1307E+03
0.77972E+04	0.1354E+03	0.1318E+03
0.78222E+04	0.1354E+03	0.1327E+03
0.78472E+04	0.1354E+03	0.1339E+03
0.78722E+04	0.1368E+03	0.1350E+03
0.78972E+04	0.1368E+03	0.1361E+03
0.79222E+04	0.1397E+03	0.1370E+03
0.79472E+04	0.1398E+03	0.1378E+03
0.79722E+04	0.1398E+03	0.1387E+03
0.79972E+04	0.1425E+03	0.1395E+03
0.80222E+04	0.1425E+03	0.1403E+03
0.80472E+04	0.1425E+03	0.1413E+03
0.80722E+04	0.1454E+03	0.1424E+03
0.80972E+04	0.1454E+03	0.1435E+03
0.81222E+04	0.1482E+03	0.1446E+03
0.81472E+04	0.1482E+03	0.1458E+03
0.81722E+04	0.1482E+03	0.1469E+03
0.81972E+04	0.1511E+03	0.1478E+03
0.82222E+04	0.1511E+03	0.1489E+03
0.82472E+04	0.1511E+03	0.1498E+03
0.82722E+04	0.1538E+03	0.1507E+03
0.82972E+04	0.1538E+03	0.1518E+03
0.83222E+04	0.1567E+03	0.1527E+03
0.83472E+04	0.1567E+03	0.1533E+03
0.83722E+04	0.1567E+03	0.1545E+03
0.83972E+04	0.1565E+03	0.1553E+03
0.84222E+04	0.1566E+03	0.1562E+03
0.84472E+04	0.1567E+03	0.1573E+03
0.84722E+04	0.1595E+03	0.1582E+03
0.84972E+04	0.1595E+03	0.1590E+03
0.85222E+04	0.1595E+03	0.1601E+03
0.85472E+04	0.1623E+03	0.1610E+03
0.85722E+04	0.1622E+03	0.1619E+03
0.85972E+04	0.1651E+03	0.1630E+03
0.86222E+04	0.1651E+03	0.1639E+03
0.86472E+04	0.1651E+03	0.1650E+03
0.86722E+04	0.1679E+03	0.1650E+03
0.86972E+04	0.1679E+03	0.1670E+03
0.87222E+04	0.1708E+03	0.1681E+03
0.87472E+04	0.1708E+03	0.1693E+03
0.87722E+04	0.1707E+03	0.1704E+03
0.87972E+04	0.1698E+03	0.1712E+03
0.88222E+04	0.1698E+03	0.1724E+03
0.88472E+04	0.1698E+03	0.1732E+03
0.88722E+04	0.1727E+03	0.1741E+03
0.88972E+04	0.1727E+03	0.1752E+03
0.89222E+04	0.1727E+03	0.1761E+03
0.89472E+04	0.1755E+03	0.1772E+03
0.89722E+04	0.1755E+03	0.1784E+03
0.89972E+04	0.1784E+03	0.1793E+03
0.90222E+04	0.1784E+03	0.1801E+03
0.90472E+04	0.1784E+03	0.1811E+03
0.90722E+04	0.1812E+03	0.1819E+03
0.90972E+04	0.1812E+03	0.1828E+03
0.91222E+04	0.1812E+03	0.1838E+03
0.91472E+04	0.1841E+03	0.1845E+03
0.91722E+04	0.1841E+03	0.1854E+03
0.91972E+04	0.1841E+03	0.1862E+03
0.92222E+04	0.1867E+03	0.1870E+03
0.92472E+04	0.1867E+03	0.1878E+03
0.92722E+04	0.1867E+03	0.1890E+03
0.92972E+04	0.1897E+03	0.1899E+03
0.93222E+04	0.1897E+03	0.1908E+03
0.93472E+04	0.1897E+03	0.1913E+03
0.93722E+04	0.1926E+03	0.1922E+03
0.93972E+04	0.1926E+03	0.1930E+03
0.94222E+04	0.1925E+03	0.1939E+03
0.94472E+04	0.1925E+03	0.1944E+03
0.94722E+04	0.1954E+03	0.1953E+03
0.94972E+04	0.1954E+03	0.1958E+03
0.95222E+04	0.1953E+03	0.1967E+03
0.95472E+04	0.1982E+03	0.1978E+03
0.95722E+04	0.1982E+03	0.1987E+03
0.95972E+04	0.1982E+03	0.1995E+03
0.96222E+04	0.2011E+03	0.2001E+03
0.96472E+04	0.2010E+03	0.2010E+03
0.96722E+04	0.2011E+03	0.2018E+03
0.96972E+04	0.2011E+03	0.2027E+03
0.97222E+04	0.2038E+03	0.2035E+03

REFERENCES

Baker, W. C. and Pouchot, J. F. (1983), "The Measurement of Gas Flow," Control Technology News, Vol. 33, No. 1 Jan.1983.

Beck, J. V., Blackwell, B., and St. Clair, Jr., C. R.(1985) Inverse Heat Conduction, Wiley Interscience, New York, NY.

Berglund, and Liu, B. Y. H., (1973), "Generation of Monodisperse Aerosol Standards", Environ. Sci. Technology, 7, 147-153.

Bradley, D. R. and Copus, E. R. (1986), Interaction of Hot Solid Core Debris With Concrete, NUREG/CR-4558, SAND85-1739, Sandia National Laboratories, Albuquerque, NM.

Brockmann, J. E. (1987), "Ex-Vessel Releases: Aerosol Source Terms in Reactor Accidents", Progress in Nuclear Energy, Vol. 19, 117-68.

Brockmann, J. E., Liu, B. Y. H., and McMurry, P. H. (1984), "A Sample Extraction Diluter for Ultra Fine Aerosol Sampling", Aerosol Science and Technology, Vol. 3, Number 4, pp 441 - 451.

Brockmann, J. E., Rader, D. J., and Lucero, D. A. (1987), "Experimental Determination of Dynamic Shape Factors", Paper presented at 1987 Annual Meeting of American Assoc. for Aerosol Research, Sept. 14-17, 1987, Seattle, WA.

Cushing, K. E., Lacey, G. E., McCain, J. D. and Smith, W. B.(1976), Particulate Sizing Techniques for Control Device Evaluation: Cascade Impactor Calibrations, EPA-600/2-76-280, U.S. Environmental Protection Agency.

Davies, C. N. and Subari, M. (1982), "Aspiration Above Wind Velocity of Aerosols with Thin-Walled Nozzles Facing and at Right Angles to the Wind Direction," J. Aerosol Sci. Vol. 13, Number 1, P. 59-71.

Eckert, E. R. G. and Drake, R. M., Analysis of Heat and Mass Transfer (1972), McGraw-Hill, New York, p. 415.

Gronager, J. E., Suo-Antilla, A. J., and Brockmann, J. E. (1986), TURC2 and 3: Large Scale $UO_2/ZrO_2/Zr$ Melt-Concrete Interaction Experiments and Analysis, NUREG/CR-4521, SAND86-0318, Sandia National Laboratories, Albuquerque, NM.

Gutfinger, C. and Tardos, G. I. (1979), Atmospheric Environment, Vol. 13, p. 853 - 876.

Holman, J. P. (1966), Experimental Methods for Engineers, McGraw-Hill, Inc., New York, NY.

Jayasekera, P. N. and Davies, C. N. (1980), "Aspiration Below Wind Velocity of Aerosols with Sharp Edged Nozzles Facing the Wind", J. Aerosol Sci., Vol. 11, pp 535-547.

Lee, K. W. (1981), Journal of Aerosol Science, Vol. 12, p. 79 - 87.

Marple, V. A. and Willeke, K. (1979), "Inertial Impactors in Aerosol Measurement," Lundgren, et al. editors, University Presses of Florida, Gainsville, p. 90-107.

McFarland, A. R., Ortiz, C. A., and Bertch, R. W., Jr. (1978) "A High Capacity preseparator for collecting Large Particles," AIHA Paper No. 80, Texas A&M University, Civil Engineering Department, Air Quality Lab Publication 3718/04/78/ARM.

Powers, D. A., Brockmann, J. E., and Shiver, A. W. (1986) VANESA: A Mechanistic Model of Radionuclide Release and Aerosol Generation During Core Debris Interactions with Concrete, NUREG/CR-4308, SAND85-1370, Sandia National Laboratories, Albuquerque, NM.

Tardos, G. I., Yu, E., Pfeffer, R. E., and Squires, A. M. (1979), A Journal of Colloid and Interface Science, Vol. 71, No. 3, p. 616 - 621.